Laser treated surfaces in particle accelerators : relation between superficial topography, particle adhesion and compatibility for ultra-high vacuum applications

Lucie Baudin

PSL
UNIVERSITÉ PARIS

THÈSE DE DOCTORAT
DE L'UNIVERSITÉ PSL

Préparée à MINES ParisTech

Laser treated surfaces in particle accelerators: relation between superficial topography, particle adhesion and compatibility for ultra-high vacuum applications

Structuration de surface par laser dans l'environnement des accélérateurs de particules: relation entre topographie superficielle, adhésion des particules et compatibilité aux applications ultravide

Soutenue par

Lucie BAUDIN

Le 10 Décembre 2020

Ecole doctorale n° 621

ISMME : Ingénierie des Systèmes, Matériaux, Mécanique, Énergétique

Spécialité

Sciences et génie des matériaux

Composition du jury :

Isabel MONTERO HERRERO Directeur de recherche, CSIC Madrid	*Présidente*
Michel, BOUSTIE Directeur de recherche, CNRS	*Rapporteur*
André ANDERS Professeur, Leipzig University	*Rapporteur*
Stéphane VALETTE Professeur, Ecole Centrale Lyon	*Examinateur*
Francesco, DELLORO Chargé de recherche, MINES ParisTech	*Examinateur*
Cédric, GARION Dr, CERN	*Examinateur*
Alain, THOREL Directeur de recherche, MINES ParisTech	*Directeur de thèse*

MINES ParisTech | PSL

Au Magnifique, dompteur des cimes,

Je laisse Sisyphe au bas de la montagne! On retrouve toujours son fardeau.
Mais Sisyphe enseigne la fidélité supérieure qui nie les dieux et soulève les rochers. Lui aussi juge que tout est bien. Cet univers désormais sans maître ne lui paraît ni stérile ni futile. Chacun des grains de cette pierre, chaque éclat minéral de cette montagne pleine de nuit, à lui seul, forme un monde.
La lutte elle-même vers les sommets suffit à remplir un cœur d'homme.
Il faut imaginer Sisyphe heureux.

Albert Camus

Abstract

Keywords:
secondary electron yield, laser surface structuration, morphology characterisation, particle adhesion, LASAT, particle accelerator.

In the Large Hadron Collider (LHC), at CERN, two proton beams are accelerated and brought into head-on collisions in different parts of the ring, where gigantic detectors collect the newly formed particles. To avoid collisions with the gas molecules present in the accelerator, particle beams circulate in an ultra-high vacuum chamber, partly cooled to 1.9 K. Electron multipacting leading to electron cloud formation in the vacuum system has been identified as a major limiting factors for the beam quality and a critical source of heat-load on the cryogenic system in the LHC. Laser-assisted surface structuration is a promising electron-cloud mitigation technique, as it could be directly applied *in-situ*, in already installed chambers.

Pico-second pulsed laser irradiation of copper in a parallel pattern creates grooves by material ablation. A part of the ablated material is redeposited as particle aggregates. This two-scale roughness decreases the Secondary Electron Yield (SEY) of surfaces, governing the multiplication of the electrons in the beam chamber, by geometrical effects. Nevertheless, the rugosity increase has a detrimental effect on other surface functionalities, in particular on the electrical impedance. During the operation of the LHC, the surface is submitted to electro-mechanical forces (around 30 $N.mm^{-3}$) and cooling cycles from room temperature to 4 K, which may affect the integrity of the structuration and alter the efficiency of the treatment. The objective of this work is thus to select a set of laser treatment parameters providing the best compromise between an efficient electron cloud mitigation and a limited detrimental impact on other surface properties.

For this purpose, a assessment methodology has been specifically developed. The multi-scale surface morphology transformations occurring during the pulsed laser treatment have been described based on a literature review of laser-matter interaction and on microscopic observations carried out on laser treated samples and could be related to the treatment parameters. Transmission Electron Microscopy microstructural analyses highlighted the presence of a 30-nm-thick oxide layer formed at the surface of the laser-processed material, despite the nitrogen protective atmosphere used during the treatment. The mass of ablated material, estimated from microscopic cross section analysis, showed a linear increase with irradiating energy density. A fraction of this matter,is re-condensed on the grooved surface creating the particle overlay. The rest is unattached

dust. Electron tomography was applied for qualitative characterisation of particles at the nano-scale, in particular concerning their size distribution.

Mechanical characterisations focused on applying non-contact forces on particles to assess their adhesion. Two extraction techniques, relying on inertia forces, were developed, aiming to explore on a large range of amplitude and duration. In centrifuges, the acceleration on the sample surface reached 275 000 g, leading to a reproducible static force field up to 24 $N.mm^{-3}$ pulling the particles out of the surface.

The LAser Shock Adhesion Test (LASAT), initially developed to assess the adhesion of coatings by spallation, was utilized to accelerate the surface of treated samples. Pressure shock waves generated by nanosecond laser irradiation produce sharp velocity variations of the surface. Deceleration and, therefore, applied inertia force were evaluated from the dynamics of the sample macroscopic surface.

The diverted use of LASAT required a calibration study based on velocity measurement by VISAR (Velocity Interferometer System for Any Reflector) to determine the surface dynamics as a function of LASAT experimental configurations. The influence of cryogenic temperatures was evaluated using both samples which underwent thermal cooling/warming cycles and sample cooled to 70 K during the laser shocks. Recuperation and analysis of detached particles allowed the quantification of ejected material as a function of mechanical stresses. The mass of particles which could be detached during the accelerator operation has been extrapolated from these results.

It is shown that the SEY would not be detrimentally increased by particles detachment due electromagnetic forces. Nevertheless, the detached material and even more, the large dust quantity produced during the treatment raise issues that should motivate the choice of alternative treatment parameters or an implementable cleaning strategy.

The main achievement of the thesis is the development of quantitative characterization methodologies of the dust created during laser-assisted surface structuration, the amount of matter present as sub-micrometre particle network overlay after the treatment and the amount which could be detached due to mechanical stresses during accelerator operation.

Résumé en français

Mots clés:
taux d'émission d'électrons secondaires, structuration de surfaces par laser, caractérisation morphologique, adhésion de particules, LASAT, accélérateurs de particules.

Dans le *Large Hadron Collider* (LHC), le faisceau de particules, accélérées à haute énergie, circule dans un tube inséré dans un système magnétique supraconducteur, refroidi à 1.9 K. Afin d'éviter les collisions avec des molécules de gaz, le faisceau circule sous ultra-vide. Un des facteurs limitant l'intensité des faisceaux est la production en cascade d'électrons, dans le système à vide du faisceau, qui accroit la désorption gazeuse des surfaces et augmente, préjudiciablement, la charge thermique sur le système cryogénique.

La structuration de surface par laser offre une voie prometteuse pour réduire le taux d'électrons secondaires (ou, SEY) de la paroi du tube et atténuer les effets du nuage d'électrons, en traitent *in-situ* les écrans de faisceau des aimants déjà installés dans le LHC

Le balayage de la surface par le faisceau laser pulsé creuse des sillons en ablatant le cuivre, dont une partie est redéposée sur la surface en une distribution de particules majoritairement sphériques, de l'ordre de quelques micromètres de diamètre. Cette rugosité à deux échelles permet l'absorption efficace des électrons.

Néanmoins, l'augmentation de la rugosité de la surface détériore d'autres fonctionnalités de la surface, en particulier l'impédance de la surface Le choix de la topographie optimale permettant de réduire la SEY de la paroi, tout en limitant les impacts négatifs sur le reste du système, est donc un équilibre qui repose sur la connaissance détaillée de la modification de la morphologie et de la physico-chimie de surface en fonction des paramètres utilisés pour l'irradiation laser. Pour cette raison, une analyse quantitative et qualitative des caractéristiques à l'échelle des sillons et des particules a été menée.

L'étude microstructurale par Microscopie Electronique en Transmission (MET) a mis en évidence les changements de microstructure et les transformation morphologiques et chimiques lors du traitement. En particulier, une fine couche d'oxyde (30 nm) a été observée malgré l'atmosphère d'azote protectrice utilisée pendant le traitement.

La masse de matériau évaporé durant le traitement a été évaluée à partir de l'observation des profils de la surface en vue de coupe. Elle augmente proportionnellement à la densité d'énergie déposée par l'irradiation laser. Une partie de cette matière, estimée à 17 % pour une irradiation à 532 nm et 10 ps, est re-condensée sur la surface sous forme de

particules. Le reste est perdu sous forme de poussière pendant le traitement laser. Ceci représente 11.8 mg de cuivre per centimètre carré de surface traitée.

La distribution en taille des particules présentes sur la surface traitée par laser a été évaluée par nano-tomographie effectuée par MEB-FIB.

Lors du fonctionnement du LHC, la paroi du système à vide est soumise à des forces électromagnétiques de l'ordre de 30 $N.mm^{-3}$ et à des variations entre température ambiante et 4 K. Afin de qualifier l'adhérence des particules dans des conditions similaires, mais en laboratoire, deux méthodes d'extraction de particules ont été mise en place, reposant sur l'application d'accélérations générant des forces d'inertie dont les durées d'application et les amplitudes ont été sélectionnées.

Les accélérations atteintes (jusqu'à 275 000 g) à la surface des échantillons placés dans des centrifugeuses ont permis d'atteindre des forces statiques volumiques de l'ordre de 24 $N.mm^{-3}$. Le LAser Shock Adhesion Test (LASAT), habituellement dédié aux essais d'adhérence de revêtements par délamination, a aussi été appliqué pour l'extraction de particules présentes à la surface. Cette application détournée a nécessité une vaste campagne de calibration à partir de mesures de vitesse réalisées grâce au dispositif d'interférométrie VISAR. Les caractéristiques des accélérations appliquées sur les particules ont ainsi été déterminées en fonction des configurations expérimentales du LASAT et de la température de l'échantillon qui a été portée à 70 K.

Pour les deux méthodes, la collecte et l'analyse des particules détachées ont permis la quantification de la masse et de la morphologie du matériau éjecté en fonction des sollicitations mécaniques et de la température de la surface. 4 % des particules présentes originellement à la surface – soit 0.1 $mg.cm^{-2}$ sont décollées par les sollicitations mécaniques considérées dans ce travail.

Il a été montré que le SEY de la surface ne serait pas affecté par le détachement de particules à la suite aux sollicitations mécaniques des forces électromagnétiques dans l'accélérateur. Néanmoins, la quantité de cuivre ainsi décollée, et plus encore, l'importante production de poussière suite au traitement robotisé, in-situ, en milieu confiné, sont des questions qui demeurent ouvertes et devraient motiver le choix de paramètres de traitement alternatifs, ou bien d'une stratégie de nettoyage.

Acknowledgements

This thesis is made of many inputs from people who contributed directly or indirectly. We shared a piece of this work, a slice of life. I take the opportunity to acknowledge you.

First of all, I would like to thank my CERN supervisors, Cedric GARION and Paolo CHIGGIATO. You opened me the doors of vacuum group and gave me confidence and motivation. I am grateful for your support and you trust: I tried (and will keep on trying) my best to be worthy of that. Thank you!

Then, I wish to thank Michel JEANDIN, Alain THOREL and Francesco DELLORO for accepting me as their PhD student at Mines ParisTech and for their help during this work. I could benefit from resources and help of skilled and dedicated people at *Centre des Matériaux*.

I would like to thank Michel BOUSTIE and Andre ANDERS for agreeing to be rapporteurs for this thesis. I also thank Stephane VALETTE and Isabel MONTERO HERRERO for their participation in the jury.

Thank you for the time, interest and attention given to my work.

I would like to highlight the scientific and technical contributions of my colleagues from CERN and external partners those works were used in this thesis.

At CERN, many colleagues were involved the laser treatment project:
Moniko SIKTO and Marcel HIMMERLICH as project leaders at CERN;
Pedro COSTA PINTO, Sergio CALATRONI, Mauro TABORELLI and all the contributors to *aC-LESS* meetings.

Samples preparation, SEY analysis, SEM observations and cross sectional specimen preparations are the common work of a large amount of people among several groups and sections at CERN. The results gathered in this thesis are presented on the behalf of all of them. In particular:
Anité PEREZ FONTENA, Elisa GARCIA TABARES, Karolina BOGDANOWICZ, Sindre FORSETLOKKEN, Aidan GRAHAM and Stephan PFEIFFER for microscopic ob-

servations;
Danilo ZANIN, Martino RIMOLDI and Delphine LETANT-DELRIEUX for SEY and XPS measurements;
Colette CHARVIN and Benoit TESSANDIER for support at chemistry laboratory;
Hendrick KOS for mechanical support for experiment and sample preparation;
Laetitia DUFAY-CHANAT and Torsten KOETTIG for support at Cryolab;
Alexander LUND for FIB tomography image acquisition.

External partners have been involved for the laser treatment of the samples:
Stefan WACKEROW, David BAJEK and Amin ABDOLVAND for preparing the samples at Dundee University.

External partners have been involved to TEM analysis:
Fabrice GARSLAIN, CDM Mines ParisTech, for the FIB preparation of the TEM specimens at CentraleSupélec;
Mohamed SENNOUR, CDM Mines ParisTech, for the TEM observation and analysis.

External partners have been involved to performed the mechanical characterisation tests:
Antoine DEBRAY, Gerard BRABANT and Alexandre COTTIN, CDM Mines ParisTech, provided a very valuable help of LASAT;
Hugo DURAND, CDM Mines ParisTech, installed and operated the high speed camera recording the detached particle cloud expansion during LASAT;
Michel BOUSTIE, Universté de Poitiers, for the access to the laser shock setup at Poitiers University, and the conception a batch of years ago of the cryogenic sample holder;
Praxedis RODRGUEZ-MARTIN and Miguel DANTA, Université de Genève, and Florence POFER, EPFL, for the access to the centrifugation facilities;
Maud FUMEAUX and Alejandro PUIG I BARANAC, Novelis Sierre, for the access to the drop test facilities.

This work uses the results of several simulation tools applied to the problematic of copper particles attached on the LHC beam screen surface:
Anton LECHNER, CERN, for particle-beam interaction simulations;
Phillipe BELANGER, TRIUMF Vancouver, for particle-beam interaction, and particle dynamics simulations;
Suzanna IZQUIERDO BERMUDEZ and Michal MACIEJEWSKI, CERN, for input information on magnets;
Marco MORRONE, CERN, for thermo-magneto-mechanical simulations;
Francois CADIOU, INSA Lyon, and Francois WILLOT, CMM Mines ParisTech, for FIB Tomography image post treatment;

Beside the scientific work, my colleagues and the many opportunities I had to meet and share time and experiences with passionate and energising people made this time at CERN a unique experience. I am grateful for that.

Last but not least, a thanks goes to my friends, the μ-adventurers and my family: people with who I share my life. They provide me energy and positive spirit for adventures and experiences. That is the first step towards the tiny, but essential, discoveries which make life so exciting. Time we spent, memories we made and bonds we build are the priceless gifts and inexhaustible resource for upcoming explorations.

Thanks you all.

List of acronyms

CERN: European Organization for Nuclear Research

UHV: Ultra-High Vacuum

LHC: Large Hadron Collider

SPS: Super Proton Synchrotron

HL-LHC: High-Luminosity Large Hadron Collider

IP: Interaction Point

BS: Beam Screen

OFE: Oxygen-Free Electronic grade

LSS: Long Straight Section

COLDEX: Cryogenic temperature in the COLD bore EXperiment

SEY: Secondary Electron Yield

SEM: Scanning Electron Microscope

TEM: Transmission Electron Microscope

SAED: Selected Area Electron Diffraction

EDX: Energy-Dispersive X-ray spectroscopy

EELS: Electron Energy Loss Spectroscopy

EFTEM: Energy-filtered Transmission Electron Microscopy (EFTEM)

FFT: Fast Fourier Transform

FIB: Focused Ion Beam

LASAT: LAser Shock Adhesion Test

VISAR: Velocity Interferometer System for Any Reflector

Table of contents

Introduction

Electron multipacting, leading to electron cloud build-up, is a source of beam instabilities and heat load on cryogenic systems. As a consequence, it has been identified as a major limiting factor to the performance of high-intensity positive particles accelerators. Laser surface structuration is a promising *in-situ* treatment method to address this issue if applied to copper surfaces of vacuum chambers. Pulsed laser irradiation, leading to local material ablation, can be used to pattern copper surfaces in parallel lines. Moreover, ablated material can undergo redeposition on the grooved surface. Copper particles, those size is in the range of a few hundreds of manometers to several micrometers, can be found on laser treated surfaces. This two-scale (grooves and particles) surface structuration decreases the Secondary Electron Yield (SEY) of surfaces by geometrical effects.

Although tests undertaken at CERN have shown that this surface morphology modification was effective in reducing electron clouds, consequences of surface laser treatment in terms of particle detachment and dust generation have not been addressed yet.

Chapter 1 presents the accelerator complex at CERN, the vacuum system of the LHC and an overview of the main challenges raised by the high luminosity upgrade program, in particular concerning electron clouds. The principle of laser-assisted surface structuration is described, as well as the main parameters of the technique. An historical overview of investigations on the effect of treatment parameters on relevant aspects of surface treatment applications in ultra-high vacuum and particle accelerator is presented, such as SEY and electron cloud measurements, surface oxidation, vacuum compatibility at cryogenic temperatures and electrical impedance evolution. Previous works have already revealed constraints and potential limiting factors of the deployment of this technology, which requires a careful choice of treatment parameters relying on the knowledge and characterisation of the surface morphology.

Chapter 2 provides a characterisation of thermal and mechanical properties of materials used in this study, as well as a description of surface laser treatment methods. In particular, parameters used for the treatment of the samples analysed in this thesis are given. Finally, methods deployed for surface analysis are presented, such as microscopy for the groove-scale analysis and the extraction method based on ultrasonic cleaning, used for particle overlay quantification.

In chapter 3, multi-scale surface morphology transformations occurring during pulsed laser treatment are first described in a literature review. These transformations are then

illustrated by microscopic observations performed by TEM, FIB Tomography and SEM on treated samples with dedicated laser parameters.

The work presented in chapter 4 aims at characterizing the amount of detached particles as a function of the mechanical stress applied on the surface. Adhesion of particles created by laser treatment was assessed by applying non-contact, reproducible forces using centrifugation and laser shock techniques. Amplitudes and durations of applied forces varied on a large range, depending on the extraction technique used. Influence of cryogenic temperatures was evaluated using samples which underwent thermal cooling/warming cycles and also by cooling down samples during the tests.

Chapter 5 explores some aspects of the implementation of surface *in-situ* laser treatment in a particle accelerator environment. In particular, the focus is on particle detachment when the beam screen surface is subjected to mechanical stresses during accelerator operations. Forces induced by a rapid decrease of the surrounding magnetic field, the interaction of detached particles with the proton beam and consequences on SEY of variations in the density of particles covering the surface are discussed.

An extended abstract in French can be found in the introduction of each chapter.

Introduction en français

Le détachement d'électron en cascade et le nuage d'électrons ont été identifiés comme étant les principaux facteurs limitants pour la qualité du faisceau ou pour le système cryogénique des accélérateurs de particules positives de haute intensité. Le traitement de surface au laser est une méthode prometteuse pour traiter *in-situ* les surfaces en cuivre des chambres à vide. L'irradiation laser pulsée du cuivre dans un motif de lignes parallèles conduit à l'ablation locale créant une surface rainurée. Une partie de la matière ablatée et redéposée sous la forme d'un réseau complexe de particules dont la taille varie entre quelques centaines de nanomètres et plusieur micromètres. La structuration de surface à deux échelles, celle des rainures et celle des particules, diminue le rendement en électrons secondaires (SEY) des surfaces par un effet géométrique.

Si les essais réalisés au CERN ont montré que la modification de la morphologie de la surface diminue l'intensité du nuage d'électrons, les conséquences du traitement laser sur la résistance mécanique et la génération de poussières n'ont pas encore été abordées.

Le Chapitre 1 présente le complexe d'accélérateurs du CERN, le système de vide de LHC, les défis liés au programme de mise à niveau de haute luminosité, en particulier ceux liés au nuage d'électrons. Le principe de la structuration de surface assistée par laser utilisée dans le but de la réduction du SEY dans les accélérateurs de particules est décrite, ainsi que les principaux paramètres du traitement. Un historique est présenté sur les recherches effectuées sur les effets des paramètres de traitement sur les aspects pertinents de l'application de surface en UHV et accélérateur de particules tels que le SEY et la mesure des nuages d'électrons, l'oxydation de surface et la compatibilité du vide à des températures cryogéniques et, enfin, la modification de l'impédance électrique. Des travaux antérieurs ont déjà révélé des contraintes et des facteurs potentiellement limitants du déploiement de la technologie, qui nécessitent un choix judicieux des paramètres de traitement basé sur une connaissance et caractérisation appronfondies de la morphologie de surface.

Le chapitre 2 s'articule en trois parties : la caractérisation du matériau utilisé dans l'étude, la description du traitement laser de la surface des échantillons et, enfin, les méthodes déployées pour leur analyse.

Le chapitre 3 traite des transformations morphologiques et chimiques aboutissant à la modification multi-échelle de la surface traitée par laser pulsé.

Dans le chapitre 4, les stratégies déployées pour les essais d'adhérence des particules sont exposées. Il s'agit de faire varier la densité de particules couvrant la surface

sans altérer la composition chimique de celle-ci. L'application de force sans contact a été privilégiée. Les effets de la température sur l'adhérence des particules ont été appréhendés, à la fois en utilisant des échantillons ayant subi des cycles thermiques, ou bien en refroidissant les échantillons pendant les essais de détachement de particules.

Le chapitre 5 explore certains aspects de l'implémentation du traitement laser *in-situ* des surfaces pour l'accelerateur de particules : le détachement des particules lorsque la surface est soumise aux sollicitations mecaniques lors de l'operation, en particulier, les forces induites par la décroissance rapide du champ magnétique environnant, l'interaction entre le faisceau de protons et les particules détachées pendant l'opération de l'accélérateur et, enfin, les consequences sur le SEY des variations de la densité de particules couvrant la surface.

Un résumé détaillé en français est present en introduction de chaque chapitre.

Chapter 1

Context of the study

Abstract

The CERN accelerator complex consists of a succession of accelerators of increasing energy. In the last element of the chain, the Large Hadron Collider (LHC), two counter rotating beams of particles (usually protons) circulate in opposite directions, are accelerated to the record energy of 7 TeV per beam and collide in the particle detectors. Particle beams are confined in a very low pressure environment to avoid collisions with gas molecules which would result in beam losses. In the present LHC configuration Ultra High Vaccum (UHV) is required which corresponds to pressure below 10^{-8} Pa.

The beam vacuum system comprises the cold bore of the superconducting magnets, which allows cryosorption. A beam screen made of co-laminated stainless steel and Oxygen-Free Electronic (OFE) copper is inserted in the cold bore. The perforated beam screen is actively cooled to 5 to 20 K and ensures the transmission of the gas molecules toward the cold bore. Furthermore it shields the components operating at cryogenic temperatures, *i.e.* 1.9 K, from beam induced effects such as synchrotron light, energy loss by nuclear scattering, image currents or electron clouds.

Although the pressure in the beam vacuum chamber is very low, residual gas molecules and free electrons remain. Charged particles are accelerated by electric fields generated by the circulating proton beam. Accelerated electrons hitting the walls with enough energy trigger the emission of secondary electrons. This mechanism can be quantified by the Secondary Electron Yield (SEY). When the SEY is higher than a threshold value, electron production takes place in cascade, namely *electron multipacting*, resulting in a so-called *electron cloud*. Electron clouds can be dense enough to cause beam instabilities, an increase in beam emittance or in electron stimulated desorption of gases, thus rising pressure in the vacuum chamber. In addition, electron impacts against the walls of the beam screen increase the heat load for the LHC cryogenic system. Electron multipacting becomes more important when the bunches of protons forming the beams are dense and close to each other. In the framework of programs devoted to increase accelerator luminosity (such as the High-Luminosity LHC project at CERN), electron clouds, which are the main source of thermal loads in beam vacuum system, are becoming a major

limiting factor. Laser surface structuring is proposed to mitigate electron cloud formation through the increase of surface multiscale roughness. The process creates various structures at the micron and sub-micron scales that can trap impinging electrons.

Preliminary tests undertaken at CERN have confirmed the ability of laser treatment to decrease SEY, electron cloud formation and the subsequent head load on the cryogenic system. Nevertheless, it has also been shown that the increased surface roughness leads to a higher surface impedance and to Joule power losses, resulting in higher heat loads for the cryogenic system. The optimal surface morphology is a compromise between the gain resulting from SEY reduction and the drawbacks on the entire system. The choice of the optimal surface structure is based on the analysis of the topography characteristics.

Résumé en français

Le complexe d'accélérateurs du CERN est formé d'une succession d'accélérateurs d'énergies croissantes. Dans le grand collisionneur de hadrons, *Large Hadron Collider*, le LHC – l'ultime élément de la chaîne – chaque faisceau de particules est accéléré jusqu'à une énergie de 7 TeV. Deux faisceaux de particules (le plus souvent des protons) circulent en sens inverse et sont accélérés par le champ électrique à très haute fréquence des cavités accélératrices. Ils tournent dans deux tubes parallèles, insérés dans un même système magnétique supraconducteur. Afin d'éviter des collisions avec les molécules de gaz présentes dans l'accélérateur, les faisceaux de particules circulent dans un vide poussé. La pression dans les tubes circulaires de 27 kilomètres de circonférence où progressent les particules est de 10^{-8} Pa. Un écran de faisceau est introduit à l'intérieur du tube -appelé tube froid- servant d'interface entre l'enceinte à vide et le fluide cryogénique de l'helium superfluide à 1.9 K. Il est chargé d'intercepter le rayonnement synchrotron afin de protéger le système cryogénique et de masquer le gaz cryo-pompé par la masse froide refroidie à 1.9 K des photons induits par faisceau.

Si le vide dans l'enceinte est très poussé, des molécules résiduelles de gaz demeurent piégées sur les parois des écrans de faisceaux. Lorsque les particules circulent, les parois libèrent des électrons qui sont accélérés par le champ électrique généré par le faisceau. Ces électrons accélérés frappent à leur tour les parois avec suffisamment d'énergie pour y arracher les molécules piégées, dégradant ainsi la qualité du vide. Ils déclenchent en même temps l'émission d'électrons secondaires. Se forment alors des nuages d'électrons qui peuvent être suffisamment denses pour déstabiliser le faisceau de protons et en augmenter l'émittance, Les impacts des électrons contre les parois de l'écran de faisceau accroissent la désorption gazeuse de ces surfaces et augmentent la charge thermique pour le système cryogénique du LHC. La production d'électrons en cascade et le nuage d'électrons résultant est d'autant plus important que les paquets de protons qui forment les faisceaux sont nombreux et rapprochés. Si bien que ce phénomèn,e observé pour la première fois en 1976, est désormais identifié comme étant l'un des facteurs limitants majeurs de la qualité du faisceau dans les accélérateurs de particules positives à haute intensité dans le cadre des programmes d'augmentation de la luminosité de ces

accélérateurs.

Des techniques opérationnelles de conditionnement -ou de nettoyage par le faisceau- sont déjà utilisées : elles consistent à faire circuler suffisamment de protons pour libérer les molécules de gaz piégées sur le métal et réduire le taux d'électrons secondaires, textitSecondary Electron Yield, le SEY de la paroi du tube. Des solutions conceptuelles de traitement de surface telles que le revêtement de carbone amorphe ou la structuration mécanique de la surface sont néanmoins étudiées afin de réduire le SEY initial de l'enceinte à vide.

La structuration de surface par laser offre une voie prometteuse pour l'atténuation du nuage d'électrons, en particulier, parce ce qu'elle pourrait permettre le traitement robotisé, in situ, à pression atmosphérique des écrans de faisceau. La conception d'un robot capable de traiter via fibre optique l'intérieur des tubes à vide a été amorcée. La surface créée par traitement laser est une structure de base sinusoïdale régulière sur laquelle est présente une distribution de particules majoritairement sphériques de l'ordre de quelques micromètres de diamètre entre lesquelles un grand nombre de vides micro-nanométriques sont observés.

Les études sont menées au CERN en collaboration avec l'Université de Dundee et l'institut britannique ASTeC STFC. Les essais sont effectués sur les échantillons plans pour l'optimisation du choix des paramètres de traitement laser et la mesure du SEY en laboratoire ainsi que sur des écrans de faisceau pour des mesures dans l'accélérateur *Super Proton Synchrotron*, SPS . Ces études ont montré que la modification de la morphologie de surface contribue à la diminution du SEY, l'atténuation du nuage d'électrons et finalement de la charge thermique à prendre en compte par le système cryogénique. Néanmoins, il a aussi été montré que l'augmentation de la rugosité de la surface nécessaire à la diminution du SEY, contribue à l'augmentation de l'impédance de la surface. Etant donné le courant électrique haute fréquence (dit courant image du faisceau) que doit conduire l'écran de faisceau, l'impédance de la paroi et la charge thermique associée constituent une préoccupation majeure pour le système cryogénique.

Il apparait d'ores et déjà que le choix de la morphologie de surface optimale permettant de réduire la SEY de la paroi tout en limitant les impacts négatifs sur le reste du système est un équilibre délicat. Ce travail repose sur la connaissance détaillée de la morphologie de surface. Des caractéristiques majeures de la surface traitée liées à la morphologie et pouvant avoir un impact sur l'utilisation de la surface dans les accélérateurs de particules restent à être évaluées notamment les propriétés structurelles à différentes échelles -résistance mécanique et la propension à la génération de poussière (particules de cuivre détachée de la surface). Le lien entre la topographie superficielle obtenue par traitement laser et la réponse de cette surface aux sévères sollicitations et exigences de l'environnement ultravide et cryogénique d'un accélérateur de particules doit être établi.

1.1 CERN accelerator complex

This section briefly presents the CERN accelerator complex and especially its larger collider, the LHC. Elements of the the machine where the laser treatment technology is foreseen to be deployed are described and basic accelerator physics notions, such as impedance and luminosity, are introduced. This introduction aims to explain the motivations of the study, environment constrains (cryogenic temperatures, geometry and materials) and possible consequences of the deployment of laser treatment in the accelerator vacuum system.

The European Organization for Nuclear Research (CERN) has been founded in 1954 and is located at the Franco-Swiss border. CERN is currently operating the world's largest particle physics laboratory. High energy physics experiments are conducted to study the structure of the matter, in particular the so-called Standard Model, which describes elementary particles and fundamental forces acting on them. CERN's instruments are also dedicated to the investigation of other fundamental questions, such as, among others, the existence of matter and antimatter, supersymmetry and the origin of dark energy [1].

Beside its mission in fundamental research, CERN is constantly facing the development of the technologies of the future. High energy physics requires unprecedented performances in many domains, such as, to name a few of them, superconducting magnets, vacuum, cryogenics, machine protection, collimation, diagnostics materials science, computing.

High energy physics experiments run at CERN mostly involve the analysis of high-energy particle collisions. The accelerator complex at CERN consists of a succession of increasing energy accelerators, as presented in figure 1.1. The whole accelerator complex has been designed, frequently updated and is currently operated to progressively accelerate charged particles. The last element of this accelerating chain, namely the Large Hadron Collider (LHC), can bring particle beams to an energy of 7 TeV [2].

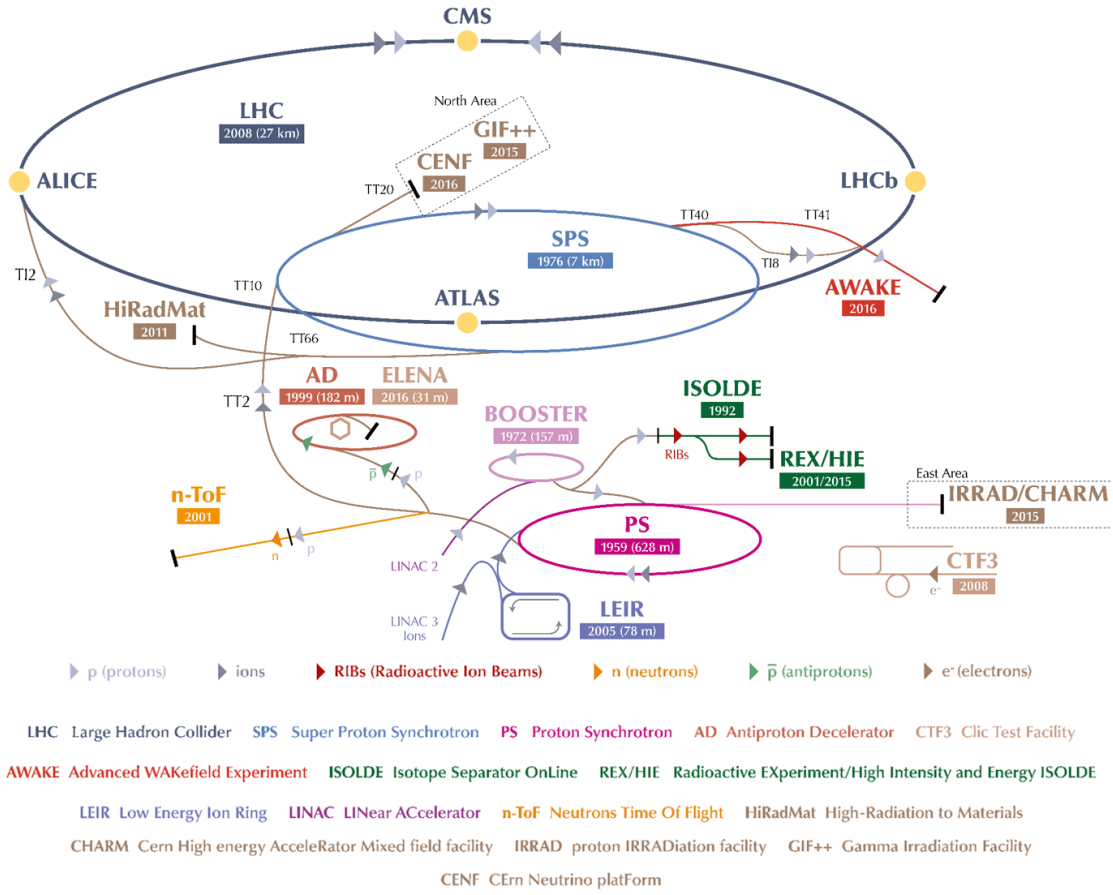

Figure 1.1: The CERN accelerator complex in 2017 [3]. Proton beams are created from hydrogen atoms and first accelerated by the linear accelerator LINAC2. Beams are successively transferred to the Proton Synchrotron Booster (PSB), then to the Proton Synchrotron (PS), to the Super Proton Synchrotron (SPS) and finally injected into the LHC. Other accelerators and experiments dedicated to high energy physics experiments are also shown. Dates correspond to the year of first operation of each machine.

1.1.1 The Large Hadron Collider

The LHC is an accelerator producing head-on collisions, mainly of protons. It has been built between 1998 and 2008 and installed in the former Large Electron Positron collider (LEP) 27-km-long ring, lying about 100 m underground. In the LHC, two beams of particles circulate in opposite directions, each in its own separate vacuum chamber. They are accelerated by high frequency electric fields in accelerating cavities.

Although the LHC is dedicated to heavy ions collisions one month per year, during standard runs the machine is typically colliding protons. Therefore, the proton beam operation is the framework of this study and the mention of *circulating particles* stands for protons circulating in the LHC.

LHC general layout, as well as parts of the machine where the laser treatment technology could be deployed (*i.e.* the main dipoles and the so-called *inner triplet* are presented in the following paragraphs.

LHC general layout

The LHC ring is an alternation of 2.8-km-long cryogenic arcs, where dipole bending magnets curve the beam around the accelerator, and 600-m-long room temperature Long Straight Sections (LSS). A schematic layout of the LHC can be found in figure 1.2.

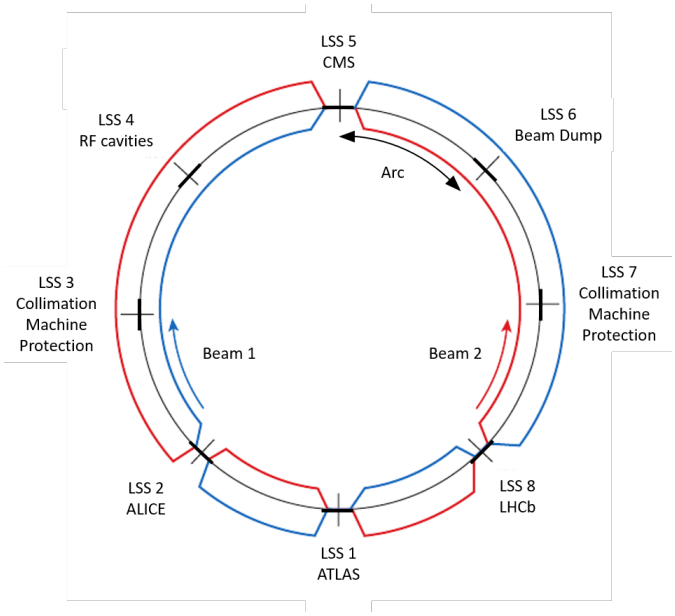

Figure 1.2: Schematic layout of the LHC, split into 8 sectors. Each of them includes a 2.8-km-long cryogenic arc and a 600-m-long straight section (LSS) The blue line illustrates the path followed by the proton beam 1, injected in LSS 2 and turning clock-wise, while the proton beam 2 (red) is injected in LSS 8 and travels counter-clock wise. Beams are circulating in the LHC in two separate vacuum chambers that merge in the interaction points (situated in LSS 2 and 8 for low intensity experiences and in LSS 1 and 5 for high intensity collisions.

The LHC is a particle-particle collider, the vacuum chambers of the two beams merge in the interaction points (IP) to allow the beams to collide in one of the four particle detectors (ATLAS, CMS, ALICE and LHCb), where collision products are analyzed. Interaction points are located in the LSS, which are also dedicated to the insertion or extraction of beams (the injection system for beam 1 and beam 2 are installed in LSS 2 and 8, respectively and the beam dump is in LSS 6), to collimation and machine protection systems (in LSS 3 and 7) and, finally, to beam acceleration, thanks to the radio frequency system (in LSS 4) [4].

LHC main bending dipoles

Each cryogenic arc of the LHC is divided into half-cells, composed of 3 dipoles (bending the trajectory of the beam) and a quadrupole (alternatively focusing or defocusing the beam). In total, 1232 superconducting dipoles are installed in the LHC. A simplified view of the dipole cross section is given in figure 1.3. The coil of the electromagnets is produced from Rutherford cables made of fine superconducting filaments of niobium-titanium (NbTi), surrounded by a 5 μm stabilizer of high-purity copper, used to redistribute the current in case of superconductivity loss or flux jumps.

In order to generate the 8.3 T magnetic fields required to circulate protons at their

maximum energy, the main dipoles are cooled to 1.9 K by superfluid helium. In this twin bore magnet, the two beam vacuum pipes and their respective magnet coils are embedded in a single cryostat, 0.91 m in diameter. The full assembly of the cryostat is 15-m-long and weights 35 tons.

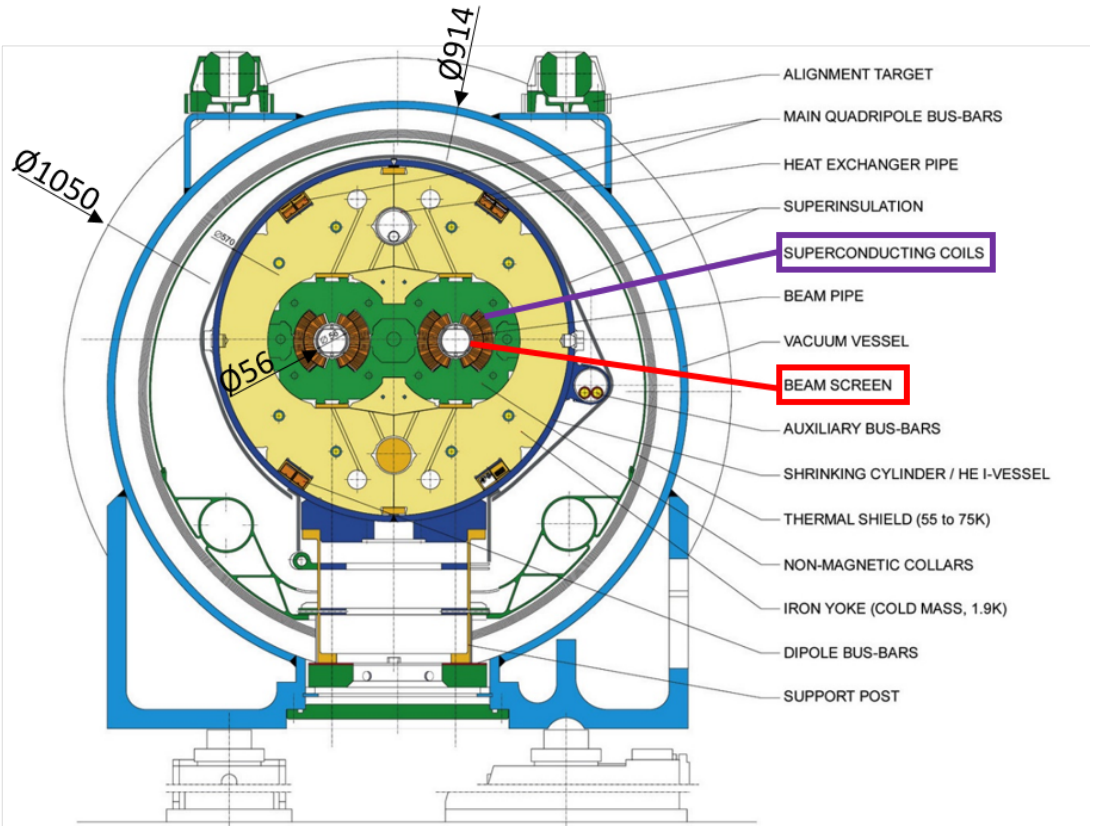

Figure 1.3: Diagram of the cross section of a standard dipole magnet in LHC, after [5]. The beam screen is highlighted in red, the magnet coils in purple. Attention should also be paid to some dimensions of the LHC dipole as, for instance, the inner diameter of the coil, 56 mm, compared to the outer diameter of the cryostat, 914 mm.

Dipole arc bending magnets are by far the most common kind at CERN. Nevertheless, more than 50 types of magnets can be found in the accelerator complex: quadrupoles have four magnetic poles arranged symmetrically around the beam pipe to squeeze the beam either vertically or horizontally. Sextupole, octupole and decapole magnets are used to correct beam optics. Some of these magnets might also be laser-treated, in particular, the so-caller inner triplets, presented in the next section.

So-called inner triplets in LHC

For the reasons explained in paragraph 1.2.2, a group of quadrupole magnets are considered a priority for the laser treatment deployment. Their characteristics are briefly presented in this paragraph.

The so-called inner triplets are located upstream and downstream of the interaction points. Four high-gradient quadrupole magnets (*Q1, Q2a, Q2b, Q3*) provide the final focusing of the beam before the collision. They reduce the amplitude function (the so-

called β function) of the transverse beam size and are, therefore, called low β magnets. They must operate reliably at the high gradient of 217 T/m, sustain extremely high heat loads in the coils and high radiation doses during their lifetime. They must have a very good field quality and a wide aperture of the cold bore [4].

In the LSS, the inner triplets are associated with a cryogenic and power distribution box (*DFBX*) and a separation/recombination dipole magnet (*D1*) which merges the two beams in one vacuum chamber. Going through these sets of magnets, the beam is "squeezed", the transverse beam size in the LHC arcs is 300 µm (at maximum energy) and is locally reduced down to 16.7 µm at IP 1 and 5.

Impedance

LHC beams interact with their environment, *i.e.* elements of the vacuum system and beam diagnostic via electromagnetic fields. In particular, image currents are induced by travelling charged particles at the beam pipe surface. Effects of surface modifications, such as the laser treatment, has to be taken into account. The notion of impedance is introduced in this paragraph.

The LHC beam time structure is described as a succession of 2 or 4 batches spaced by 225 ns, each containing 72 bunches of 1.15×10^{11} protons. When the LHC beam scheme is complete, *i.e.* the LHC is filled, it contains 2808 bunches spaced by 25 ns (7.5 m) [4]. This beam structure, made of spaced particle groups, is needed by the accelerating RF cavities and defines the induced image current characteristics on the beam screen.

The beam image current circulating in a resistive material causes Joule losses which must be evacuated by the cryogenic system. The dissipated power is proportional to the square of the image current intensity (related to proton beam charge) and to the electrical resistivity of the vacuum chamber wall material. This calls for a lower resistivity of the wall material, hence a lower operating temperature [6].

In addition to Joule losses, the induced current as charged particles flowing in the inner surface of the pipe walls generates a electromagnetic field (the total electromagnetic field vanished outside the chamber). Wake fields are identified as the electromagnetic fields emitted by the image current. They act back on the beam circulating particles [7] and can trigger oscillations of the beam in the transverse directions, leading to instabilities which may limit the achievable current per bunch or the total current [8].

Figure 1.4 illustrates the image current circulating though the walls of the beam pipe and two origins of wake fields. The coupled system is sensitive to the geometry of the chamber as, for instance, to the beam aperture. Particles keep moving on the axis of the chamber but image current trajectory is bent, resulting in synchrotron radiation emission. This radiation field is the first wake field illustrated in figure 1.4.

The second origin of wake fields comes from the deceleration of the image current travelling through a material with finite conductivity. This results in the emission of Bremsstrahlung radiation, called "resistive wall wake fields" [7]. In sum, the image current must circulate as smoothly as possible in order to not disturb and slow down the proton beam.

The wake function characterizes the electromagnetic action of a source particle

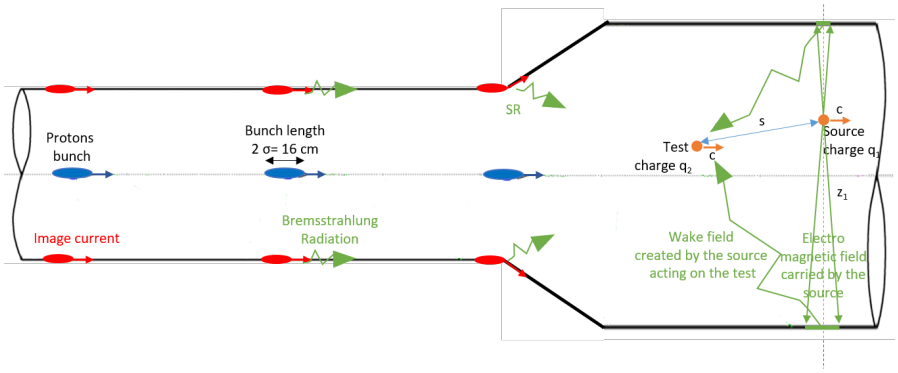

Figure 1.4: The intensity longitudinal profile of a proton bunch can be approximated by a Gaussian curve [9]. The bunch length defined as the twice standard deviation is around 16 cm. Circulating bunches induce an image current in the conductor. The electromagnetic field generated by the image current acts on the proton bunches. In particular, wake fields are generated as the image current is circulating in a resistive conductor (Bremsstrahlung radiation is emitted when the image current is "slowed down") and when the trajectory of the current is modified to follow the beam aperture (Synchrotron Radiation (SR) is emitted). As an introduction of the notion of wake function, the wake field created by a particle q_1 acting on a particle q_2 are also illustrated.

charged q_1 travelling in the beam pipe at a given position along the longitudinal axis z_1 to a following charged test particle q_2 at the same speed but at a given distance s. It is not the direct influence of the electromagnetic field of the source but rather the influence of the electromagnetic field induced in the beam pipe close to the longitudinal position of the source particle q_1. The situation is illustrated in figure 1.4.

The wake function describes the coupling between the particles depending on the environment. The longitudinal impedance or coupling-impedance is defined as the Fourier transform of the negative longitudinal component of the wake function. The frequency-domain description of the impedance (instead of the time-domain description of the wake function) is introduced to simplify the description of the coupling thanks to the few coefficients defined for the frequencies of interest of the electromagnetic coupling. The power spectrum corresponding to a Gaussian proton bunch is characterised by a reduction of -40 dB at 2 GHz [10].

For instance, the resistive power loss (and therefore the heat load which has to be evacuated by the cryogenic system) is equal to [9, 10]:

$$P_{loss} = M I_b^2 \, \Re(Z_{loss}) = 2{I_b}^2 M^2 \sum_{p=0}^{\infty} \Re[Z_L(pM\omega_0)] \times PowerSpectrum[pM\omega_0] \qquad (1.1)$$

where M is the number of bunches in the accelerator, $I_b = N_b \, e \, f_0$ is the bunch current (with N_b the number of protons per bunch, e the elementary charge and f_0 the revolution frequency, $f_0 = 11.25$ kHz for the LHC), Z_{loss} is the convolution of the longitudinal impedance Z_L with the beam power spectrum, $\omega_0 = 2\pi f_0$ is the angular frequency.

The resistive power depends on the characteristics of the proton beam and on the real part of the longitudinal impedance of the vacuum chamber. As a numerical example,

equation 1.1 is applied to the case of a simplified design of LHC beam screen, considering a Gaussian profile of the bunches. Power loss per unit length is given by equation 1.2 [10]:

$$P_{loss} = \frac{1}{C}\Gamma\left(\frac{3}{4}\right)\frac{M}{b}\left(\frac{N_b\, e}{2\pi}\right)^2\sqrt{\frac{c\,\rho\, Z_0}{2}}\,\gamma_t^{-3/2} \tag{1.2}$$

where $C = 26658$ m is the LHC circumference, Γ the Euler function, $\gamma_t^{-3/2} = 0.25$ ns the *r.m.s* beam length, ρ the resistivity of vacuum chamber material, for which temperature dependence must be taken into account, c the speed of the light, b the beam screen half height and Z_0 the free-space impedance.

Considering LHC beam and beam screen parameters, Joule losses are expected to be around 100 mW/m. It appears in equation 1.2 that Joule power losses are proportional to the resistivity of the material facing the beam.

A transverse impedance is also defined. Rise times (growth rate) and bunch intensity thresholds for different beam instabilities can be calculated based on the real and the imaginary part of transverse impedance, respectively [11].

In conclusion, impedances quantify in the frequency domain the effects of the environment on the beam coupling. They give rise to both Joule induced heating and beam instabilities. Constraints of the cryogenic system and beam stability set a maximum "budget" for longitudinal and transverse impedances, therefore adding further requirements, not only on the design and the choice of materials of vacuum system walls [4], but also on potential surface modifications such as laser treatment.

1.1.2 Beam vacuum system

Requirements for the LHC beam vacuum system in the arcs are driven by beam lifetime [4]. Particle beams circulate in Ultra High Vacuum (UHV), in order to avoid protons loss by scattering with residual gas molecules thus reducing the beam lifetime. The required lifetime associated with vacuum performance is set to 100 h, which leads to the requirement to keep vacuum system pressure below 10^{-8} Pa [12]. In experimental areas, a stringent limitation on the vacuum pressure is given to minimise the background noise to the detectors [4].

Characteristics (operation temperature and elements of design) of the beam vacuum system deployed to address vacuum requirements are briefly introduced in this section. In particular, the beam screen is presented, as it is the component modified by the surface laser treatment.

Temperature of operation

In field-free sections (representing 18 % of LHC circumference), at room temperature, gaz pumping during the operation is mainly assured by sputter ion pumps and Non-Evaporable-Getter (NEG) coatings. The LHC NEG coating is a ternary Ti-Zr-V alloy allowing chemisorption of most of the gases present in the UHV system. After dissolution in the native oxide bulk, this material establishes thermally stable chemical compounds with gas molecules (except methane and noble gases). NEG coating acts as a diffuse

pump [13]. When exposed to air, the getter is saturated in gas molecules, but it regains his pumping function after a mild thermal annealing, the so-called activation (heating under vacuum) [14, 15].

In the cold part of the machine, where superconducting magnets are used to guide the proton beam, the beam vacuum chamber is cooled at cryogenic temperatures. There, the pumping function relies entirely on the physisorption of gas molecules on the vacuum enclosure, which is at 1.9 K (temperature of superfluid helium bath). The vacuum enclosure is therefore called cold bore. At this temperature, the saturated vapour pressure of most of the gases is lower than the pressure required for the operation of the accelerator leading to cryosorption of the gas molecules [16]. For cost reasons related to available budget for cooling systems in development studies for future colliders or LHC upgrades, the beam screen operation temperature has been proposed to be higher: in the range 40-60 K for the Future Circular Collider (FCC) and 60-80 K in HL-LHC [17]. Saturated vapor pressures of adsorbed gas species must be assessed for the surfaces used in the beam screen, on these ranges of temperatures as well.

Although the combination of NEG coating and laser-assisted structuration is foreseen as a treatment for surfaces operated at room temperature and some of the results obtained can be extended to room temperature, the framework of this study will be focused to the beam screen in a cryogenic environment, where the effect of the electron cloud and, therefore, the need of a mitigation technique are more significant. The elements of the beam vacuum system design at cryogenic temperature are described in the following section.

LHC beam screens

Despite the need to maximize accelerator aperture, the concept of a beam screen standing between the beam and the magnet bore first appeared in 1994. The purpose was to protect the surface used as a cryosorber from photons emitted by particles circulating in the Superconducting Super Collider (SSC), thus avoiding desorption phenomena (in particular photodesorption) [18]. It also appeared as a priority to protect the large cryogenic system required to cool superconductive magnets from energy deposition induced by the high energy particle beam [19].

The beam screen shields components operating at cryogenic temperatures by intercepting beam-induced heat and transferring it to the cryogenic cooling fluid. The heat load is mainly generated by synchrotron light [20], image currents and electron clouds (which can be triggered by photo-electrons). Particles scattered by the residual gas or produced by nuclear reactions during collisions can also contribute to the heat load.

In addition to reducing heat deposition on the cold bore, the beam screen should also ensure numerous functions, as presented in figure 1.5. The diagram also shows processes and design features already implemented in currently used beam screens.

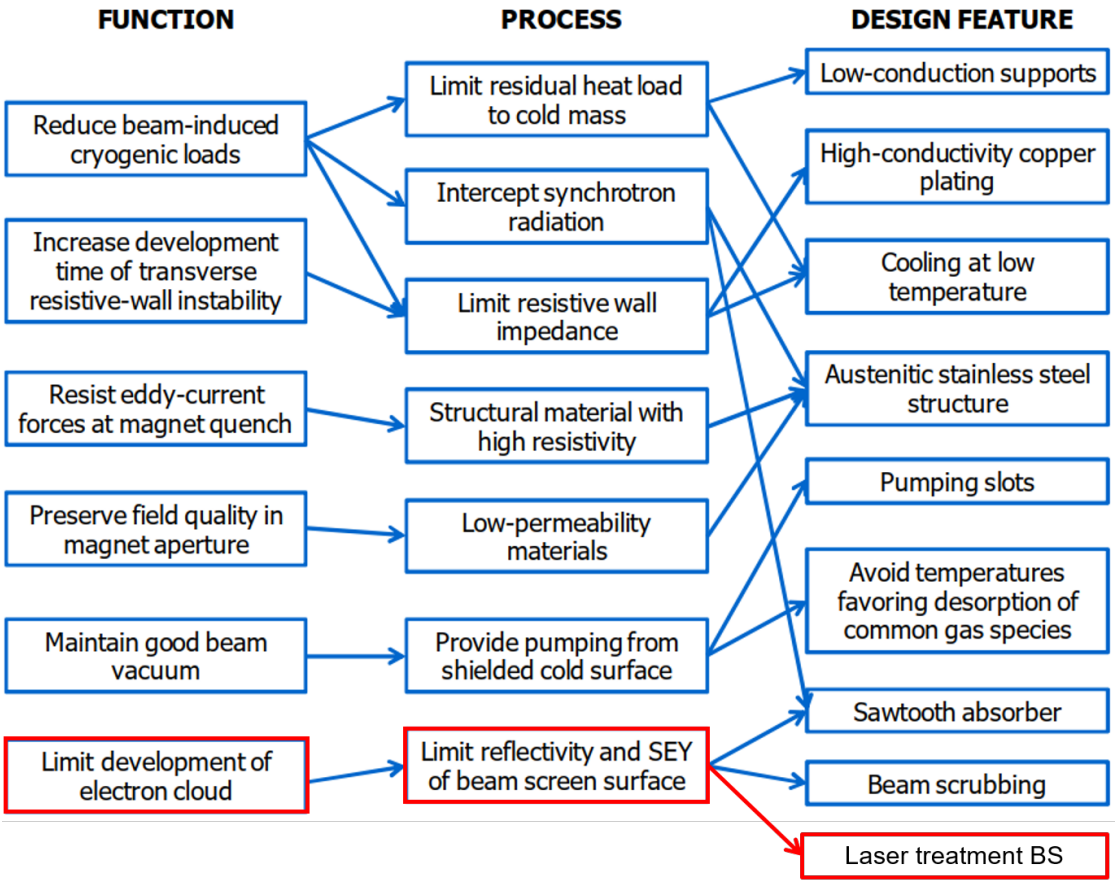

Figure 1.5: Functional design map of the beam screen, adapted from [19]. Laser treatment appears as a design feature aiming to reduce the SEY of beam screen surfaces.

Design features of standard beam screens which are relevant in the laser treatment framework are described in the following and presented in figure 1.6.

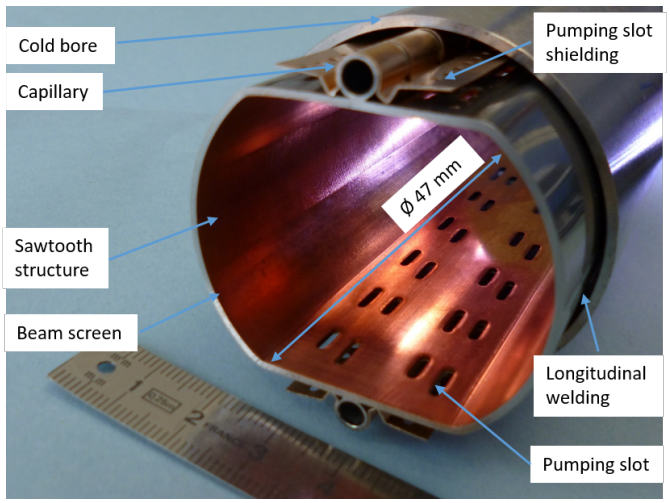

Figure 1.6: Picture of the standard beam screen inserted in arc dipoles. Photograph by Cedric Garion.

Beam screens are actively cooled between 5 and 20 K by super critical helium flowing through two capillaries welded on the screen. A cold temperature of the beam screen reduces firstly heat transfer to the cold bore by conduction and radiation and, secondly, resistive power losses.

The cross section of a LHC beam screen has a round flattened shape (a cylinder flattened at the bottom and at the top). This shape maximizes the horizontal aperture and allows the integration of two cooling capillaries. The dimensions of the racetrack-shape beam screen of LHC main dipole are 36.8 mm and 46.4 mm (vertical and horizontal apertures, respectively). The racetrack shape is obtained by continuous roll-forming and longitudinal welding.

Beam screens are manufactured by colamination of a 1-mm-thick sheet of high-manganese high-nitrogen stainless steel and a 75-μm-thick one of Oxygen-Free Electronic (OFE) copper. The copper layer colaminated at the inner surface of beam screens ensures a better image current flow in the beam screen, fulfilling the impedance requirements (comparing the skin effect and degradation of the copper layer after colamination). However, the presence of the highly conductive copper increases the currents and forces induced during a magnet quench. A stainless steel structure has been designed to withstand these induced forces and static loads. In addition, the high manganese and nitrogen contents of the P506 grade steel confer a low magnetic permeability, required for a low impact on the magnetic field quality.

In order to satisfy the vacuum requirements, the beam screens are perforated by oblong so-called pumping holes. The surface of the holes covers 4 % of the total surface and allows the beam-induced desorbed gas molecules to escape from the inside of the beam screen towards the cold bore where they are cryosorbed. The holes are shielded by a copper-beryllium sheet to prevent direct electron impact on the cold bore.

A saw-tooth structure (30 μm depth over 500 μm period) is rolled onto the outer wall of colaminated beam screens. It absorbs synchrotron radiation at normal incidence and reduces photon reflectivity. Therefore, without reflection of the synchrotron radiation, photo-electron emission is restrained to this area of the beam screen and electrons can be confined by the dipole field.

Sliding rings ease the insertion of the beam screen inside the cold bore during system assembly. They are the only contacts between the "warm" beam screen and the cold mass.

In conclusion, LHC vacuum system has been designed to address vacuum requirements in the framework of nominal and ultimate LHC beam characteristics (see table 1.1 in the following section) at room and cryogenics temperatures. Part of the existing vacuum system installation is planned to be upgraded (including surface modification) to fit the performances aimed by the so-called HL-LHC project introduced in the following paragraph.

Table 1.1: Nominal LHC, ultimate LHC and HL-LHC beam parameters [22].

Parameters		Nominal LHC	Ultimate LHC	HL-LHC
Beam Energy in collision	[TeV]	7	7	7
Number of protons per bunch	[1]	1.15×10^{11}	1.7×10^{11}	2.2×10^{11}
Total number of bunches	[1]	2808	2808	2748
Beam current	[A]	0.58	0.86	1.09
Max luminosity in IP 1 and 5	[$cm^{-2}.s^{-1}$]	1×10^{34}	2.3×10^{34}	5.3×10^{34}

1.1.3 High-Luminosity upgrade

In the framework of the project called High-Luminosity (HL-LHC), the LHC is going through two upgrade phases practically implemented during the Long Shutdowns (LS) 2 and 3. LS2, from 2019 to 2022, is dedicated to LHC maintenance and to the upgrade of injectors and experiments, while LS3, from 2025 to 2027, to the final installation. After these updates, the performance of the accelerator, *i.e.* the ability to produce collisions, will be increased by a factor of 5 [21, 22].

Luminosity, L, is an indicator describing the performance of the collider in producing useful interaction events. Indeed, the production rate R of a given physics event is given by the product of luminosity and production cross section [23]:

$$\frac{dR}{dt} = L\,\sigma_p \tag{1.3}$$

where σ_p [cm^2] is the production cross-section and L [$cm^{-2}s^{-1}$] is machine luminosity.

The luminosity related to two beams with a Gaussian beam distribution of particles, colliding heads-on (opposite velocity vector of the beams) is expressed as [23]:

$$L = \frac{N_1 N_2 n_b f}{4\pi\sigma_x\sigma_y} \tag{1.4}$$

where N_1 and N_2 are the number of protons per bunch of the two beams, n_b is the number of bunches per beam, f is the revolution frequency and σ_x and σ_y the horizontal and vertical root mean square (*r.m.s.*) bunch sizes.

The integrated luminosity is the integral value of luminosity over time $\int Ldt$ and is expressed in inverse femtobarn [$fb^{-1} = 10^{39} cm^{-2}$].

Equation 1.4 illustrates that LHC luminosity can be improved by increasing the bunch intensity and/or decreasing the transverse bunch size. The nominal LHC, ultimate LHC and HL-LHC beam parameters are given in table 1.1.

Many upgrades involve all accelerator technologies to achieve the objective of beam

intensity and to withstand related effects in all the domains: vacuum, cryogenics, machine protection, collimation and diagnostics. The development of new superconducting magnets (11T bending dipole and large bore quadrupole) based on niobium-tin superconductor technology [24], new radio frequency cavities, so called crab-cavities [25, 26], are probably the most emblematic projects of HL-LHC upgrades.

Collateral effects of the increase of beam current are expected, such as the increase of beam coupling impedance of the beam screen, of Synchrotron Radiation (SR), the diffractive losses at primary collimators, the number and the penetration of collision debris. For instance, in the framework of the HL-LHC project, the new magnets installed in the inner triplet area of IP 1 and 5 required the design of a new beam screen, able to shield the magnet coils and the cryogenic system from debris and heat load induced by the more numerous collisions [27].

Another collateral effect of the proton beam intensity increase aimed in the HL-LHC project is the development of electron clouds, which might become a major limiting factor of accelerator performances, need to be taken into account for the design of new component or require modification of the existing installation. Electron cloud presence in accelerators is further described in the following section.

1.2 Electron cloud in accelerators

Electron cloud has been observed in many accelerators of positively charged beam worldwide [28]. The production of electrons cascades is called electron multipacting. The avalanche multiplication of electrons leads to an exponential increase of electron density and results in a so-called electron cloud, detrimental in the operation of the accelerator. Strategies have been deployed to counteract this phenomenon. Build-up mechanisms, as well as the impact of electron clouds in particle accelerator performances and mitigation techniques, is described in this section.

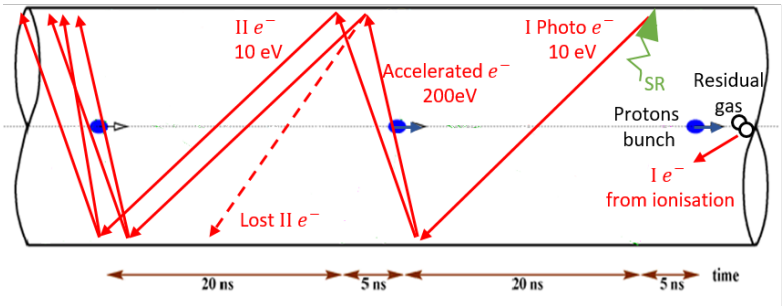

Figure 1.7: Schematic of electron cloud build-up mechanisms in positive-particle accelerator beam pipes. Primary electrons are liberated by residual gas ionisation or by Synchrotron Radiation impinging on the beam pipe surface (green). Primaries are accelerated up to 200 eV by the electric field generated by the passing bunch (blue). When impinging the opposite surface, some emitted secondary electrons survive until the next bunch and get accelerated or get lost, after [29].

1.2.1 Electron cloud mechanisms

The build-up of an electron cloud can be separated into 3 steps: generation of primary electrons, acceleration of primary electrons via the electric field generated by a bunch of protons and, finally, secondary-electron emission. These mechanisms are illustrated in figure 1.7 and further developed in the following paragraphs.

Generation of primary electrons

Despite the ultra-high vacuum, residual gas molecules remain trapped in the enclosure and can be ionized by collisions with the proton beam and therefore liberate electrons. Ionisation rate depends notably on gas pressure and beam intensity [30]. More than the ionisation of residual gas molecules, the photo-electric effect is (and will be for high energy machines) the principal source of primary electrons. Electrons are emitted from the surface of the beam screen facing the beam, when the surface is irradiated by synchrotron-generated radiation. The minimum incident-photon energy required to extract an electron form copper is between 4 and 5 eV (equal to the work function of the material) [31]. This threshold is reached, for synchrotron radiation generated in the LHC, if the proton beam energy is higher than 450 GeV [30]. The number of emitted primary photo-electrons per incident photon is called photo-electron yield (PY) and is a characteristic of the material.

Energy gain, acceleration of primary electrons via the electric field generated by a bunch of protons

If the space between bunches is short enough, electrons emitted after the passage of the bunch *N* survive long enough in the vacuum chamber to receive a kick due to the electric field generated by the bunch *N+1*. The energy gained by an electron in kick regime is proportional to the square of the bunch population [30] and depends on the azimutal position of the primary electron. Simulations showed that the energy of electrons rises from 10 eV when they are emitted to several tenths after the first bunch passage.

Secondary electron emission

Once accelerated, electrons hit the walls with enough kinetic energy to extract cryosorped molecules, increasing gas density. At the same time, they trigger the emission of secondary electrons. Secondary Electron Yield (SEY) is a material parameter characterising the mechanism of electron release from a surface. It is further explained in section 1.2.3.1. It is defined as the ratio between the number of primary electrons hitting a surface and the number of secondary electrons emitted. Materials can be classified as electron absorbers or multiplicators comparing their SEY value with a critical one. Electron-multiplicator materials have an SEY above 1. However, in reality, this critical value depends on the geometry and on field conditions. For example, for a bunch population of 1.1 10^{11} protons/bunch, it has been evaluated at 1.25 and 1.05 for, respectively, main dipoles and quadrupoles [32]. Figure 1.8 gives PyECLOUD simulation results on the sensibility of electron clouds to bunch population.

Figure 1.9 presents typical SEY curves measured on as received materials commonly used in vacuum systems. The maximum SEY can be equal to 2 or even greater. It is much higher than the critical value exhibited in figure 1.8. Without countermeasures,

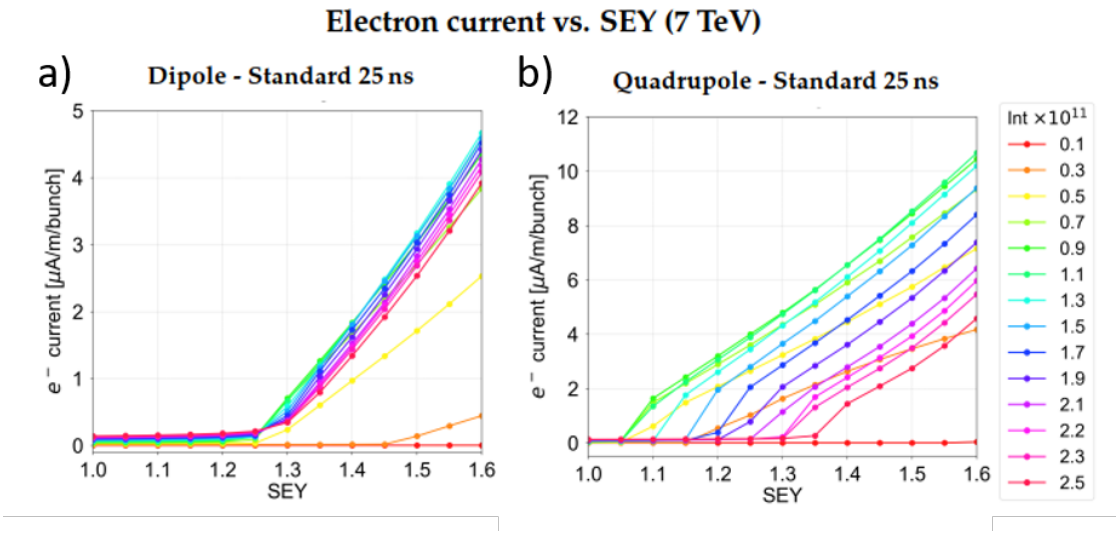

Figure 1.8: Evolution of electron-cloud current as a function of the maximum SEY of beam-pipe surface for LHC arc dipoles (a)) and quadrupoles (b)), for different bunch intensities. Simulations for 25 ns bunch spacing and 7 TeV beam energy [32].

this would lead to an exponential increase of electron density in the vacuum chamber [33].

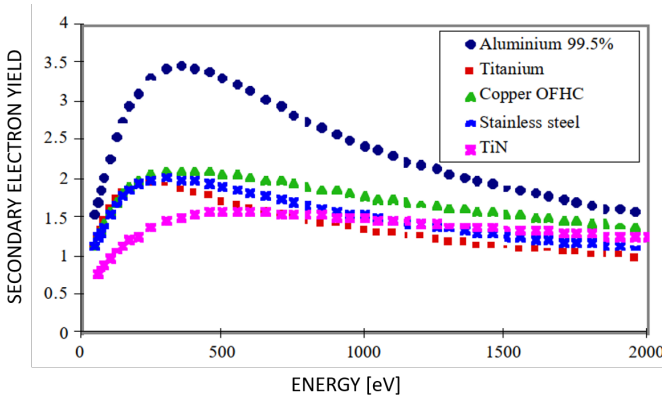

Figure 1.9: Typical SEY curves measured on materials used in vacuum systems [33].

A detailed description of modelling and simulation of electron cloud build-up with PyECLOUD can be found in [34]. Spatial distribution of electron clouds depending on magnetic field are reported in figure 1.10. It appears that the density of electrons is strongly influenced by the surrounding magnetic field. It is homogeneous in a field-free region. In the dipole, electron impacts on beam pipe surface are concentrated on the top and bottom parts of the beam screen whereas, in a quadrupole, they are concentrated on the four corners.

In conclusion, the description of electron-cloud build up mechanisms exhibits the preponderant influence of beam parameters and the beam screen surface SEY. Consequently, SEY reduction in the inner surface appears to be a relevant strategy to mitigate the heat induced by the electron cloud. Before further describing the strategies deployed to reduce the surface SEY, detrimental effects of electron clouds on accelerator

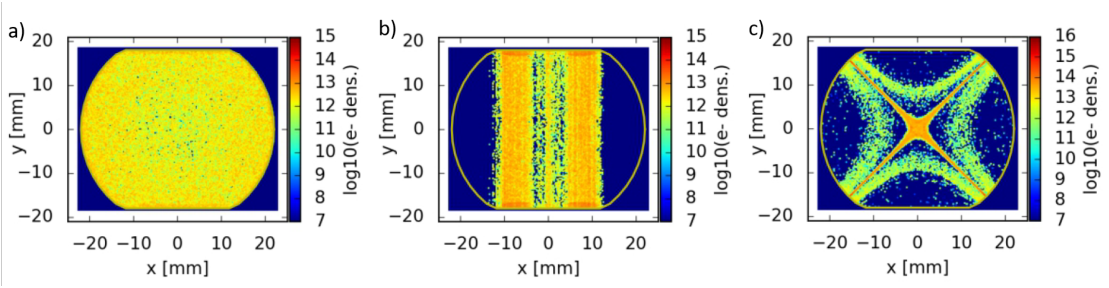

Figure 1.10: Electron cloud spatial distribution in a cross section of the beam pipe, at cryogenic temperatures, a) in a magnetic-field-free region, b) in a dipole, and c) in a quadrupole [34, 35].

performance are described in the following paragraph.

1.2.2 Impact of electron clouds on accelerator performance

Electron clouds can be dense enough to have negative consequences on the operation of the accelerator:

- can be responsible for a pressure rise driven by electron-stimulated desorption of gas molecules absorbed on inner surfaces [36];
- may have a detrimental effect on beam quality, as it increases beam emittance (*i.e.* the transverse dimension of the beam), and on beam stability [30];
- electron bombardment onto the walls of the beam screen increases the heat load to the cryogenic system. The following part of the study will be mainly focused on this aspect.

In cold regions, mainly constituted by the arcs, additional constraints originate from the cryogenic environment. The beam vacuum system is indeed embedded in the superconducting coil, inside the cold mass filled with liquid helium at 1.9 K. Several sources of beam-induced heat load on the beam screen, cooled by a the supercritical helium circuit, have been identified (values for nominal machine parameters) [4]:

- energy loss by nuclear scattering on the residual gas: 0.03 W/m/beam;
- generated synchrotron radiation: 0.2 W/m/beam;
- resistive losses of image currents (impedance): 0.2-0.3 W/m/beam [11];
- deposited power due to electron clouds: 0.7-0.8 W/m/beam (for $\delta_{max} = 1.1$) [37].

Electron clouds are the main source of thermal loads on beam vacuum system. Considering the finite cryogenic cooling capacity, electron cloud is the major limiting factor in the performance of high-energy accelerators [29, 35, 38]. Its effects have to be taken into account in design updates of current machines and in the development of future accelerators, especially as accelerator upgrades target an increase of beam intensity [39].

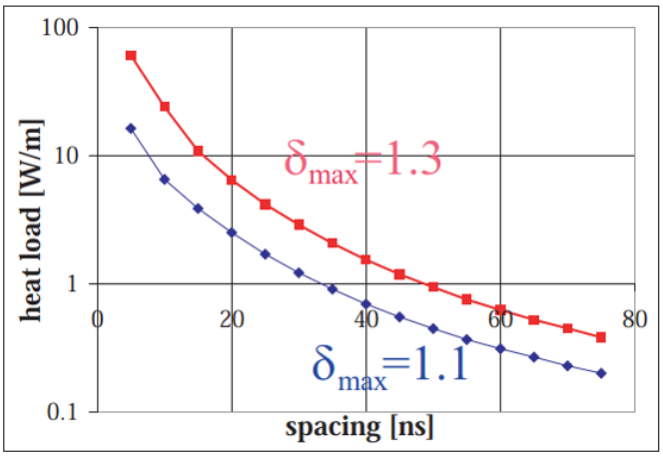

Figure 1.11: Simulated heat load in LHC arcs as a function of bunch spacing for the design bunch population of 1.15 10^{11} and for two values of maximum secondary emission yield $\delta_{max} = 1.1$ and $\delta_{max} = 1.3$. Nominal bunch spacing in LHC is currently 25 ns [37].

Figure 1.11 also exhibits a strong influence of the SEY of the beam pipe surface on deposited heat load. Consequently, SEY reduction of the inner surface appears to be a relevant strategy to mitigate heat induced by electron clouds.

Figure 1.11 illustrates the influence of bunch spacing on heat load deposited by electron clouds. Many parameters affect the appearance and the development of electron clouds, such as beam parameters (intensity, number of bunches, space in-between bunches), the geometry of the vacuum chamber and the surrounding magnetic field [34]. The electron multipacting gets more and more important when the bunches of protons, which form the beams, are numerous and close to each other, and a fortiori with for the beam characteristics aimed in the framework of HL-LHC project.

Targeted area in the framework of the HL-LHC project

The High-Luminosity LHC (HL-LHC) project is an illustration of both, the prohibitive increase of the heat load due to the electron cloud and the deployment of the strategy for the SEY reduction of the beam screen inner surface to counteract the effects of the electron cloud. In the framework of the HL-LHC project, the magnet string around the two high-luminosity experiments, ATLAS (IP1) and CMS (IP5), will be upgraded. However, in the two low luminosity experimental insertions, ALICE (IP2) and LHCb (IP8), the magnets and the vacuum chambers will not be changed during the upgrade program [40]. The aim is to prepare the current magnet setup composed by the inner triplet quadrupoles and the *D1* dipole presented in section 1.1.1, to handle and compensate the effects of the electron cloud expected due to the increase of the beam intensity. Although, no beam instability driven by electron cloud is expected with nominal HL-LHC beams in IP2 and IP8 [40], electron cloud simulations indicate that HL-LHC nominal beams would transfer much higher power in the beam screen than the cooling capacity would allow. Indeed, the heat load extracted from the beam screens of the magnets was about 160 W (in 2006), it was estimated that this heat load is mostly due to electron cloud [40]. The ultimate value of the heat load that can be extracted by the

cryogenic system has been estimated to be around 195 W [41].

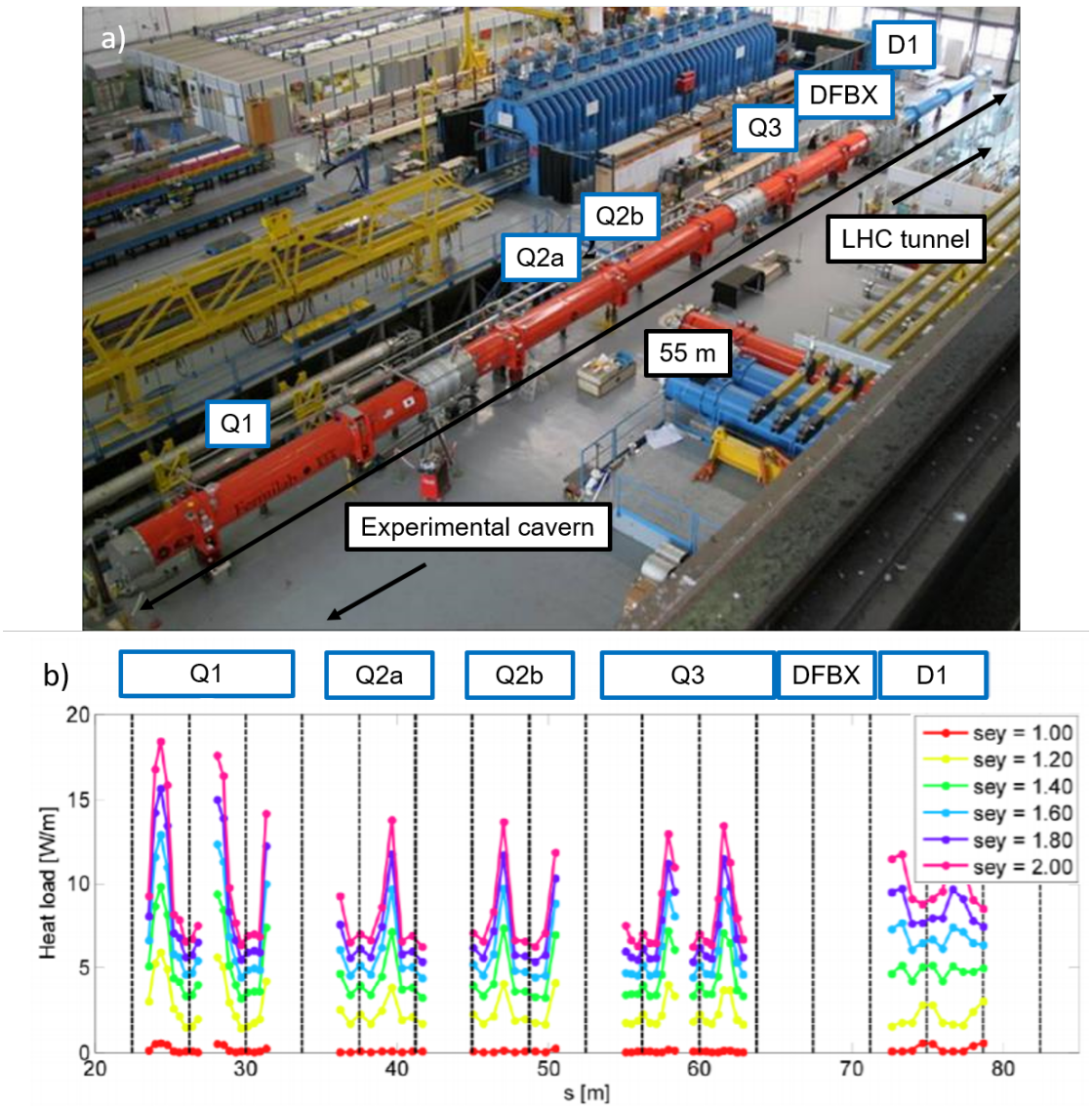

Figure 1.12: a) Picture of the components of the inner triplet installed in building 181. The inner triplet contains three quadrupole magnets (*Q1, Q2, Q3*), a cryogenic and power distribution box (*DFBX*), and a separation dipole magnet (*D1*), after [42]. b) Simulation of the heat deposition due to the electron cloud along the inner triplet depending on the SEY of the inner surface [43].

The heat load value in the inner triplets simulated with surfaces with a SEY of 1.3 is estimated to be 1000 W [44]. This can be drastically reduced to 50 W with a SEY of 1.1 [41], which would allow not to exceed the cryogenic system operational limits.

It has been decided not to modify the cryogenic circuit to increase the cooling power but rather to remove the heat source. The current setup has to be modified *in-situ*, *i.e.* without removing the magnets from the tunnel, during Long Shutdown LS3 in 2025 to reduce the electron emission of the beam screen surface. Although amorphous carbon coating (see section 1.2.3.2) is the current baseline, laser surface is considered as

an alternative method to treat the surface of this area to reduce electron cloud. The challenges raised by the *in-situ* treatment of beam screens of these magnets (about 55 m machine length x 4) will be the framework of the application cases made in this work, meaning that the numerical applications will rely on the characteristics (geometries, length and magnetic fields) of these magnets. In addition to the magnets of the LSS, the study will also take into account *arc* dipoles or *MB* dipoles: these 1232 superconductiong dipoles curve the beam orbits in the arcs of the LHC. They are not targeted in the mitigation of electron-cloud during the HL-LHC project but it was considered relevant to study the influence of the laser treatment on the most common magnets in the LHC, as well.

The case of inner triplets in IP2 and IP8 is the illustration of the detrimental effect of electron cloud (on the cryogenic system in this case) and the need to develop techniques to mitigate it locally. A brief description of the mitigation strategies is given in the following paragraph, especially the one relaying on the SEY reduction.

1.2.3 Mitigation techniques of electron cloud

After the presentation done of the electron cloud build-up mechanism and the demonstration of the need of its mitigate in the particle accelerators, this section focuses on the mitigation strategies of the electron cloud. Although some operational strategies can be found, the techniques mostly rely on the SEY reduction of the surface facing the particle beam.

As mentioned in section 1.2.1, the electron cloud is strongly linked with the bunch spacing. If despite the conditioning, the operation of the accelerator is disturbed by the electron cloud, doubling or tripling the bunch spacing or changing the filling pattern of the accelerator can reduce the electron cloud heat load to an acceptable level, at cost of the luminosity reduction [32]. Mitigation strategies can also be deployed to reduce the generation of primary electrons for instance to deflect or absorb the synchrotron radiation or disturb the acceleration of the electrons adding a solenoid field [45] or cleaning positively biased electrode on the surface [46,47]. From a practical point of view, the solenoid field or electrodes require modification of the infrastructure, additional electricity costs, power supply, maintenance the modification while the mitigation techniques can be part of the chamber design [48]. Most of the mitigation techniques aim at decreasing the SEY value of the surfaces facing the beam [49]. The mechanisms of the secondary emission are briefly presented before introducing some of the strategies deployed to reduce the SEY value of the surfaces.

1.2.3.1 Secondary electron emission mechanisms

When an electron at a given energy hits a surface, several concomitant phenomena are involved to produce secondaries electrons. They can be distinguished by measuring their energy [50]. One part of the impinging electrons are elastically reflected, these electrons keep their original energy. Another part penetrates and actually interacts with

the solid. The penetrating part will encounter two phenomena: elastic collision with the atomic nuclei which changes the direction of the primaries electrons partly reversed motion toward the surface. If they escape, they are called rediffused electrons (on their way, they also contribute to interaction with electrons). Finally, the main part of the distribution consists of low energy electrons, they had interact and loss energy through interaction with the electrons present in the crystal. These excited crystal electrons can make their way to the surface and eventually escape. These electrons that are back scattered electron are referred to as *true secondary* electrons.

The energy spectrum of emitted electrons generated by a monoenergetic electron beam is given in figure 1.13. The fraction of each category of secondary electrons depends on the incident electron energy; nevertheless the fraction of *true secondary* is stable at around 75 % if the incident energy is above 30 eV. The fraction of the reflected electrons is 65% with 10 eV electron beam energy, it decreases below 10 % above 100 eV [51]. The energy of most secondary electrons is below 10 eV quite independently of the incident energy [51].

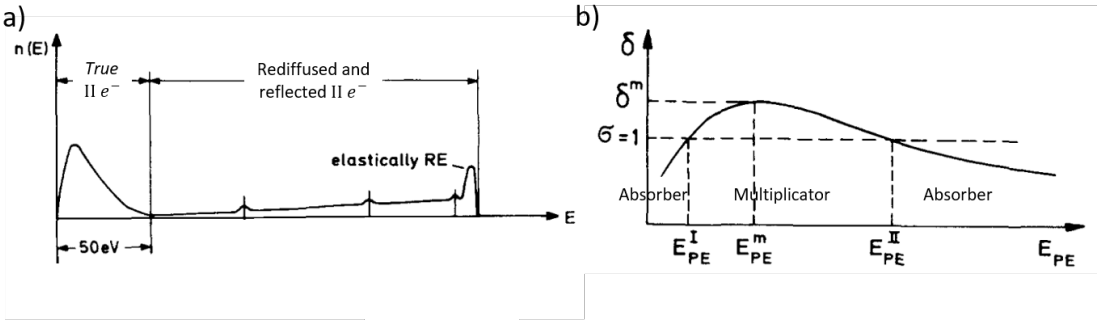

Figure 1.13: a) Example of energy distribution of emitted electrons under bombardment by electrons at the energy E. b) Example of SEY curve δ depending on the primary electron energy noted E_{PE}, after [52].

In the accelerator application case, all the secondaries electrons emitted by a solid upon primary irradiation contribute to the electron clouds, regardless their production phenomena. Therefore, in this frame, all emitted electrons are gathered under the term *secondary* electrons:

$$I_{sec} = I_{truesec} + I_{rediffused} + I_{reflected} \tag{1.5}$$

The Secondary Electron Yield (SEY), δ, is defined as the total number of emitted electrons per incident electron at a given primary energy E_{PE}:

$$\delta(E_{PE}) = \frac{I_{sec}(E_{PE})}{I_{prim}(E_{PE})} \tag{1.6}$$

In the literature, this ratio is sometime named Total Electron Yield TEY, and the term SEY is dedicated to the yield of the *true secondary* electrons [53].

A secondary electron yield curve as a function the energy of irradiating primary electron is given as an example in figure 1.13. Four parameters are used to describe the

energy dependence of the SEY:

- the maximum secondary electron yield δ^m. In this work, unless explicitly stipulated, the term of *SEY* will simply stand for δ^m, sometimes also noted as $\delta_{\max}$;
- the energy E_{PE}^m at which δ^m occurs, typically around 400 eV for copper;
- the crossover energies E_{PE}^I (respectively E_{PE}^{II}) defined as the energy below (respectively above) which the SEY is less than unity. For copper, these values are typically between 200 eV and 1500 eV [52].

The general shape of the SEY curve as a function of the primary energy is a trade off between the penetration of the incident electron, which follows law Beer-Lambert relationship (exponential decrease with the depth), and the secondary electrons escape probability to migrate and to escape from the surface. Primary electrons with a very low energy can only liberate a few secondaries located close to the surface. On the contrary, primary electrons with a very high energy penetrate too deeply into the bulk and deposit their energy in regions from where the excited secondaries cannot escape.

Phenomenological models based on the decomposition of the secondaries electrons into the three components of the SEY (true, back scattered, rediffused) have been developed to describe the yield, emitted-angle, emitted energy distributions and emission probabilities of the secondaries. Models have been fit on the experimental data [51, 53].

Two characteristics of the secondary emission involved in the SEY reduction based on geometrical effect (further described in 1.2.3.2) worth being underlined: the emission angular distribution of the secondary electrons and the effect of the incidence angle of the primary electrons.

Emission angular distribution of the secondary electrons

Although the elastically reflected electrons are expected to be "optically" reflected [50], the angular distribution of the *true secondary* and rediffused electrons from polycrystalline surfaces is a cosine distribution independent of the angle of incidence of the impinging electron [52].

Effect of the incidence angle of the primary electrons

The primary electrons penetrating the material dissipate their energy close to the surface. Therefore, for a given incident energy, the expected SEY increases when the trajectory of the impinging electron stays close to the surface *i.e.* the angle of incidence increases (0° corresponding to normal incidence). Low energy secondary electrons which cannot escape with normal incidence, do escape with a grazing incidence. This effect is enhanced when the energy of the primary electrons increases. For instance, with an incident energy of 200 eV, the SEY value increases by 25% between a normal incidence and an grazing incidence (80°) [51].

The mean escape depth of secondaries is evaluated around 1 nm for metals consequently, secondary electron emission is a very surface sensitive process [52]. Therefore, the typical SEY values depend on the material, cleanness and roughness of the surface

top layer [33]. The SEY mitigation strategies, presented in the following section, rely on these properties.

1.2.3.2 SEY reduction techniques

SEY reduction techniques have been developed to mitigate the electron cloud in the particle accelerator. They rely on both operational after installation of the surface in the vacuum system or conceptual engineering solution aiming to modify the surface state of the material itself (chemical and morphological). Electron and photon scrubbing and techniques based on coating or structural modification of the surface are presented in a short bibliography.

Electron and photon scrubbing

The beam scrubbing is the operational mitigation technique used to decrease the SEY. The conditioning of the surface is based on the modification of the surface when irradiated by electrons or photons [49]. Practically, it involves circulating enough protons to release absorbed gas molecules and electrons from the metal. During the conditioning phase, intense beams (containing many bunches) at low energies circulate during a few days. The maximum value of SEY decreases as a logarithm function of the irradiating dose [33]. The beam screen scrubbing process is the LHC baseline for the surface conditioning to prepare the vacuum system at the beginning of each operational run. After this operation, the LHC is ready to be ramped up to higher-energy beams for physics and to restart with 25-nanosecond bunch-spacing. Nevertheless, the efficiency of this conditioning is limited and it requires several weeks at the beginning of each run as the benefit is lost when the vacuum system is vented for maintenance. Therefore, conceptual engineering surface solutions have been investigated to decrease the initial SEY of the vacuum chambers surfaces.

Surface coating

The surface SEY can be decreased by cleaning (detergent, plasma discharge, bake-out), changing the electronic properties of the surface, *e.g.* by thin film deposition of material with lower SEY.

Titanium nitride (*i.e.* TiN) coatings have been deployed to reduce the SEY of the surfaces in many accelerators world wide [33, 54]. This coating needs photon conditioning, it was not applied at CERN. Indeed, in addition to the pumping capacity of NEG coating already discussed in section 1.1.2, they also exhibit a low SEY [55, 56]. However, this property is observed after an *in-situ* activation [33]. The magnet coil and the cryostat surrounding the vacuum chamber in cryogenic parts do not allow the heating of the beam screen. The technology cannot be deployed in this part of the machine.

Amorphous carbon coating (*i.e.* aC-coating) relies in a plasma deposition on the surface of a material with a low SEY thanks to the electronic properties of carbon (orbital hybridization sp^2) [57,58]. A thin film coating of amorphous carbon is produced using DC magnetron sputtering of graphite targets. Study started at CERN in 2007 in the framework of the SPS upgrade working group [59]. Amorphous carbon coating has been successfully deployed at CERN in the framework of the LHC Injector Upgrade: the

Super Proton Synchrotron (SPS) vacuum system has been upgraded in order to inject 25 ns bunch spaced beams of higher intensity in the LHC. The inner surface of the beam pipe in 40 selected magnets was treated *in-situ* by inserting a train of segmented graphite hollow cathodes. Development for HL-LHC started in 2014. Experimentation at the cryogenic test bench COLDEX [60, 61] installed in SPS LSS 4, demonstrated the efficiency of the coating at beam-screen operating temperature [62, 63]. Good adhesion of the coating has been observed even on contaminated irradiated copper samples up to 200 MGy [64]. Implementation of the method during LS2 to treat *in-situ* a selected number of Q6 and Q5 standalone magnets has demonstrated the technical feasibility. A 250-nm-thick titanium pre-coating has been applied before the 90-nm-thick amorphous carbon coating. Additional cryogenic instrumentation has been implemented to measure the heat load reduction with HL-LHC beams during the Run 3 [64].

Surface structural modification

Solutions based on topographic surface structuration offer a promising alternative for SEY mitigation. These solutions aim at increasing the surface roughness which "traps" the electrons by geometrical effects. The principle of this technique and short historic of the investigation made toward this direction are given in the following paragraphs.

Principle

The principle of the reduction of SEY when increasing the surface roughness can be explained based on the phenomenon already described in section 1.2.3.1: despite the enhancement of SEY due to the non-normal incidence, the kinetic energy of the secondary electron emitted, contributing to SEY, is very low. Surface roughness causes a shift of the peak of the energy distribution of the secondaries towards the low-energy electrons side [65]. The scattered electrons lose energy in multiple collisions with the surface where, at low energy, the SEY is lower than 1. Secondaries can be captured by the adjacent topography surface structure [57]. In this case, the effective SEY of the macroscopic surface is reduced. The roughness shifts towards higher energy the curve of the dependency of the SEY on the energy of primaries electrons [57].

In addition, given the cosine emission angular distribution only a few number of secondary electrons, emitted with a grazing angle, leave the local surface with the possibility to escape the surface roughness and be exposed to the electromagnetic field of the beam. The electron clouds formation is mitigated by taking advantage of morphological modifications [48, 66].

Investigations have been performed on various surface structuration processes. The effects of the surface modifications (most of the time the "grooves" machined into the material) have been theoretically analyzed. Simulations have been run as well as SEY measurement in laboratories or electron cloud signal in experimental chamber of the accelerator. A quick review of these works is given in the following.

Bibliography on structural modification of the surface applied to the SEY reduction

Monte Carlo simulations have been performed on bowl-structured beryllium surface with an array pattern of Gaussian bowls [67] or 2D ripple aluminum surface with cosine profile at nanoscale [65]. An aspect ratio high/width was introduced to compare these surfaces.

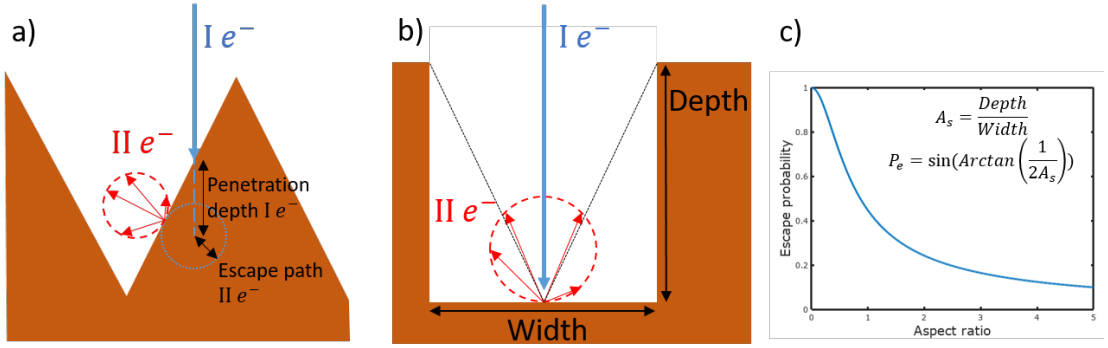

Figure 1.14: a) Triangular surface characterized by the angle α under normal to the macroscopic surface impinged by a primary electron. The penetration depth of the primary electron and the escape path of the excited secondary electron, the cosine-distribution of the emitted secondary electrons are illustrated. b) Rectangular surface structure characterized by an aspect ratio of the trench depth and width. c) Escape probability of the secondaries from the dwell in the case of an normal incident primary electron in the center of the trench 2D model.

The results of the simulations were focused on SEY of the macroscopic surface and energy and angle emission distributions of the secondaries. For the two surface morphologies investigated in this work, the two opposite effects involved in SEY mitigation on rough surfaces were observed. On one hand, the effect of *the inclined surface* - the enhancement of SEY when the incident angle of the impinging electron increases- is the dominant effect for low aspect ratio roughness. On the other hand, the effect of *re-entrance* - once-emitted electrons re-interact with an adjacent part of the consecutive topographic surface- is dominant for high aspect ratio. The simulations highlight the need to obtain high aspect ratio features covering the surface to efficiently decrease the SEY.

In 2004, in the framework of the particles accelerators, a method of angular coefficients [68], simplified for 2D case, originally developed for the calculation of the pumping speed of di-hydrogen molecules in the LHC for various design configurations, has been applied on dynamics of the electrons impinging triangular grooves. The method has been fed with phenomenological models of the influence of the incidence angle and the energy distribution [51]. The models assumed that the reflected electrons follow an elastic specular reflection. The method exhibits the secondary electron emission suppression by the toothed surface which is seen as a possible electron cloud mitigation technique for particle accelerators in the future.

SEY and/or electron cloud suppression of a mechanically machined roughened metal surfaces has been studied from the millimeter to the nanometer scale in several applications.

A rolling tap method was first developed to implement the saw tooth structure with a pitch of 1 mm in a circular beam screen chamber. Measurements in the experimental chamber showed a photo-electron emission reduction. Nevertheless it was also observed that an external magnetic field or a moderate beam field is required to enable electron clouds mitigation thanks to the surface roughness. It was also predicted that engraved grooves with a large pitch (compared to the spatial bunch length) induce beam sta-

bility problems [69]. Monte Carlo simulations based on a phenomenological model fed with experimental data [56] have been performed on saw tooth and isocele triangle machined surfaces, with or without surrounding magnetic field [70]. They revealed a SEY dependency on the angle of the triangular features but not on their period. On contrary, secondary electron emission simulations on rectangular grooved patterns showed a dependency on the size and on the presence of a magnetic field [70]. For instance, a period smaller than 63 μm was required to reduce the SEY of a surface immersed in a 1.6 T magnetic field perpendicular to the surface. In these simulations, it appeared that an higher aspect ratio of the engraved pattern reduces the SEY and that the secondary emission rate depends on the incident angle to the normal of the macroscopic surface. It was also underlined that smooth tips of the pattern should be used to reduce the impedance of the structured surface. Experimental measurement corroborated the simulations. The electron cloud density measurement of a TiN-coated triangular [46] and rectangular [48] grooved surfaces showed a reduction with respect to a flat surface by a factor of 4 and 20 respectively. These experiments were performed with orthogonal magnetic field. In these cases, the presence of a magnetic field enhances the SEY reduction due to the additional spinning of the emitted electrons along the field lines within the grooves. Monte Carlo simulations and experimental measurement on TiN films, NEG films (activated or not) and un-coated copper and aluminium samples are exposed in [48]. Concerns about impacts on the impedance (grooves orientation along the beam orbit was prescribed) and on the energy dissipated by the circulation of the image current running on the ridge of the grooves were raised. The installation of two kind of grooved surfaces (millimeter scaled triangular and rectangular grooves reduced with a cutting tool) in a SPS electron cloud monitor at CERN showed a reduction by a factor of 2 and 4 of the electron cloud signal [57]. Nevertheless, this study highlights the limits of mechanical machining processes to obtain the small size and high aspect ratio features required for the SEY decrease.

Beside the accelerator-oriented studies, simulations and SEY measurement have been performed on surfaces engraved with arrays of micropores that bring insights on the effects of the surface microscale structuration on SEY.

Photolithography has been used to engrave a micro-porous array on the sample surface [71]. Several samples have been engraved with a micro-porous pattern with an aspect ratio around 0.3 (with diameter around 12 μm and depth around 5 μm). The porosity is defined as the ratio of the porous surface over the total surface of the sample, varied between 0.25 and 0.57. SEY measurement showed a strong influence of the aspect ratio of the pores and the surface porosity. This was in a good agreement with the results from Monte Carlo simulations. Phenomenological 2D modeling assuming normal incidence of impinging electrons was used as an input of an electron-tracking simulation. The trajectory of the emitted electrons from the bottom of the rectangular hole allowed the evaluation of the probability that an electron escapes from the dwell. The contribution of both, the 1^{st} generation of secondary electrons that escape directly from the hole, and the contribution of the 2^{nd} generation of secondaries, emitted after

the 1^{st} generation had been re-captured by the walls of the hole, were identified [72]. Numerical applications of this model exhibit that the contribution of the 2^{nd} generation was maximum for an aspect ratio between 0.5 and 1 and 15.6 % of the total SEY for an aspect ratio of the rectangular hole of 0.6. As the SEY contribution of the bottom of the hole takes the major part, simulations were run introducing an hybrid structure with both holes and nano-structuration of the bottom of the holes (groove or nano-porous) and showed a significant SEY decrease. The two-scale surface modification appeared like the effective way to decrease further the SEY of the surfaces.

A 3D model was proposed to simulate the SEY of micro scale porous surfaces [73]. It has been applied to electroplated microporous gold surface. Five microporous patterns have been designed with regular array of pores in the range of 16 μm to 40 μm in diameters and with aspect ratios in the range of 0.15 to 0.375. Results of the 2D, 3D models and the experimental SEY measurement were close. The difference between the 2D and 3D models remained below 10 %. The 2D model, which allows an analytical solution, is shown in figure 1.14 c).

Besides the array of micro pores, micro or sub-micro surface roughness can be produced by chemical treatments. For instance, a strongly 200 nm period dendritic surface was obtained by ion-texturing, exposing copper samples to an argon ion bombardment in a low-pressure environment [33, 74]. Another experiment involved the coating of a standard silver plating by a wet chemically etching process. A roughness of high aspect ratio has been created in the scale of microns. The surface was protected by a 2 μm overlayer of magnetron sputtered gold. A highly porous or sponge-like chaotic surface roughness with a distribution of protuberances ranging 1–5 μm in height and 1–2 μm in width was observed [75]. In both cases, the chemical process successfully resulted in the production of an anti-multipactor surface with a low SEY even after one year of air exposure underlining the interest for sub-micro features structuration.

In conclusion, the literature selection which has been presented in this paragraph shows the effect of the surface structural modification on the SEY reduction and consequently the positive effect on the electron cloud mitigation. Because the laser treatment allows to create various micro- and nano-structures, and because it could be scaled to industrial production, it appeared as a promising method of increasing the roughness by taking advantage of morphological modifications of the surface that traps emitted electrons. Additionally, by controlling laser power, a selective treatment would also be possible on complex elements in case of treatment-sensitive components, such as electrodes in beam position monitors [76]. The studies dedicated to this mitigation technique of electron clouds are presented in the next section.

1.3 Laser treatment as a SEY reduction technique

The tests undertaken at CERN in collaboration with the University of Dundee and the British Institute ASTeC STFC have shown that the surface roughening by pulsed laser light can be deployed to decrease the SEY of the surface facing the beam in particle

accelerators. The surface morphology is modified by increasing roughness at different scales. The treated surface traps electrons by a geometrical effect, thus attenuating the electrons clouds.

The principle of the laser-assisted surface structuration used with the purpose of SEY reduction in particle accelerators is described in this section as well as the main parameters of the treatment. A historic is presented about investigations performed on the effects of treatment parameters on relevant aspects of the surface application in UHV and particle accelerator such as SEY and electron cloud measurement, surface oxidation and vacuum compatibility at cryogenic temperatures and finally impedance. Previous works have already revealed constrains and potential limiting factors of the technology deployment which require a careful choice of the treatment parameters.

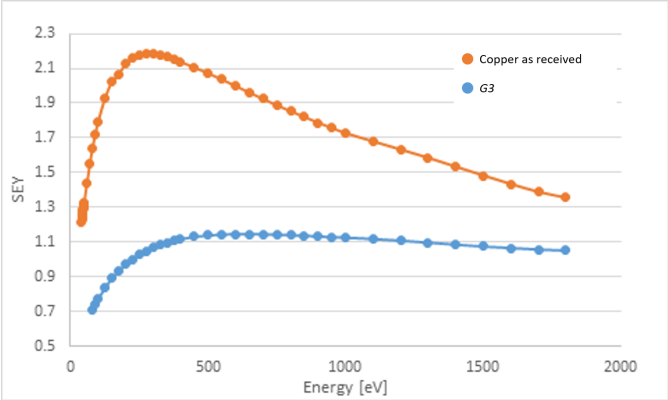

Figure 1.15: SEY curve as a function of the primary electron energy on an as received copper surface and on a laser-treated surface. The laser parameter used for the treatment so-called *G3*: Repetition rate 200 kHz, Pulse energy 25 μJ, Hatch distance 55 μm, Scan speed 15 mm.s^{-1}.

Principle and main parameters of the laser-assisted surface structuration
The laser surface structuring has been carried out with a pulsed laser focused on the surface of the sample. The laser has been coupled with the scanning head. It irradiates the sample following a given pattern (parallel lines in figure 1.16).

As shown in figure 1.16, the surface topography after the laser treatment is characterized by a trench pattern (generated by the scanned laser) covered by an in-homogeneous coral-like structure made of agglomerated nano-particles forming a sub-micrometric highly porous network.

The parameters of the surface laser-assisted treatments are:

- wavelength of the monochromatic light used (UV (332 nm), green (532 nm) or IR (1064 nm));
- duration of the pulse tau_P;
- pattern followed by the scanning head (two patterns have been mostly investigated: parallel rectilinear or perpendicular cross hatching), distance between adjacent linear lines ($Hatch\,distance$);

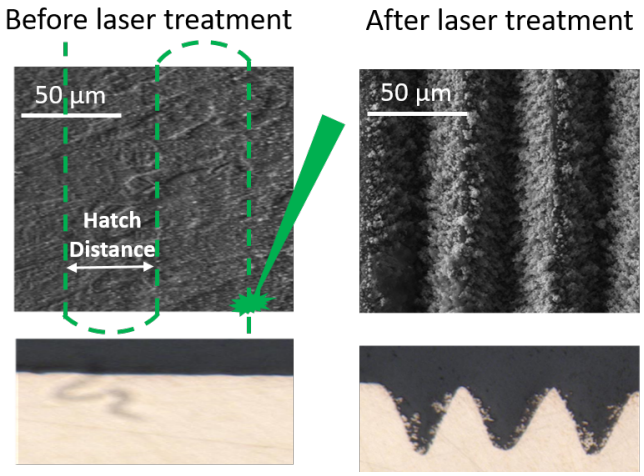

Figure 1.16: On the left, original surface top and cross section views, and scanning pattern of the laser head. On the right, surface after the laser treatment

- diameter of the laser beam ($Ø_{1/e^2}$);
- deposited energy on the sample is characterised by the energy of each pulse ($PulseEn$), the frequency rate ($Rep\,rate$) and the scanning speed ($Scanning\ speed$) of the head;
- atmosphere during irradiation (gas, flow, feeding setup).

Two scanning patterns have been compared: parallel rectilinear hatched (LH) and perpendicular cross hatched (CH) [77]. Although the SEY of the CH pattern is lower than the LH one, the CH treatment requires a twice longer processing time and the depth of the groove measured at the crossing points of the lines is also deeper. Therefore,linear pattern is preferred.

As illustrated in figure 1.17, the laser beam has a Gaussian shape defined by a diameter $Ø_{1/e^2}$ and a quality factor M^2.

The beam radius (and the related beam diameter $Ø_{1/e^2}$) is defined as the distance from the beam axis where the intensity drops to $1/e^2$ of the peak value. The fluence (energy density) distribution of each laser pulse is given by Gaussian spatial distribution.

$$F_{Pulse}(r) = F_{PulseMax}\, e^{\frac{-r^2}{2\sigma^2}} \tag{1.7}$$

where r is the radius from the center of the beam, σ is the standard deviation of the Gaussian pulse, defined as $1/e^2 = exp(\frac{-Ø_{1/e^2}{}^2}{2\sigma^2})$, $F_{PulseMax}$ is the maximum energy density for one pulse, defined as $PulseEn = 2\pi F_{PulseMax}\sigma^2$.

Therefore, the fluence of the laser pulse can be derived from the laser parameters as:

$$F_{Pulse}(r) = \frac{PulseEn}{2\pi\,\sigma^2}\, e^{\frac{-r^2}{Ø_{1/e^2}}} \tag{1.8}$$

The radial fluence profile of one laser pulse of 25 μJ for a spot diameter defined at $1/e^2$ of 52 μm is shown in Figure 1.17 as the blue curve.

The quality factor M^2 describes the divergence of the beam depending on the distance to the focal plan though the so-called Rayleigh length: [78]

$$z_R = \frac{\pi \, \text{Ø}_{1/e^2}{}^2}{4 \, \lambda \, M^2} \tag{1.9}$$

where λ is the wavelength of the laser. The diameter of the beam depending on the focal-depth z is then defined as:

$$D(z) = D_0 \sqrt{1 + \left(\frac{z}{z_R}\right)^2} \tag{1.10}$$

where D_0 is the diameter of the beam in the focal plane, for instance defined as $D_0 = \text{Ø}_{1/e^2}$

The smaller the beam diameter at the focal plane is, the larger is his divergence (see in Figure 1.17). It is also worth to note that the divergence is larger when the wavelength is longer.

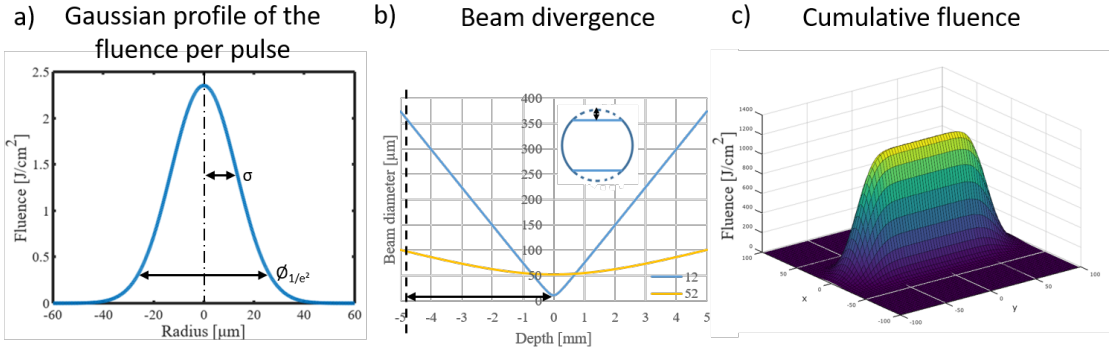

Figure 1.17: a) Radial fluence profile of one pulse of 25 μJ for a spot diameter of 52 μm at $1/e^2$ intensity. b) Illustration of the beam divergence. The beam diameter defined at $1/e^2$ is plotted as function of the focal depth for $D_0 = 12\mu$m and $D_0 = 52\mu$m. The inset represents the shape of the beam screen profile. The black arrows illustrate the maximum offset between the focused plane (on the curved part) and the flat part surface. c) Surface representation of the cumulative fluence over one line of treatment. The maximum cumulative fluence reaches 1200 J.cm^{-2}.

The overlapping rate in the direction of the treatment is specified by the scan speed and the repetition rate for a given beam spot size, whereas the overlapping rate for consecutive engraved lines is defined by the hatch distance.

Depending on the set of parameters chosen, the energy locally deposited to the sample varied. In order to allow comparison between the samples treated with different sets of parameters, one common figure of merit called cumulative fluence, has been defined as follows:

$$F_{Cumul}(x,y) = \sum_{i,\, nb\, of\, pulses} F_{Pulsei}(x,y) = \sum_{i,\, nb\, of\, pulses} F_{PulseMax}\, e^{-\frac{(x-x_i)^2+(y-y_i)^2}{2\sigma^2}} \tag{1.11}$$

The cumulative fluence represents the total energy deposited to a point during the full

duration of the laser treatment, taking into account the overlapping rate of the laser pulses. It is illustrated in figure 1.17 c).

Depending on the scanning pattern chosen for the treatment, in particular the distance between adjacent lines, *i.e.* the hatch distance, the average energy deposited to the sample can be defined as:

$$Sample\,Average\,Fluence = \frac{PulseEn \times RepRate}{Hatch\,Distance \times Scanning\,Speed} \tag{1.12}$$

The laser irradiation can create highly organised surface microstructures transforming reflective metals to absorbor of electromagnetic radiation on a large range of wavelengths [79, 80] or give to the surface an high wettability [81, 82]. The application of the low reflectivity surface, in general high rugosity surface are plenty [83]. Nevertheless, this section is focused on the technology application in the framework of the electron cloud mitigation in particle accelerators. The challenges faced and the results achieved are presented.

SEY measurement on laser-treated surfaces

The SEY measurement of metal surfaces modified with a nanosecond pulsed laser irradiation, leading to the formation of highly organised surface microstructures were first reported in 2014, in [83]. The laser treatment was performed under an argon atmosphere, on copper with a green laser (532 nm) and on aluminium and stainless steel with an infrared laser (1064-nm-wavelength). The scanning pattern was a grid along two perpendicular directions. Treated and untreated samples were conditioned by a bombardment with 500 eV electrons to a dose between 3.5 10^3 and 2.0 10^2 C.mm^{-2}. SEY curves were measured for all samples in four conditions: with and without laser treatment and with and without conditioning. It turned out that the treatment reduced the SEY of the copper, aluminium, and stainless steel from the as-received values of 1.90, 2.55 and 2.25 to 1.12, 1.45 and 1.12, respectively after the laser treatment. The later are lower than the SEY values of the conditioned untreated surfaces. After conditioning, the SEY of the treated samples was further reduced to 0.76–0.78 for all three treated metals. These results are shown in figure 1.18.

The decrease of SEY after treatment has been observed in the primary energy range of 50-1000 eV [83], and in the range of 100-1700 eV at CERN [77]. Later, the reduction of SEY at low energy below 50 eV has also been measured [84]. The aging effect on the SEY after one year, in dry air, have been measured as an increase of 0.1 compared to the original sample, for all impinging energies. This was not judged detrimental [77].

The effort has been focused on the copper surface. In [85], copper samples have been irradiated in air, by a nanosecond pulsed laser operated at basic infrared (IR) (1064 nm) and third harmonic ultraviolet (UV, 355 nm) wavelengths, the pulse duration were 70 and 25 ns, respectively. Various repetition rates ranging from 2.5 to 100 kHz and various scanning speed have been used leading to different deposited energy on the samples. Top views and cross section SEM views have been performed and SEY have been measured. The results are compared with measurement made at CERN and given in the literature

in the appendix B.

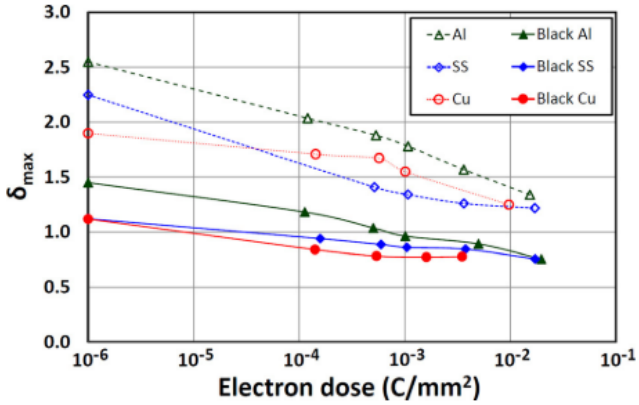

Figure 1.18: SEY as a function of the electron dose during conditioning. "Black" stands for laser-treated surfaces. The point at the dose of 10^{-6} C.mm^{-2} can be considered as the point before conditioning [83].

Electron cloud measurement on laser-treated surfaces

Although the measured SEY of the laser-treated surface was below the calculated electron cloud threshold, validation of the effect on the electron cloud had to be performed.

This was first done at room temperature, in the electron cloud monitors (ECM), installed in the SPS, LSS 5. Liners were installed in two custom-made SPS chambers, installed in a dipole field, at room temperature. One has been treated at Dundee University, the other has been treated by STFC with 532 nm wavelength and 12 μm diameter and UV 355 nm 15 μm diameter laser parameters, respectively. The electrons created in the chamber are collected by the grid located behind the perforated beam screen (7 % transparency). The beam characteristics were the followings: 26 GeV proton beam, 4*72 bunches, 25 ns bunches spacing and a bunch charge of 1×10^{11} protons. Thanks to the laser treatment the electron cloud signal (deduced from the current measured on the grid) has been reduced by 4 orders of magnitude, the electron cloud was prevented, in both chambers [77]. The first results were obtained during the Machine Development (MD) run in June 2016. The sample from Dundee University remained in the SPS for long-term studies, similar positive results were obtained during the MD run of July 2017.

At CERN, the COLD bore EXperiment (COLDEX) test bench installed in the SPS, LSS 4, allows to validate the results at cryogenic temperature in the range of 10 to 60 K. The COLDEX chamber is a perforated tube which allows electrons to escape and be collected. In order to laser-treat the 2.2-m-long beam screen with an inner diameter of 67 mm, the chamber has been divided in nine 245-mm-long sections installed in a gear-driven rotary stage mounted on a linear stage. This treatment was performed at Dundee University by a laser beam of 13 μm diameter, under a nitrogen flow of 3 l/min. The sections were welded at CERN [62]. The experiments were carried out during several MD and have confirmed the full suppression of the electron cloud. No heat load was measurable within the detection limit (100 mW/m). Nevertheless, the welds needed for the assembly did not allow conclusions about impedance losses. The mitigation effect of

the surface was also demonstrated after several thermal cycles from room to cryogenic temperature.

The efficiency of the laser treatment to prevent the electron cloud in a vacuum chamber calls for the development of a dedicated robot able to treat the surface inside a tube.

Oxidation states of laser-treated surfaces

First studies exhibited that the surface chemistry is sensitive to the atmosphere used during the laser treatment. For instance, XPS measurement revealed the presence of CuO oxide layer on samples treated in air [85]. At CERN, a study has been dedicated to analyse the consequences of the gas environment on the chemical composition and furthermore to assess the influence of the oxidation states of the surface on the surface morphology (through observations by SEM) and on the SEY measured at room and cryogenic temperatures [86]. The copper samples were treated at atmospheric pressure either in air or by irradiating the samples through a glass enclosure, which was filled with argon or nitrogen. The results were also compared with samples treated in air before and after thermal annealing (heating process, during 4 h, at 300°C, in vacuum, no air exposure after the treatment).

SEM observations exhibited differences depending on the gas used for the treatment: more particles have been observed on the top of the surface treated in air (before or after thermal annealing, no visible change in the surface morphology were observed after the thermal annealing) than on the surface of the samples treated in inert gas, argon or nitrogen.

The chemical composition has been measured by XPS. Sample treated in air presented a strong oxidation spectrum showing the presence of CuO on the surface. After annealing, the spectrum of the sample was close to the one of a sputtered-cleaned copper. The annealing triggered the chemical reduction of the CuO surface to Cu_2O illustrated by a strong decrease of the oxygen content. The spectrum of the sample treated in argon also suggests oxidation of the surface (the presence of Cu_2O and hydroxide surface groups was detected) which could be explained by reactions with impurities in the inert gas during laser treatment or by post-treatment reactions in air, if the surface is not passivated. The sample treated in nitrogen displayed an almost entirely metallic copper state.

The SEY measurement showed that samples treated in nitrogen exhibit the lowest and more stable SEY values. For the sample treated in air, the SEY could not be precisely measured at low temperature due to the thickness of the oxide which charged up during SEY measurement. Indeed, at low temperature, the surface oxide layer of air-treated samples charges upon electron exposure, leading to fluctuations in the SEY. This charging effect is due to the presence of copper oxide which behaves as insulator at low temperatures. After chemical reduction of the CuO surface to Cu_2O by thermal annealing, the SEY at room temperature decreased but the dispersion of the SEY at low temperature was still observed. The Cu_2O seems be to preferable but still causes charging effect at low temperature.

As a consequence of the study [86], the treatment in inert gas atmosphere nitrogen that presented better results at room and cryogenic temperatures has been recommended.

After treatment in air, a tentative trial to remove the copper oxide by chemical treatment by immersion in MC20 solvent (without ultrasonic cleaning) was also performed. SEM analysis revealed that the cleaning treatment detached the particles covering the surface due to either the mechanical action of the fluid on the surface or the dissolution of the oxide. Consequently the dispersion and the charging effect at low temperatures was greatly decreased but SEY increased due to lower roughness [87].

Vacuum compatibility of the laser-treated surfaces at room and cryogenic temperature

Static and dynamic vacuum behavior due to the increase of the roughness the surface have been investigated at room and cryogenic temperatures. At room temperature, pumpdown curves (pressure decrease versus time) revealed a lower decrease of the pressure over the time due to the presence of roughness and open porosities which increase the effective surface [62]. After 10 hours pumping, water outgassing was measured to be 30 times higher than the reference unbaked, untreated copper [62]. Other measurements resulted 100 times higher values than the plain copper [77]. The large uncertainty of the outgassing measurement does not permit to precisely characterize the effective surface of the treated sample compared to the geometric flat surface. Although the water outgassing could be an issue it has not been judged too detrimental to use the surface in an accelerator [77].

In the vacuum system of accelerators, pumping of the residual gas H_2, CO, CO_2, H_2O, and CH_4 is ensured by the absorption on the cryogenic walls if the temperature is low enough. The molecules are either physisorbed or condensed depending on the thickness or the number of layers of gas molecules present on the surface. Nevertheless, the vacuum stability must be insured regardless the temperature fluctuations of the beam screen surface. The vacuum transient and pressure increases due to desorpion of gas species consecutive to the fluctuation of the temperature have been studied for laser-treated surface thanks to thermal programmed desorption (TPD) measurements. In the COLDEX test bench, the desorption spectrum showed a peak of H_2 at 15 K, peaks of argon, CO at 20 K, $C0_2$ at 63 K, similar to bare copper spectrum. At 10 K, the gas composition was stable. At 60 K, only H_2 was not physisorbed [62]. More precised TPD measurement have been performed in laboratory for argon [88] and for CO and CH_4 [84]. Measurements were consistent for the three species: compared to the untreated copper surface, the gas desorption are spread over a broad temperature range. Whereas the desorption peaks of an untreated copper sample are narrow (4 K FHWM) and located around 25 K, the peaks observed for the laser-treated surface is located between 40 and 80 K for argon and between 50 to 100 K for CH_4 and CO.

The beam screen of the LHC is currently operating below 20 K, the range of temperature is not covered by the studies [84,88], but considering their saturated vapor pressure curves, desorption of the mentioned species is not expected. Based on the studies per-

formed, the implementation of the laser-treated surfaces, in UHV environment, below 20 K do not show detrimental drawbacks. Nevertheless, for cost reason and available cooling budget, operating temperature of the cold bore and the beam screen of future machines or updates of LHC has been proposed to be increased between 40 and 60 K. Within this range of temperature, finding temperature intervals where vacuum transients can be excluded for all gas species condensed on the laser-treated surface might be a difficulty [84].

Impedance of the laser-treated surfaces

It has been explained in section 1.1.1, that the circulating image current in the conductive layer, the surface impedance can have an effect both on the beam stability and on the heat deposited in the conductor. The influence of morphology modifications due to the laser surface treatment on the impedance has been evaluated in this section.

An alternating electrical current flows mainly close to the surface of the conductor. It decreases exponentially from the surface. The skin depth, δ, is defined as the depth where the current density is $1/e$ of the nominal value on the surface. It is a function of frequency of the alternating current and copper resistivity. It is given by:

$$\delta = \sqrt{\frac{2\rho(T)}{\mu_0 \omega}} \tag{1.13}$$

where $\rho(T)$ is the temperature dependent resistivity and μ_0 is the vacuum permeability.

At room temperature, the skin depth is 3.2 μm at 400 MHz and 738 nm at 7.8 GHz. At cryogenic temperature, the skin depth is 33.3 nm at 400 MHz and 19.2 nm at 1.2 GHz. The characteristic dimensions of the grooves are typically several tenths of micrometers whereas the size of the particles is micrometric and the total thickness of the particle layer is typically around 10 μm. All these dimensions are much larger than the skin depth.

Analytical models describing the influence of the grooves (and their direction compared to the image current flow) were used to evaluate the influence of the laser treatment on the impedance and subsequently on the beam stability and Joule losses [89, 90].

The effect of traversal grooves with respect to the direction of the current on the imaginary part of the longitudinal impedance have been evaluated thanks to the model used for rectangular cross sections cavities: [91, 92]

The formula used in [89] is

$$\frac{\Im(Z_L)}{n} = \Im(Z_L)\frac{f_{rev}}{f} = \frac{Z_0\, w_{groove}\, d_{groove}}{2\pi R b} \tag{1.14}$$

where the intrinsic impedance $Z_0 = 120\pi$, w_{groove} is the groove width and d_{groove} is the groove depth.

It is worth noting that the longitudinal (and consequently also the transverse) impedance increases linearly with the depth of the grooves. For such a longitudinal impedance, the additional imaginary part of the transverse impedance due to the grooves and the surface roughness is estimated to be 80 kΩ/m while the LHC budget is around 25 MΩ/m

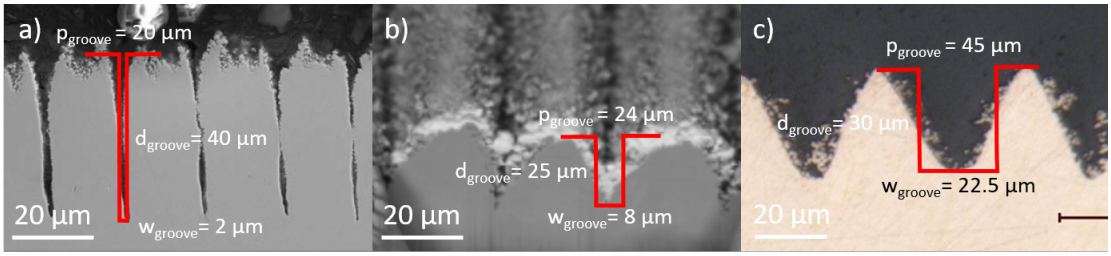

Figure 1.19: Cross section views of laser-treated surface with different parameters resulting in different morphologies and characteristics of the grooves. The period, depth and width of the assimilated rectangular pattern are illustrated a) Sample treated in 2015 used as a reference sample in [89]. b) Sample treated with the so-called *COLDEX* parameters used as a reference sample in [77, 93]. c) Sample treated with the so-called *D7* parameters defined in section 2.2.1.

in both direction horizontal and vertical (*i.e.* 0.4 % increase). The impact of the laser treatment on the beam stability seems to be reasonably low [89].

It is worth noting that the imaginary impedance is proportional to the groove cross-section areas [91]. In [89], the methodology was applied to the surface geometry represented in figure 1.19 a), The morphologies obtained with other laser treatments, so-called *COLDEX* and *D7* shown in 1.19 b) and c), respectively, lead to area of the grooves and subsequently transverse impedance which are 2.5 times and 12.65 times respectively, larger than the one used in [89].

As a conclusion of the approach, the lowest the material ablation is during the laser treatment, the lowest is the impact of the laser treatment on the beam stability criteria.

As presented in equation 1.2, the heat load induced by the beam current is proportional to the square root of the real part of the impedance of the beam screen surface, the surface resistivity. Surface resistance measurements have been performed at 7.8 GHz at room temperature, on two samples treated with different scanning speed (consequently different fluence and different morphologies). Several orientation of the grooves with respect with the electric current have been measured. No trend can be extracted from the measurement of these dependencies. The samples exhibited an increase of the surface resistance by a factor of 4-4.5 compare to the untreated sample independently on the morphology or the orientation [94]. At CERN, measurements on similar laser-treated surfaces gave a factor of 1.5 [89].

A phenomenological model has been used to calculate the correction coefficient between the smooth surface and the rough surface resistance, respectively, R_{smooth} and R_{rough} [89].

$$R_{rough} = K_{HJ} \times R_{smooth}(RRR, T) \tag{1.15}$$

$$K_{HJ} = 1 + \frac{2}{\pi} tan^{-1}\left(1.4\left(\frac{R_q}{\delta}\right)^2\right) \tag{1.16}$$

where K_{HJ} is the coefficient of correction, R_q is the rms-roughness of the surface, δ is the skin depth as defined in equation 1.13.

Nevertheless, Hammerstad and Jensen model is limited to low RMS-roughnesses and

low frequency. For highest roughness or frequency values, an increase by a factor of 2 could be expected [95].

The surface resistance of laser-treated copper was measured at cryogenic temperature using the superconducting quadrupole resonator (QPR) and compared to a smooth sample [93]. The setup allowed the measurement with an electric field perpendicular and parallel to the grooves, at three frequencies (400, 800 and 1200 MHz) and in a temperature range between 2 and 15 K. After a laser treatment in air, the surface morphologies was made of 24-μm-spaced and 35-μm-deep grooves. For both configurations (parallel or perpendicular orientation), the surface resistance is constant on the temperature range and increase with the frequency as a function of $f^{\frac{2}{3}}$. The normal skin effect varies proportional to $f^{\frac{1}{2}}$. This difference might be the result of the particles covering the surface or a change of conductivity due to the oxide layer. A clear difference was measured between the surface resistance of the patterned surface where the current circulated along the grooves (the resistance is then close to the untreated copper) and when the current circulates perpendicularly to the grooves. In the later case, the surface resistance increased by a factor of 4-5 compared to the smooth sample. The characteristic dimension of the grooves is much larger than the skin depth. The electrons travelling through the surface are following the profile of the grooves when crossing the grooves perpendicularly. The distance they have to cover is longer. This explains why the resistance measured is higher.

Assuming that the surface resistance of the copper surface increases by a factor of 5, the dissipated Joule power increased by a factor of $\sqrt{5}$ (see equation 1.2). The heat deposition due to the impedance could rise from 0.9 W/m to 1.7 W/m. The heat load deposition in Q1 due to the electron cloud is estimated to be 2.3 W/m for a SEY of 1.1 [93]. Although the laser treatment increases the heat deposition due to the impedance, the suppression of the electron cloud should result in a reduction of the overall heat load.

In the case of the interaction region 8 (IR8) of the HL-LHC, for example, it can be estimated that the power from wake losses would increase up to about 65 W. With a SEY of the inner surface of the beam screen lower than 1.1, the power dissipated due to electron cloud is estimated to be 120 W. The total dissipated power (*i.e.* 185 W) would remain lower than the local estimated ultimate cryogenic capacity, *i.e.* 195 W. Nevertheless, it appeared that the counter-effect of the increase of impedance due to the morphology modification has a strong effect and reduces the margin. The depth of the grooves has to be carefully monitored and maintained as low as possible.

As a conclusion, the measurement and calculation made on the impedances of the laser-treated samples are a strong motivation to develop a treatment system engraving grooves parallel to the beam and to define a maximum groove depth.

1.4 Description of the open challenges

The implementation of an *in-situ* laser treatment of the inner surface of the beam screen is currently under development at CERN for the mitigation of the electron cloud. The laser irradiation generate two-scale morphology modification of the surface: 50-μm-period sinusoidal grooves covered by a population of sub-micrometric particles. It efficiently reduces the SEY by geometric effect below the threshold of the electron cloud build-up.

Nevertheless, the implementation of the laser-treated surface already appears like a compromise between mitigating the electron cloud, and, as a counterpart, increasing the heat load because of the impedance enhancement due to the surface roughness. Both characteristics are linked to the morphological properties of the surface. It also appears that the chemical transformations of the surface during the laser treatment could give rise to critical performances issue on the behavior of the surface at cryogenic temperatures. The following thesis aims at assessing the mechanical integrity and suitability of such surface treatment for an application in accelerators operating at cryogenic temperature. The study is oriented along three axes:

→ Morphological and chemical transformations of the surface under laser irradiation.
How does the laser treatment change the morphology and chemistry of the surface, at the scale of the grooves? and at the scale of the particles? How do the particles look like?
How does the laser treatment create the dust?

→ Mechanical characterisation of the treated surface.
What is the bending strength of the particles on the surface?
Will the particles detach under mechanical solicitations? In a cryogenic environment?

→ Application of the treated surface in accelerator environment.
How does the morphology modifications change the SEY? Are all the particles necessary to reduce the SEY of the surface? The decrease of SEY is based on material ablation: aspect ratio of the grooves, particles present on the surface
The issues linked to the presence of dust and particle detachment are also investigated: Do the particles also detach under mechanical solicitation/vibration during the operation of the accelerator? How to extract the dust without damaging the particles? Can the vulnerable particles be removed after laser treatment and before operation of the accelerator while ensuring good SEY performance? Can the interaction between the detached particles and the proton beam be detrimental to the accelerator operation? Would a magnetic quench deteriorate the performances of the beam screen treated surface?

Chapter 2

Materials and methods

Abstract

The chapter comprises the presentation of a selection of thermal and mechanical properties of the material used in the study, the description of the laser treatment and the analysis methods.

In the first part, as a prerequisite for investigating the impact of particle impacting the treated surface on the integrity of the particle attached on the surface, the energy required to break the physical bond between a particle of re-deposited material and the surface is evaluated. Three mechanical properties are studied: stress-strain curves, to compute the deformation energy of at break per unit volume; the toughness evaluated on macroscopic or microscopic samples and finally the impact toughness. From these analyses and for a typically observed bond, the energy of failure is evaluated at 1.6×10^{-11} J. The effects of temperature and strain rate are also briefly evaluated.

The second part of the chapter explains the sample preparation. The laser treatment is carried out on flat coupons for laboratory measurements, or robot-assisted *in-situ* on a beam screen. The parameters of laser treatment are presented. 10 ps long pulsed irradiation from a laser of 532 μm wavelength, 52 μm diameter at an energy of the order of 20 μJ causes the partial ablation of the material. About 50 μm wide grooves are formed. As not to alter the surface impedance detrimentally, their depth must be limited to 30 μm. To simulate the cooling cycles to cryogenic temperatures that the surface of the beam screen of superconducting magnets must undergo during its lifetime, the flat samples were subjected to 10 thermal cycles carried out in the laboratory between room temperature and 70 K.

The surface analysis techniques are presented in the last part of this chapter. Microscopic surface analysis methods, such as cross-sectional or SEM observations are dedicated to the analysis at the groove scale, Immersion of the sample in an ultrasonic bath is used as a method of particle extraction. It allows to detach the particles from the surface treated by laser without altering its chemical composition. Detached particles, in suspension in the ultrasonic bath, are collected by filtration. The objective is twofold: first, to assess the amount of particles and their size distribution and second, to analyze

by SEM and SEY measurement the surface of the sample with a lower particle density. Automatic particle counting based on SEM images are used for a qualitative description of the detached particles Physical and chemical surface analysis methods -SEY and XPS measurements- are briefly presented.

TEM, FIB tomography and test set ups for the evaluation of particle adhesion on treated surfaces are presented in the dedicated sections, 3.2, 3.4.3 and 4, respectively.

Résumé en français

Le chapitre s'articule en trois parties : la description de certaines propriètés du matériau utilisé dans l'étude, la description du traitement laser de la surface des échantillons et enfin les méthodes déployées pour leur analyse.

La première partie du chapitre présente les propriétés thermiques et mécaniques du cuivre électronique sans oxygène (noté Cu-OFE), le matériau couvrant la surface interne du système à vide de l'accélérateur des particules LHC. L'attention a été particulièrement portée sur l'évaluation de l'énergie nécessaire à la rupture de la liaison physique entre une particule de matière redéposée au cours du traitement et la surface. Trois propriétés mécaniques ont été étudiées : les courbes contraintes/allongement qui permettent l'évaluation de l'énergie de déformation jusqu'à la rupture par unité de volume, la ténacité évaluée sur des échantillons macroscopiques ou à l'échelle microscopique et enfin la résilience. A partir de ces analyses et pour les géométries typiquement observées pour une liaison entre la surface et une particule, l'énergie de rupture est évaluée à 1.6×10^{-11} J. Les effets de la température et du taux de déformation ont aussi été brièvement évalués.

La préparation des échantillons traités par laser dans le cadre de l'étude menée au CERN est exposée dans la suite du chapitre. Le traitement laser a été réalisé sur des coupons plans pour les échantillons destinés aux mesures en laboratoire ou, assisté d'un robot, sur une section d'un écran de faisceau tubulaire dont la première réalisation de 2.2 m a été reçue au CERN en Décembre 2019. Les paramètres du traitement laser sont présentés. L'irradiation de la surface de cuivre par des impulsions de 10 ps d'un laser de longueur d'onde 532 μm, de diamètre 52 μm à une énergie de l'ordre de 20 μJ provoque l'ablation partielle du matériau creusant des sillons d'une largeur d'une cinquantaine de micromètres et dont la profondeur doit être limitée à 30 μm pour ne pas dégrader l'impédance de la paroi. Pour simuler les cycles de refroidissement aux températures cryogéniques que doit subir la surface de l'écran de faisceau des aimants supraconducteur pendant sa durée de vie, les échantillons plans ont été soumis à 10 cycles thermiques réalisés en laboratoire entre la température ambiante et 70 K.

Les techniques d'analyse de surface sont présentées dans la dernière partie de ce chapitre. L'immersion de l'échantillon dans un bain à ultra-sons a été utilisée comme une méthode d'extraction de particules. Elle permet de détacher les particules de la surface traitée par laser sans altérer sa composition chimique, de mettre les particules en suspension et de les récupérer après filtration. L'objectif est double : d'une part, évaluer

la quantité des particules et leur distribution en taille, et d'autre part, analyser par MEB et mesure SEY la surface de l'échantillon avec une densité de particules moindre. Les méthodes d'analyse de surface microscopique, physique et chimique, telles que les observations en vue en coupe ou au MEB, le comptage automatique de particules, et les mesures de SEY et XPS, sont brièvement présentées.

La Microscopie Electronique par Transmission (MET), la tomographie assistée par érosion ionique ainsi que les essais mis en place pour l'évaluation de l'adhésion des particules à la surface sont présentés dans les sections 3.2, 3.4.3 et 4, respectivement.

2.1 Literature review on materials thermal and mechanical characteristics

To comply with impedance requirements [4], the inner surface of the beam screens is made of Oxygen-Free Electronic (OFE) grade of copper which aims to minimise resistive losses of the image current circulating in the beam screen, as described in section 1.1.2. Indeed, its Residual-Resistivity Ratio (RRR), *i.e.* the ratio between the resistivity at 273 K and the one at 4 K is equal to 100. In view of an application of the laser treatment to the accelerator component, this study was thus performed on OFE copper.

An overview of the properties of the OFE copper are presented in the appendix A. The thermal properties justifying the choice of the sample temperature for the experiment carried out in this thesis are presented in the following.

2.1.1 Thermal properties of Oxygen-Free Electronic (OFE) copper

The thermal dilatation as a function of the temperature is plotted in figure 2.1. It can be seen that 94 % of thermal expansion is reached at 70 K. The experiments made at cryogenic temperature in the framework for this thesis, have been performed at 70 K to be handled by liquid nitrogen.

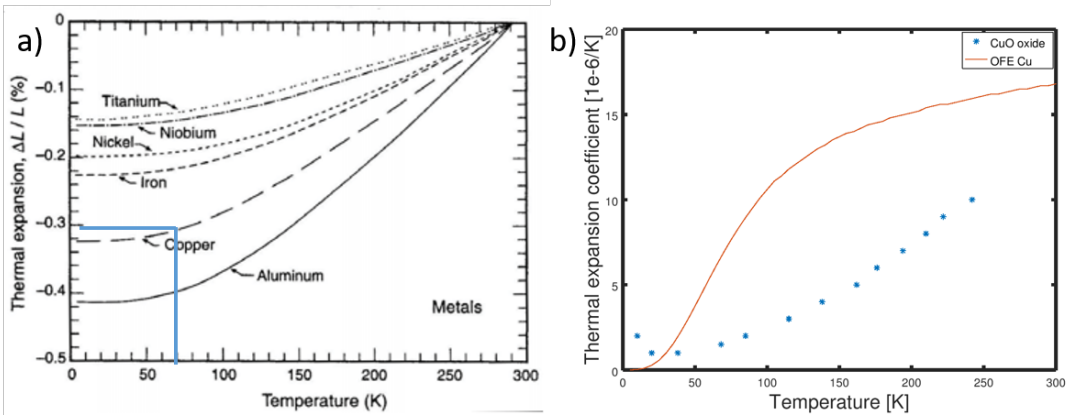

Figure 2.1: a) Thermal expansion compared to the room temperature as a function of the temperature for OFE copper [96]. b) Thermal expansion coefficient as a function of the temperature for OFE copper [97] and CuO oxide [98].

The microscopic observations in section 3.2 revealed oxide layer between the particles and the bulk. The thermal expansion coefficient of CuO oxide [98] and OFE copper [97] are compared in figure 2.1 b). A difference of thermal expansion between copper and the oxide layer may generate stresses in the bond between the particles and the bulk which could reduce the adhesion of the particles on the surface. That point motivates the choice to perform mechanical characterisation of cryogenic temperature, or one samples which have been submitted to thermal cycles to mimic the constrain that the surface undergo in the LHC.

2.1.2 Mechanical bond between the particles and the local surface

This section is dedicated to the evaluation of the dissipated energy in the fracture during the detachment of the particles from the grooved surface. The analysis is based on microscopic observations and materials properties.

Microscopic observations

To evaluate the volume of the material which undergoes mechanical stress during the detachment of the particle from the surface, assumptions on the material and the geometry of the connection between the particle and the surface have been done based on microscopy observation (further developed in section 3.2). It has been assumed that most of the stress is localized at the interface in between the particle and the surface.

The corresponding volume is estimated based on the microscopic observation to the circular section of the contact and the height of 1 μm. It gives:

- refined grained OFE copper;
- area fracture = 0.44 μm^2;
- volume undergoing plastic deformation= 0.44 μm^3.

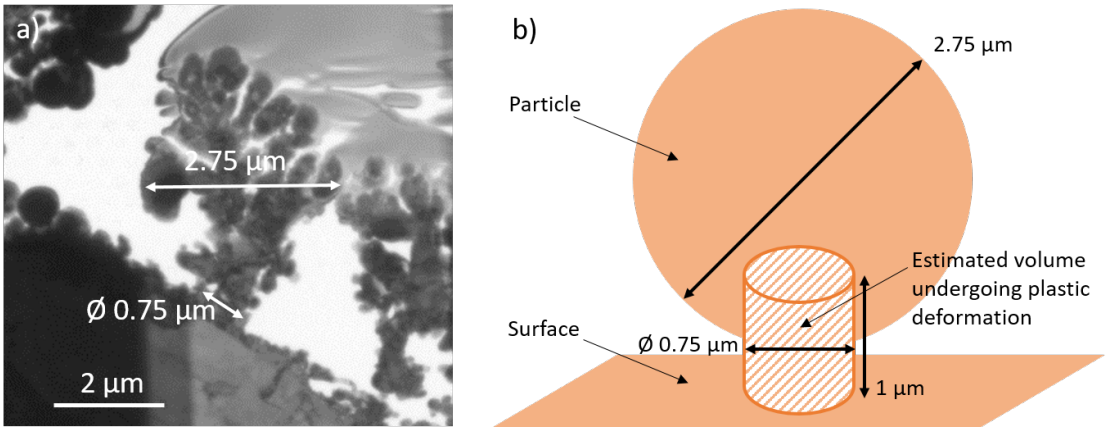

Figure 2.2: a) Bright field TEM image of a particle attached on the near surface. Other images can be seen in section 3.2 b) Model of the connection between the particle and the surface.

Although the microscopic observations in section 3.2 revealed oxide layer between the particle and the bulk surface, the material properties of OFE copper are presented in this section, as a simpler approach.

Material toughness

The material toughness is the ability of a metal to deform plastically and to absorb energy in the process before fracture. The evaluation of the plastic energy absorbed before the rupture has been done based on the strain-stress curves of the material. Two rupture modes have been considered: tension and compression. The area under the curve defined the energy absorbed by a given volume (in $J.m^{-3}$).

Figure 2.3 presents the stress-strain curves for annealed OFE copper for a tensile test and a compression test. The effect of the strain rate, has also been considered comparing quasi-static tests with a curve obtained in high strain compression on Hopkinson bars [99].

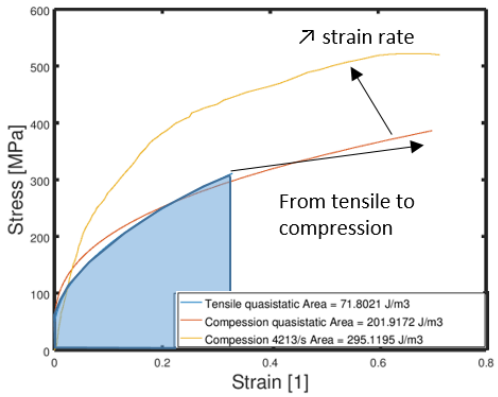

Figure 2.3: Strain stress curves of annealed OFE copper illustrating the effects of the strain rate (quasi-static *vs* high strain rate (about 4000 s^{-1})) and of the rupture mode (tension *vs* compression) [97, 99]. The area under the curve calculated for each case is indicated in the legend box.

The material toughness depending on the rupture mode and the strain rate, estimated based on figure 2.3 can be summarised up as it follows:

- traction, quasi-static: 72 $J.m^{-3}$;
- compression, quasi-static: 202 $J.m^{-3}$;
- compression, high strain rate deformation: 295 $J.m^{-3}$.

The increase of the strain hardening coefficient has been observed when the specimens were compressed with a higher strain rate. Up to 1 s^{-1} the strain rate effects are visible. Numerical modelling was based on Johnson Cook hardening model identification of the strain rate and temperature dependency based on the experimental data. Measurement data from Hopkinson bars for compression and test deforming set up based on electromagnetic forces for tensile test. Coefficients of the strain rate sensitive Johnson Cook model have been identified, these coefficients are given in the appendix A used in laser induced shock waves simulations in section 4.2.3.

The energy necessary to the fatal damage of such a volume of copper is estimated to be 3.15×10^{-11} J considering a quasi-static traction That is a conservative approach, in

case of high strain compression the amount of energy that the volume can absorb rises up to 1.3×10^{-10} J.

It is worth noting that these results are based on annealed copper at room temperature.

The effects of the micro-structure, *i.e.* the grain size, and the effects of the temperature are taken into account in the following.

The grain size effect on the tensile strength has been evaluated in [97] and [100], via comparison between annealed cold worked which exhibit a smaller grain size. The smaller the grain size is, the higher is the tensile strength. In figure 2.4, it can be seen that for a given temperature the tensile yield increases as the cold work percent increases, but the maximum elongation decreases. Therefore, the energy of the fatal damage of the volume decreases. For instance, at room temperature. the energy is divided by a factor of 3. For half hard cold work material, the energy of the fracture of a particle is 1.15×10^{-11} J.

The effects of the temperature have also been evaluated from the curves stress-strain, in figure 2.4. For a given grain size, when the temperature decreases from 295 K to 4 K the tensile yield strength increases as well as the elongation. Therefore, the energy which can be absorbed before the fracture is higher at low temperature.

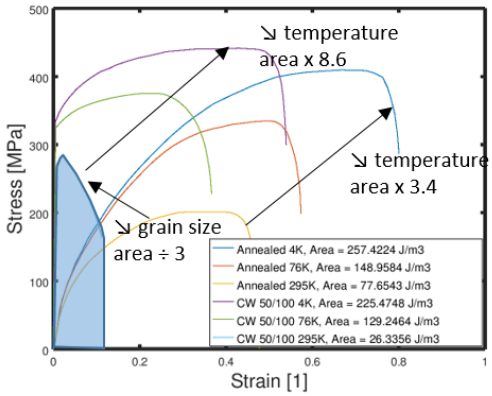

Figure 2.4: Strain stress curves on C10400 copper of a tensile test. The effects of grain size (via comparison between annealed and cold work 50 % copper) and the temperature (at 4 K, 76 K and 295 K) are illustrated. The area calculated under the curves are indicated in the legend box. Experimental data from [97, 100].

As a conclusion of the analysis of the effects of the mode of rupture, the strain rate and the temperature, it appeared that assessing the detachment of the particles in tension, quasi-static, at room temperature is a conservative approach compared to dynamic compression, at croygenic temperature. Indeed, under the mentioned conditions the energy required for the fatal damage of the copper volume is minimum. This information has to be remembered when comparing the solicitations during the mechanical characterisation of the treated surface, in chapter 4.

Fracture or notch toughness

Sharp angles are observed at the surface of the bulk which can trigger crack formation.

The notch toughness has to be taken into account, as it is the ability of the material to absorb energy in the presence of a flaw. The material develops plastic strains in the region near the crack tip as the yield stress is locally exceeded. However, the amount of plastic deformation is restricted by the surrounding material remaining elastic. The fracture toughness, or notch toughness, is an indication of the amount of stress required to propagate a pre-existing flaw. A parameter called stress-intensity factor (K) is used to determine the fracture toughness of most materials, it depends on the mode of fracture opening. The mode I, corresponding to a tensile stress normal to the plane of the crack is considered, it also depends on the crack size and the structural geometry.

The R-ratio curve is used to determine the value of the stress intensity factor on copper macroscopic samples as shown in figure 2.5 a) [101]. Based on this curve, the critical stress intensity factor, $K_{I\,c}$, has been evaluated at 40 MPa.m$^{1/2}$.

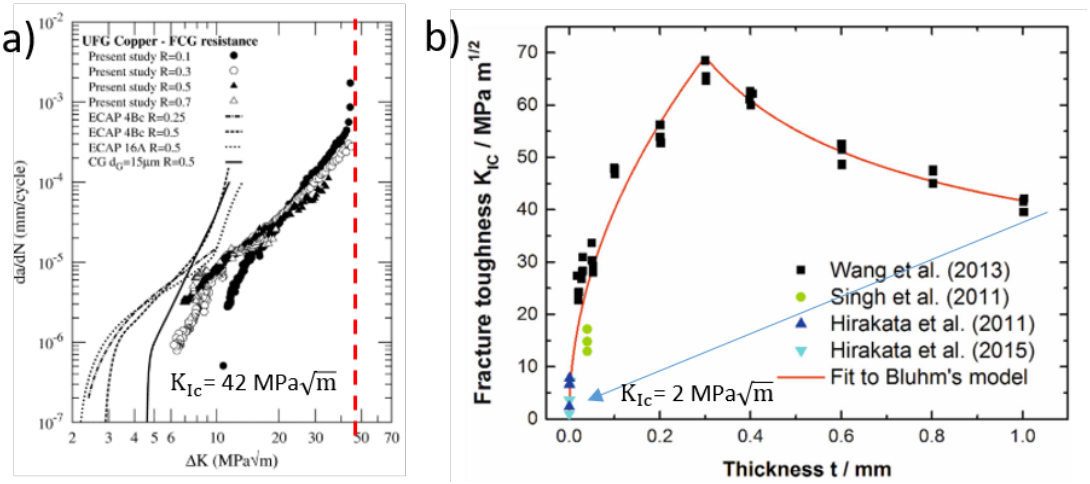

Figure 2.5: a) Macroscopic specimen, after [101]. b) Nanoscale effects: effect of the thickness of the nano-film specimen: plane strain vs plane stress, after [102].

At macro-scale, for thick samples, in plane strain condition ($E' = E$), the strain is constrained by the thick surrounding body), the fracture toughness of metallic material increases when the sample thickness decreases. For a thinner sample, in plane stress condition (absence of stress in thickness direction) the fracture toughness decreases with thickness. Both of these trends are illustrated in figure 2.5 b).

The effects of the thickness of the freestanding copper nano-films on fracture toughness have been measured by [102] on high purity copper films deposited by electron beam evaporation. The thickness was in between 800, 500 and 100 nm, the fracture toughness was estimated on the basis of the R-curve concept to be respectively 1.22, 6.63 and 2.34 MPa.m$^{1/2}$.

Fracture toughness can be used to calculate the maximum stress that a material flaws of a given size can sustain [102, 103].

The energy release during the propagation of the cracks can be estimated, in case of metallic structural material with plastic deformation by the critical strain energy release

rate for fracture is given in equation 2.1, [104]:

$$G = \frac{{K_{I\,c}}^2}{E} \tag{2.1}$$

where, G is the critical strain energy release, $K_{I\,c}$ is the critical stress intensity factor and E is the Young Modulus.

In plane stress condition, the Young modulus has to be replaced by:

$$E' = \frac{E}{1-\nu^2} \tag{2.2}$$

where, ν is the Poisson coefficient.

With a $K_{I\,c}$ of 40 MPa.m$^{1/2}$, the energy fracture for a standard particle would be estimated to be 6×10^{-9} J. Taking into account the effect of nanoscale morphology, the value of the energy fracture for an observed particle would be estimated to be 1.6×10^{-11} J.

Impact toughness: determined with a Charpy test

The Charpy impact test is used to evaluate the impact toughness of materials under high strain rates (strain rate 1300 s^{-1}) [97, 100]. The height of the pendulum times the weight of the pendulum produces the potential energy and the difference in potential energy of the pendulum at the start and the end of the test is equal to the absorbed energy.

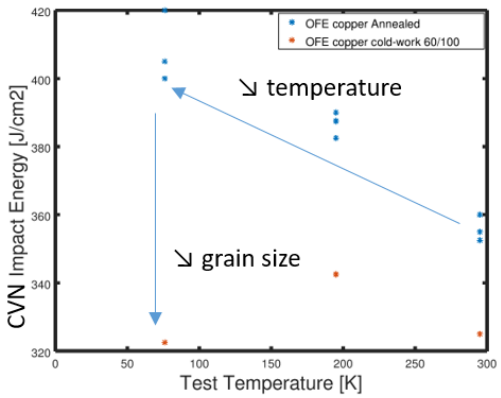

Figure 2.6: The impact energy (also called Charpy V-notch toughness (CVN) or the energy absorbed during a shock) is normalized by the sample cross section and shown as a function of the sample temperature for annealed (blue stars) and 60 % cold-work (red stars) OFE copper, after [97]. Data at lower temperature are not reported here because of the large temperature rise occurring in impact tests below 76 K for ductile materials.

Figure 2.6 illustrates the effects of the temperature and of the grain size on the energy absorbed in the impact. As mentioned previously, the lower the temperature is, the higher is the energy absorbed in the impact. On the other hand, when the grain size is smaller, less energy is absorbed in the rupture of the sample.

In [100], the absorbed impact energy is measured, based on an instrumented Charpy test at room temperature. The impact toughness, normalized by the cross section ob-

tained is this case is 48 J.cm^{-2} for ultra-fine grained copper and 55 J.cm^{-2} for coarse grained copper.

Although the values obtained in the literature are rather spread, the lower one, and therefore, the conservative one is considered in the following.

The fracture toughness can be obtained from the impact toughness. A correlation is given for several alloys based on aluminium or titanium in [105]. The Barsom end Rolfe empiric correlation [106] is used in this work:

$$\frac{{K_{I\,c}}^2}{E} = 0.222(CVN)^{3/2} \tag{2.3}$$

where, CVN is the Charpy V-notch toughness or the impact energy.

Under this assumption, from the value of impact toughness found in the literature, the energy dissipated in the rupture of a typical connection between a particle and the near surface has been evaluated at 2.12×10^{-7} J, significantly higher than the values estimated based one the material properties previously mentioned.

Conclusion

The range of the estimated values of the energy dissipated in the rupture of a typical connection between a particle and the near surface is rather broad. The minimum value, 1.16×10^{-11}, will be used as an input of a model for the detachment of particles under impacts, in section 5.2. The order of magnitude has been confirmed in experimental measurement presented in section 4.3.3.

2.2 Preparation of the laser-treated samples

This section is dedicated to the presentation of laser-treated sample preparation.

Although the final objective is the implementation of a *in-situ* beam screen treatment, the preliminary development has proceeded in laboratory, on plane samples, as the treatment itself and the analysis of the samples are easier this way. First tests started, at Dundee University, in December 2018, on a 2.2-m-long straight beam screen with a maximum inner diameter of 72 mm.

The section presents the preparation of plane, and beam screen samples, the laser parameter used in the treatment, and thermal cycling to reproduce on samples the constrain that the surface would undergo once installed in a LHC magnet.

2.2.1 Plane samples laser treatment in laboratory

The first laser-treated samples were analysed at CERN in 2016. The preliminary tests have been performed to assess the SEY reduction, the vacuum compatibility... Then, about 160 samples were treated with various combinations of laser treatment parameters in order to find the best compromise for the application of surface laser treatment of accelerator vacuum systems.

Plane coupons preparation: cut and cleaning

Both copper and colaminated sample coupons of 15×20 mm^2 were prepared at CERN.

Copper samples were cut from a 1-mm-thick cold rolled sheet of oxygen-free electronic (OFE) copper. Two kinds of colaminated samples were used corresponding to the beam screen installed in standard LHC *MB* dipole and the so-called beam screen *Type 74* installed in inner triplet magnets. The thicknesses of stainless steel P506 grade and OFE copper are respectively 1 mm and 0.08 mm for *MB* beam screen. The stainless steel thickness is reduced to 0.6 mm for *Type 74* beam screen.

After being cut the coupons were cleaned with ethanol and acetone, de-greased with alkaline detergent and ultrasonic agitation, de-oxidized with hydrochloric acid, passivated with chromic acid and dried in nitrogen and baked by hot air flow in order to remove residues as described in CERN proceedings for components of the vacuum system [107]. Then, cleaned coupons were packed in *kraft* paper and in plastic bag and shipped to Dundee University where the laser treatment was performed.

Laser treatment setup

The laser treatment was performed at Dundee University for all the samples mentioned in this work, between 2017 and 2020.

A diode-pumped solid state pulsed Nd:YAG laser was operated at the second harmonic (*i.e.* 532 nm wavelength) and 200 kHz repetition rate. The laser was linearly polarized and produced 10 ps pulsed Gaussian beam. The laser was coupled into the scanning head. The beam diameter defined at $1/e^2$ was fixed according to the position of the upper surface of the sample compare to the focal point at 52 μm with a Gaussian intensity profile ($M_2 < 1.3$). The beam standard deviation is 13 cm. These parameters were considered fixed in this work and won't be discussed anymore.

The laser processing has been performed at normal incidence onto the sample surface, in air with a laminar nitrogen flux toward the sample. Laser surface structuring of the samples was carried out over a defined area of 15×15 mm by writing a pattern of parallel one directional grooves.

Laser treatment parameters

Beyond the parameter above mentioned fixed by the choice of the laser, 160 configurations of the laser processing input parameters have been tested so far, varying scanning speed, pulse energy and hatch distance as the examples given in table 2.1. Once laser-treated, the samples were sent back to CERN pack in optical lens paper and aluminum paper in individual plastic boxes, in order to prevent any deterioration of the treated surface. The time between the treatment in Dundee University and the analysis at CERN was typically in the range of several weeks.

These samples were used on three purposes:

- to study the influence of the treatment parameters on the morphology characteristics (see section 3.3 groove profile measurement and section 3.4.2 for particle overlay quantification) and on SEY performances (see section 5.3);

- to analyse the surface transformation after laser treatment by Transmission Electronic Microscopy (TEM) and nano-tomography (see section 3.2 and 3.4.3) on the so-called *G3, D12* samples;

- for mechanical characterisation on the so-called D7 samples (see chapter 4).

Influence of the treatment parameters

In total, 9 series of samples have been prepared at Dundee University and analysed at CERN between 2017 and 2019 (*16 serie, 36 serie, alpha, beta, gamma, delta, epsilon, zeta* and *eta*) to investigate the influence of the treatment parameters on the surface topography and on the SEY performance. This parametric study went on over several years and lead to the definition of the optimal set of parameters as the best compromise between the SEY reduction and a groove depth lower than 30 μm.

A large range of treatment parameters were investigated. An exhaustive compilation can be found in the appendix B while table 2.1 summarizes them. The laser beam irradiated samples by scanning parallel lines (as illustrated in 1.16) at a speed between 10 and 43.33 mm.s^{-1}. In the transverse direction, the hatch distance, *i.e.*, the distance between adjacent line scans, was varied between 26 and 145 μm. The energy of each pulse was between 5 and 94 μJ.

The corresponding SEY and groove depth measurement are given in section 5.3.1.

Table 2.1: Range of laser treatment parameters investigated.

Fixed parameters		
λ	nm	532
τ	ps	10
Spot size $\emptyset_{1/e^2}$	μm	52
Repetition rate	kHz	200
Varying parameters		
Pulse energy	μJ	$5 \rightarrow 94$
Hatch Distance	μm	$26 \rightarrow 145$
Scanning speed	mm.s^{-1}	$10 \rightarrow 43.33$

So-called G3, D12: samples dedicated to TEM and nano-tomography

As the optimisation process was going on, some samples -*G3* and *D12*- treated with sets of parameters presenting relatively low SEY and low groove depth have been selected for more extended microscopy investigations by Transmission Electronic Microscopy (TEM) and nano-tomography (see section 3.2 and 3.4.3)

The details of the associated laser parameters is presented in table 2.2 as an example. The table presents characteristic figures calculated basing on the irradiation parameters such as the *Sample average fluence* used to compare the sample performance in section 5.3.1. Finally, the SEY and the groove depth measured for these samples are given in the last rows of the table.

For instance, *G3* samples have been treated at the scanning speed of 15 mm.s^{-1}, in the direction of the lines. In transverse direction, the hatch distance is 55 μm. The energy of each pulse is 25 μJ. In this configuration, the average fluence across the sample is 593 J.cm^{-2}. *D7* and *D12* samples present slightly different parameters and results.

Table 2.2: Laser treatment parameters, corresponding figures of merit and SEY and groove depth measurement for samples called *D7*, *G3* and *D12*. The column *BS74* corresponds to the irradiation characteristics obtained on the flat part of the beam screen when the *D7* parameters are applied on the curved part. See section 2.2.2 for further explanations.

Name		D7	G3	D12	BS74
λ	nm			532	
τ	ps			10	
Spot size $\emptyset_{1/e^2}$ defined at $1/e^2$	μm	52	52	52	98
Repetition rate	kHz	200	200	200	200
Pulse energy	μJ	20	25	20	20
Hatch Distance	μm	45	55	45	45
Scanning speed	mm.s^{-1}	15	15	10	13
Power	W	4	5	4	4
Fluence/pulse	J.cm^{-2}	0.9	1.18	0.9	0.3
Max Fluence/pulse	J.cm^{-2}	1.89	2.36	1.89	0.53
Max Fluence total	J.cm^{-2}	782	977	1173	479
Sample average fluence	J.cm^{-2}	593	606	889	684
Distance between pulse	μm	0.075	0.075	0.05	0.065
Pulse/spot		693	693	1040	1508
SEY		0.89	1.19	0.86	1.2
Groove depth	μm	32.17	33.04	44.48	Not measured

So-called D7: samples dedicated to mechanical study

Results of parametric study showed that *D7* set of parameters led to the best performance in terms of SEY and impedance. These samples were thus selected for further mechanical characterisation.

Several batches of these samples have been requested to Dundee University over the duration of this study.

The laser treatment parameters can be found in table 2.2 as well as corresponding figure of merit, and results from SEY and groove depth measurement.

However, the surface morphology, and the particle coverage in particular, of the received samples was not always reproducible, probably due to slight modification of the nitrogen atmosphere.

As an explanation of the sample labels used further in the document and an illustration of the logistic constrains due to sample treatment outside CERN, a chronology of the so-called *D7* samples processing is briefly presented:

- plan samples from *delta* series were received and analysed at CERN in April 2018. The sample is called *D7 2018*. Based on these analysis, *D7* parameters were identified as the optimized choice, in the current state of knowledge. It was decided to order a batch of identical samples treated by this set of parameters to perform further analysis;

- 54 identical plan samples were ordered for preliminary analysis (impedance, room temperature SEY, cold SEY, outgassing, ageing, carbon coating dust and shocks). One sample of the *Zeta* and *Epsilon* series were also treated by *D7* set of parameters. They were received at CERN in February and March 2019. All these samples actually presented similar surface tomography and SEY results than *delta* series, they are labelled *D7 2019*;

- 30 identical plan samples dedicated to mechanical tests arrived at CERN in September 2019. Nevertheless, the surface tomography were dramatically different due to an unsuccessful trial to change of the nitrogen supply. These samples were not used for further analysis;

- finally, 30 identical plan samples dedicated to mechanical analysis were received at CERN, in February 2020. Although the surface tomography and the SEY performance were not strictly identical to the *D7 2018* and *D7 2019*, the samples were used for centrifugation and laser shock. They are called *D7 2020*;

- in addition, *D7* parameters were applied *in-situ* on the 2.2-m-long beam screen in November 2018 (samples further called *BS74*) as described in section 2.2.2. It is worth noting that the treatment of this tube has been started in September 2018 but was finally ready to be shipped to CERN on April 2019, due to multiple technical issues. Parameters of the laser beam have been changed several times over this period. The reproducibility of the samples is far from being insured.

2.2.2 Robot assisted *in-situ* laser treatment of beam screens

The optimal *D7* set of parameters has been applied on the beam screen *in-situ*. This robot-assisted treatment is presented in the following.

The electron cloud mitigation based on laser-engineered surface structures have been demonstrated by many studies in the laboratories and in the accelerators (as explained in bibliographic elements in chapter 1). Nevertheless, one challenge is now to prove the feasibility of an implementation in long beam pipes.

As a first step in investigating large-scale deployment of this technology, a laser device aimed at *in-situ* treatment of the HL-LHC triplet surfaces has been developed by CERN conjointly with General Electric. The robot had to fit the beam screen geometry of the different magnets of all the inner triplet area presented in section 1.1.1.

Robot design and functionalities

The design of a robot capable of processing the inside of the vacuum tubes via fiber optics includes a crawling movement along the beam screen by means of pneumatic clamps, a rotational movement of the laser head, a hollow core optic fiber provided by GLPhonotinics, an optical fibre carriage system and a beam delivery system able to couple the laser into the optical fiber.

Parameters chosen for *in-situ* treatment application

The choice of some of the treatment parameters has been required by the constrains of

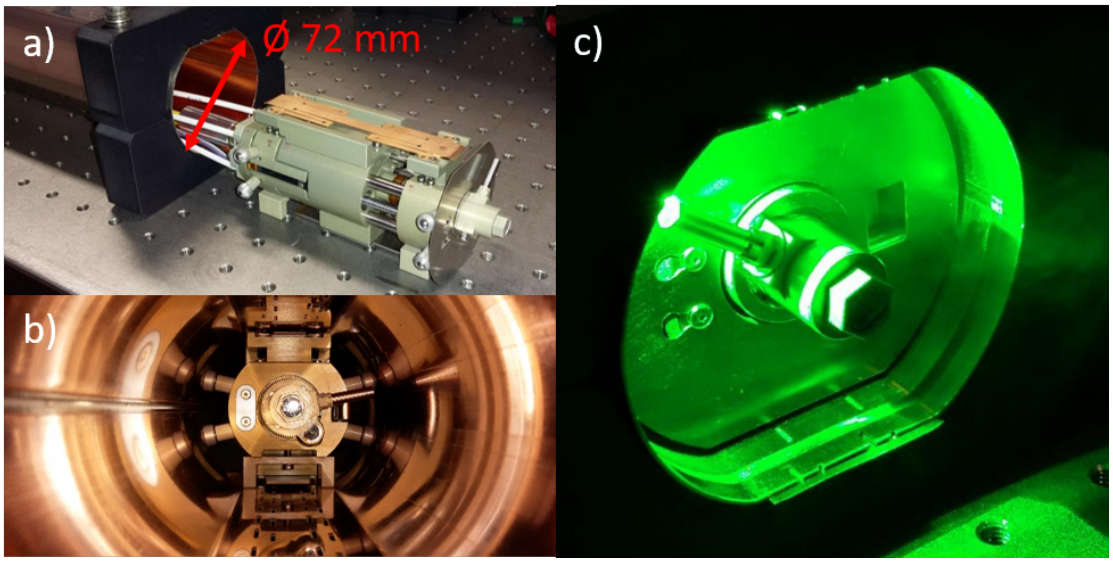

Figure 2.7: Pictures of the robot a) Before insertion in *Type 74* beam screen. b) Robot inserted in the beam screen. c) When irradiating the beam screen, the rotations movement of the head around the longitudinal axis allows a scanning along the perimeter of the beam screen. Courtesy of Monika Sitko.

the robot-assisted *in-situ* treatment of beam screen geometry. These are briefly explained in the following section.

Picosecond technology was chosen for fast ablation, industrial equipment used for machining process (drilling, cutting) [78].

The choice of the 532 nm wavelength to treat copper surface as the results of a trade off between the transmission in the optic fiber and the reflectivity of the copper. In one hand, the loss due to Rayleigh diffusion evolves as a function of $\frac{1}{\lambda^4}$ which makes transmission of the laser light more difficult for short wavelengths [78]. On the other hand, the reflectively of the copper significantly increases on the range of wavelengths considered in the study as it can be seen in figure 3.1 a). 532 nm appeared to be a compromise which motivated the choice of this wavelength.

It is worth noting that the focal length is fixed as an intrinsic parameter of the robot (*i.e* it does not change with the angular position of the scanning head). Considering the beam screen geometry, the focal depth varies while treating the flat part of the beam screen (see figure 1.17). Therefore, as shown in the equation 1.9 and 1.10 the diameter and thus the fluence deposited to the sample change with the distance to the center of the beam screen.

The tests were first performed at CERN with a laser beam diameter of 12 μm. Considering that the needed fluence can be achieved with a larger diameter, the option of enlarging the laser beam to 52 μm has been chosen to be able to treat the beam screen with more stable parameters along the perimeter. With this diameter, the effect of the laser beam divergence on the averaged deposited energy is balanced by the 14 % decrease in the scanning speed between curved and flat parts of the beam screen.

A larger beam diameter also increases the time-efficiency of the laser treatment as a

larger area is treated at each scan.

As an example in the so-called *Run 3*, *D7* parameters have been applied on the curved part of the beam screen (where the distance to the center of the beam screen is maximum). The irradiation characteristics applied to the flat parts of the beam screen have been calculated taking into account both the beam divergence and scanning speed increase. The laser treatment parameters and irradiation characteristics for the flat and curved part of the beam screen are reported in table 2.2, columns *BS7A* and *D7*, respectively,

For further analysis, the 2.2-m-long beam screen has been cut into samples on the 20 x 20 mm size. SEM top view images of the curved part and flat part can be found in figure C.6 and in figure 3.44 b) respectively.

2.2.3 Cooling cycles at cryogenic temperature

As discussed in section 1.1.2, the beam screen hosted in the LHC are operating between 5 and 20 K. In its life time, the beam screen surface will undergo several thermal cycles between the room and cryogenic temperature as its hosting magnet may be warmed up for maintenance. Since the cool down process of the LHC magnets requires several weeks, the temperature is supposed to stay homogeneous in the copper sheet of the beam screen and thermal shocks are avoided. Nevertheless the effect of the thermal contraction of the material on the mechanical properties and SEY have to be assessed, especially because the chemical composition of the surface is changed by the laser treatment due to the presence of oxide.

Experimental proceedings

In order to approach, the mechanical constrains due to the thermal cycles in LHC, 10 identical *D7 2020* samples were submitted to thermal cycles.

The samples were mounted on a cooling flange thanks to a custom-made holding plate, as shown in figure 2.8 a), which allowed to press the sample on the platform, thus ensuring a good thermal contact without damaging the central part of the treated surface. The platform was placed into a cryostat cooled by liquid nitrogen and submitted, under vacuum, to 10 thermal cooling cycles from room temperature to 80-70 K.

Although this remains higher than the operational temperature of LHC beam screens, around 90-92 % of the thermal deformation is already reached when cooling from 293 K (see figure 2.1).

The cool down rate was typically around 50 K/h. Thanks to the high thermal conductivity of the copper platform, the sample temperature is expected to be uniform. The platform temperature has been monitored during the operations, and typical evolution of the temperature during a single cycle is shown in figure 2.8 b).

The effects of the thermal cycles on the mechanical properties (*i.e.* particle adhesion) and the SEY of the surface are addressed in chapter 4.

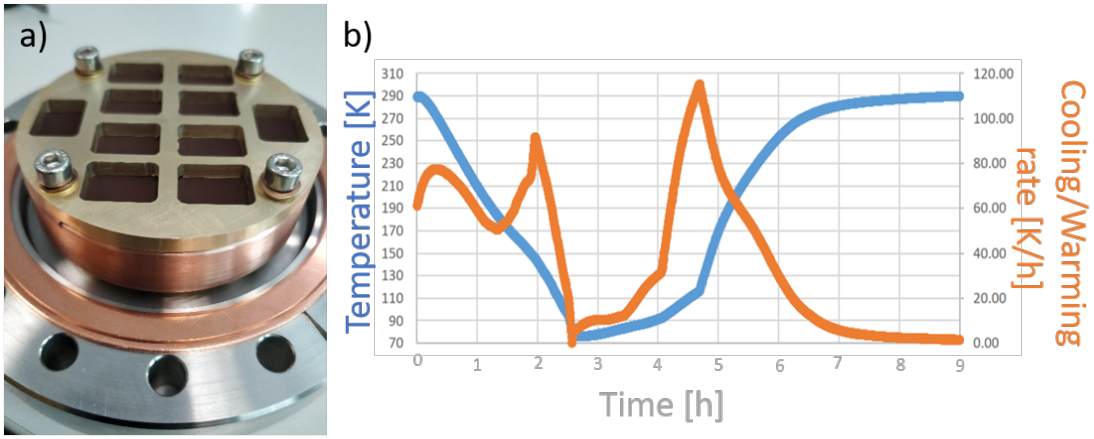

Figure 2.8: a) Picture of the 10 samples installed on the mounting flange of the cryostat b) Temperature measurement in Kelvin and cool down/warm-up rates during one thermal cycle from the room temperature to 70-80 K. Courtesy of Laetitia Dufay-Chanat and Torsten Koettig.

2.3 Surface analysis of the laser-treated samples

As explained in chapter 1, the surface topography after the laser treatment is characterized by a trench pattern (generated by the scanned laser) covered by an in-homogeneous coral-like structure made of agglomerated nano-particles, and forming a sub-micrometric highly porous network. The surface performance has been shown to be strongly correlated with its topography. Therefore, the observation and characterisation of the treated surface morphology are fundamental in this work.

The observation methods deployed for the analysis of two-scales -grooves and particles- surface are presented in this section. They are based on surface observations and analysis of particles collected after extraction.

2.3.1 Analysis of groove morphology based on cross sectional microscopy

Cross sectional microscopy is a tool dedicated to groove morphology analysis. The particles covering these grooves could not be observed as they were damaged when preparing the cross sections.

Experimental proceedings

To prepare cross-sections, samples were mounted vertically in a transparent resin with metal supports. After mounting, the samples were ground with SiC papers down to grit P1200 and polished with diamond suspensions gradually reducing the particle size from 3 μm to 1/4 μm. Cross-Section images and dimension analysis was performed using a *KEYENCE VHX 6000* optical digital microscope or a *ZEISS FEG Sigma* SEM.

In figure 3.41 a), the top of the groove is the position of the surface before the laser treatment.

Image post-treatment

ImageJ software was used for post-treating the microscopy images. Coordinates of the points localised on the profile of the treated copper were manually extracted, defined

as the limit between the unmodified copper and the material re-deposited during the treatment.

The weight of ablated material were evaluated from the copper density and the area defined by the groove profile and the original surface of the sample. The results are presented in sections 3.3 and 3.5.

2.3.2 Top-view electron microscopy analysis

Scanning electron microscopy was used to investigate the laser-treated surface right after the treatment and after submitting the sample to particles extracting methods.

Experimental proceedings

Top view images were measured by a *ZEISS FEG Sigma* SEM equipped with a field-emission source and an in-lens as well as an Evan-Thornley detector for Secondary Electron imaging. The acceleration voltage of 10 kV and an emission current controlled by an aperture of 60 μm. The acquisition was made of 8 bit depth gray scale images (256 shades of grey).

Several regions of each sample were analysed. Magnifications were chosen in the large range of 200 to 10 000 to be able to analyse the multi-scaled morphology modification from the grooves produced by the laser ablation to the sub-micrometer deposited structures.

Examples of SEM top view images of the surface can be seen in appendix section C.1.

Discussions

Top view SEM images were useful to qualitatively describe the particle cover but the large amount of particles and the long focal depth of the electron microscope do not allow an automatic post treatment of the SEM images for the quantitative analysis of the particles. Thus, other methods have been developed, such as Automated Particles Analysis (APA) on particles collected after extraction from the surface, for instance by ultrasonic (US) cleaning, as described in the coming sections.

A FIB assisted tomography was also attended to obtain a qualitative description of the particle coverage described in the section 3.4.3.

2.3.3 Ultrasonic cleaning for particles extraction

The ultrasonic (US) cleaning has been used as a method to remove particles from the laser-treated surface. The objectives were: assessing the effects of the particle density reduction on the surface properties of the treated sample and collecting the detached particles after filtration for morphological and chemical analysis. The experimental proceedings and discussion about the method are presented in this section.

Experimental proceedings

Each sample was fixed on one edge by a crocodile clamp and upright fully immersed into an 80 mL beaker filled with ultra-pure water. The beakers were placed into an ultrasonic bath at ambient temperature. Two cycles of 100 min were applied at an intensity of 300

W and frequency of 45 kHz. The efficiency of the ultrasonic cleaning seemed to depend on the immersion depth. Therefore, the cleaning cycles were repeated after turning the samples by 180 degrees in order to homogenize the cleaning across the sample surface. After the US bath, the samples were dried by an air jet.

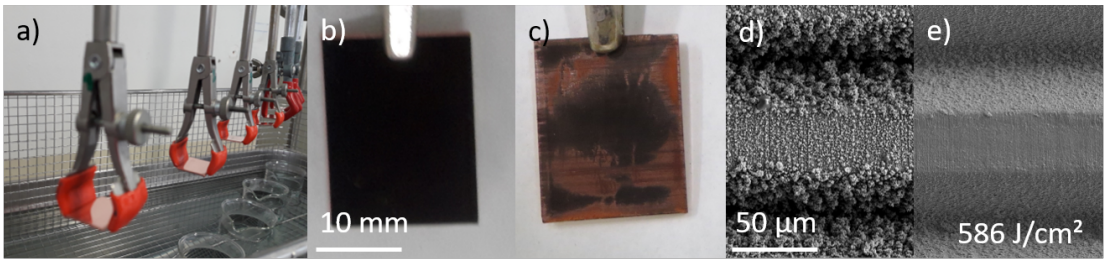

Figure 2.9: a) Picture of the samples before the immersion into the US bath (with "plan immersion"). b) Picture of the treated surface before US cleaning fixed on the top edge by a crocodile clamp. c) Picture of the treated surface after the two cycles of US cleaning. d) Top view SEM image before US cleaning. e) Top view SEM image of the same sample after US cleaning.

Once particle were removed, the sample surface was analysed by SEM (see figure 2.9) and SEY (see section 5.3). XPS analysis did not reveal major changes in the chemical surface composition upon cleaning.

The extracted particles were collected by filtration of the particle-containing water using an isopore polycarbonate, hydrophilic membrane. The size of the pores was measured to be 500 nm based on microscopic observations. The membrane were dried in the oven ($70°C$, from 2 to 12 h). Particles would then be observed by microscopy. If the particles are too numerous in the solution, they are superposed and stacked on the membrane after filtration, making the observation difficult. When the amount of detached particles is important the solution is diluted by a factor 10 %.

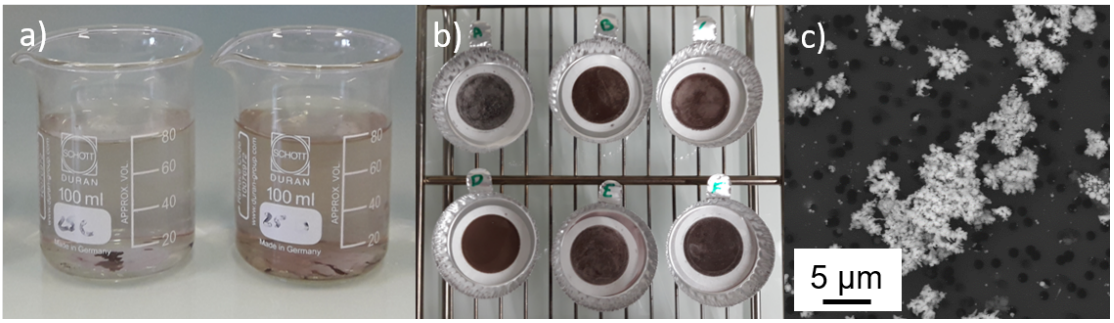

Figure 2.10: a) Picture of two beakers after US cleaning, detached particles are in suspension in the distilled water or precipitated on the bottom of the beaker. b) Picture of six membranes after the filtration of the particle-containing water. The black/brown disks on the white membranes are formed by the accumulation of detached macroparticles. c) SEM view of the detached particles. The black round dots in the background are the pores of the membrane.

As it can be seen in figure 2.9 c), the efficiency of the cleaning process seems to be higher in the area between 3 and 5 mm under the water surface of the US bath.

Consequently, the cleaning was not strictly uniform over the sample. An alternative way to handle has been successfully tested as illustrated in figure 2.9 a). The sample is handled the treated face down, placed 3 mm under the surface. In this way, the cleaning seemed more uniform across the sample surface.

The homogeneity of the US cleaning into the US bath and repeatability of the particle extraction have been assessed: 3 samples treated with identical parameters have been placed into different beakers. For these samples, the surfaces looked similar after US cleaning and the standard deviation of the measured extracted weight was 15 %.

Quantitative description of detached particles

The samples were weighted before and after the ultrasonic cleaning process to assess the mass of nanostructures detached from the surface. The collected particles were weighted as well. According to the weight-loss analysis, on average 93% of the detached nanostructures were collected in the membrane. A correlation between the parameters of the laser treatment and the amount of detached particles during ultrasonic cleaning has been found. In particular, the correlation between the laser energy deposited to the sample during the treatment and the weight of detached particles is further illustrated in section 3.4.2.

Qualitative description of detached particles

Although SEM analysis can be performed to observe the particles directly on the isopore membrane (as it can be seen on figure 2.10 e) and in section 3.4.2.2) a charging effect appears when the exposition of the sample to the electrons is too long. Thus, the automatic particle analysis (APA) could not be performed on this substrate. Particles had to be transferred from the membrane to a specimen pin stub covered by conductive carbon sticker where the SEM analysis could be performed without charging effect even after long exposure.

Discussion about the US cleaning used as an extraction method

The particles transfer on the carbon sticker required for SEM observation of the particles is not fully handled as explained in the following paragraph, as it can be seen in figure 2.11. Although a similar amount of particle were present on the two filters shown in the picture, when applying once the carbon sticker on the membrane on the left more particles were collected than when applying several times a sticker on the membrane on the right, as it can be seen in figure 2.11. The quantitative characterisation of particles collected after filtration is not consistent as probably biased by the transfer of the particles from the filter to the carbon sticker.

Qualitative description of the size distribution has been used and provided valuable input on the size distribution as presented in section 3.4.2.2. Nevertheless, is also worth noting that the qualitative size description of the detached particles based on SEM observations can be biased by effects of the ultrasonic bath and filtration (agglomeration or segmentation of particles after the detachment of the treated surface).

Conclusion

In conclusion, US cleaning has been found to be an efficient method to modify the treated surface morphology without altering its chemical composition. It has been applied in

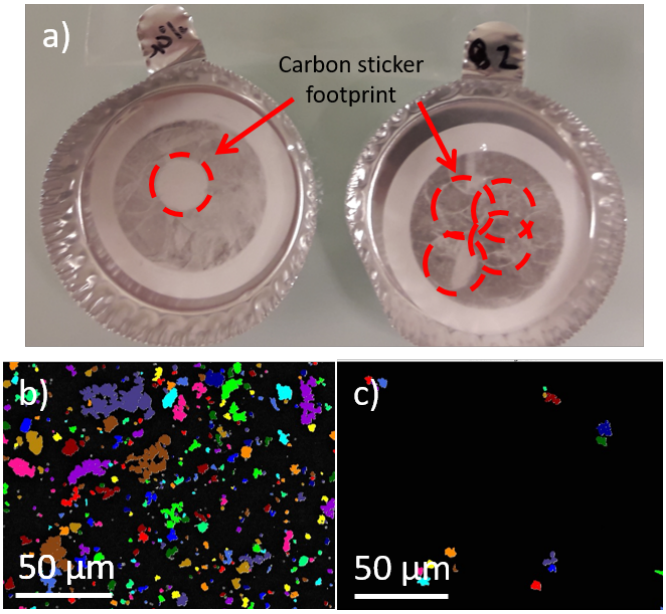

Figure 2.11: a) Picture of two membranes after US cleaning after the collect of the particle on the carbon sticker, b) SEM view of the detached particles. after binarisation of the image, and particle detection after transfer on the carbon sticker from the membrane on the left. c) From the membrane on the right.

[108] to study the effects of the particle coverage on SEY. This is further developed in section 5.3. US cleaning is also used to evaluated the particle coverage depending on the laser treatment parameters (results in section 3.4.2). Concerning the particles size distribution analysis, US cleaning showed some limitations, Thus another method based on image treatment after FIB tomography has been deployed, described in section 3.4.3.

2.3.4 Automated Particles Analysis (APA)

The Automated Particles Analysis (APA) has been used for qualitative description of the particles detached from the laser-treated surface. The use of a systematic proceeding also aims to compare the amount of detached particles while submitting the treated samples to several extraction methods. The proceeding is described in this section.

Experimental proceedings

At CERN, the *ZEISS FEG Sigma* SEM is equipped with an Oxford AZtec® EDS system. It uses an automatic particle search to perform a statistical particle analysis using a scanning electron microscope. Particles are collected on a carbon sticker (generally 12-mm-diameter) installed in the microscope. The APA is performed in several subsequent steps:

- the operator positions 3 points on the carbon sticker edges in order to define the area of interest where the APA will be performed;
- the defined area is divided into a grid of identical fields. The field area is 3.92×10^4 μm^2 (228*172 μm^2 dimension L*l). The software randomly chooses the localisation

of one field, performs the analysis and move to the next field. The so-called *montage* shows how the analysed fields are randomly located over the area of interest, see figure 2.12 a);

- the instrument acquires a back scattered electron image of the selected field, see 2.12 b). The magnification has been fixed at 200 leading to a resolution of 550 nm. This number fixes the lowest size of a detected particle;
- in the electron image, particles usually appear with different brightness depending on their material contrast (Z-contrast), in this case the chemical composition of the collected particles is mainly copper or copper oxide. In 8 bit depth grey scale image, each pixels has its own color intensity falling in the 256 grey scale range between pure black and pure white;
- an image analysis is conducted by binarising the grey scale image using a predefined threshold. A grey scale value of 200 for 8 bits images was found to be optimum for the copper particles collected on a carbon sticker. The threshold has been chosen to be 10000 for 65536 levels of grey of the 16 bits images;
- a threshold is fixed for the detection of the smallest feature, in this work: 2 pixels;
- each feature is determined as an area composed by juxtaposed pixels, without shape criteria. For each particle the software records the following geometrical characteristics: the aspect ratio (defined as the ratio of the largest dimension over the smallest one, typically around 1.48 in average with a standard deviation of 0.3, which denotes mostly spherical particles), the largest dimension and the Equivalent Circular Diameter (ECD) (defined as the diameter of the disc which would have the same area than the detected feature);
- for this study, the choice was made to stop the analysis after 10 000 detected features. The number of the analysed fields depends, consequently, on the density of features over the area of interest. This number is typically between 50 and 1000 fields (depending on the particles density), out of 2700 frames needed to fully cover the area of interest. The time needed for the analysis of one carbon sticker was typically around 3 hours;
- the particle density is calculated depending on the analysed area, the area of the collector, and the area of the sample submitted to the mechanical solicitation as follows:

$$G = \frac{Particle\,number\ \times\ Carbon\,sticker\,area}{Analysed\,area\ \times\ Solicitation\,area} \tag{2.4}$$

  The particle density can be compared among several samples and allows a quantitative description of the number of detached particles depending on the extraction method.

Chemical composition

On all regions exceeding the grey scale threshold the electron beam will be positioned,

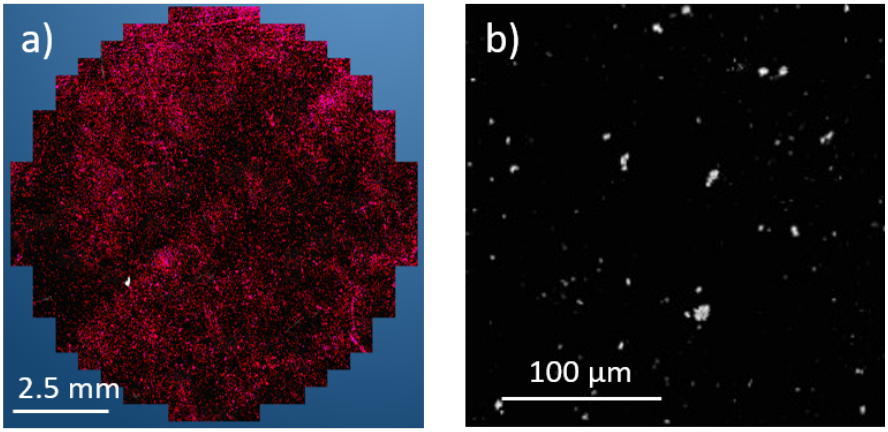

Figure 2.12: a) Montage the analysed particles appear in pink. b) SEM image of the detached particles collecting on the carbon tape.

inducing the emission of elemental specific X-rays. The X-rays are analysed using an EDS detector. The auto-ID function assigns the spectral peaks to the corresponding element and a quantification routine calculates the chemical composition of the particle. Subsequently, the particle is classified according to its composition to a predefined class. Finally the matched particles are summarised in a list. The class of the copper particles was considered. In this class, the atomic percentage of copper in a particle was in average 80 %.

Calculation of the weight of extracted particles

For each sample, the list of the Equivalent Circular Diameter (ECD) of the detected features is established as well as the analysed area. The size distribution of the detached particles per area unity is studied (see figure 2.13 b)). The cumulative distribution of the mass of extracted particles is extrapolated from the list of ECD and the value of the copper density. This visualisation of the detached particle mass emphasizes the role of the larger particles.

The particle porosity of large detached particles has not be taken into account in the calculation of the cumulated mass. Therefore, the detached mass might be significantly overestimated.

On a more general perspective, as concluded in chapter 3, the features of the surface morphology larger that 1 μm are actually aggregates of elementary particles of smaller dimension.

The equivalent density of such features could actually be considerably lower than the one of the bulk material. For instance, for a close-packing of equal hard spheres, the highest reachable average density is:

$$\frac{\pi}{3\sqrt{2}} \simeq 0.74048 \tag{2.5}$$

This feature gives an idea of what could be the overestimation of the detached particle mass based on APA for large aggregated structures: up to 30 %.

To conclude, the cumulative mass determined after APA does not aim at establishing the exact quantity of extracted particles but rather at allowing the comparison between samples exhibiting similar surface structures.

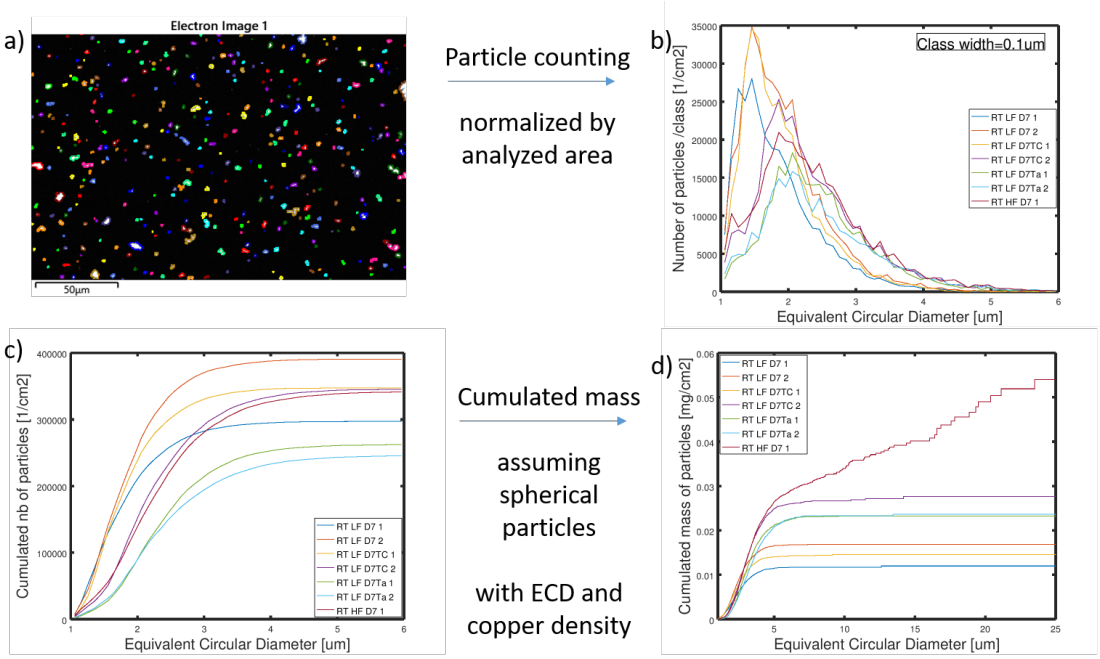

Figure 2.13: a) Typical electron image of one analysed field used for the APA. b) Size distribution of the detached particles. c) Cumulative distribution of the number of detached particles per area unity, giving for each Equivalent Circular Diameter the number of detached particles smaller than this ECD. d) Cumulative distribution of the mass of detached particles per area unity. Legends refer to samples furthers described in section 4.3.

Sensitivity of the area of analysis

Although most of the carbon sticker used to collect the particles were 12-mm-diameter, some were 8-mm-diameter, in this case the area of interested for the APA analysis was smaller. Due to the uneven distribution of the detached particles on the radius observed on laser-shocked sample (see section 4.2.3.3) a coefficient has to be applied to compare average density (defined as the detected feature number over the analysed area) when the area of interest are different. Figure 2.14 illustrates that, for a given radial detached particles distribution, the average density defined on the 4-mm-radius area of interest is 2.14 times higher than the average density defined on a 6-mm-radius area of interest. This coefficient has to be taken into account when comparing the samples.

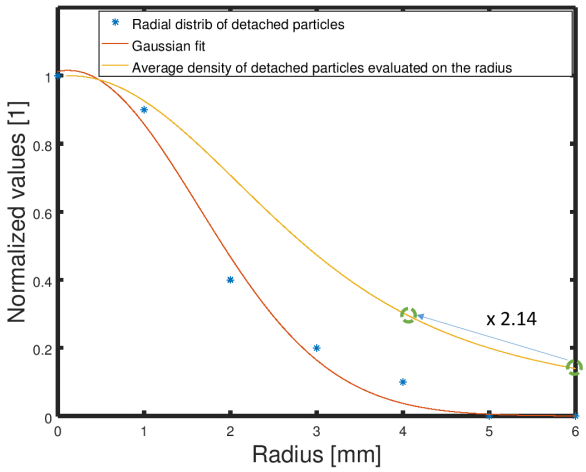

Figure 2.14: Normalized values of the radial distribution of the detached particles (blue stars) (here extracted from SEY measurement), the corresponding Gaussian fit (red curve) and the average density of the detached particles evaluated on the disc of a given radius (yellow curve). Normalisation by the maximum value of each data series.

2.3.5 Secondary Electron Yield (SEY) measurement

The Secondary Electron Yield (SEY) quantifies the number of secondary electrons emitted per primary electron. That is the phenomena that the laser treatment aims to mitigate. From this point of view, the SEY is part of the performance evaluation of treated surfaces. Main results are developed further in the document (in particular, the relation between surface tomography and SEY, in section 5.3) while the experimental proceeding is described in the following paragraph.

Experimental proceedings

The experimental setup used to perform the room temperature SEY measurement is described in [58]. The samples are inserted in the UHV measurement chamber (base pressure of 5×10^{-10} mbar). An electron gun irradiates the sample at normal incidence while the current in to sample and to the secondary electron collector are measured. The SEY is calculated as the ratio of these values. The primary energy was scanned from 50 to 1800 eV. The diameter of the primary electron beam is around 1 mm, *i.e.* much larger than the size of the grooves engraved by the laser treatment. SEY measurements are performed usually on five different spots over the sample to assess homogeneity of the laser treatment across the treated surface.. The total dose delivered during the measurement of one SEY curve is about 1×10^{-6} C.mm^{-2}, which is low enough to prevent any conditioning during the measurements. No surface charging was detected, the maximum value of SEY was determined within the experimental uncertainty estimated to be 0.05.

2.3.6 X-ray Photo-electron Spectroscopy (XPS) for chemical analysis

The chemical composition of the surface is a key parameter influencing its SEY. To correlate the change of SEY with a modification of the surface morphology, it is important

to validate that the laser surface treatment, and extraction methods do not modify the surface chemical composition. Thus, X-ray Photo-electron Spectroscopy (XPS) analysis was systematically performed after SEY measurement.

Experimental proceedings

The surface composition of the samples was analysed by XPS. The description of the setup can be found in [109] or [110]. The experiments were carried out at room temperature in a baked UHV system at the pressure of 5×10^{-9} mbar equipped for XPS analysis at 45° emission with a nonmonochromatic Mg Kα source. It is worth noting that the XPS analysis area is around 1 mm in diameter while groove period is 52 μm, the XPS signal is an average over several grooves. The samples were transferred from the SEY vacuum chamber to the XPS one under vacuum through a transfer line

Main results

According to the resulting spectra, the surface created upon the laser-treatment is slightly oxidized and nitrogen is incorporated into the top surface. Based on a calculation assuming homogeneous elemental distribution, the surface stoechiometry of *D7 2019* was estimated to be 38.8 atomic (at.)% copper, 41.1 at.% oxygen, 7.8 at.% nitrogen, 12.3 at.% carbon for laser-treated samples.

The chemical composition of the surface submitted to methods of particles extraction (US cleaning, centrifugation or laser shock) was controlled.

In case of US cleaning for instance, the atomic content of copper, oxygen, nitrogen and carbon was respectively, 28.5, 41.1, 5.3 and 37.7 [108]. XPS analysis do not indicate any significant chemical change apart from the amount of carbon impurities which is increased after the ultrasonic cleaning.

The carbon content measured on samples after centrifugation or laser shock did not show difference. For instance, the atomic % of carbon was measured to be 23.3 before the laser shock and 21.1 after the laser shock on *D7 2020* (Martino RIMALDI TE-VSC, in private conversations). Therefore, the increase in the SEY observed on centrifugated or laser-shocked samples would be due to topography changes and not induced by chemical surface changes.

2.4 Conclusions on material and methods

The chapter provides a characterisation of the thermal and mechanical properties of the materials used in the study as well as a description of the surface laser treatment and methods deployed for their analysis.

Conventional SEM and APA analysis were adapted and standardised for the systematic analysis of the numerous samples produced. The US cleaning has been adapted to the specific needs as well.

The development and the standardisation of these experimental proceedings are part of the achievements of this work, as the know-how is transferred and documented and can be applied to other specimens in the future.

TEM, FIB tomography and tests set up for evaluation of particles adhesion on treated

surfaces are presented in dedicated sections, 3.2, 3.4.3 and 4, respectively.

Chapter 3

Surface transformations during the laser treatment

Abstract

This chapter starts with a literature review on the multi-scale surface morphology transformations occurring during the pulsed laser irradiation. In the second part, the results of the microscopic surface observations (TEM, FIB Tomography, SEM observations) of the laser irradiated samples, treated in the framework of this thesis, are presented together with their corresponding laser parameters.

Laser irradiation excites electrons at the target's surface. The optical energy is converted into kinetic energy of the electron. Depending on the dissipation mechanisms of the kinetic energy and the transfer to the lattice structure, the ablation processes and the resulting morphology modifications of the target are reported to be different.

The picosecond pulsed laser irradiation scans the surface, ablates the copper which is then re-condensed on the surface creating complex multi-scale morphology. Using Transmission Electron Microscopy (TEM) and Energy Dispersive x-ray Spectroscopy (EDS), microstructural analyses were performed to investigate metallographic structures, composition and phase transformations at the surface of the laser-processed material. In particular, the thick oxide layer formed at the surface of the sample despite the nitrogen protective atmosphere during the treatment has been given evidence.

The size, shape and salient geometrical surface morphology features resulting from the various phenomena involved in the laser process are interesting. Qualitative and quantitative multi-scale analyses of the surface morphology of samples treated are carried out.

Both groove and particle characteristics have been characterized using Scanning Electron Microscopy (SEM), Focused Ion Beam (FIB) assisted preparation,

The ablated material mass was estimated, based on microscopic grooves cross view observations. It was highlighted that the mass of ablated material evolved linearly with the irradiating energy for a selection of samples.

The particle coverage was analysed both based quantitatively and qualitatively.

The weight difference before and after ultrasonic cleaning showed that the particle coverage mass is linear with the irradiating fluence as well and represents about 17 % of the ablated material. Electron nanotomography by FIB-SEM has been applied to go into the particle qualitative characterisation at the nano-scale giving the size distribution of the particles covering the surface.

The quantity of dust, *i.e.* the fraction of material during the ablation which is not redeposed as attached particles on the surface, appeared to be proportional to the fluence, for given irradiation conditions.

Résumé en français

Le chapitre traite des transformations morphologiques et chimiques aboutissant à la modification multi-échelle de la surface traitée par laser pulsé.

Une étude bibliographique des travaux menés sur l'irradiation laser pulsée d'une cible métallique appliquée au traitement de surface met en évidence les mécanismes de l'interaction laser-matière. Les électrons de la structure métallique sont mis en mouvement par l'onde électro-magnétique, puis ces vibrations sont transmises au réseau atomique. Les agitations électroniques ou atomiques peuvent être mesurées en termes de température dont l'évolution temporelle et spatiale sont modélisées par la loi de conduction de chaleur. La dépose rapide d'énergie sur un espace restreint conduit à des phénomènes hors équilibre aboutissant à l'ablation de la cible via différents procédés en fonction des paramètres du traitement laser (durée du pulse laser, longueur d'onde de la lumière, densité d'énergie locale (*i.e.* la fluence) définie par l'énergie totale d'une pulsation et la distribution spatiale de cette énergie).

La liquéfaction et l'évaporation du métal sont attendues lorsque les températures de changement de phases sont atteintes. A plus hautes fluences -et particulièrement dans un contexte de confinement de contraintes lorsque l'élévation de la température est plus rapide que la relaxation mécanique- des ondes de pression se propagent liées à l'expansion thermale non-uniforme de la cible. Lorsqu'elles sont réfléchies sur une surface libre, des contraintes de tension peuvent être générées et conduisent à l'apparition de fissures et de cavités quelques nanomètres sous la surface, lesquelles augmentent considérablement l'efficacité de l'ablation laser. A hautes fluences, le liquide métastable peut être chauffé au-delà de la température d'évaporation et atteindre la température du point critique de l'équilibre thermodynamique. A cette température, les contraintes de cohésion dans le liquide disparaissent, une mixture de gouttes de métal liquide et d'atomes est expulsée de la surface à haute vitesse par explosion de la phase liquide.

Les résultats des travaux menés pour modéliser et simuler ces différents phénomènes donnent des indications sur la taille des cavités présentes sous la surface ainsi que sur la dynamique d'expansion du panache de matière expulsée (la taille des gouttelettes et leur vitesse). La revue bibliographique a ensuite été orientée sur l'aspect morphologique de la surface de cuivre lors de traitements laser similaires à celui envisagé au CERN. Le rôle du gaz environnant le site d'ablation sur le présence et la taille des particules de

cuivre recouvrant la surface traitée et l'effet sur les propriétés physiques de la surface ont notamment été mis en évidence. La présence d'oxyde de cuivre sur la surface traitée a aussi été commentée.

Il apparait que les sillons parallèles créés par l'ablation de matière constituent la première échelle des modifications de la morphologie de la surface par le traitement laser. D'autre part, le choix de certains paramètres du traitement laser favorise l'apparition à l'extrême surface d'agglomérats de matière resolidifiée après éjection du site d'ablation sous l'irradiation. L'analyse de la surface des échantillons traités pour le CERN a été entreprise et exposée dans la suite du chapitre.

L'analyse microstructurale a été réalisée par microscopies électronique à balayage (MEB) et en transmission (MET) dans le but d'identifier les structures, la composition chimique et les transformations de phase à la surface du matériau traité au laser lors de l'irradiation pulsée en fonction de la valeur de la fluence. Ainsi, il a été observé qu'en-dessous d'un seuil d'ablation identifié autour de 0.45 J.cm^{-2}, la surface de cuivre irradiée ne subit pas de transformation mais est recouverte d'une couche d'oxyde Cu_2O issue de l'ablation de la matière adjacente. Lorsque la valeur de la fluence augmente, les signes de recristallisation et de liquéfaction de la surface apparaissent; des gouttelettes et des éclaboussures figées lors de la re-solidification sont notamment visibles. Au-dessus d'une valeur seuil de fluence, établie autour de 1.88 J.cm^{-2}, des porosités apparaissent au-dessous de la surface. Ces porosités pourraient être le résultat de contraintes de tension lors de refroidissement du bain de fusion du matériau irradié. La taille et la profondeur des porosités augmentent lorsque la fluence augmente. La surface est alors recouverte d'une couche d'oxyde CuO d'une dizaine de nanomètres.

L'observation des structures déposées sur la surface après ablation a permis l'identification de deux types de morphologie : des particules sphériques et des agglomérats de matière.

La taille des gouttelettes sphériques est comprise entre 80 et 300 nm en dehors des vallées alors que des gouttes plus volumineuses ont été observées dans le fond des vallées, plus proches du lieu de l'ablation, et peuvent être le résultat de l'agglomération de plusieurs gouttes élémentaires de liquide expulsé.

D'autre structures de surface sont formées d'agglomérats de matière dont la taille peut atteindre 5 μm. En dépit de l'atmosphère d'azote protectrice utilisée lors du traitement laser, les analyses révèlent la présence d'oxyde de cuivre CuO autour des particules sphériques et d'oxyde Cu_2O sur le contour des particules et à l'extrême surface du substrat. Les processus de refroidissement rapides décrits dans le cadre de l'ablation laser favorisent la solidification des structures avant leur re-déposition sur l'extrême surface. Leur adhésion au substrat est un point de questionnement.

L'investigation des vallées creusées par le traitement laser a été rendue possible par des observations au microscope optique de vues en coupe, et ce pour des échantillons obtenus en variant les paramètres laser utilisés pour le traitement. Le volume de cuivre évaporé a été évalué à partir du profil de la surface observée sur ces vues de coupe. Ce volume augmente lorsque la fluence à laquelle est exposé l'échantillon augmente.

La caractérisation des particules recouvrant les vallées a été fondée sur deux outils

: l'observation des particules, après leur détachement de la surface dans un bain à ultrasons, la tomographie couplée au FIB et la prise d'images au microscope électronique. Le nettoyage de la surface traitée par ultrasons est une méthode rapide permettant d'obtenir une première évaluation de la quantité de matière redéposée en fonction des paramètres du traitement laser utilisés. Cette quantité augmente proportionnellement avec la fluence irradiant l'échantillon. Pour les paramètres du traitement laser déterminés comme optimaux, la masse de matière présente sous forme de particules à la surface de l'échantillon a été évaluée à 2.6 mg.cm^{-2}.

La distribution en tailles des particules a été déterminée à partir de l'analyse automatique des particules détachées par les ultrasons. Le seuil de détection a été fixé à 500 nm; au-dessus de cette limite, une distribution logarithmique a été observée 95 % des particules détachées ont un diamètre inférieur à 5 μm.

L'analyse tridimensionnelle des particules recouvrant la surface repose sur les résultats de la nano-tomographie électronique par FIB-MEB et un traitement d'images, en vue d'une caractérisation topographique à l'échelle nanométrique. Ces travaux ont confirmé la valeur de la quantité de particules déterminée par pesée après le lavage au bain à ultrasons, et permettent d'établir la distribution en taille des particules.

Enfin, en comparant le volume de cuivre extrait du sillon creusé par l'ablation laser au volume de cuivre présent sous forme de particules à la surface de l'échantillon traité en laboratoire, près de 80 % du volume évaporé n'est pas redéposé sous forme de particules liées à la surface. Cette matière est qualifiée de poussière, elle n'a pas été recueillie ni analysée mais sa quantité a été évaluée par défaut de masse, en fonction des paramètres utilisés pour le traitement laser.

La connaissance plus approfondie des caractéristiques morphologiques de la surface traitée par laser, et notamment des quantités de matière non ou faiblement attachée à la surface, met en évidence le besoin d'une caractérisation des propriétés mécaniques des particules couvrant la surface pour l'évaluation du seuil de détachement de ces particules et des possibles conséquences pour l'opération de la surface dans l'accélérateur.

3.1 Literature review on pulsed laser surface treatment

The laser energy deposition is both fast and localized creating nonequilibrium conditions of electronic, thermodynamic, and mechanical states of the matter. Laser irradiation is possible in different ways via interfererometry [111] or via direct laser writing. This work is focused on the latter.

The possibility to focus the energy deposition to a small volume explain the many industrial applications of laser such like welding, surface alloying and cladding, laser annealing, high-precision processing, micromachining, selective material modification... Laser ablation on biological tissues is used in laser surgery or for matrix-assisted laser desorption/ionization (MALDI) of biomolecules for mass-spectrometric investigation [112]. Laser ablation can clean archaeological objects from the external deposited layer by nanosecond pulsed irradiation [113]. Pulse laser ablation in liquids can be used for

fabrication of copper nanoparticles [114, 115]. In air the plasma generated by laser ablation can be deposited into thin films and coatings during the pulsed laser deposition (PLD) [116].

The fast disintegration and vaporization creates conditions for rapid cooling quenching and freezing of the transiently liquid structure, leading to multiscale surface modification [117] with the formation of surface sub-microstructures [118]. The surface texturation change surface properties, approaching sometimes bio-inspired functional surfaces [119]. Textured surfaces can have interesting optical properties in some application: highly absorptive surfaces are used for solar cell [120]. Antireflective, enhanced Raman Scattering (SERS) effect [114], or coloured metals were fabricated by producing nanostructures on the surface. Such structural colors were attributed to the specific nanostructures formed on the metals that induce higher plasmonic absorbance at certain wavelengths. The structuration of the surface can increase the contact angle and, therefore, change the wettability properties [81, 82]. Superhydrophobic surfaces have many applications like anti-icing, anti-corrosion, self-cleaning, drag reduction, anti-bacterial low friction surfaces [121]. The biological interactions with a surface depends on its surface morphology, the texturation can reduce or enhance adhesion for the desired type of cell.

In this section, various works present the basic mechanisms of pulsed laser interaction with materials to describe the nonequilibrium processes caused by the fast deposition of laser energy, which results in material removal and modification of the surface structure or composition at meso, micro and nanoscopic leves.

The comprehension of the mechanisms involves nonlinear complex and collective processes that are not well understood [118], and the development of models is difficult because of the lack of well-quantified thermophysical and optical properties [122]. This literature review mostly aims to summarize phenomenological and experimental oriented approaches.

A laser pulse is defined by a:

- temporal intensity $I(t)$ distribution following a Gaussian profile, defined by the pulse duration τ_p defined at Full Width Half Maximum (FWHM). Nanosecond, picosecond or femtosecond regimes can be considered;
- wavelength λ;
- intensity spatial distribution $I(r)$, following a Gaussian profile defined by a diameter at $\emptyset_{1/e^2}$;
- a pulse energy, which leads to a value of irradiating fluence.

The effects of some laser parameters will be investigated and focused when possible in laser interaction with a copper target.

3.1.1 Laser Matter Interaction: Transfer of optical energy to the material

In this section, the processes of transfer of optical energy to the material, *i.e.* the Laser Matter Interaction (LMI) are discussed based on bibliographic elements.

The processes induced by laser irradiation can be separated into three groups: [118]

- laser excitation of optically active electronic states in the irradiated material;
- energy transfer from the excited electron to atomic lattice vibrations;
- the dissipation of the energy by thermal cooling by heat transfer and solidification of the irradiated area.

Optical energy deposition, Absorption

The laser light is a polarized electromagnetic wave, forced vibration of electrically charged particles are initiated due to the electric force when the light passes over a media. In a metal, energy of a short laser pulse is mainly transferred to electrons, specially the ones that form the conduction band, which are set in movement by "inverse bremsstrahlung effect" (the bremsstrahlung effect is the emission of photon from excited electrons) [118]. When it reaches the surface, three optical phenomena are involved in the interaction: the reflection, the transmission (both due to the re-radiation of the photons by excited electrons) and the absorption. The emitted photons are restrained by a lattice of phonon, the bonding energy in a structured phase, liquid or solid.

The energy absorption by the irradiated substrate is defined taking into account the reflectivity, the Beer-Lambert Law of absorption and the spatial and temporal distributions of the laser pulse as follows:

$$S(r,z,t) = I(r,t)\,(1-R)\,\alpha\,exp(-\alpha z) \tag{3.1}$$

where, $\alpha = \frac{4\pi k}{\lambda}$ is the absorptivity, or coefficient of absorption, with k the extinction coefficient, $R = \frac{(n-1)^2+k^2}{(n+1)^2+k^2}$ is the reflectivity with n the real part of refractive index defined as $n_i = n + ik$.

As it is shown in figure 3.1 a), for a given material, the optical properties depend on the wavelength of the laser irradiation. For metals, the reflectivity goes down as the wavelength is shorter (a shorter wavelength means more energetic photons which can penetrate the material and be absorbed by the bound electrons of the metals).

The optical properties also depend on the irradiated substrate: the material and its temperature. Indeed, the higher the temperature of the substrate, the more intense the vibrations of the atomic lattice, and consequently the more likely are the electrons to collide and interact with the structure rather than re-emit photons. The reflectivity of the material decreases when the temperature of the lattice increases, as illustrated in figure 3.1 b) where both the absorption coefficient and the reflectivity are plotted in the case of the irradiation of copper by 800 nm laser light.

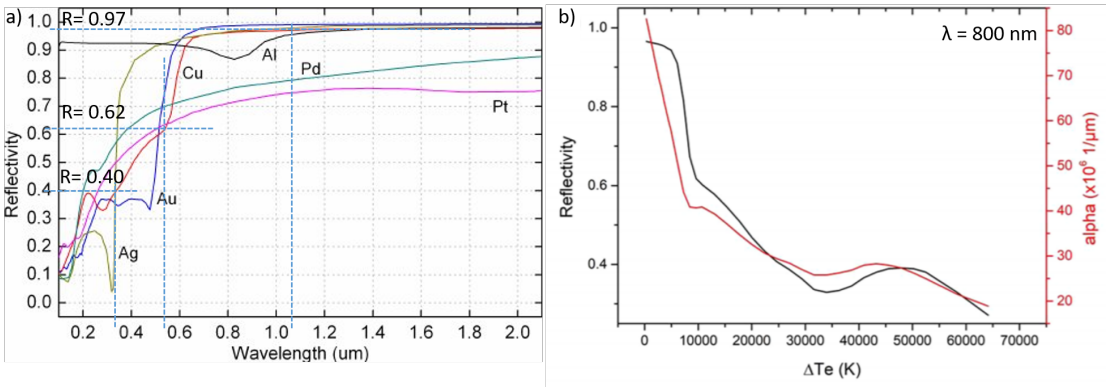

Figure 3.1: Reflectivity of smooth surfaces of metals (Silver, Gold, Aluminium, Palladium and Platinum) depending on the wavelength irradiating electromagnetic wave, at room temperature. For copper the reflectivity coefficients are presented for the wavelengths typically used in laser treatment 336 nm, 532 nm and 1064 nm. The reflectivity is respectively 0.40, 0.62 and 0.97 [123]. b) Decreases of reflectivity and absorption coefficient of copper with the increase of the electron temperature for a wavelength of 800 nm [111].

Optical models have been developed to describe the evolution of these values depending on the temperature of the lattice and electrons [122]. For instance, it has been simulated that the reflectivity goes from 0.96 down to 0.25 during the first 100 fs of the irradiation of copper at fluence 10 J.cm^{-2} [122]. The decrease of the reflectivity contributes to increase the laser energy being absorbed by the material over the irradiation. A lower coefficient of absorption also means a larger optical penetration depth, the laser energy is deposited deeper into the material.

In addition, in this case, the substrate temperature, chemical or topographical surface modifications such as oxidation or laser induced surface roughening also tend to increase the laser absorption of the substrate surface. Despite shielding effects and redeposition of material during processing [124], it has been observed for instance that the ablation of material is significantly enhanced in dual pulsing, in comparison to single pulse processing [111]. A strong decrease of reflectivity was also observed with surface pre-modification, for instance thanks to sandpaper roughened to 50 μm or sandblasted before the laser treatment [78].

In conclusion, the transfer of the laser light energy to the electrons strongly depends on the medium (material, temperature, surface quality), the wavelength and the intensity of the pulses.

Energy transfer to the atomic lattice

The energy of the optically excited electrons is then transferred to the atomic vibration by electron-phonon coupling. The vibration can be seen as heat which is transferred to the surrounding material via the network of molecules following the Fourier heat conduction law. The thermal process can be modeled in a Two Temperature Model (TTM) where the temperatures of both the electron system T_e and the lattice system T_l are considered separately [125]. The one dimensional distribution of T_e and T_l oriented

orthogonal to the substrate surface is defined by the following equations:

$$C_e(T_e)\frac{\delta T_e}{\delta t} = k_e(T_e)\frac{\delta T_e}{\delta z} - G(T_e - T_l) + S \tag{3.2}$$

$$C_l(T_l)\frac{\delta T_l}{\delta t} = k_l(T_l)\frac{\delta T_l}{\delta z} - G(T_e - T_l) \tag{3.3}$$

where, C_e and C_l are the specific heat capacities of electron system and lattice respectively, k_e and k_l are the thermal conductivities of electron system and lattice respectively, G is the electron-phonon coupling coefficient. S is the source term of the heat input induced by the laser irradiation as defined in the equation 3.1.

As heat diffusion in metals is related up to 99 % to transmission by collisions within the electron system, the contribution of the lattice conductivity to the thermal diffusion is often neglected [111]. The electron thermal properties and coupling factor strongly depend on the irradiated medium (material, and electron and matrix systems temperatures) they are the object of various modelling works.

Electron conductivity and heat capacity are varying with the electron and lattice temperatures as follow $C_e = C_{e0}\,T_e$ and $k_e = k_{e0}\,T_e/T_l$. More detailed models have also been developed [111].

The value of the electron-phonon coupling coefficient depends on the metals considered: noble metals (gold, silver and copper) exhibit a lower coefficient compared to other metals [126]. ($G_{Cu} = 10 \times 10^{16}\ Wm^{-3}K^{-1}$ and $G_{Al} = 56.9 \times 10^{16}\ Wm^{-3}K^{-1}$ [127]). The electron-phonon-coupling coefficient also varies with the temperature difference of the system $T_e - T_l$ [128]. The commonly used linear temperature dependency can show differences with the more sophisticated computational analysis of the electron density of states in electronic structure [129]. Depending on the material considered, with the increase of the electron temperature, the electron-phonon coupling can be increased (in the case of aluminium, silver or copper) or decreased (in the case of nickel and platinum). In the case of copper, the enhancement of the coupling at higher temperature leads to a faster transfer to the lattice, the generation of higher thermoelastic stresses and a reduction of the threshold value of fluence for laser melting and ablation, shorter time scale for phase transformation with strong consequences on the surface modification.

The TTM is used to determine the volume of the heated material as well as the temperature distribution throughout that volume, as it is illustrated in figure 3.3. The model allows the calculation of the time required to reach the equilibrium in the material, between the electrons and the lattice of atoms, this characterizes a time constant for the energy transfer from electrons to the atoms. Figure 3.2 shows the results of the simulation of TTM after a pulse of 100 fs: the equilibrium between the electrons and the lattice is achieved at τ_{eq} after a few picosecond (around 4 ps in case of copper).

The pulse duration has to be compared to τ_{eq} equilibrium to understand which relaxation mechanisms are dominant and which subsequent transformations the material will undergo after irradiation [130]:

- in case of nanosecond pulses, the temperature of the electrons and the lattice are

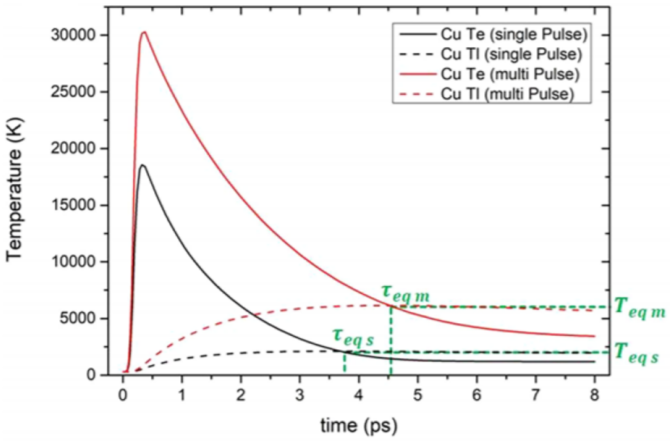

Figure 3.2: Electron and lattice heating calculated for copper at the surface area exposed at a fluence of 1.1 J.cm^{-2} at single and multiple 100 fs pulse irradiation. The thermal relaxation time τ_{eq} as well as the corresponding equilibrium temperature T_{eq} are marked for both single (s) and multi-pulses (m) irradiation [111].

equal. The optical energy is transferred to the atomic lattice where the conventional thermal diffusion drives the heat dissipation in the material which undergoes thermal processes of transformation;

- in case of picosecond pulses by transfer from the excited electrons to atomic vibrations. The rapid equilibrium of the two temperatures leads to ultrafast heating rates 10^{14} K/s of the lattice, illustrated in the temperature rise in figure 3.2. The vibration of the lattice can modify the inter-atomic bonding, the material undergoes ultrafast phase transitions [131], solid-solid or it can be melted, evaporated or ionized if the absorbed energy is high enough to stretch bond or create free-electron;

- in the case of femtosecond pulses, the pulse duration is shorter than the time needed to transfer the optical energy to the lattice, it is even shorter than the mean free time between collisions of electron in a conductor (0.1 ps). Conduction, electron-phonon coupling nor lattice heating happen, the material undergoes non-thermal processes, ejection of a mixture of clusters and atoms rather than an equilibrium surface evaporation.

Transformations occurring during the cooling phase also depends on the ablation regime via the proportion of evaporated material. In fact, the evaporation of the material can produce sharp temperature gradients and high cooling rates (in the order of 10^{12} K/s). It leads to a rapid quenching of the transiently melted material [118]. The generation and relaxation of compressive stresses and the high speed of re-crystallisation can lead to the formation of metastable phases and complex surface microstructures, exhibiting high densities of crystal defects.

Figure 3.3 illustrates the spatial and temporal temperature distributions when the material is irradiated by the same fluence in a femtosecond regime and in a nanosecond

regime. Facing different heating and cooling rates and gradients, the material undergoes transformations leading to various ablation processes and, subsequently, the surface morphology is different (see figure 3.4).

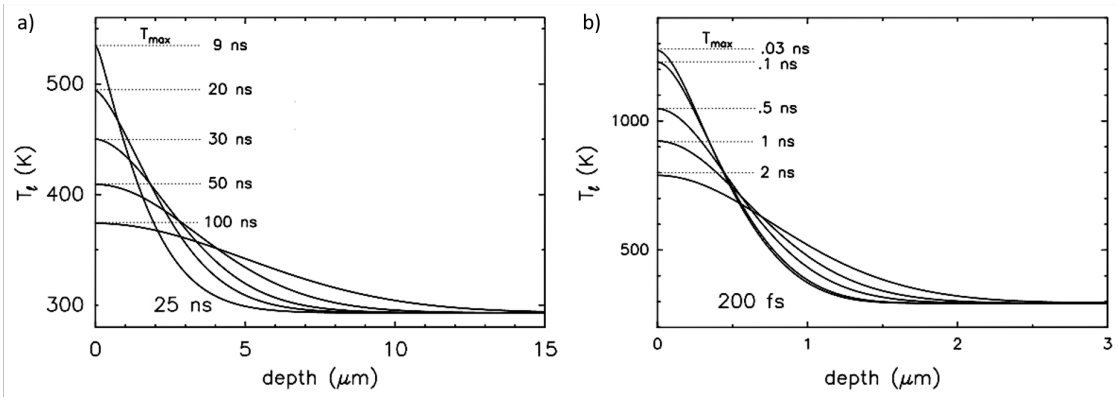

Figure 3.3: Spatial lattice temperature distributions at certain times after excitation of a gold sample by Gaussian pulses of $\tau_P = 25$ ns a) and 200 fs b) with a fluence of 130 mJ.cm^{-2}, after [126]

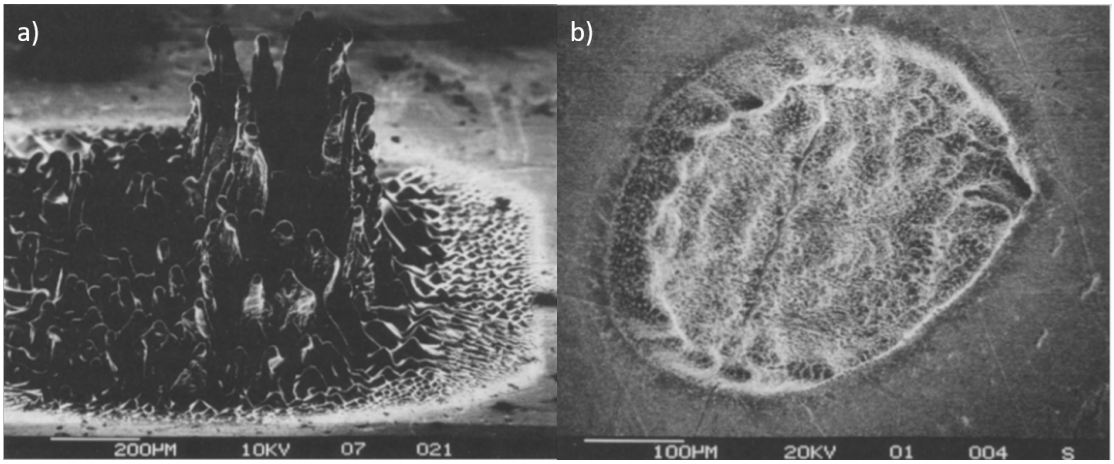

Figure 3.4: SEM images of ablation site on indium after ablation with $\tau_P = 15$ ns a) and 500 fs b). Both experiments were performed in vacuum, after [132]

3.1.2 Phenomenological description of ablation processes

In addition than the ablation regime i.e the pulse duration, the mechanisms observed for the ablation of highly conductive metals like copper after ultrashort pulsed irradiation depend on the irradiating fluence. Due to the spatial variation of the laser intensity within the laser beam with a Gaussian profile, phenomenon can coexist as ablation mechanisms triggered by the same laser pulse. They can be described as follows:

Melting and Vaporization, phase changes

The solid-liquid phase transition induced by ultrashort laser pulses is mainly controlled by nucleation dynamics, instead of energy balance [122]. Due to the high heating rate,

the solid-liquid interface can be heated well above the normal melting point during the melting process, in which the solid becomes super-heated. On the other hand, the interface can be cooled far below the normal melting point in the solidification process, in which the liquid becomes undercooled.

Photomechanical spallation, mechanical fracture

The fast rate of energy deposition by short laser pulses may lead to the generation of compressive laser-induced stresses due to the non-uniform thermal expansion in the target. The magnitude of the laser-generated stresses is significantly enhanced in stress confinement regime (also called inertial confinement) [133]. The stress confinement regime is obtained when the time of the laser heating is shorter or comparable to the time required for the mechanical relaxation (expansion) of the heated volume.

The heating time is defined by the maximum of the laser pulse duration, τ_p, or the time of the electron–phonon equilibrium or thermal relaxation, τ_{eq} (also noted τ_{e-ph} in literature).

The mechanical relaxation time is defined as the ratio of the velocity of sound in the target material over the characteristic dimension of the laser energy, $\frac{Cs}{L}$ deposition. The optical penetration depth is often used as characteristic dimension. Nevertheless, in case of metals, the depth of diffusive/ballistic energy transport during τ_{eq}, (also called electron ballistic range) can be added to the optical penetration depth to take into account the effects of the ballistic motion and hot electron diffusion that spreads the absorbed laser energy into a deeper part of material [122]. This depth has been estimated to be L_P = 16 nm for aluminium [134] and L_P = 100 nm for copper [127] (in noble metals the electron-electron collision probability is lower than in other metals so the penetration of ballistic electrons is enhanced). If the thickness of the sample is thinner than the hot electron diffusion length, the thickness is taken as the input for the calculation. It can have an impact on ablation mechanism threshold fluence for instance [135]. In case of copper, submitted to a 532-nm irradiation, $1/\alpha + L_P$ = 110 nm leading to a mechanical relaxation time of 30 fs. Despite these figures, stress confinement regime has been reported for sub 10-ps laser irradiation of copper [136].

In case of stress confinement, the temperature rise is faster than mechanical relaxation in the system, therefore the laser-induced heating occurs in a nearly constant volume which leads to a thermoelastic pressure increase [137]. The consecutive compressive wave propagates through the material reflects at the free surface, creating tensile wave. If the tensile stresses exceed the mechanical strength of the material, subsurface voids appear. The growth and the coalescence of these voids can lead to the ejection of significant pieces of irradiated material [118]. The mechanical fracture or spallation is a relaxation mechanism of the high thermoelastic pressure.

At even lower laser fluence, close to the ablation threshold, a layer of large and relatively intact cold chunks of material can be separated from the bulk and ejected. The material disintegration is driven by nucleation, growth and coalescence of voids/microcracks localized within the spallation region, at a certain depth under the surface [112].

The term of spallation describes the dynamic fracture of the material as a result

of reflection of the compressive wave on the back surface of the sample [138]. This phenomenon is involved in the LASAT, discussed in chapter 4.2. Talking about ablation of the "warm" material under laser irradiation the term of "front surface spallation" could rather be used.

In other words, spallation (or foaming) also refers as heterogeneous vapour nucleation in a sub-critical liquid phase a cavitation-like process taking place in a melted part of the material [111].

Phase explosion

At higher fluences, with high heating rates, the molten material undergoes a large overheating well above the normal boiling point close to the thermodynamic equilibrium critical temperature (T_{cr} = 7696 K in copper) without boiling. When the temperature reaches the phase explosion threshold (around 90 % of T_{cr} [122]) the tensile strength of the superheated, metastable liquid will fall to zero. Consequently, homogeneous bubble nucleation occurs at an extremely high rate [139]. This evaporative super-critical fluid expansion is called phase explosion (or explosive boiling). It leads to a strong impulse, the decomposition of the overheated material and the ejection of a mixture of liquid droplets and vapour-phase atoms out of the bulk surface at high velocities [111]. The fraction of individual molecules is related to the degree of overheating and increases with laser fluence [137]. Phase explosion significantly enhances ablation as the kinetic impulse also removes a considerable amount of molten material [111] and increases the pressure already high due to the constant volume heating of the solid [137]. The explosive removal of hot matter provides fast cooling of the ejected plume but also initiates a strong convective cooling effect at the surface, which is limiting further heat diffusion and freezes the agitated, churn-up melt-front. Ejection of the largest droplets is attributed to the hydrodynamic motion in the vicinity of the molten surface, especially active in the regime of stress confinement [112].

Coulomb Explosion

At even higher fluences, electrostatic disintegration of a superficial layer of the irradiated material can be observed and called *Coulomb Explosion*. It is caused by photo and thermionic emission of the excited electrons and associated with a non-electronic equilibrium positive charging of the surface. This process of ablation is mainly observed in dielectric materials. In semi conductor or metals, the high mobility of charge carriers prevents accumulation of the positive charge up to the level of disintegration of the surface by electrostatism.

The quick phenomenological description of the ablation process highlights the complexity of the laser-induced ablation because of the many mechanisms involved. The simulation of ablation process needs a set of physical models: optical models to characterise the temperature dependence of optical parameters which describe the laser absorption by the material (this includes the thermal transport from electron temperature (T_e) to lattice temperature (T_l) using a TTM), two phase change models for melting and evaporation under superheating, a hydrodynamic model for liquid and vapor motion, and a phase explosion model for ejection of metastable liquid decomposing into droplets

and vapor phase.

3.1.3 Modelling, simulations and experimental insights on laser induced structural and phase transformation of the target

In this section, a selection of the reports focused on the modelling, and simulation of the target disintegration are presented. Some of them are compared with experimental results reported in literature. The simplest models based on TTM aim to predict the ablation rates depending on the irradiating conditions. Approaches based on fluid dynamics equations try to assess the behavior of the molten material. Simulation based on molecular dynamics are also presented as it aims to simulate spallation and phase explosion mechanisms.

Ablation depth

The ablation rate is estimated from energy conservation by the assumption that all the energy of the laser pulse leads to the evaporation of material. The energy of the laser pulse is applied in order to heat up the material to evaporation temperature and to overcome the latent heats of melting and evaporation. Material in a vapor state is ablated.

The energy conservation during the laser ablation, only considering the material evaporation, can be written as:

$$N\,E_{Pulse} = m\,(c_{p_{Sol}}\,(T_{Fus} - T_{RT}) + L_{Fus} + c_{p_{Liq}}\,(T_{Vap} - T_{Fus}) + L_{Vap}) \tag{3.4}$$

where N is the number of pulses, E_{Pulse} is the pulse energy, m is the ablated mass, $c_{p_{Sol}}$ and $c_{p_{Liq}}$ are the heat capacities of solid and liquid states, respectively, L_{Fus} and L_{Vap} are the heat or enthalpy of fusion and evaporation, respectively, T_{Fus} and T_{Vap} are the temperatures of fusion and evaporation, respectively. The values for copper are summed up in A and can be founded in [140].

The model assumes 100 % energy absorption and neglects heat conduction effects as well as overheating of metal vapor, there it overestimates the ablation rate as it can be seen in [141].

Another expression of the ablated mass, based on the TTM has be proposed for short pulse irradiation by [132]:

$$m = N\,\rho\,A\,\alpha^{-1}\,ln\left(\frac{F_{inc}}{F_{th}}\right) \tag{3.5}$$

where N is the number of pulses, m is the ablated mass, ρ is the density, F_{th} is the threshold fluence for ablation. A is the area irradiated by the incident fluence F_{inc}, If the fluence is constant over the irradiated area, $F_{inc} = \frac{E_{Pulse}}{A}$.

This expression needs the following assumptions to be done:

- absorption can be described using Beer's law, with a constant absorption coefficient; although it has already been discussed that optical properties may change with the temperature;

- the reflectivity is considered as a constant; although it may decrease with the increase with the surface roughness during multi-pulse irradiation;
- ablation takes place after the laser pulse is over, so that shielding of pulse energy by the generated ablation plume does not have to be taken into account;
- heat conduction is negligible, the thermal diffusion length ($L_D = \sqrt{D\,\tau_P}$) is much smaller than the optical penetration;
- the absorbed energy per volume has to exceed a threshold density;
- re-deposition does not occur significantly as it is the case in vacuum.

The ablation threshold can be determined by various methods that include diameter (D^2 method) and/or crater depth (or ablation rate) measurements [142]. The logarithmic dependency of the ablation depth on the irradiating fluence is in a good agreement with the experimental measurement performed in many works [132, 141, 143, 144].

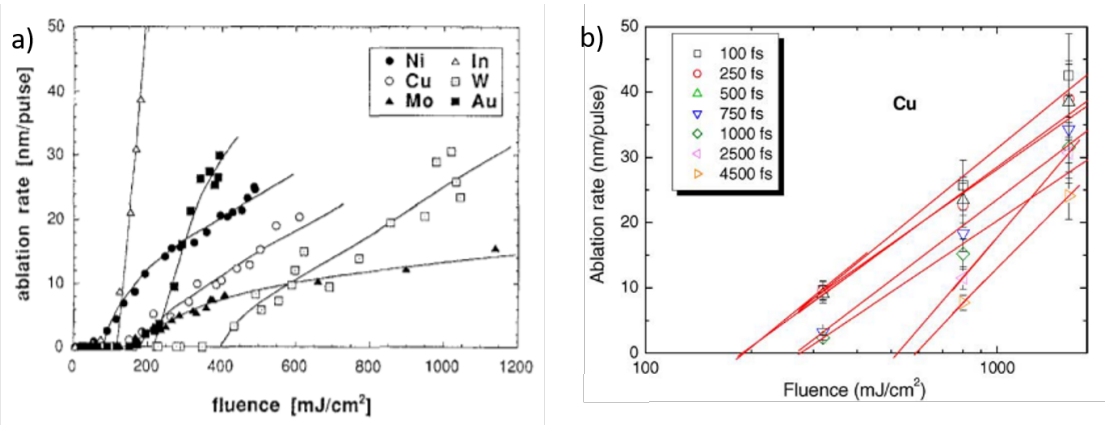

Figure 3.5: Ablation rate (nm/pulse) as function of incident laser fluence in the low fluence regime for different metals at $\tau_P = 500fs$ a) [132] and for pulse duration of 100, 250, 500, 1000, 2500 and 4500 fs for copper b) [143]. In both case, the solid lines represent the best fits according to equation 3.5.

The ablation rate is strongly influenced by the ambient atmosphere of the ablation site: the threshold fluence is doubled for ablation of aluminium, copper, iron and lead with a 12 ps, 532 nm laser in air compared to in vacuum [144]. While the slope of the ablation rate decreases by a factor of 2-3 when samples were treated at atmospheric pressure compared to treatment under vacuum [132, 144]. This latter point might be explained by the re-deposition on the ablation site of a fraction of ablated material.

Ablation thresholds depend on the irradiated material (see figure 3.5a)), for copper it has been evaluated at 170 mJ.cm^{-2} for 500 fs irradiation [132], and it depends on the pulse duration (see figure 3.5b)) It was shown that below 1 ps the threshold fluence and melting depth are independent on the pulse duration, then it increases as a function of $\tau^{0.5}$ [145] which leads to the threshold fluence value of 850 mJ.cm^{-2} for a 10 ps irradiation on copper.

It has been shown that the oxidation layer on copper (composed of CuO and Cu_2O) may have a lower damage threshold than copper [146].

The ablation threshold $F_{Th}(N)$ for N the number of pulses can be related to the single pulse ablation threshold $F_{th}(1)$ according to the following equation, which is based on the accumulation model of [146]:

$$F_{Th}(N) = F_{Th}(1)\, N^{S-1} \tag{3.6}$$

where S is the incubation coefficient which characterizes the degree of incubation in the material.

The incubation coefficient is material dependent. It is lower than the unit therefore the pulse accumulation behavior, also called incubation effect, has the effect to lower the ablation threshold. For 10 ps irradiation, on copper, the incubation coefficient has been evaluated from experimental work at 0.77 [147]. This value lowers the ablation threshold down to 189 mJ.cm^{-2}.

The influence of the repetition rate, shown in [142], may explain the low value of threshold found in [144]: 230 mJ.cm^{-2} in air with a repetition rate of 4.1 MHz and an important number of pulses.

Hydrodynamic effects

Hydrodynamics of the molten pool play an important role in structure formation. Different mechanisms were proposed and described with a continuum computational approaches based on a numerical 2D model including Navier-Stokes equations to explain the ejection of droplets and the formation of various laser-induced nanostructures,surface roughness or sub-surface bubble cavitation.

Hydrodynamic effects can be formation and desorption (the ejection) of micrometer large metallic droplets. Thermal and hydrodynamic simulations of nanosecond regime irradiation of gold [148] also showed that formation of the droplets or more generally the surface morphology depends on both, the balance between the acceleration of the melt and the surface tension, and on the value of surface tension itself. For instance, if the surface tension is low, the growth occurs but not the ejection. If the tension is too high, the droplet formation process is suppressed.

Absorbed energy induces a surface tension driven flow owing to the high temperature gradient [78]. Surface-tension-driven convection mechanisms of heat transfer contributes to molten material movement at the surface of the target. Evaporation and high thermal conduction to the bulk of the target provide fast cooling and can lead to solidification of the asperities. It freezes the transient liquid surface features [149]. These processes could be responsible for the formation of hydrodynamic patterns/asperities observed experimentally for metal targets. The kinetics of the transient melting and resolidification depends on the laser irradiation and define the shape of the surface topography [150].

The progress of the liquid-solid interface toward the surface also depends on the ablation regime; it results in a re-solidified layer a few tens of nanometers in thickness with a pico second irradiation [150]

Target disintegration via vaporization (spallation and phase explosion)

Coarse-grained Molecular Dynamics (MD) simulations are useful to investigate the disintegration of the irradiated target as well as the dynamics of the early stages of the ablation plume formation and the mechanisms of cluster ejection. It provides interesting insights on the characteristics of the surface and sub-surface modifications.

In classical MD models, electrons are not explicitly represented, the vibrational excitation of random matrix molecules is simulated using the model of breathing spheres [137]. In this model each molecule (or appropriate group of atoms) is represented by a single sphere owing translational degrees of freedom. The effect of the laser irradiation is simulated by transferring kinetic energy to the random spheres during the time of the laser pulse. The probability for a given molecule to be excited depends on the fluence of the laser pulse and the initial position of the molecule under the surface (comparatively to the optical penetration depth appropriate for a given wavelength and material properties). The wavelength of the laser light defines the kinetic energy transferred to each sphere. In addition of laser pulse absorption, MD simulation can model the relaxation processes leading to laser-induced crystal defects [151] and phase transformations.

Classical MD model does not include processes involving electron excitation (for short laser pulses); in order to include it an hybrid computational model has been developed [133]. In the combined continuum-atomistic model TTM-Molecular Dynamics (MD), the differential equation of diffusion of T_e defined in TTM is coupled with the MD equation of motion of the lattice as explained in [151].

TTM-MD simulations performed on aluminum substrate for 100 fs irradiation are given as an example of the results achieved by these simulations [134]. The characteristics (occurrence and volume) of the subsurface voids are simulated depending on the irradiating fluence (from just below the spallation threshold to 60 % above). The analysis of the ablation plume generated by the phase explosion (size distribution of the cluster, velocity and temperature) can also be performed. It is worth noting that in this irradiation case, the melting front was located around 200 nm below the initial surface, the voids appeared around 120-125 nm under the surface. Depending on the local irradiating fluence, the thickness of the top layer ejected by spallation was around 25 nm just above to spallation threshold to a few nm at higher fluences. All these results are summed up in figure 3.6. The input of this work is the absorbed fluence, the optical model are not presented [134]

For comparison, the results of a similar TTM-MD simulation performed on nickel substrate for 15-ps-irradiation can be found in [133]. The nucleation and the growth of subsurface voids were also investigated. In that case, a power law void volume distribution has been reported in simulation with power law exponent going from -3.3 at 30 ps to -1 at 125 ps after laser pulse due to the coalescence of some of the initial voids. After the irradiation, 10-nm-diameter voids were present 30 or 40 nm below the original surface.

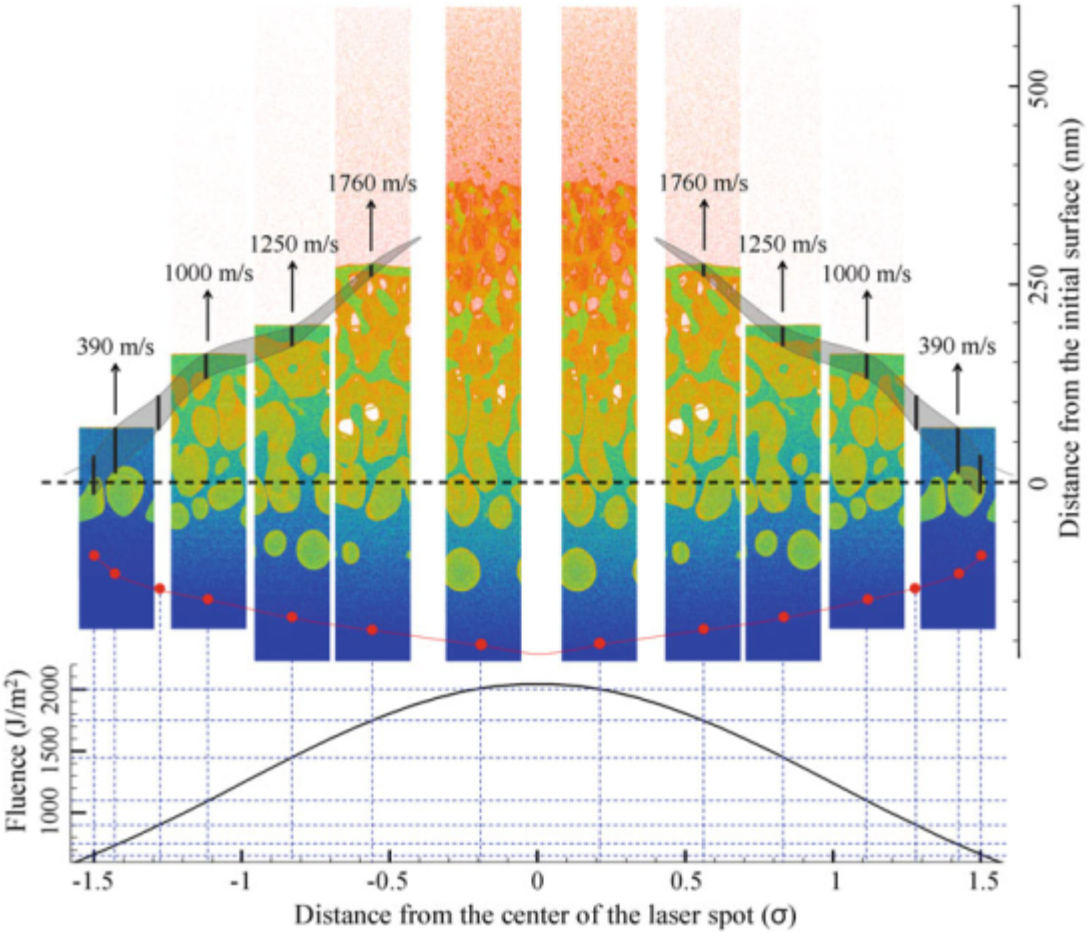

Figure 3.6: The integral visual picture of melting, generation of subsurface voids and material ejection from an aluminium target irradiated by a 100 fs laser pulse. The laser beam has a Gaussian spatial profile with a peak absorbed laser fluence of 2,050 $J.m^{-2}$. Snapshots from 5 individual TTM-MD simulations taken at the same time of 150 ps after the laser pulse are aligned with locations within the laser spot that corresponds to the values of local fluence used in the simulations. The atoms in the snapshots are colored by their potential energy, from blue for atoms in a low potential energy state, in the bulk of the target, to red for the atoms in the vapor phase . The red dots mark the depth of the melting front. The thicknesses and locations of the top void-free layers are shown by black bars. The velocities of the liquid ejectat in $m.s^{-1}$ at 150 ps after the laser pulse are provided in the figure [134].

3.1.4 Modelling, simulations and experimental insights on plasma formation and plume dynamics

In this section, a selection of works reported in literature are presented, based on the simulation and experimental results, and focused on the plume dynamics consecutive to the target vaporisation. The role of the plume in the ablation processes and the re-deposition of the ablated particles influenced by the plume dynamics play role in the morphology modification of the irradiated surface.

The vaporization of the target and subsequent gas dynamic processes in the expanding plume can be investigated by MD simulation in the first few nanoseconds [137].

Other material removal processes such as plume dynamics or liquid ejection may take place on a substantially longer time scale; other computational tools based on Direct Simulation Monte Carlo (DMCS) (using MD simulations results as an input) and Direct numerical simulation (DNS) have been developed to simulate these processes.

The size and speed distribution of the ejected particles as well as the plasma composition for instance the degree of ionisation are investigated depending on the gas environment.

Simulations of 15-ps-long irradiation on copper [137] showed that spallation of material leads to ablation of large molecular clusters in addition to monomers. The first kinds of particles formed are nanoparticles [137], with sizes varying from a few to several tens of nanometers. The velocity distribution of the ablated molecules fit to a Maxwell Boltzmann distribution. The evolution of the average axial velocity of the molecule ablated over the first 500 ps is rather constant around 150 $m.s^{-1}$ at the bottom of the plume (these molecules were originally located at 22 nm under the surface) up to 700 $m.s^{-1}$ at the top of the plume (for the molecules localized in the top monolayers of the original surface). In [112], the ejection of 20-nm-diameter droplets was found just above the ablation threshold.

MD simulations provide interesting insights on the material ablation, the initial plume composition depend on the irradiation conditions [112]. Nevertheless, MD simulations have to be associated with Direct Simulation Monte Carlo (DMCS) [152–155] to perform larger time and length scales simulations taking into account not only the target material disintegration and processes of cluster ejection but also their following evolution during the laser plume expansion as a result of the gas-phase collisions. Indeed, processes such as elastic and inelastic collisions, sticking reaction in cluster (molecule collisions), aggregation reaction in cluster (collisions of clusters) and cluster evaporation are included in DSMC simulations. Practically, MD simulation results obtained at 1 ns after the laser pulse are used as the initial conditions for the direct simulation Monte Carlo for the calculation of large-scale three-dimensional plume evolution [154]. The collision probabilities in DSMC calculations are parameterized to describe the material properties in a gas phase, such as viscosity coefficient and velocity dependence of the equivalent collision cross sections.

Following this methodology, cluster evaporation and condensation processes have been simulated for a picosecond regime of ablation in [154]. The expansion of a same set cluster parameters (material, initial size and temperature) was simulated with various properties for the surrounding gas (density and temperature). It has been shown that both the evaporation and condensation rates are proportional to the gas density and the square of temperature. It has also been shown that the initial cluster parameters can strongly change the final cluster size as either the evaporation or condensation is dominant over the other processes.

Experimental measurements including fast imaging of plasma expansion and ablation rate measurement based on measuring the volume of craters by microscopy, have been performed for a laser irradiation of copper, under vacuum [156]. Depending on the

irradiating fluence, the velocities have been measured for the Cu^+ ions (constant around 25 000 m.s^{-1}), the atoms of copper (5000 to 8000 m.s^{-1}) and the nano particles (150 to 120 m.s^{-1}). The analysis via atomic force microscopy of the size distribution of nanoparticles collected on a substrate placed in front of the laser target indicates that two populations of nanoparticles exist within the plume: particles smaller than 7 nm which are supposed to be directly emitted from the target, whereas larger particles are expected to be formed by collisions and agglomeration during the plasma extension. The size distribution for larger particles exhibits a $r^{3.5}$ dependence which is in a good agreement with MD-DSMC simulations [153].

MD simulations associated with DSMC were also performed for femtosecond laser interaction, in an inert background gas [155].

A simple model of the cooling processes of the extracted droplets from the ablation site was reported in [136]. To handle the long time scale phenomena (several microseconds), the cooling process was modeled assuming the heat radiation as the dominant dissipative effect, the power dissipated by a grey body sphere can be estimated by the Stephan-Boltzmann law:

$$P_{Dissipated} = \epsilon \, \sigma \, \pi D^2 \, T^4 \tag{3.7}$$

where $\epsilon = 0.15$ is the emissivity of the copper, $\sigma = 5.670 \times 10^{-8} \; Wm^{-2}K^{-4}$ is the Stefan–Boltzmann constant, D is the diameter of the sphere, and T is the surface temperature.

This power has to be compared with the energy which has to be dissipated to solidify a ball of the same diameter from the boiling temperature to melting temperature (see the equation 3.8) in order to determine a solidification time.

$$E_{SolSphere} = \frac{\pi D^3}{6} \rho \left(L_{Fus} + c_{p_{Liq}} \left(T_{Vap} - T_{Fus} \right) \right) \tag{3.8}$$

where ρ is the density, $c_{p_{Liq}}$ is the heat capacity of liquid states, L_{Fus} is the heat or enthalpy of fusion, T_{Fus} and T_{Vap} are the temperatures of fusion and evaporation, respectively. The values for copper are summarized in A. Under these assumptions, the temporal evolution of the temperature of the droplets depending on the diameter of the spherical particles has been plotted in figure 3.7.

The solidification of a 150-nm-diameter droplet of copper cooled down by radiation starts at 1.55 ms and finishes at 3.14 ms. In this case the maximum cooling rate is 4.8×10^6 K.s^{-1}. The solidification time would be significantly increased by the contribution of the convective cooling and if the initial temperature is lower than the boiling temperature. With the ejection speed of 120 m.s^{-1} previously reported, it means that the droplet would be fully solidified when being re-deposited to the surface several hundreds of micrometers away.

Beside MD-DCMC simulations, Direct Numerical Simulation (DNS) using governing continuum equations of both the near sample surface and adjacent and the background gas is another way to simulate the laser ablation process and subsequent plasma extension. Simulations solving the integrated conservation equations of mass, momentum,

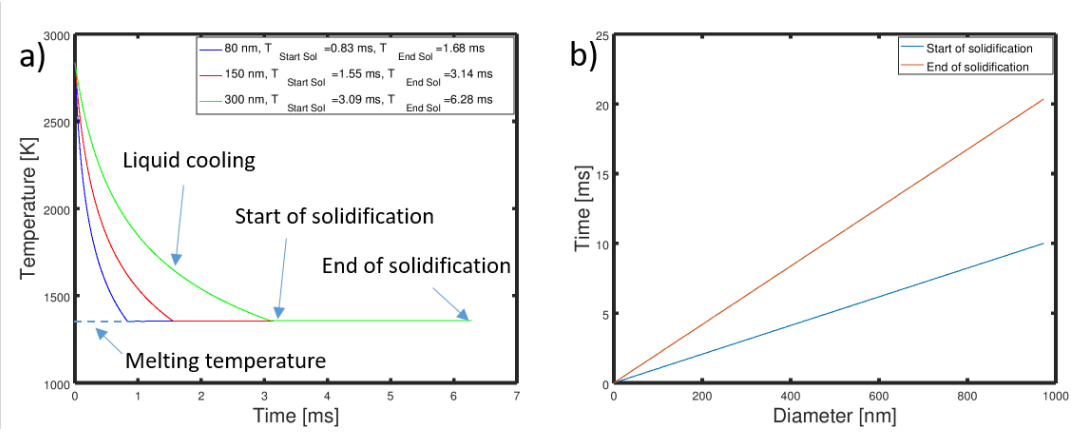

Figure 3.7: a) Temporal evolution of the droplet temperature depending on the diameters from the boiling temperature to the total solidification. b) Times of the start and the end of solidification of a droplet cooled by heat radiation cooling depending on the diameter.

and energy were used to calculate the pressure and density and identify the shock waves.

Both, laser ablation via target heating, melting and vaporisation and the gas and plasma expansion dynamics have been modeled for nanosecond 266-nm irradiation of copper with helium gas background [140]. It was found that the degree of copper ionization depends on the localisation in the plume: first order oxidation dominates in the region close to the surface within 20 μm, then in the core of the plasma the distributions between the ions Cu^{+} and Cu^{2+} were found to be rather equal. The threshold for plasma generation was set at 2 J.cm^{-2}. The expansion velocity of the laser plume has been measured around 10 000 m.s^{-1}. In [140], the author also reported that plasma shielding and vapor plume could be observed after a few nanosecond and remained a few tenths nanosecond after the laser pulse. For comparison, the frequency of the laser pulses (also called repetition rate) at 200 kHz corresponds to an interval of 5 ns in between two pulses. A pulse might irradiate the surface through the plasma generated by the ablation of the precedent pulse. The plasma shielding reduces the laser energy absorbed by the target of long nanosecond irradiation. In this case, the particles released by the ablation expand in a higher density plasma which may protect the surface from further oxidation [157].

Nanoparticle generation during copper ablation was studied, in nanosecond ablation regime, under atmospheric argon, neon and helium atmospheres [158–160]. Experimental results based on shadowgraphy and spectral emission measurement of the vapour plume and plasma, were compared with the numerical gas dynamics simulations of the nanoparticle condensation process. Although the study was made for nanosecond pulses, the main conclusions on the plume expansion dynamics and the interaction with the ambient gas should be applicable to other laser interaction regime. The ratio of the energy transferred to the plume versus the laser energy strongly depends on the surrounding gas: 75 % for helium, 35 % for argon and around 40 % in neon. However, for the same incident laser energy, the vaporized mass in the three gases was almost equal [161]. The higher the energy transfer to the plasma, the less likely the re-deposition of the ablated

mass in the vicinity of the ablation site.

The ablation environment has a strong influence on the surface morphology. This aspect will be further developed in the following dedicated section. The frame of this thesis is focused on ablation in gas environment as it suits the industrial application.

3.1.5 Experimental studies: morphological investigations

As a consequence of processes of target disintegration and evolution inside the plume, different types of particles are produced, which are partly re-deposited to the target and cause surface roughening. For some applications the deterioration of the surface finishing and the achievable dimensional accuracy in the material micro-machining might be detrimental and undesirable [157]. For some others, the surface roughening is the intended impact of the laser treatment.

In this section, some experimental studies are presented, focusing on the morphological investigations at different scales of modification, mainly on functional surfaces. For these surfaces, the effect of the morphology transformation on physical properties of the surface, mainly the reflectivity measurement, are highlighted [79, 80].

The factors influencing the surface morphology have been split as: irradiated material, laser irradiation and gas environment. Furthermore, laser-induced periodic surface structures (LIPSS) morphology is presented at the end of this section.

Effect of the material

Materials properties have impacts on the morphology, the size and the chemical composition of the nanostructures: optical properties and properties involved in the electron-lattice equilibrium defined the ablation processes of the irradiated target while thermal properties such as the thermal conductivity and the specific heat determine the lifetime of the molten phase both on the irradiated surface area and in the nanoparticles being formed. This impacts the size distribution and the propensity to aggregation and nanodroplet formation [79].

As an example, the surface morphology of titanium, silver and copper, are pictured in figure 3.8 after a 100 fs laser irradiation in air. The different morphological characteristics of the re-deposed material is illustrated as well as the effect on the reflectivity of the treated surface. Titanium surface shows a dense overlay of re-deposed material which reduces the surface reflectivity. It can be explained as followed. Compared to the two noble metals, the untreated surface of titanium presents a low reflectivity, therefore, a higher proportion of the laser energy is absorbed, a higher coupling coefficient leads to a stronger stress confinement, and stronger processes of laser ablation. The high specific heat enhances nanoparticles aggregation and re-deposition compared to the noble metals as it can be seen in figure 3.8

In a given gas environment, the chemical composition of the irradiated surface is also influenced by the reducing ability of the irradiated material (*i.e.* low standard electrode potentials). In case of irradiation of copper (metal with a relatively high reducing ability) under air the formation of CuO is observed (XPS, EDX) [87].

Effect of the condition of irradiation fluence (disintegration of the target)

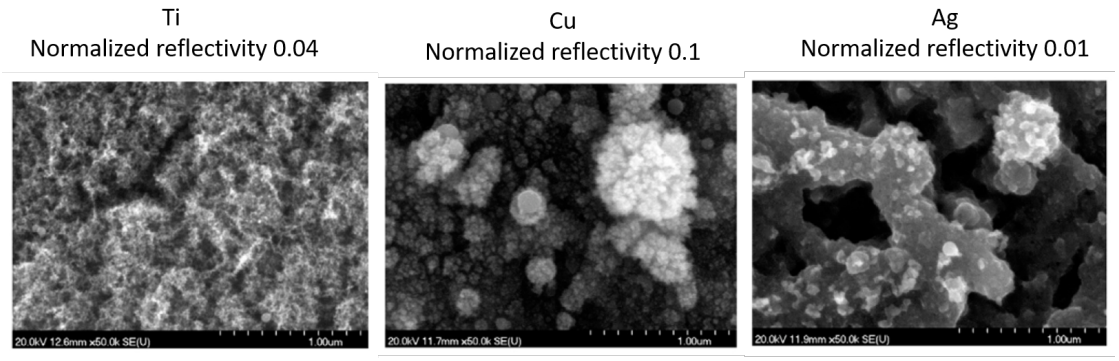

Figure 3.8: a) SEM images showing morphological progress of the nanostructures on titanium a) copper b) and silver c) surfaces irradiated in air with 100 fs laser pulses with a fluence of 0.5 J.cm^{-2}. The width of the images corresponds to 2.5 μm [79].

In [80], a study of the morphology and the subsequently reflectivity of the laser-treated surface is reported depending on the irradiating conditions: wavelength, pulse duration, number of pulses and irradiating fluence.

The morphology of copper surfaces is shown in figure 3.9 under various irradiation conditions. It can be seen that:

- at a given fluence, the nanofeatures size increases with increasing number of pulses;
- for a fixed number of pulses, the nanofeatures size increases with increasing fluence;
- similar patterns of nanoparticles are observed with the different irradiating wavelength using adapted fluences;
- filament-like structuration are observed in the fentosecond regime, while round droplets were observed with a 10 ps laser pulse.

The size and shape of nanostructures can be controlled by varying fluence and the number of pulses: generally, more nanoparticles of a bigger size are observed on the surface when the irradiating fluence (controlled by the number of pulse or the fluence of one pulse) increases as more material is ablated from the surface. The morphology also evolves from small round droplets to larger round droplets, finally to fractoides shapes at higher fluences.

Effect of the surrounding environment on the plume dynamics (ambient gas and magnetic field)

For different fluences, the impact of gas environment (nitrogen, air, oxygen, and helium) on the surface morphology and reflectivity has been studied when irradiating a copper surface with 100 repetitions of laser 150-fs-long pulses at the wavelength of 775 nm [79]. Figure 3.10 shows SEM analysis a) and the normalized reflectivity at 550 nm b) of the each irradiated sample was measured.

The effects on the reflective properties of the treated surfaces were induced in two ways: during the formation processes or because of the chemically-induced modifications

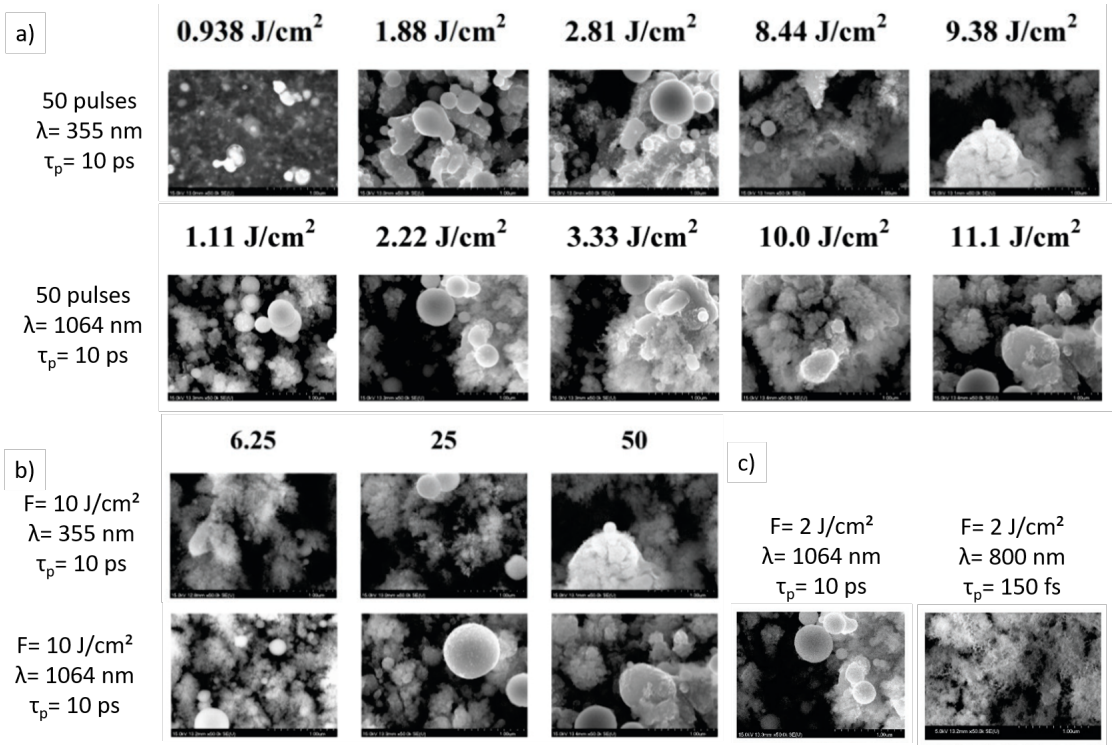

Figure 3.9: SEM top view images on copper surface under different irradiation condition. a) Comparison for different values of irradiating fluence for two wavelengths (number of pulses and pulse duration are constant) . b) Comparison for different values of the number of pulses for two wavelengths (fluence and pulse duration are constant). c) Comparison for different values of the pulse duration. The width of the images corresponds to 2.5 μm [80].

of the nanostructures. It is known that together with the roughness, the oxidation and the chemical modification of the surface have a impact on the light trapping.

The properties of the ambient gas having effects on the plume expansion dynamics and nanoparticle formation can be summarized as followed, [158]:

- the thermal conductivity of the target influences the temperature of the plasma evolution: a high thermal conductivity leads to a faster cooling rate, the condensation process starts and finishes earlier, it reduces the time for condensation and smaller nanoparticles are formed;

- the diffusion coefficient changes the dynamics of the ejected particles. With a high diffusion coefficient, the nanoparticles are more efficiently mixed with the ambient atmosphere and transported further away from the ablation site;

- the atomic or molecular weight changes the dynamics of the ejected particles. A low atomic mass or molecular weight leads to a faster and further expansion of the plasma plume. This is due to the fact that less energy is lost in the collision between the ablated material and atoms or molecules of the ambient gas [162]. The plume expansion being faster in presence of light gas ambient it moves away from the target surface. Particles have a lower tendency to be re-deposited to the

target. It leads to a decreased deposition rate in presence of light gas compared to heavier. It was experimentally observed that 14 % of the total ablated mass/pulse of copper is redeposited back on the target in argon ambient compared to 6 % in helium ambient (4 ns 266 nm irradiation) [162].

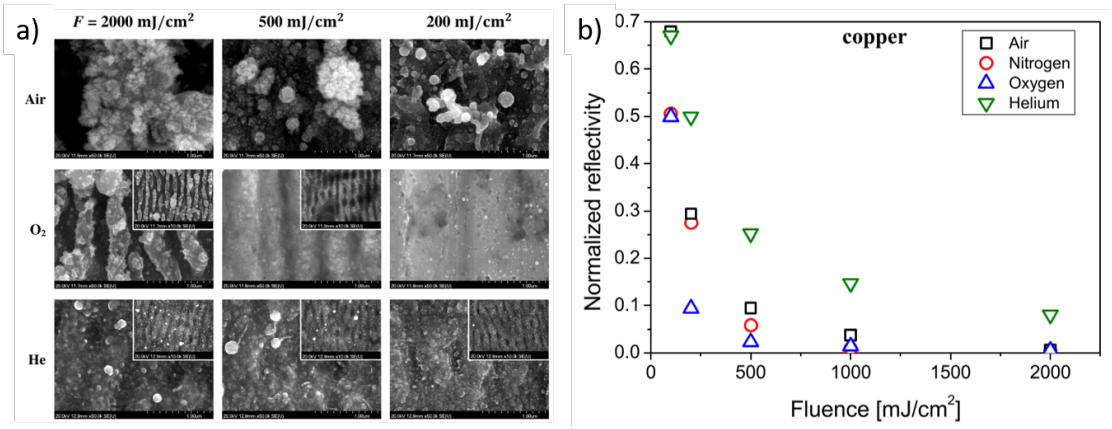

Figure 3.10: a) SEM top view images on copper surface irradiated with different laser fluences (F) in air, di-oxygen and helium. The width of the images corresponds to 2.5 μm and 12.5 μm for the lower magnification insert. b) Normalized reflectivities of the irradiated copper sample at 550 nm as a function of the applied laser fluence. The samples were irradiated with 100 laser pulses in different gas ambiences [79].

As an example, the properties of helium compared to air, argon, di-oxygen, and air explain the inhibition of the nanoparticle creation, agglomeration and deposition onto the target surfaces when helium atmosphere is used for the ablation. It was verified in [158], where the size distribution of particles created under argon had a maximum size around 30 nm while the particles created under helium atmosphere followed a logarithmic decrease from 10 nm (the minimal size measurable by the system). This trends is also visible in figure 3.10 where only a few nano size features can be observed when the sample is irradiated under helium atmosphere. The higher reflectivity of the samples irradiated under helium atmosphere was explained by the lack of nanostructures covering the surface.

Another example is given in [157], in the case of a 30-ns-long, 511 nm laser irradiation of copper samples. The samples irradiated in air and argon jet gas showed similar surface morphology at low magnification the irradiated surface was covered of spherical particles with an average size of 5 μm whereas differences appeared at nanoscale. 50-100 nm diameters features were covering the microscale particles of the sample treated in air while the nanoscale structuration was not observed with the argon atmosphere.

The influence on the ablated material re-deposition of the magnetic field surrounding the ablation site was reported in [162], as the magnetic field influences the plasma dynamic which stays more or less close to the target. It was observed that both, the number and the shape of nanoparticles are impacted. The presence of the magnetic field increased the ratio of the re-deposited over the total ablated mass from 14 % to 21 % in the case of argon and from 6 % to 16 % in case of helium ambient.

Laser-induced periodic surface structures (LIPSS)

When the treated samples are not covered by nanostructures, a laser-induced periodic surface structuration can be observed. LIPSS are also called ripples or nano-ripples and are nanostructures constituted of alternation of crests and troughs, nanoscale periodic grooves [135]. Based on their periodicity, two types of LIPSS are observed: the low-spatial-frequency LIPSS (LSFL) have a periodicity close to the laser wavelength, and the high-spatial-frequency LIPSS (HSFL) have a periodicity much smaller (typically 20 times smaller) than the laser wavelength. LSFL are perpendicular to the polarization of the incident laser beam while the orientation of the high-spatial-frequency LIPSS (HSFL) can be parallel or perpendicular to the beam polarization.

Low frequency LIPSS formation is usually explained in three steps [163]:

- due to interference between the incident light and the surface scattered waves, a periodical modulation of the electron temperature can appear at the surface of the sample;
- the amplitude modulation in the electron temperature evolves into a high-amplitude modulation in the lattice temperature upon electron-lattice thermalization; Metals with a high electron-lattice coupling coefficient allow a strong confinement of the energy and stronger temperature gradients in the molten thin layer;
- the surface gradients of temperature can also involve local Marangoni force, which relocates material along the surface and induce ripple growth. Both, thermal diffusion and hydrodynamical motion cool down the molten layer, which undergoes solidification that freezes the metal surface in a groovy shape [150]. Hydrodynamic processes in the molten surface layer form the LIPSS pattern.

Electron-phonon coupling has a role in the ripple formation and growth on metallic materials under ultrafast laser irradiation. The higher the coupling is, the more susceptible are the ripples to grow. The relative amplitudes of the surface patterns on ruthenium, tungsten, nickel, and copper match the ranking of these materials based on the electron-phonon coupling coefficient and the absorptivity [150].

LIPSS produced by long-pulsed lasers have smooth features which can be observed as long they are not densely covered with nanostructures as reported in the inserts of figure 3.10. Ripple amplitudes tend to increase logarithmically with the fluence [82]. The amplitude can reach several hundreds of nanometers [81]. LIPSS are visible from very low fluences: 0.3 J.cm^{-2}. If the fluence is higher than 1.2 J.cm^{-2} particles appear at the surface of the sample (for 1064 nm, 10 ps irradiation) [81].

For copper, the periodicity of the LSFL has been reported to be 0.5 times the wavelength for a fluence of 0.15 J.cm^{-2} and 0.85 times the wavelength at 2 J.cm^{-2} [135]. Other measurements gave a ratio of 0.676 (for 532 nm 7 ps irradiation) [163], or 0.8 on a brass copper alloy [164].

The formation processes of HSFL are still an open question: self organisation, interference of the incident laser radiation with the surface electromagnetic wave generated on

a rough interface between the metal and the air, second harmonic generation, splitting of LSFL [81].

Other self organized patterns, smaller than the beam diameter, can also be pyramids, holes structures, chaotic rugged patterns.

During a femto second irradiation of stainless steel 304 and titanium, the origin of ellipsoidal cones was explained, based on chemical, crystallographic, and topographical analyses, by un-ablated material whose conical geometry offers a significant degree of fluence reduction (35-52 %). Therefore, the rest of the irradiated area is preferentially ablated at a higher rate than the ellipsoidal cones [165]. Elsewhere, multiscale mound-like titanium structures were attributed to re-solidification of molten material from the hydrodynamic Marangoni effect driving fluid flows. FIB analysis showed porosities present in this re-solidification layer, that also confirms melting/fluid flow. Such porosities can be the results of gas bubbles or shrinkage [166].

To conclude, in this section, the link between the morphology characteristics and the functionalities of the surface has been highlighted. The effects of laser treatment parameters on the morphology have to be understood in order to then, choose optimized parameters and enhance the surface performance.

3.1.6 Oxidation of copper surfaces

This section is focused on the oxidation of copper upon conventional heating processes and upon heating induced by laser irradiation.

Two common forms of copper oxide cuprous oxide or cuprite (Cu_2O) and cupric oxide (CuO). Both are p-type semiconductors with a band gap of 1.9-2.1 eV and 2.1-2.6 eV, respectively [167]. It has been shown that the oxidation of the treated surface strongly influences the material functionality: for instance, CuO is hydrophile while Cu_2O is hydrophobic, the reflectivity of CuO and Cu_2O [168], as well the SEY behavior are significantly different. That later point has already discussed in section 1.3.

The thermodynamically stable phases in dependence of the partial pressure of oxygen and the temperature during oxidation are reported in figure 3.11.

The evolution of the oxidation state during annealing was reported in various studies [168, 170–172].

The formation of Cu_2O is reported on the film surface for temperatures lower than 300 °C while CuO developed for higher temperature [170].

For instance, in [168], relative oxide concentrations at the sample surface evolved from 78 % for Cu_2O, 20 % for CuO and 2 % for $Cu(OH)_2$ before the annealing to 20 % Cu_2O, 68 % CuO and 12 % for $Cu(OH)_2$, after annealing in air at 600 °C. The increase of the crystal size was also reported due to recrystallisation effects at elevated temperatures.

Mainly driven by the increase of the crystalites size, the oxidation of the surface also triggers a roughness increase. In [172], the thermal oxidation of thin film copper between 200 and 450 °C leads to an increase of the RMS roughness from 1.47 nm before annealing to 11.78 nm at 100 °C, the value remained constant up to 450 °C.

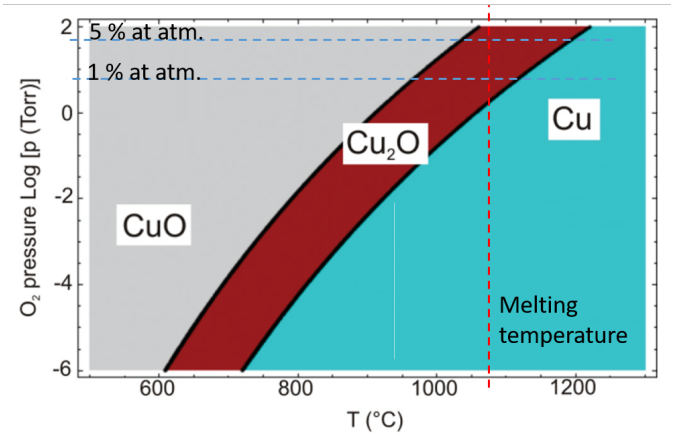

Figure 3.11: Calculated phase diagram of the copper oxide system indicating thermodynamically stable phases depending on the partial pressure of oxygen and the temperature. The melting temperature of copper is indicated, as well as the partial pressure corresponding to 1 % and 5 % concentration of di-oxygen at atmospheric pressure. Extrapolating this graph, CuO is the stable phase of oxide in air at atmospheric pressure, after [169].

In [171], the oxidation of copper was studied at low temperature in air. The composition of the oxide layer was evaluated based on XPS measurements and reported to be composed of three regions: on the top, a very thin CuO layer, a thick Cu_2O layer and a region containing oxygen. The layer thicknesses increased when enlarging the oxidation time or increasing the temperature (from 200 to 300 °C, the two temperatures considered in the study). After 1 min annealing, the layers were measured to be between 5-10 nm for CuO, 40 nm for Cu_2O and 100 nm for the oxygen-containing zone.

Some insights on the oxidised state of the copper also came from laser treatment oriented studies.

The laser-assisted oxidation of copper thin films was reported in [173]. A 75-fs-pulsed, 1040 nm irradiation was performed below the ablation threshold (0.13 J.cm^{-2}), under air atmosphere on copper thin films (thicknesses were between 50 and 200 nm). The formation of chromatic annuli of copper oxide was observed around the laser spot (see figure 3.12) and was studied by micro-Raman spectroscopy, optical and electronic microscopies. CuO was observed closer to the beam spot location and Cu_2O at larger distance. The variation of the radius of the oxide ring depending on the film thickness suggested a strong influence of the temperature and thermal history of the samples.

During the laser irradiation of copper in air, the formation of CuO and $Cu(OH)_2$ was reported [157]. It was explained by the vaporized copper particles from the plume reacting with oxygen and water vapor from the air.

It was reported that the laser treatment parameters such as the scanning speed changes the oxidation state of the surface. For instance, in [157], the chemical composition, analysed via XPS spectra of the surface, depends on the scan speed of the laser treatment. For a high velocity of 100 mm.s^{-1}, at which the laser beam is focused in a point of the surface for a shorter time (as compared to lower scanning speed) Cu^+ oxidized state (Cu_2O) was observed while at lower velocities of the beam the copper

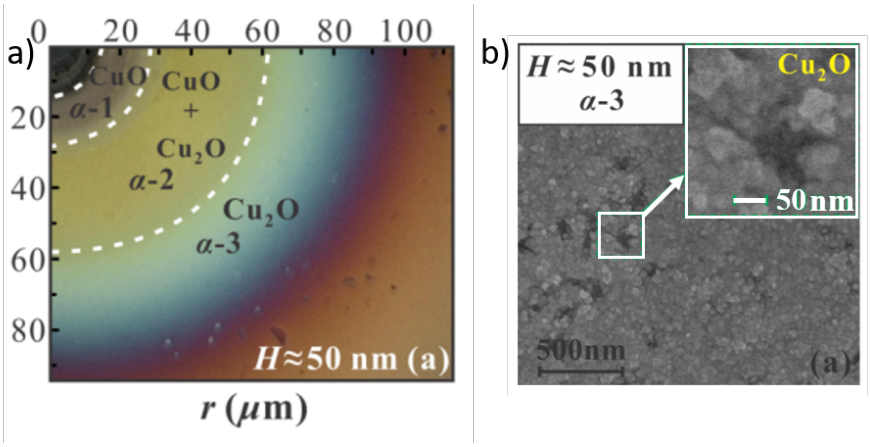

Figure 3.12: a) Optical microscopy image of the surface of the copper 50-nm-thin films, after 1 min irradiation with fs laser pulses 50 MHz at an average fluence of 0.13 J.cm^{-2} in air. The images illustrate the formation of diverse chromatic annuli on the film surface. The white circles identify different annular regions associated to the predominance of a particular copper oxide. b) SEM image of the regions occupied only by Cu_2O (noted $\alpha - 3$ in a)). The upper-right inset corresponds to the areas marked by dashed squares in white. After [173].

surface is oxidized to a Cu^{2+} state (CuO).

3.2 TEM: morphological and chemical transformations depending on fluence

The TEM analysis objective is the investigation of the effects of the absorbed laser energy in the copper target and subsequent relaxation of the energy that induces chemical and structural transformations during laser irradiation. The important input of the TEM analysis carried out in this study compared to the microscopic analysis performed in previous one ([77]) was the possibility to observe the interface region, the particles and the interface areas in between for several values of irradiating fluence.

Results have been already partly presented in [174].

It is worth noting that owing to the thickness of the specimens prepared by FIB (around 100 nm), that leads to dynamic diffraction conditions, only *lattice imaging* was achieved instead of *high resolution analysis at the atomic scale.*

3.2.1 TEM experimental proceedings

Methods used for analysis

The microstructure and the chemical composition of the surface layers have been studied in more details by transmission electron microscopy (TEM), energy-dispersive X-ray spectroscopy (EDX), high-angle annular dark-field imaging (HAADF), energy-filtered transmission electron microscopy (EFTEM), lattice imaging, selected area electron diffraction (SAED) methods in order to investigate metallographic structures, composition and phase transformation at the surface of the laser-processed material.

These analyses have been carried out on the microscope FEI TECNAI F20-ST, at Centre des Matériaux (CDM) of Mines ParisTech.

TEM specimen preparation

In this section, samples were treated with *G3* and *D12* parameters, described in section 2.2.1.

The sinusoidal shape of the surface made the extraction of the specimen from the concave area of the groove difficult. A special care was taken not to deteriorate the specimen during the polishing and handling of the specimen.

Figure 3.13 shows a SEM cross section image of the sample after FIB polishing. Although this picture has not been made during the thin sample preparation, it illustrates the size and the localization of the thin specimens compared to the general morphology of the treated surface (size of the specimens compare to the hatch distance and groove depth, localization of the specimens on the top of the groove and on the bottom of the valley).

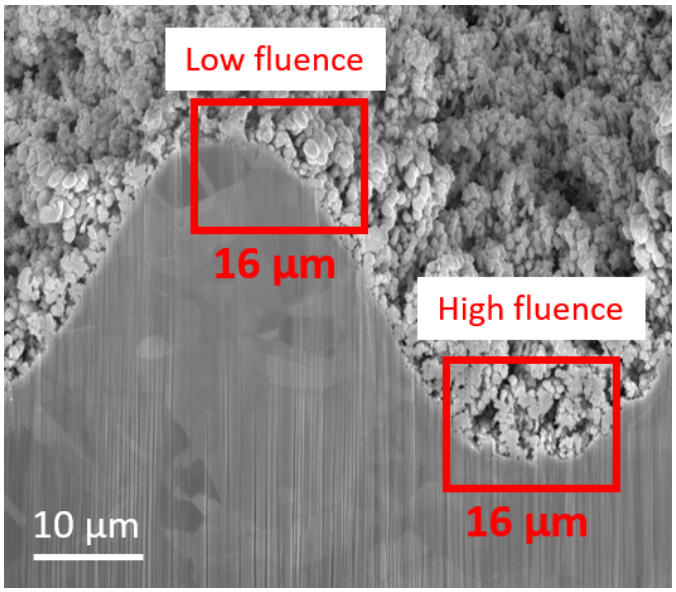

Figure 3.13: SEM image after a FIB polishing. Illustration of the location from where the specimen has been extracted from the treated sample: in the convex part of the groove at low irradiating fluence and in the concave part of the groove at high irradiating fluence.

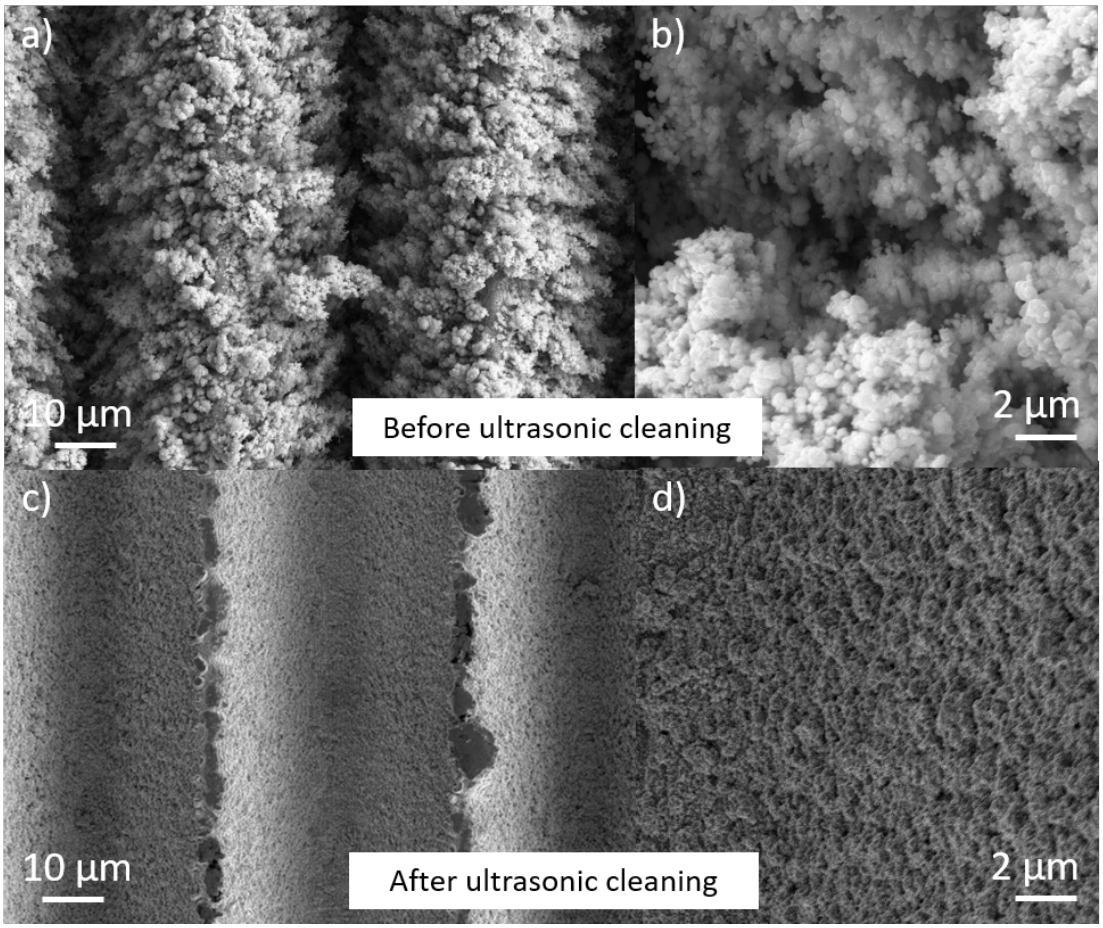

Figure 3.14: SEM images of *D12* sample before (a) and b)) and after (c) and d)) ultrasonic cleaning.

Three FIB specimens have been prepared at CentraleSupélec for the investigation on the effects of the irradiating fluence on the copper:

- surface after ultrasonic cleaning: the superficial structures were removed following the procedure described in section; 2.3.3). The ultrasonic cleaning removes most of the particles covering the surface as it can be seen in figure 3.14 c) and d). The removal of the particles eased the handling of the specimen and allowed the observation near the surface irradiated by high values of fluence (in the concave areas of the grooves).

- a specimen extracted from high laser fluence region. The extraction of a thin specimen from the concave part of a groove required elaborated sample preparation. The impregnation of the sample in slow polymerization embedding resin *LR White* from *Agar scientific* was necessary to preserve the integrity of the particles. SEM images after preparation are presented in figure 3.15. A beveled mechanical polishing (figure 3.16) was performed in order to ease the access to the bottom of the valley avoiding time-consuming ion polishing;

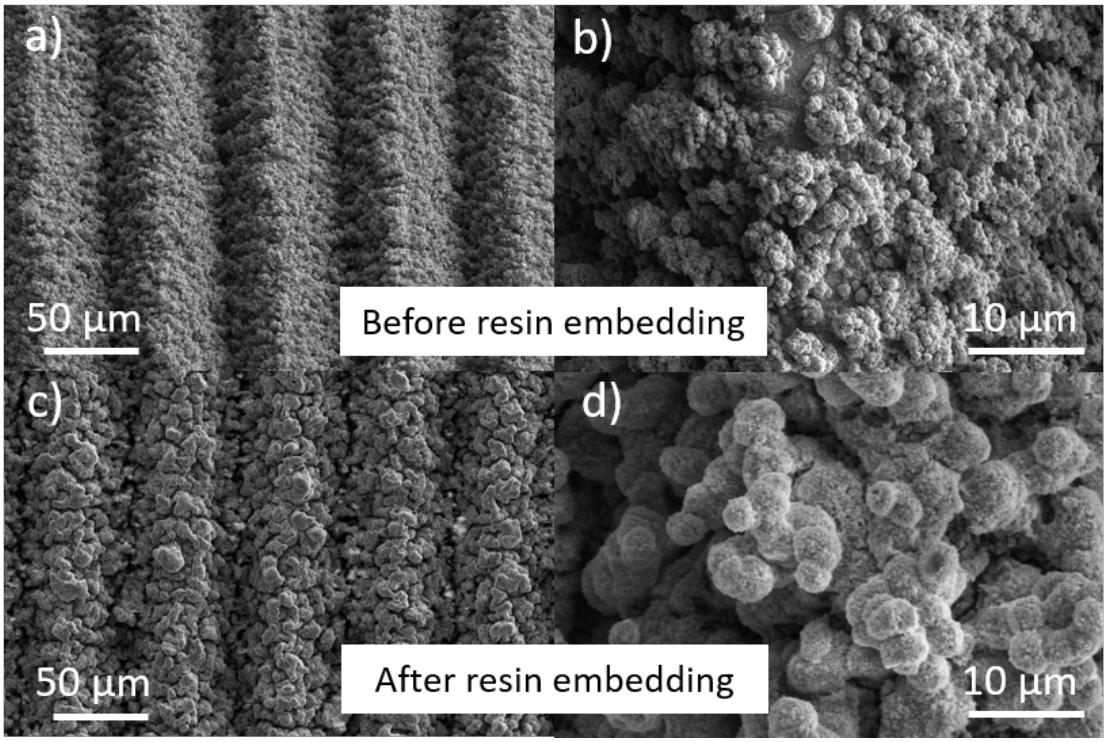

Figure 3.15: SEM images of *G3* sample before (a), b)) and after (c), d)) resin embedding.

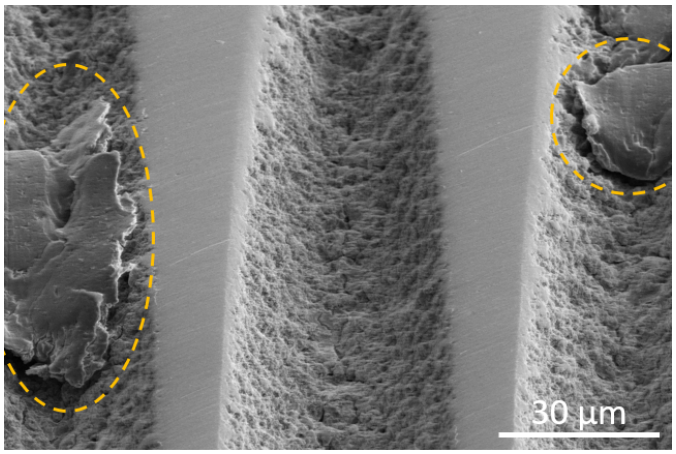

Figure 3.16: SEM images of the surface embedded in the resin after bevelled polishing. The access to the bottom of the groove is eased by the removal of the top part of the groove by bevelled polishing. The resin protects the nano-surface from chips or debris from the mechanical polishing identified by yellow circles.

- on a sample from low irradiating fluence area. The specimen has been extracted from the convex part of the groove. The lower density of particles in this area eased the extraction and the manipulation of the specimen.

Figure 3.17 presents the microscopic images made during the preparation for a thin specimen extracted from the laser-treated sample on the top of the grooves. The preparation of the other specimens is illustrated in Appendix C.

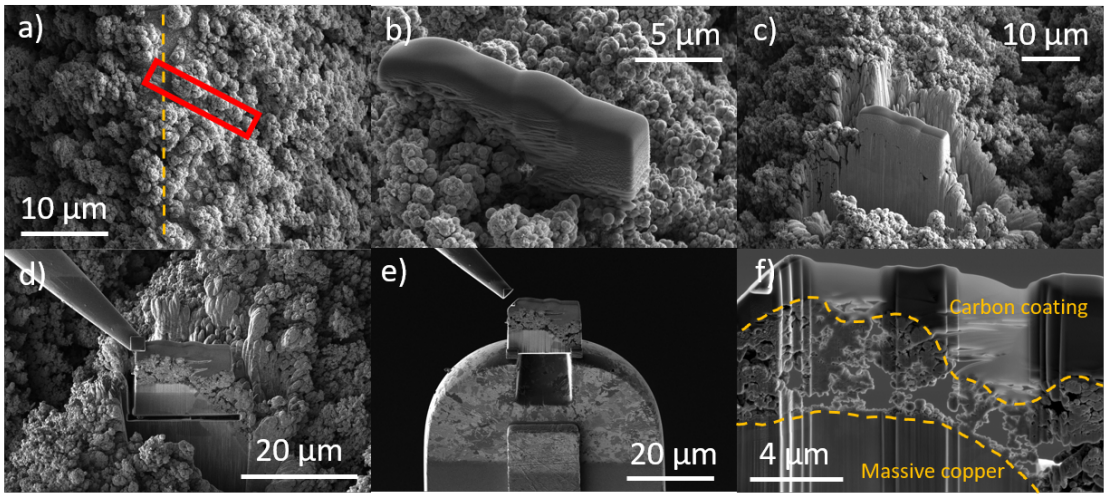

Figure 3.17: FIB specimen preparation for TEM analysis. a), b), c) SEM images of the surface of the samples. a) illustrates the selection of the area of interest (the red rectangle on the image) on the top of a groove (the yellow dashed line), b) illustrates the deposition of the carbon layer to protect the rough surface during polishing and handle the specimen. c) The volumes around the specimen are polished via ion beam etching. d), e) Ions beam images of the specimen before final polishing. d) Trenches are machined by the ion beam to detach the specimen out of the sample. The specimen is handled by a needle visible in the top left corner of the image. e) The specimen once detached from the sample is brought to the sample holder. f) SEM image of the specimen after final polishing.

In figure 3.17 f), the bulk copper shaped by laser erosion can be seen in top of a sinusoidal groove, the particles distributed over this bulk surface and the carbon protective layer. The frontier between the particles and the carbon protective layer is hard to establish, the carbon deposition could also have modified the structure of the neighboring copper particles; consequently the analysis of these particles will be focused in an area rather far away from the carbon layer.

Figure 3.18 illustrates the effects of the final polishing. Large apertures and porosities between the bulk copper and the particles appear on these SEM cross section views. The near surface of the sample seems highly porous. Nevertheless, it is worth to note that apertures have been increased by ion erosion and especially by the final ion polishing, which aims to reduce the thickness of the specimen to 100 nm. Some of the aggregates of particles are detached during the polishing process. The analysis of this specimen does not aim to quantify the amount of particles or the porosity, knowing that only a partial proportion of originally present particles remains on the surface after ion polishing. The microstructure and chemical composition will be assessed.

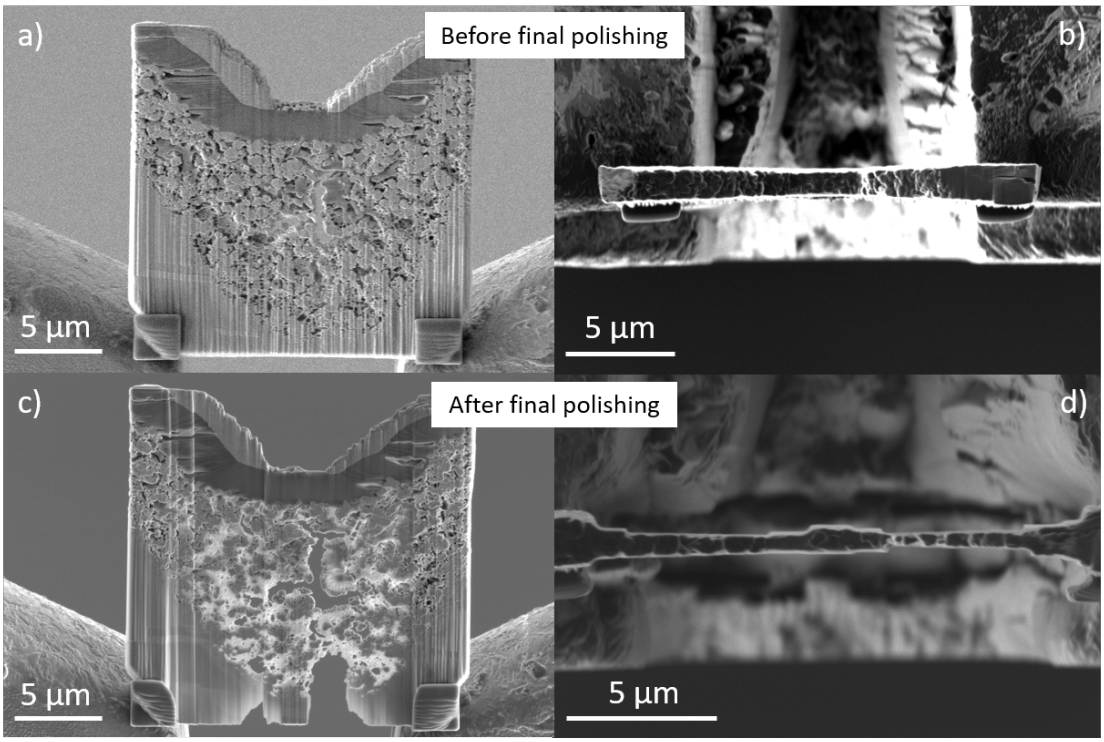

Figure 3.18: SEM images of the specimen before (a), b)) and after (c), d)) final polishing.

3.2.2 Local irradiating fluence

The three specimen have been prepared in order to investigate the effects of the laser irradiation on the copper for a large range of laser fluence. Indeed, depending on the localization of the specimen on a groove, the material is locally exposed to different fluence. The points where the TEM analysis have been focused are localized thanks to their distance to the center of a groove. For instance, the maximum irradiation received by the point localized at 27.5 μm of the center of the groove, during one pulse is 0.25 J.cm^{-2} while it is 2.35 J.cm^{-2} for the point localized right in the middle of the grooves with *G3* laser configuration. The cumulative fluence received by theses two points during the treatment is 219 J.cm^{-2} and 1010 J.cm^{-2} respectively.

Figure 3.19 presents the Gaussian profiles of fluence of each pulse irradiating the copper samples used for the TEM analysis. In the case of *G3* the energy of each pulse was 25 μJ while it was 20 μJ for the sample called *D12*. The spatial distribution of the fluence, *i.e.* the energy density, was different in the two cases and allowed analysis of material under various laser fluence. On each of these profiles the analysis points have been localized and the laser fluence irradiating these points has been identified.

For pulsed laser irradiation, the heat affected zone of the material for a single pulse is defined by the heat diffusion length or by the electron heat diffusion. In copper, the electron penetration can be in the range of $L_P = 100$ nm. Considering the thermal diffusivity of copper D_{Cu} and given the laser pulse duration $\tau_P = 10$ ps, the heat diffusion length for each pulse $L_{Cu} = 2\sqrt{D_{Cu}\,\tau_P}$ is evaluated to be 66 nm.

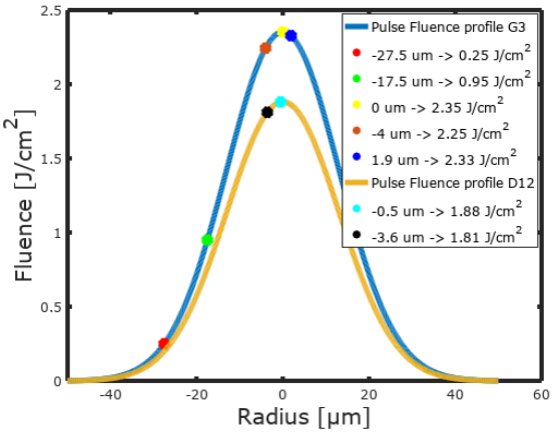

Figure 3.19: Pulse fluence profiles for *G3* laser parameters in blue and *D12* laser parameters in yellow. The dots on the curves indicate the position where TEM analysis has been performed, the corresponding fluence is also indicated.

Figure 3.20, figure 3.21 and figure 3.22 a) are general SEM of the specimens after the final ion polishing. On these images, the deposited carbon can be identified as well as a layer of copper deposited to the top of the carbon layer during the ion polishing. Figure 3.20, figure 3.21 and figure 3.22 b) show bright field TEM images of the specimen. The white areas are the porous area where there is no material. The lightness depends on both the local thickness of the sample (the two areas where the ion erosion has been more advanced and where the sample is thin appear lighter) and the local atomic composition (the carbon layer made of a lighter element than the particles presumed to be made of copper and oxygen appear lighter). The TEM pictures show the grain structure of the bulk copper, the particles area as well as the protective carbon layer. The red rings are the localization where the TEM analysis have been focused. The distance to the center of the groove is indicated for each of these points as well as the associated fluence (maximum fluence for one pulse).

TEM analysis has been performed in order to understand the mechanisms involved in the laser processing and the physico-chemical transformations and to allow an estimation of the local mechanical properties. The analysis has been focused on several distinct areas: on the interface region irradiated by 0.25, 0.95, 1.81-1.88, 2.25-2.35 J.cm^{-2}. The analysis has been focused on the particles irradiated by 0.25 and 2.25-2.35 J.cm^{-2}.

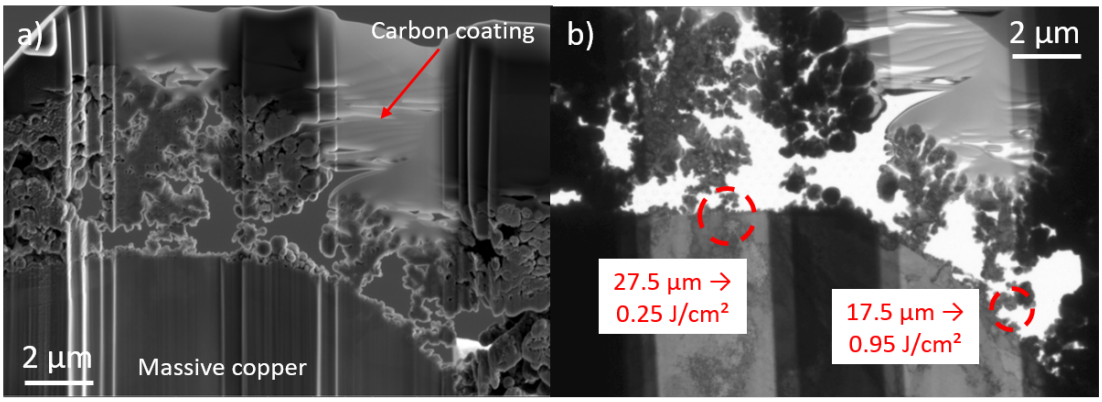

Figure 3.20: General SEM a) and TEM bright field b) images of the specimen extracted from the top of the grooves. The bulk copper can be seen on the bottom left corner of the image as well as the carbon coating deposited during the specimen preparation. In between the particles created by the laser treatment are visible. b) Red circles indicate the main area of interest on the specimen. The distance to the centre of the groove and the corresponding irradiating fluence are indicated.

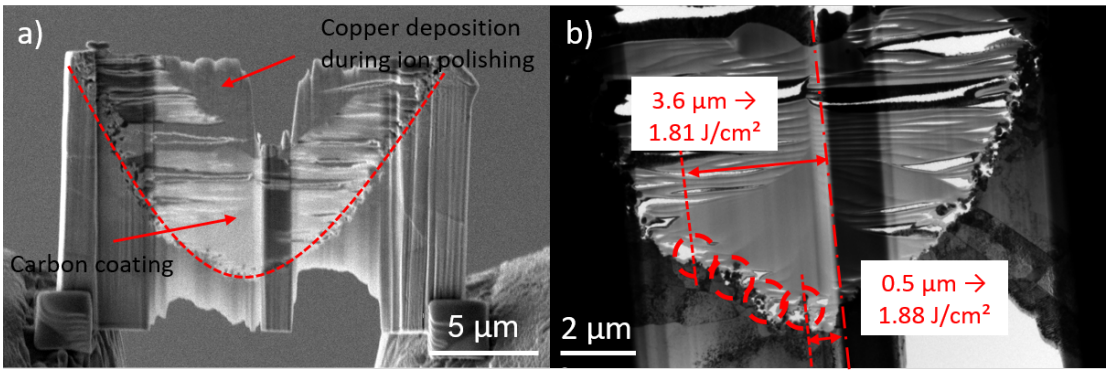

Figure 3.21: General SEM a) and TEM bright field b) images of the specimen extracted after ultrasonic cleaning of the sample. The V-shape of the bulk copper can be observed as well as the carbon coating deposited during the specimen preparation. A layer of copper ablated during the ion polishing is re-deposited to the top of the carbon coating. b) Red circles indicate the main area of interest on the specimen. The distance to the centre of the groove and the corresponding irradiating fluence are indicated.

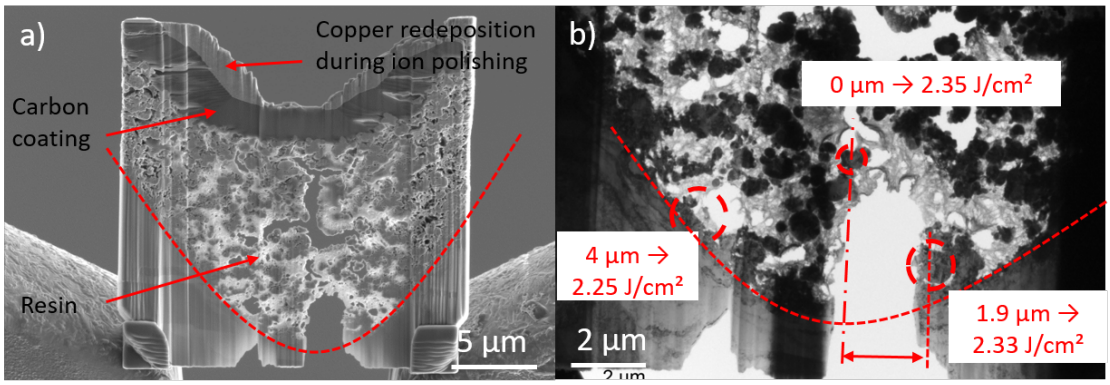

Figure 3.22: General SEM a) and TEM bright field b) images of the specimen extracted after resin embedding. The V-shape of the bulk copper can be observed as well as the resin which impregnated the copper particles, the carbon coating deposited during the specimen preparation and the re-deposed layer of copper ablated during the ion polishing. b) Red circles indicate the main area of interest on the specimen. The distance to the centre of the groove and the corresponding irradiating fluence are indicated.

3.2.3 Interface region between bulk copper and particles

Interface region irradiated at 0.25 J.cm^{-2}

Below the ablation threshold, there is an apparent distinction between the bulk copper and the surface features.

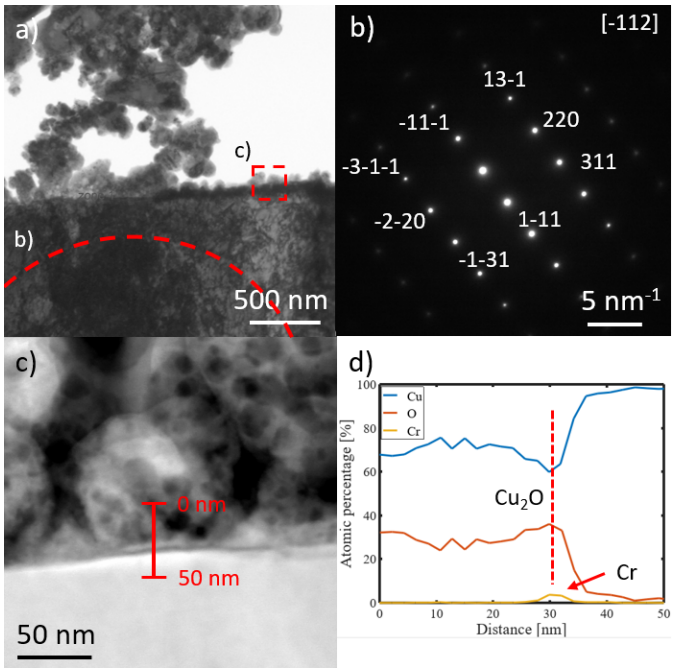

Figure 3.23: a) TEM Bright field image in an area irradiated by 0.25 J.cm^{-2}. The red square defines area selected for higher resolution images. The red dashed arc defines the area selected from the diffraction analysis. b) the corresponding SAED pattern from the indicated area. c) STEM-HAADF image of the interface region. d) Elemental distribution of copper, oxygen and chromium (in blue, red and yellow, respectively) extracted from the EDX map, every 1 nm, along the red line marked in c).

The bulk copper has been analysed by electron diffraction. The SAED pattern from the selected area presented in figure 3.23 b) (also visible in figure C.9 c)) correspond to a large area located between 200 nm and 5 μm below the surface. Analysis of the SAED pattern of this area shows a monocrystalline face-centered-cubic crystal structure (space group Fm-3m) and unit cell constant a = 3.6 Å. Without apparent crystal defect or indication for re-crystallisation, this material can be considered as not being modified by the laser treatment.

In figure C.9, the microstructure of the bulk located up to 10 μm below the surface has been analysed, and confirmed the observation of monocrystalline and uniform large-size copper grain. The visible contrast, between 1 and 8 μm below the surface changes while tilting the specimen; it is due to dislocations within one grain and not grain boundaries themselves. The SAED pattern of the area chosen in the deeper below the surface, (between 8 and 10 μm) is shown in figure C.9 c). It also exhibits face-centered-cubic monocrystalline structure but with a different crystallographic orientation. The grain size observed below the surface is typically in the range of 5-6 μm.

Figure 3.23 c) represents a STEM dark field image, obtained using a High-Angle Annular Dark-Field (HAADF) detector. In this Z-contrast image, the lighter the element is, the darker it appears. Thus, an evident interface can be seen between the uniform bulk copper in the bottom of the image and the top layer of heterogeneous structure of lighter elements. The chemical composition profile along the red arrow has been determined by quantitative EDX analysis focused on the concentration of three elements: copper, oxygen and chromium (figure 3.23 d)). The EDX profile corroborates evidence of the two distinct layers: bulk copper and oxide layer. In the oxide layer, the average atomic fraction of the two elements is approximately 33 % and 66 % for oxygen and copper, respectively, revealing the presence of cuprous oxide, Cu_2O (copper (I) oxide). A trace of chromium can also be observed on the surface of the bulk that is probably a residue after surface passivation described in section 2.2.1. This is another proof of the re-deposition of the oxide layer on the top of unprocessed copper during the laser treatment.

Exposed to a fluence lower than the ablation threshold, copper microstructure does not undergo through any re-crystallization of the lattice and keeps the same size and morphology as the microstructure of the unprocessed copper. The undamaged copper is covered by a layer of material probably coming from the ablation site in vicinity. Knowing that the laser irradiation had been performed under a laminar flux of nitrogen the oxidation of the material, which has travelled in the plume before reaching the site of observation is not fully understood. The presence of oxygen in the atmosphere may be explained by strong turbulent streams generated by the evaporation of ablated copper and ejection of particles in the ablation site.

In order to closer investigate the interface and the composition of the oxide layer lattice imaging has been performed. Figure 3.24 b) shows the precise localization of the area selected for lattice imaging at the interface between the layers in the area irradiated at 0.25 J.cm^{-2}. In this case, the bulk copper appears darker and the oxide layer is slightly lighter. Along this interface, three areas marked in b) have been selected for detailed analysis of crystal structure. The results are presented in figure 3.25. The lattice spacing of the fringes visible on the lattice imaging (figure 3.25 b)) has been deduced from the post treatment of the corresponding Fast Fourier Transformation (FFT) image (figure 3.25 c)) and revealed in this case a mono-crystalline cubic crystal structure of copper (I) oxide, Cu_2O, (space group Pn-3m) with a unit cell constant a = 4.25 Å. Similar analyses in other spots along this same interface revealed a lattice structure corresponding to cupric oxide CuO (copper (II) oxide) either in a poly-crystalline structure or in a mixture of both oxides (see in appendix figure C.10).

The observed nano-crystals of the oxidized layer on top of the copper bulk suggests a fast kinetics of cooling of ablated material after exposition to oxygen in the plume. Re-deposition of the molten material is observed on the surface of the bulk copper that has not been altered by the laser pulses below the required ablation threshold. Ablation (evaporation or melting) copper is not expected in this area. That confirms the observations on cross sectional micro-graphs: the top of the grooves is on the same level than the original copper in figure 3.37.

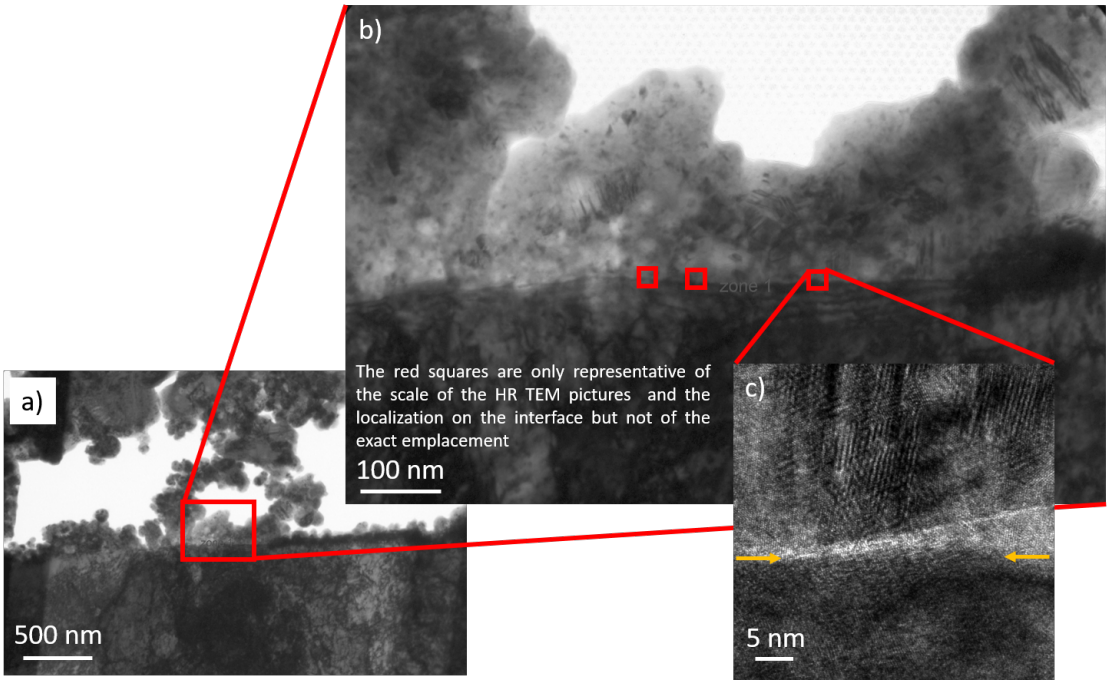

Figure 3.24: Illustration of the localisation of the area selected for lattice imaging on the interface in the area irradiated at 0.25 J.cm^{-2}. a), b) Bright field TEM images. The scale bars in TEM images is 500 nm and 100 nm respectively. c) Lattice imaging at the interface of the oxide layer. The yellow arrows indicate the position of the interface.

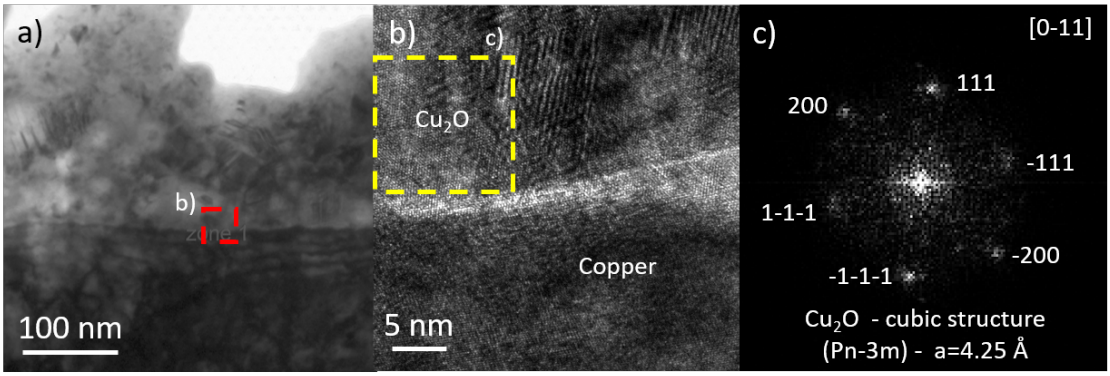

Figure 3.25: a) TEM bright field image in the area irradiated at 0.25 J.cm^{-2}. The red square defines area selected for high resolution image. b) Lattice imaging of the interface in between the oxide layer and the copper. c) Corresponding Fourier spectra from the indicated yellow squared area in b).

Interface region irradiated at 0.95 J.cm^{-2}

The bright field TEM and STEM-HAADF images of the interface region in the zone irradiated by 0.95 J.cm^{-2}, above the ablation threshold (figure 3.26) show a structural transformation of the underlying microstructure. The effect of the laser irradiation can be seen on both the sub-surface and the surface roughness.

While tilting the specimen, the contrasts visible in the bottom left corner of figure 3.26 a) disappeared, the contrasts were attributed to dislocations or defects in the crystal

rather than grain boundaries. Based on this observation the grains of size deeper than 300 nm below the surface was estimated to be in the range of 1-2 μm. Higher magnification bright field TEM and STEM-HAADF pictures (figure 3.26 b) and c)) confirm grain size transition from finer-grained copper on top of the surface to the bigger grains in the bulk. The limit of the re-crystallisation limit was visible 250 nm below the surface. It is worth noting that this limit of re-crystallisation exceeds the length of the single pulse heat affected zone already discussed. This may be an effect of the heat accumulation in the case of multi-pulse irradiation. 50-nm-diameter porosities are suspected in the re-crystallized layer, they could have originated from bubbles and gas cavities.

The roughened surface was formed by splash-like shapes up to 200 μm into the material. These shapes seem to be resulting from transient hydrodynamics of free interface of the molten copper submitted to surface tension and fluid inertia. Quantitative EDX analysis, performed at the spots shown by red circles in figure 3.26 c) indicate the presence of pure copper. This interpretation would confirm melting and on-the-spot without transport in the plume. The surface roughness is due to the transient liquid phase frozen during re-solidification of the copper, due to the fast cooling allowed by the high thermal conductivity of copper and the possible evaporation of a fraction of the molten layer created under ablation above the damage threshold. In literature, micro-eruption of molten material are reported in [136]. As the properties of the molten material driving hydrodynamic behavior and modification of surface topography (density, viscosity and surface tension) are dependent on the temperature the characteristic shape of these structures is expected to depend on the fluence.

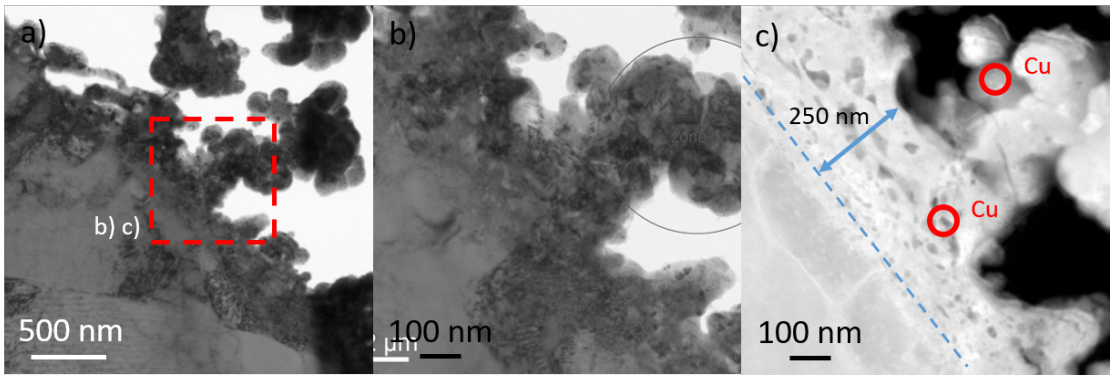

Figure 3.26: a) Bright field TEM image performed in an area irradiated by 0.95 J.cm^{-2}. b) Bright field TEM image on the red square identified in a). c) STEM-HAADF image focused on the red square identified in a). The limit between refined grain and larger grains is visible 250 nm under the surface. EDX analysis have been performed on the two points identified by red circles. Both analysis revealed copper as the dominant element (more than 90 %).

Interface region irradiated at 1.81-1.88 J.cm^{-2}

When increasing the value of fluence irradiating the surface, the local morphology changes. Laser-induced sub-surface defects were clearly observed at 1.85 J.cm^{-2} (see figure 3.27 a)). 100-nm-diameter, quasi-spherical, sub-surface voids are visible about 100-150 nm below the surface. On the oxygen and copper distribution EDX maps, pre-

sented in figure 3.27 b), it appeared that the inner walls of the apparently closed porosity exhibit a high oxygen containing area.

The surface roughness is still characterised by a feature which could result from a transient liquid phase frozen. The atomic concentration of oxygen and copper was investigated thanks to a detailed EDX inspection of the inner wall of an open cavity created by the surface roughness (see figure 3.27 c)). The cavity appeared to be covered with a 10-nm-thick layer of CuO oxide. (see figure C.20 in the appendix).

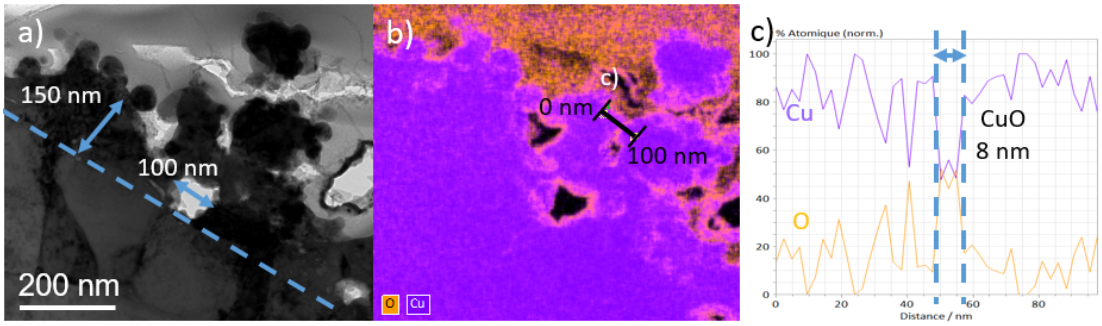

Figure 3.27: a) Bright field TEM image performed in an area irradiated by 1.85 J.cm^{-2}. b) EDX maps of element distribution of the corresponding area. The purple color corresponds to the copper-containing area. The oxygen containing area are identified in orange. c) Elemental distribution of copper and oxygen (in purple and orange, respectively) extracted from the EDX map, every 1 nm, along the segment marked in b).

More analysis treating of the surface roughness created under the range of fluence can be found in figures C.12, C.13, C.14, C.15 and C.16 in the appendix. These analyses focused on the microstructure of an emerging rugosity. Contrast changes while tilting the specimen suggested existence of grains with different crystal orientation in figure C.12. this was inspected at a lower magnification by electron diffraction, the results can be seen in figure C.14. The thickness of the copper oxide was also investigated both thanks to lattice imaging and elements distribution maps performed by EDX. Figure C.18 illustrates that in two similar splash-like rugosities, about 300 nm high exhibit different microstructures: in one case the crystal orientation along the structure was not modified while twinning structures and re-crystallisation were observed in the other rugosity. EDX analysis shown in figure C.17 confirms the presence of a 10-nm-thick layer of CuO oxide.

Figure 3.28 is a bright field TEM image of the interface region irradiated by 1.85 J.cm^{-2}. Although it could be a local artefact, some characteristics of the morphology of the surface can also be interpreted as the indication for the presence of the phase explosion threshold. The efficiency of this ablation mechanism has been reported to be significantly higher than evaporation and photo mechanical spallation (explaining the *step* observed on the profile of the interface region). This ablation mechanism is known to expel out of the surface large quantity of molten materiel, which increases the temperature gradient and cooling rates on the interface region (this would explain the local decrease of re-crystallisation depth under similar irradiation conditions on the right of the image).

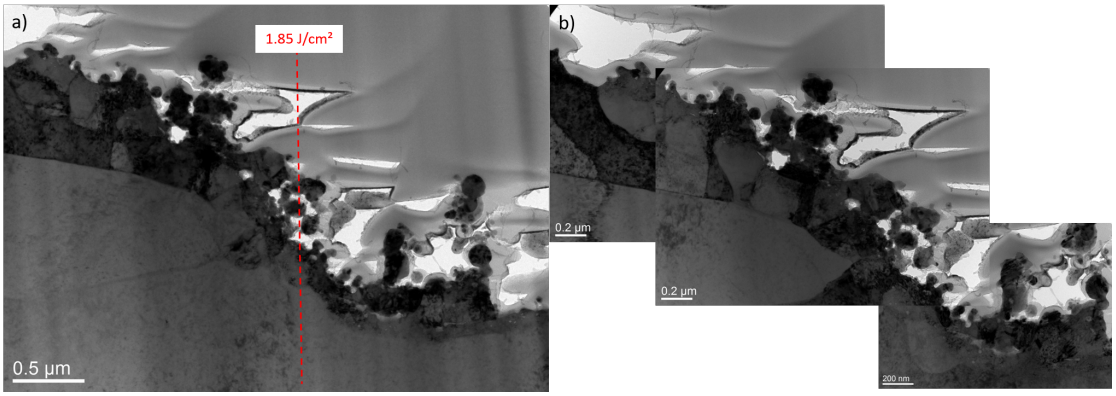

Figure 3.28: a) Bright field TEM image measured in an area irradiated by 1.85 J.cm^{-2}. On the left side of the dotted line, the fluence is lower than 1.85 J.cm^{-2}, on the right side it is higher. b) Compilation of bright field TEM images made with different tilts.

Interface region irradiated at 2.25-2.35 J.cm^{-2}

At the maximal fluence, the effects of the irradiation are enhanced such as an increase of the ablation rate. First quite spherical (see figure 3.27 a)), the shape of the sub-surface voids became elongated in the direction parallel to the surface (see figure C.20). Their size and their number increased, they can merge and create 1 μm long fractures as it can be seen in figure 3.29 a), which may detach out of the surface piece of material with sizes in the range of 1-2 μm. The creation of sub-surface voids has been reported in the literature, as an effect of the laser-induced tensile stresses. The stresses result from the thermal expansion of the atomic lattice due to the increase of the temperature consecutive to the laser irradiation. The higher the irradiating fluence is, the sharper is the temperature gradient in the lattice and the stronger are the stresses in the sub-surface. This phenomena would explain the growth and the coalescence of the voids at higher fluence.

Figures 3.29 b) and c) and C.19 illustrate the increase of the re-crystallisation layer: the volume of material undergoing laser-induced transformations is enhanced when the fluence increases. SAED pattern obtained below the boarder of re-crystallisation showed the monocrystal structure of copper. While, closer to the surface the SAED pattern showed a poly-crystallized structure composed of both copper and copper oxide. The oxidation of this inner volume of material is not fully understood. It may be the result of convective hydrodynamic flow in the molten material which could eventually reach the free surface, be oxidized and be moved deeper into the volume.

The characteristic of the oxidised layer observed at the free surface of the material has been investigated thanks to lattice imaging and image post-treatment based on FFT analysis (see figure 3.30). The thickness of the CuO oxide layer was measured to be 20 nm. This is considerably thicker than the oxidation layer observed after heat treatment as reported in the bibliography review (in section 3.1.6). It is worth noting that the thickness of the oxide increases with the increase of the irradiating fluence.

Under high irradiating fluences the localisation of the minority elements detected in the EDX spectra (shown in figure C.21) is visible on the spatial distribution cartography

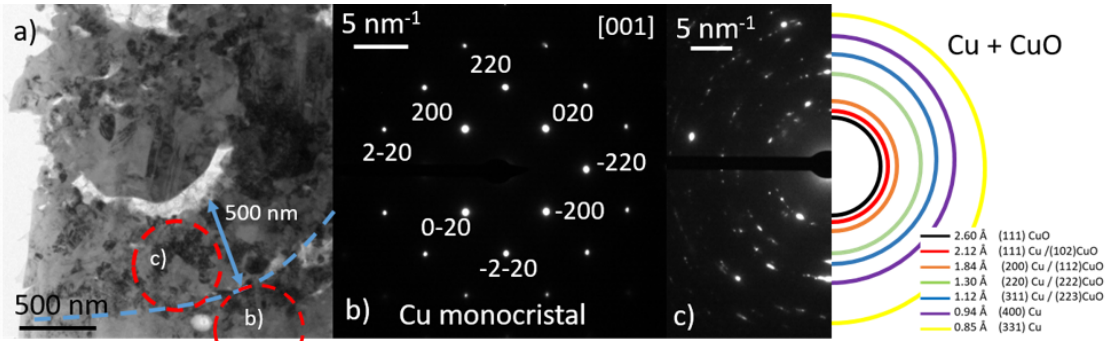

Figure 3.29: a) Bright field TEM image in an area irradiated by 2.25 J.cm^{-2}. The red dashed circles define the areas selected for the diffraction analysis. b) and c) SAED patterns from the indicated area in a).

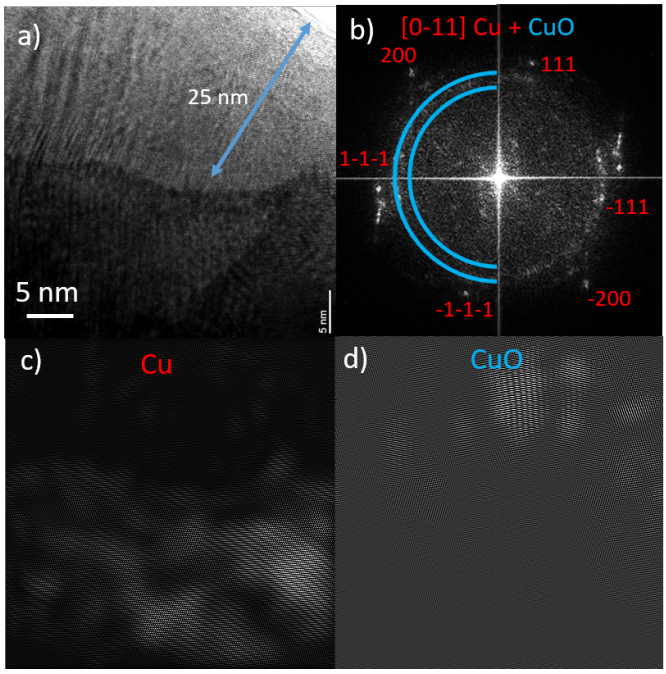

Figure 3.30: a) Lattice imaging in an area irradiated by 2.25 J.cm^{-2}. b) corresponding Fourier Fast Transformation (FFT) spectra from a). c) Inverse FFT image with the contribution of copper. d) Inverse FFT image with the contribution of CuO. The thickness of the oxide layer is around 25 nm.

in figure C.22. The presence of silicon, iron, phosphor, sulfur, aluminium, chromium, and nitrogen was only detected in the embedded resin itself. The low concentrations of nitrogen (despite the nitrogen gas jet used during the laser irradiation) and sulfur excluded the presence of structured crystal of Cu_3N, and $CuSO_4$. $CuCO_3$ and $Cu(OH)_2$ have been excluded because of the mismatch of inter reticular distances deducted from the SAED patterns and the low concentration of oxygen measured in the material.

Conclusion on interface region observation

The interface region between bulk copper and particle, observed above the damage threshold, presents evident indications for liquid transient transformation. The expulsion

of the liquid phase material out of the surface has been reported, it is generated by hydrodynamic effects in the molten pool and gas and plasma dynamics. Furthermore, despite the fact that 10 ps irradiation is on the limit of the stress confinement regime, sub-surface voids have been observed. They are the indication for tensile stresses in the material which can trigger photo-mechanical spallation thus expulsion out of surface of massif pieces of molten material.

The indications for phase explosion are hard to identify based on the observation of the post-irradiation interface region. Nevertheless, given that the difference between the spallation and the phase explosion fluence threshold have been reported to be pretty close, this ablation mechanism may occur also well under the irradiation conditions applied on the characterised sample. The transformation of the liquid reaching the critical point would result in the massive expulsion of a mixture of liquid droplets and gas atoms.

All the ablation regimes result in the ejection of the ablated material. A part of the material is re-deposited to the surface enhancing the surface roughness and forming the particle coverage or surface structures. The particle observation is related in the following section.

3.2.4 Particles, surface structures observation

It has been reported that the proportion of the re-deposed material relatively to the ablated material, the shape, and the chemical composition are sensitive to the laser treatment parameters and the environment where it was performed. The microscopy inspection of the surface objects to study the morphological characteristics, solidification process of the object may bring insights on their mechanical attachment at the surface.

Particles irradiated at 0.25 J.cm^{-2}

The observation of the surface in area irradiated at 0.25 J.cm^{-2} indicated that no transformation of the surface occurs at this irradiating fluence, the enhancement of the roughness in the local area only originates from re-deposited material.

Figure 3.31 a) shows a bright field TEM image of the superficial particles located on the surface of the copper in an area irradiated by 0.25 J.cm^{-2}. Two main morphological groups could be distinguished based on their general structure:

- aggregates of material of size bigger than 1 μm without any characteristic shape.In figure 3.31 a), the maximum dimension of the aggregate is more than 5 μm long;
- spherical particles of average diameter around 80-200 nm, which agglomerated to larger clusters. An example of those particles can be seen in the STEM-HAADF image in 3.31 e).

The Energy-filtered transmission electron microscopy (EF-TEM) method allows a mapping of the oxygen-enriched material (white areas in figure 3.31 c)). At the bottom of this picture, the nearly uniform distribution of oxygen on the interface region of the bulk corresponds to the oxide layer described in the previous section. In the re-deposited

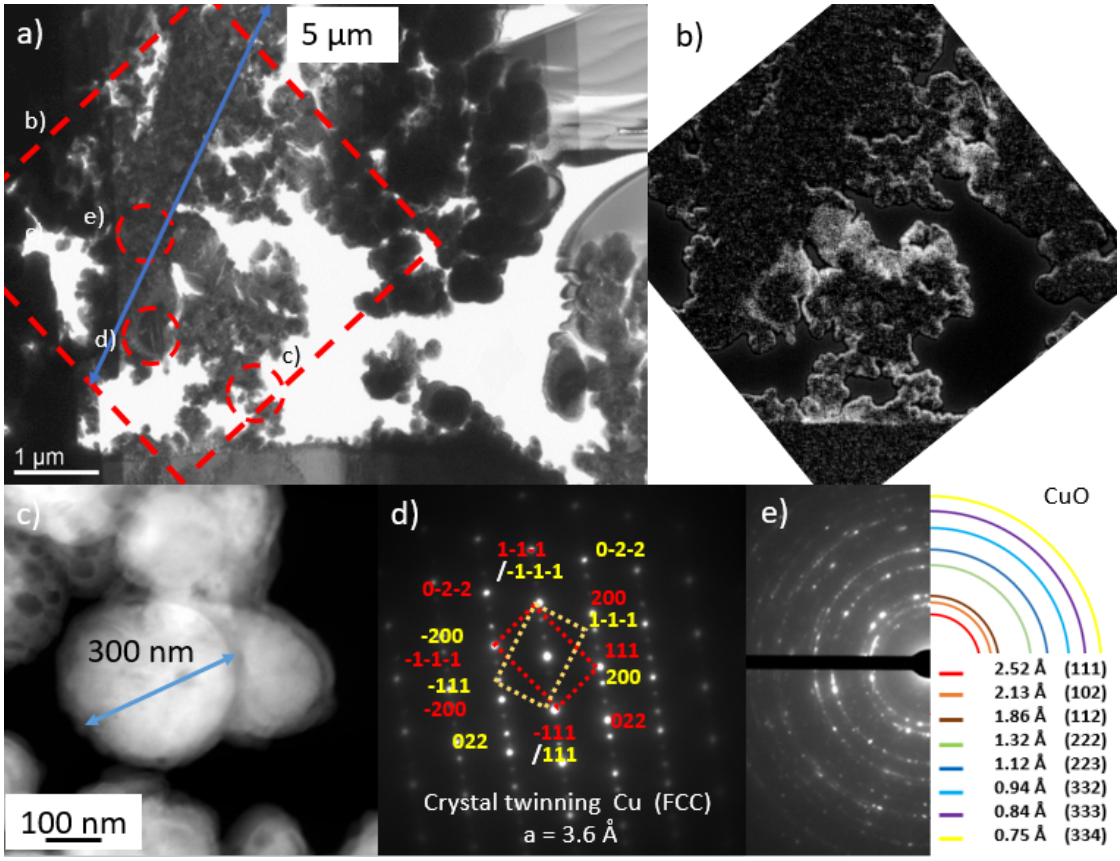

Figure 3.31: a) TEM Bright field image of the re-deposed structure in an area irradiated by 0.25 J.cm^{-2}. The red dashed square defines the area selected for EF-TEM analysis, The circles noted b) and d) are the areas selected for the diffraction analysis. The circle noted e) is selected for STEM-HAADF analysis. b) SAED patterns from the indicated area in a). c) EF-TEM analysis of the area selected in a). Oxygen contained area appear in bright in the image d) SAED patterns from the indicated area in a). e) STEM-HAADF image of a droplet.

surface area the distribution of oxygen appeared to be more disparate. Oxygen-enriched areas were generally detected in a most external layer. However, still high concentration of oxygen could be observed inside some of the material aggregates. Since EF-TEM is a method that is sensitive to the thickness of the specimen EDX analysis was performed to quantitatively evaluate the oxygen content in selected points. EDX analysis locally made on the aggregates also confirmed a mixture of copper and copper oxide and the non-uniform micro-structural transformation of the superficial structures. These results are presented in the appendix (figure C.23), the areas subjected to EDX analysis are marked by red circles on a dark field STEM-HAADF image of redeposited material.

Figure 3.31 b) is the SAED pattern corresponding to the aggregates (red dashed circle with a diameter of 650 nm marked b)). The colourful circles illustrate the inter-reticular distances corresponding to cupric oxide, CuO (copper (II) oxide). The presence of rings indicates that the re-solidified region is poly-crystalline with random grain orientation. Another zone (red circle marked as d)) has been chosen for diffraction analysis in an area where grain boundaries were visible as vertical color variations (this location is also

visible in figure C.23, in appendix, as clearer bean-shaped area), The SAED pattern of this area (3.31 d)) showed a face-centered-cubic twinning crystal structure with the unit cell constant a = 3.6 Å. Material twinning has been reported as structural signatures of transient melting and re-solidification submitted to strain which could originate from a temperature gradient during the solidification process [118].

The size, microstrcucture and chemical composition of the droplets have been further investigated.

In figure 3.32 a), the bright field image shows spherical droplets distributed all over the surface of the specimen. In the centre of the droplet, the EDX analysis has been performed across a larger area represented by the red dot in figure 3.32 a). The atomic percentages of copper and oxygen found are 90.34 % and 9.65 %, respectively. This confirms that the droplet is composed of mostly pure copper. The small quantity of oxygen can be attributed to an artefact explained by slight oxidation of the specimen during the FIB polishing. However, detailed quantitative EDX analysis made in one localized zone of the oxide layer (red dot with arrow) reveals atomic percentages of oxygen and copper of 36.56 % and 63.43 % respectively, which corresponds to copper (I) oxide. Figure 3.32 c) shows lattice imaging of a representative area of the outer layer of the droplet. The image shows complex lattice fringes, associated with different crystal grains in the oxide. The FFT treatment is shown in figure 3.32 d). The colourful circles illustrate the interplanar spacing 1.40, 1.54, 1.75, 1.92 and 2.45 Å corresponding to (221), (220), (211), (201) and (111) plans respectively. These rings confirmed poly-crystalline cubic structure (space group Pn-3m) and unit cell constant a = 4.25 Å of the copper (I) oxide. The post treatment of the lattice imaging corroborated the EDX analysis revealing the presence of this oxide around the spherical particles. The thickness of the oxide layer observed in this area was evaluated to be around 20 nm.

Analysis of SAED pattern shown in 3.32 b) indicated that the 120-nm-diameter droplet particle is face-centered cubic copper and indicated a mono-crystalline structure. The ring present on the pattern is the indication for the presence of an oxide on the surface. Depending on the diameter both mono and poly-crystalline structures can be observed in the droplets, it might be explained by different local cooling rates. Figure C.24 in the appendix, showed a poly-cristalline microstructure for a 300-nm-diameter droplet.

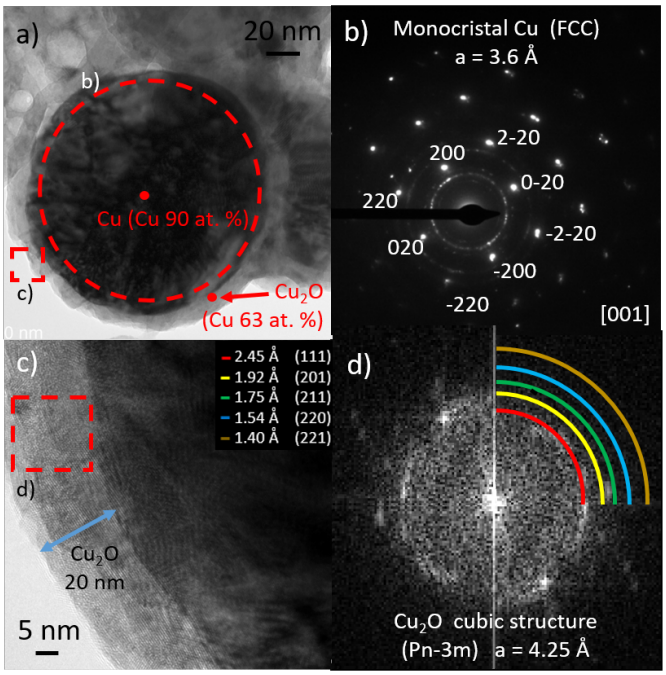

Figure 3.32: a) TEM Bright field image of a droplet in an area irradiated by 0.25 J.cm^{-2}. The circle noted b) defines the area selected for the diffraction analysis. The red dashed square noted c) defines the area selected for lattice imaging, EDX analysis have been performed on the two points identified by red circles: in the center of the droplet the analysis revealed copper as the dominant element (90 atomic %), in the outer layer of the droplets, the atomic percentage was measured at 63 %, Cu_2O was identified. b) SAED patterns from the indicated area in a). b) Lattice imaging of the area selected in a). The outer layer oxide thickness is 20 nm. the red squared noted d) is the area selected for FFT analysis d) corresponding Fast Fourier Transformation spectra highlighting the Cu_2O structure of the outer layer.

Particles irradiated at 2.35 J.cm^{-2}

Particles also exist at the bottom of the groove. Figure 3.33 a) shows a bright field TEM image of the particles which can typically be observed in this area. Particles are around 1 μm larg in diameter. They can be round or could be the result of the agglomeration of the smaller droplets. The oxygen and copper concentration map (figure 3.33 c)) indicated a thin layer of high concentration of oxygen which could be the interface between two droplets which agglomerated before the solidification.

The SAED pattern in figure 3.33 b) presents a mono-crystalline structure of copper. Further SAED patterns realised on the same particle are shown in the appendix (figure C.25), and show similar grain orientation. The agglomeration of the droplet may happen in the liquid phase or in the very early stages of solidification.

The profiles of the oxygen and copper atomic concentration performed along the segment presented in figure 3.33 c) showed a thick layer of CuO oxide (close to 30 nm) surrounding the particle.

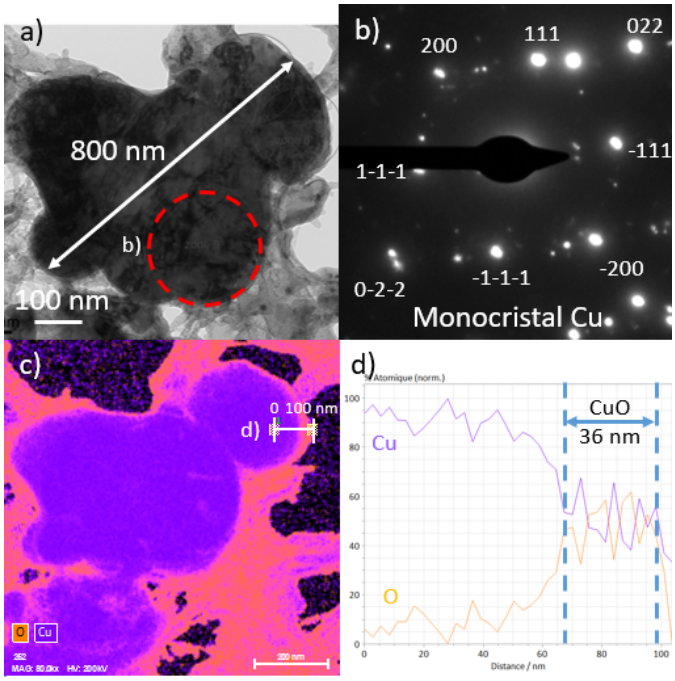

Figure 3.33: a) TEM Bright field image of a droplet in an area irradiated by 2.35 J.cm^{-2}. The maximal dimension of the particle is 800 nm. The circle noted b) defines the area selected for the diffraction analysis. b) SAED patterns from the indicated area in a). c) EDX maps of the element distribution of the corresponding area. The purple color corresponds to the copper-containing area. The oxygen containing area are shown in orange. d) Elemental distribution of copper and oxygen (in purple and orange respectively) extracted from the EDX map, every 1 nm, along the segment marked in c).

Conclusion on particles observation

The oxide has been identified incorporated inside the aggregates, inside the surface structures. That has been reported as an indication for an atomisation during the ablation process,

It is worth noting that the oxide observed (which can be as thick as 30 nm) is mainly present on the outside layer of the spherical particles. The particle clusters free of oxygen would be formed after solidification of molten copper, ejected by spallation.

The difference between the particles observed in the bottom of the groove and the one observed on the top of the groove (at low fluence) may be due to the cooling environment. The latter remained in the plume in the vicinity of the ablation site in a probably *warmer* environment which may favour the agglomeration of droplets in liquid phase.

On the other hand, the particles re-deposited around 30 μm away from the ablation site, may encounter a sharper transition of temperature.

3.2.5 Conclusion on structural analysis

The analysis of the laser-treated surface showed that the morphology, the microstructure, the chemical characteristics and the mechanical strength of the treated surface depend on the local irradiating fluence.The main morphological features observed on the interface

region (roughness, oxidation layer and sub-surface voids) are presented in figure 3.34.

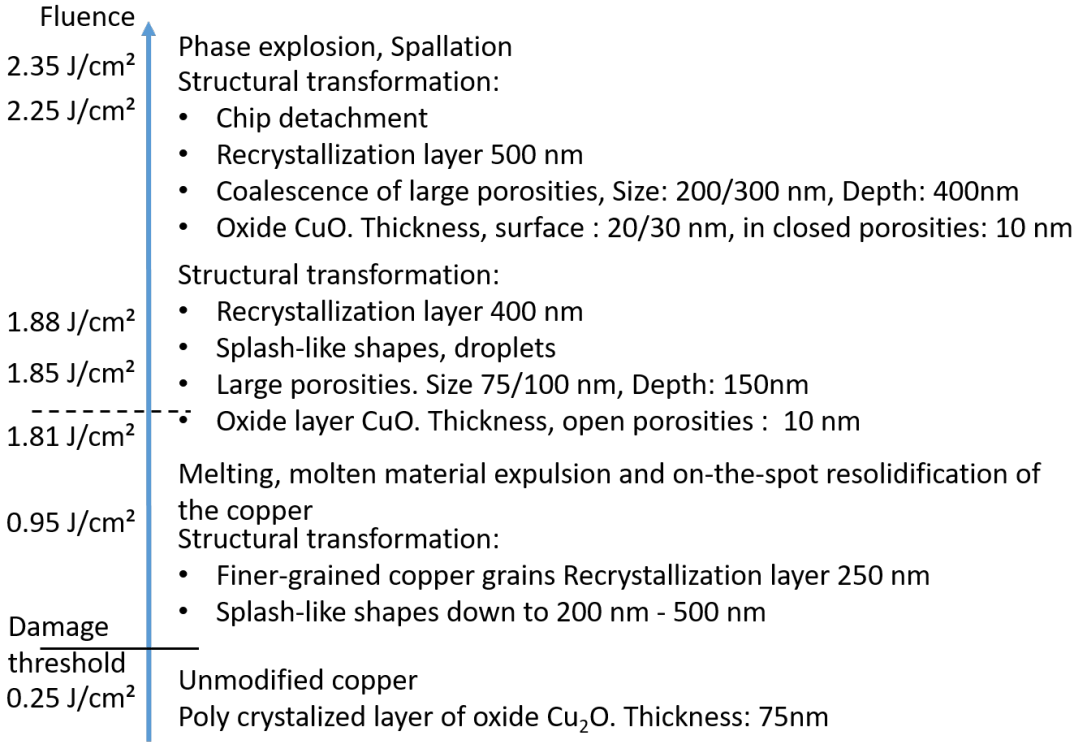

Figure 3.34: Observed transformations of the interface region depending on the local irradiating fluence for 10 ps 532 nm laser irradiation on OFE copper.

In the area exposed to an irradiating fluence lower than the ablation threshold, the copper microstructure did not recrystallize and kept the same size and morphology as the microstructure of the unprocessed copper. This confirmed that the portion of the Gaussian laser beam below the ablation threshold was not able to modify the copper bulk. The surface roughness was made of nanocrystals of the oxidized layer on top of the copper bulk, suggesting fast cooling kinetics of the ablated material after exposition to the oxygen in the plume.

Under a fluence higher than the ablation threshold, the picosecond laser processing removed material from the bulk copper. The interface region structures can be attributed to re-solidification of the molten copper and have not been transferred during the ablation process. The absence of oxides insight the interface region rugosities might indicate that the material was not exposed to the surrounding atmosphere. The continuity of the material might suggest good adhesion to the surface. The sub-surface voids were an indication for sub-surface tensile strain which may lead to the detachment of chips from the surface.

Observations were also performed on the material re-deposited at the surface (shape, size and oxidation). The analyses showed a non-uniform microstructural transformation of the superficial structures. Based on their general shape, two main morphological groups were distinguished: aggregates of material with heterogeneous mixture of copper

and oxides and spherical droplets of pure copper which could be agglomerated in larger clusters, especially in the bottom region of the grooves. These particles are re-deposited to the interface region after evaporation in the ablation site. The origin of the aggregates is not fully understood; it could be the result of sublimation during the ablation process.

It is worth noting that, despite the high cooling rate reported during re-solidification processes after ultra-short laser pulses ablation (larger than 10×10^{11} K.s^{-1}), no indication of the presence of amorphous material was found in the specimen. The analyses have shown that the re-deposed structures attached to the surfaces and the interface region itself kept crystalline character.

A thick oxide layer was observed on the interface region and around the particles despite the nitrogen laminar jet gas used during the laser treatment.

3.3 Morphological characterisation at groove scale

As mentioned in section 1.3, a parametric study aiming to find the best compromise between a low SEY, maximum allowed ablation depth of 30 μm and other requirements of the application of the laser-treated surface in the accelerator environment (time of processing, production of dust) has been performed and is still ongoing to define the optimal set of parameters of the laser processing.

In section 5.3, the observations about the morphology will be coupled with the SEY measurement in order to choose the best compromise for a laser treatment applicable to mitigate electron cloud formation while respecting the criteria in terms of groove depth. The following section focuses on the characterisation of grooves created in laboratory by varying laser parameters on plane samples. The groove observation is mainly done based on cross sectional microscopy as presented in section 2.3.1.

Figure 3.35 presents groove depths measured at CERN on samples treated at Dundee University in the framework of the parametric study for optimisation of the treatment parameters. Groove depths are plotted as a function of the average laser fluence which has been found to be a convenient figure of merit to compare samples. The figure also includes the results of studies found in the literature [85, 94].

Although a large spread of measurements can be observed, the general trend is the increase of groove depth when the fluence increases. The large dispersion of the measurement is not fully understood. The ablation process involves complex phenomena sensitive to the irradiation conditions, the surface reflectivity (which depends on surface roughness and oxidation for instance)...

To better highlight the effects of the fluence on the morphology, a set of samples was chosen: *G3*, *D9*, and *Zeta* series samples whose treatment parameters can be found in appendix B. For this batch of samples, special care was taken to keep the gas environment as constant as possible and to improve the packing.

12 groove profiles extracted from the same sample *G3* are plotted in figure 3.36 a). The areas indicated in the legend are the areas of the ablated cross sections for each groove profile. The averaged value of 933 mum^2 has been estimated with a standard

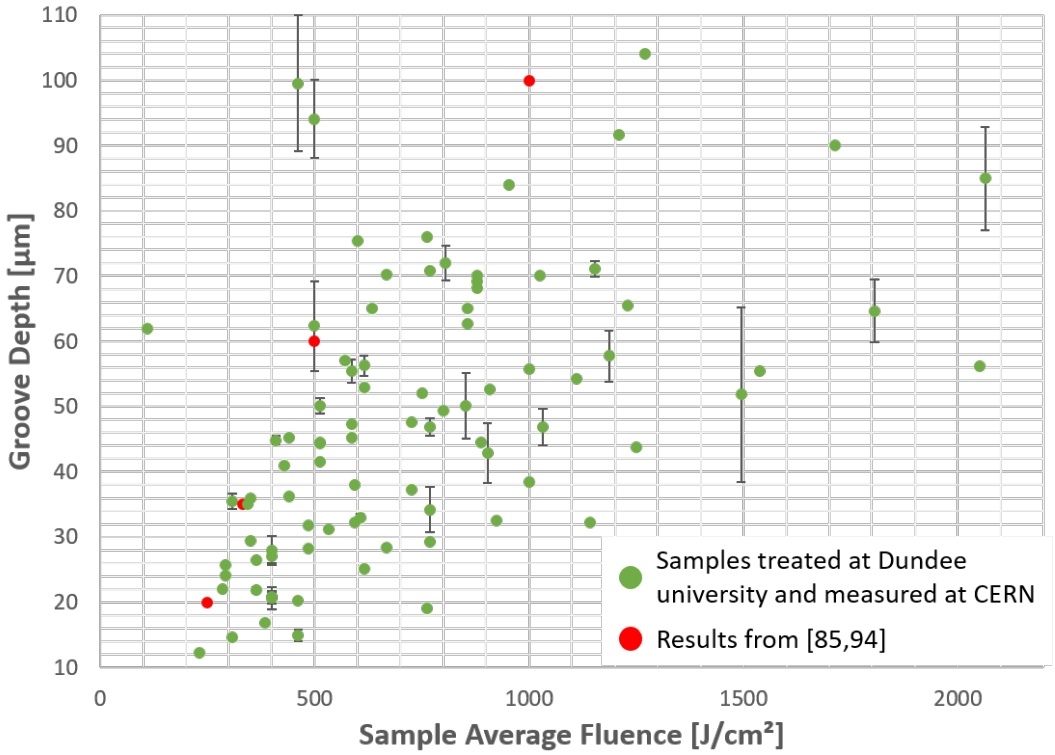

Figure 3.35: Groove depth as a function of the average irradiating fluence measured on the samples treated in the frame of the parametric study between 2017 and 2020 (green dots). The parameters used for the treatment are described in the appendix B. The results are compared with data found in the literature [85, 94] (in red).

deviation of 4.3 %, that shows a reasonable repeatibility of the measure. In the following, the measure of the groove profile area is used to determinate the ablated mass.

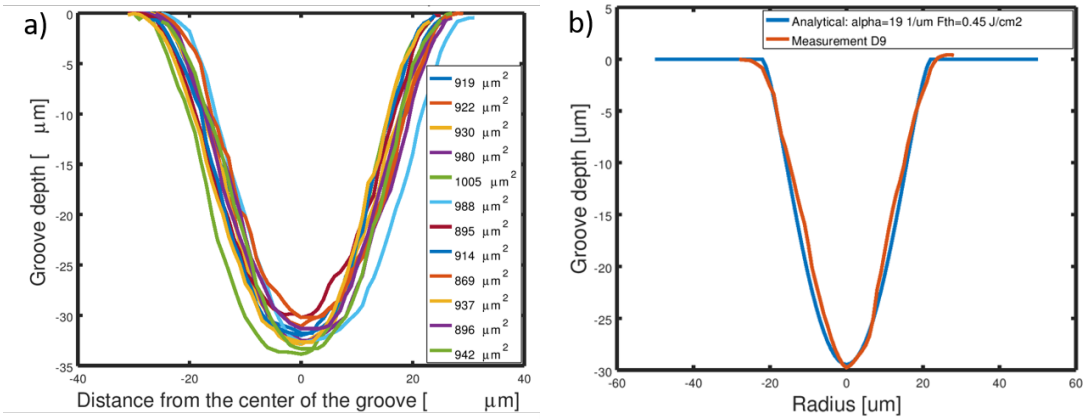

Figure 3.36: a) 12 Grooves profiles measured on a *G3* sample. b) Groove depth profiles measured on sample *D9* (in red) and calculated based on the analytical model presented in equation 3.9 (in blue) with the parameters: F_{Th}= 0.45 J.cm^{-2}, $\alpha = 19$ μm^{-1} chosen to fit the measured profile.

As suggested [175], the groove profile has been calculated taking into account the

local fluence for each pulse. For each pulse, the ablation depth have been deduced by calculations of the local fluence including pulse overlap, scan speed, spot diameter and repetition rate.

$$L_{Total}(x,y) = \sum_{i,\, nb\, of\, pulses} \frac{1}{\alpha} ln\left(\frac{F_{Pulsei}(x,y)}{F_{Th}}\right) \tag{3.9}$$

where $\frac{1}{\alpha}$ is the optical penetration depth, F_{Th} is the ablation threshold fluence.

In figure 3.36 b) the measured groove profile is compared to the ablation obtained with the analytical formula presented in the equation 3.9. The value of the ablation threshold has been fixed to 0.45 J.cm^{-2} (after TEM observations) while the value of the optical penetration depth was chosen in order to fit the measurement. The identification $\alpha = 19$ μm^{-1} leads to an optical depth of 55 nm compared to the 13.5 nm reported in the literature [143]. With the *G3* parameters the number of pulses per spot is 693. The groove depth has been measured at 33 μm, leading to an average ablation rate of 50 nm/pulse, which is close to the optical penetration depth identified on the analytical model. The longitudinal distance between two pulses along the scanning direction is 75 nm.

Influences of the laser treatment parameters

To identify the influence of the laser parameters on the surface morphology at the groove scale, study has been performed on *Zeta* series samples. For each sample, the hatch distance was kept constant, while the fluence was varying (as the scanning speed was varying).

Part of the results presented in the following have been the object of a publication [108], specifically the results about the influence of the groove morphology on the SEY, also presented in section 5.3.

SEM cross-sectional micro-graphs are presented in figure 3.37, and the groove profiles, determined after image analysis, are plotted in figure 3.38 a). It appeared that the higher the fluence was, the deeper the grooves were,

Aspect ratio has been introduced as a figure of merit to characterize the surface morphology at the groove scale. For each groove, the aspect ratio has been defined as:

$$Aspect\ ratio = \frac{Groove\ Depth}{Groove\ Width} \tag{3.10}$$

where *Groove Depth* and *Groove Width* are defined as illustrated in figure 3.38 a).

The groove aspect ratios are plotted in figure 3.38 b), they increase logarithmically with the average fluence irradiating the samples. The aspect ratio has been used as a morphological characteristic of the treated surface to evaluate the influence of the morphology on SEY [108].

The mass of copper ablated during the laser treatment has been calculated from the groove profiles, presented in figure 3.38 a), and taking into account the copper density. For the *Zeta* series, the results are shown in figure 3.39. It shows a linear increase of the ablated mass when the laser fluence increases.

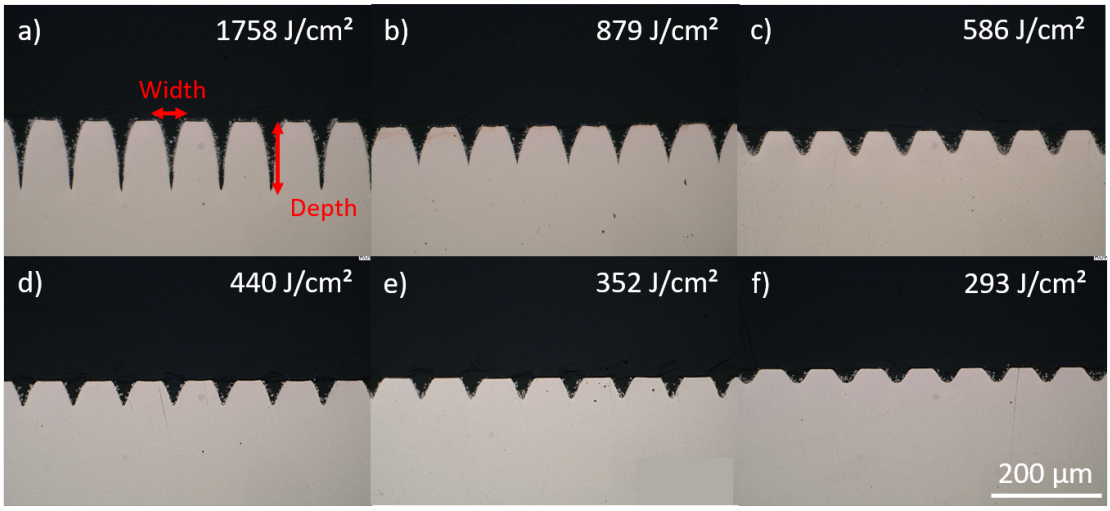

Figure 3.37: Cross sectional characterisation in a optical microscope of *Zeta 1* series samples, irradiated with a fluence of a) 1758 J.cm^{-2}. b) 879 J.cm^{-2}. c) 586 J.cm^{-2}. d) 440 J.cm^{-2}. e) 352 J.cm^{-2}. f) 293 J.cm^{-2}.

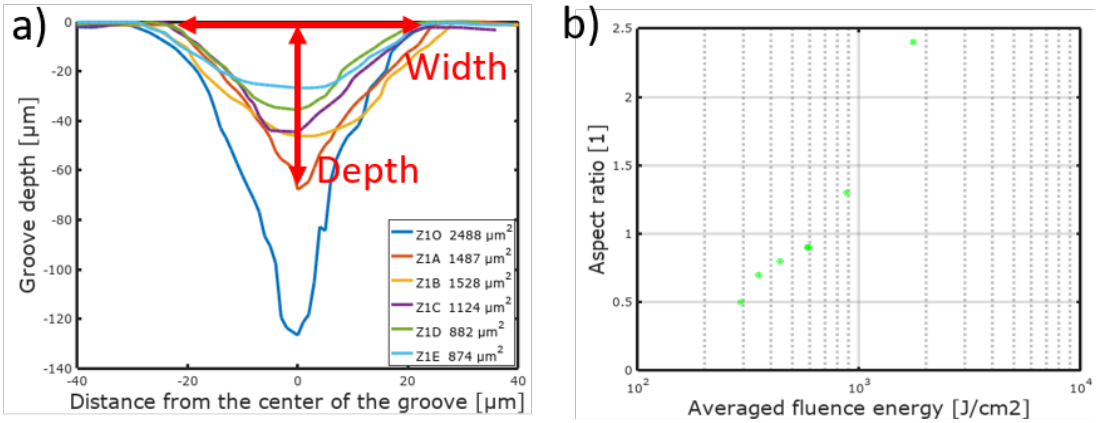

Figure 3.38: a) Groove profiles of *Zeta 1* series samples. The area ablated can be read in the legend box. b) Corresponding aspect ratios, as defined in equation 3.10 are plotted as a function of the fluence.

The energy efficiency was calculated as the ratio between the energy required to evaporate the volume of copper measured from the groove profiles and the energy deposited to the surface by the laser. This ratio is a simplified approach, for instance, it does not take into account the kinetic energy of the ablated material or non-linearities in the absorption of the laser energy by the material.. The energy efficiency of the laser ablation has been defined as:

$$Efficiency = \frac{m_{copper}\left(c_{pSol}\left(T_{Fus} - T_{RT}\right) + L_{Fus} + c_{pLiq}\left(T_{Vap} - T_{Fus}\right) + L_{Vap}\right)}{Sample\ Average\ fluence} \tag{3.11}$$

where m_{copper} is the mass of ablated copper, c_{pSol} and c_{pLiq} are the heat capacities of solid and liquid states, respectively, L_{Fus} and L_{Vap} are the heat or enthalpy of fusion and

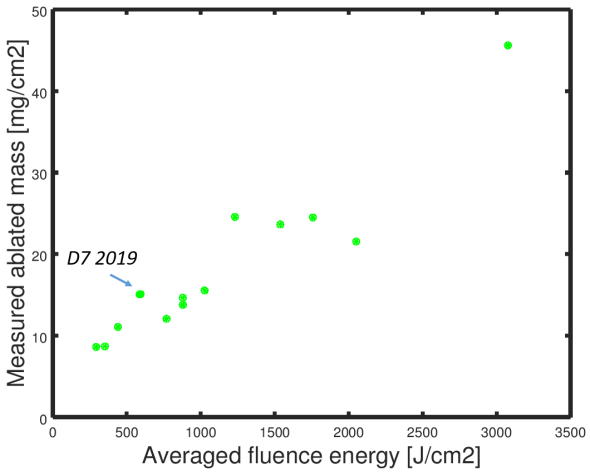

Figure 3.39: Mass of copper ablated during the laser treatment for *Zeta* series samples and *D7 2019* sample. The ablated weight is plotted as a function of the irradiating fluence.

evaporation, respectively, T_{Fus} and T_{Vap} are the temperatures of fusion and evaporation, respectively. The values for copper are summarized in A and can be founded in [140].

In figure 3.39 b), the mass of ablated material is proportional to the energy density irradiating the sample. The ratio between the energy deposited to the surface by the laser and the energy needed to evaporate the volume appears to be constant with the irradiating fluence (in the observed range), it is equal to 15 %, in this case.

Groove characteristics for *D7* samples

Table 3.1 presents the results of the analysis applied on *D7* samples. For instance, on *D7 2019* samples, based on cross sectional microscopy the ablated mass was estimated to be 15.1 mg.cm^{-2}.

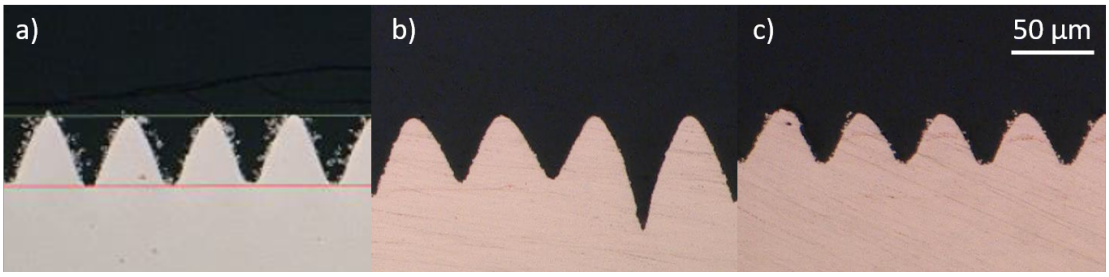

Figure 3.40: Cross sectional characterisation in a optical microscope of *D7* samples. a) *D7 2019*. b) *BS74*. c) *D7 2020*.

Table 3.1: Comparison of the ablated masses evaluated on *D7* samples. The values are expressed in mg.cm^{-2}.

Sample	*D7 2018*	*D7 2019*	*BS74*	*D7 2020*
Ablated mass	14.4	15.1	17.8	11.5

Cross sectional microscopy was also used for the identification of model of the treated

surface at the groove scale. A model of the colaminated copper layer after laser treatment was identified based on microscopy observation, as explained in figure 3.41 b). The model was based on rectangular and sinusoidal profiles whose dimensions have been identified.

It has been used for electro-magnetic-mechanical simulations in section 5.1.

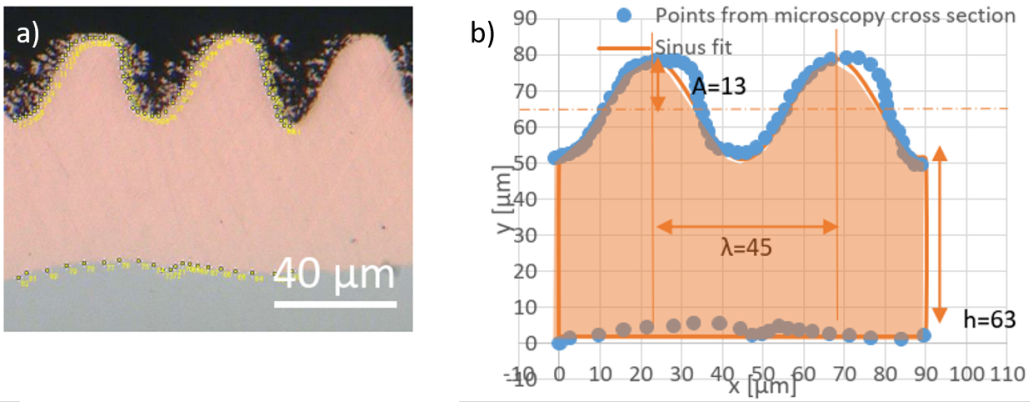

Figure 3.41: a) Cross section of a colaminated sample the surface treated by the so-called *D7 2019* parameters. The interface between the stainless steel and the colaminated copper can be seen on the bottom of the image. The resin used during the preparation of the cross-section appears on the top of the image. The yellow points are numerated, they have been localised at the contour of the copper layer. b) From the extracted points of the cross section, the parameters of model based on rectangular and sinusoidal profiles have been identified. Both cross sections (modelled one and the one measured on the microscopy) have the same area.

Conclusion

To conclude, the image post treatment of cross view observations of the groove pattern allowed the determination of the amount of copper ablated during the laser treatment for each configuration of treatment parameters. It has been shown that the ablated mass increases linearly with the fluence, on the considered range.

Part of the ablated matter is re-condensed on the grooved surface as particles. Qualitative and quantitative characterisation of the particle overlay is the object of the following section.

3.4 Morphological characterisation at particle scale

Three techniques have been deployed to describe, qualitatively and quantitatively, the surface topography at the particle scale: top view SEM observation of the treated surface, ultrasonic cleaning and nano-tomography.

3.4.1 Top view SEM observations: overall description

Top view SEM analysis can bring insights on the qualitative description of the particles created by the laser treatment.

Ejected particles

In figure 3.42, the SEM image of the edge of the treated area pictures grooves on the right of the image and an untreated area on the left. The un-treated copper is covered

by sub-micrometer large spherical particles lying freely on the surface. The spherical shape of the droplets and the small contact with the surface would suggest that the particles are solidified (or mostly) when the particles are re-deposited to the surface. For the flying particles created during the ablation process, the heat radiation would be the dominant process of heat dissipation. The spherical particles are located 50 μm away from the ablation crater. Considering, 120 m.s^{-1} as a lower estimate of the expansion speed, a direct trajectory and no friction in the ambient gas, time of flight of the particle re-deposited to the surface is estimated to be in the range of microseconds.

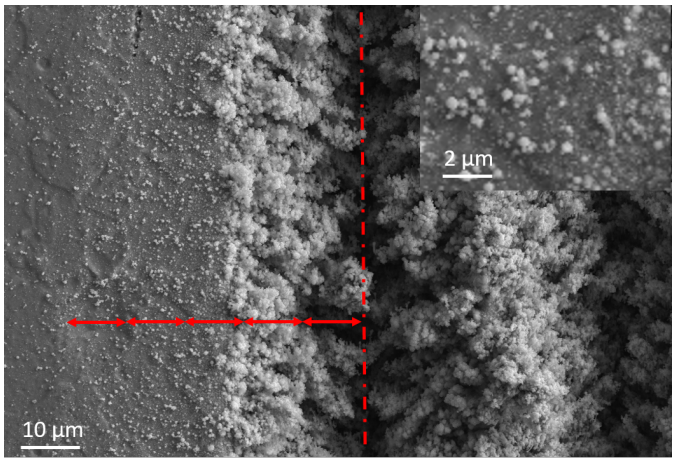

Figure 3.42: SEM top view of *D7*. The red dot line highlights the center of the groove, each arrow is 50 μm, the inset is a higher magnification of the flat part of the sample covered by deposed particles.

It has been shown that the particle morphology is sensitive to the gas environment, elongated particles were observed when the nitrogen flux was turbulent (see figure C.2 in the appendix section C.1). Special care has been asked to our partners at Dundee University in charge of the laser treatment to insure repetitive conditions for the laser treatment.

Influence of the laser treatment parameters

The SEM top views of *Zeta 1* series samples are presented in figure 3.43. For these samples, the gas environment as well as the wavelength and the pulse duration was kept constant. The average fluence was changed by varying the scanning speed (see the treatment parameters in the appendix B). For a given environment of ablation (here a gentle nitrogen flux towards the sample) and ablation regime, it appeared that the higher the fluence was, the more particles were visible on the surface.

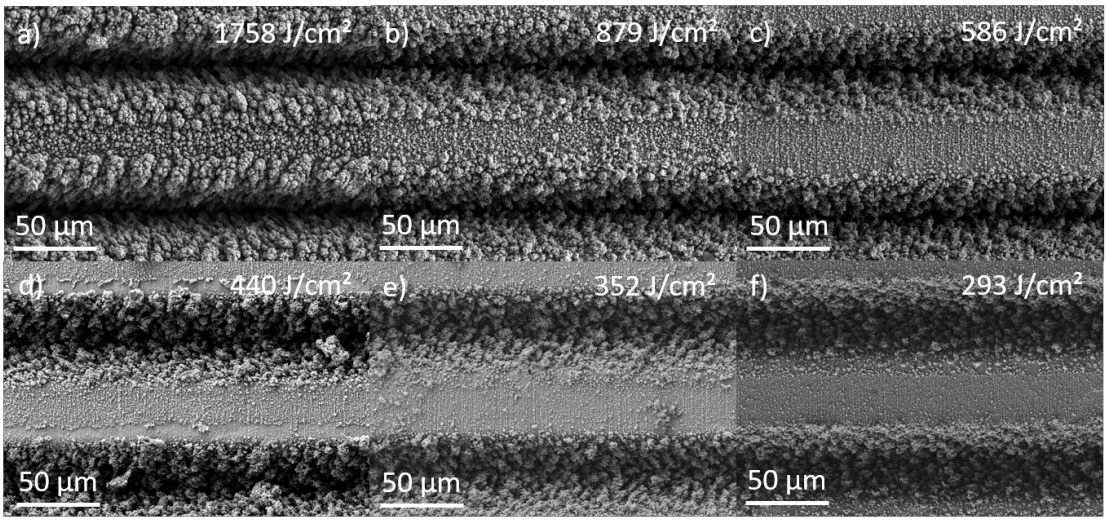

Figure 3.43: Top view SEM images of *Zeta 1* series samples, respectively irradiated with the fluence a) 1758 J.cm^{-2} b) 879 J.cm^{-2} c) 586 J.cm^{-2} d) 440 J.cm^{-2} c) 352 J.cm^{-2} c) 293 J.cm^{-2}.

Top views observation of *D7* surfaces

As an example, figure 3.44 presents top view SEM images of samples treated with *D7* parameters when produced in different batches of samples.

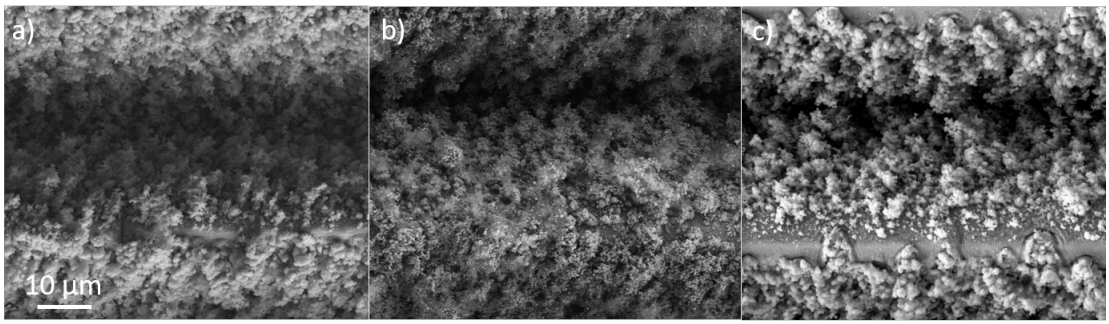

Figure 3.44: SEM top view images of samples treated by *D7* parameters a) *D7 2018*. b) when apply in the *BS74* flat part. c) *D7 2020*.

3.4.2 Particle analysis after ultrasonic cleaning

To estimate the quantity of surface structures, samples are cleaned in ultrasonic bath following the proceeding described in section 2.3.3.

Figure 3.45 shows SEM top view images of *G3* sample, before the ultrasonic (a)) and after (b)). After the ultrasonic cleaning, most of the particles were removed, the more fragile structures detached mostly from the convex part of the grooves. Nevertheless, some particles remained in the concave part of the grooves. They were mostly spherical, with a diameter measured around 1 μm. The experimental value of surface particle density obtained by weight difference after the US cleaning appeared to be underestimated.

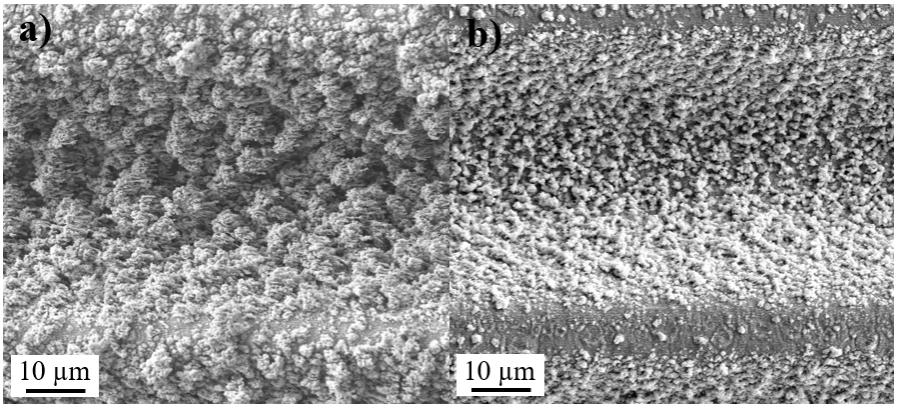

Figure 3.45: SEM top view images of the *G3* sample. a) before the cleaning. b) After 10 min of ultrasonic cleaning at the ultrasonic power of 300 W.

3.4.2.1 Quantitative description

Influences of the laser treatment parameters

In figure 3.46, the mass of particles removed during the ultrasonic cleaning has been plotted compare to the average fluence *Zeta* series samples.

In this series of samples, the wavelength and the pulse duration was kept constant, as well as the gas environment but the average fluence was changed by varying the hatch distance (*Zeta 1*) or the scanning speed (*Zeta 5*) (see the treatment parameters in the appendix B). In both cases the amount of detached particles increases linearly with the irradiation fluence.

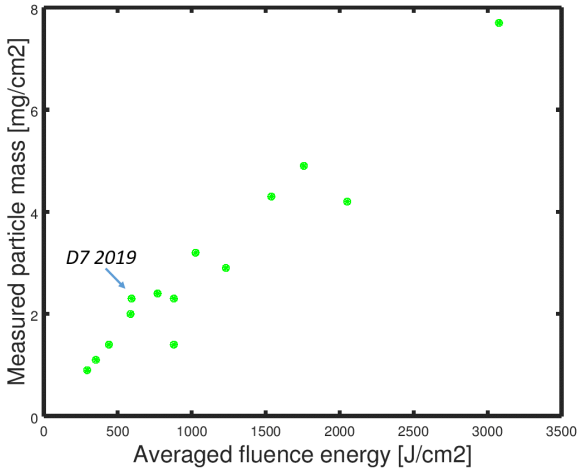

Figure 3.46: Mass of particles removed in US bath as a function of the average irradiating fluence on the samples. Results for *D7 2019* sample and *Zeta* samples are presented.

Ultrasonic cleaning technique allowed the quantification of the phenomena observed on SEM observations.

For a given irradiation regime (wavelength and pulse duration), the higher the irradiating fluence is, the more material is ablated, as shown in the previous section, and

furthermore, the more material is re-deposited to the surface as particles.

Quantification of particle coverage of *D7* surface

In addition to the conclusion on the effect of fluence, the estimated mass of particles on the overlay of samples treated with *D7* parameters is particularly meaningful for this work as they are the reference to determine the percentage of particles removed from the surface in the chapter 4.

Table 3.2 presents the results of the analysis applied on *D7* sample. For instance, on *D7 2019* samples, the mass of particles covering the surface has been measured at 2.6 mg/cm^2. While it was measured at 1.0 mg/cm^2, for *D7 2020* samples, 0.62 mg/cm^2, for *BS74* samples.

This measurement confirmed the observation made in figure 3.44, on the lower unexpected particle coverage on samples received at CERN in 2020.

Table 3.2: Comparison of the ablated masses and particle coverage evaluated on *D7* samples. The values are expressed in mg.cm^{-2}.

Sample	*D7 2018*	*D7 2019*	*BS74*	*D7 2020*
Ablated mass	14.4	15.1	17.8	11.5
Particle coverage	No data	2.6	0.62	1.0

3.4.2.2 Qualitative description the particle overlay

Automatic Particles Analysis (APA) have been performed on the particles collected after filtration of the particle-containing water of bath used for US cleaning, as described in section 2.3.4. As explained previously, because of the transfer from the membrane to the carbon sticker, APA can not be used to evaluate quantitatively the amount of particles detached during the ultrasonic cleaning. Nevertheless it can give good insights for the qualitative description of the size distribution of the detached particles.

Figure 3.47 presents the size distribution of the particles collected on *Zeta 5 B* sample when submitted to two consecutive cleanings. A 10 % dilution of the solution was necessary to perform the APA after the 1^{st} cleaning due to the high number of detached particles. Less than 5 % of the detached particles had an equivalent spherical diameter (ESD) larger than 5 μm. The size distribution of the particles follows an exponential decreasing identified as $\alpha exp^{\frac{-ECD}{1.2}}$. This size distribution has been typically observed on the other studied samples, dependently on the irradiating fluence. Although the effects of a possible bias due to fragmentation or aggregation of particles in ultrasonic bath are not quantified, fitted curve of size distribution is used in section 4.3.2 as reference to compare the size distribution of particles detached after mechanical solicitation.

After the 1^{st} US cleaning, the sample was submitted to a 2^{nd} cycle of the same US cleaning in order to evaluate the amount of particles still *detachable* after an ultrasonic cleaning and to identify any changes or sensitivity of the particle size to the US cleaning. The amount of detached particles did not require the dilution of the solution before performing the APA on the carbon sticker.

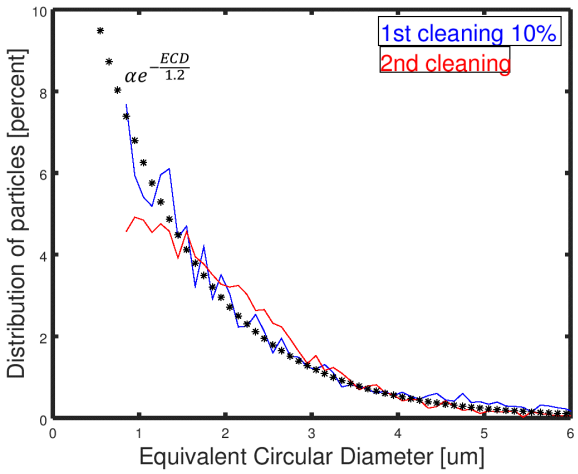

Figure 3.47: Size distribution of the detached particles depending on their diameter extracted by ultrasonic cleaning from the sample so-called *Zeta 5 B*. In blue, the size distribution of the particles obtained after the 1^{st} cleaning and filtration of the 10 % diluted solution. In red, the size distribution of the particles after the 2^{nd} cleaning of the same sample.

The size distribution of the particles detached during the 2^{nd} US cleaning appeared to be slightly different than the size distribution of the particles detached during the 1^{st}: particles below 1.5 μm Equivalent Circular Diameter (ECD) are more likely to be removed during the 1^{st} US cleaning. Below this size particles appeared to be more vulnerable to the mechanical solicitations due to ultrasonic cleaning than the bigger one. It could be explained by the faster solidification of the small particles illustrated in figure 3.7. If the solidification is already more advanced when the particles are re-deposited to the surface, the mechanical link with the bulk surface might be weaker.

To conclude, the particle extraction via ultrasonic cleaning brought valuable information on the particle density coverage and the particle size distribution. It turned out to also be a fast and easy way to modulate this quantity without changing the chemical composition. Finally, it is representative of what could be the cleaning procedure for components of the vacuum system laser-treated in laboratory (but not *in-situ*). Nevertheless, it is worth noting that the influence of the ultrasonic bath on the fragmentation or, on the contrary, the agglomeration of the particles in the particle-containing solution is unknown. Another tool was tried to characterize both the particle coverage, particle size distribution: FIB-assisted tomography is presented in the following section.

3.4.3 FIB-assisted surface tomography for particle description

Focused Ions Beam (FIB) cross sectional analysis has been performed on a sample laser-treated by *G3* parameters. It provided 341 incremental images of the surface at a resolution of 50 nm. These images can be visually examined in order to gain improved insight into the particles and voids present on the laser-treated copper surface.

The surface is highly topographical and has a regular sinusoidal base structure pattern was dug by laser ablation into the bulk copper. Particles and their aggregates of

varying size form a highly porous region, in direct contact with this bulk copper. The thickness of this outer layer is 3-4 μm on the convex curvature, on the top of the grooves, while this layer is much thicker on the concave curvature, about 10 to 12 μm. A detailed description of FIB cross section of the surface obtained with similar laser parameters is available in [77].

3.4.3.1 Experimental details

The Scanning Electron Microscope (SEM) images of the cross section of a sample cut with a FIB cross section (see figure 3.13) have been visually examined in order to gain improved insight into the local surface and the particles on the laser-treated copper sample. In order to quantitatively characterize the particles present in the interface region region and to extract a 3D model from the FIB tomography, a sequential cross-sectioning was performed on a region of approximately 100 x 50 x 15 μm^3 with a voxel size of 50 nm. Trenches were then milled on three sides of the pad using a milling current of 100 nA and an accelerating voltage of 30 keV to a depth of approximately 100 μm. Progressive refinement of this surface was performed at milling currents of 30 nA and 15 nA in order to reveal the region of interest. An automated FIB tomography protocol was then initiated in which sequential InLens SEM images were captured at a magnification of 977 times (pixel size 50 nm). SEM images were tilt *corrected* on SEM pictures: displayed dimensions on the cross section take into account the tilt. During this process a 7 nA milling current was used to incrementally polish 50 nm slices in the region of interest. Images of size 50 $\times$ 100 μm^2 were recorded at each milling increment. FIB cross sectional analysis has provided a stack of 341 incremental images of the surface at a resolution of 50 nm.

3.4.3.2 Image segmentation

A major obstacle to the image segmentation is the so-called *shine through artefact*. Due to the large field depth of the SEM images, the particles been beyond the plane milled by the FIB can be seen through the voids left by the particles of the first plane. Post-processing of the images was performed in order to correct this artefact as well as extracting the regions of interest.

The image post-treatment utilized the software *Octave* for matrix calculation and the software *Fiji*.

Grayscale threshold

Post-processing of the images was performed to correct the brightness and contrast, as well as extracting the regions of interest. Figure 3.48 a) illustrates the selection of regions of interest from the original picture of the FIB cross section. Out of the lower part of the picture is considered as copper bulk. The upper part is considered as a background.

In order to obtain improved insight into the voids and particles present within the interface region region, the images were thresholded. A grayscale value of 200 was found to be optimum for the particles. Results of this image segmentation are presented in the

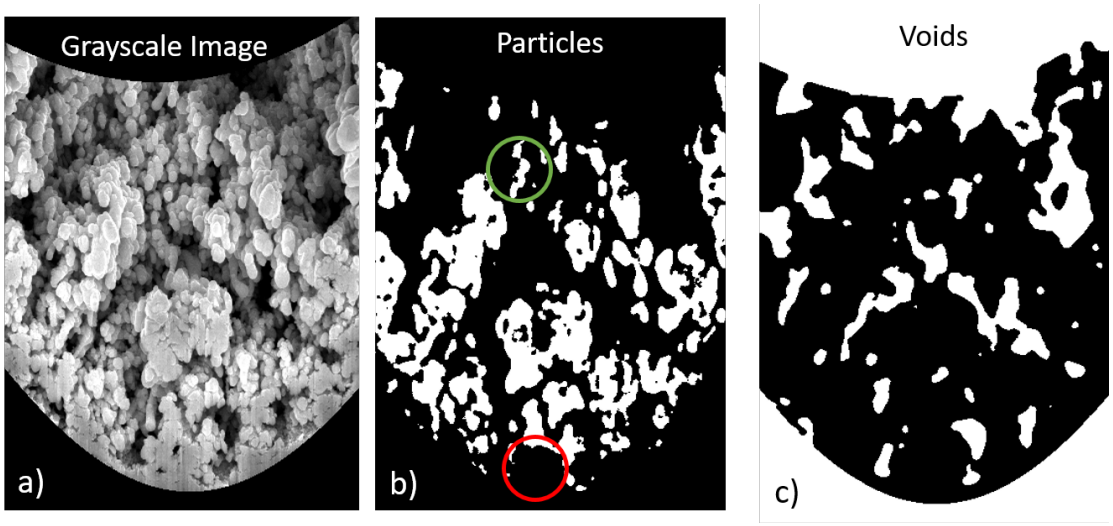

Figure 3.48: XY image extract from the FIB tomography a) SEM grayscale image. b) Binary image after grayscale thresholding with the value 200 and a median filter (radius 6 pixels).The white parts are considered as particles. The red circle highlights particles appearing on the grayscale image but not taken into account after the segmentation. On the other hand, the green circles highlights shine through effect wrongly taken into account as particles after post treatment. c) Binary image after grayscale thresholding with the value 87 and a median filter (radius 6 pixels). The white parts are considered as voids.

plan XY in figure 3.48 and in the plan YZ in figure 3.49.

In figure 3.48 b), the white areas are classified as particles part of the cross section. A grayscale value of 82 was found to be optimum for visualising the voids. In order to minimise the impact of noise on the results, a median filter was applied to the images with a radius of 6 pixels. This process reduces the minimum resolvable void size, however it is necessary for automated analysis.

In figure 3.48 c), the white areas are appraised as voids after applying both the threshold and the image filter. Based on these two estimations of particles and voids, the software Fiji was used with the plugin 3D object counter to resolve the voids and particles within the data set. Over the full volume taken into account during this FIB tomography, data thresholding and automated particle analysis have revealed that the mean particle volume is 6.42×10^{-3} μm^3, the equivalent spherical particle would have a diameter of 0.2 μm. The mean void volume is larger: 1.05×10^{-1} μm^3, which corresponds to an equivalent spherical diameter of 0.37 μm.

The quantitative results from the tomography are based on a very arbitrary image post processing. It can not be used for a quantitative description of the particle morphology. Based on the size distribution of the particles given by the software *Fiji*, the weight of the particles covering the surface has been estimated to be 0.003 mg.cm^{-2}, which is underestimated compared to the experimental value (see section 3.4.2.1).

The high porosity makes the image processing and more specifically the automatic segmentation of the particulates cut in the cross section and the background difficult, as illustrated in figure 3.49.

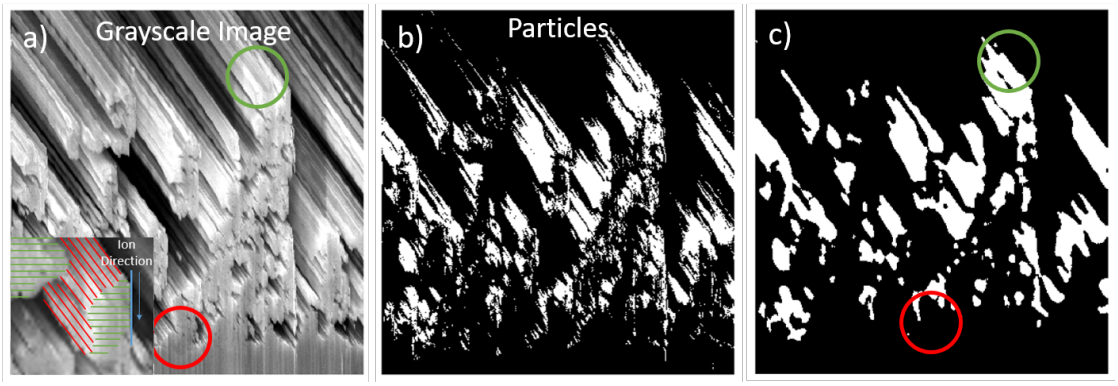

Figure 3.49: YZ image extract from the FIB tomography a) SEM grayscale image. The inset on the bottom left corner highlights the shine through effect: the green hatched region represents the *real* particle cross section, the red hatched area is due to the artefact. An artefact due to the polishing direction is also highlighted: the right edge of most of the particles appears to be vertical due to the erosion of the last piece of particles. b) Binary image after grayscale thresholding with the value 200. c) and after a median filter (radius 6 pixels). The red circles highlight particles appearing on the grayscale image but not taken into account after the segmentation. On the other hand, the green circles highlights the shine through effect.

Resin impregnation was tried to ease the image segmentation. Nevertheless, resins, traditionally used for the mechanical polishing of a cross section alter the particle coverage as it can be seen in cross sectional microscopy after mechanical polishing (see figure 3.37, for instance). Carbon coating has been used in FIB tomography (see figure 3.50 a)). The particles are altered by the coating, part of the structure is destroyed and the cavities near the surface are not filled. Silver paste has been tried as a coating without more success (Figure 3.50 b)). slow rate polymerization resin has also be unsuccessfully tested.

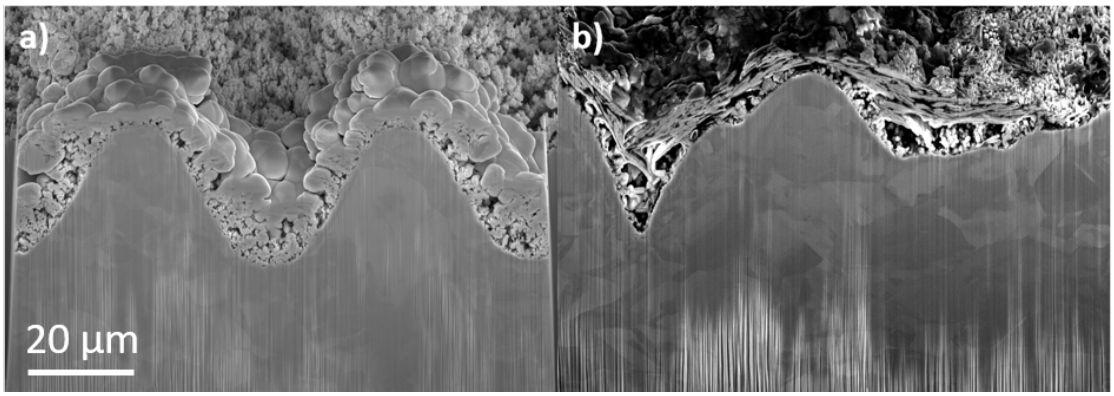

Figure 3.50: SEM image of the cross section image of a laser-treated sample prepared with a) carbon coating and b) silver paint coating.

The difficulties to ease the image segmentation by the sample preparation motivated the used of post image treatment based on *Watershed transformations*.

Watershed transformations

Image segmentation was performed on a subset of the data defined by one period of the

sinusoidal pattern. It is called region of interest in the following. Prill presented [176] a methodology based on watershed transformations which has been applied on images of laser-treated sample tomography as illustrated in figure 3.51.

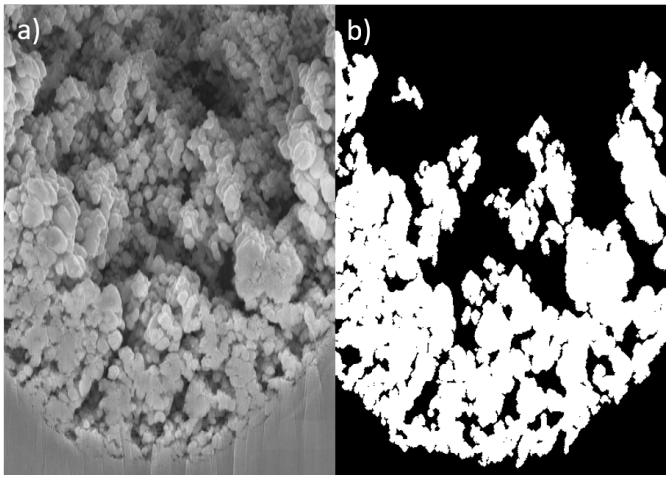

Figure 3.51: XY image extract from the FIB tomography a) SEM grayscale image b) Binary images after watershed transformations courtesy of Francois CADIOUX INSA Lyon.

3.4.3.3 Post treatment: statistics on the chord lengths

Because of the shine through effect, the volume identified in the tomography is both the volume of particles themselves and their extrusion. The direction of the extrusion is defined with an angle of 53 ° in the YZ plane. It is constant across the specimen.

The length of the shine through effect has been evaluated to know how much the extrusion increased the volume.

Another interest of analysing the dimensions of the particles in the direction perpendicular to the shine through effect is that particles are not deformed along that direction,

The post treatment investigating the feature dimensions in the direction of the shine through effect has been done pivoting the images, as illustrated in figure 3.52 b). An artefact of the matrix pivoting can be seen in figure 3.52 c). In the following, the chords smaller than 2 pixels have been removed of the study.

The expected value in direction 37 ° was estimated to be 14.525 pixels (726 nm). The expected value in direction 143 ° was estimated to be 19.533 pixels (976 nm) (+34.5 %).

Although the determination of the size distribution of the particles covering the surface was the first motivation for a nano-tomography of the treated surface, the results achieved in this works do not allow to conclude on this point because the high porosity and the associated shine through effect made the image segmentation difficult.

Nevertheless, the length chord distributions in the direction of the shine through effect and perpendicularly have been applied to the estimation of the particle coverage as explained in the following paragraph.

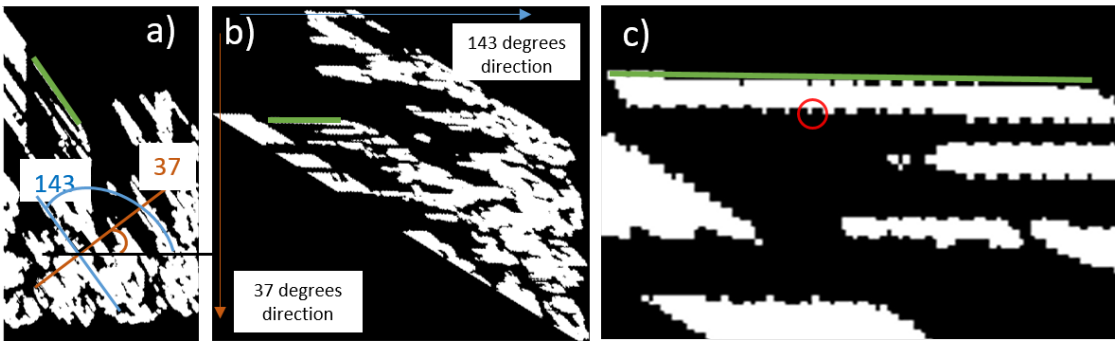

Figure 3.52: Binary images in the plane YZ. The green segment highlights the same part of the image appearing in the pictures. a) The two directions 37 and 143 appear. b) Binary image after pivoting. 37 ° direction is now vertical, 143 ° direction is horizontal. c) Zoom on a detail of the image. The artefact appeared.

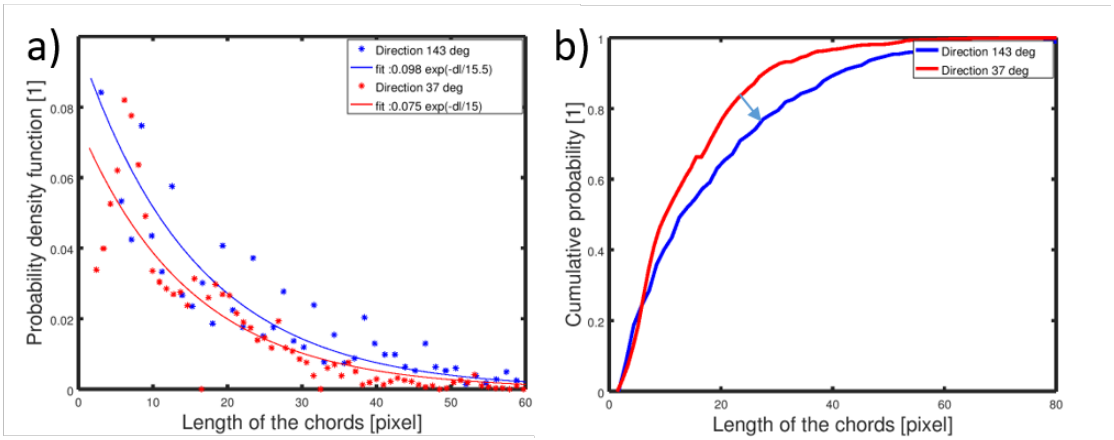

Figure 3.53: a) Probability density function. b) Cumulative distribution. of the size in pixel of chords in both directions, 143 ° in blue and 37 ° in red. The arrow highlights the effect of the shine through effect increasing the size of the particles in direction 143 °.

Particle coverage estimation

The volume of the particles has been estimated counting the number of pixels identified as particle; it has been calculated for each Z slice and summed over the Y slides. Based on the total amount of pixels, the copper density and the area of the surface analyzed, the particle density on the laser-treated surface is 10.8 mg.cm^{-2}.

The volume of copper in the tomography is over estimated because of the shine through effect. This effect could be corrected taking into account the extrusion of 134.5 % in the direction of the shine through effect. That brings the particle coverage estimation down to 8 mg.cm^{-2} based on the analysis of the sub-selection selected for watershed transformation.

The area analyzed was a 15-μm-large sub-selection of the tomography in the bottom of the groove. In this area, the particle coverage is thicker than on the top of the grooves, as illustrated in figure 3.54 a) and b).

Two models of groove and particle coverage profile are proposed in figure 3.54 c) based on the TEM specimens observation. Two cross-sectional areas can be defined and

evaluated:

- a_2, the cross sectional area of the particle coverage over one period of the grooved surface, equal at 467 μm^2;
- a_1, the cross sectional area of the particle coverage studied after watershed transformation equal at 174 μm^2.

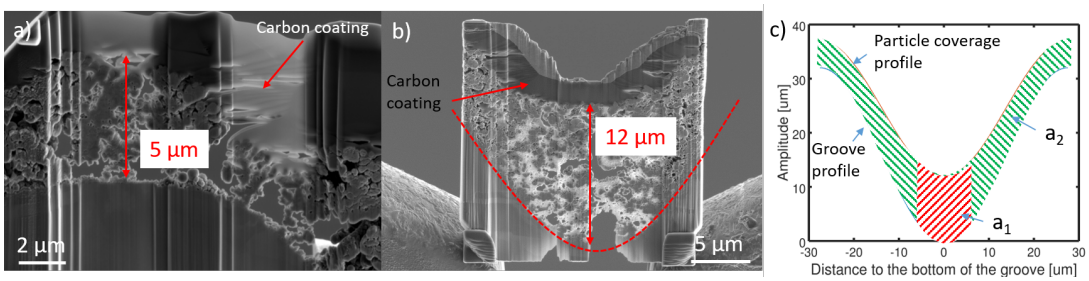

Figure 3.54: a) SEM image of the TEM specimen presented in figure 3.20 for estimation of the thickness of the particle coverage on the top of the groove. b) SEM image of the TEM specimen presented in figure 3.22 for estimation of the thickness of the particle coverage on the top of the groove. c) Models of groove and particle coverage profiles. The green area a_2 is the cross sectional area of the particle coverage over one period of the grooved surface. The red area a_1 is the cross sectional area of the particle coverage studied after watershed transformation.

Taking into account the ratio of the two areas, and considering that the particle density is uniform on the cross-sectional area, the particle coverage averaged estimated based on nano-tomography is 2.97 mg.cm^{-2}.

As further work, it is planned to carry out the watershed transformation on an entire period of the grooved interface region in order to better estimate the average particle coverage.

To conclude, the post-treatment performed on nano-tomography allowed the determination of the particle coverage at the microscopic scale. The estimated value is in a good agreement with the experimental value at 2.6 mg.cm^{-2}, determined at the macroscopic scale, after ultrasonic cleaning, as described in section 3.4.2.1.

3.5 Dust, the *un-re-deposed* ablated material

Comparing the mass of ablated material (figure 3.39) and the mass of particles present on the top of the surface (based on ultrasonic cleaning, figure 3.46) it appeared that only a small proportion of the ablated material is actually re-deposited to the surface.

The re-deposition rate is defined as the ratio of the copper re-condensed on the surface compared to the copper evaporated during the laser ablation.

Influences of the laser treatment parameters

In figure 3.55, in the case of 10 ps 532 nm laser irradiation, with nitrogen protective atmosphere, illustrated by samples from *Zeta* series, the ratio appears to be rather constant independently on the irradiating fluence. The observed ratio, around 17 %, is in good agreement with the value reported in literature [162].

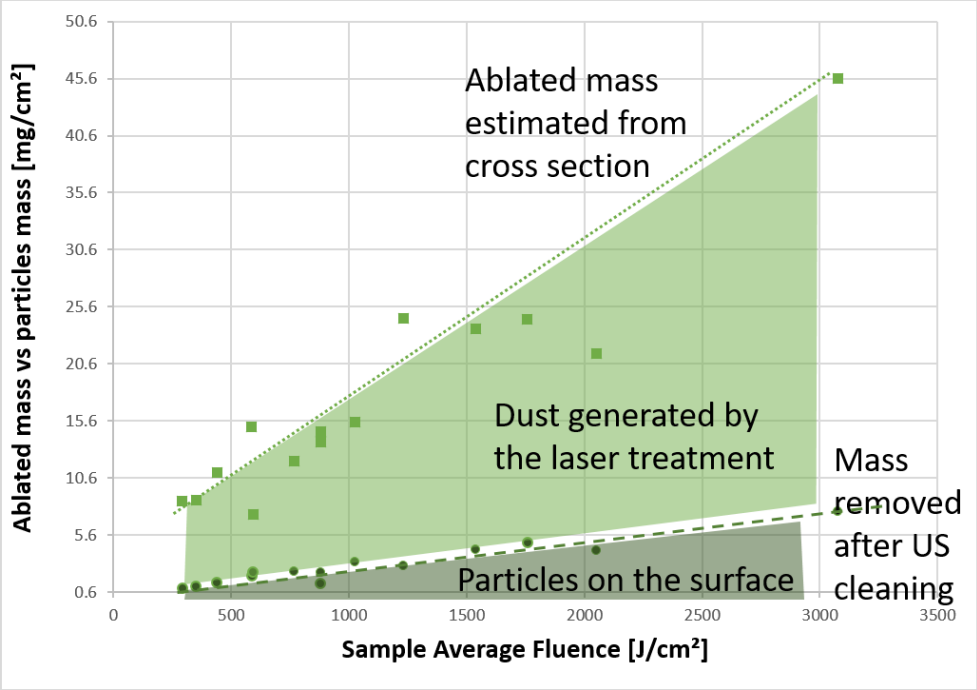

Figure 3.55: Ablated mass estimated from the groove profiles observed in cross sectional microscopy and mass of particles estimated after ultrasonic cleaning for *Zeta* series samples. The difference between the ablated mass and the mass re-deposed as particles is the dust generated by the laser treatment.

Similar studies have been performed on flat copper samples treated by an infrared laser, in the frame of collaboration with partners equipped with such a laser technology:

- at Dundee University the samples treated with 1034 nm at 300 fs, in air without nitrogen flux;
- at Leibniz Institute of Surface Engineering (IOM), the samples treated with 1064 nm at 12 ps.

The re-deposition rate measured on the sample treated by infrared light in a 300 fs regime, in air (without nitrogen) is equal to 6 %, it is significantly lower than the re-deposition rate previously presented. While the molecular mass of the gas is similar (air or nitrogen), femtosecond regime may emphasise stress confinement regime and favors the spallation and phase explosion, ablation phenomenon. The re-deposition rate decreases as more energy is transferred to the plume. As reported in literature, plume dynamics depends on gas environment and regime of laser material ablation.

In figure 3.56, the ratio between the energy deposited to the surface by the laser and the energy needed to evaporate the volume (defined in the equation 3.11) appears to be constant with the irradiating fluence (in the observed range), and to be depending on the wavelength of the laser irradiation. It is equal to 15 % in case of 532 nm irradiation and 5 % in case of infra-red irradiation.

It is worth noting that the higher absorptivity of copper for the green light (12.67 times higher that the absortivity of the 1034 nm wavelength light, see figure 3.1) does not

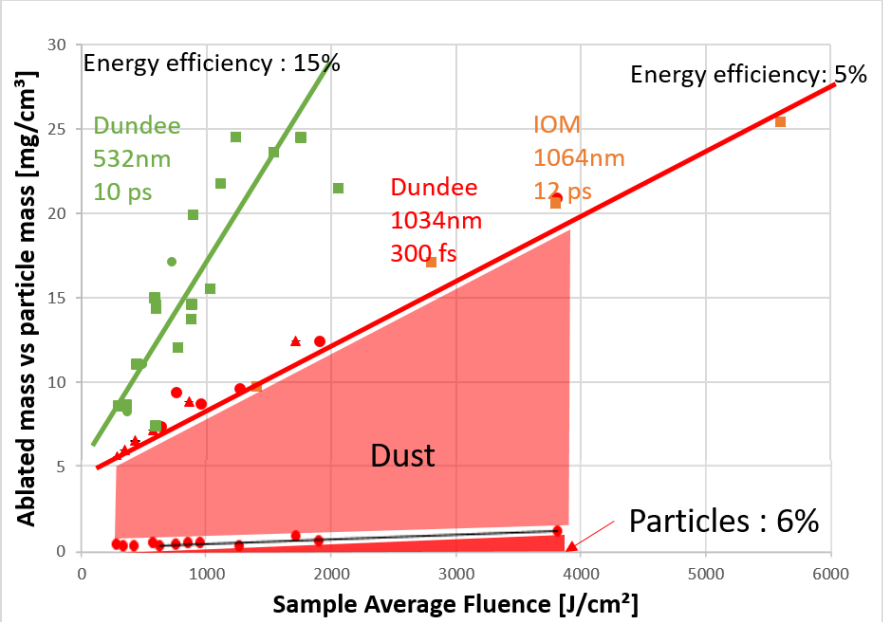

Figure 3.56: Ablated mass estimated from the groove profiles observed in cross sectional microscopy and mass of particles estimated after ultrasonic cleaning for samples treated by infrared light. Tow groups of samples are presented: samples treated at Dundee University with 1034 nm at 300 fs (in red) and samples treated in IOM institute with 1064 nm at 12 ps (in orange). The results for samples treated at Dundee University with 532 nm at 10 ps presented in figure 3.55 have been added for comparison (in green),

explain the higher *energy efficiency* of the laser treatment performed with 532 nm irradiation. Complex, non-linear phenomena are involved in the laser material interaction: for instance the surface reflectivity depends on the surface temperature, roughness...

For infrared irradiation, no differences in the energy efficiency have been observed in between the 300 fs and 12 ps irradiation regimes.

Observation of *in-situ* treated surface

Figure 3.57 shows SEM images of the *BS74* sample extracted from the 2.2-m-long beam screen *in-situ* treated. Large foamy features are observed on the top of the laser-structured surface or the un-treated surface, That features were not observed on plane samples treated in laboratory, they might be the effect of dust present on the confined space of the beam screen.

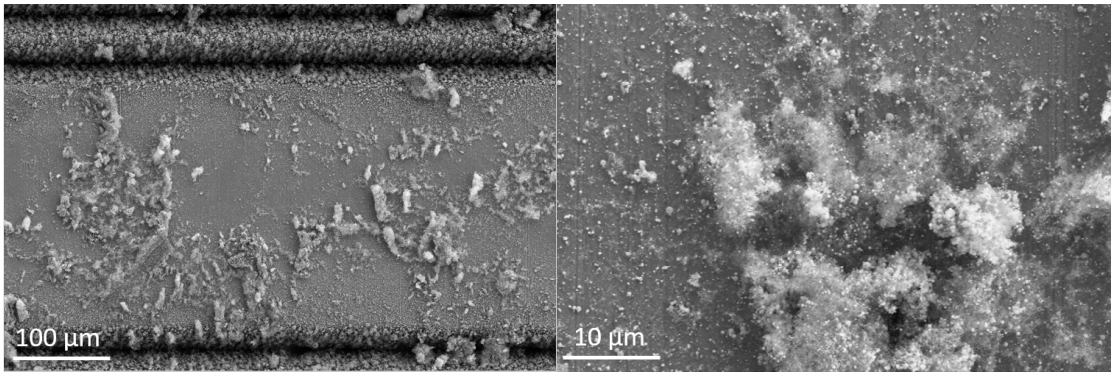

Figure 3.57: SEM surfaces top view observations of *BS7A* samples extracted from the 2.2-m-long beam screen, treated by robot *in-situ*.

Dust quantification for *D7* samples

Table 3.3 presents the results of the analysis applied on *D7* sample. For instance, on *D7 2019* samples, the created dust during the treatment of these plane sample was estimated to be 10.3 mg.cm^{-2}.

Table 3.3: Comparison of the ablated masses, particle coverage and generated dust evaluated on *D7* samples. The values are expressed in mg.cm^{-2}.

Sample	*D7 2018*	*D7 2019*	*BS7A*	*D7 2020*
Ablated mass	14.4	15.1	17.8	11.5
Particle coverage	No data	2.6	0.6	1.0
Created dust	No data	10.3	17.2	10.5

Conclusion

In this section, it has been shown that the re-deposition rate during the irradiation of flat copper samples in an open environment with a nitrogen flux is 17 % creating particles which cover the formed grooves.

In other words, 83 % of the ablated copper from a plane sample treated in an nitrogen flux is not re-deposited to the surface. This *missing matter* is the dust generated by the treatment.

The dust could be an issue if the ablation happens in a confined space as it is the case for *in-situ* treatment of the beam screen. The large amount of material vaporised or ionised could disturb the operation of the robot or escape through the pumping slots and pollute the space between the beam screen and the cold bore. Part of the dust would remain unattached on the treated surface. Extraction of this dust has to be considered during or after the treatment of the surface.

3.6 Conclusions on the surface transformation during the laser irradiation

In the literature, the ablation mechanisms and therefore the morphological characteristics of the structured surface are linked to the ablation regime (pico or femtosecond) and the parameters of the laser treatment, notably the wavelength and the irradiating fluence. Computational tools have been developed to simulate the behavior of the material in the ablation site and in the ejected plume. Morphological observations are also reported and correlated with the measure of physical properties of the treated surface such as the reflectivity or the wettability.

The overall observations performed on the treated samples at CERN showed a sinusoidal pattern of grooves and the re-deposition of ablated material in the form of microstructures and sub-microstructures. The TEM analysis illustrated the description of the ablation mechanisms. The morphological description of the surface was made related with the local value of the irradiating fluence.

Microscopic observations were carried out on treated samples. The depth of the grooves increases with the irradiating fluence as more energy is available to ablate the copper.

Once ablated, the material is partially re-deposited to the surface and create submicrometer roughness. The size distribution, as well as the particle masses have been evaluated thanks to the collect of detached material in an ultrasonic bath and the analysis by FIB/nano-tomography.

These studies established that only a fraction of the ablated material during the irradiation is actually re-deposited to the surface of the sample. The missing material, made of free particles, is released as dust.

Due to the high cooling rates usually observed in laser ablation, the particles are observed to be already re-solidifying when they reach the interface region of the sample after ejection. Consequently, they might be weakly connected and could be potentially removed when mechanical solicitation is applied. Depending on the size of the ejected liquid droplet, the solidification process might be more or less advanced when the droplet is re-deposited to the surface. Larger particles might be more strongly attached to the surface than the smaller ones.

In general, the mechanical integrity of the particles covering the surface has to be assessed; it will be investigated in the following chapter.

Chapter 4

Mechanical tests on the laser-treated surface

Abstract

The aim of this chapter is to characterize the amount of detached particle as a function of the applied mechanical stress on the surface. The adhesion of particles created by the laser treatment was assessed applying no-contact, reproductive forces on these particles. The amplitude, the duration varied on a large range of value depending on the extraction technique used. Influence of the cryogenic temperatures was evaluated both using samples which underwent thermal cooling/warming cycles or performing tests at cryogenic temperatures.

During the operation of the accelerator, the beam screen can be subjected to high electro-magnetic forces which could compromise the mechanical integrity of the treated surface. This phenomena and the consequences for the treated surface are further detailed in section 5.1 but it already give an idea of the acceleration range of interest for the application. The acceleration that leads to inertia force equivalent to the Lorentz forces expected during magnetic quench (around 30 $N.mm^{-3}$) is in the range of 350 000 g.

Test setups have been considered to apply a no-contact force on the particles using inertia forces. These forces, also called pseudo-forces or fictitious forces, are acting on objects whose motion is described in a non-inertial frame of reference. A frame is not an inertial frame if it is not in a state of rectilinear and constant motion compare to the inertial frame of reference (also called Galilean reference frame). The forces arise from the acceleration of the non-inertial frame of reference compared to the Galilean reference frame. The following equation links the equivalent acceleration and the forces density:

$$\gamma = \frac{F_{Vol}}{d_{copper}} \tag{4.1}$$

where γ is the acceleration, d_{copper} is the copper density, F_{Vol} is the inertia force, a force density *i.e.* a force per unit volume. The force applied on a particle is the integrate over

the volume of the particle $F = \iiint_V F_{Vol} dV$.

The range of targeted acceleration did exclude mechanical conventional drop tests, as, in that case the acceleration reported is typically in the range of 300 g.

Two methods have been used to submit the laser-treated samples to acceleration field: centrifugation and acceleration of the surface triggered by laser shocks.

The centrifugal acceleration has been used to submit the sample to a static and reproducible force field up to 24 N.mm^{-3}.

The experimental setup, usually dedicated to LAser Shock Adhesion Test (LASAT), has been used to accelerate the surface of treated samples. In this configuration, when the sample accelerates, in the non-inertial reference frame attached to the accelerating sample an inertia force pushes the particles backward into the surface. On the other hand, when the surface of the sample decelerates, in the non-inertial reference frame attached to the sample, an inertia force pulls the particles away from the decelerating surface. In the case of acceleration in a straight line, inertia force is evaluated from the value of the acceleration of the macroscopic surface. The application of LASAT setup to the particle extraction required a calibration study in order to determine the surface dynamics as a function of the LASAT configurations.

Using these two extraction methods, detached particles were counted and analysed to determine the quantity of dust detached per unit surface submitted to the mechanical stress and subsequently, by weight difference the density of particles still attached on the sample surface. It turned out that about 4 % of the particles originally present on the surface were detached when applying the mechanical solicitations. This amount was more important if the samples were at cryogenic temperature or if it had been submitted to thermal cycles before the mechanical tests. SEM and XPS analysis of sample surfaces after particle extractions did not revealed strong modifications neither of the surface morphology nor the surface physical properties.

Résumé en français

Dans ce chapitre, les stratégies déployées pour les essais d'adhérence des particules à la surface sont exposées. Il s'agit de faire varier la densité de particules couvrant la surface sans altérer la composition chimique de celle-ci. L'application de force à distance est privilégiée. Les effets de la température sur l'adhérence des particules ont été appréhendés, à la fois en utilisant des échantillons ayant subi des cycles de refroidissement ou bien en réfrigérant les échantillons pendant des essais de détachement de particules.

$$\gamma_{eq} = \frac{F_{Vol}}{d_{cuivre}} \tag{4.2}$$

ou γ_{eq} est l'accélération équivalente, d_{cuivre} est la masse volumique du cuivre, F_{Vol} est la force volumique définie par la force par unité de volume. La force F appliquée sur une particule correspond à la valeur intégrée de la force volumique $F = \iiint_V F_{Vol} dV$.

Pendant l'opération de l'accélérateur, la surface traitée pourrait être soumise à d'importantes forces électro-magnétiques qui sont discutées dans une section dédiée (sec-

tion 5.1) mais dont l'ordre de grandeur est estimé autour de 30 N.mm^{-3}. Afin d'obtenir une telle force volumique d'inertie, l'accélération que doit subir les particules de cuivre est de l'ordre de 350 000 g excluant par la même, l'utilisation des tours de chute ou l'accélération obtenue est de l'ordre de 300 g. Deux techniques ont été appliquées à l'extraction des particules.

Les accélérations obtenues (jusqu'à 275 000 g) à la surface des échantillons placés dans des centrifugeuses ont permis d'atteindre des forces statiques volumiques de l'ordre de 24 N.mm^{-3}.

D'autre part, le dispositif de choc laser, LAser Shock Adhesion Test (LASAT) habituellement dédié aux essais d'adhérence par spallation a été utilisé. Un tir laser est effectué sur la surface avant d'un échantillon. L'expansion du plasma ainsi créé génère une onde de chocs qui se propage dans l'épaisseur de l'échantillon jusqu'à déboucher à la surface libre opposée ou elle est alors réfléchie. L'interaction des ondes incidentes et réfléchies conduit à des contraintes de traction à l'origine du phénomène de spallation. Dans ce travail, le LASAT est utilisé pour mettre en mouvement la surface traitée et la soumettre à des variations de vitesse d'amplitudes importantes mais de courtes durées et, par conséquent, à une large gamme d'accélérations et de décélérations.

Cette application détournée du LASAT à l'extraction de particules présentes à la surface de l'échantillon a réclamé une vaste campagne de calibration visant à déterminer la dynamique de la surface à partir de mesures de vitesse réalisées grâce au dispositif Velocity Interferometer System for Any Reflector (VISAR). Les caractéristiques des forces volumiques appliquées sur les particules sont ainsi déterminées en fonction des configurations expérimentales du LASAT. Il s'agissait notamment d'évaluer l'influence de paramètres tels que la densité d'énergie du laser impactant, l'épaisseur de l'échantillon, la présence d'une couche de matériau à haute impédance acoustique ou encore la nature du milieu de confinant l'expansion du plasma.

Ces essais de calibration ont aussi servi à l'identification des paramètres d'un outil de simulation de propagation d'onde de choc dans le cas d'échantillons de cuivre plans. Les tirs laser ont ensuite été réalisés sur des échantillons traités, qui ont ainsi été soumis à des forces volumiques d'amplitude 1.4-4.6 kN.mm^{-3} mais pour des durée d'application de l'ordre 100 ns.

Par ailleurs le banc LASAT, a été utilisé pour enregistrer la vitesse d'éjection des particules lors du choc laser à l'aide d'une caméra à haute vitesse d'acquisition. L'énergie dissipée dans la rupture de la liaison entre les particules et le substrat a été estimée. A défaut de pouvoir enregistrer le déplacement individuel des particules, il s'agit de tester la faisabilité d'enregistrer le déplacement du nuage créé par un détachement massif de particules. Les tirs ont donc été réalisés à haute densité énergétique.

Pour les deux méthodes d'extraction de particules, la collecte et l'analyse des particules détachées doivent servir à la détermination de la quantité de matériau éjecté en fonction de la densité de puissance et de la température de la surface (qui a été portée à des températures cryogéniques dans le cas des chocs laser). Les résultats ont montré que près de 4 % des particules présentes originalement à la surface sont décollées par les

sollicitations mécaniques considérées dans ce travail. Ce chiffre est plus important si la surface traitée a été refroidie à température cryogénique, ou si l'échantillon a subi des cycles de refroidissement avant d'être sollicité à température ambiante.

Les analyses de la surface de l'échantillon ayant subi les sollicitations mécaniques n'a pas présenté de modifications profondes et préjudiciables de la topographie et des propriétés physiques et chimiques (SEY, degré d'oxidation).

4.1 Centrifugation applied on particle detachment

4.1.1 Principle of centrifugation applied on particle detachment

A centrifugal force is an inertial force acting on the object placed in a rotating frame of reference. More specifically, in a centrifuge, the reference frame spins around an axis, the centrifugal force is orthogonal to the axis of rotation, radial, outwards from the axis. Centrifugal forces can be used to generate artificial gravity (rotating space station, high-G simulators), in a washing machine to wring water out of the fabrics, or in science and industry to separate substances: low-density elements are pushed inward and denser elements move outward under the influence of the centrifugal force.

Centrifugal force for a given mass rotating around and axis can be expressed as following:

$$F_{Vol}(r) = d_{copper}\,\gamma = d_{copper}\,r\omega^2 \tag{4.3}$$

where γ is the centrifugal acceleration, d_{copper} is the copper density, ω is the rotational speed and r is the distance of the point to the axis of rotation.

To test the adhesion of particles in treated surfaces, centrifugal forces were applied on samples, specifically placed into a centrifuge, as illustrated in figure 4.1, with the treated surface facing outwards with respect to the rotation axis.

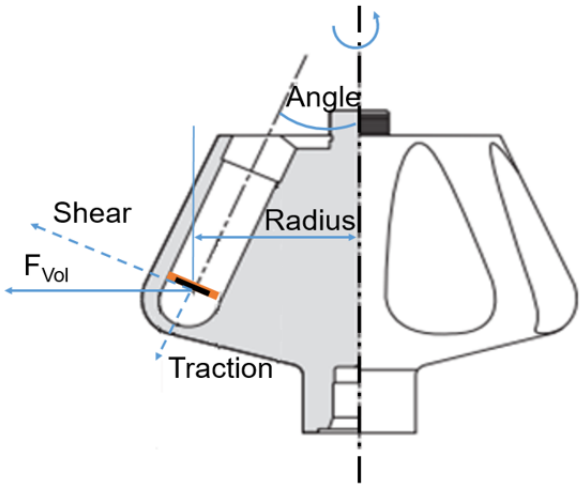

Figure 4.1: The centrifuge force applied on the sample depends on the rotational speed and on the radius. Force orientation with respect to the macroscopic surface of the sample depends on the angle of the rotor and on sample orientation in the holder.

Due to the high density of copper and to the force density that the experiment attempted to approach (30 $N.mm^{-3}$, as further discussed in section 5.1), the targeted value acceleration for centrifugation tests was 350 000 g. Given typical rotor geometry of commercial equipment (related in particular to the distance between the rotational axis and the centrifuged sample), the targeted rotational speed was around 70 000 RPM.

It is worth noting that, in this project, an unconventional use of equipment usually dedicated to the centrifugation of liquid substances was made. In addition, entirely custom-made holders were been used in centrifuge at very high speeds. Preliminary attempts and proof of concept studies were necessary to set up experimental procedure at *low* speed (*i.e.* 13 000 RPM), aiming to guarantee the integrity of centrifuges and rotors.

4.1.2 Description of experimental setups

Different experimental setups were tested in this study, during three test campaigns. Centrifuges and rotors used are listed below:

- at Ecole Polytechnique Fédérale de Lausanne (EPFL), the *Sorvall* Lynx 600 centrifuge with the *ThermoFisher Scientific* SS-34 rotor, used at 30 000 g (13 000 RPM) for proof of concept study;
- at Geneva University, the *Sorvall* RC-5b Plus centrifuge with the *ThermoFisher Scientific* F14-14 x 50cy rotor, used at 45 000 g (20 000 RPM) for proof of concept study;
- at Geneva University, the *Beckman Coulter* Optima L-100 XP ultra-centrifuge with the *Beckman Coulter* 70 Ti rotor, used up to 276 000 g (57 000 RPM) for preliminary study and 136 000 g (40 000 RPM) for final experiments.

Laser-treated samples were placed into the centrifuge tube thanks to a sample holder specifically designed and manufactured according to the rotor model and the centrifugation speed. The tube was placed into the rotor and allowed mechanical support to the sample during the high speed centrifugation..

Figure 4.2 a) presents, as an example, the sample holder used with the *Beckman Coulter* 70 Ti rotor. A tilt angle of 23° ensures the vertical position of the sample once it is installed in the rotor, as illustrated in figure 4.2 b). In this condition, inertia forces applied on particles are perpendicular to the macroscopic surface. Considering the local topography of the treated surface, as illustrated in figure 4.2 c), a mixed load with shear and tension is locally applied on bonds between the surface and the particles.

After centrifugation, both the sample surface and collected detached particles were observed. A carbon sticker was placed in front of the sample surface, on an aluminum stub, in order to collect detached particles. It is visible on the lower part of figure 4.3. Detached particles were collected and analysed following the procedures described in section 2.3.4. The mass of detached particles scaled with the surface submitted to centrifugal forces has been determined depending on the experimental conditions.

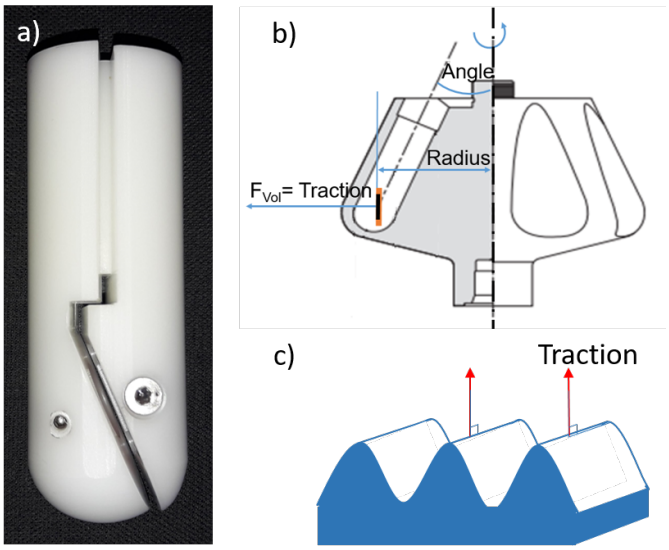

Figure 4.2: a) Picture of an assembled sample holder used with the *Beckman Coulter* 70 Ti rotor. b) Schematic of the sample placed in the rotor, the angle of the sample with respect to the tube axis allowed the sample to be placed vertically once the assembly was installed in the rotor. c) Schematic view of the local surface topography and the direction of centrifugal forces in a tilted sample holder.

The sample surface (visible on the upper part of figure 4.3) was analysed by SEM, SEY and XPS

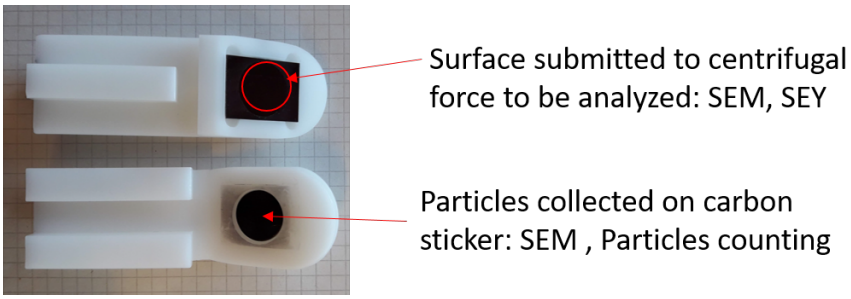

Figure 4.3: Picture of the sample and sample holder after the centrifugation. The surface of the sample was analysed by SEM and SEY measurement, While particles collected on the carbon tape were counted by APA.

Other pictures and further considerations about the realization of these experiments can be found in the appendix D.2.

4.1.3 Description of samples and experimental configuration

Samples used in centrifugation tests

The description and results of proof of concept studies at lower rotational speeds will not be presented in this document.

This paragraph describes the samples and experimental conditions used in centrifugation experiments performed at Geneva University, using the *Beckman Coulter* Optima L-100 XP ultra-centrifuge with the *Beckman Coulter* 70 Ti rotor.

- 1-mm-thick copper samples, labelled *D7 2019*, were used for preliminary studies and for the determination of the rotational speed;
- 1-mm-thick copper samples *D7* (*i.e. D7 2020*);
- *Thermo cycled* samples are *D7 2020* samples which underwent 10 thermal cycles between ambient temperature and 70 K, as described in section 2.2.3. The aim was to assess if thermal dilatation could fragilize the particle bonding and enhance their detachment;
- samples called *BS74* were taken from the 2.2-m-long laser-treated beam screen, as described in appendix section C.2.

Except for preliminary studies, all samples were centrifuged at 40 000 RPM, corresponding to an inertia force value of 12 N.mm^{-3}. Experiments were performed in air at standard conditions of pressure and temperature. Depending on the target RPM value and the centrifuge model, the maximum rotation speed was reached after several tens of seconds. In this test setup, forces applied on samples can be considered as static.

Choice of the rotation speed for experiments

Preliminary studies were performed on *D7 2019* samples to determine the rotational speed which could be applied on samples without risk for the rotor and centrifuge.

The rotational speed and, therefore, inertia forces applied on particles were ramped up to 57 000 RPM, corresponding to the advised maximum value for the equivalent density allowed for the rotor. Before reaching the maximum speed, the integrity of the rotor and of the sample holder were regularly assessed before increasing further the speed. In between each speed increment, detached particles were collected on the carbon sticker and analysis to determine the detached mass was performed as explained in section 2.3.4. At 57 000 RPM, the acceleration was 276 000 g and an inertia force of 24 N.mm^{-3} was produced in that condition.

Figure 4.4 presents the cumulated total mass of detached particles as a function of inertia forces applied on the surface.

When applying 24 N.mm^{-3}, on *D7 2019* sample around 0.09 mg of particles per square centimeter could be detached. Compared to the mass of particle estimated from the analysis presented in section 3.4, it means that 3.8 % of the particles present on the surface has been detached, as it can be seen in figure 4.4.

The amount of detached particle reached a saturation value after 8 N.mm^{-3}. The final centrifugation campaign has been performed at 40 000 RPM, leading to 12 N/mm^3. This value was chosen as a compromise between the number of detached particles and the risk of damaging the equipment. The speed was enough to detach the particles, with limited forces applied on the experimental setup.

The amount of detached particles will be compared with results obtained on other samples and with other extraction techniques. More information about the size distribution and analysis of the samples will be further discussed in section 4.3.

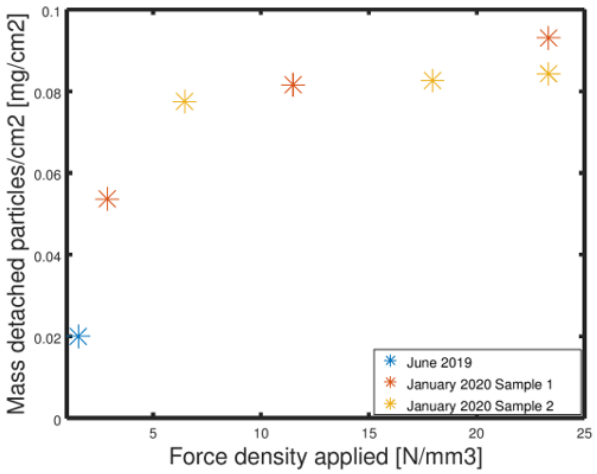

Figure 4.4: Mass of detached particle per 1 cm^2 depending on the force density applied on sample surfaces.

Several loading cycles

In order to assess the effect of multiple successive loading cycles on the surface, a *D7 2020* sample was submitted several times to the same rotational speed of 40 000 RPM. Particles were collected and counted after the 1^{st}, after the 2^{nd} and finally after the 5^{th} cycle. Over the total amount of detached particle after the test, 96.71 % were detached after the 1^{st} cycle, 1.44 % between the 1^{st} and the 2^{nd} cycle and 1.85 % between the 2^{nd} and the 5^{th} cycle.

No additional particle detachment have been observed after 5 loading cycles. Once the most vulnerable particles were detached during the 1^{st} loading cycle, the remaining particles seemed to be strongly attached on the surface. In view for the final application, this result suggests that a cleaning strategy could be developed to clean the surface from the most vulnerable particles.

4.2 LASAT on the laser-treated surface

It is worth noting that the term *fluence*, used in this chapter and more largely in the LASAT scientific community, does not stand for the *energy density* in [$J.cm^{-2}$] expected by the physical definition, and as it used in chapter 3 for instance. As the pulse duration is a key parameter it has been found convenient to divide the energy density of the laser by the pulse duration, and to use the *power density* in [$W.cm^{-2}$] to compare LASAT configurations. When the term *fluence* is used in this chapter, it wrongly refers to the *power density*.

4.2.1 Principle and application of the laser shocks on laser-treated surface

Plasma generation and its rapid expansion at the surface irradiated by a pulsed laser beam has been reported as an effect of the laser-material interaction in section 3.1.1.

Laser pulses and plasma expansion phenomena could be used for propulsion in space, avoiding space debris re-entry as exposed in [177]. Pulsed laser can be used to induce high amplitude stress waves in a material, generated by material ablation and plasma expansion after the pulse strikes the target. Laser peening (LP), or laser shock peening (LSP), is a surface engineering process which takes advantage of laser-driven shock waves to generate beneficial residual stresses in materials. Residual stresses strengthen the surface and increase resistance to fatigue and stress corrosion cracking. [78]

Mechanical shock waves generated by laser and propagating through the material are the phenomena exploited in the LAser Shock Adhesion Test (LASAT), as described in the following section.

Principles of LASAT

The LASAT is a contact-less method to determine the adhesion of coatings, based on spallation phenomena. Coating thickness can vary from few μm to several mm, depending on the laser set-up characteristics.

As illustrated in figure 4.5, during LASAT, a high power pulsed nanosecond laser is focused on the front side of the sample. The high energy delivered in a short time is absorbed by a thin material layer and triggers sublimation, vaporization and ionization of the irradiated surface. This highly energetic material state corresponds to plasma. Its fast expansion produces a high pressure shock pulse and triggers a compressive shock wave on the front side of the sample. The incident compressive shock wave propagates across the sample and is reflected on the opposite surface (*i.e.* rear free surface). The superposition of the incident and reflected waves can generate a tensile stress, which can bring to material failure or to the decohesion of internal interfaces [178–180].

A containment (or confinement) layer is added to confine and delay the plasma expansion, in these conditions the induced pressure is reported be be an order of magnitude greater and the shock wave duration up to 3 times longer than in the direct irradiation regime at the same power density [181–183].

In this work, the dynamic behavior of the free opposite surface (*i.e.* the acceleration and deceleration of the macroscopic surface) was used to generate inertia force on the particles present on the surface. Detached particles were then collected on a carbon sticker for further analysis. Figure 4.5 illustrates how LASAT setup was used to assess the detachment of the particles. The density of particles on treated surface decreases after application of mechanical stresses. The consequence of particle density reduction on treated surfaces on SEY were measured and are exposed in section 5.3.

Figure 4.6 is an illustration of the direction of inertia force applied on the particles depending on the dynamics of the sample macroscopic surface during a laser shock. For each emergence of the shock wave at the free surface, a velocity peak is measured. During the acceleration phase, the surface moves down and the inertia forces acting on particles

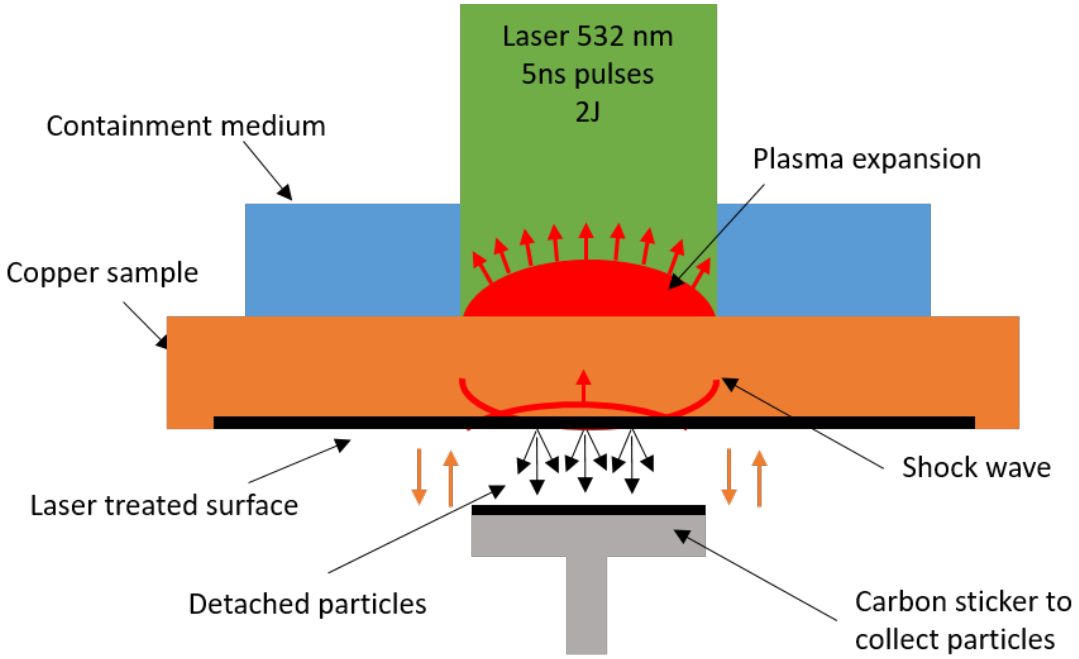

Figure 4.5: Sketch of LASAT setup for the assessment of particle adhesion on a laser-treated surface. A high power short pulse laser (532 nm, 5 ns, up to 2 J) is focused on the back surface of the treated sample. The expansion of the generated plasma produces an intense compressive stress wave which propagates through the material. Reflection at the free surface of the sample changes the incident compressive shock wave into a tensile one which propagates to the opposite direction. The movement of the surface generates inertia forces on particles which may detach from the surface and be collected on a carbon sticker for further analysis.

push them toward the surface. On the other hand, during deceleration the inertia forces pull particles away from the surface.

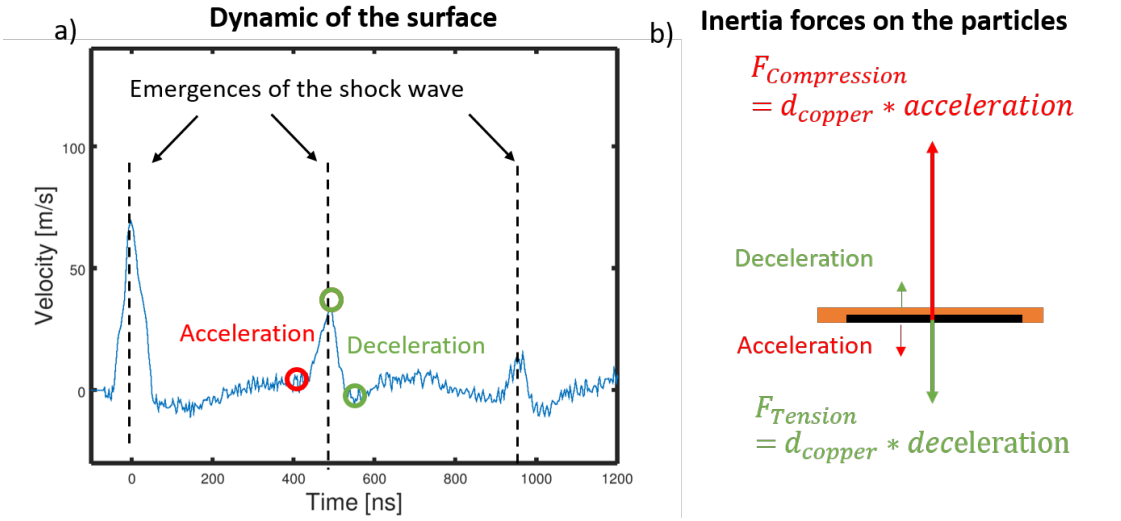

Figure 4.6: a) Velocity measured on the free surface of an untreated 1-mm-thick copper sample, with tape as confinement media, at the power density of 2.72 GW.cm^{-2}. b) Sketch of the sample submitted to acceleration and deceleration, showing inertia forces in tension or in compression depending on the dynamics of the surface during a laser shock experiment.

Objectives and applications to laser-treated surfaces

LASAT experimental campaigns were divided into two phases: test calibration and experiment on laser-treated samples.

The first objective of the work was to determine the movement of the rear surface with a high time resolution during laser shocks, as a function of the experimental configuration. More precisely, velocity peak amplitudes and the duration of acceleration and deceleration phases were measured. Samples and configurations used for the calibration and achieved results are presented in the following section.

A simulation tool has been developed and calibrated based on the results of the velocity measurement experimental campaign. Some application of the tool help the interpretation of the results.

The aim of laser shocks experiments was to collect and analyse particles detached during the shock and to determine how surface particle coverage evolves under fast dynamic loads. Experimental methods will be presented in section 4.2.4 and results in section 4.3.

4.2.2 Calibration based on velocity measurements

Objectives

The aim was to determine acceleration and deceleration and consequently the inertia forces applied on the surface as a function of the LASAT configurations: laser parameters such as pulse duration, beam diameter and energy and the sample characteristics (material and thickness).

The final objective of the calibration phase is to determine the deceleration of the free surface as a function of the energy of the laser irradiation: more specifically, knowing

the sample thickness, the law of the deceleration as a function of the power density (*i.e. fluence*) $Deceleration = f(Fluence)$ as well as the validity range have been determined based on experimental measurement.

The velocity of the rear face of the untreated copper sample was measured during laser shots thanks to a velocity interferometer system for any reflector (VISAR) system. The tests on un-laser-treated samples were also performed to calibrate the pressure loading induced by the laser shock for flat samples, knowing the power delivered by the laser and measuring the velocity of the opposite surface. These measurements were necessary for the validation of a LASAT simulation tool, that will be introduced in section 4.2.3.

LASAT configuration parameters that were varied in this study were the confinement medium, the sample thicknesses, the laser pulse duration, the presence of the impedance layer, the laser pulse power density (via pulse energy and spot diameter to investigate the influence of the pressure spatial profile) and the temperature.

Bibliographic elements

Many authors have analysed the effects of the experimental LASAT configuration on surface dynamics. For instance, experimental measurement, using VISAR of temporal profiles of mechanical shock waves generated laser shocks in water confinement regime, as well as effect of the target thickness for aluminum [181, 184–186], nickel [178, 187], tantalum [184] or tin [187], nickel-based super-alloy [185], zirconium [185], aluminium oxide [185], Al_2Si alloy and on 10 μm aluminium coated 316L steel [188] targets are reported.

Characterization of shock waves in copper has been studied in the framework of bi-layers targets made of copper/chromium and aluminum/copper [184]. In that case, the copper layer was deposited on the aluminum substrate (by projections, or electro-deposition, plasma deposition...).

Thick copper targets (thicker than 500 μm) are not commonly reported and more importantly, the literature do not report on the acceleration and deceleration phases but rather on the velocity peak amplitude. A deep calibration campaign was, therefore, justified.

4.2.2.1 Description of the experimental setup used for the calibration

The section is dedicated to the description of the experimental setup developed for calibration tests. The effects of LASAT experimental parameters on the rear surface dynamics of copper targets were, first, broadly investigated. The study was then oriented toward the application of LASAT for the investigation of particle adhesion, in the framework of surface laser treatment in accelerator vacuum systems. In particular, LASAT target were constituted by materials used in vacuum systems, as presented in section 1.1.2. Moreover, special LASAT configurations were developed and tested, with limited amplitudes of applied inertia forces, to approach targeted values typical of magnetic quench, as given in section 5.1.

Samples used in calibration tests

Laser shocks were performed on oxygen-free electronic (OFE) copper alloy, on 20x15 mm^2 cold rolled planar samples. Four thickness values have been tested (200 μm, 500 μm, 1 mm and 2 mm), with the objective to assess its influence on rear surface dynamics.

Calibration tests were also performed on standard colaminated beam screen samples for dipole MB and $Type74$ beam screen. An extended description of these materials and thicknesses can be found in section 2.2.1. During LASAT experiments, the front face - illuminated by laser shock - was the stainless steel side, while the rear face, whose dynamic is recorded by a VISAR system, was the copper side.

As an attempt to investigate more LASAT configurations to modify dynamics of the free surface, a layer of high acoustic impedance material has been glued on the sample front face as illustrated in figure 4.7 a)

Among possible materials with high acoustic impedance, tantalum was chosen for its availability in thin plates. 99.00 % pure tantalum, 10-μm-thick foils, from *Goodfellows* company were cut and glued on copper samples using an epoxy glue. In order to assess the influence of a thicker layer of a material with high acoustic impedance on the surface dynamics, several tantalum and epoxy layers were superposed and glued on the sample surface. Three configurations were tested with a total thickness of tantalum equal to 10 μm, 20 μm and 50 μm. A uniform pressure was maintained during glue polymerisation to obtain a uniformly thick glue layer over the whole sample. The uniformity of glue thickness has been checked on cross section optical micrographs presented in figure 4.7 b).

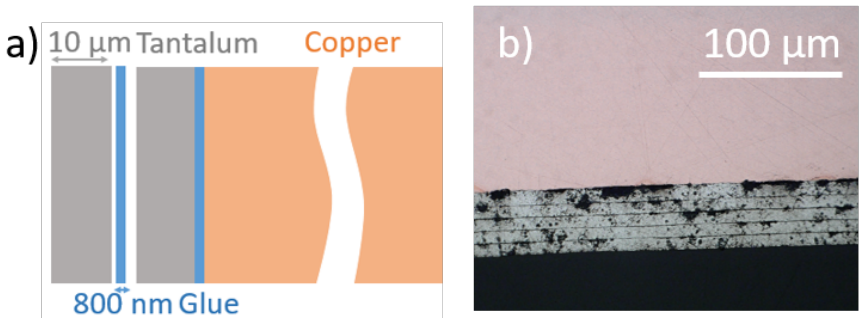

Figure 4.7: a) Sketch of two 10 μm-thick tantalum layers glued on copper sample surface. b) Optical microscope cross-sectional view of an assembly made of five 10-μm-thick tantalum layers glued on a copper sample. Copper appears on the top of the picture, while the five tantalum layers are visible on the bottom. Darker lines between tantalum layers are epoxy glue layers (their thickness was enhanced by metallographic sample preparation (cutting and polishing)).

Before the shock tests, all samples were degreased and passivated, washed in isopropyl alcohol and dried, to remove residues from the surface, as exposed in section 2.2.1. Front surfaces of copper samples were roughened using a P400 grade abrasive paper to enhance the absorption of laser light.

Sample holders used in calibration tests

Pictures illustrating experimental setups used in calibration studies are available in the appendix section D.3.

Copper samples were clamped in an assembly which maintained the sample in the

laser beam trajectory. The upper part of the clamp assembly was made by a 5-mm-thick rubber plate and an aluminium plate, both presenting a 10-mm-diameter hole which allowed to expose the sample front surface to the laser beam. The lower part of the assembly consisted in an aluminium plate with a 10-mm-diameter hole, to allow VISAR measurements on sample rear surface.

In this thesis, two confinement medium have been used: water and transparent tape. In water confined regime configuration, the space between the copper sample surface and the rubber layer thickness was filled of water. When the adhesive tape has been used as a containment media, acrylate-based polymer was stuck on this polished surface as already presented in [189].

The laser beam power density in LASAT experiments was adjusted changing the beam energy through polarizing optics and the beam spot size on the sample front surface. The latter is determined by the distance between the laser beam focusing lens and the sample front surface. The variation of the shock diameters was obtained changing the distance between the lens and the sample: the laser beam has a diameter of 22 mm before the lens, the lens focal is 198 mm-focal therefore the sample must be placed respectively 171 mm and 153 mm away from the lens for a shock diameter of 3 mm and 5 mm, respectively. The energy distribution on the target was checked by impact on photo sensitive paper.

Description of LASAT setups

Three laser shocks campaigns were dedicated to the calibration of the LASAT configurations at the *Centre des Matériaux MINES ParisTech* (CDM) and at ENSMA Poitiers University.

- at CDM Mines ParisTech, experiments were performed with a *Saga 330* laser shock generator by *Thales* (Paris, France), described in [185]. The laser delivers 532 nm waveleght pulses of an approximately Gaussian temporal profile, characterized by 5.2 ns full width at half-maximum (FWHM). Laser output energy could be varied between 0.5 J and 2 J and was controlled by a rotating half-waveplate and a polarizing beam splitter. The spatial intensity distribution of the laser beam were close to a flat-top profile of 3 mm or 5 mm in diameter. The laser energy and the spatial distribution led to power densities ranging between 0.5 and more than 5.44 $GW.cm^{-2}$.

- at ENSMA in Poitiers, experiments were performed with a 1053 nm wavelength Nd-Glass source, described in [190]. It could deliver up to 20 J with a pulse duration about 30 ns. The laser beam was focused on a 4-mm-diameter spot, The laser energy and the spatial distribution led to power densities ranging between 0.64 and more than 4.08 $GW.cm^{-2}$.

The experiments were performed in air at standard conditions of pressure and temperature.

Setup used for velocity measurement: VISAR and signal post-treatment

Several diagnostic devices applicable to laser shock experiments to measure rear surface

velocities could be found in literature, such as shadowgraph camera, heterodyne velocimetry [187, 191], Fabry-Perot Laser-Doppler Interferometry (LDI) [179], polyvinylidene fluoride (PVDF) and electromagnetic (EMV) gauges [188].

In this work, a VISAR developed by Valyn Company (Albuquerque, New Mexico, USA) (Serial N. VLNV-04-1023-532) has been used during LASAT experiments. The system consisted mainly in a Michelson-type optical interferometer. The velocity of a reflecting surface can be measured taking advantage of the Doppler effect between incident and reflected light. The light source for the VISAR was a continuous laser probe (532-nm-wavelenght, 2 W maximum power, VERDI laser by Coherent). Light reflected by the surface was collected by a beam delivery system (a drilled tilted mirror and a convergent lens), named "cyclope" by its developing company *Nucletudes* (Les Ulis, France). It was then transmitted via an optical fibre to the interferometer, where photo-sensors allowed the analysis of interference fringes. The analysis of the fringes allows frequency and phase differences of incident and reflected light, from which surface velocity can be calculated with a temporal resolution smaller than 1 ns. Both principle and set-ups are further described in many references, as for example [192, 193].

More details about signal post-treatment are available in the appendix section D.3.2.

4.2.2.2 Velocity measurement results: influence of experimental parameters

A more detailed report on velocity measurements during experimental calibrations can be found in the appendix D.3.2. An example of velocity measurements obtained via the VISAR system can be seen in figure 4.6.

A qualitative description of the influence of each parameter of the LASAT setup is given in the following.

Overall description

Velocity measurement curves exhibit peaks corresponding to emergences of shock waves at the free surface. The amplitude of the peaks decreased (the amplitude of the 3^{rd} peak is 25 % of the amplitude of the 1^{st} peak) as the wave travels back and forth, through the sample, due to energy dissipation.

In order to ease the comparison of velocity measurements for different sample thicknesses, time scales of all curves have been scaled on their maximum value, corresponding to the 1^{st} shock wave emergence at the free surface. In these plots, vertical black dotted lines mark the expected times for shock wave emergence. This time was calculated based on sample thickness and shock velocity. The value of longitudinal shock velocity in copper was found to be around 4300 $\mathrm{m.s^{-1}}$ from VISAR data, which is in good agreement with shock celerity calculated as follows:

$$D = C_0 + S\,u \tag{4.4}$$

where D is the shock velocity, $C_0 = 3933$ $\mathrm{m.s^{-1}}$ is the bulk sound celerity in copper [178], u is the particle velocity and S the Hugoniot coefficient for copper, which can be found in literature.

Strain-rate estimation based on velocity curves

Surface dynamics can be used to experimentally determine the strain rate in the sample as suggested in [194]:

$$\dot{\epsilon} \simeq \frac{\Delta u}{\Delta t} \frac{1}{2C_0} \tag{4.5}$$

where Δu is the pullback velocity, *i.e.* the difference between the first maximum and the first minimum free-surface velocity, Δt is the difference in the corresponding times, $C_0 = 3933$ m.s^{-1} is the bulk sound celerity [178]. Using values typically observed during LASAT experiments, strain-rates resulted to be in the order of magnitude of 1×10^5 s^{-1}.

Discussion on reproducibility

Among all LASAT configurations tested, some of them have been measured in both campaigns at CDM in December 2018 and in December 2019. It can be noticed that amplitudes of velocity peaks were systematically lower in December 2019. The reasons for this decrease are not yet fully understood and can be due to the laser shock beam generator, to beam diagnostics and/or to the measurement setup.

Influence of sample characteristics on velocity measurements

Three sample characteristics were varied: copper thickness, presence (and thickness) of a material layer with high acoustic impedance and front surface state.

In addition to results on copper samples shown here, measurements performed on colaminated samples are presented in the appendix section D.4.

Influence of sample thickness

Rear surface velocity measurements on samples of various thicknesses, irradiated with the same laser power density of 4.08 GW.cm^{-2} and using water as confinement media, are presented in figure 4.8. Time intervals between velocity peaks depend on sample thickness, as well as on the amplitudes of maximum peaks. Another important effect of sample thickness is energy dissipation: for thicker samples, the energy dissipated during wave propagation will be higher and, as a consequence, measured velocity peaks on the free surface will be lower.

Comparing velocity profiles measured on different thicknesses, three considerations can be made:

- velocity profiles measured on 1-mm-thick copper samples were close to those measured on beam screen samples (see figures in appendix section D.3.2);
- velocity amplitudes and decelerations measured at a given power density were smaller when the thickness of the sample was larger;
- laser driven shock waves obtained irradiating a spot of diameter greater than sample thicknesses (typically 2 or 3 times larger [195]) avoid perturbations due to two-dimensional ($2D$) effects, affecting velocity measurements as described in [195]. Shock waves in this approximation can be considered one-dimensional ($1D$).

Although it will be further explained in the following, it can be already noticed that the measured velocities/accelerations during the laser shocks generated solicitations on

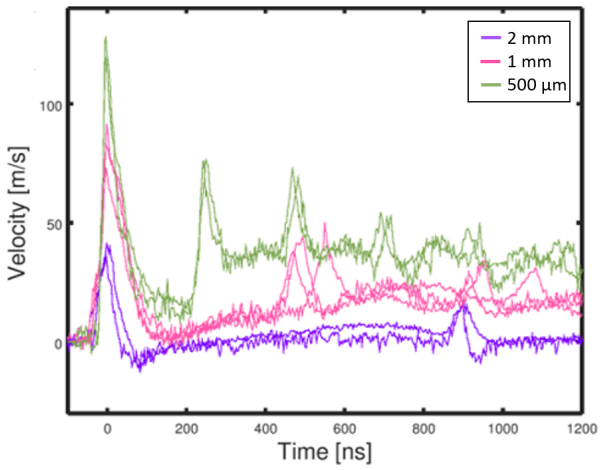

Figure 4.8: Comparison of VISAR measurements on copper untreated samples, with thickness varying from 500 μm to 2 mm. Tape was used as confinement medium and laser power density was set to 4.08 GW.cm^{-2}.

particles more severe than mechanical solicitations foreseen in case of use of the surface in the accelerator (presented in section 5.1). The objective of the calibration phase was then, also, to investigate laser shock experimental conditions which tend to reduce the deceleration of the rear surface.

For these reasons, it was decided to focus further analysis on 1-mm-thick copper samples.

Influence of a layer of material with high acoustic impedance on velocity measurement
As a tentative to reduce the deceleration during the laser shock and to spread the velocity peak measured on the rear surface, an high impedance layer was glued on the sample front surface.

The effect of tantalum layer thickness is illustrated in figure 4.9. Rear surface dynamics of three 1-mm-thick copper samples (one without any tantalum layer, the others with a 10-μm-thick and a 50-μm-thick layers) can be compared. Laser power density was kept at 1.36 GW.cm^{-2} and water used as confinement medium. Clear effects were visible only with the 50-μm-thick tantalum layer. Although velocity amplitude and average decelerations were not modified, peaks were significantly larger, especially because accelerations were lower (a factor of 3 was typically observed) and negative velocity peaks were larger.

The addition of a layer of high acoustic impedance material was initially foreseen to slow down the shock wave, with the hope of reducing mechanical solicitations on the particles covering the laser treated surface. From velocity measurements presented in figure 4.9, it appeared that the tantalum layer increased the shock duration without altering the maximum deceleration, so it was not effective in getting closer to the target acceleration value.

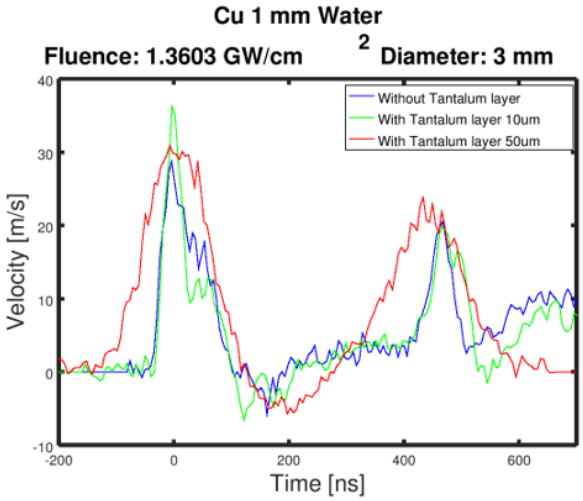

Figure 4.9: Comparison of VISAR measurements on three untreated 1-mm-thick copper samples: in blue no tantalum layer, in green 10-μm-thick and in red 50-μm-thick layer.

Influence of the front surface state on velocity measurement

All the samples were polished before being shocked in order to insure an identical front state surface for all the single laser shocks.

In this paragraph, the surface state modification has to be understood as modifications due to previous laser shocks. The objective was actually to assess the possibility of submitting the surface to several solicitation cycles despite the fact that the laser shock modifies the front surface state as illustrated in the figure D.8, in appendix.

In [184], 11 shoots have been performed on a copper (300 μm)/nickel(20 μm) target at a power density of 160 GW.cm^{-2}. velocity profiles of all these shoots were perfectly reproducible and no influence of the surface state and of wave propagation conditions through the sample (which could have been changed because by local material hardening) were noticed.

A similar experiment was performed at CDM, to verify the influence of sample surface state at lower power densities. A 1-mm-thick copper sample was submitted to 3 laser pulses on the same spot, with a laser power density of 1.36 GW.cm^{-2}. For each shot, the recipient of water used for the confinement was refilled but both the sample and the sample holder were kept in place. The rear surface velocity was measured by VISAR for the three laser shoots and shown in figure 4.10. Velocity peaks measured for the third shot are significantly different to the previous ones. In particular, the maximum speed is reduced to about 1/3 of the value for the first and second shots.

This difference can be explained by chemical and morphological alterations of the front surface irradiated by the previous laser pulses. The surface modifications changed laser matter interaction (LMI) such as the absorption of the laser energy or the plasma generation mechanisms. Subsequently, the pressure impulse on the front surface and the dynamic of the rear surface can be affected by previous laser irradiations of the sample.

As a conclusion, rear surface dynamics are dependent on sample surface state. For this reason, velocity measurements are not repeatable when irradiating the same area

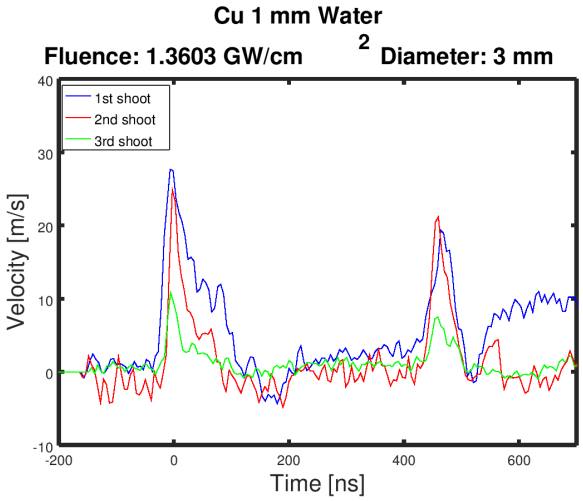

Figure 4.10: Comparison of VISAR measurements on a 1-mm-thick copper untreated sample for three consecutive shots on the same spot. Water was used as confinement medium and the power density was set around 1.36 GW.cm^{-2}.

for several shocks, at the laser power densities used in this study. Therefore, LASAT can not be used to submit samples to multiple consecutive loading cycles.

Influence of confinement media on velocity measurement

Although most of the study was performed in a water confinement regime, transparent tape had to be used for samples at cryogenic temperatures (see section 4.2.4). Thus, the influence of confinement medium has been assessed comparing velocity measurements of two signals obtained with water and one obtained with transparent tape.

Figure 4.11 shows velocity measurements on copper untreated 1-mm-thick samples laser shocked at the power density of 2.72 GW.cm^{-2}, using water and tape as confinement media. No significant difference could be observed in amplitudes and shapes of the first velocity peaks.

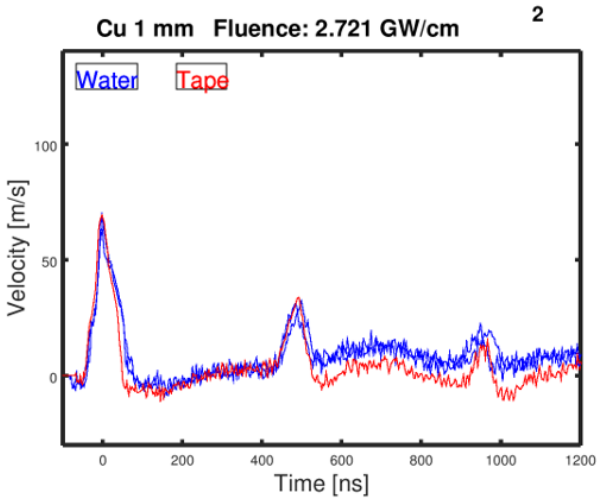

Figure 4.11: Comparison of VISAR measurements on copper untreated 1-mm-thick samples at the power density of 2.72 GW.cm^{-2}, with tape (in red) and water (in blue) as confinement media.

Influence of the laser characteristics on velocity measurement

Several configurations of laser beam characteristics could be tested, varying the laser power density (via laser energy and beam diameter) and the beam duration. The latter is generally machine-dependent for laser shock systems. In this study, as previously mentioned, two systems with different laser pulse durations and power densities were tested, at University of Poitiers and at CDM.

Influence of the laser power density on velocity measurement

For a given laser system (*i.e.* a given pulse duration), the laser power density irradiating the sample is fixed by two parameters: the laser energy and the beam diameter. 1-mm-thick samples have been irradiated with various power densities, varying laser energy with fixed beam diameter and using water as confinement medium. The higher was the power density of the laser irradiating the sample, the higher was the pressure shock generated by the plasma on the rear surface and, finally, the higher was the velocity peak measured on the front surface. A factor of 2.2 separates the maximum velocities obtained with power densities of 1.36 and 5.4 GW.cm^{-2}.

The width of the peaks did not depend on power density: the acceleration phase was 50 ns long and the decelerating phase was 100 ns long, independently of laser energy. The average value of both accelerations and the decelerations was proportional to the maximum velocity.

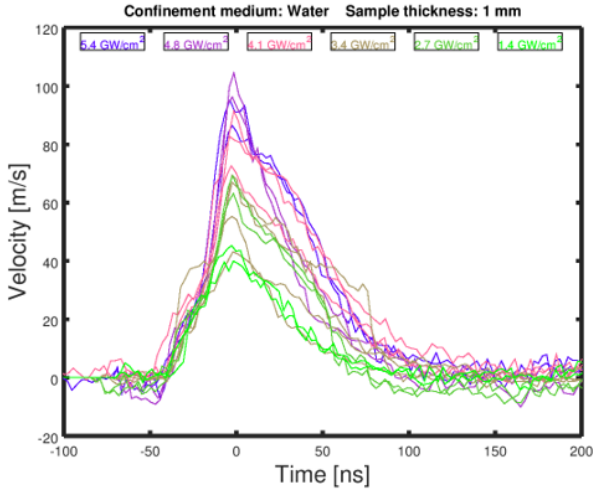

Figure 4.12: Comparison of VISAR measurements on untreated 1-mm-thick copper samples, with water as confinement medium and power densities varying from of 1.36 to 5.4 GW.cm^{-2}.

Influence of laser pulse duration on velocity measurements

The calibration study was started at CDM, using a 5-ns-long pulsed laser. As a tentative to reduce the deceleration during the laser shocks and to spread the velocity peak measured on the rear surface, laser shocks were also performed using a 30-ns-long pulsed laser at University of Poitiers.

The influence of the pulse duration is illustrated in figure 4.13 at power density around 0.7 GW.cm^{-2} and at power density around 3.7 GW.cm^{-2}.

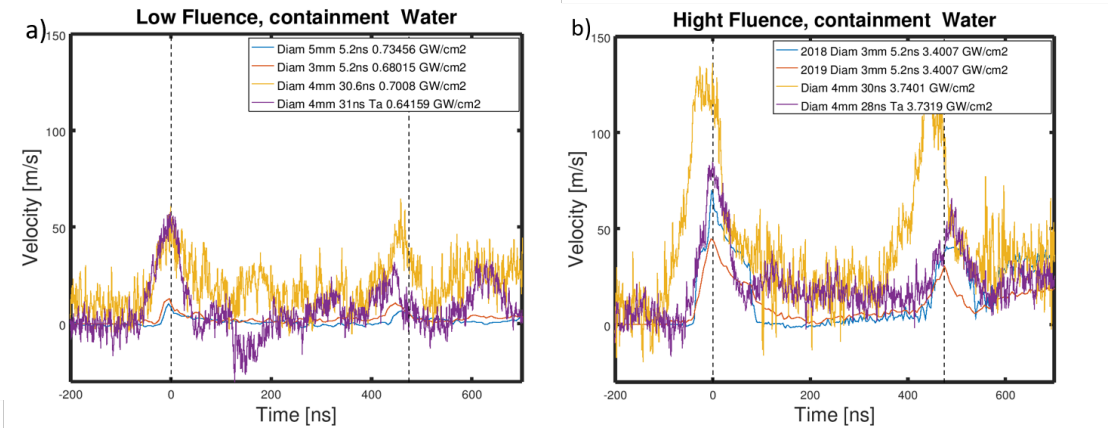

Figure 4.13: Comparison of the VISAR measurements on an untreated 1-mm-thick copper sample, with tape as confinement media, at the power density around 0.7 GW.cm^{-2} (a)) and 3.7 GW.cm^{-2} (b)).

It is worth noting that the laser wavelength used for the 30-ns-long pulses laser shocks was 1064 nm while it was 532 nm for the 5-ns-long pulses. The corresponding reflectivity coefficient are 0.97 and 0.62 respectively (see figure 3.1). For the same irradiating power density, the actual absorbed power density might be lower in the case of the 1064-nm irradiation.

The signal-to-noise ratio is notably lower for the measurement made after 30-ns-long pulses laser shocks. Despite the background sound level, the first peak of velocity is visible and does not show any significant change of shape which would generate rear surface dynamics and consequently inertia force applied on particles very different than the one obtained after 5-ns-long pulses.

To conclude, as the deceleration duration was not significantly enhanced by longer pulses, and because the quality of the signal was better at CDM, the study was pursued with 5-ns-long laser pulses.

The influence of the initial sample temperature on the shock response
The velocity measurement on untreated samples at cryogenic temperature could not be performed in this work, this experimental campaign is scheduled at CDM, in 2021.

The work found in the literature did not reveal major differences between the shocks responses observed at ambient and cryogenic initial temperatures. In [196], spallations under laser shocks were studied down to 30 K, for gold and aluminum. No changes were measured, in the amplitude and shape of the velocity peak after mechanical shocks on nickel samples between between 150 and 1150 K [197] and on iron samples in the temperature range 143-1275 K [198].

Although no data have been found for copper, it has been assumed that the acceleration reached with a given laser power density is the same for samples at room or cryogenic temperatures.

4.2.2.3 Post-treatment: experimental laws on surface dynamics

As previously explained, the values of interest when considering the application of LASAT to particle detachment in the LESS framework are the acceleration and deceleration of the macroscopic surface, as they determine the inertia force applied on particles during the test. After a qualitative description of the influence of each parameter of the laser shock experimental configuration, quantitative results based on the automatic detection of velocity peak amplitudes and calculation of accelerations and decelerations are given in this section.

Velocity measurement performed during the experimental calibration campaigns are exhaustively reported in the appendix D.3.2. In velocity vs time curve plots, red points were placed at the maximum amplitude of each velocity peak. Black points were defined as the inflection points which were considered as the beginning of the velocity peaks, they were used to evaluate the average acceleration during the velocity peaks. Blue points were defined as the inflection points which were considered as the end of the velocity peaks, they were used to evaluate the average deceleration during the velocity peaks.

The time intervals in between, on one hand, black and red points, and, on the other hand, red and blue points were found to be over a range of duration of 40-50 ns and 90-100 ns, respectively. In between these points both accelerations and decelerations were found to be uniform,

Figures 4.14 and 4.15 summarize the results of the tests campaign aiming to determine the dynamic solicitation at the sample surface during laser shocks.

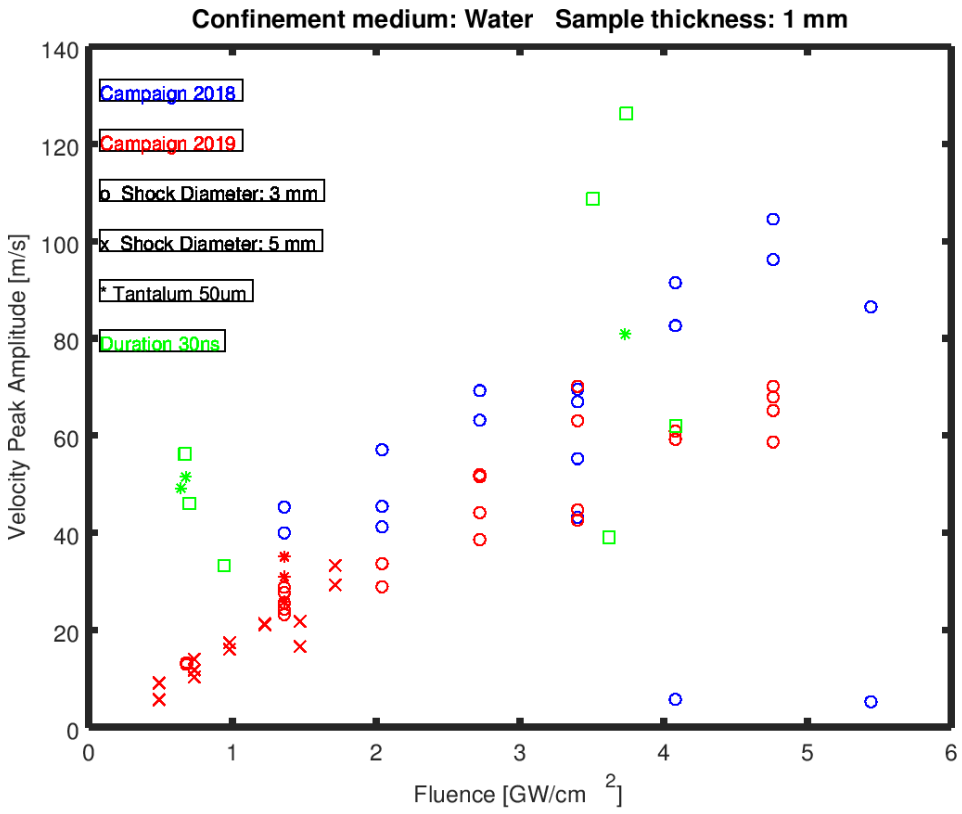

Figure 4.14: Maximum amplitude of the first velocity peak as a function of the power density irradiating the sample. Several configurations are compared: laser beam diameter 3 mm (circle) or 5 mm (cross), with tantalum layer (star), laser pulse duration 30 ns (in green) or 5 ns (the others), test campaign December 2018 (in blue) or December 2019 (in red). Water was used as containment medium on 1-mm-thick samples.

The velocity amplitude increases linearly with the power density (independently on the shock diameter). An amplitude difference between the test campaigns performed at CDM in December 2018 and December 2019 appears clearly in the plots. This can be due to instabilities of the laser source which, although stable in the short term, could deliver different energies over a long time span. Results obtained at University of Poitiers are more dispersed for same power density, this can be also due to laser source instabilities on the short period.

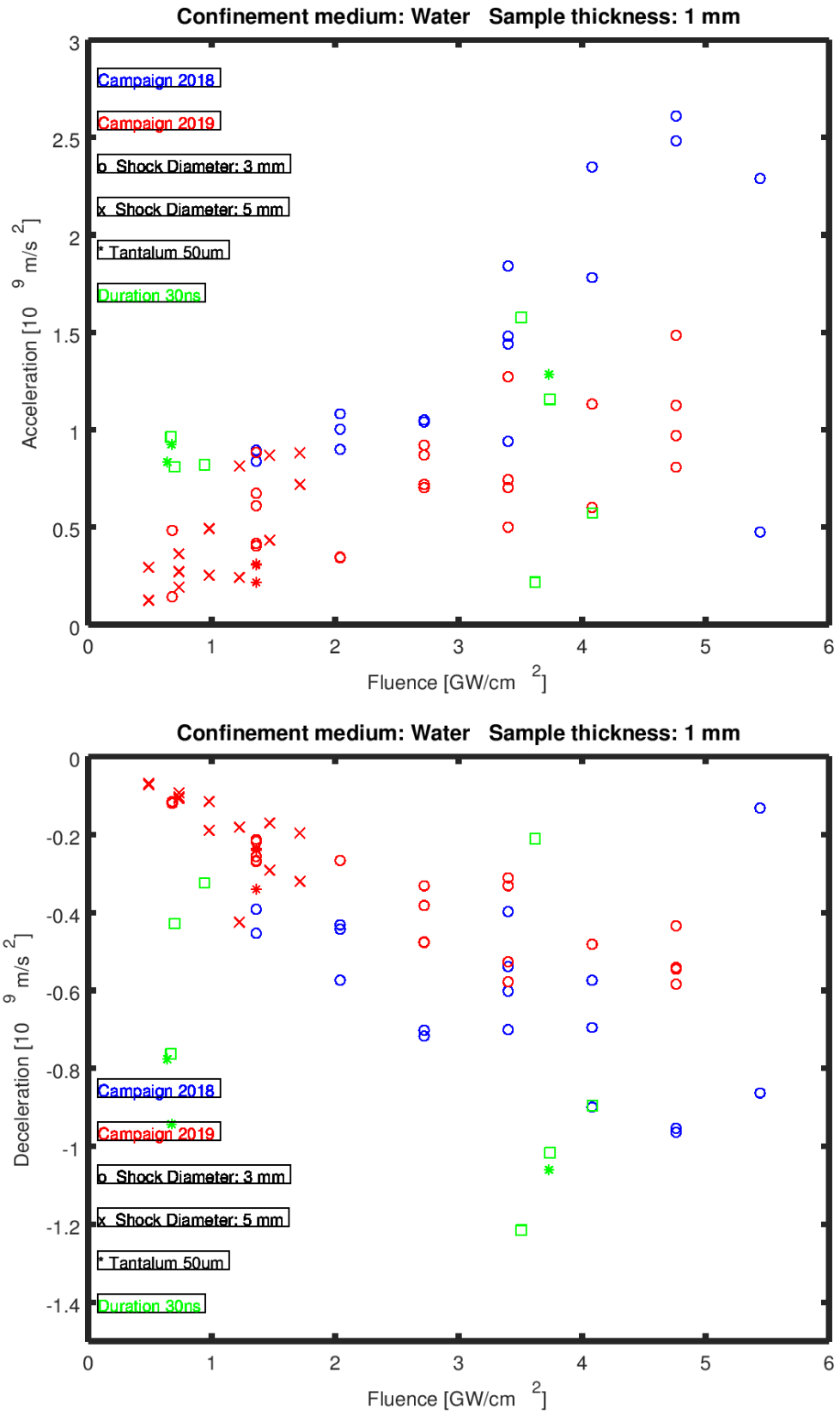

Figure 4.15: Average acceleration (on the top) and deceleration (on the bottom) in the first velocity peak as a function of the power density irradiating the sample. Conditions and labeling are the same as in figure 4.14

Saturation due to plasma breakdown

The averaged values of the peak velocity amplitude and the related calculated acceleration and deceleration increased linearly with the irradiating power densities up to 4.8 GW.cm^{-2}. Between 4.8 and 5.5 GW.cm^{-2}, the values unexpectedly decreased. This can be due to the so-called plasma breakdown, a phenomena reported in literature [183]. With sufficient power density, plasma can be formed before the target surface, inside the confinement medium or in the air above. Generated plasma screens a significant amount of incident photons, limiting the laser energy reaching the confined plasma, immediately above the target. As a consequence, the pressure induced on the target surface is reduced with respect to the unsaturated case. Plasma breakdown appears above a given laser power density threshold, which depends on laser pulse characteristics, sample material and confinement medium. In the case of aluminum as a target and water as confinement medium, the saturation value was evaluated at 10 GW.cm^{-2} for a 1064 nm, 25–30 ns pulsed laser irradiation [181]. On aluminium target, breakdown thresholds were found to be comparable for water and tape, around 7 GW.cm^{-2} for a 532 nm, 9 ns pulsed laser irradiation [189].

Based on the observations collected during the calibration test campaign on copper with a 532 nm, 5 ns pulsed laser irradiation, with water and transparent tape confinements the value of the plasma breakdown threshold was situated between 4.8 and 5.5 GW.cm^{-2}. Therefore, 5 GW.cm^{-2} can be considered the upper bound of the validity range of the experimental law developed in this section.

Threshold for plasma generation

On the other side of the validity range, for very low power densities, threshold for plasma generation was assessed in water confined regime by experimental measurements performed on copper, in [182]. Depending on the wavelength of the laser source, the threshold was determined at 0.2 GW.cm^{-2} and 0.036 GW.cm^{-2}, for respectively 1064 nm and 532 nm. The thresholds were reported to be lower on tantalum target: 0.06 at 1064 nm and 0.023 at 532 nm.

These values have been compared with the theoretical threshold values determined in [199] and turned out to be the same than in direct irradiation regime. It was concluded, then, that the difference between direct and confined regimes are due to plasma expansion rather than to plasma generation. Therefore, the same threshold is also expected to be valid for transparent tape confinement. Other authors reported a minimal power density for plasma generation located around 1 GW.cm^{-2} [185].

Based on the measurements presented in the present study, on copper with a 532 nm, 5 ns pulsed laser irradiation and with water confinement, the lowest power density used (0.49 GW.cm^{-2}) still follows the same linear behavior valid for higher power density values. Linear regressions could thus be used in the range suggested in [182], going from 0.36 GW.cm^{-2} to 5 GW.cm^{-2}.

Average values: experimental laws

Averaged values of the peak velocity amplitude and the related acceleration and deceleration have been calculated in given configurations (confinement medium, presence of

a high impedance layer, copper thickness and irradiated power density). The standard deviation was calculated in each case.

The effect of irradiating power densities is shown in figure 4.16 for 1-mm-thick copper samples with water confinements. Results for tape confinement are shown in the appendix, in figure D.57.

Linear regressions of averaged maximum velocity peaks, accelerations and decelerations as functions of power density were calculated in the range between 0.48 and 4.76 GW.cm^{-2}. The power density of 5.44 GW.cm^{-2} was excluded from the data set since it exceeded the observed value of threshold for plasma breakdown in water.

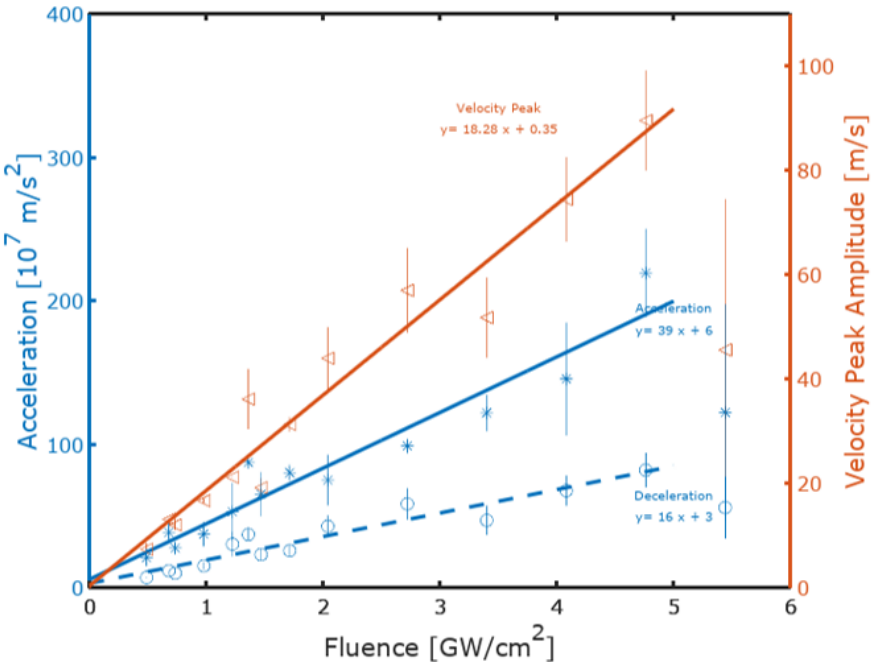

Figure 4.16: Average amplitudes and calculated related accelerations and decelerations of the first peaks of measured velocities, as functions of irradiating power density (named *Fluence* on the graph). Water was used as confinement media on 1-mm-thick copper samples.

Experimental laws have been extracted from the linear regressions presented. These relationships allow the estimation of velocity amplitudes, accelerations and decelerations depending on power densities irradiating 1-mm-thick copper samples. Equations 4.6, 4.7 and 4.8 exhibit these relations in the case of water confinement regime.

$$V_{max} = 16.19 \times PD \ + \ 2.77 \tag{4.6}$$

where V_{max} is the maximum velocity amplitude of the first peak in m.s^{-1} and PD the power density in GW.cm^{-2}.

$$a = 36 \times PD \ + \ 8 \tag{4.7}$$

where a is the acceleration in 1×10^7 m.s^{-2}.

$$a = -16 \times PD \; - \; 3 \tag{4.8}$$

where a is the deceleration (negative acceleration) in 1×10^7 m.s^{-2}.

4.2.2.4 Conclusions on the calibration campaign

Velocity measurements on laser-shocked sample rear surfaces, in the power density range from 0.48 to 4.76 GW.cm^{-2}, allowed the determination of experimental linear laws giving surface accelerations as function of power density.

Inertia forces pulling particles out of the sample macroscopic surface during laser shocks were calculated based on the deceleration values, as given in equation 4.9 below:

$$F_{Vol} = a \times d_{copper} \tag{4.9}$$

where a is the deceleration measured on the macroscopic surface, $d_{copper} = 8960$ kg.m^{-3} the copper density and F_{Vol} the inertia force (a force density *i.e.* a force per unit volume).

Based on equation 4.9, the inertia forces applied on particles have been calculated in the configurations which will be used for the mechanical characterisation of the laser treated samples. In particular, on a 1-mm-thick copper sample, with water confinement, a 1.4 GW.cm^{-2} irradiation (further called low fluence (LF) irradiation) generates an inertia force of 4.6 kN.mm^{-3}. Adding this high acoustic impedance layer, the inertia force applied on the particles is around 3.5 kN.mm^{-3} but with a duration slightly higher. A 4.76 GW.cm^{-2} irradiation (further called high fluence (HF) irradiation) generates an inertia force of 8.6 kN.mm^{-3}. In parallel, based on the deceleration measured on beam screen colaminated samples, the inertia force generated by a 1.4 GW.cm^{-2} irradiation has been evaluated to be 31.9 kN.mm^{-3}. Measurement on beam screen sample is shown in the appendix (see figure D.58).

The duration of forces applied on particles during laser shock experiments was evaluated around 90-100 ns, independently on power density.

It is worth noting that inertia forces values represent a force per unit volume. The total force applied on a particle can be calculated as the integral over its volume $F = \int F_{Vol} dV$. For a spherical particle and a uniform force density, it scales with the cube of particle diameter.

4.2.3 Shock response simulation tool

A finite elements model was developed to simulate the shock response of copper samples as a function of spatial and temporal pressure profiles generated by plasma expansion triggered by laser irradiation.

Bibliographical elements

Different models have been developed for the entire full laser shock process: light absorption by the material, plasma generation, pressure wave propagation thought the sample

thickness and reflection at multi-material layer interfaces or at free surfaces [186].

Nevertheless, most of the codes developed in LASAT framework simulate the final part of the process, involving only mechanical models. They are able to predict the free surface velocity and spallation phenomena as a function of the pressure load on the sample. Three codes can be cited on this purpose: *HUGO* based on analytical simulation, *1D SHYLAC* standing for *Simulation HYdrodynamique LAgrangienne de Choc* and *2D/3D RADIOSS* explicit finite element model (3 of them have been used in [184] for copper targets).

In [185], $P_{Max} = f(I)$ curves of the pressure applied as a function of the laser power density in the range between 0.8 and 5 GW.cm^{-2}, were obtained by comparison with velocity measurements, with water confinement regime, on aluminum targets (thicknesses in the range between 100 and 500 μm), using a 532 nm, 5.2 ns pulsed laser irradiation.

Overall objectives

The identification of spatial and temporal parameters of the pressure load was based on VISAR measurements. This calibration of the simulation led to the determination of a relationship $P_{max} = f(Fluence)$ for 532 nm, 5.2 ns laser irradiation of copper with water as confinement medium.

Once the expression of the pressure load as a function of the power density was known, the model could be used to predict surface dynamic response as a function of sample thickness and power density. The estimation of the shock response (especially the first velocity peak deceleration) was the main application of the simulation tool in the present study. It could help limiting calibration studies based on VISAR measurements, when changing the sample thickness or the power density.

In addition, the simulation tool has then been applied for several purposes:

- determination of surface dynamics in every point of the sample, contrarily to VISAR measurements which allow measurement only in one point;
- estimation of other physical quantities of interest, such as pressure and temperature, helping to analyze sample behavior during laser-shock tests;
- analysis of effects of the local surface morphology.

It is worth noting that colaminated samples were not treated in this section.

4.2.3.1 Presentation of the simulation model

A 1-D axisymmetrical model was developed in Abaqus/Explicit®to simulate shock wave propagation and stress distribution in the whole sample. Simulation inputs, such as material constitutive models, boundary conditions and loadings, are firstly presented.

Constitutive material model

The Mie-Grüneisen equation of state is a relation between the pressure, the volume and the internal energy of a solid at a given temperature. It is used to model solid materials

at high pressures and, in particular, in presence of shock waves.

$$P(V) - P_{ref}(V) = \frac{\Gamma_0}{V_0} \ (E - E_{ref}) \tag{4.10}$$

where P is the pressure, V is the volume, E is the internal energy, Γ_0 is the Grüneisen parameter of the material, ref stand for a reference state of the material, usually assumed to be the state at which the temperature is 0 K.

Laser shocks can induce high strain rates in materials, up to 1×10^6 s^{-1}. For this reason, an adapted mechanical model was chosen, the viscoplastic semi-empirical Johnson–Cook constitutive model. The comparison of this constitutive law with a perfect elasto-plastic law have been illustrated in [184]. The Johnson–Cook model expresses the yield stress as the product of three terms, as shown in equation 4.11 below:

$$\sigma = \left(A + B\epsilon_p^n\right) \left(1 + Cln\left(\frac{\dot{\epsilon}}{\dot{\epsilon_0}}\right)\right) \left(1 - \left(\frac{T - T_0}{T_{melt} - T_0}\right)\right) \tag{4.11}$$

where A is the initial yield stress, B the hardening modulus, ϵ_P the equivalent plastic deformation, n the hardening coefficient, C the strain rate sensitivity parameter, $\dot{\epsilon}$ the strain rate during the process, $\dot{\epsilon_0}$ the reference strain rate, T_{melt} the melting temperature and T_0 a reference temperature.

The first term accounts for the strain-hardening effect, the second for the strain rate effect and the last one for the thermal softening. The values of Johnson–Cook parameters used in the simulations were found in [200, 201] for OFE copper and are reported in the appendix A.

The mesh size was chosen as 2 μm, based on the mesh size convergence analysis shown in the appendix, in figure D.59. The velocity peak simulated with mesh size varying between 10 and 1 μm showed the convergence of the results for a mesh size smaller than 2 μm. Boundary conditions were defined as if the sample was clamped on his perimeter. Gravity was neglected.

Spatial and temporal pressure loading models

Spatial pressure loading model

The laser energy deposition was assimilated to an equivalent pressure loading with a 1.5 mm radial top-hat distribution based on observations on photo-sensitive paper and previous works on the laser source [185]. The spatial distribution of the pressure loading is shown in figure 4.21 d) and is given by equation 4.12 below:

$$P(r, \lambda, R) = 1 - \frac{1}{1 + exp(-\lambda(r - R))} \tag{4.12}$$

where r is the distance to the center of the laser spot, R the laser spot radius and λ was fixed to 3, as suggested in [185].

Temporal pressure loading model

In this work, a model has been proposed to describe the temporal evolution of pressure loadings generated by laser shock. It is defined as a succession of four phases and determined by six parameters ($Pmax_{4GW.cm^{-2}}$, $FWHM$, $Pmax$, P_{pl}, $t3$, $t4$), as follows:

- Gaussian evolution with $Pmax_{4GW.cm^{-2}}$ and $FWHM$;
- exponential decrease from the value $Pmax/2$ to time = $t3$ constant $beta$;
- plateau P_{pl} from $t3$ to $t4$;
- linear decrease, from P_{pl} at $t4$ to 0 at 1000 ns.

The profile is illustrated in figure 4.17.

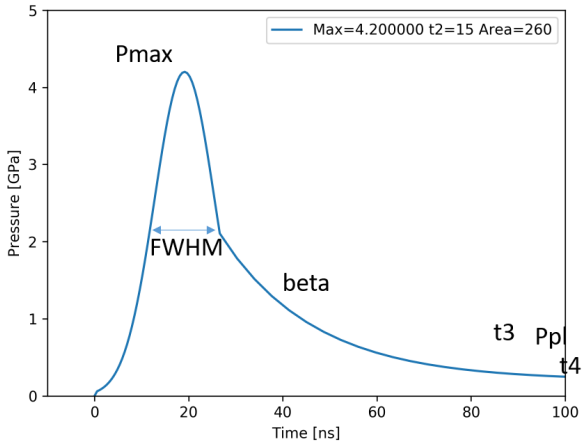

Figure 4.17: Temporal pressure loading profile. The model has 6 parameters.

4.2.3.2 Determination of the pressure load as a function of the power density

The calibration of the pressure load as a function of the power density followed two steps. First, the six parameters of the previously described temporal profile were identified, comparing simulation results to experimental measurements, for a given power density on several thicknesses of sample. In this work, 4.08 GW.cm^{-2} was chosen. Then, once the *shape* of the profile was fixed for a given power density, amplitude variation as a function of the power density was determined. It was, then, assumed that power density did not alter the temporal profile, but acted as a simple scale factor for pressure amplitude.

Identification of temporal pressure profile parameters

Parameter identification was performed in an iterative trial and error process, which started from an initial guess of parameter set E_0 and iterated the following steps until reaching a good agreement between experimental and simulated data for laser shock performed with water confinement at the power density of 4.08 GW.cm^{-2}:

- simulation of rear surface velocity with parameter set E_i;
- comparison with VISAR measured data for three sample thicknesses: 500 μm, 1 mm and 2 mm;

- trial of a new parameter set E_{i+1}.

As general observation it can be said that the first velocity peak amplitude was scaled with area under the pressure loading curve. The coefficient of the exponential decrease and the amplitude of the plateau had effects on the shape of the second velocity peak. The choice of the new parameter set was a trial based on fitting the amplitude of the two velocity peaks.

Figure 4.18 presents the results of profile parameters identification.

Simulations were performed with the temporal profile of the pressure loading which can be seen in figure 4.17 with parameters presented in the table 4.1.

Simulation showed a good agreement with VISAR measurement. In particular, amplitudes and widths of the first and the second peaks were estimated quite accurately.

Table 4.1: Best fitting parameters of the model of the pressure loading temporal profile, based on experimental and simulated data comparison for laser shock performed with water confinement at the power density of 4.08 GW.cm^{-2}

Parameters	$Pmax_{4GW.cm^{-2}}$	$FWHM$	$t3$	$beta$	$t4$	P_{pl}
Values	4.4	15	100	0.05	600	0.2

It is worth noting that the pressure load due to plasma expansion was significantly longer that the laser pulse, assimilated to a 5.2-ns-FWHM Gaussian profile. As reported in [185], this is likely to be the effect of the confinement medium .

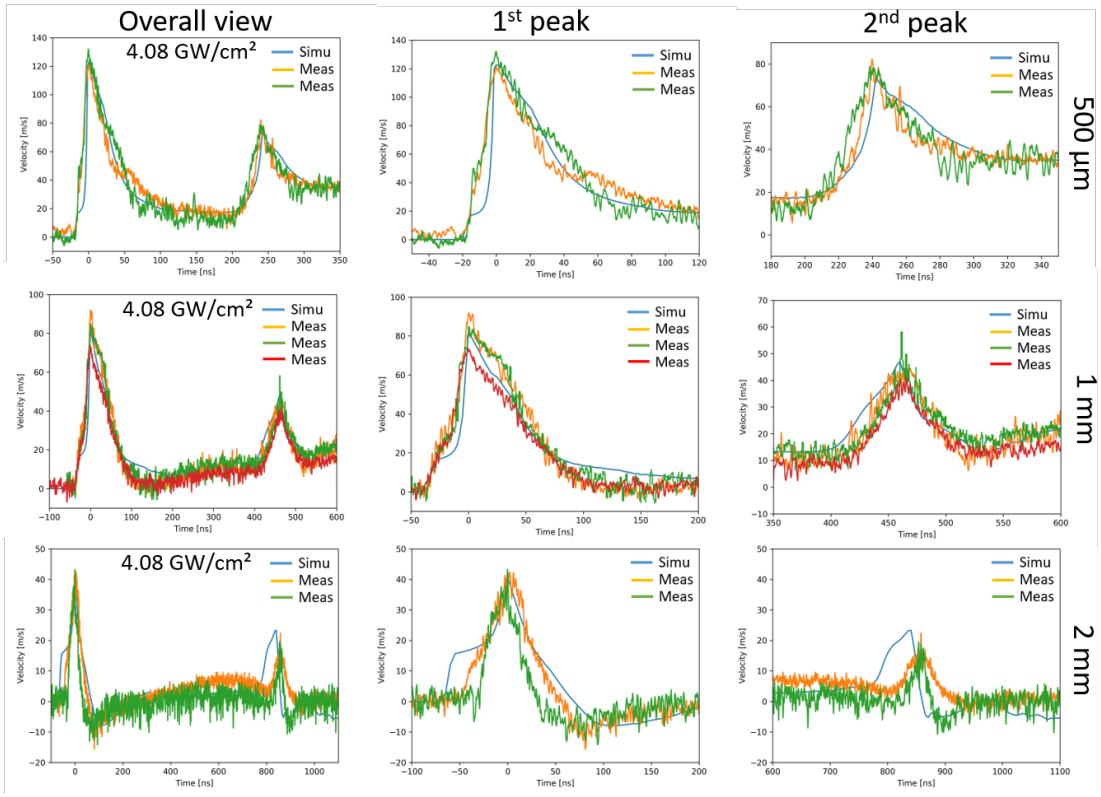

Figure 4.18: Comparison of velocity profiles for a 4.08 GW.cm^{-2} laser shock. Simulated data are in blue and measured ones in green, yellow and red for copper samples with thicknesses of, respectively, 500 μm, 1 mm and 2 mm. Plots in first column on the left show the first two velocity peaks. Plots in the second and third columns represent zooms on the fist and second velocity peak, respectively.

Determination of P_{max} as a function of power density

The *shape* of the temporal pressure profile has been assumed independent of power density on the considered range. For this reason, the pressure profile was normalised and a scaling factor was introduced, namely P_{Max}. For each power density in the experimental data set, the value of P_{Max} was identified by an iterative, trial and error process, based on comparison of simulated and measured amplitude of the first velocity peak. The identification was performed using simulations and measurements made on 1-mm-thick copper samples with water as confinement medium. Table 4.2 presents the result of that identification on the power density range considered in this study.

Figure 4.19 shows the comparison of experimental and simulated velocity profiles, showing a good agreement between them. In particular, amplitudes and widths of first

Table 4.2: P_{max} scaling factor applied on normalised pressure temporal profile of the pressure loading.

Power density	[GW.cm^{-2}]	4.76	4.08	3.40	2.72	2.04	1.36
P_{max}	[GPa]	4.9	4.4	3.9	3.4	2.8	2.3

and second peaks were accurately estimated.

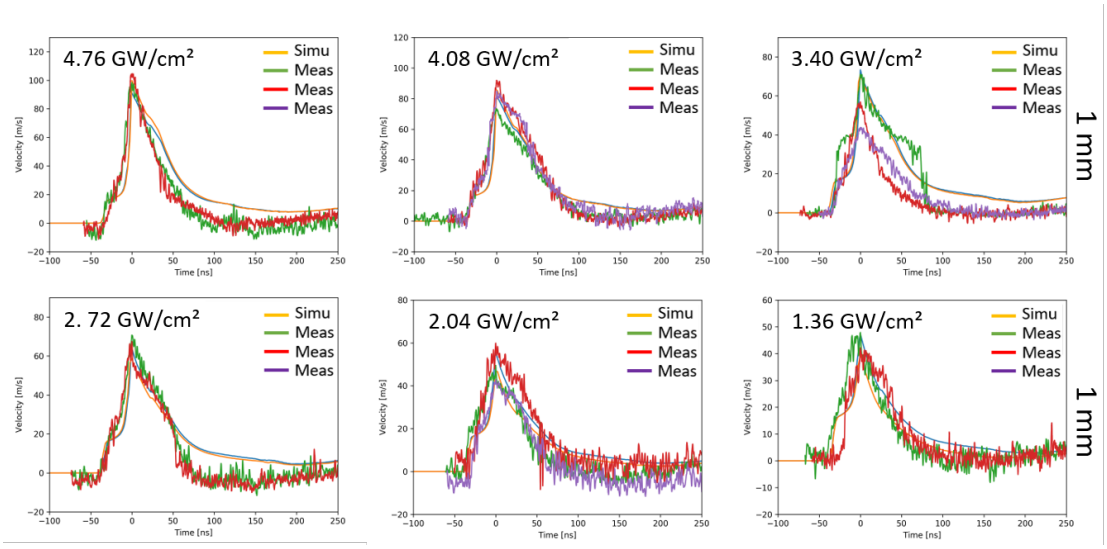

Figure 4.19: Comparison of VISAR measurements on a copper untreated samples of a thickness of 1 mm, with water as confinement medium, at power densities of 1.36, 2.04, 2.72, 3.4, 4.08 and 4.76 GW.cm^{-2} with simulations.

A linear regression was performed to determine a semi-empirical $P_{max} = f(PowerDensity)$ law, as described in equation 4.13 below:

$$Pressure_{Max} = 0.77 \times PD \ + \ 1.05 \tag{4.13}$$

where P_{Max} is the scaling factor applied on the normalised pressure profile.

LASAT test calibration, *i.e.* the determination of the acceleration depending on the experimental configuration, should be preferably based on VISAR measurements, as presented in the previous section. However, a VISAR was not permanently installed at CDM. Thus, the model developed has been used to simulate the dynamic behavior of the free surface when submitted to laser shock at a given power density. All model parameters were based on the experimental data already acquired and, in particular, on the $P_{max} = f(PowerDensity)$ law previously identified.

t=75 ns was found to be an inflection point of the velocity curves (especially for the higher values of power density). Average deceleration can be calculated based on simulated velocity profiles between the maximum of the velocity peak and 75 ns. as illustrated in figure 4.20.

For instance, the first peak deceleration at 0.5 GW.cm^{-2} was estimated by simulation to 3.2×10^8 m.s^{-2}, while it has been measured at around 2×10^8 m.s^{-2} from VISAR data collected during the campaign of December 2019.

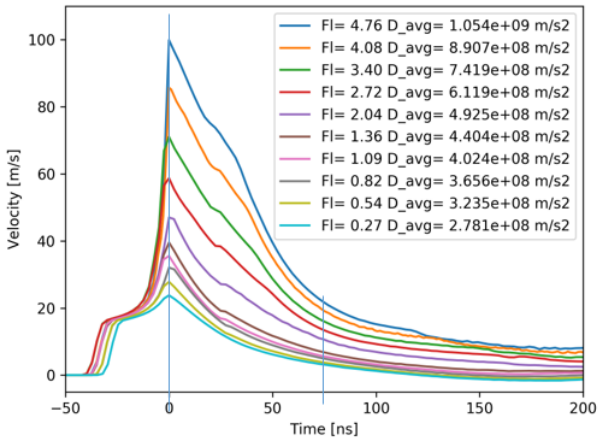

Figure 4.20: Simulation of free surface velocity at the center of the 3-mm-diameter laser spot, for power densities in the range 0.27 to 4.79 GW.cm^{-2} (Power densities are noted *Fl* in the legend). The zero on the time scale corresponds, for each curve, with the velocity maximum.

4.2.3.3 Other applications of the laser shock model

Once the parameters of the simulation tool identified based on comparison with experimental measurements, simulations have been for several applications described in the following sections: the definition of the region from where particles are detached, the calculation of the pressure through the sample thickness, the evaluation of the groove influence on the surface dynamics.

Definition of particle extraction area

The model developed allowed the determination of dynamics of free surfaces during laser shocks everywhere on the target, while VISAR measurements can be performed in one point only, usually at target center. In this section, the model was used to bring relevant information about accelerations and, therefore, inertia forces acting on particles, depending on their position along the radius.

Figures 4.21 a) and b) show SEM images of particles collected on a carbon tape placed in front of the treated rear surface of shocked sample. The space between the sample and the tape was about 1 mm. Most of detached particles were collected in a disk with a radius of about 0.93 mm, highlighted by a green dotted circle in the figures.

In figure 4.21 c), velocity profiles out of the axis are shown, *i.e.* for points placed on the surface at a given distance from the center of the laser beam spot. The green dotted line corresponds to the average value of deceleration calculated on the radius of 0.93 mm.

On each velocity profile, the average deceleration was calculated between the time corresponding to the maximum velocity (t_{max} found around 250 ns) and $t_{max} + 50$ ns. The green dotted line corresponds to the average value of deceleration calculated on the radius of 0.93 mm.

Deceleration are shown in figure 4.21 d) as a function of the distance from the center

of the laser beam spot, in comparison with the applied pressure profile and the maximum simulated velocity. The green line correspond to the radius of the disc highlighted on the microscopy images. It corroborates the microscopy observations: inside the disc the deceleration remains constant, the deceleration decreases when the distance is larger than 0.93 mm, leading to a lower particle detachment.

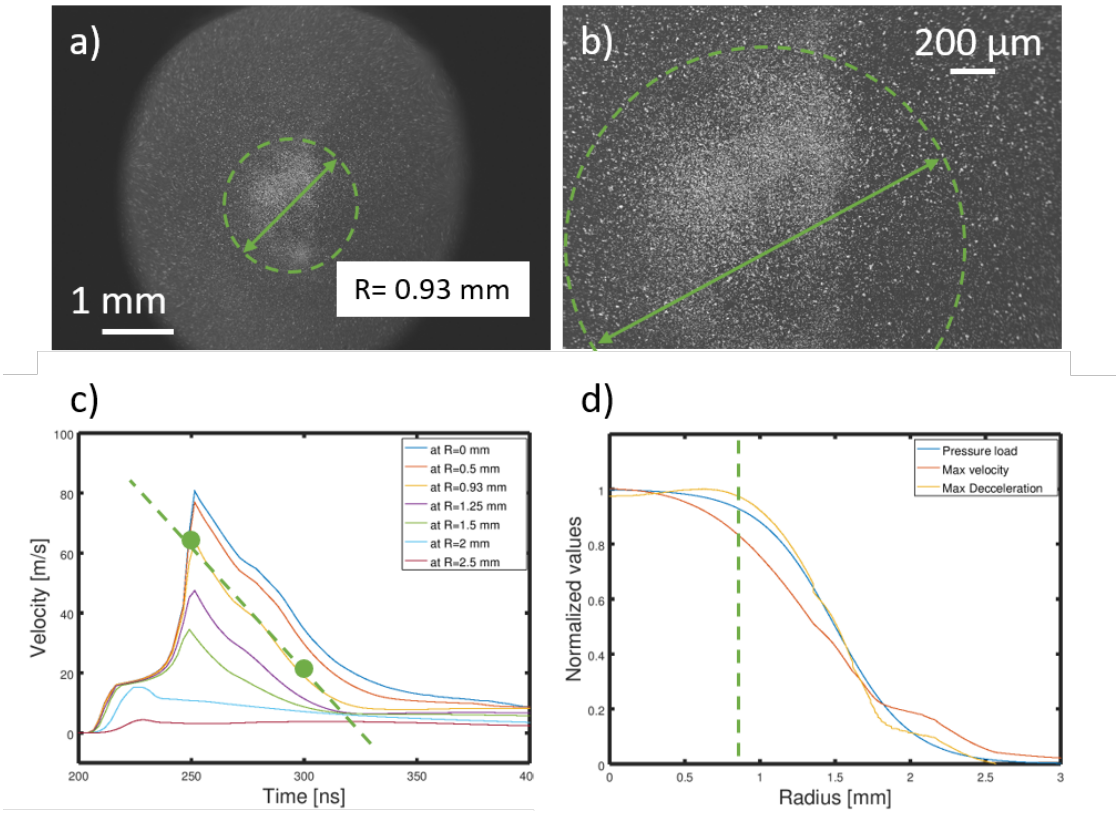

Figure 4.21: a) b) SEM top views at different magnifications of the carbon tape with collected particles after a 3-mm-diameter shock with 3.4 GW.cm^{-2} power density, on a 1-mm-thick treated copper sample. The green dot circle has a radius of 0.93 mm. Most of the particles lay inside this circle. c) Simulated velocities at the free surface for points placed on the radius, at distances displayed in the legend. The shock diameter was 3 mm. d) Normalised spatial pressure load applied on the front surface, normalised maximum velocity and deceleration, simulated on the free rear surface as a function of the radius.

The diameter of the extraction area, where the force is applied on particles, can be estimated as the disc slightly smaller than the diameter of the impacting laser, around 2 mm in the case of the 3 mm laser beam diameter considered in the test campaigns.

Simulations confirmed that outside of the impacted area inertia force are not applied on particles. The localized application of the force allows the presence on the same sample of areas both affected and non-affected by the mechanical solicitation. This makes the analyse of the thin effects of the particle detachment on the surface of a same sample easier and more reliable, for instance SEM observations (see section 4.3.1 and SEY measurements (see section 5.3.2.2).

Equivalent pressure stress along the thickness

The model developed also allowed stress estimation into the sample during laser shocks. The equivalent pressure stress is defined as:

$$Pressure_{eq} = -\frac{1}{3} \times trace(\bar{\bar{\sigma}}) \tag{4.14}$$

where $\bar{\bar{\sigma}}$ is the stress tensor.

The compressive wave applied on the front surface propagates and is reflected at the rear surface as a tensile wave. A tensile stress maximum results from the interaction of incident and reflected stress waves, not far from the rear surface where it can trigger spallation phenomena when exceeding the local tensile strength of the material (or of the interface in the case of an assembly).

Figure 4.22 b) presents the maximum values of compressive and tensile stresses simulated as a function of the depth.

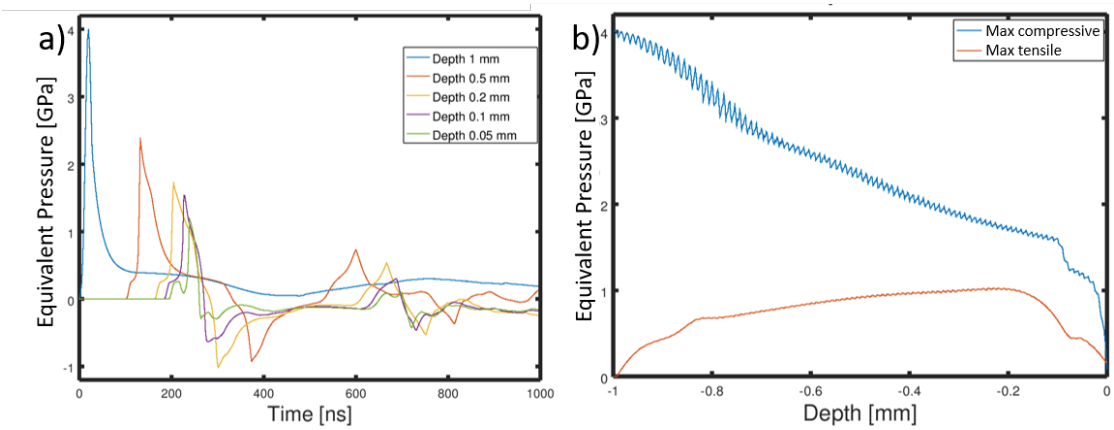

Figure 4.22: Simulated values of the equivalent pressure stress along the axis. The shock diameter was 3 mm. a) Temporal evolution of pressure stress for points placed on the axis, at different depths, as displayed in the legend. The depth -1 mm corresponded to the front free surface of the sample and 0 to the rear free surface. b) Maximum value of simulated compressive and tensile stresses, as a function of the depth.

The maximum value of the tensile pressure stress was located 200 μm below the rear surface and reached 1 GPa. Although this value should exceed copper ultimate tensile strength, as commented in chapter 2, no spallation of 200 μm fragments of copper sample has been observed during the experiments.

More importantly, the maximum tensile stress, drops when getting closer to the surface. For instance, at the depth of 30 μm, has been evaluated to be lower than 50 MPa, it does not exceed the tensile strength illustrated in the stress-strain curve in figure 2.3 (*i.e.* 300 MPa for tensile quasi-static test). The structural modifications created by the laser treatment such as porosities or roughness are located within a depth of 500 nm where the tensile stress generated by the pressure wave propagation is almost zero. The detachment of the surface morphology features observed during laser shocks is not the result of spallation phenomena, it is due to the stress generated by the inertia force rather.

Influence of the grooves

LASAT calibration was performed on flat samples. The question risen in this section concerns the influence of the grooves created by the laser treatment on local acceleration values.

Surface roughness influence on local dynamics was studied in [184]. The distribution of positive and negative maximum local velocities on the rear surface as a function of the radial position, depending on the surface roughness can be seen in figure 4.23.

Compared to a smooth surface, the maximum amplitude of positive and negative simulated velocities increases if the surface is rough. The increase is higher when the spatial period and the peak-to-peak amplitude of the roughness are small: +20 % for 200×100 μm^2 and +39 % for 100×50 μm^2 (with the roughness defined as $a \times b$, where a is the spatial period and b is the peak-to-peak amplitude).

Simulations also show that the maximum velocity can vary locally on the grooved surface: for groove tops it was higher than for groove bottoms.

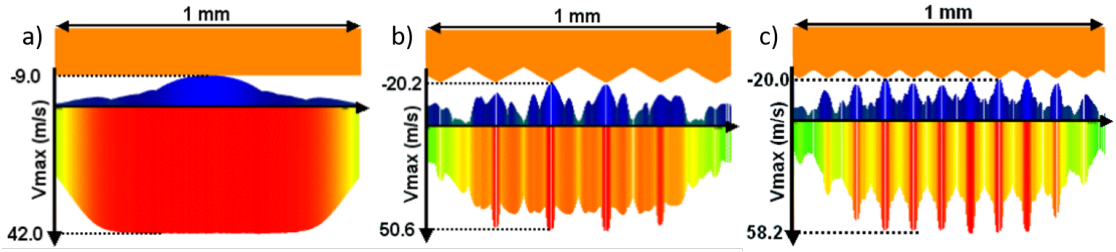

Figure 4.23: Positive and negative maximum local velocities on the rear surface as a function of the radial position, depending on surface roughness, after [184]. Simulations were performed on a smooth surface a), surface with a roughness (noted as $a \times b$, where a is the spatial period and b is the peak-to-peak distance) of 200×100 μm b) and 100×50 μm c) on a 300 μm-thick copper sample with a shock diameter of 1 mm.

Measurements, performed in [184] are shown in figure 4.24. Slight variations of the maximum velocity are measured but can depend on the position of the probe beam of the VISAR compared to the spatial period. More importantly, VISAR measurement did not show sharp differences on average decelerations due to the roughness with respect to the smooth surface, highlighted, in the figure, by the red dotted line, especially is the ratio spatial period to peak-to-peak amplitude is higher than 2.

The roughness observed on the laser treated surface is made of parallel sinusoidal grooves with a spatial period of 50 μm and a 35 μm peak-to-peak amplitude. Although, some differences in term of velocity amplitude are expected between the top and the bottom of the grooves, no difference of the *shape* of the velocity peak are expected depending on the position over the spatial period and comparing to a smooth surface, Therefore, groove influence, in the present study, has to be neglected. Accelerations measured on smooth surface samples and, therefore, inertia force estimation was considered as uniformly applied on the surface of laser-treated samples during laser shocks.

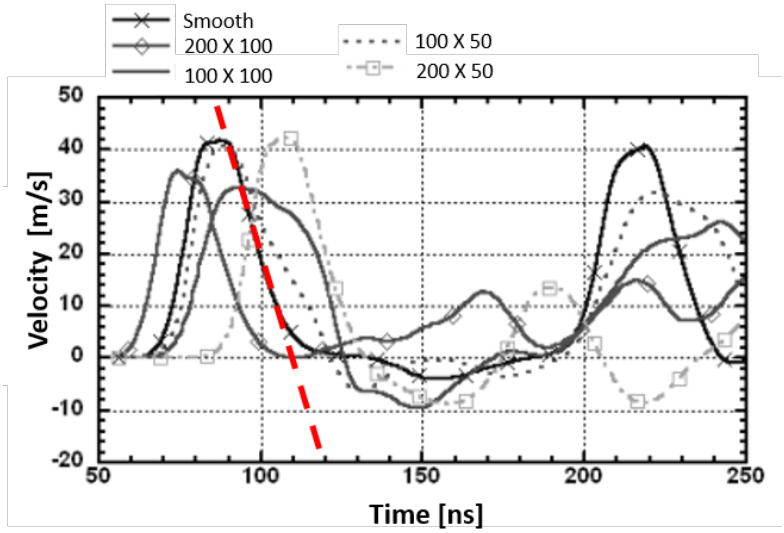

Figure 4.24: Velocities measurement on the rear surface at the center of the target, depending on surface roughness, after [184]. The measure is an average on a 20-μm-diameter area of the VISAR probe beam. Measurements were performed on a smooth surface and on surfaces with a roughness (noted as $a \times b$, where a is the spatial period and b is the peak-to-peak amplitude) of 200 $\times$ 100 μm, focused on the bottom of a groove, and 100 $\times$ 100 μm, 100 $\times$ 50 μm and 200 $\times$ 50 μm, all focused on the top of a groove,

4.2.4 LASAT on laser-treated samples: description of setup and experiments

In the second part of the present chapter, laser shocks applied on laser-treated samples are presented. Particle adhesion was assessed as a function of the intensity of mechanical stresses acting on the surface.

Objectives

The objective was to study the adhesion of copper particles lying on the treated surface when samples were subjected to laser shocks. Both sample surfaces and ejected particles were analyzed by XPS and SEY measurement, and SEM top view imaging. Analysis on sample surfaces after laser shocks, in particular SEY, aimed to determine if physical properties of the surface were modified by particle detachment.

Aims of particle analysis were to assess the number and sizes of particles peeled off from the surface and to determine if the amount of detached particles depended on the applied force, on sample temperature and on sample thermal history (*i.e.* if the thermal dilatation during thermal cycles fragilizes the particles and enhance the detachment).

Test setups

In literature, Photonic Doppler Velocimetry (PDV) technique was developed in [191], where it was used to quantify the number and sizes of particles extracted from the surface after a laser shock. This technique was especially relevant as shocks performed were destructive for the target. In the present study, ejectas were collected on carbon stickers, while in other works, as for example [202], they were collected in a gel, allowing further analysis by tomography.

Collection of ejected particles

Laser shocks were performed on laser-treated samples with the help of a sample holder allowing the collection of detached particles. The experimental set up used for these tests can be seen in figure D.7, in the appendix. An aluminum pin stub of 12 mm diameter was placed in front of the sample and covered with a double-sided adhesive tape to collect detached particles. Such carbon stickers were conductive and allowed analyses with SEM/EDS systems, avoiding electrical charging effects.

Shocks were performed both at room temperature and at cryogenic temperatures. Indeed, in order to evaluate particle adhesion at cryogenic temperatures, samples were cooled to 60 K. The experimental setup is presented in appendix section D.2. Preliminary work validated the use of liquid nitrogen to cool the sample holder and the sample during laser shocks. For samples at cryogenic temperature an acrylic tape was used as confinement medium, instead of water, to avoid icing and alteration of confinement behavior.

High speed imaging

A high speed imaging system has been installed in the LASAT test bench, at CDM Mines ParisTech by Hugo DURAND. This camera was used to study the trajectory of detached particles during laser shock on the laser-treated surface.

The camera settings -1.985 μm pixel size, 4-mm-large frame and 90 KHz acquisition frequency- did not allow to record and track the displacement of single particles, as their size is mostly smaller than 2-μm-diameter. It was, nevertheless, possible to image the cloud created by the detachment of numerous particles. For this reason, laser shocks with high power density were used in this part of the study to enhance to particle detachments.

The results obtained thanks to this tool are shown in section 4.3.3.

Samples, laser shock configuration and corresponding characteristics of mechanical solicitations

The choice of samples and LASAT configurations used for mechanical tests on treated samples, as well as the determination of the corresponding characteristics of mechanical solicitations, took advantage of the calibration already presented in 4.2.2.

The labels of the samples, depending on experimental conditions, are given in the following:

- 1-mm-thick copper samples *D7 2020* after laser treatment;
- *Thermo cycles* samples are *D7* samples which underwent 10 thermal cycles between ambient temperature and 70 K, as described in section 2.2.3;
- *LF* corresponds to samples shocked with the low power density of 1.36 GW.cm^{-2}, leading to an inertia force of 3.5 kN.mm^{-3}. The duration of forces applied on particles was evaluated around 90-100 ns, independently on power densities;
- *HF* corresponds to samples shocked with the high power density of 4.6 GW.cm^{-2}, leading to an inertia force of 8.6 kN.mm^{-3};

- *D7 Ta* indicates D7 2020 samples with the addition of a 50-μm-thick glued tantalum layer, as described in section 4.2.2.1. In this case, with a power density of 1.36 GW.cm^{-2}, inertia force applied on the particles was around 3.5 kN.mm^{-3} and with a slightly higher duration (from 100 ns to 150 ns, typically) when compared to samples without tantalum layer;

- *BS74* samples were extracted from the 2.2-m-long laser-treated beam screen, as described in appendix section C.2. Inertia force generated at 1.4 GW.cm^{-2} was about 20 ns long with an amplitude of 31.9 kN.mm^{-3}.

It is worth noting that mechanical solicitations applied on *D7 2020* and *BS74* samples during the laser shock campaign are not identical in term of amplitude and duration. It did not allow the direct comparison of particle adhesion of surfaces treated in laboratory and *in-situ* based on laser shock extraction technique. More investigations could be seen as a further work to find on the LASAT configuration where the deceleration measured on the 1-mm-thick copper sample is identical than the one measured on colaminated beam screen sample. In particular, high acoustic impedance material could be added on the front surface of *BS74* to enlarge the velocity peak and power density on colaminated could be reduced.

4.3 Analysis of surface properties after mechanical tests

Mechanical loading applied to treated samples, using centrifugation and laser shock techniques, resulted in partial particle detachment. This section will focus on the study of surface properties after mechanical loading. Both sample surfaces and ejected particles were analysed.

4.3.1 Analysis of sample surfaces

Both extraction techniques allowed the analysis of treated surfaces after mechanical solicitations, although a part of the surface was damaged by the sample holder (see figure 4.25). It must be also noted that all samples had to be handled, packed and shipped at CERN for analyses and this might have altered their surface properties.

As a general remark, differences observed when comparing SEY, XPS and SEM top views of centrifuged samples and a treated sample which did not undergo mechanical solicitation were so little that they could not be attributed undoubtedly to the detachment of particles under a static force of 12 N.mm^{-3}.

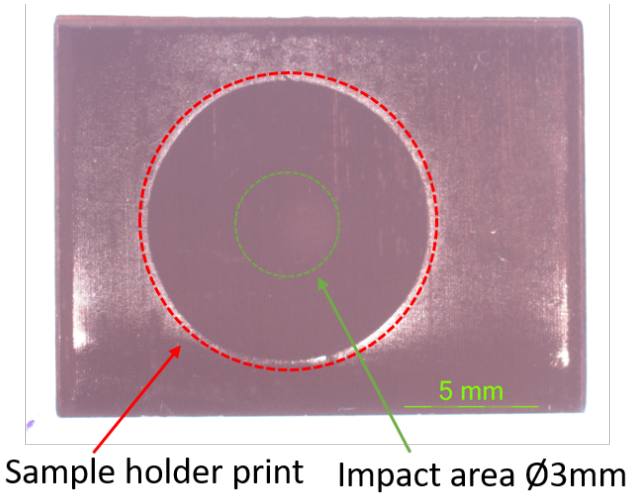

Figure 4.25: Top view picture of a treated surface after laser shock. Outside of the red dotted circle, the surface was damaged by the sample holder. Laser shock related phenomena affected only the part of surface inside the green dotted circle.

Analysis on sample surfaces after laser shocks brought more information. In this case, more particles could be detached and, moreover, on each sample the presence of areas unaffected by mechanical loadings (those outside the shock diameter and inside the sample holder diameter, as illustrated in figure 4.25) allowed a direct comparison and evaluation of shock effects.

Three analyses were performed on samples after mechanical solicitation: SEM, XPS and SEY. SEY measurements are discussed in section 5.3.2.2 and are directly linked with the performance of the surface in the accelerator environment.

Morphology analysis via SEM observations

Top view SEM analysis was performed on a *D7 2020* sample submitted to a laser shock, at room temperature and high power density (4.6 GW.cm^{-2}). In figure 4.26, images taken from two areas are compared: on the left, the zone was not affected by the laser shock while, on the right, shock induced inertia force was maximal (8.6 kN.mm^{-3}). Slightly less particles are visible on the surface affected by the mechanical solicitations, in particular on the top of the grooves.

An image post-treatment was developed to quantify particle detachment. It was based on the measurement of areas on the groove top, which is not covered by particles even in non-shocked zones. Three 150-μm-long segments of groove tops were randomly selected on SEM images of both areas. The surface uncovered by particles was measured using ImageJ software on each selected groove, as illustrated in yellow on figure 4.26 b). On average, the uncovered surface increased from 607 μm^2 for non-shocked areas to 730 μm^2 for shocked zones, corresponding to a 20 % increase.

The effect of the slight change of surface topology on the SEY are presented in the chapter dedicated to the use of the surface as mitigation technique of electron cloud in accelerators (see section 5.3.2.2).

To conclude, particle density on the sample surface after mechanical solicitations

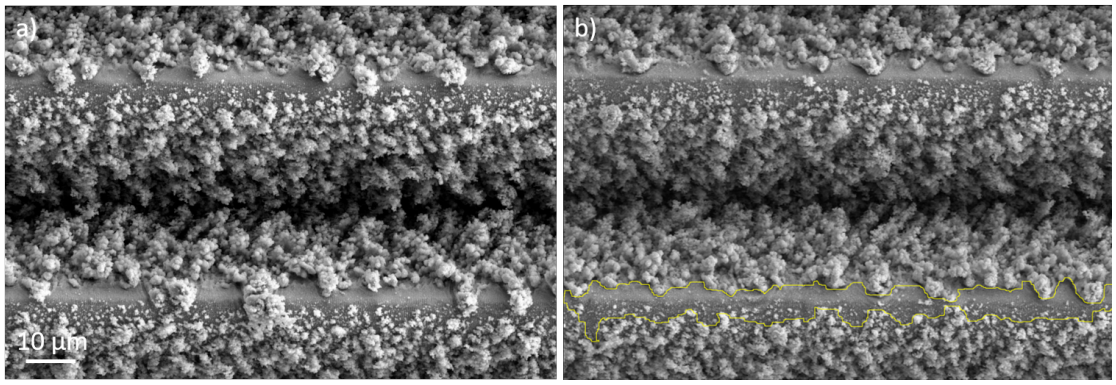

Figure 4.26: SEM top views of the treated surface a) in an area non affected by the laser shock, b) in an area affected by the laser shock (corresponding inertia force of 8.6 kN.mm^{-3}). The yellow line highlights an uncovered area on the groove top.

remained too important to be quantified by SEM top views. That motivated the analysis of extracted particles in order to achieve a quantitative comparison of the applied mechanical stresses on the particle detachment, as presented in section 4.3.2.

Chemical analysis by XPS

XPS analysis was tentatively applied to a *D7 2020* sample submitted to a laser shock at room temperature and high power density (4.6 GW.cm^{-2}).

Based on XPS spectra analysis the copper oxidation states I and II, were interpreted as Cu_2O and $Cu(OH)_2$, respectively (from Martino RIMOLDI, CERN TE-VSC, in private communication).

CuO measured by TEM (see section 3.2) was not observed on XPS (from Martino RIMOLDI, CERN TE-VSC, in private communication). It could be explained by the fact that the particles surrounded by CuO were located in the bottom of the grooves, maybe covered by other particles and were not accessible for XPS measurement, which is limited to a depth of 5 nm, typically.

The $Cu(OH)_2$, in amorphous phase, could not be observed an TEM, a layer may be formed around the surface structures due to air exposure.

XPS measurement performed on the *D7 2020*, comparing areas submitted or not to laser shock, are shown in 4.27.

Small but detectable variations in copper oxidation state were measured on the rear surface of laser shocked *D7 2020* samples and are presented in 4.27 b). In particular, XPS profiles allowed to quantify the $Cu(I)/Cu(II)$ ratio, revealing a decrease in $Cu(II)$ amount relative to $Cu(I)$ when moving from the center to the edge of the sample. This same trend was followed by SEY values, as further discussed in section 5.3.2.2.

These changes in copper oxidation states could not be attributed to a thermal effect. In fact, heat deposition due to laser shock on a 1-mm-thick copper sample could not generate a significant temperature increase on the opposite face of the sample. This was shown in [203], where temperature evolution was given as a function of shock pressure for copper. Considering pressure profiles shown in figure 4.22, pressure loading did not exceed 4 GPa during all the experimental campaigns, so that the temperature at the

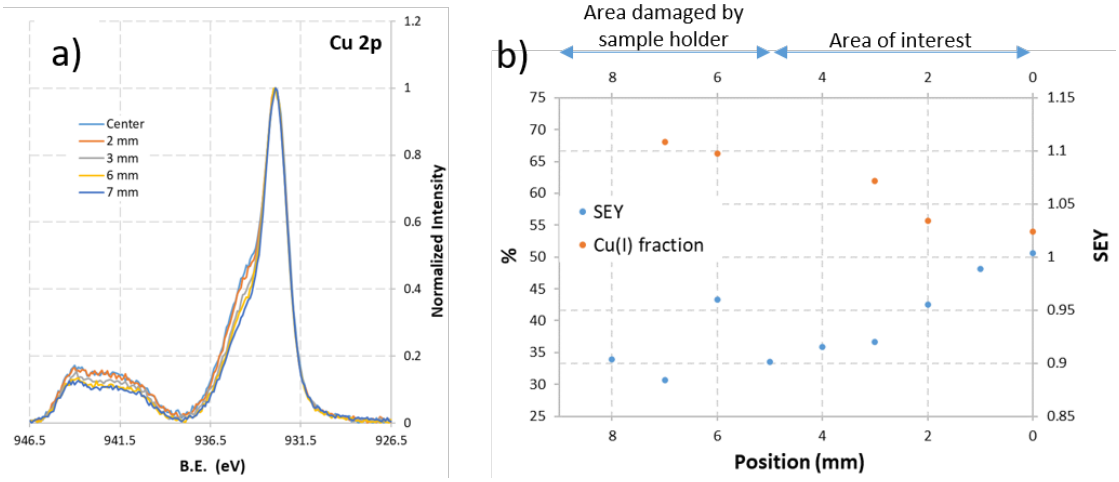

Figure 4.27: a) XPS profile focused on the range of binding energies (noted *B.E.*) between 946.5 and 926.5 measured at different distances from the center of the laser beam spot. b) Corresponding SEY (blue dots) and $Cu(I)$ fraction (red dots), Figure from Martino RIMOLDI, CERN TE-VSC, in private communication.

free surface should not have exceeded 300 K. This small temperature increase could not explain local changes in the oxidation state of the surface.

The slight oxidation change it might have been the result of local particle detachment. TEM analysis (see section 3.2) revealed an inhomogenous oxide distribution on the surface of the treated sample, at the groove scale. In particular, copper particles attached on groove tops are surrounded by a Cu_2O layer, while particles observed at groove bottoms present a CuO layer. The decrease of the Cu_2O to $Cu(OH)_2$ ratio, observed by XPS measurement could, then, be explained by a particle detachment, in particular particles from the top of the groove tops.

To conclude, although not very pronounced, the changes detected by XPS analysis, might be attributed to mechanical solicitations on sample surfaces. In any case, only minor changes could be detected, XPS measure can not bring further insights on characterisation of the surface after mechanical solicitation.

4.3.2 Analysis of ejected particles

This sections presents the analysis of detached particles that were collected on carbon stickers during mechanical solicitations of treated samples, based on two extraction techniques, laser shocks and centrifugation.

The aims of this analysis were to assess the size and the number of detached particles, in order to

- compare the two extraction techniques and assess the effects of amplitude and duration of applied forces on particle detachment;
- assess the effects of initial surface topography, temperature and sample thermal history (*i.e.* if it has been submitted to thermal cycles) on particle detachment.

Presentation of APA results

Automated Particle Analysis (APA) was carried out, as described in section 2.3.4. A list of 10 000 particles with their Equivalent Circular Diameter (ECD) was established, as well as the surface area to be analysed to reach this quantity. Detached particles density could then be calculated. The mass of each particle was calculated based on its ECD, assuming spherical shape and pure copper density. The total mass of detached particles was deducted.

APA results were displayed by two graphs:

- size distribution graphs (as, for instance, figure 4.28 b)) highlight differences for the detachment of particles smaller than 6 μm in ECD. It is worth noting that particles smaller than 1 μm were not taken into account by APA;
- cumulated detached particle mass (as, for instance, figure 4.28 a)), representing the cumulative mass distribution of detached particles per unit area. For a given ECD, the mass of all detached particles smaller than this value is given. Such graphical representation emphasizes the contribution of large particles to the total mass detached, despite their small number.

On average for these tests, only 0.1 %, in number, of the detached particles were larger than 6 μm. Although their small number, bigger particles may have a more detrimental effects on accelerator operation. Therefore, both the distribution and cumulative mass graphs were used to describe the full size spectrum of particles, as they bring complementary information to the study.

Comparison of extraction techniques

Plane D7 2020 samples

Figure 4.28 compares results of detached particle mass and number, obtained for identical samples *D7 2020* when submitted, at room temperature, to the following mechanical solicitations:

- low power density laser shock, generating 90-ns-long forces of 4.6 kN.mm^{-3};
- high power density laser shock, generating 90-ns-long forces of 8.6 kN.mm^{-3};
- low power density laser shock with high impedance layer (labelled LF Ta), generating 150-ns-long forces of 8.6 kN.mm^{-3};
- 40000 RPM centrifugation, generating a static load of 12 N.mm^{-3}.

The total amount of detached particle is 66 times higher for high power density laser shocks than for centrifugated samples. Using laser shocks, the amount of detached particles can be modified either by increasing the amplitude of the force applied on particles by changing the power density, or by increasing force duration, adding a high acoustic impedance layer.

It is worth noting that size distributions of collected particles were different depending on the kind of mechanical solicitation. In particular, the distribution curve was much

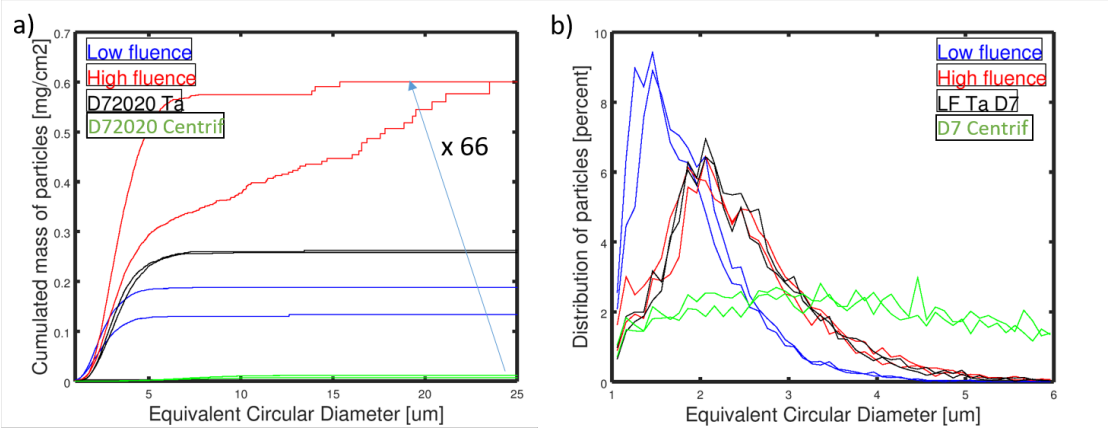

Figure 4.28: Comparison of extraction techniques applied to *D7 2020* samples at room temperature. a) Cumulated mass per square centimeter, b) Particle size distribution.

broader for static loads than for laser shocks. Moreover, for laser shocks, a longer duration or a larger amplitude of generated inertia forces could move the size distribution towards larger ECD. This point is further discussed below, in the *Discussion* paragraph.

Beam screen samples

Figure 4.29 compares the results obtained for identical *BS74* samples submitted to the following extraction techniques, at room temperature:

- low power density laser shock, generating 20-ns-long inertia force of 31.9 kN.mm^{-3};
- 40000 RPM centrifugation, generating a static load of 12 N.mm^{-3};

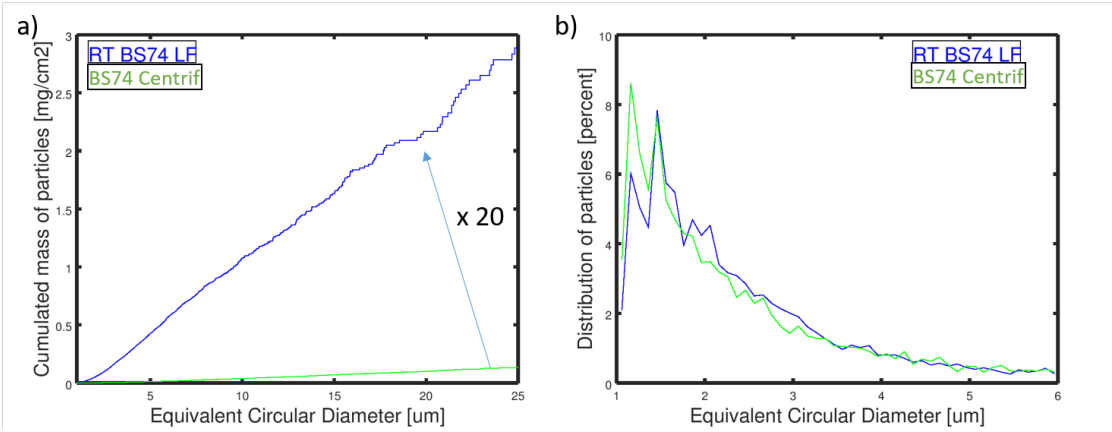

Figure 4.29: Comparison of extraction techniques applied to *BS74* samples, at room temperature. a) Cumulated mass per square centimeter, b) Particle size distribution.

The same trend previously observed for *D7 2020* samples was measured for *BS74* samples. In particular, the total detached mass was 20 times higher for low power density laser shocks than for centrifugation. However, no significant difference could be noticed in size distribution between the two extraction techniques.

To conclude, a large range of particle detachments can be obtained applying different extraction techniques. Due to the higher magnitude of forces applied on particles, laser

shock could detach significantly more particles than centrifugation. The number of detached particles could be modified changing laser shock parameters, as the power density or the presence of a high impedance layer.

Sample comparison

Three series of samples, all treated with the same set of laser parameters (*D7*) were compared: plane copper samples *D7 2019* and *D7 2020* and samples extracted from the 2.2-m-long beam screen, *BS74*.

Despite identical laser parameters applied during the treatment, the surface morphology of these samples looked slightly different, as illustrated in figure 3.44. More particles were present on *D7 2019* and *BS74*. This has been confirmed by particle mass density measurements performed by ultrasonic cleaning, in section 3.4.2.1, and qualitative surface observation by SEM, in section 3.4.1.

In figure 4.30, cumulated mass per unit surface and particle size distribution for these samples are compared, after centrifugation (static force of 12 N.mm^{-3}).

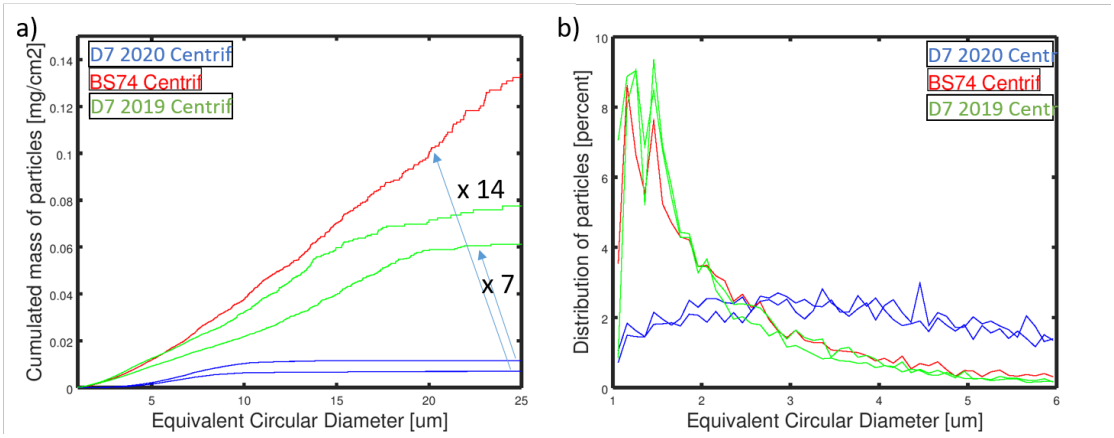

Figure 4.30: a) Cumulated detached mass per square centimeter and b) particle size distribution, after centrifugation on different samples (*D7 2019*), *D7 2020* (*BS74*).

More particles were extracted from *D7 2019* samples than for *D7 2020* samples.

The amount of particles extracted out of *BS74* beam screen samples is 14 times higher than the amount extracted on plan sample. That difference should be mainly explained by the presence of the large foamy particles observed by SEM on the top of the surface before the mechanical characterisation, those weight is overestimated by the analysis based on APA of the detached particles after centrifugation or laser shocks.

Conclusions

To conclude, under a same mechanical solicitation -here a static force of 12 N.mm^{-3}-, the amount and the size distribution of detached particles was different,

Extraction techniques can be used to quantify this adhesion and compare samples with different surface morphologies.

Influence of cryogenic temperatures

In real life operation in the accelerator environment, laser treated beam screens would be submitted to temperatures down to 5 K and, moreover, would undergo several thermal

cycles from room temperature to cryogenic temperature before installation in the LHC and during maintenance operations on the magnet. As a consequence, it is important to assess if cryogenic temperatures could affect particle adhesion on treated surfaces. This was possible thanks to the use of sample which have underwent thermal cycles before the mechanical characterisation and the possibility to cool down the sample temperature during the laser shocks.

Influence of thermal cycles

Particle extraction techniques previously described were applied to thermally cycled *D7* samples. Figure 4.31 compares cumulated detached masses and particle size distributions for *D7* samples with and without thermal cycles. Both centrifugation and laser shock at high and low power densities were applied. Independently of the extraction technique chosen, the total amount of detached particles was significantly higher for samples that underwent thermal cycles.

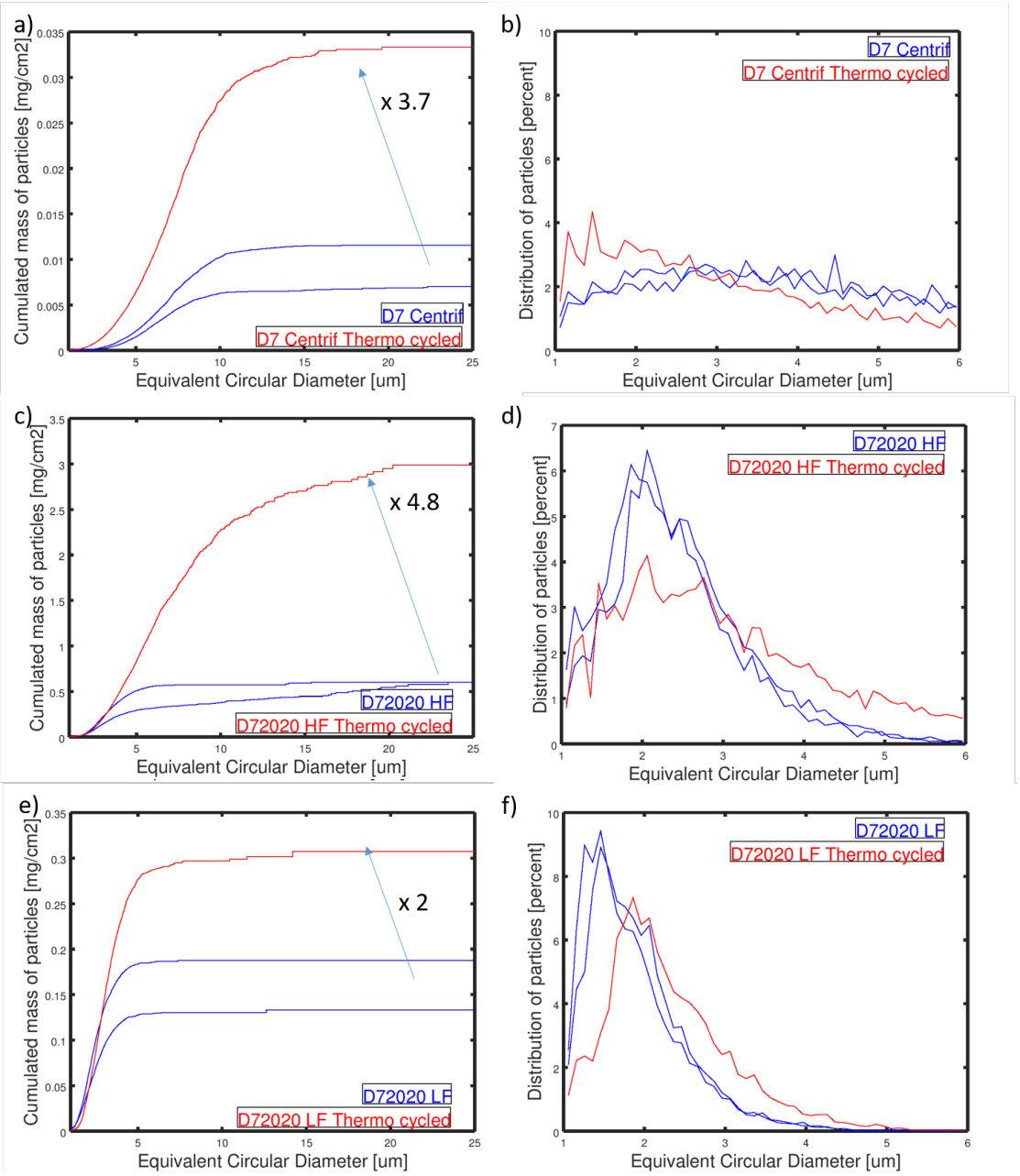

Figure 4.31: Influence of thermal cycles performed on *D7 2020* samples. Cumulated detached mass per square centimeter (first column) and size distribution (second column) are shown for samples submitted to 40 000 RPM centrifugation (first line), high power density laser shock (second line) and low power density laser shock (third line).

Influence of sample temperature during shocks

Laser shock experiments could be performed at cryogenic temperature, aiming to assess the effect of sample temperature on particle detachment. In figure 4.32 and 4.33, results for *D7* and *BS74* samples, respectively, compare the characteristics of detached particles for low power density laser shocks at Room Temperature (RT) and at cryogenic temperature (70 K).

The analysis based on the OFE copper material properties, in section 2.1.2, showed a larger energy would be absorbed by the particle-surface bond before the fracture at cryogenic temperature than at room temperature. Nevertheless, the experimental campaign showed a larger amount of detached particles during the mechanical solicitations at low temperature.

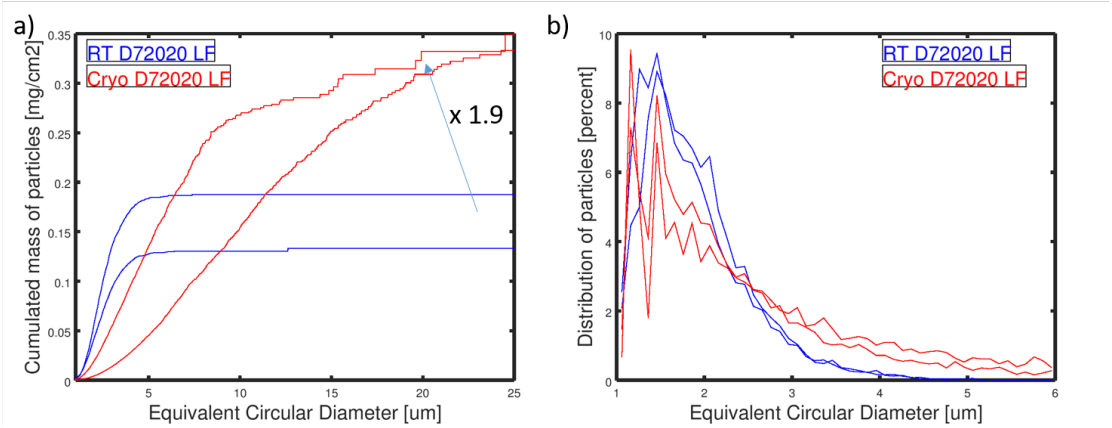

Figure 4.32: Influence of sample temperature during laser shock at low power density for *D7 2020*, comparing results at room temperature (RT) and at 70 K (Cryo). a) Cumulated detached mass per square centimeter. b) Particle size distribution.

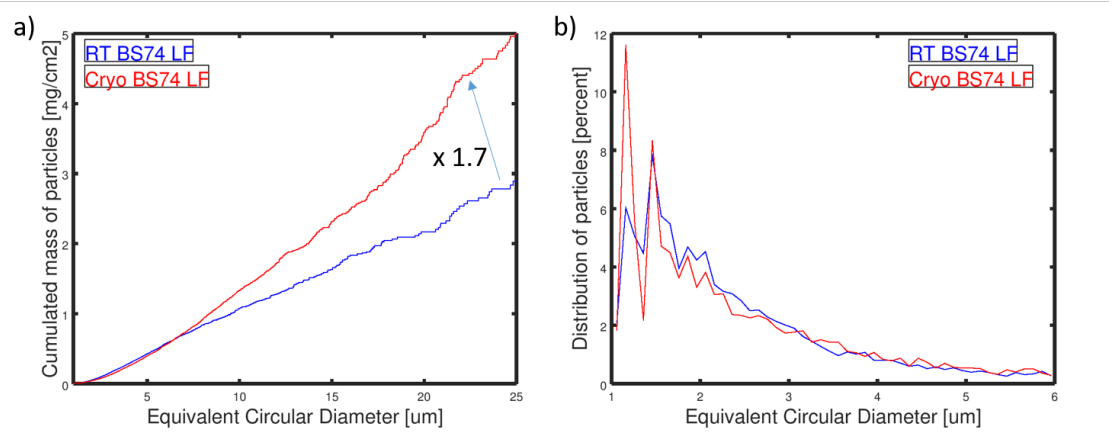

Figure 4.33: Influence of sample temperature during laser shock at low power density for *BS74* samples, comparing results at room temperature (RT) and at 70 K (Cryo). a) Cumulated detached mass per square centimeter. b) Size distribution.

Conclusions

To conclude, the effect of temperature (both thermal cycles on samples and actual sample temperature during laser shock) was notable.

Effects of sample temperature were studied using laser shocks at low power density. Results show a significant increase of detached particle amount. Temperature effects should be taken into account in future tests. As a rule of thumb, a factor of 2 on the total detached particle mass, can be applied on results obtained at room temperature to extrapolate at cryogenic temperatures.

The effects of thermal cycles were notable with all extraction techniques. The total amount of particle detached was systematically higher for samples previously submitted to thermal cycles. The size distribution of detached particles was shifted toward larger diameters. The effect of thermal cycles should be taken into account in future tests. As a rule of thumb, a factor of 5 can be applied on results obtained on non-thermally-cycled samples to extrapolate for thermally cycled samples.

Copper material characteristics, presented in section 2.1.2, showed that, at cryogenic temperature, the energy required for particle-surface bond rupture is higher than at room temperature. Nevertheless, microscopic analysis of the surface and of particle-surface connections, presented in section 3.2, highlighted the presence of a thick nano-crystallised oxide layer. The difference in dilation expansion coefficient of OFE copper and copper oxide may explain the detrimental effect of cryogenic temperatures (both thermal cycles and actual sample temperature) on particle adhesion, as highlighted in this work. In fact, the difference in thermal expansions and contractions at low temperature may have raised internal stresses close to particle-surface interfaces and fragilize their bond. As the same phenomena are suspected to cause the increased detachment on both thermally cycled samples and cooled samples, the two effects are not expected to be cumulative. That means that a factor of 5 should be applied on the results obtained for non-thermo-cycled samples solicited at room temperature to extrapolate the detachment of a thermo-cycled surface at cryogenic temperatures. To prove this hypothesis, laser shock tests at cryogenic temperatures on thermally cycled samples should be performed in the future.

Discussion

Comparison of detached mass and particle surface coverage

As already explained, cumulated mass was calculated, based on volume estimation from SEM image processing, to quantify the amount of detached particles in each test configuration, in order to compare samples and extraction techniques.

Although some exceptions may be noted and are not fully understood (*cryo D7 2020 LF*, *RT D7 2020 HF*), only a very small number of particles larger than 10 μm could be extracted from planar samples. This can be explained by the fact that their number, originally present on the surface is low, as observed from SEM top views (see section 3.4.1) and characterized by APA after US cleaning (see 3.4.2.2). Less than 5 % of the detached particles had a ECD larger than 5 μm.

Important differences were observed between planar samples and those extracted from the 2.2-m-long beam screen. The latter underwent a different *in-situ* laser treatment in a confined environment, as explained in section 3.5. This is probably the origin for the different surface features observed. In particular, *BS74* samples were covered by large foamy structures, which are not visible on planar samples treated in laboratory (see figure 3.57). A low mass density was assumed for these structures, based on their SEM observation.

During mechanical characterisation, foamy structures were collected and were detected by APA. They have been wrongly taken into account in the estimation of cumulated mass of detached particles applying the same method than those applied for dense

spherical particles, *i.e.* using the copper density to calculate the mass of the particle based on the volume estimated by SEM. This led to a large overestimation of detached mass for *BS74* samples.

On a more general perspective, particle porosity of large detached particles was not taken into account in the calculation of cumulated detached mass. Therefore, the detached mass might be significantly overestimated as discussed in section 2.3.4.

Nevertheless, the detached mass under centrifugation can be compared to the mass of the particles originally present on the sample surface estimated after ultrasonic cleaning of *D7* samples, as shown in table 4.3.

Table 4.3: Comparison of masses of particles extracted by US cleaning and by centrifugation with inertia force of 12 N.mm^{-3}, in [mg.cm^{-2}].

Sample	*D7 2019*	*BS74*	*D7 2020*
US cleaning	2.6	0.62	1
Centrifugation	0.07	0.13	0.009
Percentage	2.69%	20.97%	0.90%

Mass of detached particles was not proportional to the one originally present on the surface. It may mean that not only the number of particle were different but also the way the particles are connected to the surface.

The specific case of *BS74* sample has already been discussed above.

Concerning *D7 2020* and *D7 2019* planar samples, which present similar surface structures before the mechanical solicitations (*i.e.* no foamy structure), the differences highlighted in table 4.3 are more likely due to differences in particle adhesion. The same mechanical solicitation tended to detach more particles from *D7 2020* samples than from *D7 2019* ones. This can be interpreted as a reduced particle adhesion for *D7 2020* samples, probably due to a different gas environment during laser treatments.

Size distribution for particles smaller than 6 μm

Size distribution of particles detached by ultrasonic cleaning, was determined by APA as presented in section 3.4.2.2. This could be fit by the function $\alpha_0\, exp(\frac{-ECD}{1.2})$, where ECD is particle equivalent circular diameter. Despite the agglomeration or segmentation phenomenon, which may occur by the cleaning process, it gives an idea of what could be the size distribution of particles present on the treated surface.

Comparing the size distribution of the extracted particles during mechanical solicitation may bring insights on the particle adhesion depending on the particle size.

The following three considerations have to be taken into account when investigating particle adhesion, assuming they have spherical shapes:

- the applied mechanical solicitation being a force density, it scales with particle volume, *i.e.* with the cube of the diameter D^3;
- particle-surface bond is expected to be proportional to their contact area, which scales approximately with the square of the diameter D^2;

- during particle re-deposition, solidification time is expected to increase proportionally with particle diameter D (see figure 3.7). If the solidification is more advanced when they are re-deposited to the surface, smaller particles are less strongly connected to the surface, and, therefore, they might be more likely to be detached under mechanical solicitations.

These assumptions may suggest that particle detachment is relatively independent on particle size.

Although, the decay constant was smaller (identified around 0.7), at low power density, the size distribution was close to the exponential distribution determined by US, confirming above assumptions.

On the contrary, for high power density shocks, particle size distribution was consistently different, in particular for particles smaller than 2 μm. The shape of the curve might more suggest $\alpha_1 ECDe^{\frac{-ECD}{1.2}}$ or $\alpha_2 ECD^2 e^{\frac{-ECD}{1.2}}$. That difference is not understood but might highlights non linear phenomena on the dimensions of the contact region between the particles and the surface or on the adhesion properties depending on the solidification of the particles when they are redeposited on the surface.

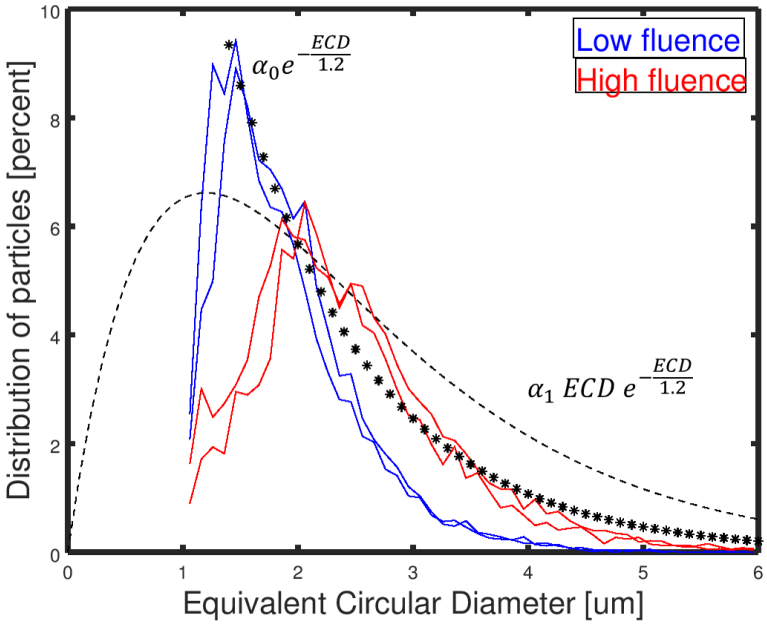

Figure 4.34: Size distribution of detached particles during laser shocks at low and high power densities. $\alpha_0 e^{\frac{-ECD}{1.2}}$, $\alpha_1 ECDe^{\frac{-ECD}{1.2}}$ curves are plotted for comparison.

4.3.3 Analysis based on ejected particle velocity

This section presents the analysis of trajectory and velocity of the detached particles recorded by high speed imaging system during laser shock experiments on treated samples. The aim of this analysis was the evaluation of energy dissipated in particle-surface

bond fracture evaluated as the difference of kinetic energy of the particle when it is attached on the surface and after the detachment.

Laser shock set up delivered a power density of 4.76 GW.cm^{-2} irradiating 1-mm-thick copper samples.

In this configuration, the maximum rear surface velocity was measured at 68 m.s^{-1} during calibration experiments, as reported in section 4.2.2. It is assumed to be the velocity of the particle before its detachment.

The velocity of the particles after the detachment is based on sequential pictures of the expansion of a particle cloud ejected from a *D7 2020* sample, presented in figure 4.35 a). The cloud front position was tracked on each frame. Knowing the time interval between successive frames, it was possible, then, to estimate cloud velocity.

Cloud displacements as a function of time are shown in figure 4.35 b) for three identical samples. The average value of cloud velocity could be estimated to be 1.5 m.s^{-1}.

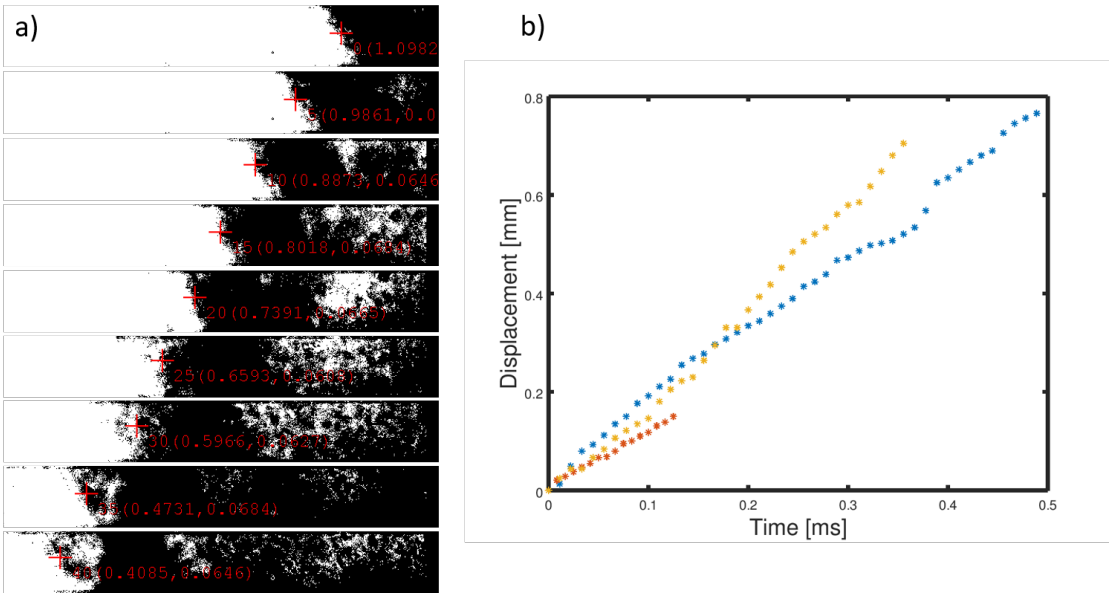

Figure 4.35: a) Pictures extracted from high speed imaging system recording particle detachment during high power density laser shock on a *D7 2020* sample. The position of particle cloud front was tracked (red crosses). b) Curves of particle cloud displacements as a function of time, for three *D7 2020* samples.

As shown in figure 4.34, most of the detached particles had an ECD of 2 μm. Considering copper density, the mass of an average particle could be calculated. Together with velocity measurements, this allowed the estimation of energy dissipated during the bond break, as the difference between particle kinetic energies, when they were attached on the free surface (same speed as the surface) and when they were flying, after their detachment. The calculation is presented in equation 4.15 below:

$$E_{Fract} = \frac{1}{2} m_{Part} \left({v_i}^2 - {v_f}^2 \right) = 8.7 \times 10^{-11} J \tag{4.15}$$

where E_{Fract} is the energy dissipated during bond break, m_{Part} is the average particle mass, v_i is particle velocity before its detachment (equal to rear surface velocity), v_f is flying particle velocity measured by high speed imaging system.

The order of magnitude of dissipated energy is consistent with the estimation based on material properties, as evaluated in chapter 2. This value was further used as an input in simulations of the cascading effect in particle detachment, presented in section 5.2. Other experiments can be performed with the high speed imaging system, to evaluate the energy dissipation as a function of treatment parameters or of thermal and mechanical history of samples. This was not possible during the present work, but can be suggested for a further work.

4.4 Conclusions on mechanical tests for particle adhesion

During accelerator operation, the beam screen can be subjected to high electro-magnetic forces which could compromise the mechanical integrity of treated surfaces. These phenomena and their consequences for treated surfaces are further detailed in section 5.1. Nevertheless, an estimation of the acceleration range of interest for the application can be anticipated here. Accelerations leading to inertia force equivalent to those expected during a magnetic quench (around 30 N.mm^{-3}) are in the range of 350 000 g.

The objective of mechanical tests applied to laser-treated surfaces was to assess particle adhesion. The main achievements of this chapter can be summarized as follows:

- development of reproducible techniques based on non-contact forces to extract particles out of treated surfaces;
- quantification of the amount of detached particles, in order to:
  - compare samples;
  - estimate the quantity of particles detached during a quench.

Both static centrifugation and dynamic laser shock techniques -allowing to reach high accelerations in a short duration- have advantages and drawbacks which are summarized in table 4.4. The two developed methods can be considered as complementary. The amplitude and the duration of the force applied on particles varied on a large range of values, depending on the extraction technique used. The influence of cryogenic temperatures was evaluated in two testing configurations: ambient temperature laser shocks on samples which underwent thermal cooling/warming cycles and laser shocks at cryogenic temperatures.

The development of other extraction techniques could be considered. Preliminary measurement on a drop-test setup at Novelis company (Sierre, Switzerland), showed that mechanical test could generate forces in the order of 0.1 N.mm^{-3} with a duration of 300 μs. This duration range has not been explored by the two techniques developed in the present study. Nevertheless, due to the low force magnitude, it has been decided not to investigate further drop test techniques. Although electromagnetic forces could

Table 4.4: Advantages and drawbacks of extraction techniques developed for particle adhesion study on laser-treated surface, in particular concerning its application in vacuum systems of particle accelerators.

Centrifugation	Laser shocks
Advantages	
Allows the collection of ejected material and sample surface analysis after mechanical solicitation	Allows the collection of ejected material and sample surface analysis after mechanical solicitation
Precise, repeatable and adjustable amplitude of applied forces based on the rotational speed of the centrifuge	Diverted use of a setup dedicated to research on coating adhesion, available at several research centers
Force orientation compared to sample macroscopic surface can be chosen by modifying sample holder geometry	Allows test at cryogenic temperatures
Applied static forces are in the same order of magnitude as forces during a quench	Precise definition of the solicited area, allowing precise analysis of sample surface
Compare the surface of planar copper samples treated in laboratory with beam screen samples	Allows the detachment of a large number of particles to study the effects on a larger range of surface modifications
Allows multiple loading cycles	Many parameters (e.g. sample thickness, laser duration and power density) can be adjusted to achieve different mechanical solicitations
Drawbacks	
Unconventional use of an expensive (74000 CHF based on the quote established in 2019 by Beckman Coulter) equipment not available at CERN	Inertia forces higher than forces generated during magnetic quench (116 times higher in the tested configuration)
Does not allow test at cryogenic temperatures	Calibration based on VISAR measurement and simulations needed to identify mechanical solicitation characteristics
Maximum amplitude of applied force limited by the maximum rotational speed of centrifuge and rotor (70 000 RPM at Geneva University)	

have been an interesting way to apply non-contact forces on particles, this option has not been considered in this work. In fact, preliminary calculations on electrostatic interaction showed that a too high electric field would be necessary to achieve forces in the range of

interest for the application.

Quantification of ejected material was based on particle counting. It was shown that detached material mass could have been overestimated due to particle porosity, which was not taken into account. Nevertheless, this method allowed the quantification of the effects of mechanical solicitation characteristics and surface morphologies. The APA has to be associated with SEM top view observations of the surface before the mechanical characterisation to detect the presence of large foamy structures, which have to be taken into account to relativise the contribution of large particles in the detached mass extrapolated from the APA.

Three step were necessary for particle coverage analysis on laser treated surfaces:

- SEM observations, to identify foamy structures;
- US cleaning, to quantify the mass of particle overlays;
- mechanical tests, to evaluate particle adhesion based on APA of the detached particles.

Estimation of detached particle amounts during a quench

The mass of detached particles during a quench could be extrapolated based on measurements after centrifugation. For *D7 2019* samples, 0.01 mg.cm^{-2} were detached when applying a 24 N.mm^{-3} static force on the surface. After applying a factor of 5 to take into account thermal cycle effects experienced by the surface in the accelerator, that led to an extrapolated amount of 0.05 mg.cm^{-2}. When scaled to the total beam screen surface in a magnet, the amount of detached particle during a quench could be estimated in the order of 1 g (see table 5.3).

This dust lying on the beam screen could be exposed to ionizing radiation from the proton beam circulating in the accelerator (18 mm away at the minimum distance). The dust is volatile and can be spread during the venting of the vacuum system. The large amount of material, exhibited after he mechanical characterisation of the surface, opens radio-protection issues which will require heavy protective measures for maintenance operations of the vacuum system in the vicinity of the laser treated beam screens.

Chapter 5

Laser-treated surfaces in the accelerator environment

Abstract

The chapter explores some additional constraints of the implementation of laser-assisted surface treatments in particle accelerators: the particle detachment when the beam screen is subjected to mechanical stresses during the operation, in particular, the forces induced by a fast decrease of the surrounding magnetic field, the interaction of copper particles detached from the treated surface with the proton beam and, finally, the consequences on SEY of variations in particle coverage density on treated surfaces.

The most detrimental mechanical solicitation on treated surfaces during accelerator operation could be the electromagnetic forces induced in the copper layer during a magnet *quench*, *i.e.* the fast transition from superconducting to normal state of the magnet.

The fast decay of the magnetic field generates large eddy currents and Lorentz forces which act on beam screen copper layer. Based on analytical models and thermo-electromagnetic mechanical simulations, mechanical stresses during the quench (of the order of 30 N/mm^3) and dynamic solicitations of the beam screen walls were evaluated. Simulations also allowed to quantify the influence of surface topology, which concentrates the induced currents in the bottom of the grooves. It showed that the denser micrometric network formed by the particle overlay is, the better flow the induced currents through the structures.

Particle extraction techniques presented in chapter 4 aimed at submitting the treated surface to forces in the range of those estimated during a quench by simulations.

The possibility that certain particles, elements of the surface topology, detach, fall into the beam trajectory and interact with proton beams is a major concern for the use of laser surface structuration in particle accelerators. The effects of the detachment of a copper particle from the surface during the operation of the accelerator and of its interaction with the beam were evaluated depending on the size of the incident particle.

If the diameter of the particles falling into the beam is larger than 20 μm, inelastic

collisions between the particle and the proton beam could cause sufficient beam losses and trigger a beam dump. Based on the particle size distribution on treated surface, this event seems unlikely since particle diameters are mainly distributed around 1 μm.

Without causing beam losses prejudicial for accelerator reliability, copper particles of diameters smaller than 20 μm still interact with the proton beam: as they become electrically charged, and are subjected to forces due to the electric field generated by the beam. Their trajectory is deflected, they are rejected out of beam trajectory and hit the beam screen wall. Simulations of particle dynamics interacting with the beam give the speed and position of the particle upon impact with the wall. The kinetic energy of particles striking the beam screen surface was estimated between 10^{-11} J and 10^{-10} J, which is in the energy range required to break the mechanical bond between the particles and the surface (see section 2.1.2).

Scenarios of particle detachment after collision of an incident particle have been considered (the detached particles are called *secondaries*), as well as the cascading detachment of particles after successive collisions. The size-velocity distribution at each *generation* of released particles was evaluated from a simplified model of impact. It was shown that, under the model assumptions, for 1 initial particle falling and interacting with the beam, only 0.31 detached secondary particles would interact with the beam. It turns out that a chain reaction is very unlikely.

Finally, an experimental study demonstrated the influence on SEY of the characteristics of two-scales topology features created by laser structuration: the groove depth/width ratio and the mass of the particle overlay redeposited on the sinusoidal surface.

Morphological features are governed by laser treatment parameters such as pulse energy, repetition rate, scanning speed and hatch distance, as presented in chapter 3. SEY has been measured on samples treated by 160 combinations of laser treatment input variables.

The contribution of the groove-scale morphology modification was identified by measuring the SEY of a treated surface after particle removal by ultrasonic cleaning. The SEY decreased when the groove depth/width ratio increased. This study also revealed that surface structuration at particle-scale is necessary to reach a SEY close to 1 and a groove depth lower than 30 μm, in other word to obtain a SEY below the threshold for creating the electron cloud while limiting the depth of the grooves to the requirements related to the impedance. Large variations of surface particle density, for instance generated by a cleaning treatment, might strongly degrade SEY reduction performances of treated surfaces.

Nevertheless, conditioning (*i.e.* SEY reduction when the surface undergoes electron bombardment during a dedicated phase of the accelerator pre-operation) was shown to be very effective on laser-treated surfaces, including those with low particle density and therefore the initial SEY greater than the target value. A SEY below the electron cloud creation threshold is obtained after a dose of 7×10^{-5} C.mm^{-2}.

Measurements on treated surfaces, whose particle density has been reduced after

mechanical stresses close to that foreseen during a *quench* did not show a detrimental increase in SEY, it did not deteriorate the electron cloud mitigation function of the treated surface.

Résumé en français

Le chapitre explore certains aspects de l'implémentation du traitement laser *in-situ* des surfaces pour l'accélérateur de particules. En particulier, il sera étudié le détachement des particules lorsque l'écran de faisceau est soumis à des sollicitations mécaniques, comme celles induites par la décroissance rapide du champ magnétique environnant, ainsi que l'interaction entre le faisceau de protons et les particules de cuivre se détachant de la surface traitée pendant l'opération de l'accélérateur et, enfin, les conséquences sur le SEY des variations de densité de particules couvrant la surface.

Les sollicitations mécaniques sur la surface traitée les plus préjudiciables pendant l'opération de l'accélérateur pourraient être les forces électromagnétiques induites dans le cuivre pendant le *quench*, *i.e.* la transition rapide de l'état supraconducteur à l'état normal de l'aimant. La décroissance rapide du champ magnétique génère d'importants courants de Foucault et des forces de Laplace qui agissent sur le cuivre de l'écran de faisceau. Un modèle analytique et des simulations mécano-thermo-électromagnétiques ont permis d'évaluer les sollicitations mécaniques pendant le *quench* (de l'ordre de 30 N/mm^3) et les déformations et contraintes dynamiques des parois de l'écran de faisceau. La simulation a également permis de quantifier l'influence de la topologie de la surface, qui concentre les courants induites dans le fond des sillons. Plu le réseau formé par les particules est dense, plus la circulation des courants au travers ces structures est facilitée.

Les méthodes d'extraction de particules décrites dans le chapitre 4 ont permis de solliciter la surface dans une gamme de forces proche de celle attendue dans l'accélérateur en cas de *quench* de l'aimant supraconducteur.

L'éventualité que certains éléments de la morphologie se détachent de la surface traitée et interagissent avec le faisceau de protons est une préoccupation majeure dans le cadre de l'utilisation de la structuration laser pour application aux accélérateurs de particules. Les effets du détachement d'une particule de cuivre au cours de l'opération de l'accélérateur et de son interaction avec le faisceau ont été évalués en fonction de la taille de la particule. Si son diamètre est supérieur à 20 μm, les collisions inélastiques entre la particule et le faisceau de protons pourraient causer des pertes de faisceau, suffisantes pour être détectées et déclencher l'extraction du faisceau. Au regard de la distribution des tailles des particules observées sur la surface traitée, cette possibilité parait peu probable puisque les diamètres des particules sont majoritairement inférieurs à 1 μm.

Sans provoquer des pertes de faisceaux préjudiciables pour la disponibilité de l'accélérateur, les particules de cuivre d'une taille inférieure à 20 μm, interagissent tout de même avec le faisceau de protons : elles se chargent électriquement et sont alors soumises aux forces dues au champ électrique généré par le faisceau. Leur trajectoire est modifiée et elles

sont rejetées hors du faisceau de protons, heurtant la paroi de l'écran de faisceau. Des simulations de la dynamique des particules interagissant avec le faisceau ont permis d'estimer la vitesse et la position des particules lors de l'impact avec la paroi. L'énergie cinétique des particules heurtant la surface de l'écran de faisceau a été évaluée entre 10^{-11} J et 10^{-10} J. L'ordre de grandeur est similaire à l'énergie nécessaire à la rupture de la liaison mécanique entre les particules et la surface (voir section 2.1.2). Des scénarii de détachement de particules (dites alors *secondaires*) aprèsl'impact sur la surface traitée d'une particule incidente ont donc été envisagés, tout comme le détachement en cascade des particules après des impacts successifs. La distribution en taille et en vitesse des particules détachées à chaque *génération* a été évaluée à partir d'un modèle simplifié de collision. Finalement, avec seulement 0.31 particules secondaires détachées et interagissant avec le faisceau pour 1 particule initiale tombant et interagissant avec le faisceau, la possibilité d'une réaction en chaine menant à un détachement massif de particules est peu probable dans les hypothèses du modèle.

Une étude expérimentale a mise en évidence l'influence sur le SEY des caractéristiques de la morphologie à deux échelles : le rapport profondeur/largeur des sillons et la présence des particules redéposées sur la surface sinusoïdale. Ces caractéristiques sont contrôlées par les paramètres du traitement laser, telles que l'énergie et la fréquence de répétition des impulsions, la vitesse d'avancement et la distance entre deux sillons consécutifs. Cent soixante combinaisons des variables d'entrée du traitement laser ont été appliquées en ce sens. En mesurant le SEY d'une surface traitée, aprés un bain à ultra-sons qui a permis de diminuer le nombre de particules, la contribution de la modification de morphologie à l'échelle des sillons a été identifiée : le SEY diminue quand le rapport profondeur/largeur augmente. Cette étude a aussi révélé que la structuration de la surface à l'échelle des particules est nécessaire pour atteindre un compromis entre un SEY voisin de 1 et une profondeur des sillons inférieure à 30 μm. La présence des particules couvrant la surface est essentielle pour obtenir un SEY en dessous du seuil de création du nuage d'électron tout en limitant la profondeur des sillons, pour limiter l'augmentation de l'impédance électrique. En consequence, toute procédure de nettoyage qui éliminerait les éléments fragiles de la morphologie pourrait augmenter significativement le SEY de la surface. Néanmoins, le conditionnement (c'est à dire la réduction de SEY quand la surface est soumise à un bombardement d'électrons) s'est montrée très efficace sur les surfaces traitées par laser, y compris celles avec une faible densité de particules et dont le SEY initial était supérieur à la valeur cible. Un SEY en dessous du seuil de création du nuage d'électron a été obtenu après une dose de 7×10^{-5} C.mm^{-2}.

Les surfaces traitées dont la densité de particules a été réduite par des sollicitations mécaniques proches de celles envisagées pendant un *quench* ne montrent pas d'augmentation rédhibitoire du SEY remettant pas en cause l'efficacité de ce traitement de surface pour l'élimination du nuage d'électrons.

5.1 Forces acting on the treated surface during accelerator operation

Laser treatment of the beam screen surface is foreseen for selected cryogenic magnets. This section aims at evaluating mechanical solicitations acting on treated surfaces during the operation of the accelerator.

As illustrated in figure 1.3 in section 1.1.1, the beam screen is inserted inside the magnet cold bore. Although the beam screen is inserted in the magnet after the training and tests that LHC magnets undergo in the laboratory, it can be submitted to constrains during the re-training which might be required after the transport in to the LHC tunnel. Vibrations of the magnet during the transport have been documented [204] to be on the order of 1.2 $m.s^{-2}$ in longitudinal, vertical and lateral directions.

If laser treatment is performed *in-situ*, when the magnet is already installed in the LHC tunnel, the surface has to undergo thermal cooling cycles from room temperature to cryogenic temperatures. This effect has been assessed by the test described in section 2.2.3.

The most detrimental constrains applied on the beam screen structuration have been identified in case of a magnet *quench*.

5.1.1 Calculation of forces acting on beam screen surfaces during a quench

Overall description and objective

A magnet quench is a resistive transition of the superconducting magnet surrounding the beam screen [205]. If a resistivity increase is detected, the beam is extracted out of the accelerator and the quench protection system discharges the magnet current. The magnetic field of the dipole (or the magnetic gradient of a quadrupole) decays from its nominal value to 0 in a few hundreds of milliseconds. This rapid magnetic field variation induces high magnitude eddy currents and Lorentz forces in the highly conductive components of the beam screen assembly. Such an event is not rare and has to be considered for the design of magnets and of beam screens. 75 quench events were recorded in 2018 for LHC magnets [206].

Depending on the assembly configuration, induced magnetic forces can generate deformations and dynamic movements of the beam screen which have to be evaluated. The presence of a stainless steel shell, with lower electrical conductivity and higher Young Modulus than copper, limits deformations and displacements of the beam screen.

Electromagnetic forces directly applied to the particles could be a detrimental effect for the particle adhesion. Lorentz forces are the result of the interaction between electrically charged particles in the conductor and the varying surrounding magnetic field. The surface topology is made of copper, therefore, induced eddy currents are circulating through the surface morphological features and the features are submitted to the induced force field.

Massive particle detachment from the treated surface during a magnet quench could

be a major obstacle to the use of laser-treated surfaces in particle accelerators. The Lorentz force intensity has to be estimated based on the geometry of the assembly, on the electro-thermal-mechanical properties of the materials and on the magnet field decay dynamics.

Hypothesis about the chemical composition of the surface

Despite the presence of a thin oxide layer, as revealed by TEM characterisation presented in section 3.2, in the following calculations the material was considered to be pure copper, with a uniform resistivity. That is a conservative approach, since the high electrical resistivity of the oxide should reduce the intensity of eddy currents circulating through the particles, thus reducing Lorentz force amplitude, as compared to the homogeneous copper hypothesis.

Analytical description of the electromagnetic forces applied during a quench

Forces induced by temporal variations of magnetic field amplitude are described in [207] and illustrated in figure 5.1. In the case of a dipole magnet, with a vertical magnetic field, the induced eddy currents circulate orthogonally to the magnetic field, in the longitudinal direction of the beam screen. Lorentz forces are orthogonal to both magnetic field direction and current direction, they are horizontal and oriented towards the outside of the beam screen. The force amplitude increases linearly with the distance to the vertical plane of symmetry of the beam screen. This tends to deform the beam screen in the horizontal direction.

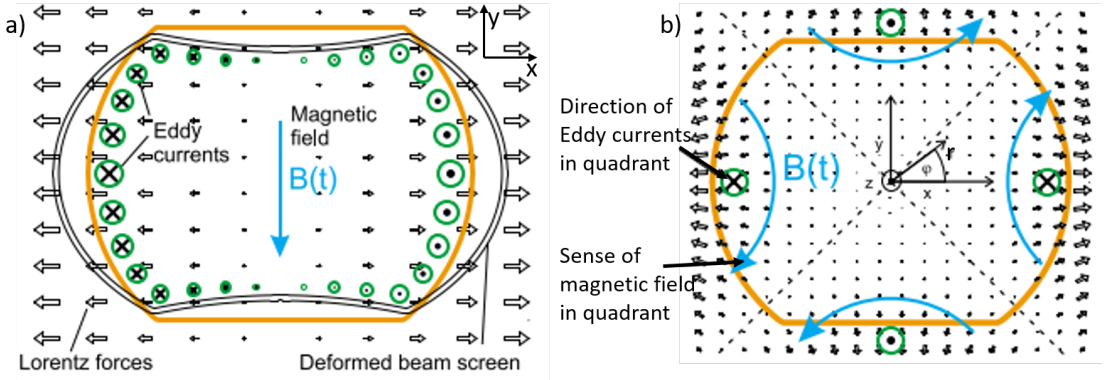

Figure 5.1: a) Sketch of eddy current, Lorentz force and deformations of the beam screen in a dipole field during a quench, after [208]. b) Beam screen in a quadrupole field during quench with superposed field of Lorentz forces, after [209].

Analytical formulas have also been used to calculate induced forces, bending moment, stresses and beam screen deformation in a dipole field [208] and in a quadrupole field [209]. In particular, the maximum force applied on the surface is given by equation 5.1 and equation 5.2 for the dipole and quadrupole cases, respectively.

$$F_{Vol\,MAX}(x,y) = \frac{B(x,y)\dot{B}(x,y)\,x}{\rho_{elec}} \tag{5.1}$$

where $B(x,y) = B$ is the value of the magnetic field considered as uniform over the section, ρ_{elec} is the local resistivity.

$$F_{Vol\,MAX}(x,y) = \frac{G(x,y)\dot{G}(x,y)\,r^3}{2\rho_{elec}} \tag{5.2}$$

where $G(x,y) = G$ is the value of the magnetic field gradient, $r = \sqrt{x^2+y^2}$ is the distance to the magnetic center assumed concentric with the beam screen, ρ_{elec} is the local resistivity.

Analytical calculations to validate the mechanical load are based on an electrical resistivity value of $\rho_{elec} = 1.68 \times 10^{-10}\ \Omega.m$ (between 4 and 20 K). The Residual-Resistivity Ratio (RRR) is the ratio between the resistivity at 273 K and the resistivity at 4 K. In the case of the material selected for the beam screen, the ratio is equal to 100 between 4 and 20 K.

The analytical model has been applied to LHC beam screen geometries, in particular to determine the deformation of the beam screen during the main dipole magnet quench. The maximum horizontal deformation was estimated to 0.86 mm. The maximum stress is in correspondence of the horizontal direction. It has been compared with measurement on a 4-m-long [210, 211] and on a real size 15-m-long beam screens [212, 213] during quench tests.

The analytical formulation was found to provide conservative results due to multiple simplifications of the model: the electrical resistivity was kept constant since resistive losses were not taken into account, the particularities of the 3D geometry such as the stress concentration due to the pumping slots, the variations of electrical and thermal properties as a function of temperature, the magneto-resistivity and the magnetic self-inductance have not been taken into account. It called for the development of more sophisticated models which implement the two-way coupling between the magnetic and mechanical phenomenon.

An analytical formulation was used to give an upper bound for forces seen by the screen during quenches of magnets were the laser treatment could be potentially applied: in particular, the main bending dipole *MB* and magnets in targeted area in the framework of the HL-LHC project presented in section 1.1.1. The dipole *D1* is equipped with the magnet *MBX*, and the quadrupoles *Q1*, *Q2* and *Q3*, are equipped with the magnets *MQXA*, *MQXB* and *MQXA*, respectively. The nominal field generated by these magnets is illustrated in figure 5.2.

The characteristics of the magnets such as the number of poles (mainly quadrupoles or dipoles), the nominal magnetic field or magnetic gradient, the decrease in time of the magnetic field or magnetic gradient, as well as the characteristics of the beam screen such as the geometry, the orientation -vertical or horizontal- inside the magnet, the nominal temperature, have been gathered for the magnets relevant in this study.

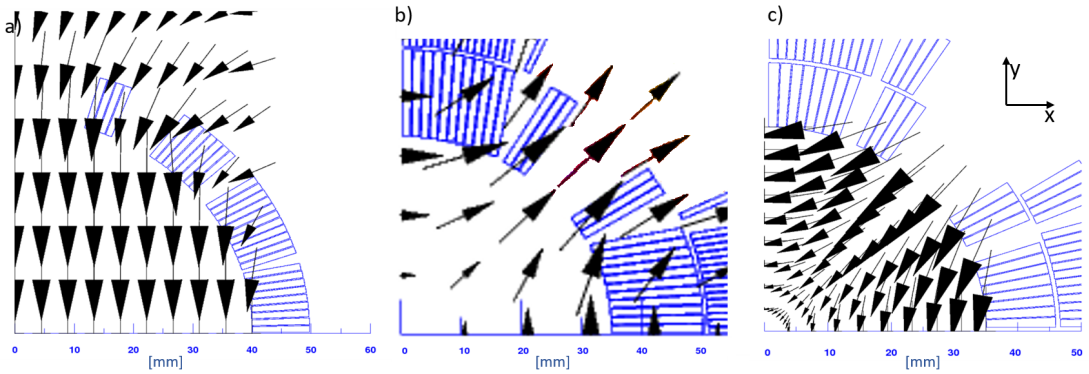

Figure 5.2: Field map in inner triplets for a) MBX. b) $MQXA$. c) $MQXB$. Susanna IZQUIERDO BERMUDEZ, CERN, TE-MSC, private communication.

Magnetic field or magnetic gradient decrease

The electrical current supplying the magnets is monitored and recorded during tests and during operation in the LHC. The decrease of the magnetic field (or of its gradient in the quadrupole case) have been calculated based on measurements of current intensity decay during magnet quenches recorded during LHC operation.

A linear equation can be used to approximate the relationship between the current I in the superconductor and the magnetic field measured when powering the magnet on test bench. This linear regression, called the *load line* of the magnet, is valid for high current values. The parameters were provided by Susanna IZQUIERDO BERMUDEZ, CERN, TE-MSC, in private conversation and are summarized, as follows:

- $B_{MB}[T] = -0.0007\, I[A] \; + \; 0.0105$;
- $G_{MQXA}[T/m] = -0.03017\, I[A] \; - \; 2.827$;
- $G_{MQXB}[T/m] = -0.0182\, I[A] \; + \; 0.9332$;
- $B_{MBX}[T] = -0.0007\, I[A] \; + \; 0.0695$.

Curves of current decrease are based on measurements during quench test in the training phase, before the operation or during LHC operation. For MB magnets, they have been described in [210] and in [208], while for magnets $MQXA$ and $MQXB$ they have been provided by the Magnet Circuits, Powering, and Performance Panel (so-called MP3) team from CERN, in private conversations.

Since the MBX magnet has never quenched in the machine at high current, there is no available data of electrical current decrease in the LHC database. Magnetic field decrease in $D1$ dipole was estimated based on the nominal magnetic field value found in the LHC design report [4] and the exponential decay constant identified on MB dipole.

Figures 5.3 and 5.4 show the magnetic field and gradient decays in the inner triplet during a quench. Products $B\dot{B}$ and $G\dot{G}$ are also plotted, since their maximum value appears in the analytical model for the estimation of the maximum induced force (see equation 5.1 and 5.2).

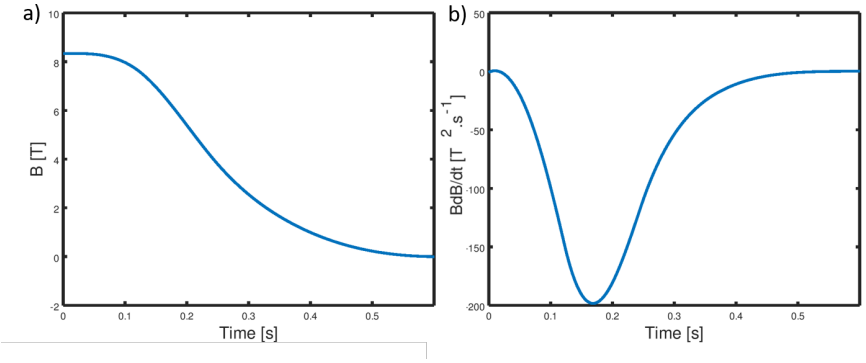

Figure 5.3: Time decrease of the magnetic field (a) and amplitude-time derivative product. $B\dot{B}$ (b) in *MB* based on measurement of the electric current during magnet quench tests.

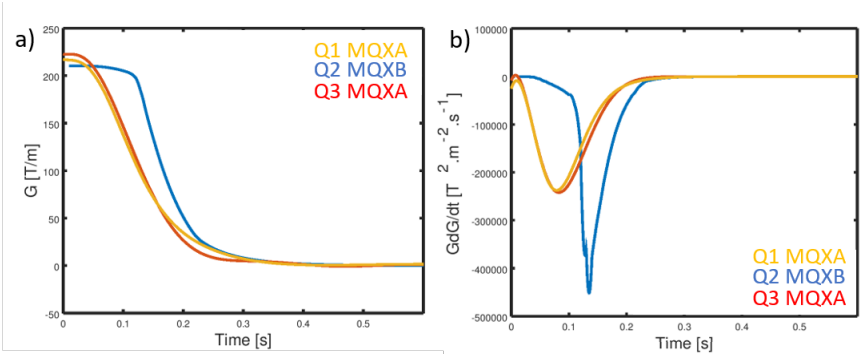

Figure 5.4: Time decrease of the magnetic field (a) and amplitude-time derivative product. $G\dot{G}$ (b) in *Q1*, *Q2* or *Q3* based on measurement of the electric current during magnet quench tests.

Results of analytical calculation of Lorentz forces

Table 5.1 presents the evaluation of the maximum volumetric force applied on the beam screen surface, for five specific magnets (dipoles and quadrupoles). Force values were calculated based on equations 5.3 and 5.4 and depend on geometrical dimensions and magnetic field characteristics of each magnet considered in the study.

Table 5.1: Force density calculated by the analytical model for five different magnet configurations.

Name	Magnet	BS diameter $[mm]$	$B\dot{B}_{max}$ $[T^2 \cdot s^{-1}]$	$G\dot{G}_{max}$ $[T^2 \cdot m^{-2} \cdot s^{-1}]$	Force density $[N \cdot mm^{-3}]$
MB	MB	48.5	200		29
D1	MBX	72	70		15
Q1	$MQXA$	53		250 000	25
Q2	$MQXB$	63		450 000	23
Q3	$MQXA$	63		250 000	42

Multiphysics simulations

The simulation of the mechanical behavior of the beam screen during the quench has been developed at CERN using the *Comsol Multiphysics* software [214]. It allows the two-way coupling between magnetic, thermal and mechanical phenomena.

The main dipole magnet has been used as a study case for multiphysics simulations.

Figure 5.5 shows the magnetic field properties given as an input of the quench simulations: the amplitude of the magnetic field was considered spatially constant in the beam screen section and varying temporally as described in b).

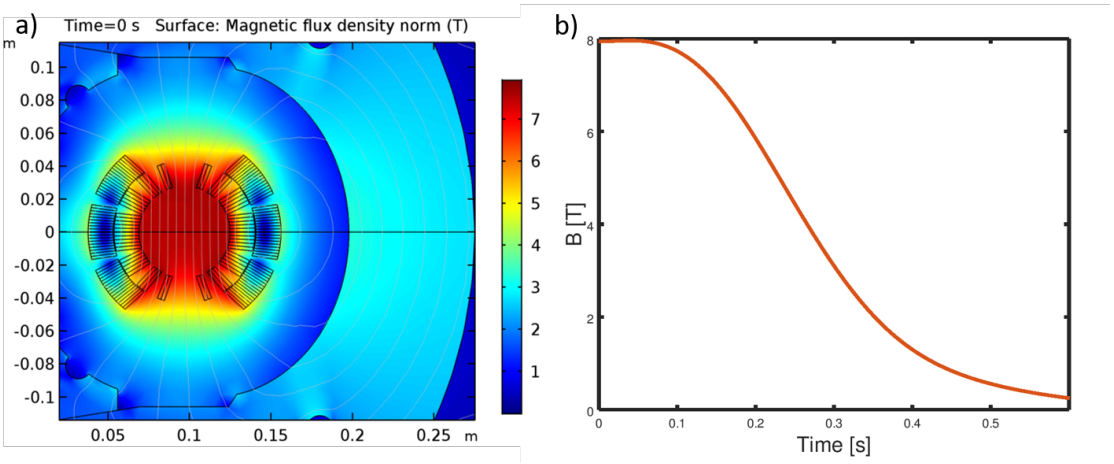

Figure 5.5: a) Magnetic field map from a simulation based on the current circulating in the superconductor magnets. Figure from Michal MACIEJEWSKI, CERN, TE-MPE, private communication. b) Field decay used as an input of quench simulation.

As already commented for figure 5.1 a), the induced forces tend to extend the beam screen in the horizontal direction. Figure 5.6 presents the main results of the simulation: the maximum horizontal displacement is obtained in the round part toward the outside of the beam screen. It was evaluated to be 0.52 mm (lower than the conservative estimation from the analytical study: 0.86 mm). The Lorentz force acting on the beam screen surface was given as a function of the time and reached the maximum value of 20 $N.mm^{-3}$.

Transient simulations also provided insights on the time constant of the mechanical

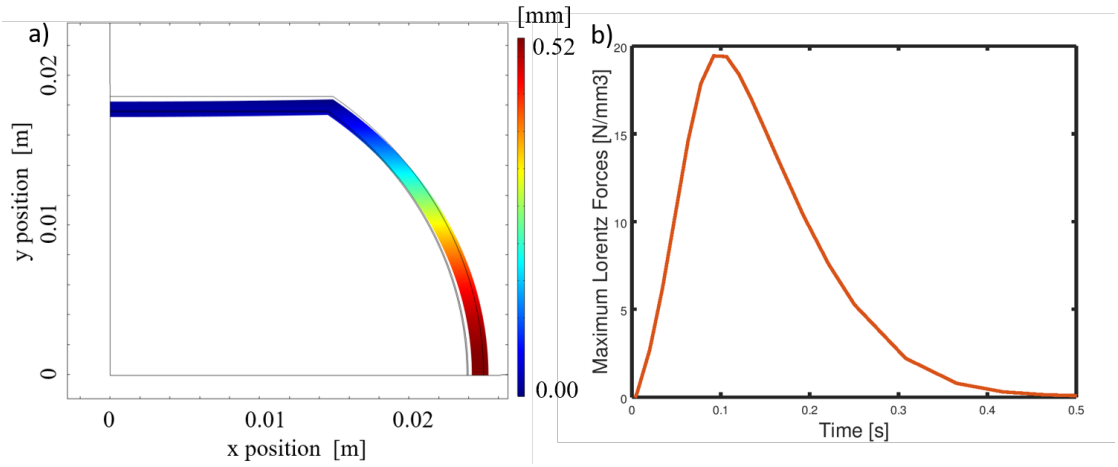

Figure 5.6: a) Map of the horizontal displacement of one quarter of the beam screen at t = 0.1 s, when the displacement is maximum. b) Time evolution of the maximum value of the Lorentz force applied on the structure, from simulation based on the current circulating in the supraconductor magnets. Figure from Marco MORRONE, CERN, TE-VSC, private communication.

solicitation: 200 ms at the FWHM of the maximum force applied on the surface and the strain-rate estimated to be 0.15 s^{-1} at maximum. The maximum amplitude of the force was reached after 100 ms.

It is worth comparing induced force time constants with those of the extraction and dilution kicker system: the fast-pulsed extraction magnet field rise time is at most 3.0 μs and the kicker field *flat-top* must be at least 90 μs to extract the particle beam of one circumference turn in LHC [4]. Detached particles would not interact with the proton beam.

Simulations allowed the calculation of the maximum value of acceleration and deceleration on the beam screen surface. It has been estimated to be 275 m.s^{-2}. The effects of the inertia force of 2.5×10^{-3} N.mm^{-3} are orders of magnitude lower than the specific Lorentz force and can be neglected.

Finally, the thermo-mechanical module allowed the determination of the beam screen temperature increase during the quench: from 20 K to 58 K.

To conclude, the analytical formulation allowed the calculation of an upper bound for forces applied on the particles during a quench, based on the geometry of the beam screen and the decay of the magnetic field generated by the magnet. The main dipole case, studied in simulations, showed that the force analytically evaluated is a conservative estimation (around 30 % higher) and gives insights into the time characteristics of mechanical stresses.

5.1.2 Influence of treated surface topology: grooves and particles

The simulation tool in *Comsol Multiphysics* has also been used to estimate the effect of the two-scale surface local topology on the induced force in the particles. Both effects of grooves and particle stacks are investigated in this section.

The characteristics of the main dipole, MB magnet, were used as inputs for the simulation.

Influence of the grooves

The larger scale (30 μm) of the surface topology is constituted by grooves, that were described in the model as sinusoids in the cross-section normal to the laser trajectory. The geometrical characteristics of the copper layer model (such as the period, the peak-to-peak amplitude and maximum thickness) were based on the microscopical cross-sectional observations presented in section 3.3.

Grooves were considered as engraved in the circumference of the beam screen. Therefore, the induced current was circulating perpendicularly to them. As illustrated in figure 5.7 a), groove effects have been evaluated in two configurations:

- in the flat part of the beam screen (see figure 5.7 b)), the surface is orthogonal to the magnetic field, so that the induced force and groove direction are parallel. In this configuration, particles on the beam screen surface would be submitted to longitudinal forces (*i.e.* along groove direction);
- in the round part of the beam screen, at y=0 mm, (see figure 5.7 c)), the surface is parallel to the magnetic field, so that the force is oriented towards the surface and perpendicular to groove direction. In this configuration, particles on the beam screen surface would be compressed toward the macroscopic surface.

In both cases, the simulated value of current density (A.mm^{-2}) was more than twice higher in the bottom than on the top of grooves (around 75 A.mm^{-2} and 32 A.mm^{-2}, respectively). These values were compared to the current density simulated at the surface of a flat beam screen (without groove pattern), which amounted to 53 A.mm^{-2}. The presence of grooves enhanced current density and, therefore, the induced force in groove bottoms by 40 %. A correcting factor of 1.4 will then be applied, to take into account groove presence, on simulation results performed on flat samples for simplicity.

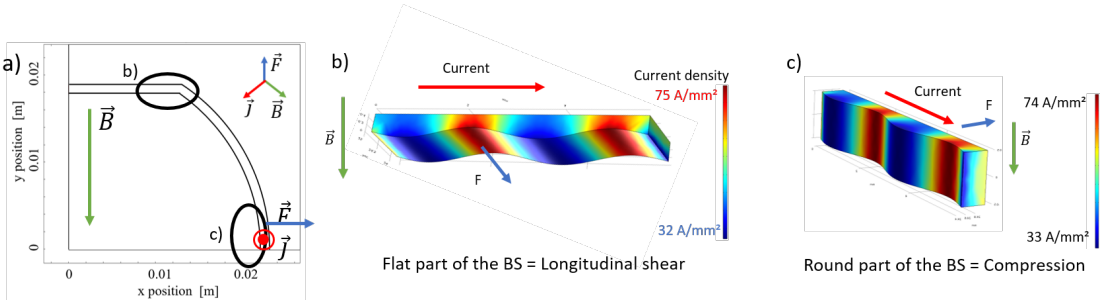

Figure 5.7: Simulation results of the current density induced in the beam screen during a quench, taking into account the presence of grooves, in a dipole field. a) Sketch of the beam screen cross section and orientation of the magnetic field, of induced current and induced force; b) grooves placed in the flat part of the BS, where the surface is submitted to a longitudinal shear; c) grooves placed in the round part of the BS, where the surface is submitted to compression.

It has to be noted that a scale factor was applied in the model to ease simulation convergence. Simulations with different scale factors were done to assess its effect. it was

found that the ratio between the maximum density of current measured in the bottom of the grooves and the minimum current density found at the top of the grooves is the same when using a scale factor in the range from 5 to 30 so, we can conclude that scale factor has no influence in the range tested. The results obtained for factor 5 are extrapolated to 1

To conclude, the presence of grooves perpendicular to the induced current flow direction increased current density in groove bottoms. Therefore, the amplitude of Lorentz forces, proportional to current density, was enhanced by the grooved pattern.

Influence of particle overlay

Particle overlay influence on the induced current flow has been evaluated comparing two particle stacking configurations:

- a particle stacked on the top of another one;
- three particles forming a *bridge*, as illustrated in figure 5.8 c).

In both cases, the ratio R of the integrated force on the particle called "*Top*" on the integrated force on the particle called "*Down*" has been calculated assuming, conservatively, a perfect bonding between particles (the oxide layer has been neglected). Particles were placed in the bottom of a groove, on the flat part of the beam screen, where the induced force is maximum and its direction tangential to the macroscopic surface.

Figure 5.8 b) and c) are graphical representations of simulation results showing the 3D structure, as well as the lines followed by the induced current (in red) and the vectors, whose amplitude is proportional to the induced force.

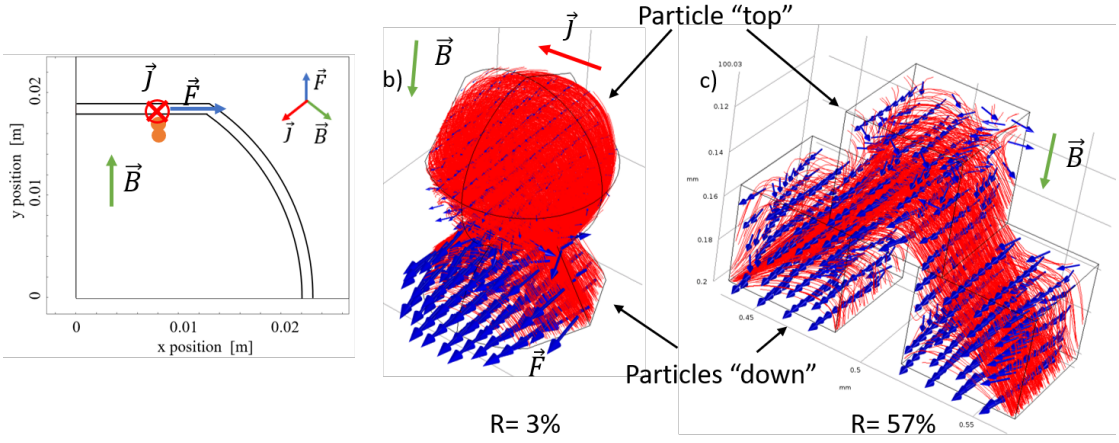

Figure 5.8: Simulation results of the current density, taking into account particle presence in groove bottoms on the flat part of the beam screen (BS), during the quench of a *MB* dipole magnet. a) Sketch of the beam screen cross section with the orientation of the magnetic field, of the induced current and of the induced force. b) Two spherical particles stacked the one on the top of the other. c) Three cubic particles in a bridge configuration. R is the ratio between the force on the upper particle (called "Top") and the one on lower particles (called "Down").

When two particles were stacked one on top of the other, the current flowing through the upper particle was negligible and R was as low as 3 %. In the *bridge* configuration,

current densities on upper and lower particles were closer and R increased to 57%. This result can be extrapolated intuitively as follows: the more complex the particle network is, the more numerous particle contacts are likely to exist, the more probable is that induced current flows in the network upper part, as illustrated schematically in figure 5.9.

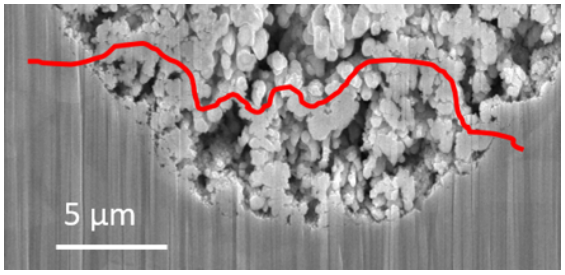

Figure 5.9: SEM cross-sectional image of the structured surface. The red line illustrates an hypothetical path followed by the induced current to flow across the groove, through particle overlay.

Simulations based on a more complex model, taking into account density and size distribution of particles, could be considered in a further work. In the current state of knowledge, based on these preliminary simulations, a conservative approach has been followed: the current density flowing through particle overlay was considered equal to the current flowing on the beam screen surface, evaluated in the previous sections.

5.1.3 Conclusion on particle detachment during accelerator operation

The resistive transition of the superconducting magnet has been identified as the accelerator operation during which a beam failure, due to the structuration of beam screen surface, is most probable. Forces induced in particles during the *quench* have been assessed in this section.

The amplitude of the force field acting on particles was conservatively estimated based on an analytical model. Simulations allowed also to assess the effect of the groove pattern and of particle network overlay. Forces applied on particles were estimated to be in the range from 20 to 40 N.mm^{-3}. Their direction could be parallel to the macroscopic surface or oriented toward the surface. Temperature was considered in the range between 20 and 58 K. Quench simulations were performed considering electrical resistivity of pure copper. In reality, the oxide layer present in between the particles and the bulk surface can decrease the induced force.

Comparison with extraction techniques used for mechanical characterisation

Extraction techniques presented in chapter 4 were chosen to be representative of mechanical solicitations occurring during a magnet quench. Either if none of the proposed techniques could reproduce exactly the target loading conditions, they were complementary and each gave an interesting piece of information on particle adhesion. In particular, centrifugation techniques allowed to reach the target amplitude, although at

ambient temperature and with a static force. Laser shocks, even though they induced forces higher than the target value, had a dynamic nature and moreover allowed the evaluation of cryogenic temperature effects.

Based on the experimental campaign of particle extraction, the amount of particles which might be extracted from the laser treated beam screen surface during a quench is estimated to be around 0.05 mg.cm^{-2}.

Some limitations have to be considered:

- the strain-rate achieved during the quench (around 0.15 s^{-1}) was not reachable by the propose extraction techniques. In fact, centrifugation was quasi-static and laser shock submitted surfaces to high strain rates, in the order of 10^5 s^{-1}).

  Based on material properties presented in section 2.1.2, material toughness was higher for high strain rates than in quasi-static conditions. Therefore, the mechanical solicitation generated by centrifugation can be considered more conservative when compared to those occurring during a quench.

- during a quench, particles are submitted to shear and compression (considering the macroscopic surface), while the direction of inertia forces applied by the two extraction techniques was always orthogonal to the macroscopic surface.

  Due to the grooved pattern of the near surface, locally, during a quench, the stress applied on a bond between a particle and the near surface is a composition of both shear and compression. Inertia forces during mechanical tests, orthogonal to the macroscopic surface, also generate a mixed-mode loading on the complex particle network, which can locally undergo shear, compression and traction. Material properties presented in section 2.1.2 show that the maximum strength of the OFE copper in compression is higher than in traction.

In the current state of knowledge, particle detachment occurring during a quench, as it has been conservatively evaluated based on extraction techniques, does not show a detrimental effect on the integrity of the surface morphology itself, due to the relatively small amount of particle overlay that would be detached. Effects of particle detachment on SEY are assessed in section 5.3.

Dust production, which can be activated during accelerator operation, raises radioprotection issues for maintenance operations.

5.2 Copper particle interaction with the proton beam

This section discusses interactions between the proton beam circulating in the accelerator and copper particles, features of the treated surface that could be detached from it by induced forces. Two consequences of the interaction between the proton beam and a detached particle are described: beam losses and cascading detachment of particles. Reasons of spontaneous detachment are not investigated in this thesis.

5.2.1 Beam losses due to beam/particle interaction

Beam losses

In the LHC, the beam energy at collision is 7 TeV. Each proton beam has an energy of more than 330 MJ threatening to damage the accelerator environment in case of uncontrolled beam loss [215].

Beam losses are monitored by Beam Loss Monitors (BLM). These devices measure the ionization produced in a gas by lost particles, scattered from the beam trajectory. They consist of an ionization chamber filled with a noble gas (e.g. argon) and of electronics able to read the signal produced by the ionization chamber. The BLM's signal feed the beam interlock system, it is compared with predefined thresholds for the identification of dangerous beam losses. The fastest reaction time of the BLM system is 40 μs [4].

To prevent damages in accelerator equipment, in case of beam losses surpassing the so-called *dump threshold*, kicker magnets are turned on to extract the beams into dump blocks which safely absorb the beam energy [215]. The extraction takes advantage of the particle-free gap in the circulating beam, during which the field of the extraction kicker magnets rise to its nominal value in 3 μs. The kicker field *flat-top* is 90-μs-long to extract the particle beam of one circumference turn in LHC [4]. Beam losses were responsible for 33 of the 975 faults of the LHC in 2018 [206]. The introduction of beam screen surface treatment could have an impact on beam losses, due do dust detachment. In fact, if inelastic collisions between the proton beam and detached particles would surpass the *dump threshold*, a beam dump would be triggered, reducing accelerator availability. Beam/macroparticle interaction simulations have been performed to investigate this probability.

Simulation inputs and hypothesis of beam-macroparticle interaction simulations

The simulations of macroparticles of copper interacting with the proton beam have been prepared by Philippe BELANGER, working for TRIUMF, in Vancouver. The relevant characteristics of the macroparticles to assess the consequence of the beam interaction are the size, the shape, the chemical composition, the transverse position, the longitudinal position and finally the initial electrical charge (charging effect due to the electron cloud).

Input parameters of Monte-Carlo simulations related to the beam characteristics were:

- beam intensity: 2.4×10^{14} protons;
- proton beam energy: 6.5 TeV;
- beam size: randomly selected within standard arc cell.

It is worth noting that the beam characteristics used as inputs in the simulation are not strictly conservative: as shown in table 1.1, during HL-LHC operation the beam intensity will reach 6×10^{14} protons at the energy of 7 TeV. The beam size in the inner triplet is also larger.

The macroparticle characteristics were:

- macroparticle geometry: spherical with a between 1.5 μm and 10 μm, logarithmically distributed;
- macroparticle material: copper;
- macroparticle initial charge: neutral;
- macroparticle initial location: on top flat part of the beam screen (18 mm), with randomly selected horizontal offset (0-1 mm) (see figure 5.10 a));
- macroparticle initial speed: no initial speed.

The proton beam is assumed centered in the beam screen.

Comments on the initial charge of the particle

For a neutral copper macroparticle, gravity is the driving force for the dynamics, which leads to a 5σ (around 2 mm in diameter) interaction limit as it can be seen in figure 5.10 a) (outside of that, they simply fall beside the beam). Results could be detrimentally modified if the particle would be negatively charged due to the presence of an insulating oxide layer (shown in section 3.2) and bombarding electrons. If the copper macroparticle is negatively charged, gravity would become negligible compared to the electric force of the beam and the interaction region would increase significantly. Highly charged copper could also orbit the beam.

Nevertheless, this possibility has been excluded since the conditioning of the surface at room temperature was effective, meaning that bombarding the surface with electrons, the SEY of the surface is reduced, and the surface was not charged. The same experiment is planned to be performed at cryogenic temperatures.

On the other hand, the macroparticle being charged positively because of the photoelectron emission under synchrotron radiation for instance would tend to expel particle out of the proton beam and reduce inelastic collisions rate.

Comments on the material

In the simulation, the macroparticle material was considered to be copper despite the observation of oxide layer. Most of the macroparticles are spherical droplets of copper of 800 nm diameter surrounded by an oxide layer with a thickness typically close to 20 nm. Depending on the laser parameters chosen for the treatment, several of these droplets can be agglomerated and can create larger macroparticles of typically 3 μm diameter. The volume distribution is 86 % copper and 14 % of Cu_2O oxide. Taking into account the copper and oxide densities (8.96 g/cm^3 and 6 g/cm^3, respectively) the copper element is dominating at 95 %.

Comments on the initial speed

Macroparticle are considered as falling into the beam screen only by gravitational forces acting on the particle. The force induced during a quench, presented in section 5.1 would reach its maximum at 100 ms, more longer than the time required to extract the

beam. Therefore, detached particles under mechanical solicitations due to an induced force during a quench would not interact with the beam.

Results of the simulation of beam-macroparticles interaction

Figure 5.10 b) and c) present the inelastic interaction between macroparticles and the proton beam depending on the initial position and the diameter of the macroparticle, respectively. The detection limits in figure 5.10 b) and c) comes from the smallest and largest UFO event detected during run 2. It aims to illustrate the range of signal amplitudes tagged as a *UFO event* during LHC operation.

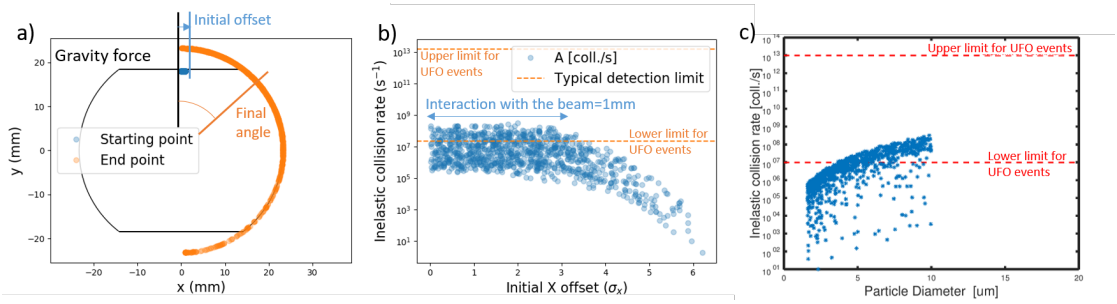

Figure 5.10: a) Sketch of the beam screen. The starting point (blue point) of the macroparticle, before interaction of the proton beam are located on top the flat part of the beam screen, the initial offset of the macroparticles is presented. The orange points are the end point location. Figure from Phillipe BELANGER, Triumf, private communication. b) Inelastic collision rate depending on the initial offset of the macroparticle. The offset is expressed as a function of σ_X, beam size characteristic calculated from the emittance ϵ of the proton beam and the β of the magnet, $\epsilon = \frac{\sigma^2}{\beta}$. Figure from Phillipe BELANGER, Triumf, private communication. c) Inelastic collisions as a function of the particle diameter.

Under these assumptions, the beam losses caused by interaction between the particles detached from the treated surface and the proton beam are substantially lower than the *dump threshold* (Private communication with Anton LECHNER, CERN, EN-STI). For copper, the minimum size of particle, which could trigger a beam dump, has been estimated to be 20 μm in diameter (Private communication with Anton LECHNER, CERN, EN-STI).

Based on the size distribution of the particle extracted from *D7 2020* samples by centrifugation, the density of particles larger than 20 μm is around 500 particles/cm^2.

5.2.2 Multi detachment of particles: simulations of macroparticle dynamics

Particles smaller than 20 μm won't trigger the extraction of the beam in case of interaction. Nevertheless, particles are charged when falling in the electric field generated by the proton beam. Once charged, these particles are repelled from the beam and hit the inner surface of the beam screen. The treated surface is covered by particles which might detach due to the impact and might interact with the beam or impact the beam screen surface and detach another *generation* of particles.

A scenario of cascading detachment of particles is considered in this section. The scenario is based on the simulations of dynamic of the macroparticles of copper interacting

with the proton beam prepared by Phillipe BELANGER, Triumf.

5.2.2.1 Dynamic simulation of 1^{st} generation macroparticles

The 1^{st} generation are macroparticles falling from the surface into the beam as presented in the previous section and illustrated in figure 5.10 a). They are positively charged while interacting with the proton beam, repelled by electric force and impinge the inner surface of the beam screen.

Figure 5.11 shows the simulation results on the macroparticle dynamics: the final velocity and localization (via the final angle compared to the vertical axis) of the impact of the repelled particles on the beam screen surface.

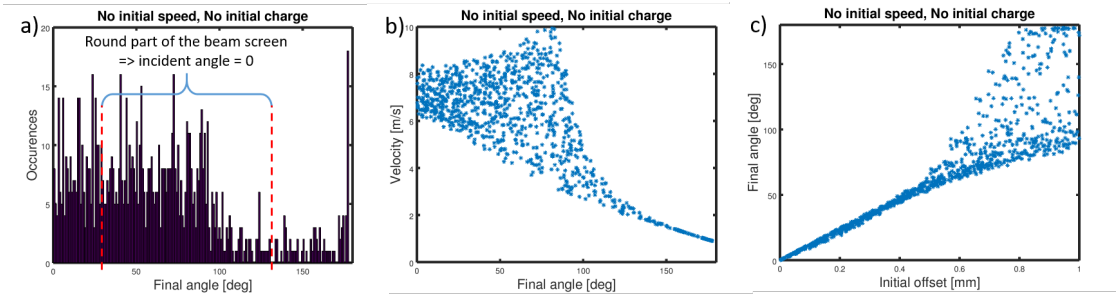

Figure 5.11: a) Histogram of the final angle compared to the vertical axis of the particles when impinging the beam screen surface after interaction with the proton beam. Particles with a final angle between 37° and 137° impinge the round part of the bean screen, in normal incidence. b) Velocity of repelled particles when impinging the surface of the beam screen. c) Final angle depending on the initial offset.

As illustrated in figure 5.11, particles can speed up to 10 m.s^{-1} after interacting with the proton beam. For spherical copper particles with a radius of 5 μm, the kinetic energy of the expelled particle when impacting the surface of the beam screen is 1.82×10^{-10} J. It is in the range of the energy required to detach a particle bond to the surface (see section 2.1.2).

62 % of the 1^{st} generation, repelled from the proton beam and impacting the beam screen surface have a normal incidence compared to the macroscopic surface of the beam screen as illustrated in figure 5.11 a).

5.2.2.2 Charge of macroparticle after interaction with the proton beam

The charge of the copper macroparticles after interacting with the proton beam has been estimated to be in average 1×10^{-13} C from simulation.

When charged particles are repelled by the beam, they attach on the surface of the beam screen after the collision due to image forces (until it gets neutralised when contacting the beam screen).

The image force amplitude and the time of discharge of the particle when in contact with the beam screen surface are estimated based on the geometric characteristics and material properties of the particle and the oxide layer covering the copper.

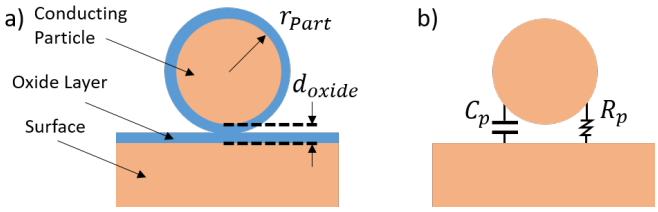

Figure 5.12: a) Physical description of the macroparticle in contact with the bulk surface. b) Corresponding electrical model. A resistor–capacitor circuit (RC circuit) composed of a resistor R_P and capacitor C_P is used to model the presence of the oxide layer, the copper oxide being a semi-conductive material [216].

As illustrated in figure 5.12, a RC circuit is used to model the contact resistance and capacitive effect between a spherical particle and the surface. The values of the equivalent capacitor and particle charging resistance have been calculated as well as the charging and discharging time constant of the particle in the presence of an insulating oxide layer.

The equivalent capacitor, C_P, is given by equation 5.3 [216].

$$C_p = 4\pi\,\epsilon\left(1+\alpha_p+\frac{{\alpha_p}^2}{1-{\alpha_p}^2}+...\right) \tag{5.3}$$

where C_P is the equivalent capacitor, $\epsilon = \epsilon_R/.\epsilon_0$ with ϵ_R, the relative permittivity or dielectric constant of the copper oxide layer (were found to be equal to 7.6 and 18.1 for Cu_2O and CuO, respectively [217]), α_P is a geometric coefficient defined in equation 5.4,

$$\alpha_p = \frac{r_{Part}}{2(r_{Part}+d_{oxide})} \tag{5.4}$$

where r_{Part} is the radius of the copper macroparticle, based on the microscopic observations and the model deduced in section 2.1.2. $r_{Part} = 1.5$ μm has been taken as an illustration, d_{oxide} is the layer of oxide observed in between the macroparticle and the bulk surface, typically 50 nm.

The particle charging resistance, R_p, depends on the contact area between the macroparticle and the bulk, A_p, defined as 1 % of the maximum cross-sectional area.

$$R_p = \frac{d_{oxide}}{A_p\,\sigma_{oxide}} \tag{5.5}$$

where σ_{oxide} is the conductivity of the oxide layer.

For Cu_2O oxide conductivity values were found in the range of 0.18 to 0.92 S.m^{-1} in [172, 218]. For CuO oxide conductivity values were found in the range of 0.52 to 3.2 S.m^{-1} in [172, 219].

Based on the geometry and electrical parameters of the oxide layer, the charg-

ing/discharging time constant has been estimated from the equation 5.6 [216].

$$\tau_p = R_p C_p = \frac{8\pi\epsilon\, r_{Part}\, d_{oxide}}{A_p\, \sigma_{oxide}} = 47 - 786\ s \tag{5.6}$$

The range of values found for semiconductor conductivity is broad therefore, the discharging time constant is evaluated in the range of 47 to 786 s. For this thesis, only the order of magnitude of the time constant matters: several tens of seconds.

The image force is the electrostatic force from the image of a charge placed inside of a closed conductor such as the beam screen. A charged copper particle close to the beam screen is attracted until it is discharged. The value of this force depends on the charge of the macroparticle and the particle and oxide layer geometries, it can be calculated thanks to equation 5.7 ([220]) and has to be compared to the weight of the particle.

$$F_{image} = \frac{{q_{Part}}^2}{4\pi\ \epsilon_0 2(r_{Part} + d_{oxide})^2} \tag{5.7}$$

where ϵ_0 is the vacuum electric permittivity (or electric constant).

The image force is 5 orders of magnitude higher than the weight so it contributes to attach the charged macroparticles to the beam screen surface until these particles are discharged (in several tens of seconds).

5.2.2.3 Cascade effect simulations

The scenario of a multiple detachment cascade effect has been justified by the *high* kinetic energy gain by the particle due to the interaction with the beam. The kinetic energy of the impinging particles could be partly transferred to resting particles and detach them from the surface. If the kinetic energy of the released particles is important, a chain reaction could be triggered as follows:

- 1^{st} generation particles, fall into the beam and are repelled and accelerated. They impact the beam screen treated surface covered by particles and detach 2^{nd} generation particles. This is *Impact 1*:
  - 1^{st} generation particles are charged and stuck on the surface by image force;
  - 2^{nd} generation particles are released and:
    - interact with the beam, are charged, repelled and accelerated, impinge the surface in *Impact 2*. They are stuck on the surface by image force but detach 3^{rd} generation particles;
    - impinge the surface in *Impact 2'* detach 3^{rd} generation particles;
- ...
- generation *N* particles impinge the surface and detaching generation *N+1* particles;

- generation *N+1* particles either interact directly with the beam either impact the surface to trigger the detachment of generation *N+2* particles, *etc.*

Figure 5.13 illustrates the collision of one particle m_1 with the treated surface and the detachment of the particle m_2.

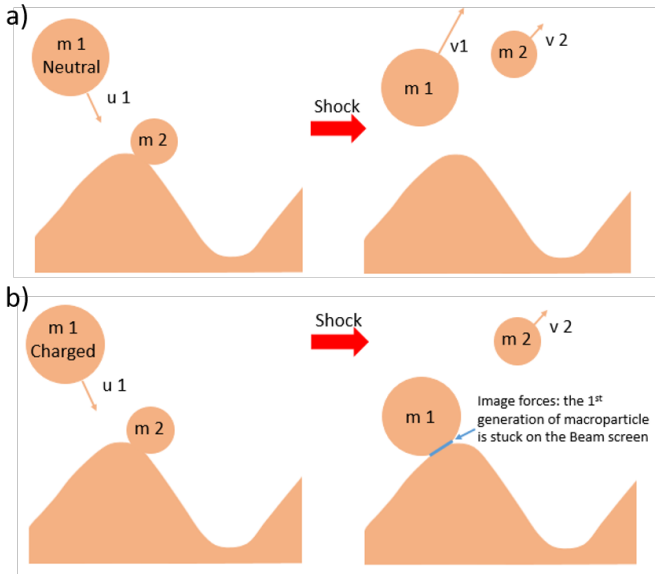

Figure 5.13: a) Model for one neutral particle impinging the surface being reflected. b) Model for one charged particle impinging the surface staying attached one the surface due to the image force. The scale between the diameter of the particles and the characteristics of the grooved surface is not respected.

Simple assumptions on the collisions between the N generation particles and the surface were made to evaluate:

- the angular distribution of the released *N+1* generation particles as a function of the incident angle of the N generation particle;
- the velocity of the released *N+1* generation particles as a function of the kinetic energy of the N generation particle;
- the number of the released *N+1* generation particles as a function of the kinetic energy and electric charge of the N generation particle.

Distribution angle

Assumptions have been used on the collisions between the incident particles and the surface to evaluate the distribution angle of the released particles. The main objective is to evaluate what is the proportion of the released particles which will interact with the beam. 2^{nd} generation particles interact with the proton beam if the incident angle is equal to the emitted angle, with angles defined from the macroscopic surface normal.

Assumptions on the local surface geometry and the emitted angle are illustrated in figure 5.14:

- sinusoidal grooves based on the surface model identified in section 3.3 (45-μm-period, 26-μm-peak-to-peak amplitude);
- emission is dominated by reflection on the local microscopic surface. For a specular (*i.e.* regular) reflection, the incident angle to the local surface normal is equal to the angle of reflection, $\alpha_1 = \alpha_2$.

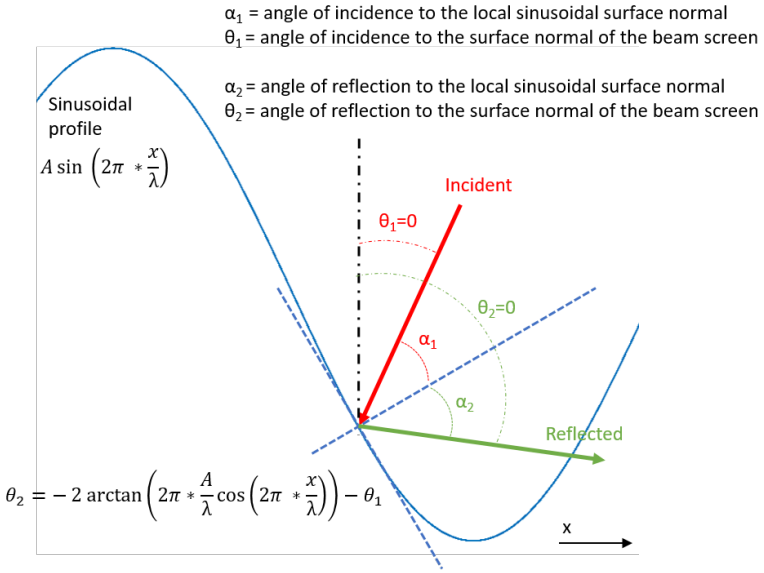

Figure 5.14: Reflection of the particle by the locally grooved surface. The angles θ are defined compared to the normal of the macroscopic surface, The angles α are defined compared to the normal of the local surface. The reflected angle θ_2 is defined depending on the characteristics of the sinusoidal grooves and the incident angle.

The reflection angle depends on the impact localisation of the 1^{st} generation particles on the microscopic surface *i.e.* in the sinusoidal groove (as illustrated is figure 5.15 a) b)). As r, the ratio of the spatial period is randomly chosen, probability density function and cumulative distribution function of the reflected angle have been calculated in figure 5.15 c) and d), respectively.

Figure 5.16 shows the same approach for the maximum incidence in the given beam screen geometry.

The probability that released particles interact with the proton beam has been calculated and is shown in figure 5.17. Depending on the incident angle, between 9 and 15 % of the 2^{nd} generation macroparticles will interact with the proton beam.

The distribution of the final angle of the 1^{st} generation particles impinging the beam screen surface (see figure 5.11), gives the incident angle distribution of the 1^{st} generation particles, knowing the beam screen geometry. Taking into account the incident angle distribution, the 2^{nd} generation particles reflected back to the beam are 10 %.

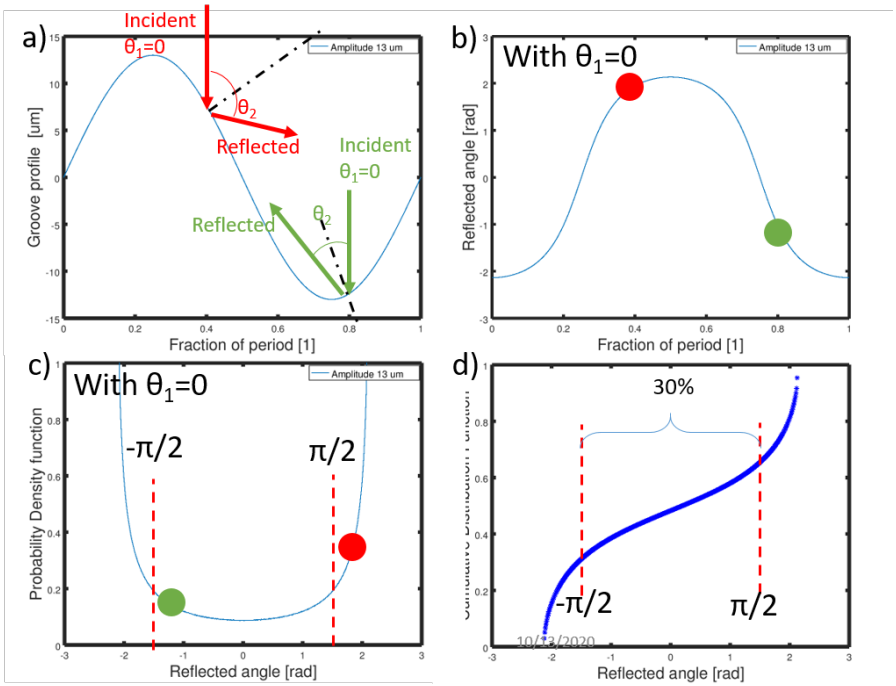

Figure 5.15: a) Spatial period of the local sinusoidal surface. Illustration of two normal incident (with respect to the macroscopic surface) and regular reflection compared to the local surface. b) Reflected angle defined from the macroscopic surface normal depending on the position of the impact. Red and green dots are cases illustrated in a). c) Probability density function of the reflective angle. If the reflected angle is between $-\pi/2$ and $\pi/2$ the particles escape the surface, in the other case it will impact the surface again. d) Corresponding cumulative distribution function. 30 % of normal incident particles escape the surface.

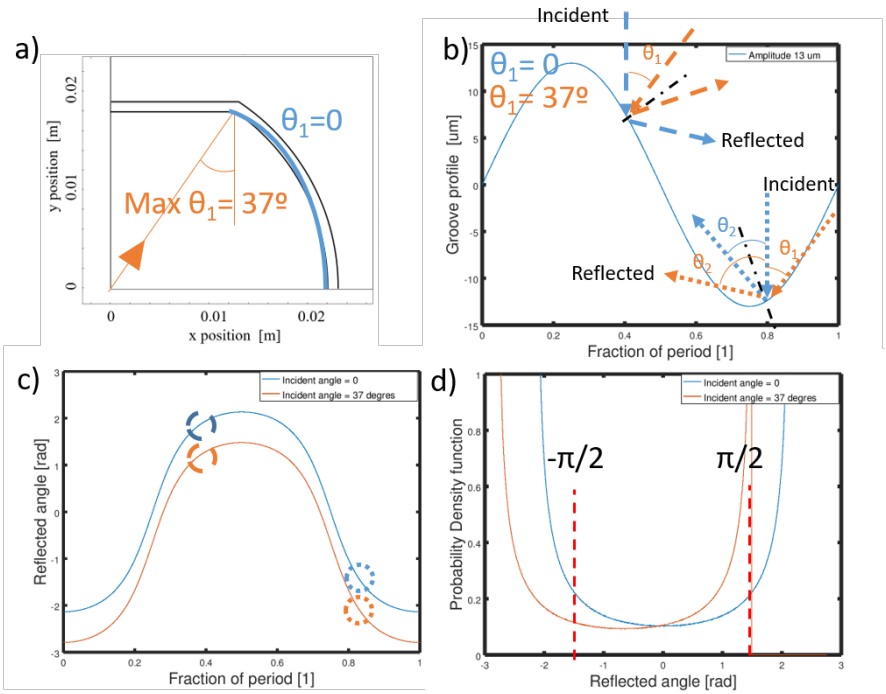

Figure 5.16: a) Sketch of the top left corner of the beam screen section. In the blue area, impinging particles have a normal incidence compared to the macroscopic surface. In orange, the maximum incidence is 37°. b) Spatial period of the local sinusoidal surface. Illustration of normal incidence and 37° incident in the point of the period. c) Reflected angle defined from the macroscopic surface normal depending on the position of the impact, in the two position illustrated in b). d) Probability density function of the reflective angle. If the reflected angle is between $-\pi/2$ and $\pi/2$, particles escape the surface.

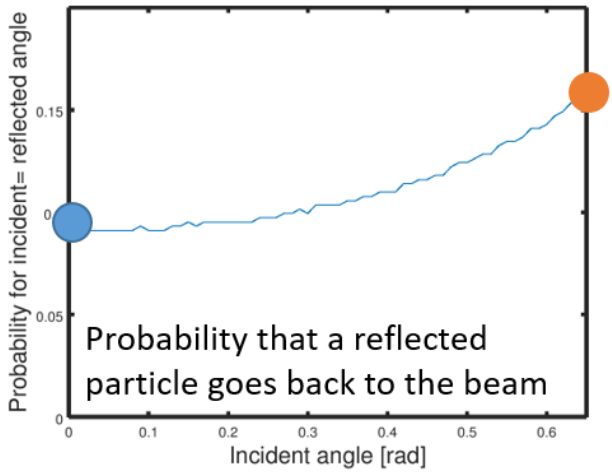

Figure 5.17: Probability that the reflected is equal to the incident angle, depending on the incident angle.

Velocity amplitude and number of released particles

For a given particle size distribution, the macroparticle dynamic simulations provide the velocity distribution of the 1^{st} generation particles after the interaction with the proton beam, it is shown in figure 5.18 (blue stars).

The collision of each incident particle m_1 with an initial velocity u_1 is considered with the immobile macroparticle m_2 of random size chosen among the size distribution of particles initially present on the surface. After the shock, the particles m_1 and m_2 have a velocity of v_1 and v_2, respectively.

Hypotheses on the impact

- non isolated system of two macroparticles: impulsion of the force acting on m_2 is added on the momentum conservation equation shown in equation 5.8;
- non elastic shock: the kinetic energy of m_1 before the shock is partly transferred to m_2 and partly dissipated in the fracture, En_{Fract}=1.16 $\times$ 10^{-11} J. The value is estimated based on mechanical material properties in section 2.1.1. The order of magnitude has been confirmed in experimental measurement in section 4.3.3;
- assumption to solve the system $v_1 = v_{1 isolated\, elastic} = \frac{m_1-m_2}{m_1+m_2}u_1$.

These hypotheses lead to the equation system:

$$\begin{cases} m_1u_1 = m_1v_1 + m_2v_2 + J_{Fract},\ with\ J_{Fract} = \int F_{Fract}dt \\ \frac{1}{2}m_1u_1^2 = \frac{1}{2}m_1v_1^2 + \frac{1}{2}m_2v_2^2 + En_{Dis},\ with\ En_{Dis} = En_{Int} + En_{Fract} \end{cases} \tag{5.8}$$

where m_1 and m_2 are the mass of the particles, u_1 is the velocity before the impact, v_1 and v_2 are the velocities after the impact.

Based on these hypothesis, the velocity of the released particles is calculated depending on their mass and the energy dissipated in the fracture. For example, the velocities can be calculated in the following configuration:

- impinging particle: radius 5 μm, velocity 9 m.s^{-1}, kinetic energy 1.82 $\times$ 10^{-10} J;
- impinged particle: radius 1.5 μm.

The calculated value of v_1 is 8.5 m.s^{-1}.

With an energy dissipated in the fracture estimated to be 1.16 $\times$ 10^{-11}, v_2 is evaluated to be 10.7 m.s^{-1}.

If the kinetic energy of the impinging particle is *low*, the model gives v_2 equal to zero, that relates a situation where the impinging particle does not trigger further particle detachment when impinging the treated surface.

Impact 1

The model of collision between one incident, charged, 1^{st} generation particles and one particle on the surface with an energy dissipated in the fracture of 1.16 $\times$ 10^{-11} J has been applied to the size-velocity distribution given after dynamic simulation of particle/beam interactions.

Over 1000 1^{st} generation particles, the size-velocity distribution of 2^{nd} generation particles has been calculated and is shown in figure 5.18 b) (red stars). The ratio, $R_{1\to2}$, is the number of 2^{nd} generation particle compared to the number of 1^{st} generation particles, it is 16.7 %.

The probability that one 1^{st} generation particle detaches a 2^{nd} generation particle which will interact with the proton beam is 1.7 %. The probability that one 1^{st} generation particle detaches a 2^{nd} generation particle which will directly impact the surface of the beam screen is 14.6 %.

The Impact 1 changes the size distribution of the detached particles eliminating the small ones which are not triggered and do not trigger particle detachment during the collision.

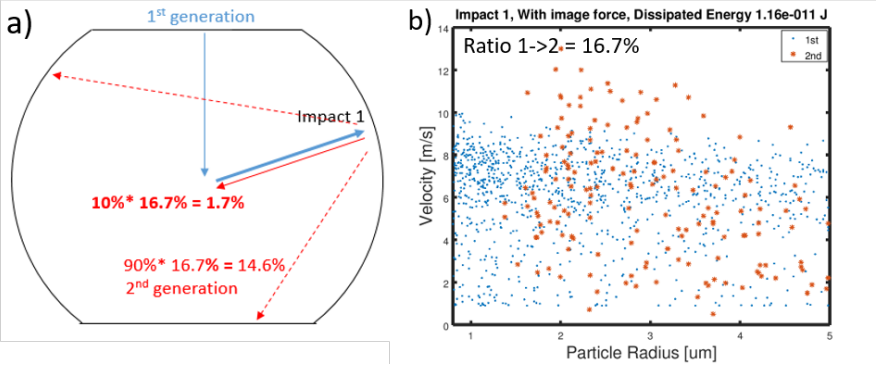

Figure 5.18: a) Sketch illustrating the Impact 1. b) Size and velocity distribution of the 1^{st} generation particle after interaction with the proton beam and before the Impact 1 and of 2^{nd} generation particle after Impact 1.

Impact 2 and Impact 2'

After Impact 1, 2^{nd} generation particles (charged or neutral) impact the beam screen and trigger the release of 3^{rd} generation particles. The same assumptions than in Impact 1 are applied to model but two cases have been considered depending on the electric charge of the impacting particle:

- collision of charged particles, Impact 2: after the Impact 2, impinging particle are submitted to the image force and remain stuck on the surface of the beam screen.

  The ratio, $R_{2\to3}$, in between the population of the 2^{nd} and 3^{rd} generations is calculated to be 29 %;

- collision of neutral particles, Impact 2': it has been assumed that impinging particles have not been charged and their kinetic energy has not been modified by the proton beam electric field. Without image force, these particles are re-emitted, the 3^{rd} generation includes the 2^{nd} generation particles which reflect the surface and the particles detached during Impact 2'.

  After Impact 2', the ratio, $R_{2'\to3}$, is 132 % between the number of particles from generations 3^{rd} and the number of particles from 2^{nd}.

Figure 5.19 illustrates the Impact 2, and shows the results of the model when it is applied on the size-velocity distribution calculated after Impact 1. The ratio $R_{2\to3}$ is equal to 29 %.

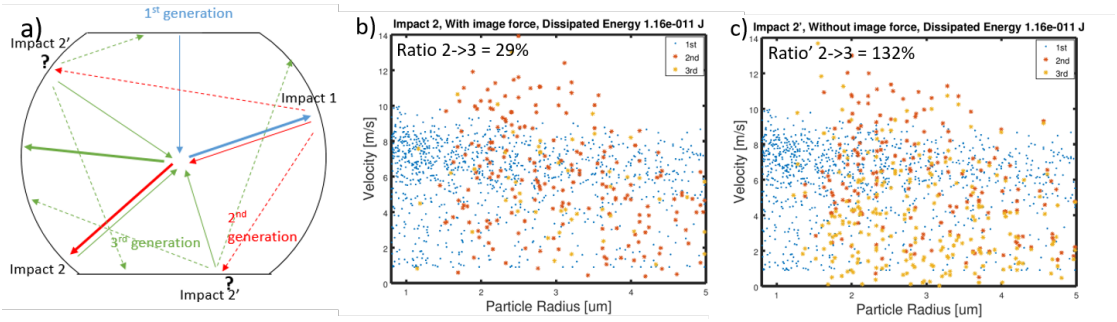

Figure 5.19: a) Sketch of a beamscreen section representing the trajectories of of particles from generation 1, 2 and 3. b) Size and velocity distribution of the 2st generation particle after interaction with the proton beam and before the Impact 2 and of 3^{rd} generation particle after Impact 2. c) Size and velocity distribution of the 2st generation particle after interaction with the proton beam and before the Impact 2' and of 3^{rd} generation particle after Impact 2'.

Asymptotic effect

Applying the model, the ratio during collision of charged particles quickly decreases for the further generations, as particles lose kinetic energy in the collisions, and charged impinging particles are trapped by the image force.

After several collisions the particles lose energy in the collisions with the beam screen. The kinetic energy of the particles decreases and they do not trigger detachment of $N+1$ generation of particles, the ratio during collision of neutral particles: decreases toward 1 (it goes even lower if particles with $v_1 = 0$ are removed).

The ratio $R_{2'\to3}$ which is the maximal ratio is applied to characterize the collision of the charged particles with the surface of the beam screen, for all the impacts.

Independently on the incident angle of the N generation particles, and the positions of the Impact N around the beam screen, it has been assumed that 10 % of the emitted $N+1$ generation particles will *directly* interact with the proton beam, as evaluated in figure 5.16.

It is worth noting that the fact that these particles are actually accelerated when interacting with the proton beam has not been taken into account.

Total probability

For each generation, the probability of direct interaction between a particle and the proton beam has been calculated by equation 5.9.

$$P_{Gen_n} = 90\% \times Ratio_{1\to2} \times \prod_{i=2}^{n-1} Ratio_{i'\to i+1} \times 10\% + P_{Gen_{n-1}} \times Ratio_{1\to2} \times 10\% \quad (5.9)$$

where $Ratio_{i'\to i+1}$, is the ratio for collision of uncharged particle between generations i and $i+1$. It is considered that $Ratio_{i'\to i+1} = Ratio_{2'\to}$. 10 % is the proportion of the emitted particles which will interact with the proton beam, $P_{Gen_{n-1}}$ is the probability

that a particle from the generation $N-1$ interact with the proton beam.

The total probability of interaction for one 1^{st} generation particle is obtained when summing the probability of all the generations, as shown in equation 5.10.

$$P_{Total} = \sum_{n=2}^{\infty} P_{Gen_n} \simeq \sum_{n=2}^{50} P_{Gen_n} \tag{5.10}$$

It appeared that this total probability is stable when taking into account several tens of generations (which would correspond to 0.2 s after the interaction of the first particle.). The convergence indicates that there is no cascading effect of the detachment of particles.

The number of particle interacting with the beam is calculated as the sum of the probability for each generation of particle. After 40 generations that number converges, as shown in figure 5.20

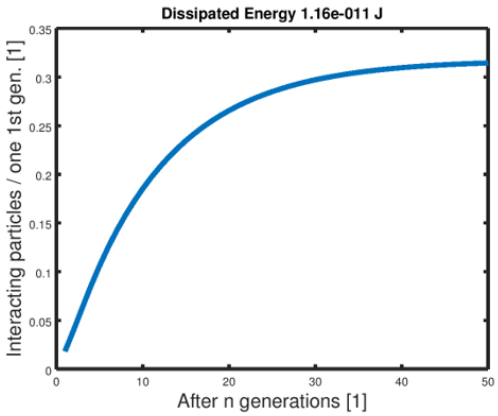

Figure 5.20: Calculated number of macroparticle being detached from the surface after impacts of n generations of particles interacting with the beam. Based on equation 5.10.

The number of interacting particles increases when the energy dissipated in the fracture of the mechanical considered in the model decreases.

For the value of the dissipated energy considered in this study, it was found that for one particle detached vertically to the beam without initial charge without initial velocity and interacting with the beam, 0.3 particles would detach and interact with the beam.

In these conditions, the cascade effect does not happen.

A scenario of multiple detachment of *N+1* particles when impinged by *N* generation particle has been considered and lead to a similar total number of interacting particle and similar conclusion.

5.2.3 Conclusions on released particle-beam interactions

This section investigated the possible detrimental effects of the interaction between particle released form the laser-treated surface morphology and the proton beam circulating

in the vacuum chamber during the operation of the accelerator. The hypothesis of a neutral copper particle falling into the beam has been considered.

The beam losses due to inelastic collisions between the proton and the copper particle would trigger a beam dump if the particle is larger than 20 μm in diameter. The occurrence of such a particle on the treated surface of *D7 2020* samples has been estimated to be 600 particles/cm^2 from the size distribution of particle extracted after 12 N.mm^{-3} centrifugation.

Smaller particles do not interact detrimentally with the proton because the are charged when approaching the beam, the electrical field generated by the proton beam expels them out of the beam trajectory. The beam losses resulting from the interaction of one of these particles are not critical for the operation of the accelerator.

Nevertheless the kinetic energy gain by the copper particle is in the same order of magnitude than the energy required to break the bonds between particles and the near surface. A chain reaction scenario, of multiple detachments of small particles has been considered.

Dynamic simulations gave the velocity and size distribution of the 1^{st} generation of the particles interacting with the proton beam. These results were used as an input of a simplify model assessing the risk of massive detachment after multiple collision on the inner wall of the beam screen. Under the hypotheses considered in this work, the risk of a cascade effect can been excluded.

5.3 SEY reduction dependency on surface morphology

In chapter 3, the effect of laser treatment parameters on morphological characteristics have been commented at two scales, looking at the groove characteristics and the particle coverage density.

As reported in the literature, the morphology of the surface strongly influences the SEY of the material (see section 1.2.3.2). In this section, the influences of both scale morphology characteristics of the laser-treated surface on SEY are investigated. Average irradiating fluence was found to be a convenient figure of merit to describe irradiation conditions for a given ablation regime (10 ps, in this work) and gas environment (gentle nitrogen flux, in this work) and to compare samples.

In figure 5.21, maximum value of SEY curve of treated surface is plotted as a function of average laser fluence. Although a large spread of SEY measurements is evident, the general trend is a decrease of SEY when fluence increases.

The large measurement dispersion is not fully understood. The ablation process involves complex phenomena, sensitive to irradiation conditions and surface reflectivity. Surface SEY can also be very sensitive to the damage of superficial structures due to their handling, packaging and transport.

To better highlight the effect of fluence on surface morphology, a set of samples was chosen: the so-called *Zeta 5* series, whose parameters can be found in appendix B. For this batch of samples, special care was taken to keep the gas environment as constant as

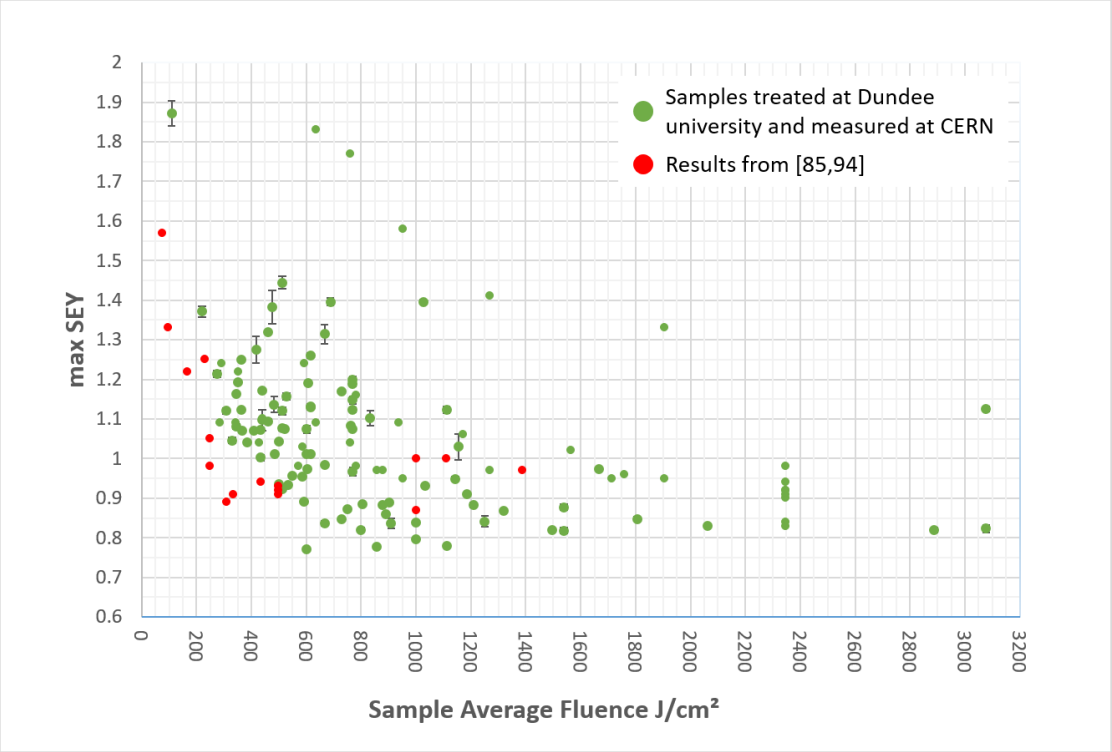

Figure 5.21: Maximum value of SEY as a function of the average value of irradiating fluence, measured on samples treated in the frame of the parametric study between 2017 and 2020, at CERN (green dots). Parameters used for the treatment are described in appendix B. Results are compared with data found in literature [85, 94] (in red).

possible and to improve the packing.

To disentangle the effects of groove-scale structuration and particle overlay in SEY reduction, SEY was measured after laser treatment, on samples having a high particle coverage density. This was compared to samples after US cleaning and, thus, without particle overlay but with the same groove characteristics.

5.3.1 Influence of groove morphology on SEY

This section presents SEY measurements on laser-treated samples where particles have been remove, to analyse the influence of groove morphology.

Part of the presented results in the following has been the object of a publication [108], where the escape probability of secondary electrons emitted from the center - in case of normal incidence - have been used to evaluate surface SEY as a function of the groove aspect ratio, as illustrated in figure 5.22. The same experimental values are also presented as a function of the average irradiating fluence, in figure 5.24.

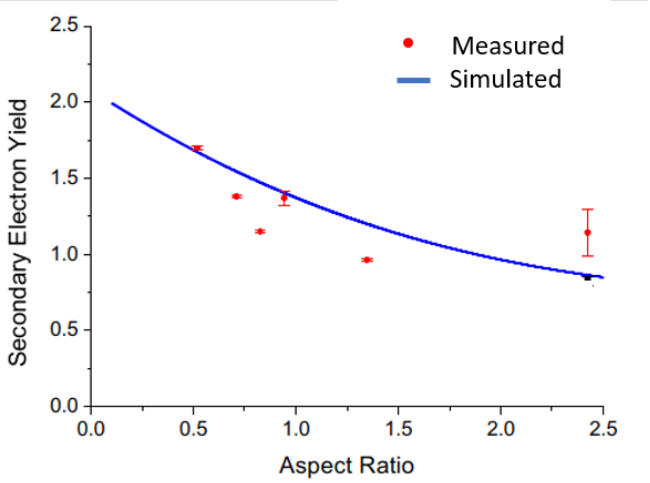

Figure 5.22: The measured maximum average SEY for each sample of *Zeta 5* series, after particle layer removal, plotted as a function of the measured trench aspect ratio and compared with the simulated trend, after [108].

5.3.2 Influence of particle surface density on SEY

5.3.2.1 Large variation of particle surface density on SEY

The role of particles in SEY reduction was first illustrated in [77]. Samples were submitted to a 5 min ultra sonic agitation and NGL alkaline detergent cleaning [221], which is a standard degreasing and cleaning procedure at CERN [107]. SEY was measured after and before. The maximal value of SEY increased slightly (0.02), but the E_{max} associated was shifted towards lower energies, from 1700 eV to around 400 eV. SEM images acquired using two different samples showed that typical cauliflower-like superficial structures were detached from surface top by the cleaning procedure. Similar observations have been made after chemical treatment in [87].

SEY curves of three surfaces are plotted in figure 5.23, *i.e.* flat as received, after laser treatment and after both laser treatment and US cleaning removing particles. It illustrates an increase of SEY value for the latter, as well as the shift of E_{max} value.

A dedicated study on the role of the particle overlay in SEY mitigation has been performed in [108]. In this study, particles were systematically removed from treated samples (*Zeta 5* series), thanks to ultrasonic cleaning.

Figure 5.24 illustrates that the SEY increased in average by 0.29, when removing the particles on the surface. The SEY of surfaces treated with the optimized parameters but without particles increased to 1.45, that is, above the required value for electron cloud mitigation.

As presented in section 1.3, two criteria were first considered to choose the best set of parameters: a maximum SEY lower than 1.1 and a groove depth not exceeding 30 μm. Opposite trends were observed: SEY decreased as fluence increased, while groove depth increased. A parametric study aiming to find the best compromise between a low SEY and an acceptable ablation depth was carried out.

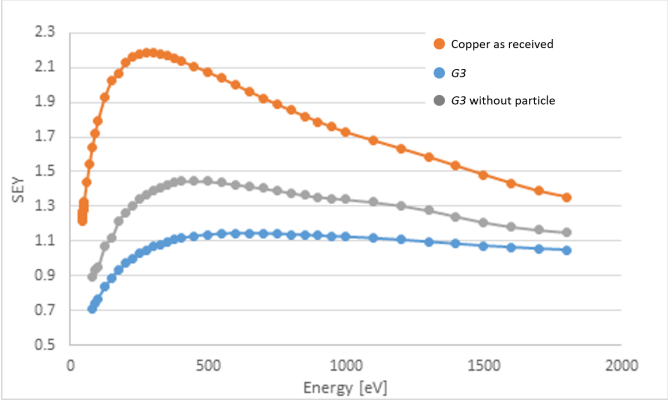

Figure 5.23: SEY curve as a function of the primary electron energy measured at CERN on a as received copper surface and on a laser-treated surface by *G3* parameters before and after that surface particles have been removed by ultrasonic cleaning.

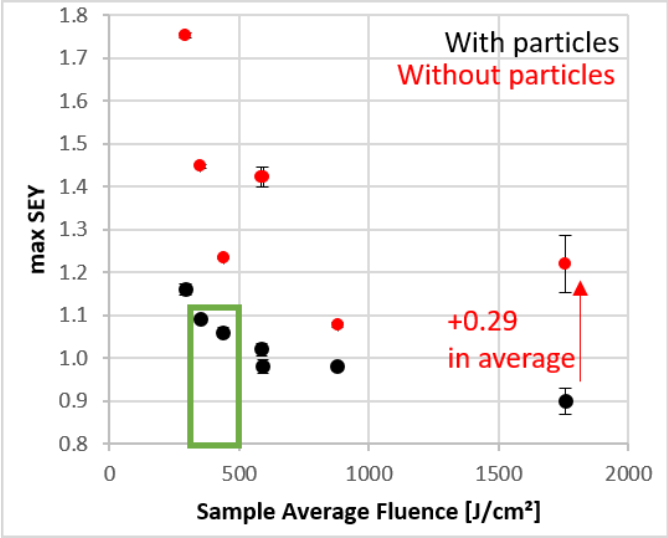

Figure 5.24: Maximum SEY curve of *Zeta 5* series samples, as a function of the average value of laser fluence. In black, samples with particles. In red, after particle removal by ultrasonic cleaning. The green rectangle defines the range of average irradiating fluence where the treated samples would fit the requirements for the application in accelerator environment (SEY < 1.1 and groove depth < 30 μm) meaning in these irradiation conditions that the average sample fluence has to be kept below 450 J.cm^{-2}.)

As illustrated in figure 3.38 c), the average fluence irradiating the sample should be below 500 J/cm^2 to fit the required groove depth. On the other hand, a value of SEY below 1.1 requires a fluence higher than 300 J/cm^2. The optimal set of parameters for the laser treatment have to be chosen as the resulting average fluence is in this window. The so-called *D7* set of parameters almost fit these requirements with an average fluence of 593 J/cm^2 (and a groove depth consequently slightly superior to 32 μm). Other requirements of the application of laser-treated surfaces in accelerator environment (time of processing, production of dust) are ongoing, to define the optimal set of parameters for laser processing.

Particle detachment when submitting the surface to mechanical solicitations has been documented in chapter 4. The influence of this modification on morphology is investigated in the following section. It was shown that a surface morphology with particles is needed to reach SEY requirements. The dependency of SEY as a function of the density of particles covering the sample had to be further investigated.

SEY measurement on *D7* samples

Table 5.2 presents the results of the analysis applied on *D7* samples. For instance, the maximum SEY measured on *D7 2019* samples was 0.98.

These results are an illustration of two scale morphology modifications in SEY reduction.

Table 5.2: Comparison of ablated mass, particle coverage and SEY measured on *D7* samples. Masses are expressed in mg.cm^{-2}.

Sample	*D7 2018*	*D7 2019*	*BS74*	*D7 2020*
Ablated mass	14.4	15.1	17.8	11.5
Particle coverage mass	No data	2.6	0.6	1.0
SEY	0.89	0.98	1.35	1.25

5.3.2.2 Small variations of particle surface density on SEY

Small variations of particle surface density would occur if treated surface is submitted to a quench during accelerator operation. Particles would be detached due to mechanical solicitations. The effect of particle detachment on SEY performance of the surface was evaluated in this section, by measuring the SEY on surfaces exposed to the extraction methods presented in chapter 4.

Comparing a reference sample and samples submitted to mechanical tests

SEY have been measured on a *D7 2019* sample exposed to 26 N.mm^{-3} static force, at room temperature, by centrifugation and compared to a reference sample.

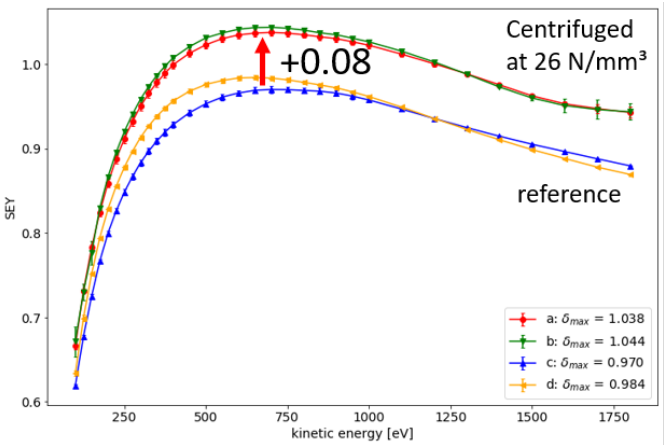

Figure 5.25: SEY curves comparing 3 measurements on a reference *D7 2019* sample and on a *D7 2019* sample submitted to 24 N.mm^{-3} static force, at room temperature, by centrifugation.

Any strong influence on SEY could be detected comparing samples before and after mechanical solicitation. Although the sample was submitted to a force comparable to the one produced during a quench, centrifugation was performed at room temperature and, therefore, particle detachment could be actually lower by a factor of 2 than the one that could occur during a quench at cryogenic temperatures. In addition, SEY measurement is sensible to surface chemical alteration. It is this difficult to link the small observed difference with the morphology change, especially after a small mechanical solicitation and considering the multiple handlings between SEY measurement and mechanical tests. For these two reasons, SEY measurements have been performed on laser shocked samples, where particle detachment was more important and where areas of reference and areas submitted to mechanical solicitations were present on the same sample.

Measurement performed on different areas of the same sample

SEY measurement were performed on laser-shocked samples, as shown in figure 5.26. High power density laser shocks detached 66 times more particles than centrifugation. For this reason, it can be considered as a conservative estimation of what could happened during a quench.

The radius indicated in figure 5.26 is the distance from the laser shock center. Laser beam radius was 1.5 mm. In this area, the surface was submitted to mechanical solicitations and particles were detached. In the range of 4 to 5 mm away from the center, the surface was not submitted to stresses. This is considered as the reference area.

SEY increase, measured on two *D7 2020* samples and one *BS74* sample, correlates the expected profile of the maximum deceleration which trigger particle detachments. SEY peak enlargement, compared to the force applied on particles, can be explained by the 1 mm wide beam radius of the electron gun used in SEY measurement. SEY increases could be attributed to mechanical stresses, without bias of chemical alteration due to a careful handling during the tests. SEY increases were 0.094, 0.103 and 0.097 for the two *D7 2020* samples and *BS74* sample, respectively. A SEY increase of such order a magnitude after particle detachment during a quench is not considered detrimental for the main function of the laser-treatment, *i.e.* electron cloud mitigation.

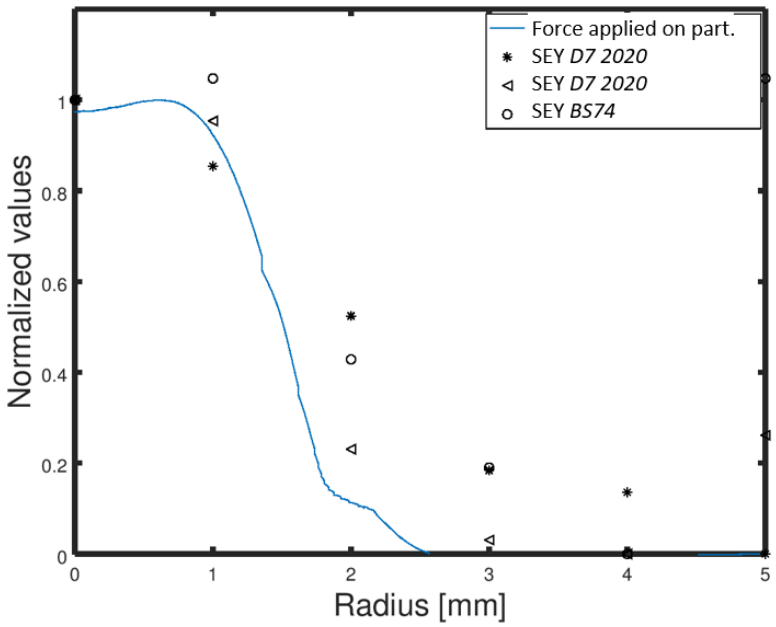

Figure 5.26: Comparison of the force applied on particles (scaled with maximum deceleration of the macroscopic surface simulated during the laser shock (blue line)) and the variation of SEY between the maximum value measured in the center of the laser shock and the minimum value measured in the range of 4 to 5 mm away from the center.

5.3.3 Conditioning of laser-treated surfaces

The conditioning effect has been first introduced in section 1.2.3.2 as an operational SEY reduction technique. The maximum SEY of the surface is reduced down to a saturated value when the surface is bombarded by electrons. The conditioning curve of an air exposed beam screen sample is illustrated in figure 5.27. From an initial value higher than 2, the SEY decreases to the minimum value of 1.15. At an irradiating dose of 1×10^{-4} C.mm^{-2}, SEY was measured to 1.5.

Conditioning measurements have been performed on laser-treated samples with a reduced particle coverage density (*i.e. BS74* whose particle coverage density was evaluated to 0.62 mg.cm^{-2}). Results showed that the dose (the quantity of electron irradiating the surface, or the duration of the beam scrubbing run) required to reach the target SEY value was significantly lower for the laser treated sample.

Even if, on a sample with reduced particle coverage density, the initial SEY value was significantly higher than 1.1, the fast (with respect to non-laser-treated samples) conditioning of these surfaces allowed to reach the value of 1 after a dose of 7×10^{-5} C.mm^{-2}.

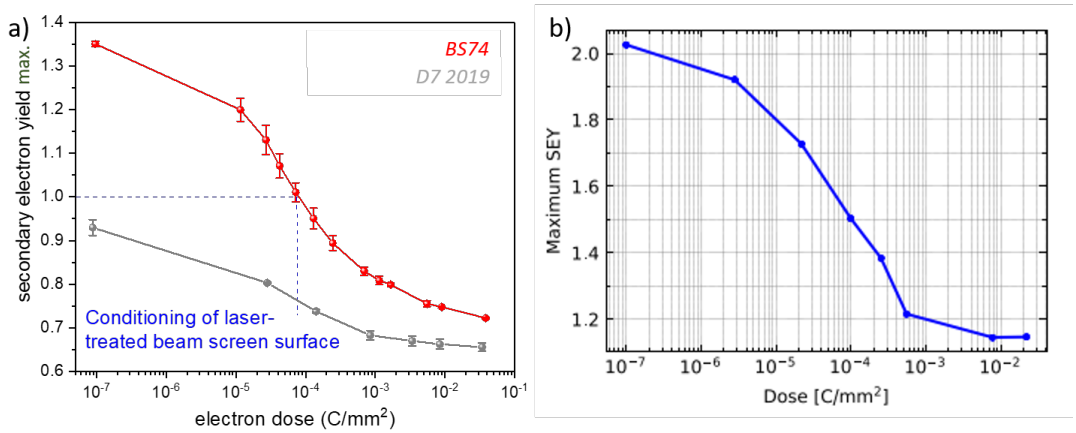

Figure 5.27: Evolution of maximum SEY of an air exposed sample as a function of irradiation dose. a) For *D7 2019* (high particle coverage density) and *BS74* (low particle coverage density) laser treated samples. Figure adapted form Marcel HIMMERLICH, CERN TE-VSC, in private communication. b) For a non-laser-treated sample extracted from the LHC beam screen [222].

5.3.4 Conclusions on laser-treated surfaces in the accelerator environment

A small decrease of particle coverage density due to particle detachment during a quench does not have a detrimental effect on SEY performance of the surface. Surface morphology was shown to be robust when exposed to the mechanical stresses expected during a quench. It could maintain its function of electron cloud mitigation.

On the other hand, it has been shown that dust is an intrinsic product of laser ablation. The two-scale (grooves and particle overlay) surface topology generated by this technique was nevertheless necessary to reach the target SEY value.

Dust produced during the treatment could rise issues for maintenance interventions on the vacuum system. Nevertheless, the deployment of a cleaning strategy to remove dust could significantly reduce particle surface density. Without the particle overlay, the surface would not fit SEY requirements. Nevertheless, it has been found that conditioning of laser treated surfaces (even without the particle overlay) is significantly better than for flat copper surfaces. This important result calls for the choice of more moderate laser treatment parameters, to limit the amount of ablated material and reduce the concern about dust generation. Even if SEY of this surface does not fit the requirement initially, it may be lower by a fast conditioning, once the accelerator operation starts.

Conclusion and perspectives

The implementation of an *in-situ* laser treatment of the inner surface of the beam screen is currently under development at CERN for the mitigation of the electron cloud. The laser pulsed irradiation generates two-scale morphology modification of the surface: 50-μm-period sinusoidal grooves covered by a population of sub-micrometric particles. It efficiently reduces the SEY by a geometric effect below the threshold of the electron cloud build-up.

Nevertheless, the implementation of the laser-treated surface already appears like a compromise between mitigating the electron cloud, and, as a counterpart, increasing the heat load because of the impedance enhancement due to the surface roughness. Both characteristics are linked to the morphological properties of the surface.

The thesis establishes relations between superficial topography, particle adhesion and compatibility for ultra high vacuum applications.

Investigations

This thesis aimed at assessing the mechanical integrity and suitability of such surface treatment for an application in accelerators operating at cryogenic temperature. Another objective of the thesis was the development of quantification methodologies of the dust created during laser-assisted surface structuration, the amount of matter present as sub-micrometric particle network layer after the treatment and the amount which could be detached due to mechanical stresses during accelerator operation.

The developed quantification methods have been applied on the characterisation of the samples treated with *D7* parameters, This configuration of parameters has been chosen among 160 tested configurations of the inputs parameters of the laser treatment. The morphology of the *D7* samples has been found to be optimal after SEY and groove depth measurement.

The multi-scale surface morphology transformations occurring during the pulsed laser treatment have been described based on a literature review of laser-matter interaction and on microscopic observations carried out on treated samples. Microstructural analyses by Transmission Electron Microscopy (TEM) highlighted the presence of a 30-nm-thick oxide layer formed at the surface of laser-processed material despite the nitrogen protective atmosphere used during the treatment.

The ablated material mass, estimated from cross sectional microscopy, showed a

linear increase with irradiating energy density. A part of this matter, estimated around 17 % for the 532-ns-long wavelength, 10 ps irradiation under nitrogen atmosphere, recondensed on the grooved surface creating the particle overlayer. The rest, unattached dust was evaluated at 11.8 mg.cm^{-2} on the treated surface. Electron tomography by FIB-SEM was applied for qualitative characterisation of particles at the nano-scale, in particular concerning their size distribution.

Mechanical characterisations focused on applying non-contact forces on particles to assess their adhesion. Two extraction techniques, relying on inertia forces, were developed, aiming to explore a large range of amplitude and duration:

- In centrifuges, the acceleration reached on the sample surface was 275 000 g leading to a reproducible static force field up to 24 N.mm^{-3} pulling the particles out of the surface.This value is representative of the mechanical solicitations which happen during a magnet quench in LHC;
- The LAser Shock Adhesion Test (LASAT), developed to assess the adhesion of coatings by spallation, was utilized to accelerate the surface of treated samples, including samples refrigerated at cryogenic temperatures. Pressure shock waves generated by nanosecond laser irradiation produce sharp velocity variations of the surface. Decelerations, and therefore applied inertia forces were evaluated from the dynamics of the sample macroscopic surface.

Recuperation and analysis of detached particles allowed the quantification of ejected material as a function of the mechanical stresses. The mass of particles, which could be detached during the accelerator operation has been extrapolated from these results.

It was shown that the SEY would not be detrimentally increased by a slight decrease of the particle coverage density due electromagnetic forces generated by a magnet quench.

The possibility that certain elements of the morphology detach from the treated surface and interact with the proton beam was a major concern when using this technology in the particle accelerator. The effects of the detachment of a copper particle from the surface during the operation of the accelerator and of its interaction with the beam were evaluated depending on the size of the incident particle.

The risk of detrimental release particle-beam interaction is limited, because the critical size of interaction which may trigger a beam dump has been estimated to be 20 μm of copper, significantly higher than the size of the particles covering the surface and because the interaction of the proton beam with small particles seems to not trigger cascading effect and massive detachment of particles.

Conclusions

To conclude, the implementation of the laser treatment technology could efficiently reduce the SEY of the surface and mitigate the electron cloud, with a contained increase of the heat deposition due to the surface impedance. Based on the mechanical and morphological characterisations performed on the laser-treated surface in the framework of

this thesis, the surface has been found to be robust to the magnet quench considered to generate the most prejudicial mechanical stress during accelerator operation. The presence of copper particles should not disturb the operation of the accelerator by triggering beam dump.

Perspectives

Although particles would not be a problem for the accelerator operation, the detached material and even more, the massive volatile dust produced during the treatment could be activated and raise some radioprotection issues for the maintenance of the vacuum system.

Based on the results of the dust quantification and the properties of the beam screen magnets, where the laser treatment could be implemented, table 5.3 presents the total weight of particles generated during the laser treatment or detached from the surface during a magnet quench. Hundreds of grams of volatile copper particles could lie in the vacuum system during accelerator operation and be activated. Particles may be spread and flushed over several meters when venting the system, which might impose a strict protocol for removal of the vacuum equipment (pumps, valves).

Table 5.3: Dust produced during the treatment and material which could be detached during a quench for each magnet where the laser treatment could be implemented. The Beam Screen (BS) type is the inner diameter of corresponding cold bore in mm.

Magnet	BS Type	Length [m]	Dust produced during the treatment [g]	Detached material during a quench [g]
MB	48.5	15.56	272	1.15
D1	74	2.62	69	0.29
Q1	53	7.92	147	0.62
Q2	63	13.23	295	1.25
Q3	63	9.74	218	0.92

The concern for maintenance operations about the amount of dust produced during the treatment should motivate the choice of alternative treatment parameters which would ablate less material. Surface structuration using a lower range of energy density is being considered. It could rely on laser-induced periodic surface structures (LIPSS) created by interference of the incident laser radiation with the surface electromagnetic wave generated on a rough interface.

An implementable cleaning strategy aiming at removing or re-fixing the unattached or weakly attached particles could also be considered. A *vacuum cleaning* will be installed to suck the dust out of the beam screen while treating the surface *in-situ*. The re-irradiation of the created features at the surface [85] could also be a strategy to investigate.

The dust creation is intrinsic for laser ablation which generates the two-scale surface

topology required to reach the SEY target value. The treated surface might not fulfill the SEY objective after a cleaning strategy which could be deployed, or after a treatment ablating less material.

Nevertheless, the conditioning of the laser treated surface (even without the particle overlay) is significantly better than the copper original surface. The important result calls for the choice of laser treatment parameters which may not ablate such a large amount of material, reducing the concern about the dust generation. Even if the SEY of this surface does not fit the requirement initially, it may be lower by a fast conditioning once the accelerator operation starts.

The characterisation techniques were applied on samples treated by the same configuration of parameters (called *D7*). A spread of the results was noticed depending on the batch of samples used and could be attributed to a slight change of the gas environment during the laser treatment. Further investigations on the laser treatment proceeding which will be now performed at CERN, should lead to a more consistent and reliable sample production. In particular, parameters have be well controlled to ensure a reliable treatment of the real components,

Another aspect to be improved for a large scale production in LHC, is the rate of treatment. In the current configuration, 24 cm^2 are treated per hour, the treatment of two beam screen of a entire main dipole magnet would require 80 days of 24/24 operation. It calls for a fully automotive and monitored treatment process or even the development of a new treatment strategy able to speed up the beam screen treatment.

Conclusion et perspectives

La mise en œuvre d'un traitement laser *in-situ* de la surface interne de l'écran de faisceau est actuellement en cours de développement au CERN pour l'atténuation du nuage d'électrons. L'irradiation pulsée laser génère une modification morphologique à deux échelles de la surface : des sillons sinusoïdaux de 50 μm de période recouverts d'une population de particules sub-micrométriques. Il réduit efficacement le taux d'électrons secondaire (SEY) par effet géométrique en dessous du seuil de formation du nuage d'électrons.

Néanmoins, l'augmentation de la rugosité de la surface détériore d'autres fonctionnalités de la surface, en particulier l'impédance de la surface.

Le SEY et l'impedance sont donc des propriétés liées à la morphologie de la surface. La thèse cherche à établir les relations entre la topologie de la surface traitée par laser, l'adhesion des particules et la compatibilité aux applications à l'ultra vide dans les accélérateurs de particules.

Travaux

L'objectif de la thèse est la caractérisation mécanique de la surface et la vérification de la compatibilité à l'opération de la surface à température cryogénique ainsi que le développement des méthodes de quantification de la poussière créée pendant le traitement laser et de la matière redéposée sous forme d'un empilement de structures submicrometriques après le traitement et la quantité pouvant être décrochée sous les sollicitations mécaniques pendant l'opération de l'accélérateur.

L'analyse quantitative et qualitative des caractéristiques à l'échelle des sillons et des particules a été menée sur les échantillons *D7* dont la morphologie a été jugée optimale après une étude paramétrique où les mesures de profondeur de sillons et de SEY permirent les choix des paramètres idéaux parmi les 160 configurations testées.

L'étude microstructurale par Microscopie Electronique en Transmission (MET) a mis en évidence les changements de microstructure et les transformations morphologiques et chimiques lors du traitement. En particulier, une fine couche d'oxyde (30 nm) a été observée malgré l'atmosphère d'azote protectrice utilisée pendant le traitement.

La masse de matériau évaporé durant le traitement a été évaluée à partir de l'observation des profils de la surface en vue de coupe. Elle augmente proportionnellement à la densité d'énergie déposée par l'irradiation laser. Une partie de cette matière, estimée à 17

% pour une irradiation à 532 nm et 10 ps, est re-condensée sur la surface sous forme de particules. Le reste est perdu sous forme de poussière pendant le traitement laser. Ceci représente 11.8 mg de cuivre par centimètre carré de surface traitée. La distribution en taille des particules présentes sur la surface traitée par laser a été évaluée par nano-tomographie effectuée par MEB-FIB.

Lors du fonctionnement du LHC, la paroi du système à vide est soumise à des forces électromagnétiques de l'ordre de 30 N.mm^{-3} et à des variations entre température ambiante et 4 K. Afin de qualifier, en laboratoire, l'adhérence des particules dans des conditions similaires, deux méthodes d'extraction de particules ont été mises en place, reposant sur l'application d'accélérations générant des forces d'inertie dont les durées d'application et les amplitudes ont été sélectionnées.

- Les accélérations atteintes (jusqu'à 275 000 g) à la surface des échantillons placés dans des centrifugeuses ont permis d'atteindre des forces statiques volumiques de l'ordre de 24 N.mm^{-3} ;
- Le LAser Shock Adhesion Test (LASAT), habituellement dédié aux essais d'adhérence de revêtements par délamination, a aussi été appliqué pour l'extraction de particules présentes à la surface, y compris pour des échantillons refroidis à températures cryogéniques.

Pour les deux méthodes, la collecte et l'analyse des particules détachées ont permis la quantification de la masse et de la morphologie du matériau éjecté en fonction des sollicitations mécaniques et de la température de la surface. 4 % des particules présentes originellement à la surface – soit 0.1 mg.cm^{-2}- sont décollées par les sollicitations mécaniques considérées dans ce travail.

Il a été montré que le SEY de la surface ne serait pas affecté par le détachement de particules à la suite des sollicitations mécaniques liées forces électromagnétiques dans l'accélérateur. Les risques pour l'opération de l'accélérateur, inhérents au détachement et à l'interaction avec le faisceau d'une particule composante de la surface ont été jugés contenus. En effet, la taille critique à partir de laquelle l'interaction de la particule avec le faisceau déclenche son extraction a été évaluées à 20 μm. Pour les particules plus petites, la possibilité d'un détachement en cascade après l'interaction avec le faisceau de ces particules et leur collision avec la surface traitée a été écartée.

Conclusions

Pour conclure, à partir des caractérisations mécaniques et morphologiques réalisées sur la surface traitée, dans le cadre de cette thèse, la mise en place de la technologie de traitement au laser pourrait réduire efficacement le SEY de la surface et diminuer le nuage d'électrons, avec une augmentation contenue du dépôt de chaleur dû à l'impédance de surface. La présence de particules de cuivre ne perturberait pas le fonctionnement de l'accélérateur et la surface s'est avérée robuste aux sollicitations mécaniques qu'elle pourrait endurer pendant un *quench* (une transition rapide de l'état supra conducteur à

l'état résistif) de l'aimant où elle est installée. Ces sollicitations sont considérées comme les contraintes mécaniques les plus sévères pendant le fonctionnement de l'accélérateur.

Perspectives

Néanmoins, la quantité de cuivre ainsi décollée, et plus encore, l'importante production de poussière à la suite du traitement robotisé, *in-situ*, en milieu confiné, sont des questions qui demeurent ouvertes.

L'estimation, certes conservative, conduit une quantité de cuivre pouvant aller jusqu'à plusieurs centaines de grammes (voir le tableau 5.4). Une valeur jugée importante dans la mesure ou cette poussière reposant dans l'écran de faisceau pourrait s'activer et être dispersée lors de l'ouverture du système à vide. La contamination radiologique des équipements tels que les pompes et vannes conduirait à des mesures de protection lourdes.

Table 5.4: Poussière produite pendant le traitement et matière détachée pendant un *quench*. Le type d'écran de faisceau correspondant au diametre interieur du tube de la masse froide correspondant en mm.

Aimant	Type d'écran	Longeur [m]	Poussière produite pendant le traitement [g]	Matière détachée pendant un *quench* [g]
MB	48.5	15.56	272	1.15
D1	74	2.62	69	0.29
Q1	53	7.92	147	0.62
Q2	63	13.23	295	1.25
Q3	63	9.74	218	0.92

Ces questions motivent la réflexion sur une procédure de traitement alternatifve qui réduirait la production de poussière. La re-irradiation de la surface traitée pour refondre les poussières ou l'utilisation des paramètres de traitements différents conduisant à une irradiation avec une fluence moindre et donc une ablation de matière moindre pourraient être envisagée. La structuration de surface reposant sur le phénomène de LIPSS est par exemple investiguée. L'établissement d'une procédure standard de nettoyage consécutif au traitement *in-situ* de l'écran de faisceau s'impose alors comme un autre aspect technique du projet de traitement laser des surfaces.

L'effet des particules couvrant la surface sur la réduction du SEY a été évalué et se révèle être essentiel pour obtenir un SEY en dessous du seuil de création du nuage d'électron en limitant la profondeur des sillons aux impératifs liés à l'impédance. Le retrait d'une partie de structures de surface réduit les performances de la surface en termes de SEY.

Néanmoins, il a été montré que le conditionnement de la surface traitée au laser (même avec une densité de particules présente à la surface plus faible) est nettement meilleur que la surface d'origine en cuivre. Ce résultat encourageant autorise le choix des paramètres de traitement au laser qui génère moins de poussière aboutissant à une

surface dont le SEY initial est superieur à la valeur cible, mais qui pourrait être abaissé par un conditionnement rapide.

Les techniques de caractérisation ont été appliquées sur des échantillons dont les paramètres de traitement étaient une configuration *D7* fixe. La dispersion des résultats constatée en fonction du lot d'échantillons utilisé pourrait être attribuée à un léger changement de l'environnement gazeux lors du traitement laser. Des investigations plus poussées quant à la procédure de traitement, qui sera désormais réalisées au CERN, devraient conduire à une production d'échantillons plus fiable et plus reproductible. *In fine*, l'ensemble des paramètres doivent etre maîtrisés pour assurer un traitement fiable des composants réels dans l'accélérateur.

La rapidité du traitement est un autre aspect à améliorer pour un déploiement de la technologie à grande échelle dans le LHC. Dans la configuration actuelle, 24 cm^2 de surface interne des écrans de faisceau sont traités en une heure. Le traitement des deux écrans de faisceau d'un dipôle *MB* entier nécessiterait 80 jours de fonctionnement 24h/24. Cela nécessite un processus de traitement entièrement automatisé et motive le développement d'une stratégie de traitement plus rapide.

Appendix A

Values applied for copper OFE

Properties	Unit	Value
Atomic Properties		
Density	$g.cm^{-3}$	8.96
Optical Properties		
Absorptivity, α (λ= 800 nm, T_e=300 K)	m^{-1}	12.8×10^7
Refectivity, R (λ= 800 nm, T_e=300 K)		0.9645
Electron heat capacity, C_{e0} (T_e=300 K)	$J.m^{-3}.K^{-2}$	96.6
Lattice heat capacity, C_l	$J.m^{-3}.K^{-2}$	3.39×10^6
Electron thermal conductivity, k_{e0} (Te=300 K)	$W.m^{-1}.K^{-1}$	401
Electron-phonon coupling coefficient, G_0	$W.m^{-3}.K^{-1}$	12×10^{16}
Optical penetration depth, $L_P = \frac{1}{\alpha}$	nm	7.8
Material specific constants C		386.5
Material specific constants s [111]		0.14
Thermal Properties		
Thermal conductivity, k [140]	$W.m^{-1}.K^{-1}$	380 (solid), 170 (liquid)
Specific heat, C_p	$J.kg^{-1}.K^{-1}$	420 (solid), 494 (liquid)
Mass density, ρ	$kg.m^{-3}$	8960 (solid), 8000 (liquid)
Melting point, T_m	K	1358
Boiling point, T_b	K	2836
Heat of fusion, ΔH_{sl}	$J.mol^{-1}$	1.3×10^4
Heat of vaporisation, ΔH_{lv}	$J.mol^{-1}$	3.048×10^5
Mechanical Properties		
Elasticity		
Yound Modulus E	GPa	130
Poissn ν		0.345
Lamé λ	GPa	108
Lamé μ	GPa	48
Plasticity		
Perfect plasticity A	MPa	90
Strain Hardening B	MPa	292
Strain Hardening n		0.31
Viscoplasticity (Johnson-Cook) C		0.022
Viscoplasticity (Johnson-Cook) m		1.09
Hydrodynamic parameters		
Sound celerity C_0 [184]	$m.s^{-1}$	3933
Hugoniot coefficient [184] S		1.489
Mie Grüneisen Γ_0		
Electrical Properties		
RRR at 4 K		100
RRR at 20 K		100
Resistivity, ρ_{elec}		1.68×10^{-10}

Appendix B

Parameters of the laser treatment

This appendix presents the parameters used to treated the samples analysed in this thesis.

The measurements (*i.e.* SEY, groove depth, ablated mass) made on that samples are also shown in the tables.

Rep rate series						
Name		1	2	3	4	5
λ	nm	532	532	532	532	532
τ	ps	10	10	10	10	10
Spot size	um	12	12	12	12	12
Rep rate	kHz	200	400	600	800	1000
Pulse energy	uJ	4.8	4.8	4.8	4.8	4.8
Hatch Distance	um	24	24	24	24	24
Scan speed	mm/s	10	20	30	40	50
Power	W	0.96	1.92	2.88	3.84	4.8
Average Fluence/pulse	J/cm²	4.24	4.24	4.24	4.24	4.24
Beam Standard deviation	um	3	3	3	3	3
Max Fluence/pulse	J/cm²	8.50	8.50	8.50	8.50	8.50
Distance between pulse	um	0.05	0.05	0.05	0.05	0.05
Pulse/spot	1	240	240	240	240	240
Real Fluence max	J/cm²	1221	1221	1221	1221	1221
Spot Average Fluence	J/cm²	800	800	800	800	800
Sample Average Fluence	J/cm²	400	400	400	400	400
SEY	1	0.87	0.92	0.96	0.97	1
Groove depth avg	um	27.98	20.65	20.80	20.74	27.00

Figure B.1: University of Dundee. April 2017.

16 series																	
Name		A	B	C	D	E	F	G	H	I	J	K	L	M	N	O	P
λ	nm	532	532	532	532	532	532	532	532	532	532	532	532	532	532	532	532
τ	ps	10	10	10	10	10	10	10	10	10	10	10	10	10	10	10	10
Spot size	um	52	52	52	52	52	52	52	52	52	52	52	52	52	52	52	52
Rep rate	kHz	200	200	200	200	200	200	200	200	200	200	200	200	200	200	200	200
Pulse energy	uJ	94	94	94	94	94	94	94	94	94	94	94	94	94	39	54	68
Hatch Distance	um	104	104	104	104	91	91	91	91	65	26	39	52	65	91	91	91
Scan speed	mm/s	10	20	30	43	10	20	30	43	10	43	43	43	43	10	10	10
Power	W	18.78	18.78	18.78	18.78	18.78	18.78	18.78	18.78	18.78	18.78	18.78	18.78	18.78	7.76	10.80	13.60
Average Fluence/pulse	J/cm²	4.42	4.42	4.42	4.42	4.42	4.42	4.42	4.42	4.42	4.42	4.42	4.42	4.42	1.83	2.54	3.20
Beam Standard deviation	cm	12.99	12.99	12.99	12.99	12.99	12.99	12.99	12.99	12.99	12.99	12.99	12.99	12.99	12.99	12.99	12.99
Max Fluence/pulse	J/cm²	8.85	8.85	8.85	8.85	8.85	8.85	8.85	8.85	8.85	8.85	8.85	8.85	8.85	3.66	5.09	6.41
Distance between pulse	um	0.05	0.10	0.15	0.22	0.05	0.10	0.15	0.22	0.05	0.22	0.22	0.22	0.22	0.05	0.05	0.05
Pulse/spot	1	1040	520	347	240	1040	520	347	240	1040	240	240	240	240	1040	1040	1040
Real Fluence max	J/cm²	5506	2753	1835	1272	5506	2753	1835	1272	5506	1272	1272	1272	1272	2275	3167	3988
Spot Average Fluence	J/cm²	3611	1806	1204	833	3611	1806	1204	833	3611	833	833	833	833	1492	2077	2615
Sample Average Fluence	J/cm²	1806	903	602	417	2064	1032	688	476	2889	1667	1111	833	667	853	1187	1495
SEY	1	0.85	0.89	1.07	1.28	0.83	0.93	1.40	1.38	0.82	0.97	1.12	1.10	1.31		0.91	0.82
Groove depth avg	um	64.66	42.91			84.95	46.81								50.11	57.78	51.83

Figure B.2: University of Dundee. May 2017.

36 series

Name		A	B	C	D	E	F	G	H	I	J	K	L	M	N	O	P	Q	R	S	T
λ	nm	532	532	532	532	532	532	532	532	532	532	532	532	532	532	532	532	532	532	532	532
τ	ps	10	10	10	10	10	10	10	10	10	10	10	10	10	10	10	10	10	10	10	10
Spot size	um	52	52	52	52	52	52	52	52	52	52	52	52	52	52	52	52	52	52	52	52
Rep rate	kHz	200	200	200	200	200	200	200	200	200	200	200	200	200	200	200	200	200	200	200	200
Pulse energy	uJ	5	10	15	20	25	30	35	40	45	50	55	60	25	25	25	25	40	40	40	40
Hatch Distance	um	91	91	91	91	91	91	91	91	91	91	91	91	91	91	91	91	91	91	91	91
Scan speed	mm/s	10	10	10	10	10	10	10	10	10	10	10	10	10	15	20	25	10	15	20	25
Power	W	1	2	3	4	5	6	7	8	9	10	11	12	5	5	5	5	8	8	8	8
Fluence/pulse	J/cm²	0.24	0.47	0.71	0.94	1.18	1.41	1.65	1.88	2.12	2.35	2.59	2.83	1.18	1.18	1.18	1.18	1.88	1.88	1.88	1.88
Beam Standard deviation	cm	13	13	13	13	13	13	13	13	13	13	13	13	13	13	13	13	13	13	13	13
Max Fluence/pulse	J/cm²	0.47	0.94	1.41	1.89	2.36	2.83	3.30	3.77	4.24	4.71	5.19	5.66	2.36	2.36	2.36	2.36	3.77	3.77	3.77	3.77
Distance between pulse	um	0.05	0.05	0.05	0.05	0.05	0.05	0.05	0.05	0.05	0.05	0.05	0.05	0.05	0.075	0.1	0.125	0.05	0.075	0.1	0.125
Pulse/spot	1	1040	1040	1040	1040	1040	1040	1040	1040	1040	1040	1040	1040	1040	693	520	416	1040	693	520	416
Real Fluence max	J/cm²	293	586	880	1173	1466	1759	2052	2346	2639	2932	3225	3518	1466	977	733	587	2346	1563	1173	939
Spot Average Fluence	J/cm²	192	385	577	769	962	1154	1346	1538	1731	1923	2115	2308	962	641	481	385	1538	1026	769	615
Sample Average Fluence	J/cm²	110	220	330	440	549	659	769	879	989	1099	1209	1319	549	366	275	220	879	586	440	352
SEY	1	1.87		1.05					0.88			0.88	0.87	0.96	1.07	1.21	1.37		0.95	1.10	1.19
Groove depth avg	um	62.00										91.72	118.90						55.43		

36 series

Name		U	V	W	X	Y	Z	AA	BB	CC	DD	EE	FF	GG	HH	II	JJ
λ	nm	532	532	532	532	532	532	532	532	532	532	532	532	532	532	532	532
τ	ps	10	10	10	10	10	10	10	10	10	10	10	10	10	10	10	10
Spot size	um	52	52	52	52	52	52	52	52	52	52	52	52	52	52	52	52
Rep rate	kHz	200	200	200	200	200	200	200	200	200	200	200	200	200	200	200	200
Pulse energy	uJ	55	55	55	55	40	40	40	40	40	40	55	55	55	55	55	55
Hatch Distance	um	91	91	91	91	26	52	91	26	52	91	26	52	91	26	52	91
Scan speed	mm/s	10	15	20	25	10	10	10	20	20	20	10	10	10	20	20	20
Power	W	11	11	11	11	8	8	8	8	8	8	11	11	11	11	11	11
Fluence/pulse	J/cm²	2.59	2.59	2.59	2.59	1.88	1.88	1.88	1.88	1.88	1.88	2.59	2.59	2.59	2.59	2.59	2.59
Beam Standard deviation	cm	13	13	13	13	13	13	13	13	13	13	13	13	13	13	13	12.99
Max Fluence/pulse	J/cm²	5.19	5.19	5.19	5.19	3.77	3.77	3.77	3.77	3.77	3.77	5.19	5.19	5.19	5.19	5.19	5.19
Distance between pulse	um	0.05	0.075	0.1	0.125	0.05	0.05	0.05	0.1	0.1	0.1	0.05	0.05	0.05	0.1	0.1	0.1
Pulse/spot	1	1040	693	520	416	1040	1040	1040	520	520	520	1040	1040	1040	520	520	520
Real Fluence max	J/cm²	3225	2149	1613	1291	2346	2346	2346	1173	1173	1173	3225	3225	3225	1613	1613	1613
Spot Average Fluence	J/cm²	2115	1410	1058	846	1538	1538	1538	769	769	769	2115	2115	2115	1058	1058	1058
Sample Average Fluence	J/cm²	1209	806	604	484	3077	1538	879	1538	769	440	4231	2115	1209	2115	1058	604
SEY	1		0.89	0.97	1.14	0.82	0.82		0.88	0.97							
Groove depth avg	um	72.02				24.29			34.16								

Figure B.3: University of Dundee. June 2017.

Alpha

Name		A1	A2	A3	A4	A5	A6	A7	A8	A9	A10	A11	A12
λ	nm	532	532	532	532	532	532	532	532	532	532	532	532
τ	ps	10	10	10	10	10	10	10	10	10	10	10	10
Spot size	um	52	52	52	52	52	52	52	52	52	52	52	52
Rep rate	kHz	200	200	200	200	300	300	300	300	300	300	300	300
Pulse energy	uJ	50	50	50	50	50	50	50	50	60	60	60	60
Hatch Distance	um	100	115	130	145	100	115	130	145	100	115	130	145
Scan speed	mm/s	20	20	20	20	30	30	30	30	30	30	30	30
Power	W	10	10	10	10	15	15	15	15	18	18	18	18
Fluence/pulse	J/cm²	2.35	2.35	2.35	2.35	2.35	2.35	2.35	2.35	2.83	2.83	2.83	2.83
Beam Standard deviation	cm	13	13	13	13	13	13	13	13	13	13	13	13
Max Fluence/pulse	J/cm²	4.71	4.71	4.71	4.71	4.71	4.71	4.71	4.71	5.66	5.66	5.66	5.66
Distance between pulses	um	0.10	0.10	0.10	0.10	0.10	0.10	0.10	0.10	0.10	0.10	0.10	0.10
Pulse/spot	1	520	520	520	520	520	520	520	520	520	520	520	520
Real Fluence max	J/cm²	1466	1466	1466	1466	1466	1466	1466	1466	1760	1760	1760	1760
Spot Average Fluence	J/cm²	962	962	962	962	962	962	962	962	1154	1154	1154	1154
Sample Average Fluence	J/cm²	500	435	385	345	500	435	385	345	600	522	462	414
SEY	1	0.94	1.00	1.04	1.08	1.04	1.07		1.16	1.01	1.07	1.09	
Groove depth avg	um	62.37				94.06						99.55	

Figure B.4: University of Dundee. August 2017.

Beta

Name		B0	B1	B2	B3	B4	B5	B6	B7	B8	B9	B10	B11	B12	B13	B14	B15	B16	B17
λ	nm	532	532	532	532	532	532	532	532	532	532	532	532	532	532	532	532	532	532
τ	ps	10	10	10	10	10	10	10	10	10	10	10	10	10	10	10	10	10	10
Spot size	um	52	52	52	52	52	52	52	52	52	52	52	52	52	52	52	52	52	52
Rep rate	kHz	200	200	200	200	200	200	250	300	400	200	200	300	300	300	300	200	200	200
Pulse energy	uJ	40	40	40	60	60	60	40	40	40	40	40	40	40	40	40	40	40	40
Hatch Distance	um	52	52	52	52	52	52	52	52	52	65	78	65	78	65	78	26	26	26
Scan speed	mm/s	20	25	30	20	25	30	25	30	40	20	20	30	30	35	35	10	20	30
Power	W	8	8	8	12	12	12	10	12	16	8	8	12	12	12	12	8	8	8
Fluence/pulse	J/cm²	1.88	1.88	1.88	2.83	2.83	2.83	1.88	1.88	1.88	1.88	1.88	1.88	1.88	1.88	1.88	1.88	1.88	1.88
Beam Standard deviation	cm	12.99	12.99	12.99	12.99	12.99	12.99	12.99	12.99	12.99	12.99	12.99	12.99	12.99	12.99	12.99	12.99	12.99	12.99
Max Fluence/pulse	J/cm²	3.77	3.77	3.77	5.66	5.66	5.66	3.77	3.77	3.77	3.77	3.77	3.77	3.77	3.77	3.77	3.77	3.77	3.77
Distance between pulse	um	0.1	0.13	0.15	0.10	0.13	0.15	0.10	0.10	0.10	0.10	0.10	0.10	0.10	0.12	0.12	0.05	0.10	0.15
Pulse/spot	1	520	416	347	520	416	347	520	520	520	520	520	520	520	446	446	1040	520	347
Real Fluence max	J/cm²	1173	939	782	1760	1408	1173	1173	1173	1173	1173	1173	1173	1173	1005	1005	2346	1173	782
Spot Average Fluence	J/cm²	769	615	513	1154	923	769	769	769	769	769	769	769	769	659	659	1538	769	513
Sample Average Fluence	J/cm²	769	615	513	1154	923	769	769	769	769	615	513	615	513	527	440	3077	1538	1026
SEY	1	1.08		1.44	1.03		1.15	1.12		1.19	1.01	1.08	1.13	1.12	1.16	1.17	1.13		1.40
Groove depth avg	um	46.88			71.14						52.88	41.53		44.54					

Figure B.5: University of Dundee. November 2017.

Gamma																	
Name		G1	G2	G3	G4	G5	G6	G7	G8	G9	G10	G11	G12	G13	G14	G15	G16
λ	nm	532	532	532	532	532	532	532	532	532	532	532	532	532	532	532	532
τ	ps	10	10	10	10	10	10	10	10	10	10	10	10	10	10	10	10
Spot size	um	52	52	52	52	52	52	52	52	52	52	52	52	52	52	52	52
Rep rate	kHz	200	200	200	200	200	200	200	200	200	200	200	200	200	200	200	200
Pulse energy	uJ	15	20	25	30	15	20	25	30	15	20	25	30	15	20	25	30
Hatch Distance	um	55	55	55	55	65	65	65	65	65	65	65	65	65	65	65	65
Scan speed	mm/s	15	15	15	15	10	10	10	10	15	15	15	15	20	20	20	20
Power	W	3	4	5	6	3	4	5	6	3	4	5	6	3	4	5	6
Average Fluence/pulse	J/cm²	0.71	0.94	1.18	1.41	0.71	0.94	1.18	1.41	0.71	0.94	1.18	1.41	0.71	0.94	1.18	1.41
Beam Standard deviation	cm	13	13	13	13	13	13	13	13	13	13	13	13	13	13	13	13
Max Fluence/pulse	J/cm²	1.41	1.89	2.36	2.83	1.41	1.89	2.36	2.83	1.41	1.89	2.36	2.83	1.41	1.89	2.36	2.83
Distance between pulse	um	0.08	0.08	0.08	0.08	0.05	0.05	0.05	0.05	0.08	0.08	0.08	0.08	0.10	0.10	0.10	0.10
Pulse/spot	1	693	693	693	693	1040	1040	1040	1040	693	693	693	693	520	520	520	520
Real Fluence max	J/cm²	586	782	977	1172	880	1173	1466	1759	586	782	977	1172	440	587	733	880
Spot Average Fluence	J/cm²	385	513	641	769	577	769	962	1154	385	513	641	769	288	385	481	577
Sample Average Fluence	J/cm²	364	485	606	727	462	615	769	923	308	410	513	615	231	308	385	462
SEY	1	1.25		1.19	1.17	1.32	1.26	1.20		1.12	1.07		1.13				
Groove depth avg	um	21.87	28.19	33.04	37.22	20.33	25.13	29.31	32.50	35.46	44.85	50.13	56.27	12.23	14.69	16.84	14.92
Ablated mass	mg/cm²	8.26	11.05	14.78	17.12												

Figure B.6: University of Dundee. January 2018.

Delta																					
Name		D1	D2	D3	D4	D5	D6	D7	D8	D9	D10	D11	D12	D13	D14	D15	D16	D17	D18	D19=G1	D20=B10
λ	nm	532	532	532	532	532	532	532	532	532	532	532	532	532	532	532	532	532	532	532	532
τ	ps	10	10	10	10	10	10	10	10	10	10	10	10	10	10	10	10	10	10	10	10
Spot size	um	52	52	52	52	52	52	52	52	52	52	52	52	52	52	52	52	52	52	52	52
Rep rate	kHz	200	200	200	200	200	200	200	200	200	200	200	200	200	200	200	200	200	200	200	200
Pulse energy	uJ	15	15	15	15	20	20	20	20	20	20	20	20	20	20	25	25	25	25	15	40
Hatch Distance	um	35	40	45	50	35	40	45	50	55	35	40	45	50	55	40	45	50	55	55	78
Scan speed	mm/s	10	10	10	10	15	15	15	15	15	10	10	10	10	10	10	10	10	10	15	20
Power	W	3	3	3	3	4	4	4	4	4	4	4	4	4	4	5	5	5	5	3	8
Fluence/pulse	J/cm²	0.71	0.71	0.71	0.71	0.94	0.94	0.94	0.94	0.94	0.94	0.94	0.94	0.94	0.94	1.18	1.18	1.18	1.18	0.71	1.88
Beam Standard deviation	cm	13	13	13	13	13	13	13	13	13	13	13	13	13	13	13	13	13	13	13	13
Max Fluence/pulse	J/cm²	1.41	1.41	1.41	1.41	1.89	1.89	1.89	1.89	1.89	1.89	1.89	1.89	1.89	1.89	2.36	2.36	2.36	2.36	1.41	3.77
Distance between pulse	um	0.05	0.05	0.05	0.05	0.075	0.075	0.075	0.075	0.075	0.05	0.05	0.05	0.05	0.05	0.05	0.05	0.05	0.05	0.075	0.1
Pulse/spot	1	1040	1040	1040	1040	693	693	693	693	693	1040	1040	1040	1040	1040	1040	1040	1040	1040	693	520
Real Fluence max	J/cm²	880	880	880	880	782	782	782	782	782	1173	1173	1173	1173	1173	1466	1466	1466	1466	586	1173
Spot Average Fluence	J/cm²	577	577	577	577	513	513	513	513	513	769	769	769	769	769	962	962	962	962	385	769
Sample Average Fluence	J/cm²	857	750	667	600	762	667	593	533	485	1143	1000	889	800	727	1250	1111	1000	909	364	513
SEY	1	0.78	0.87	0.84	0.77	1.08	0.98	0.89	0.93	1.01	0.95	0.84	0.86	0.82	0.85	0.84	0.78	0.80	0.84	1.12	0.92
Groove depth avg	um	62.75	52.00	70.25	75.46	19.09	28.34	32.17	31.14	31.72	32.21	38.47	44.48	49.40	47.63	43.75	54.21	55.75	52.61	26.43	44.34
Ablated mass	mg/cm²							14.38					19.91				21.80				

Figure B.7: University of Dundee. May 2018.

Epsilon								
Name		O	A	B	C	D	E	F (D7)
λ	nm	532	532	532	532	532	532	532
τ	ps	10	10	10	10	10	10	10
Spot size	um	52	52	52	52	52	52	52
Rep rate	kHz	200	200	200	200	200	200	200
Pulse energy	uJ	40	40	40	40	40	40	20
Hatch Distance	um	91	91	91	91	91	91	45
Scan speed	mm/s	5	10	15	20	25	30	15
Power	W	8	8	8	8	8	8	4
Fluence/pulse	J/cm²	1.88	1.88	1.88	1.88	1.88	1.88	0.94
Beam Standard deviation	cm	13	13	13	13	13	13	13
Max Fluence/pulse	J/cm²	3.77	3.77	3.77	3.77	3.77	3.77	1.89
Distance between pulse	um	0.025	0.05	0.075	0.1	0.125	0.15	0.075
Pulse/spot	1	2080	1040	693	520	416	347	693
Real Fluence max	J/cm²	4691	2346	1563	1173	939	782	782
Spot Average Fluence	J/cm²	3077	1538	1026	769	615	513	513
Sample Average Fluence	J/cm²	1758	879	586	440	352	293	593
SEY	1	0.96	0.97	1.03	1.10	1.22	1.24	1.24
Groove depth avg	um	115.72	68.22	47.27	36.23	29.45	24.04	

Figure B.8: University of Dundee. October 2018.

Zeta series															
Name		Z1O	Z1A	Z1B	Z1C	Z1D	Z1E	Z1F (D7)	Z5O	Z5A	Z5B	Z5C	Z5D	Z5E	Z5F
λ	nm	532	532	532	532	532	532	532	532	532	532	532	532	532	532
τ	ps	10	10	10	10	10	10	10	10	10	10	10	10	10	10
Spot size	um	52	52	52	52	52	52	52	52	52	52	52	52	52	52
Rep rate	kHz	200	200	200	200	200	200	200	200	200	200	200	200	200	200
Pulse energy	uJ	40	40	40	40	40	40	20	40	40	40	40	40	40	40
Hatch Distance	um	91	91	91	91	91	91	45	26	39	52	65	78	91	104
Scan speed	mm/s	5	10	15	20	25	30	15	10	10	10	10	10	10	10
Power	W	8	8	8	8	8	8	4	8	8	8	8	8	8	8
Fluence/pulse	J/cm²	1.88	1.88	1.88	1.88	1.88	1.88	0.94	1.88	1.88	1.88	1.88	1.88	1.88	1.88
Beam Standard deviation	cm	12.99	12.99	12.99	12.99	12.99	12.99	12.99	12.99	12.99	12.99	12.99	12.99	12.99	12.99
Max Fluence/pulse	J/cm²	3.77	3.77	3.77	3.77	3.77	3.77	1.89	3.77	3.77	3.77	3.77	3.77	3.77	3.77
Distance between pulse	um	0.025	0.05	0.075	0.1	0.125	0.15	0.075	0.05	0.05	0.05	0.05	0.05	0.05	0.05
Pulse/spot	1	2080	1040	693	520	416	347	693	1040	1040	1040	1040	1040	1040	1040
Real Fluence max	J/cm²	4691	2346	1563	1173	939	782	782	2346	2346	2346	2346	2346	2346	2346
Spot Average Fluence	J/cm²	3077	1538	1026	769	615	513	513	1538	1538	1538	1538	1538	1538	1538
Sample Average Fluence	J/cm²	1758	879	586	440	352	293	593	3077	2051	1538	1231	1026	879	769
SEY Before cleaning	1	0.90	0.98	1.02	1.06	1.09	1.16	0.98	0.84	0.90	0.83	0.92	0.94	0.91	0.92
SEY Aftere cleaning	1	1.22	1.08	1.42	1.23	1.45	1.75	1.42	0.87	1.13	1.14	1.07	1.14	1.15	1.44
Groove depth avg	um	127.00	70.00	45.25	45.25	36.00	25.75	38.00	78.50	56.25	55.50	65.50	70.00	69.25	70.75
Ablated mass	mg/cm²	24.50	14.64	15.05	11.06	8.68	8.61	15.01	45.61	21.54	23.63	24.57	15.53	13.78	12.04

Figure B.9: University of Dundee. March 2019.

Eta																			
Name		E1A	E1B	E1C	E1D	E1E	E1F	E2A	E2B	E2C	E2D	E2E	E2F	E3A	E3B	E3C	E3D	E3E	E3F
λ	nm	1030	1030	1030	1030	1030	1030	1030	1030	1030	1030	1030	1030	1030	1030	1030	1030	1030	1030
τ	ps	0.3	0.3	0.3	0.3	0.3	0.3	0.3	0.3	0.3	0.3	0.3	0.3	10	10	10	10	10	10
Spot size	um	22	22	22	22	22	22	22	22	22	22	22	22	22	22	22	22	22	22
Rep rate	kHz	500	500	500	500	500	500	500	500	500	500	500	500	500	500	500	500	500	500
Pulse energy	uJ	16	16	16	16	16	16	7.2	7.2	7.2	7.2	7.2	7.2	16	16	16	16	16	16
Hatch Distance	um	42	42	42	42	42	42	42	42	42	42	42	42	42	42	42	42	42	42
Scan speed	mm/s	5	10	15	20	25	30	5	10	15	20	25	30	5	10	15	20	25	30
Power	W	8.00	8.00	8.00	8.00	8.00	8.00	3.60	3.60	3.60	3.60	3.60	3.60	8.00	8.00	8.00	8.00	8.00	8.00
Fluence/pulse	J/cm²	4.21	4.21	4.21	4.21	4.21	4.21	1.89	1.89	1.89	1.89	1.89	1.89	4.21	4.21	4.21	4.21	4.21	4.21
Beam Standard deviation	cm	5.50	5.50	5.50	5.50	5.50	5.50	5.50	5.50	5.50	5.50	5.50	5.50	5.50	5.50	5.50	5.50	5.50	5.50
Max Fluence/pulse	J/cm²	8.43	8.43	8.43	8.43	8.43	8.43	3.79	3.79	3.79	3.79	3.79	3.79	8.43	8.43	8.43	8.43	8.43	8.43
Distance between pulse	um	0.01	0.02	0.03	0.04	0.05	0.06	0.01	0.02	0.03	0.04	0.05	0.06	0.01	0.02	0.03	0.04	0.05	0.06
Pulse/spot	1	2200	1100	733	550	440	367	2200	1100	733	550	440	367	2200	1100	733	550	440	367
Real Fluence max	J/cm²	11087	5544	3695	2773	2218	1848	4989	2495	1663	1248	998	832	11087	5544	3695	2773	2218	1848
Spot Average Fluence	J/cm²	7273	3636	2424	1818	1455	1212	3273	1636	1091	818	655	545	7273	3636	2424	1818	1455	1212
Sample Average Fluence	J/cm²	3810	1905	1270	952	762	635	1714	857	571	429	343	286	3810	1905	1270	952	762	635
SEY Before cleaning	1	0.94	0.95	0.97	0.95	1.04	1.09	0.95	0.97	0.98	1.04	1.09	1.09	1.28	1.33	1.41	1.58	1.77	1.83
SEY Aftere cleaning	1	1.38	1.60	1.41	1.43	1.45	1.49	1.54	1.44	1.41	1.55	1.48	1.44						
Groove depth avg	um	185.67	135.25	104.00	84.00	76.00	65.00	90.00	65.00	57.00	41.00	35.00	22.00						
Ablated mass	mg/cm²	20.94	12.41	9.62	8.74	9.42	7.35	12.45	8.87	7.18	6.54	5.98	5.60						

Figure B.10: University of Dundee. October 2019.

STFC																				
Name		6	5	4	3	2	7	8	9	2*	3*	FCC							1	
λ	nm	355	355	355	355	355	1064	1064	1064	1064	1064	1064	355	355	1064	1064	1064	1064	1064	335
τ	ps	25	25	25	25	25	70	70	70	70	70	70	25	25	25	25	25	25	5	5
Spot size	um	15	15	15	15	15	25	25	25	25	25	25	15	15	15	15	15	15	15	15
Rep rate	kHz	40	40	40	40	40	2.5	5	10	20	100	50	40	40	10	10	10	10	1.25	1.25
Pulse energy	uJ	75	75	75	75	75	760	480	390	150	10	1000	125	125	500	500	500	500	4000	4000
Hatch Distance	um	10	10	10	10	10	20	20	30	10	10	20	10	10	5	10	5	10	5	5
Scan speed	mm/s	30	60	90	120	180	125	125	30	500	500	180	216	162	200	200	100	100	30	90
Power	W	3	3	3	3	3	1.9	2.4	3.9	3	1	50	5	5	5	5	5	5	5	5
Average Fluence/pulse	J/cm²	42	42	42	42	42	155	98	79	31	2	204	71	71	283	283	283	283	2264	2264
Beam Standard deviation	um	3.75	3.75	3.75	3.75	3.75	6.25	6.25	6.25	6.25	6.25	6.25	3.75	3.75	3.75	3.75	3.75	3.75	3.75	3.75
Max Fluence/pulse	J/cm²	85	85	85	85	85	310	196	159	61	4	408	142	142	567	567	567	567	4533	4533
Distance between pulse	um	0.75	1.5	2.25	3	4.5	50	25	3	25	5	3.6	5.4	4.05	20	20	10	10	24	72
Pulse/spot	1	20	10	7	5	3	1	1	8	1	5	7	3	4	1	1	2	2	1	0
Real Fluence max	J/cm²	1027	518	343	256	168	310	196	806	61	12	1702	242	300	567	567	567	567	4533	4533
Spot Average Fluence	J/cm²	667	333	222	167	111	61	77	520	24	8	1111	154	206	167	167	333	333	1111	370
Average Fluence	J/cm²	1000	500	333	250	167	76	96	433	60	20	1389	231	309	500	250	1000	500	3333	1111
SEY at 1000eV	1	1	0.91	0.91	0.98	1.22	1.57	1.33	0.94			0.97	1.25	0.89	0.92	1.05	0.87	0.93	0.92	1
Groove depth avg	um	100	60	35	20	8														

Figure B.11: Data from literature [85, 94].

		IOM															
Name		A1	A2	A3	A4	A5	A6	A7	A8	B1	C1	D1	E1	F1	G1	H1	D8
λ	nm	1064	1064	1064	1064	1064	1064	1064	1064	1064	1064	1064	1064	1064	1064	1064	1064
τ	ps	12	12	12	12	12	12	12	12	12	12	12	12	12	12	12	12
Spot size	um	56	56	56	56	56	56	56	56	56	56	56	56	56	56	56	56
Rep rate	kHz	100	100	100	100	100	100	100	100	100	100	100	100	100	100	100	100
Pulse energy	uJ	41	39	36	28	19	14	7	1.3	41	41	41	41	41	41	41	1.3
Hatch Distance	um	50	50	50	50	50	50	50	50	50	50	50	50	50	50	50	50
Scan speed	mm/s	1	1	1	1	1	1	1	1	2	5	10	20	50	100	200	10
Power	W	4.1	0	3.6	0	1.9	0	0	0.13	4.1	4.1	4.1	4.1	4.1	4.1	4.1	0.13
Average Fluence/pulse	J/cm²	1.66	1.58	1.46	1.14	0.77	0.57	0.28	0.05	1.66	1.66	1.66	1.66	1.66	1.66	1.66	0.05
Beam Standard deviation	um	14	14	14	14	14	14	14	14	14	14	14	14	14	14	14	14
Max Fluence/pulse	J/cm²	3.33	3.17	2.93	2.28	1.54	1.14	0.57	0.11	3.33	3.33	3.33	3.33	3.33	3.33	3.33	0.11
Distance between pulse	um	0.01	0.01	0.01	0.01	0.01	0.01	0.01	0.01	0.02	0.05	0.1	0.2	0.5	1	2	0.1
Pulse/spot	1	5600	5600	5600	5600	5600	5600	5600	5600	2800	1120	560	280	112	56	28	560
Real Fluence max	J/cm²	11161	10616	9800	7622	5172	3811	1905	354	5581	2232	1116	558	224	112	56	35
Spot Average Fluence	J/cm²	7321	6964	6429	5000	3393	2500	1250	232	3661	1464	732	366	146	73	37	23
Average Fluence	J/cm²	8200	7800	7200	5600	3800	2800	1400	260	4100	1640	820	410	164	82	41	26
Ablated mass	mg/cm²	31.74	29.75	28.44	25.43	20.59	17.15	9.77	1.08								

Figure B.12: Leibniz Institute of Surface Engineering (IOM). August 2018.

Appendix C

Additional observations of treated surface

C.1 SEM observations on flat samples treated in laboratory

Figure C.1 is shown as an example that the morphology of the surface can not be simply described depending on the fluence. For rather similar fluences with different wavelengths, a very different surface morphologies are observed.

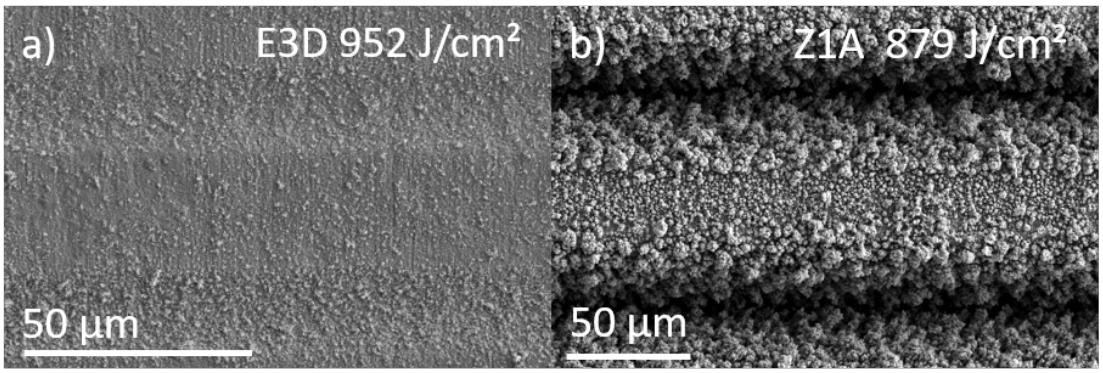

Figure C.1: SEM top views of a) *E3D* 1030 nm treated in air Averaged fluence: 952 J.cm^{-2} Absorbed averaged fluence: 19 J.cm^{-2}. b) *Z1A* 532 nm treated in nitrogen Averaged fluence: 879 J.cm^{-2}. Absorbed averaged fluence: 220 J.cm^{-2}.

Figure C.2 is shown as an example sensibility of the particle coverage of the surface of the sample treated in different gas environment. For similar parameters of the laser irradiating the samples, the morphology of the particle depends on the flux of nitrogen. The special care was asked to our partners performing the laser treatment keep this parameters as consistent as possible.

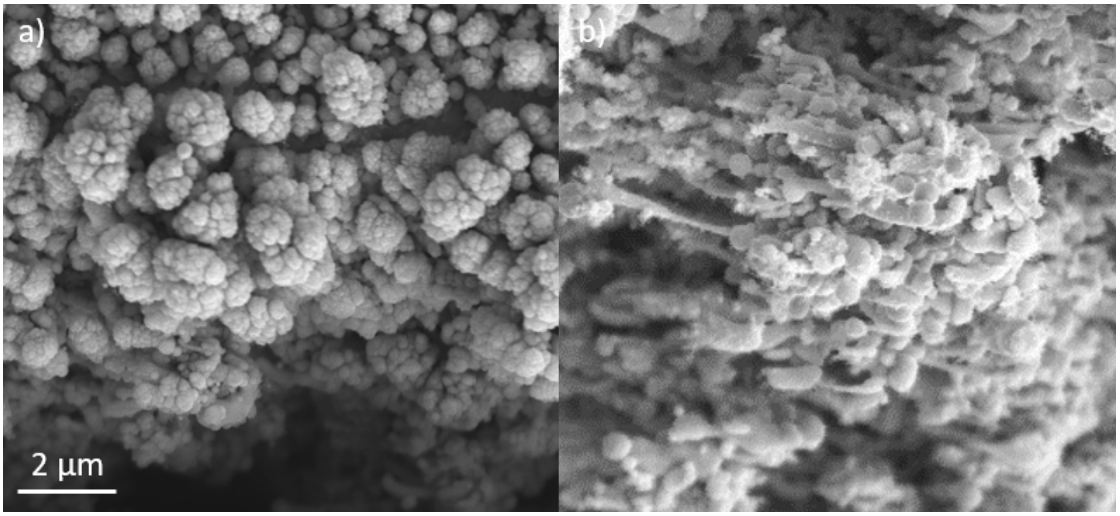

Figure C.2: SEM top views of the particles at the surface of samples treated with similar laser parameters a) with laminar nitrogen flux, b) with turbulent nitrogen flux.

Figure C.3 is an optical microscopy of the beam screen treated by *D7* parameters. The stainless steel layer can be seen in the bottom of the image, while the copper layer is on the top of the image. The regular sinusoidal pattern is the micro-scale surface modification due to the laser treatment.

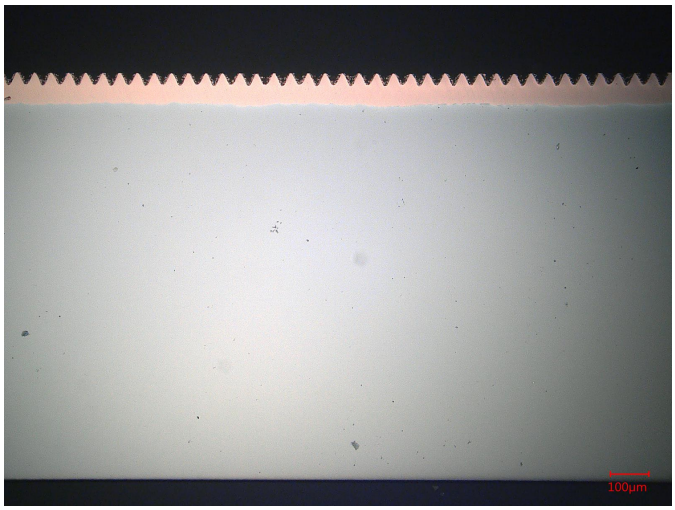

Figure C.3: Optical microscope image of a cross section of beam screen treated by *D7* parameters.

C.2 SEM observations on *in-situ* treated beam screen

A 2.2-m-long race-track-shape *Type 74* beam screen has been treated using the robot briefly presented in section 2.2.2 The parameters *D7* are applied on the curved part of the beam screen profile. Due to the radius difference between curved and flat parts the irradiation characteristics are slightly different in the flat part as presented in table 2.2.

Once treated at Dundee University and shipped to CERN, the bream screen has been

longitudinally cut in two halves in order to extract samples those the size dimensions allow analysis on conventional instruments at CERN (SEM, SEY and XPS measurement).

The 10-mm-large vertical stripes visible on the picture correspond to the area treated between two clamping movements of the robot. The irradiation characteristics and therefore the surface topography over this area is expected to be homogeneous. Each area has been numerated as shown in figure C.4 to insure the tractability with the treatment parameters used for each of these areas.

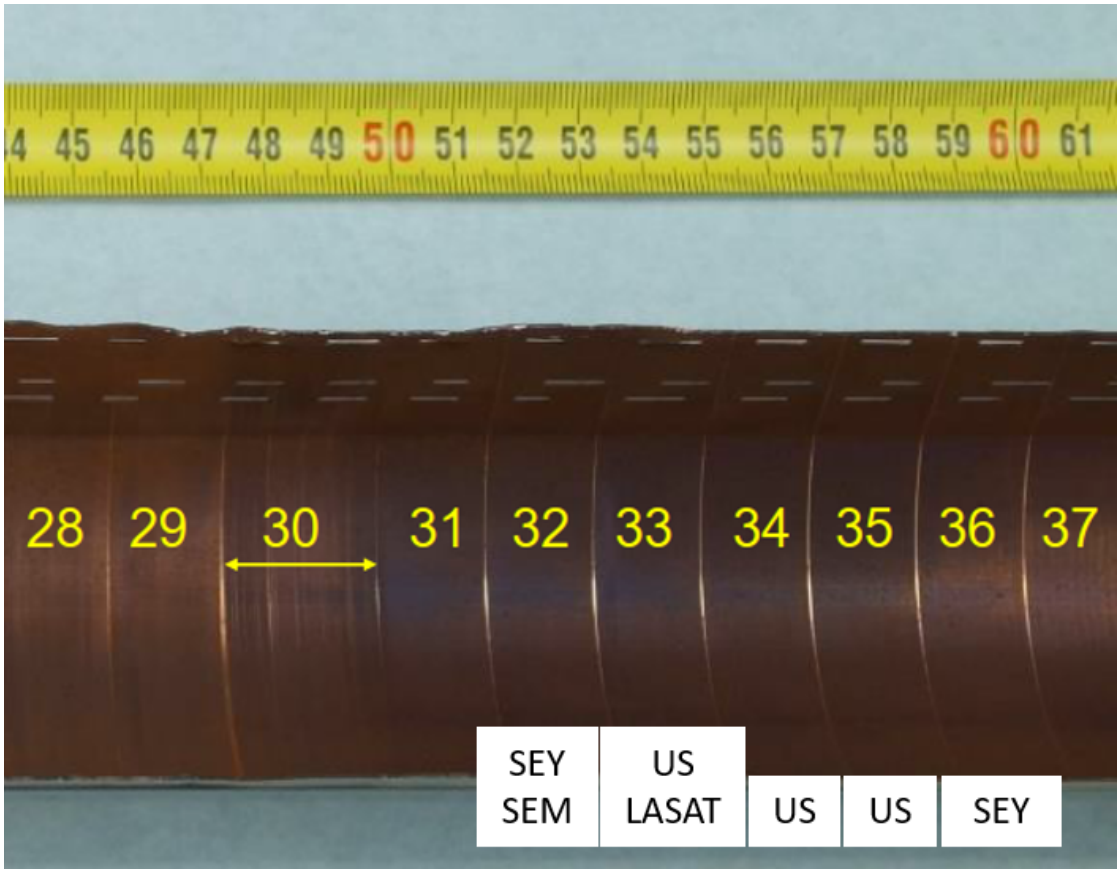

Figure C.4: Picture of the inner surface of one half of treated beam screen, in section *Run 3*, after been cut into two halves. Samples from sections 32 to 36 have been treated with *D7* parameters. they have been used for ultrasonic cleaning analysis (US), SEY, SEM, and mechanical tests (LASAT). Courtesy of Marcel Himmerlich.

Although the groove depth measured at the beam screen surface is observed to be similar than plan samples, the particle coverage appears to vary strong depending on the localisation in the beam screen, longitudinally and around a section (flat part or curved part, respectively presented in figure 3.44 b) and figure C.6).

Samples in flat part, have been used for US cleaning studies and mechanical tests as mentioned in figure C.4 and illustrated in figure C.5

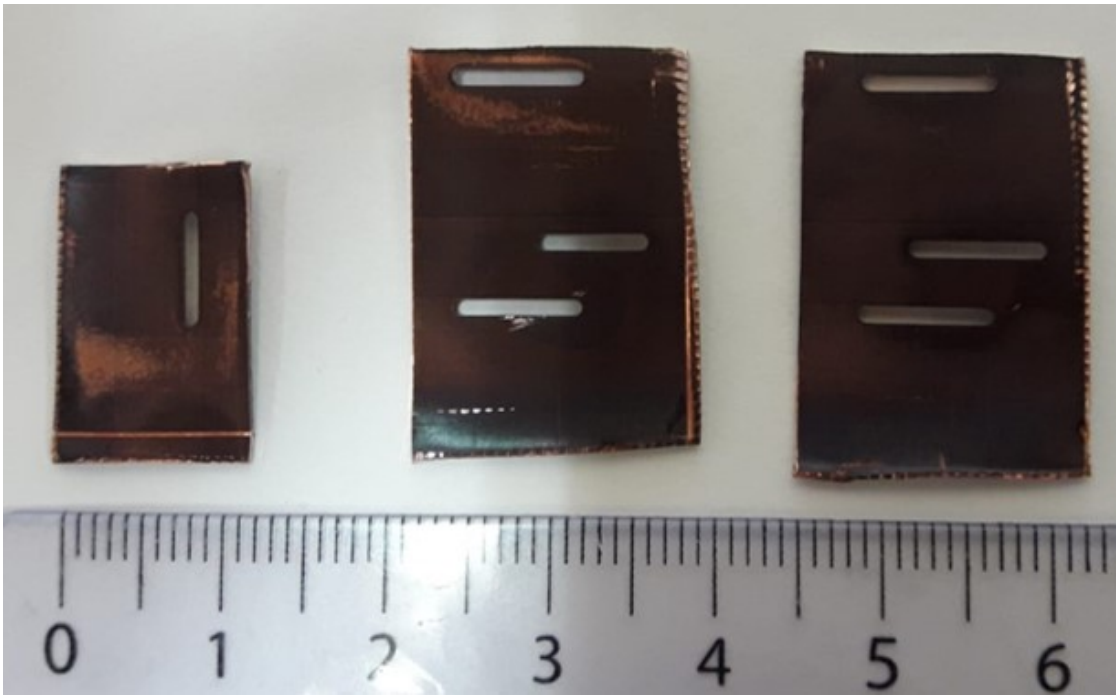

Figure C.5: Picture of the 33, 34 and 35 samples (form left to right), cut in section *Run 3*, after ultrasonic cleaning. The area of each sample has been measured to determine the particle density covering the sample.

In curved part, the particle coverage was in general significantly lower than the one observed on the flat samples. Although this fact is not fully understood, it could be due to the gas environment in the confined space. The lower particles coverage allowed the observation of features on the near surface such as the LIPSS undulations and cracks, as illustrated in C.6.

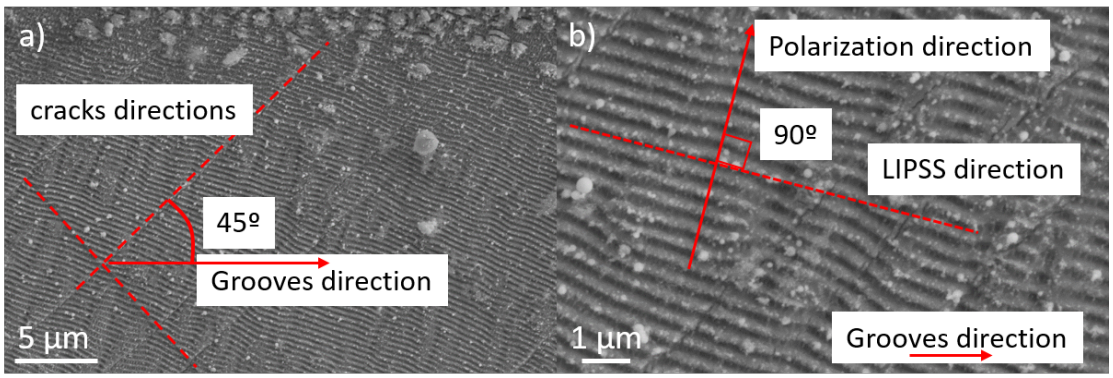

Figure C.6: SEM top view samples extracted from the treated beam screen (curved part, section 32 as referred to figure C.4) a) Cracks oriented 45 ° compare to the groove direction is highlighted. b) Higher magnification to observe LIPSS undulations. The groove direction is illustrated by the red arrow are observed, the polarisation direction has been reported to be oriented at 90 ° compare to the LIPSS direction.

The periodicity of the undulations measured on the SEM images was 340 nm. The ratio of 0.64 compare to the laser wavelength (532 nm) was in a good agreement with

the sub-wavelength Laser Induced Periodic Surface Structures (LIPSS) induced by a 532 nm laser irradiation reported in the literature.

The undulation are the effects of cumulative phenomena and interference of the linearly polarized repetitive laser pulses reported to be perpendicular to the polarization direction [163].

More generally, the LIPSS, unexpectedly observable on groove profile when the particle coverage is not present, is a laser-assisted surface structuration strategy which may be interesting to investigate. Although the peak to peak amplitude and therefore the aspect ratio of LIPSS surfaces and associated SEY performance are lower than the one obtained with high fluence etching, this structuration technique obtained without material ablation prevent the dust and weakly attached particles formation.

C.3 FIB-assisted specimen preparation for TEM analysis

In figure C.7 a), the red rectangle represents the area where the thin specimen will be taken from. 16 μm long and 3 μm large. To prevent degradation of the surface layers during etching by an ion beam, a carbon protective layer has been electro-deposited locally on the sample surface (b)). This carbon layer allows the handling of the specimen despite the high rugosity of the surface and the fragility of the particles covering the grooves. The ion beam is used to free the space around the specimen (c) and d)) . A needle has been used to carry the specimen from the laser-treated surface (e)) to the specimen holder (f)).

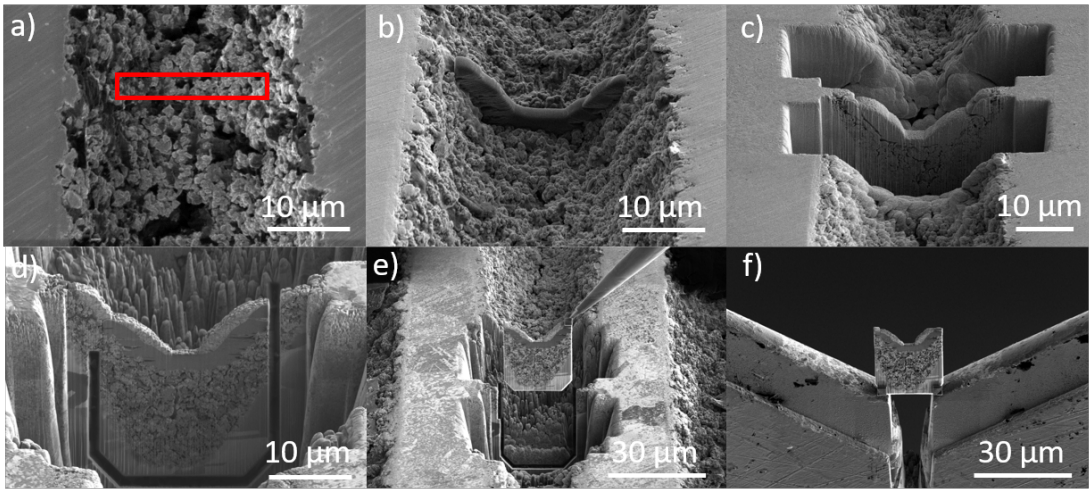

Figure C.7: Specimen preparation. a) illustrates the selection of the area of interest (the red rectangle on the image) on the bottom of a mechanically polished groove, b) illustrates the deposition of the carbon layer to protect the rough surface during polishing and handle the specimen. c) The volumes around the specimen are polished thanks to ion beam. d) Trenches are machined by ion beam to detached the specimen out of the sample. e) The specimen is detached and handled by a needle visible in the top right corner of the image. f) The specimen once detached from the sample is installed on the sample holder.

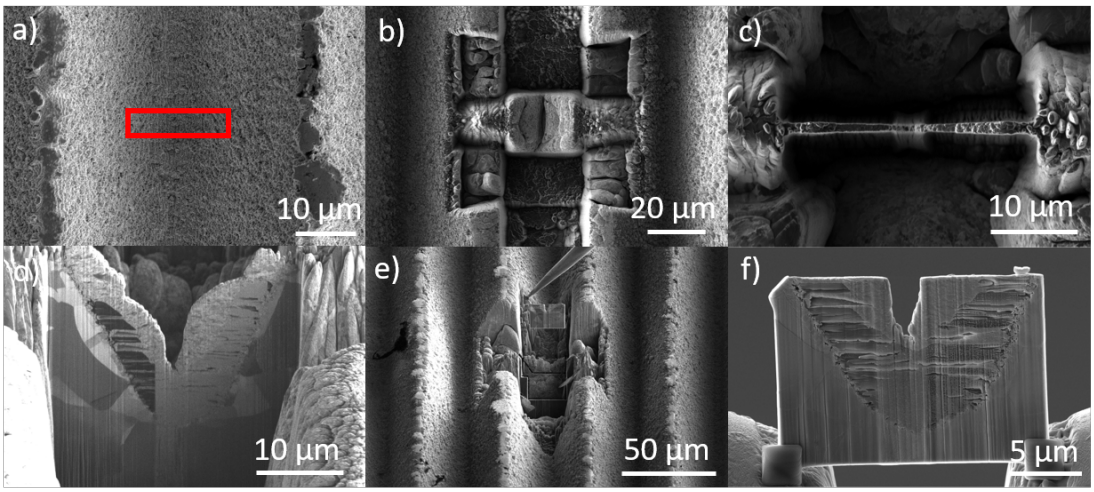

Figure C.8: Specimen preparation. a) illustrates the selection of the area of interest (the red rectangle on the image) on the bottom of a groove cleaned in ultrasonic bath, b) c) d) The volumes around the specimen are polished thanks to ion beam. e) The specimen is detached and handled by a needle visible in the top part of the image. f) The specimen once detached from the sample is installed on the sample holder.

C.4 Additional images of TEM analysis

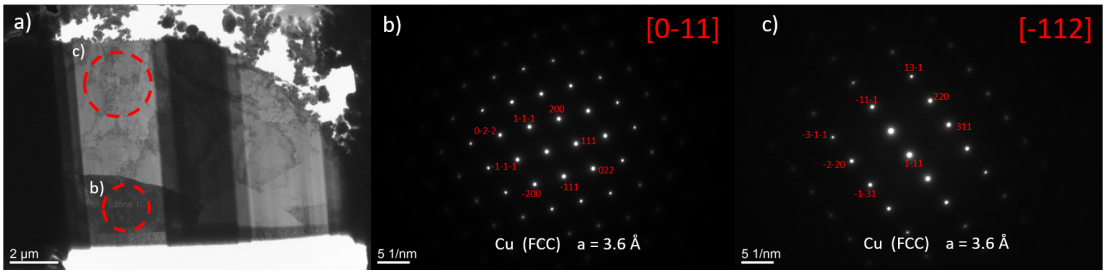

Figure C.9: a) Bright filed TEM general view of the bulk copper below the surface irradiated by 0.25 J.cm^{-2}. The red dashed circles are the area selected for the diffraction analysis . b) and c) are the corresponding SAED patterns.

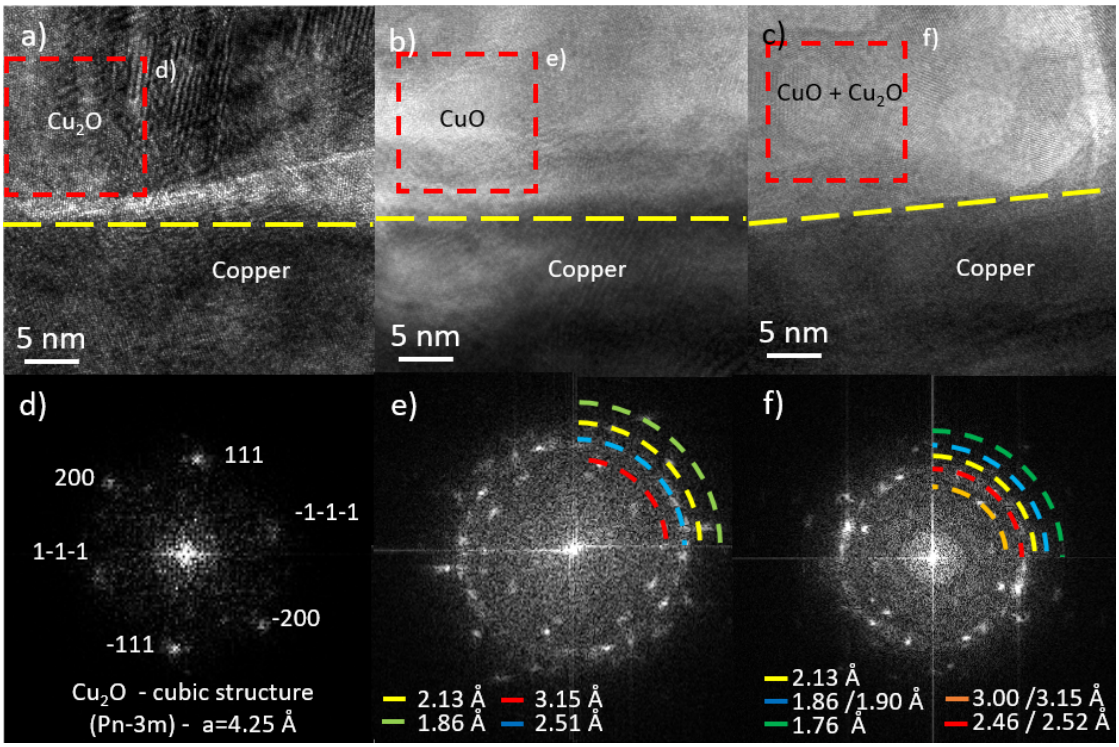

Figure C.10: a), b), c) Lattice imaging on the inter interface between copper and oxidized layer of area marked as red squares in figure 3.24 b). The scale bars are all 5 nm. d), e), f), corresponding Fourier spectra from the indicated red squared area.

Other lattice imaging pictures and Fast Fourier Transformation (FFT) analysis of three other points located in the oxide layer are shown in figure C.10. The yellow dashed lines underline the border between the copper and the oxide layer, The red dashed squares are the areas selected for the Fast Fourier Transformation shown in pictures d), e) and f) respectively. Lattice fringes are visible on the pictures, the lattice spacing has been deduced from the post treatment of the FFT images. Figure C.10 d) reveals a monocrystalline cubic crystal structure (space group Pn-3m) and unit cell constant a = 4.25 Å. This coincides with the data for copper (I) oxide. Lattice distances of 1.86, 2.13, 2.51 and 3.15 Å can be identified from the FFT image presented in figure C.10 e). These are the inter-recticular distances corresponding to cupric oxide (copper (II) oxide). Circular distributions of diffraction points indicate a polycrystalline structure. Similarly, in figure C.10 f), the FFT of a polycrystalline structure is displayed. However, the identification of the circular distribution of light is ambiguous and it may correspond to the pattern of cupric and cuprous oxides simultaneously. This could indicate the presence of a mixture of the both oxides.

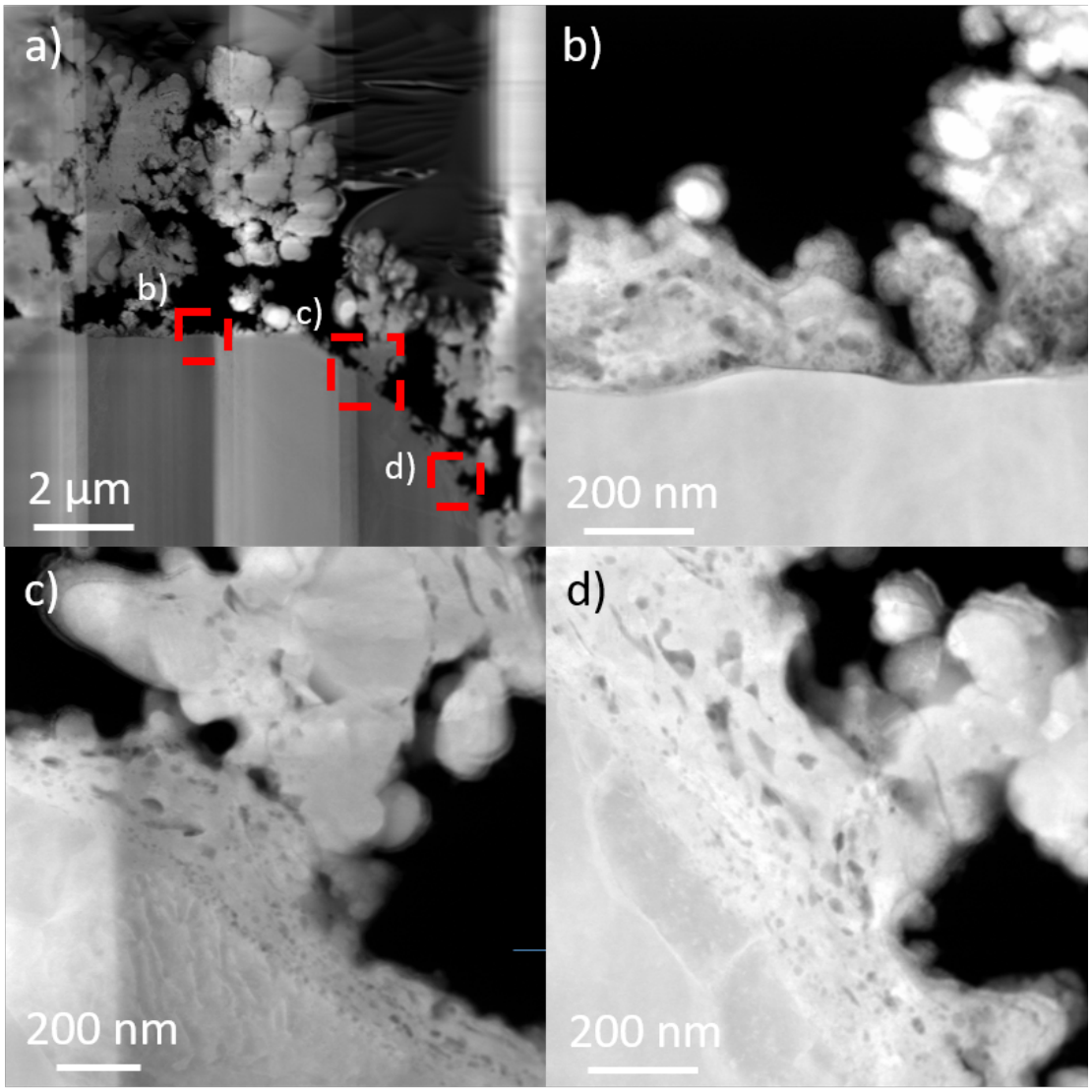

Figure C.11: STEM-HAADF image of a) general view . b) an area irradiated by 0.25 J.cm^{-2}. c) an area irradiated by 0.55 J.cm^{-2}. d) an area irradiated by 0.95 J.cm^{-2}.

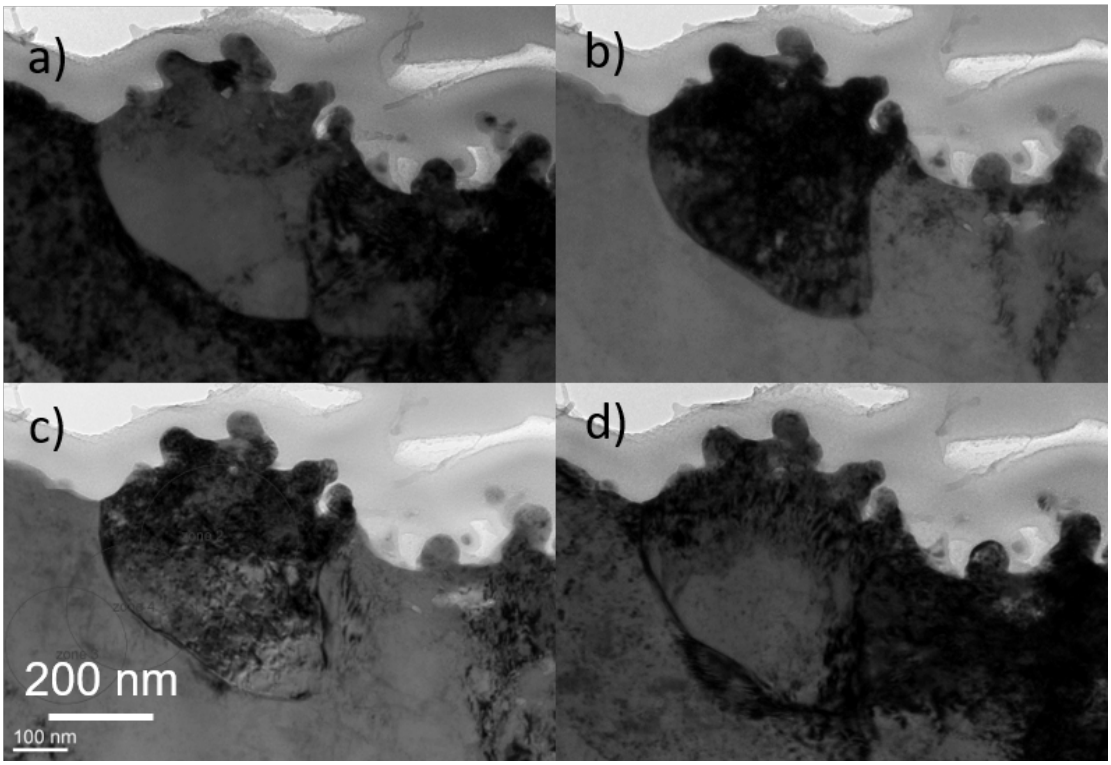

Figure C.12: a) b) c) d) Bright field TEM images performed with a different tilt, in an area irradiated by 1.81 J.cm^{-2}.

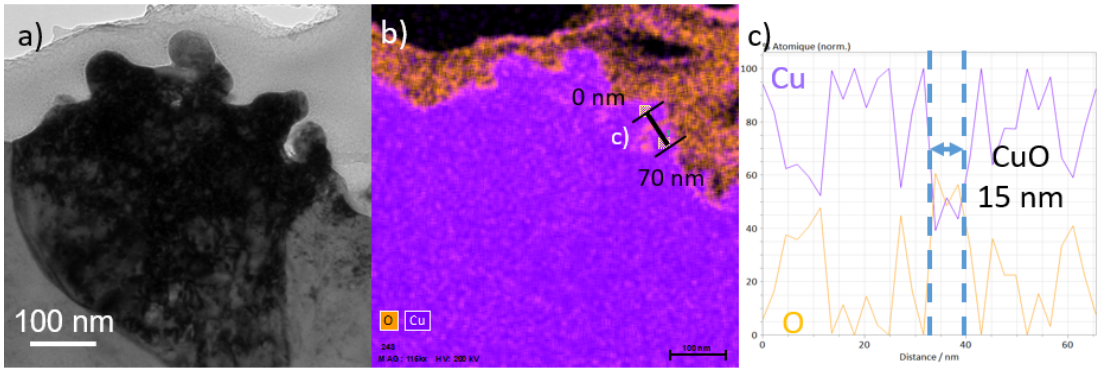

Figure C.13: a) Bright field TEM image performed in an area irradiated by 1.81 J.cm^{-2}. b) Element distribution EDX maps of the corresponding area. The purple color corresponds to the copper-containing area. The oxygen containing area are identified in orange. c) Element distribution extracted from the EDX map, every 1 nm, along the segment marked in d) of copper and oxygen in purple and orange respectively.

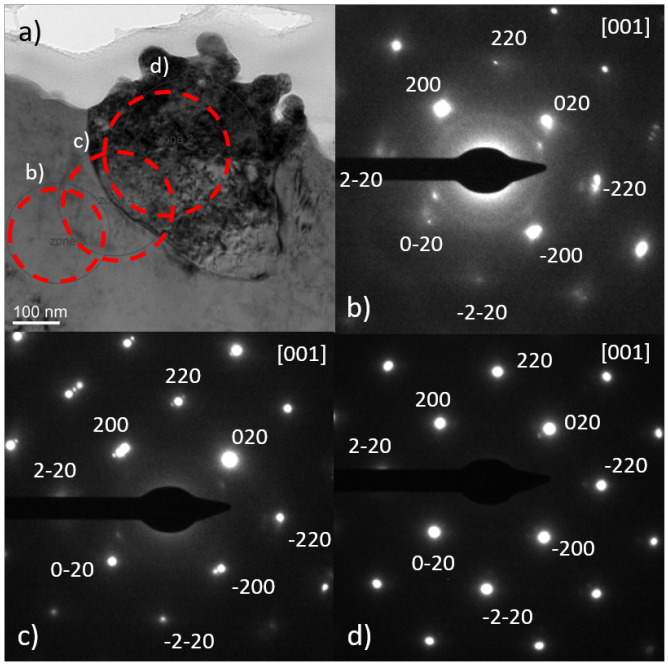

Figure C.14: a) TEM Bright field image in the area irradiated by 1.81 J.cm^{-2}. The red dashed circles are the areas selected for the diffraction analysis. b), c) and d) SAED patterns from the respectively indicated areas in a). The SAED have been obtained with different tilts in order to find the same zone axis.

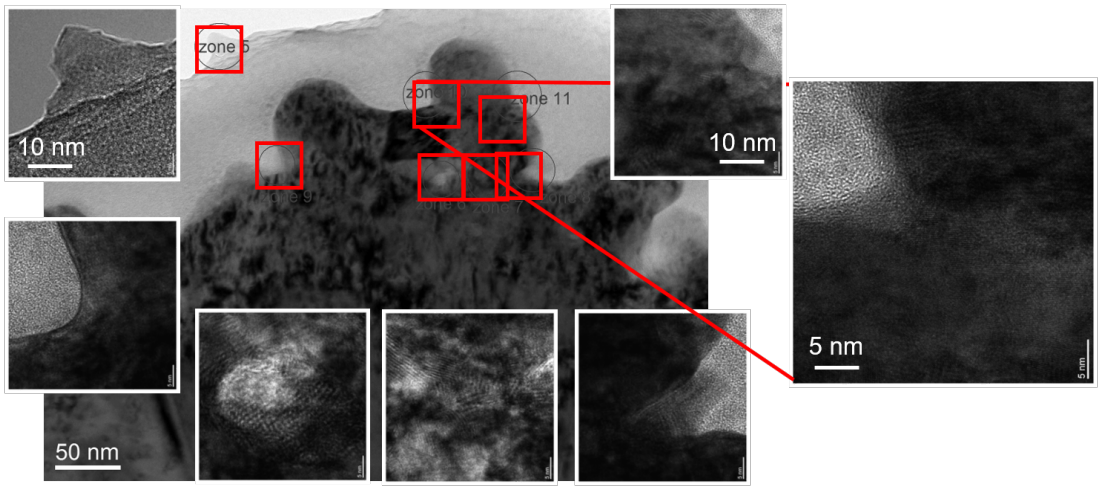

Figure C.15: Illustration of the localisation of the area selected for lattice imaging at the surface, in the area irradiated by 1.81 J.cm^{-2}. The larger image is a bright field TEM images, the red squares are the area selected of lattice imaging. The smaller images are images of the lattice.

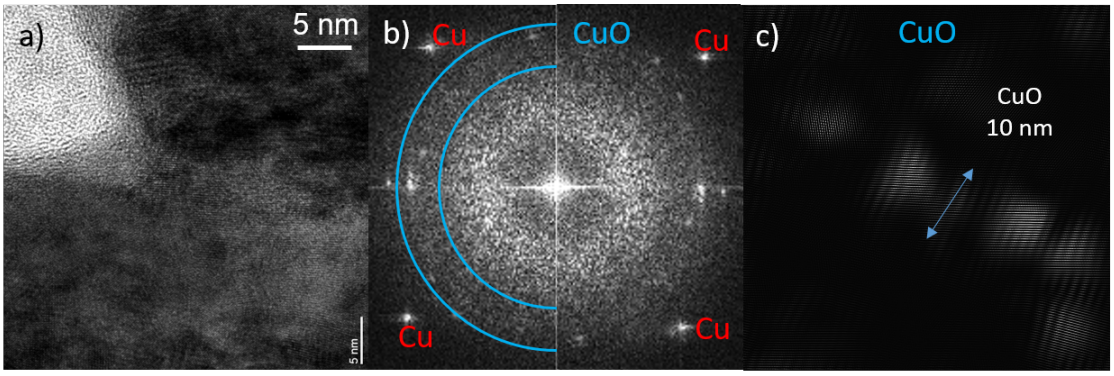

Figure C.16: a) Lattice imaging in an area irradiated by 1.81 J.cm^{-2}. b) Corresponding Fast Fourier Transformation spectra from a). c) Inverse FFT image with the contribution of CuO. The thickness of the oxide layer can be evaluated around 10 nm.

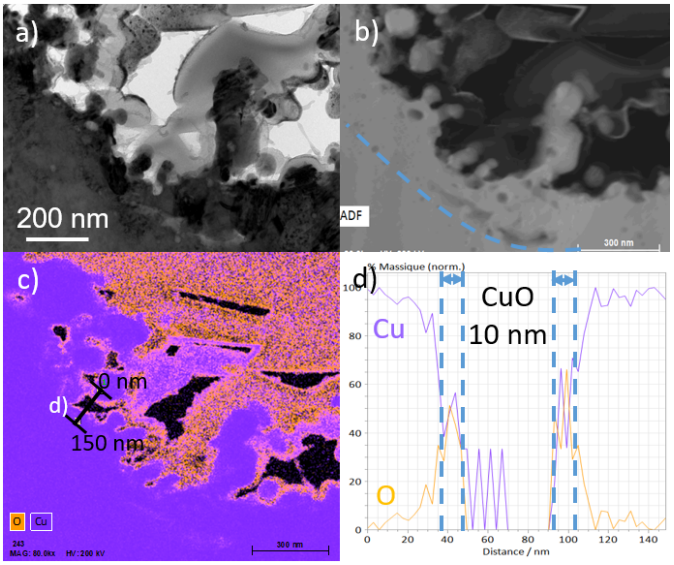

Figure C.17: a) Bright field TEM image performed in an area irradiated by 1.86 J.cm^{-2}. b) STEM-HAADF image of the corresponding area c) EDX maps of element distribution of the corresponding area. The purple color corresponds to the copper-containing area. The oxygen containing area are identified in orange. d) Element distribution extracted from the EDX map, every 1 nm, along the segment marked in c) of copper and oxygen in purple and orange respectively.

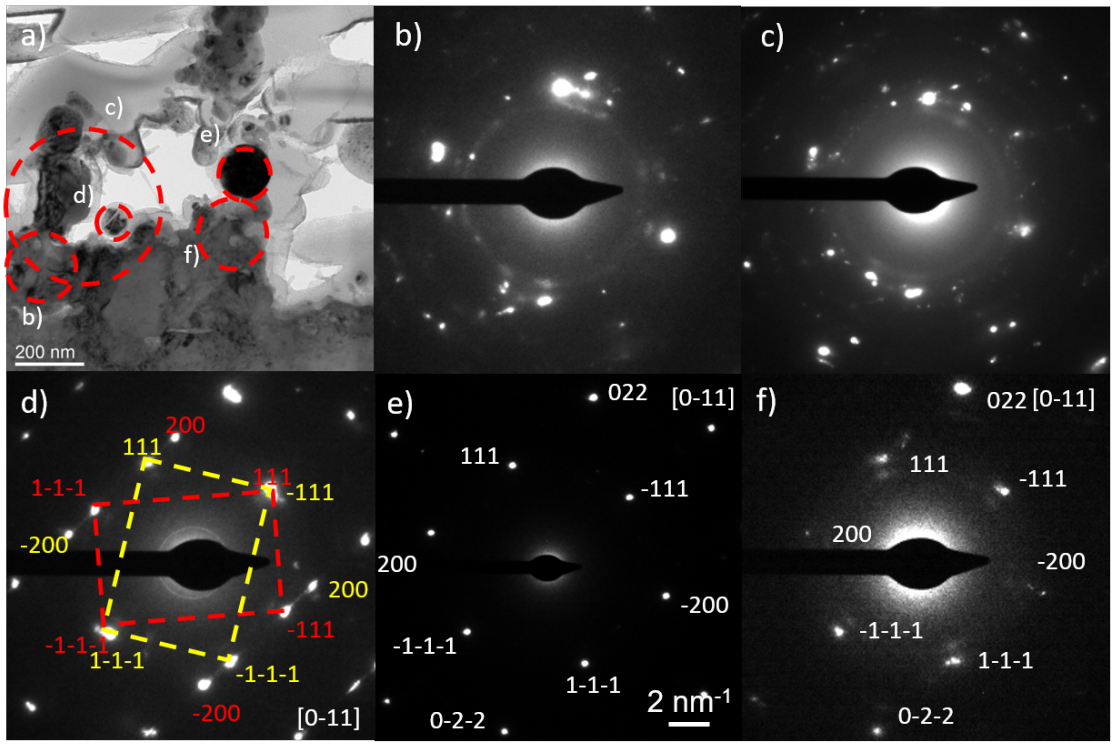

Figure C.18: a) TEM Bright field image in the area irradiated by 1.88 J.cm^{-2}. The red dashed circles are the areas selected from the diffraction analysis. b), c), d), e) and f) SAED patterns from the respectively indicated areas in a).

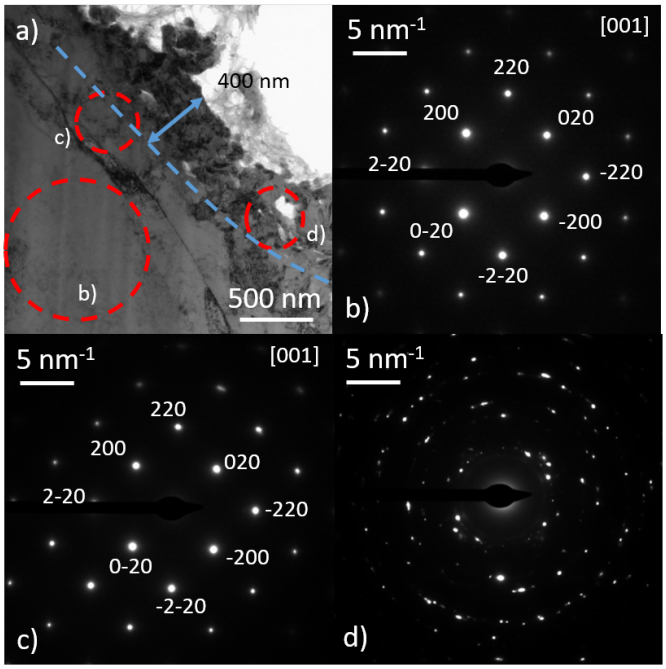

Figure C.19: a) TEM Bright field image in the area irradiated by 2.25 J.cm^{-2}. The limit between refined grain and larger grains has been identified around 400 nm under the surface. The red dashed circles are the areas selected from the diffraction analysis. b), c) and d) SAED patterns from the respectively indicated areas in a).

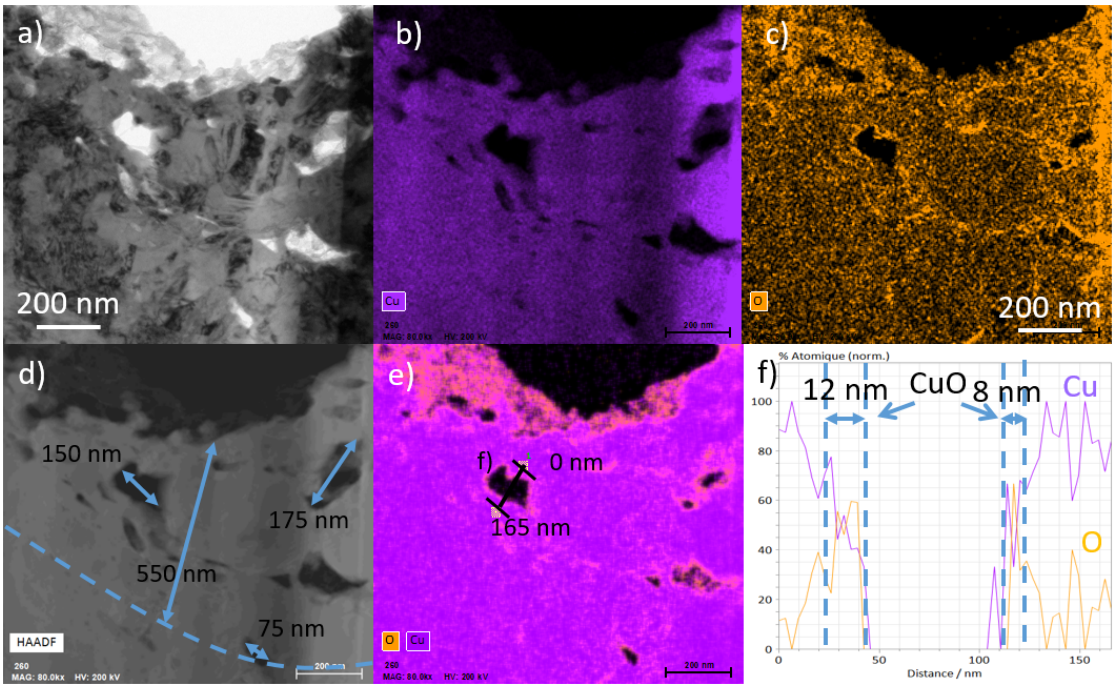

Figure C.20: a) Bright field TEM image performed in an area irradiated by 2.25 J.cm^{-2}. d) STEM-HAADF image of the corresponding area. Porosities have been identified with different diameters. The lower limit under the surface of these porosities has been identified at 550 nm. b) c) and e) Element distribution EDX maps of the corresponding area.The purple color corresponds to the copper-containing area. The oxygen containing area are identified in orange. d) Element distribution extracted from the EDX map, every 1 nm, along the segment marked in c) of copper and oxygen in purple and orange respectively. A layer of around 10 nm of CuO oxide has been identified in the inner walls of a closed porosity.

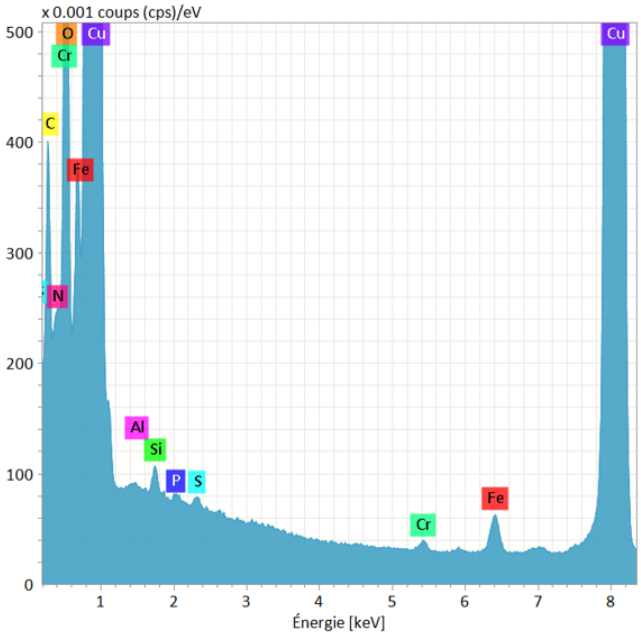

Figure C.21: Total EDX spectra of the area illustrated in C.22. The spectra is focused on the peaks whose amplitude is much lower than the one of copper and oxygen.

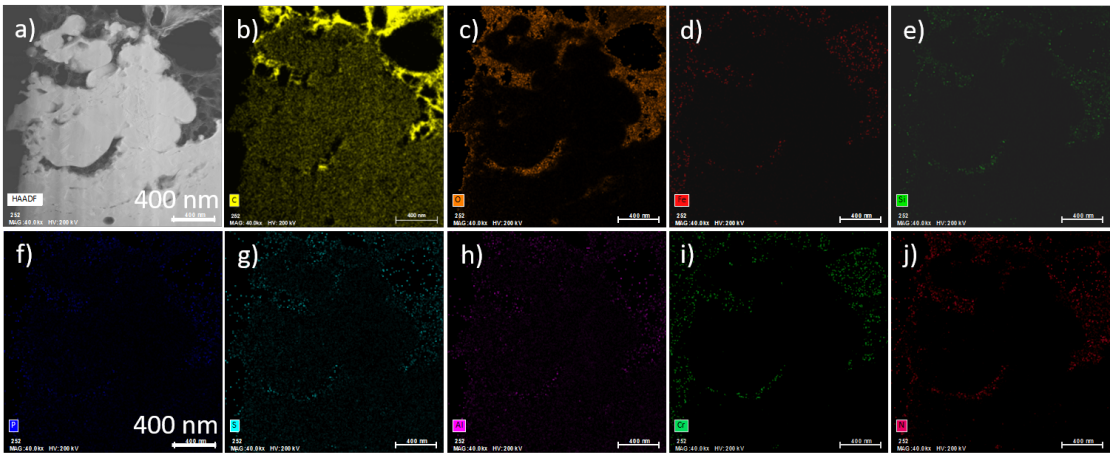

Figure C.22: a) STEM-HAADF image performed in an area irradiated by 2.33 J.cm^{-2}. d) EDX maps of the element distribution of the corresponding area. The yellow color corresponds to the carbon-containing area. c) The orange color corresponds to the oxygen-containing area. d) The red color corresponds to the iron-containing area. e) The green color corresponds to the silicon-containing area. f) The dark blue color corresponds to the phosphor-containing area. g) The cyan color corresponds to the sulfur-containing area. h) The pink color corresponds to the aluminum-containing area. i) The light green color corresponds to the chromium-containing area. j) The magenta color corresponds to the nitrogen-containing area.

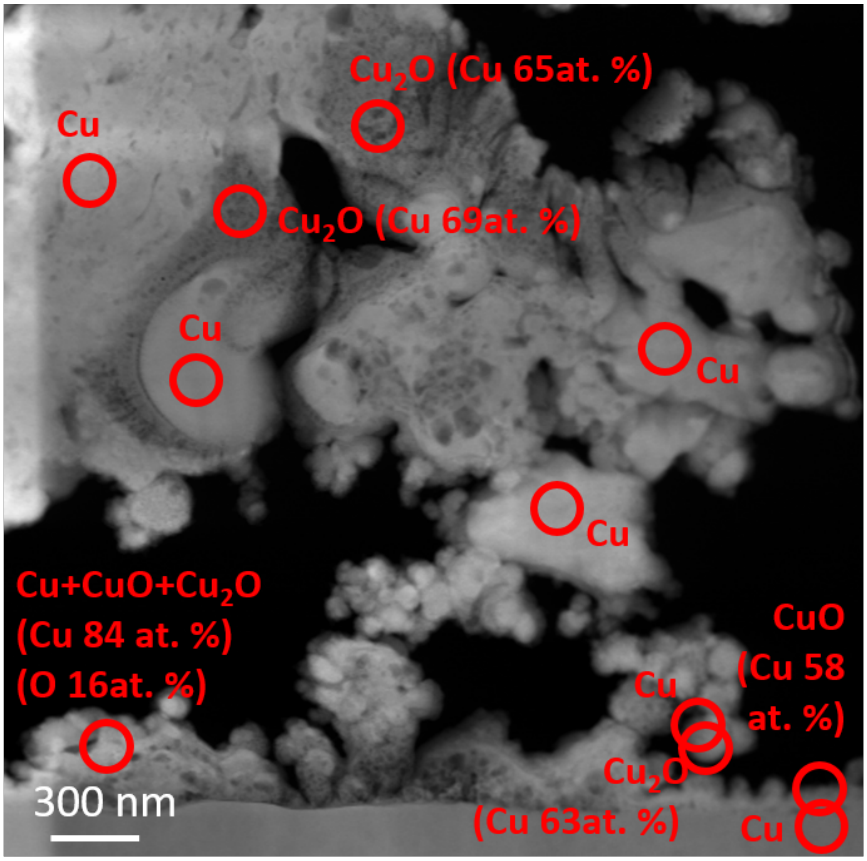

Figure C.23: STEM-HAADF image performed in an area irradiated by 0.25 J.cm^{-2}. EDX analysis have been performed on the points identified by red circles. The atomic percentage of copper is indicated when it is lower than 90%.

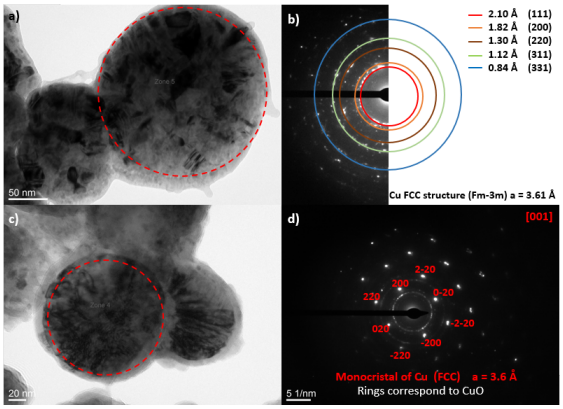

Figure C.24: Bright filed TEM images of droplets located in an area irradiated by 0.25 J.cm^{-2}. The red dashed circles are the areas selected for the diffraction analysis. a) The diameter of the droplet is 300 nm. c) The diameter of the droplet is 120 nm . b) and d) SAED patterns from the area indicated in a) and c), respectively.

In figure C.24 a) and c), bright field images show spherical droplets observed all over the surface of the specimen. The diameter of the spherical structures is evaluated respectively to 120 and 300 nm. The SAED pattern of the selected droplets can be seen

on the right hand side of each picture. C.24 b) is the SAED pattern based on the area shown in C.24 a) (red dashed circle diameter 300 nm). The colourful circles illustrate the inter-reticular distances 0.84, 1.12, 1.3, 1.82 and 2.1 Å corresponding to the (331), (311), (220), (200) and (111) plans respectively. This confirmed that droplet particle is face-centered cubic phase in nature. The presence of rings indicates that the re-solidified region is poly-crystalline. In figure C.24 d), the SAED pattern based on the area shown in C.24 c) (red dashed circle diameter 120 nm) is characteristic of a mono-crystalline material.

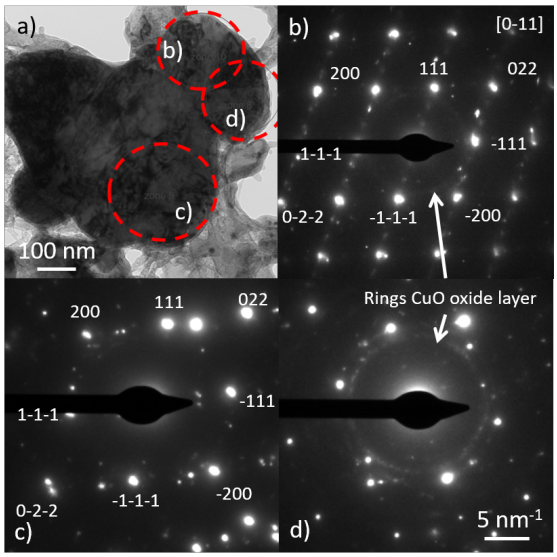

Figure C.25: a) Bright filed TEM images of droplets located in an area irradiated by 2.35 J.cm^{-2}. b), c) and d) SAED patterns from the areas noted in a).

Appendix D

details about experimental mechanical characterisation

D.1 Droptest set-up

The deceleration obtained when the fall of a mass is crashed on a metallic piece has been considered as a mean to submit the laser treated surface to inertia force. It is a diverted use of a drop test crash tower, ordinary used to analysed the deformation of the metallic piece under the shock.

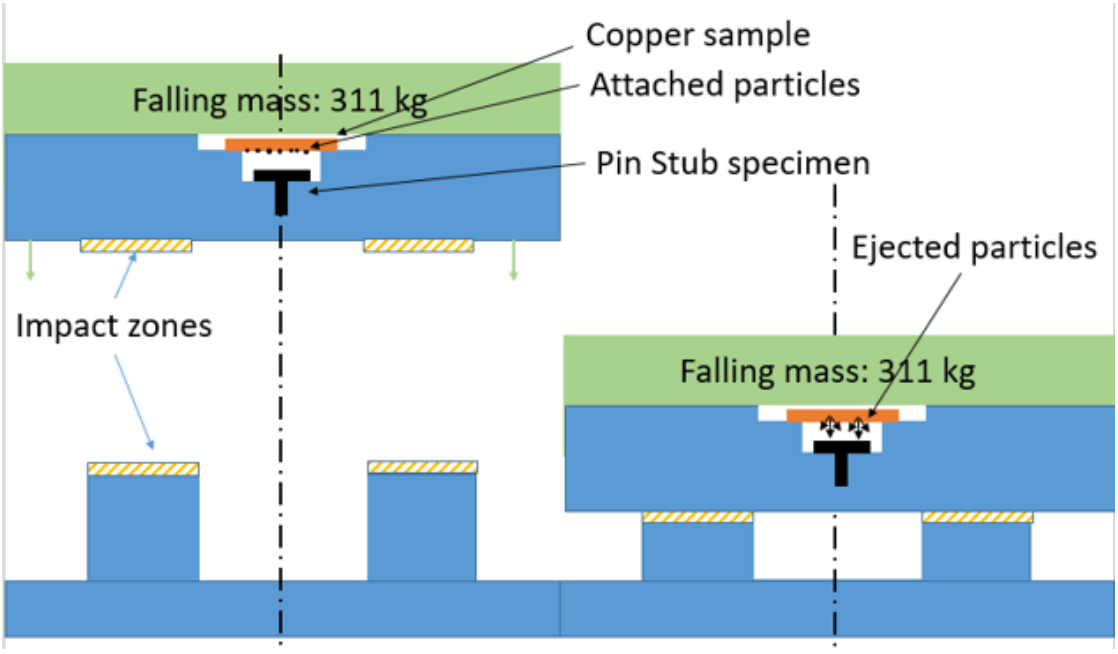

Figure D.1: Sketch of the droptest .

A preliminary test took place at *Novelis* company, in Sierre. The accelerometer was installed in the falling mass which is dropped from a height of 3 m. The falling mass is decelerated crashing on a metallic sample fixed on the ground, which absorbed the

energy.

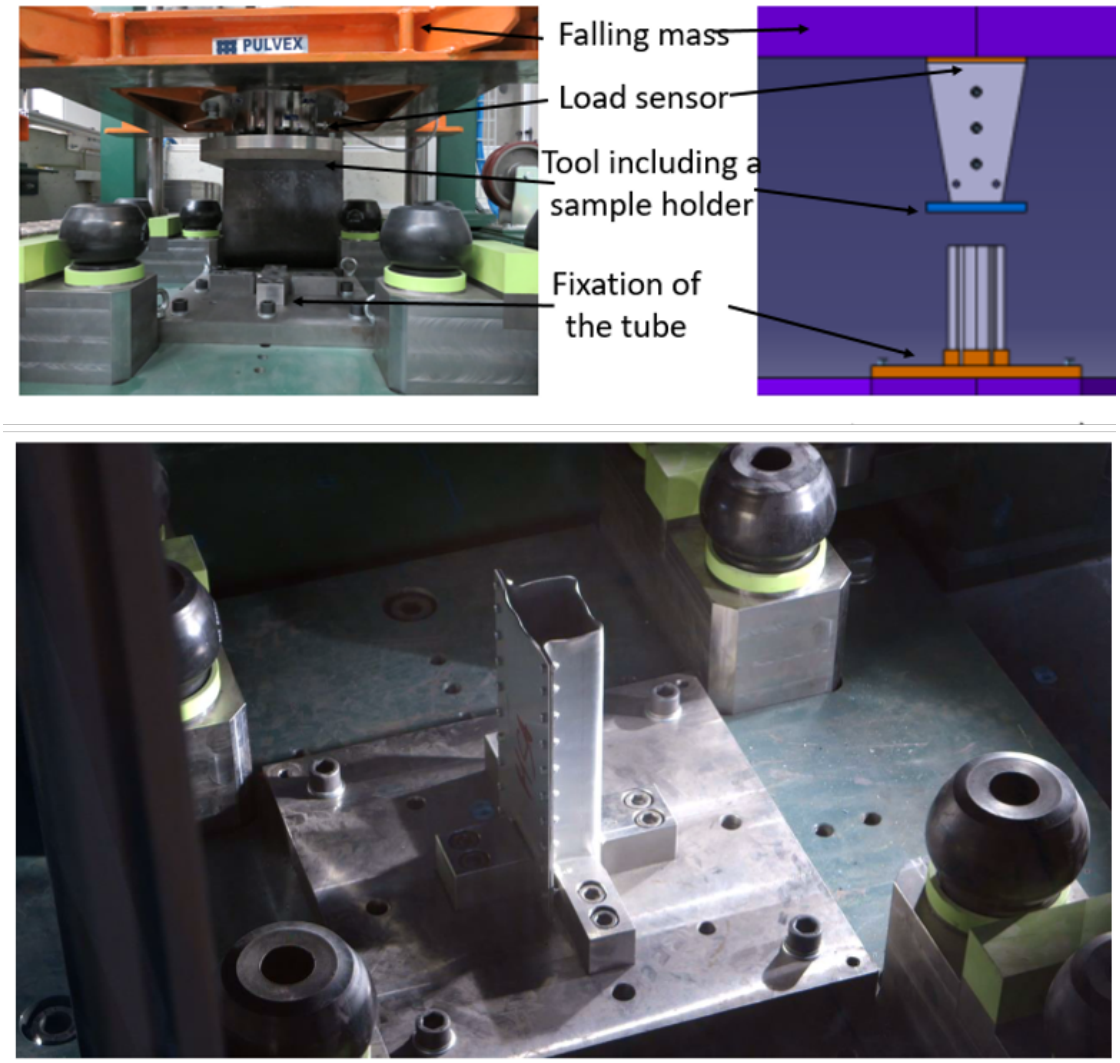

Figure D.2: Pictures of the experimental setup used at *Novelis* company.

The acceleration of the falling has been recorded as presented in figure D.3. Using the profile shown in the inset, the maximum deceleration was 80 g. Although the deceleration might have been higher using a stiffer profile, it was found to be far from the target value of deceleration aimed to approach the force applied on the surface during the accelerator operation.

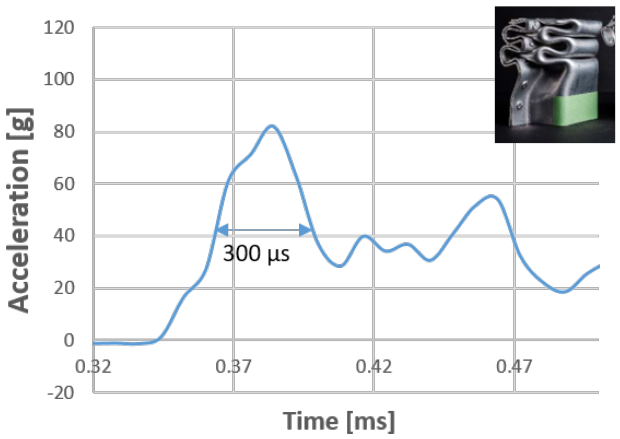

Figure D.3: Acceleration measured during the drop test of the falling mass.

D.2 Centrifugation experimental set-up

Prototype of sample holder realised for preliminary tests for centrifugation at 30 000 RPM. The sample holder material has been chosen *Delrin*, as a low density, rather high strength the easy to manufacture.

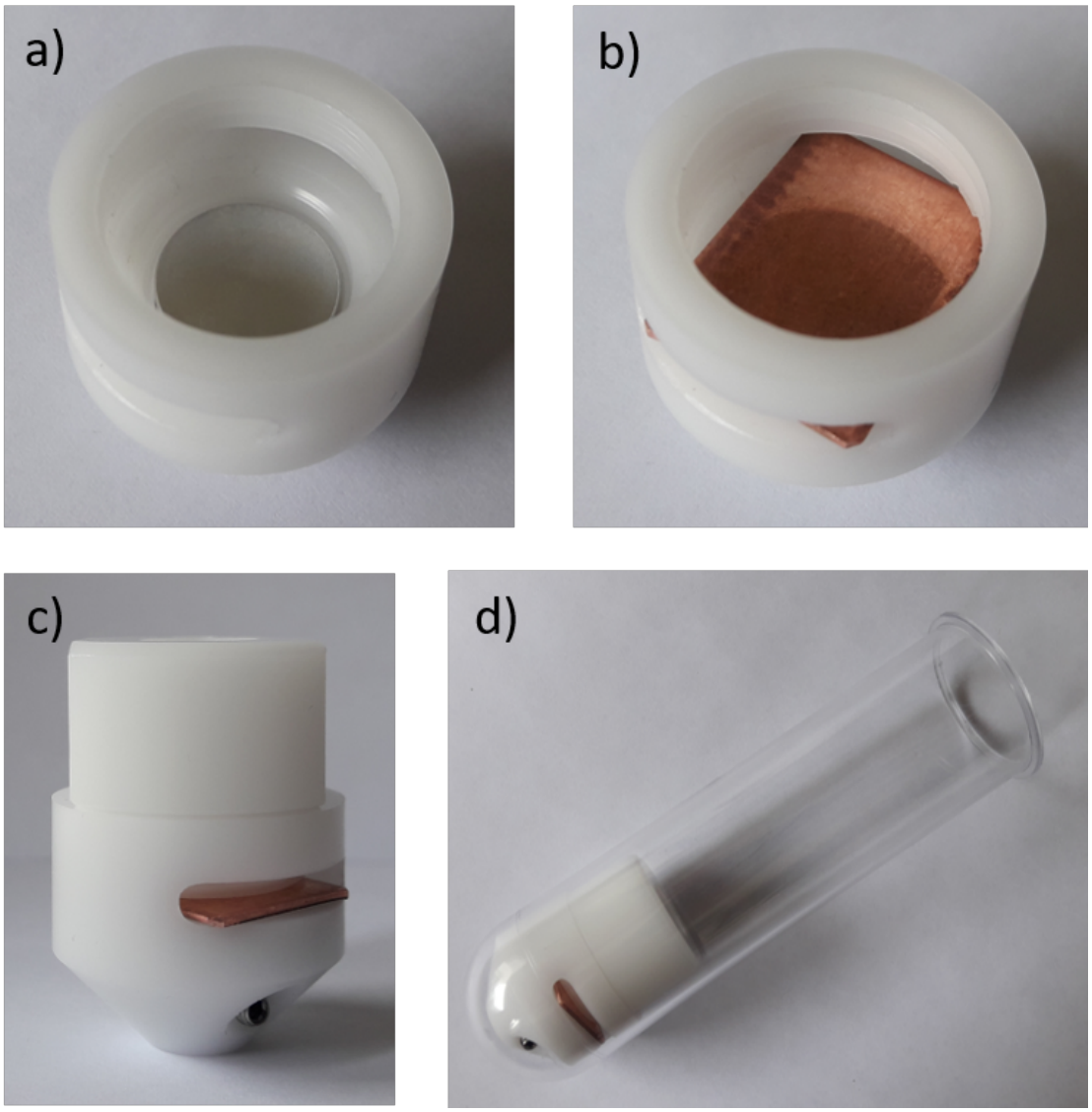

Figure D.4: Picture of the sample holder custom made for preliminary studies. a) The aluminum pin where the carbon tape has been stuck is visible on the picture. b) The copper sample is in the sample holder. c) The copper sample is fixed while screwing the upper part of the sample holder. d) The assembly in put in the tube of the centrifuge.

The design of the sample holders used at high speed has to be adapted in order to provide to the tubes sufficient internal support to maintain structural integrity. An illustration of the tube collapse in given in figure D.5. The collapse of the tube may deteriorate the rotor.

The sample holder has been designed has full filling the tube. On the other hand, the sample holder had to be as light as possible. Indeed, the equivalent density of the assembly (sample + pin stub + sample holder) had to be maintained in the range of the liquid solution usually used in the centrifuges (in this case the equivalent density was 1.29 g.cm^{-3}). Depending on this density the maximum speed that can handle the rotor is documented.

In the 70.1 Ti rotor, the tube are tilted with an 23°. The distance between the sample surface, vertical once the sample holder as inserted in the rotor, and the axis of rotation is measured at 76.15 mm.

Considering the high speed used in the test campaigns, rotors were carefully balanced before centrifugation thanks to tubes filled of water, (tolerances were 0.0001 g).

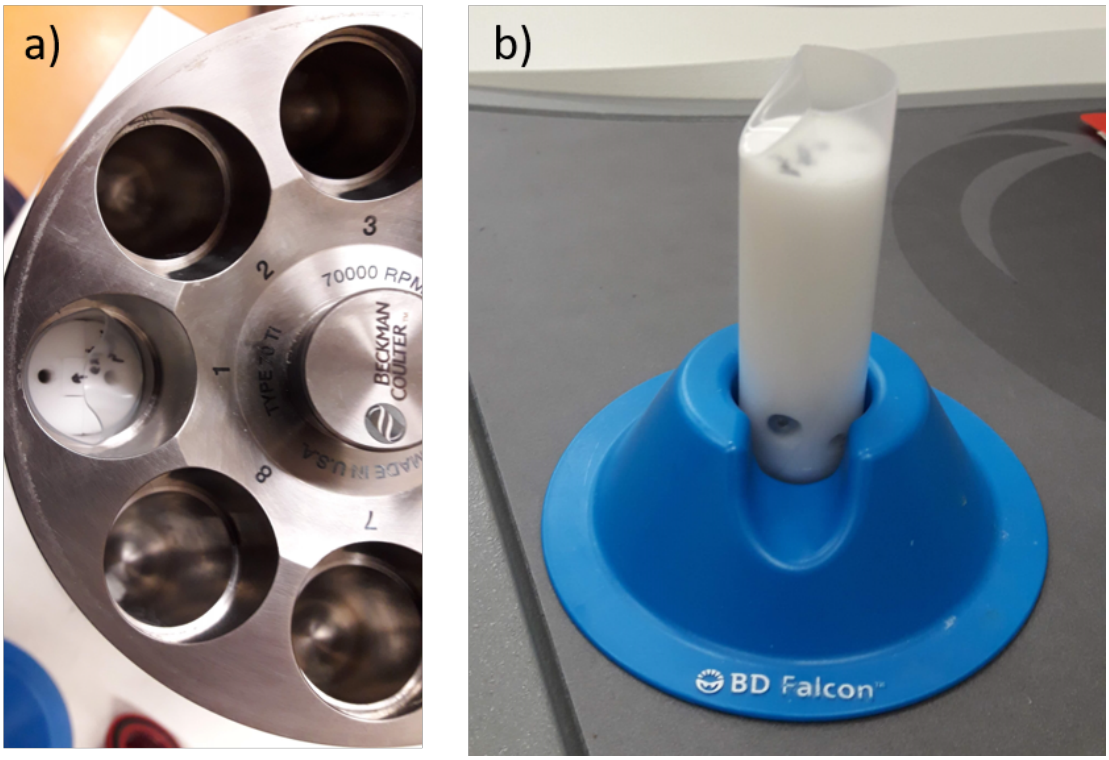

Figure D.5: Picture of the collapse of the centrifuge tube a) in the rotor b) once extracted from the rotor.

D.3 LASAT campaigns

D.3.1 Experimental setup pictures

Experimental assembly at room temperature

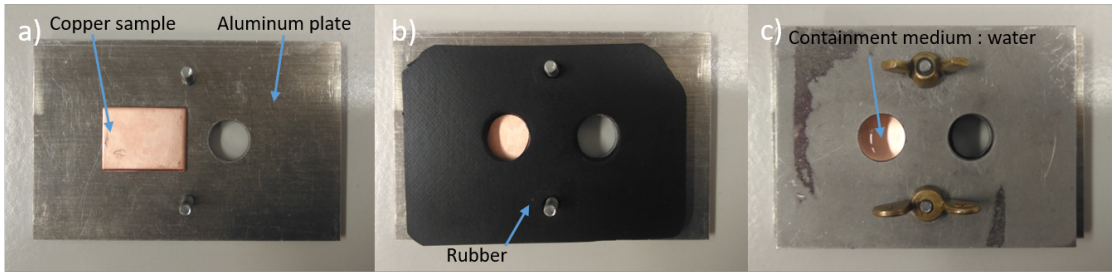

Figure D.6: Top view pictures of the sample and the sample holder, Mounting proceeding: a) The copper sample is placed on one of the two holes drilled in the aluminum plate. b) A robber layer is placed on the top of the sample, the front face of the sample is visible through the holes drilled in the rubber layer. c) A second aluminium plate is positioned. The sample holder is clamped and the space is used as a recipient for the water if used as a the containment medium.

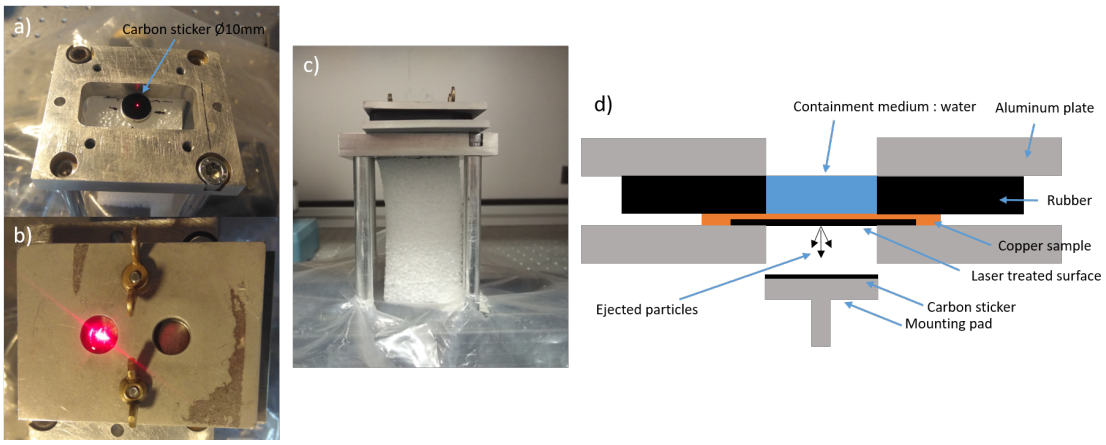

Figure D.7: Pictures of the sample holder and particles collectors. Mounting proceeding: a) The carbon sticker is stuck on the aluminium stub place in the trajectory of impinging laser (the red dot corresponding to the pointing laser can be seen). b) The sample holder is placed with the sample in the trajectory of the impinging laser. c) Side view of the assembly. d) Schematic side view of the assembly.

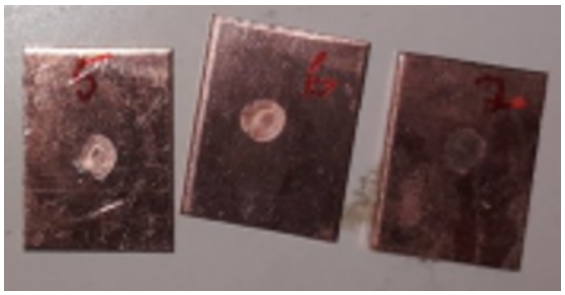

Figure D.8: Picture of the front surface of 3 samples after laser shock. In this case the diameter of shock was 4 mm. The circular spots in the center of the copper sample correspond to the impacts of the laser. Picture by Michel BOUSTIE.

Experimental assembly at cryogenic temperatures

The sample holder was first cold being immersed in the liquid nitrogen until a contained

boiling of the nitrogen bath. The sample holder was then extracted of the bath, the copper sample was assembled. The assembly was then party immersed in the nitrogen bath, the upper part of the sample holder and the sample remained out of the nitrogen and installed in the LASAT. Thanks to the evaporation of the nitrogen bath, the air is chased of the surrounding and no ice condensation has been observed on the sample holder.

The aluminum stub collecting the detached particles is placed in a expanded polystyrene base. Although the stub was maintained out of the nitrogen, on an isolating material, its temperature decreased. The no-adherence of the carbon tape on the aluminium stub has been observed that after 5 min of immersion of the base. It has been decided to manipulate the aluminum stub back at the room temperature once the adherence of the carbon tape was recovered.

The use of Kapton (polyimide) tape was considered as it remains stable at cryogenic temperatures. Nevertheless, in the absence of calibration performed with the VISAR and references without in the literature, the transparent tape already used at room temperature as a confinement media for the calibration was preferred. As the transparent tape did not show a good adherence on the copper at cryogenic temperature during preliminary tests. A 3D printed silicon ring was added of the upper flange to press on the tape and insure its contact with the copper sample.

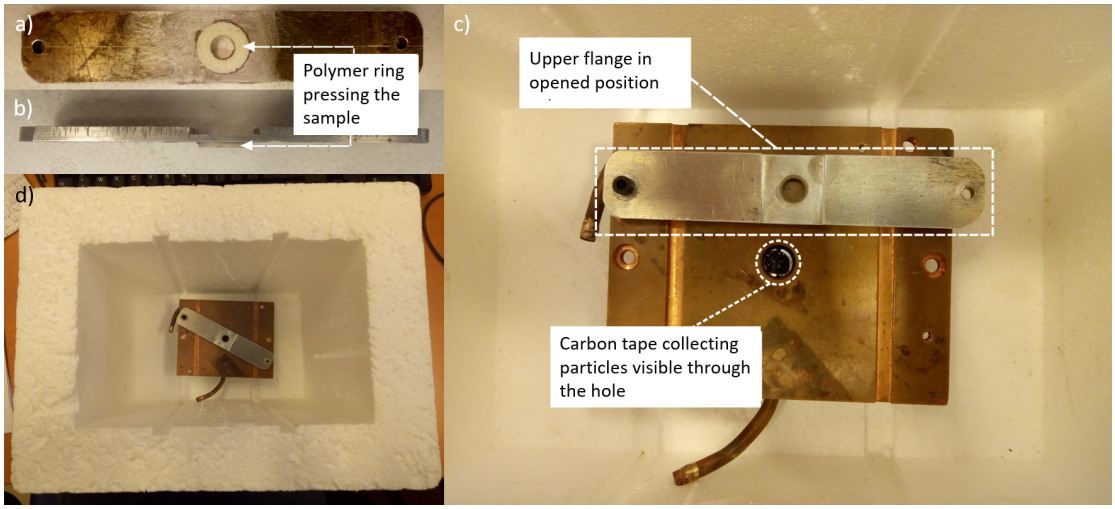

Figure D.9: a) View of the upper flange pressing the sample. B) Side view of the upper flange. c) Top view of the sample holder. d) Sample holder in closed position placed into the recipient which will contain liquid nitrogen. Picture by Antoine DEBRAY.

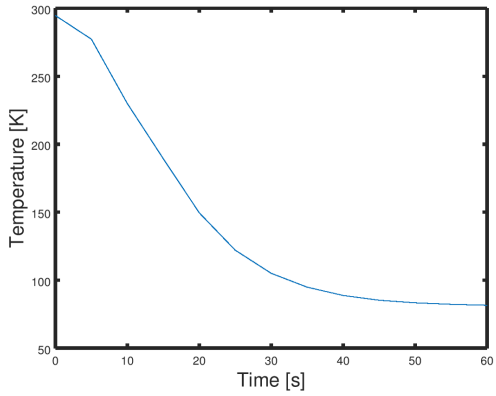

Figure D.10: Temperature measured by a K-type thermocouple brazed on the front side of a 1-mm-thick copper sample when assembled on the sample holder. t= 0 s corresponds to the immersion of the sample holder in the liquid nitrogen bath. After 1 min the temperature of the sample is stabilised around 60 K. The LASAT was performed after 2 min.

D.3.2 LASAT calibration on untreated samples

Treatment of the signal, downsampling

Post treatment of the signal from the interferometer was made with Labview software. Two velocity per fringe constants were used: 99.2 m.s^{-1}/frange when the copper sample thickness was 2 mm and 1 mm the maximum amplitude of the first peak of velocity was 104.51 m.s^{-1} and 144.7 m.s^{-1}/frange when the copper sample thickness was 500 μm and 200 μm and therefore the measured velocity was 125.8 m.s^{-1} (thickness 500 μm).

The VISAR system allowed velocity measurements from 10 m.s^{11} to several thousands of m.s^{-1}. On thick copper samples at low power densities, the velocity peak value did not exceed 10-20 m.s^{-1}. The lower sensibility limit was reached in this configuration. VISAR allowed attaining an acquisition frequency of 20 GHz (corresponding to a time interval of 0.05 ns). The signals presented in this work have been downsampled during the post-treatment with *Octave* Software, using Tchebishev low pass filtering to increase time sampling up to 2 ns to speed up data processing. Signals before and after filtering are plotted in the appendix, in figure D.11.

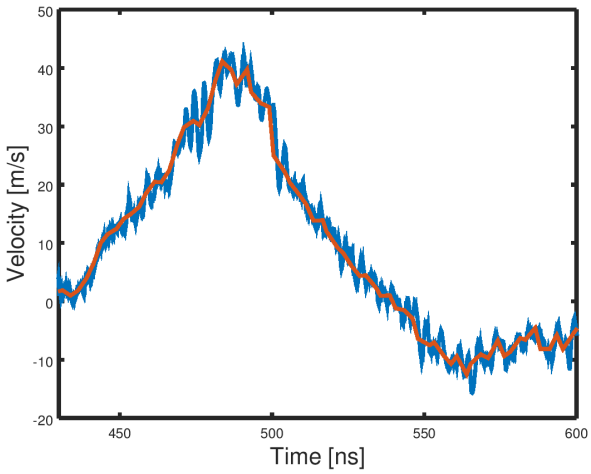

Figure D.11: Signal before (in blue) and after (in red) the downsampling.

Velocity measurement

Transparent tape confinement

Sample thickness : 2 mm

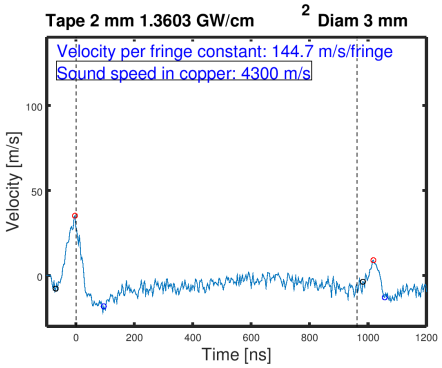

Figure D.12: Comparison of the VISAR measurements on a copper untreated sample of a thickness of 2 mm, with tape as confinement media, at the power density of 1.36 GW.cm^{-2}.

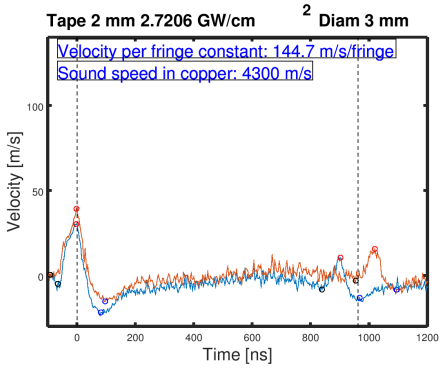

Figure D.13: Comparison of the VISAR measurements on a copper untreated sample of a thickness of 2 mm, with tape as confinement media, at the power density of 2.72 GW.cm^{-2}.

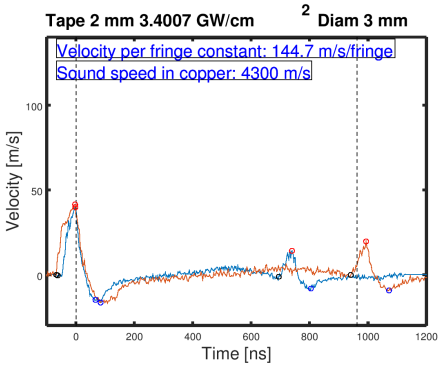

Figure D.14: Comparison of the VISAR measurements on a copper untreated sample of a thickness of 2 mm, with tape as confinement media, at the power density of 3.40 GW.cm^{-2}.

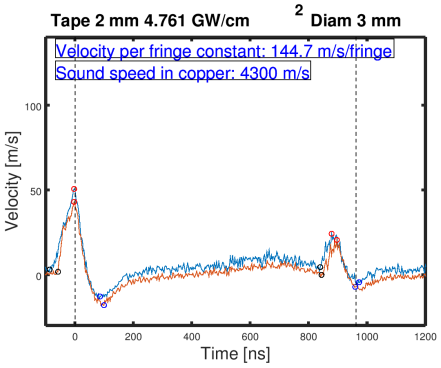

Figure D.16: Comparison of the VISAR measurements on a copper untreated sample of a thickness of 2 mm, with tape as confinement media, at the power density of 4.76 GW.cm^{-2}.

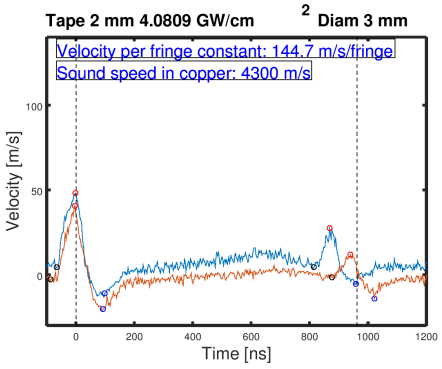

Figure D.15: Comparison of the VISAR measurements on a copper untreated sample of a thickness of 2 mm, with tape as confinement media, at the power density of 4.08 GW.cm^{-2}.

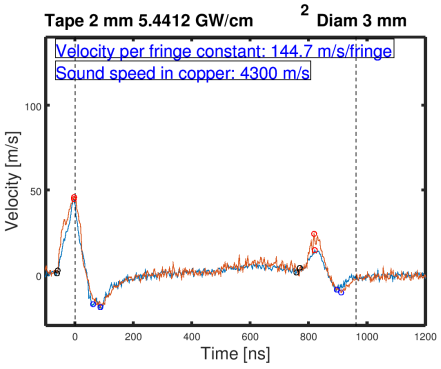

Figure D.17: Comparison of the VISAR measurements on a copper untreated sample of a thickness of 2 mm, with tape as confinement media, at the power density of 5.44 GW.cm^{-2}.

Sample thickness : 1 mm

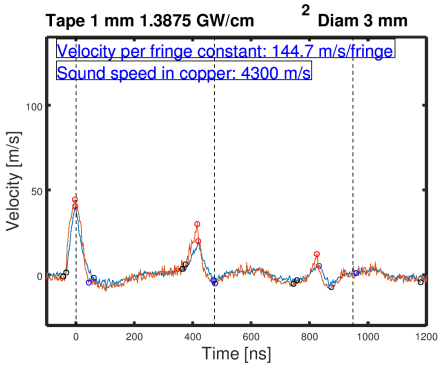

Figure D.18: Comparison of the VISAR measurements on a copper untreated sample of a thickness of 1 mm, with tape as confinement media, at the power density of 1.39 GW.cm^{-2}.

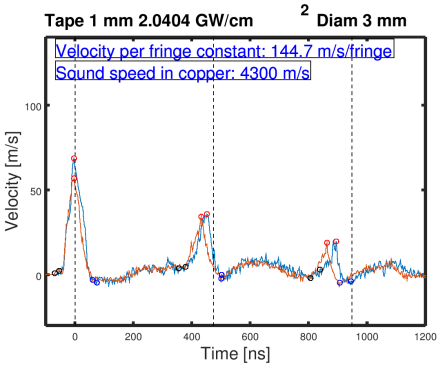

Figure D.19: Comparison of the VISAR measurements on a copper untreated sample of a thickness of 1 mm, with tape as confinement media, at the power density of 2.04 GW.cm^{-2}.

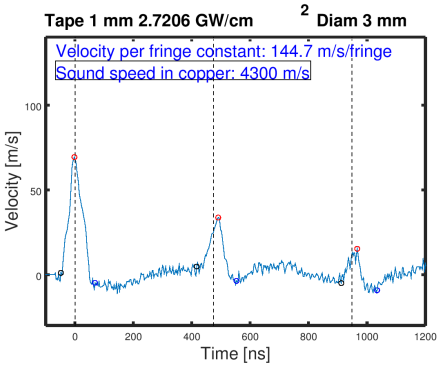

Figure D.20: Comparison of the VISAR measurements on a copper untreated sample of a thickness of 1 mm, with tape as confinement media, at the power density of 2.72 GW.cm^{-2}.

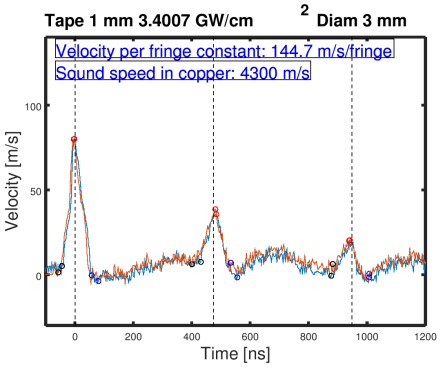

Figure D.21: Comparison of the VISAR measurements on a copper untreated sample of a thickness of 1 mm, with tape as confinement media, at the power density of 3.40 GW.cm^{-2}.

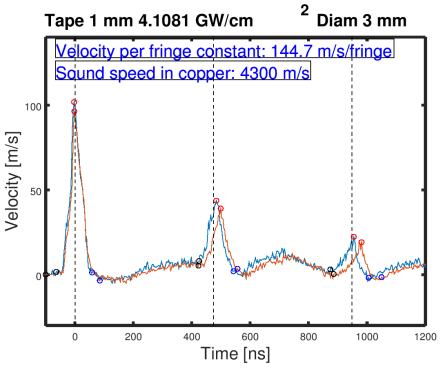

Figure D.22: Comparison of the VISAR measurements on a copper untreated sample of a thickness of 1 mm, with tape as confinement media, at the power density of 4.11 GW.cm^{-2}.

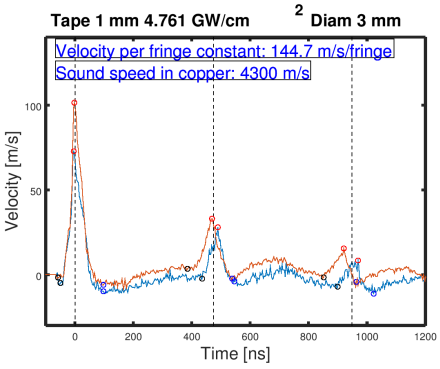

Figure D.23: Comparison of the VISAR measurements on a copper untreated sample of a thickness of 1 mm, with tape as confinement media, at the power density of 4.76 GW.cm^{-2}.

Water confinement

Sample thickness : 2 mm

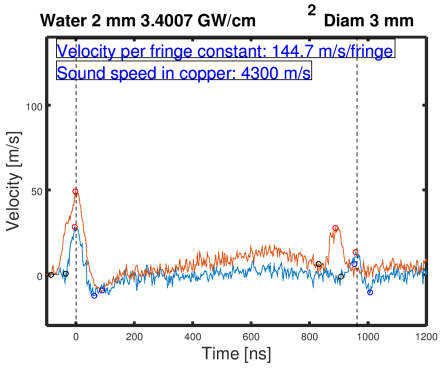

Figure D.24: Comparison of the VISAR measurements on a copper untreated sample of a thickness of 2 mm, with water as confinement media, at the power density of 3.40 GW.cm^{-2}.

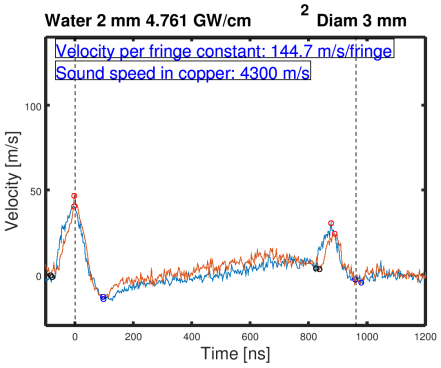

Figure D.26: Comparison of the VISAR measurements on a copper untreated sample of a thickness of 2 mm, with water as confinement media, at the power density of 4.76 GW.cm^{-2}.

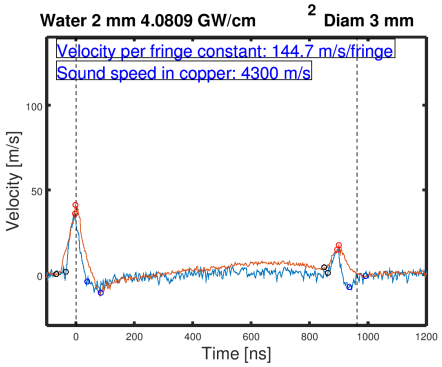

Figure D.25: Comparison of the VISAR measurements on a copper untreated sample of a thickness of 2 mm, with water as confinement media, at the power density of 4.08 GW.cm^{-2}.

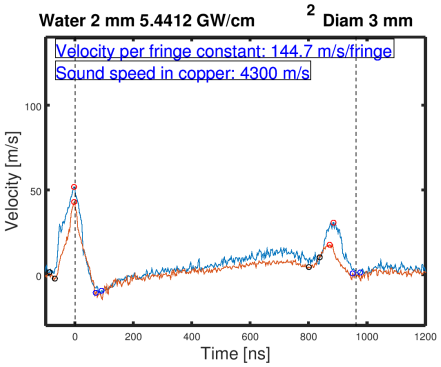

Figure D.27: Comparison of the VISAR measurements on a copper untreated sample of a thickness of 2 mm, with water as confinement media, at the power density of 5.44 GW.cm^{-2}.

Sample thickness : 1 mm

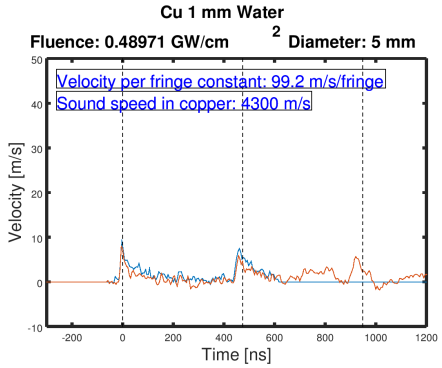

Figure D.28: Comparison of the VISAR measurements on a copper untreated sample of a thickness of 1 mm, with tape as confinement media, at the power density of 0.49 GW.cm^{-2}.

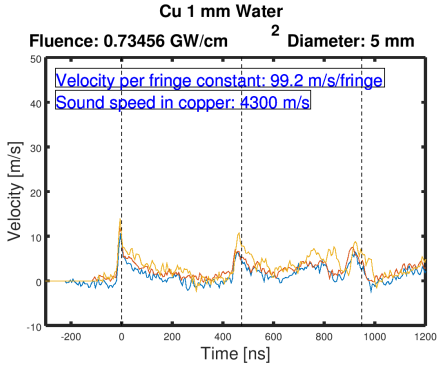

Figure D.29: Comparison of the VISAR measurements on a copper untreated sample of a thickness of 1 mm, with tape as confinement media, at the power density of 0.73 GW.cm^{-2}.

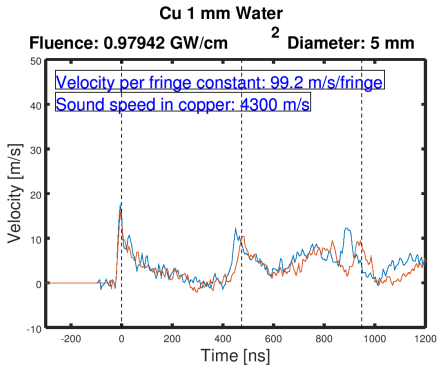

Figure D.30: Comparison of the VISAR measurements on a copper untreated sample of a thickness of 1 mm, with tape as confinement media, at the power density of 0.98 GW.cm^{-2}.

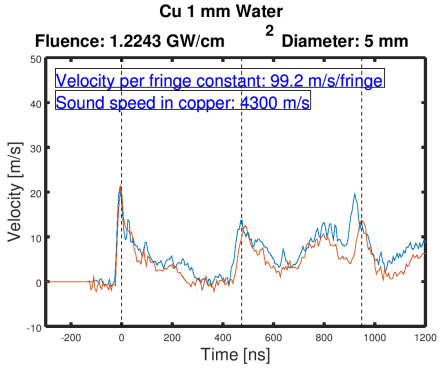

Figure D.31: Comparison of the VISAR measurements on a copper untreated sample of a thickness of 1 mm, with tape as confinement media, at the power density of 1.22 GW.cm^{-2}.

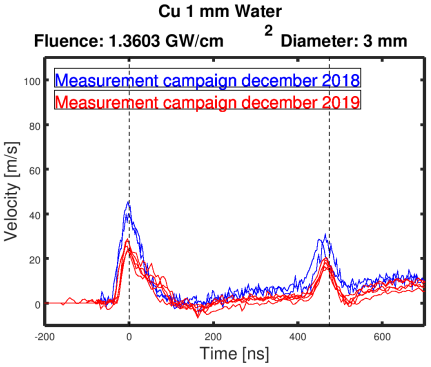

Figure D.32: Comparison of the VISAR measurements on a copper untreated sample of a thickness of 1 mm, with tape as confinement media, at the power density of 1.36 GW.cm^{-2}.

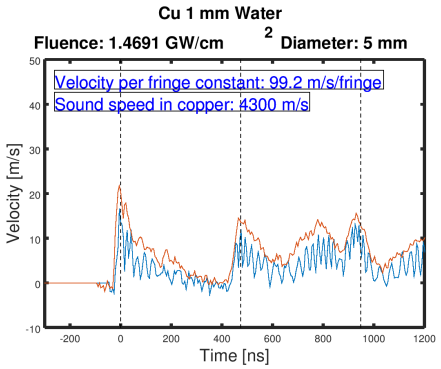

Figure D.33: Comparison of the VISAR measurements on a copper untreated sample of a thickness of 1 mm, with tape as confinement media, at the power density of 1.47 GW.cm^{-2}.

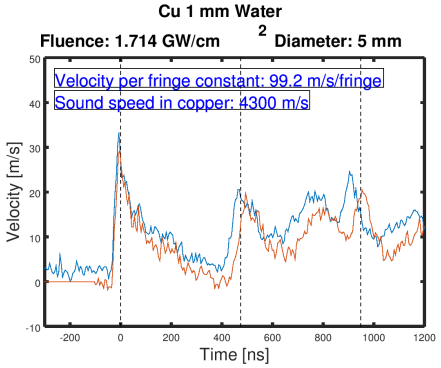

Figure D.34: Comparison of the VISAR measurements on a copper untreated sample of a thickness of 1 mm, with tape as confinement media, at the power density of 1.71 GW.cm^{-2}.

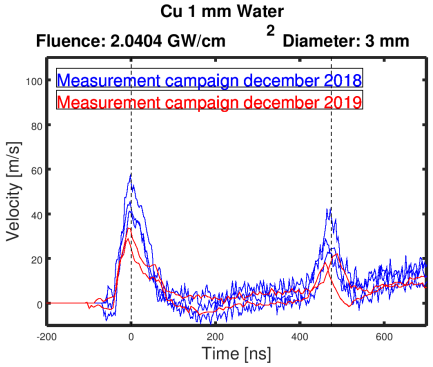

Figure D.35: Comparison of the VISAR measurements on a copper untreated sample of a thickness of 1 mm, with tape as confinement media, at the power density of 2.04 GW.cm^{-2}.

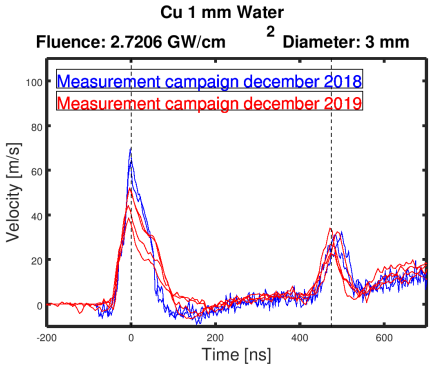

Figure D.36: Comparison of the VISAR measurements on a copper untreated sample of a thickness of 1 mm, with tape as confinement media, at the power density of 2.72 GW.cm^{-2}.

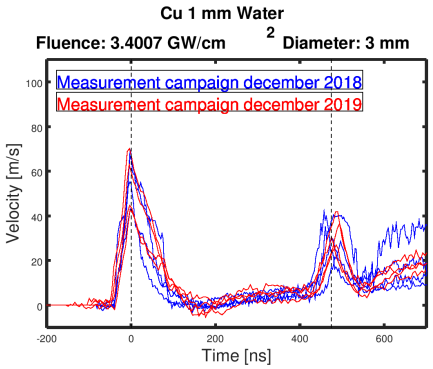

Figure D.37: Comparison of the VISAR measurements on a copper untreated sample of a thickness of 1 mm, with tape as confinement media, at the power density of 3.40 GW.cm^{-2}.

With Tantalum layer

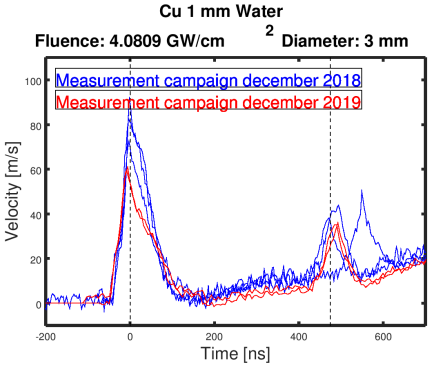

Figure D.38: Comparison of the VISAR measurements on a copper untreated sample of a thickness of 1 mm, with tape as confinement media, at the power density of 4.08 GW.cm^{-2}.

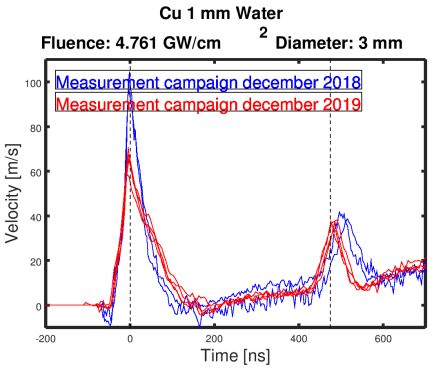

Figure D.39: Comparison of the VISAR measurements on a copper untreated sample of a thickness of 1 mm, with tape as confinement media, at the power density of 4.76 GW.cm^{-2}.

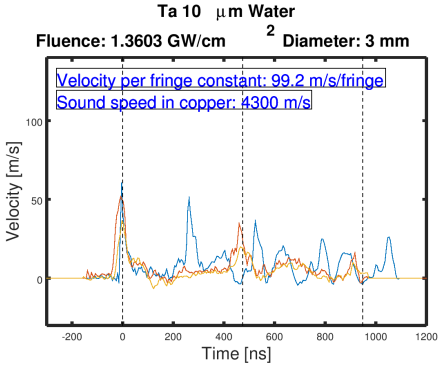

Figure D.40: Comparison of the VISAR measurements on a copper untreated sample of a thickness of 1 mm, with tape as confinement media, at the power density of 1.36 GW.cm^{-2}, with a 10-μm-thick Tantalum layer glue on the front surface.

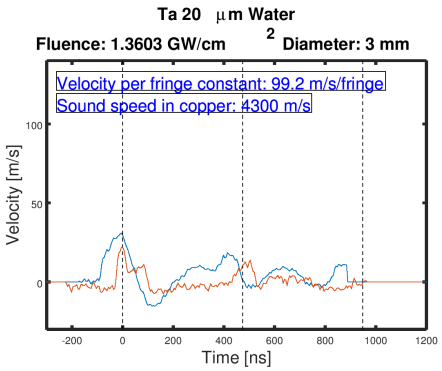

Figure D.41: Comparison of the VISAR measurements on a copper untreated sample of a thickness of 1 mm, with tape as confinement media, at the power density of 1.36 GW.cm^{-2}, with a 20-μm-thick Tantalum layer glue on the front surface.

With long pulses duration

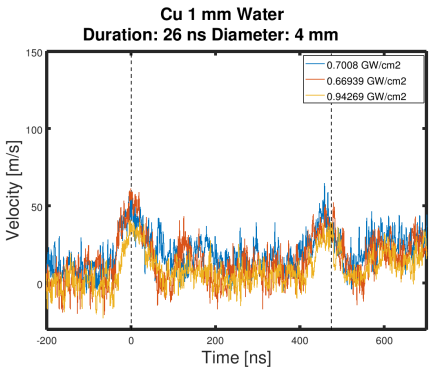

Figure D.43: Comparison of the VISAR measurements on a copper untreated sample of a thickness of 1 mm, with tape as confinement media, at the power density of 0.94 GW.cm^{-2}.

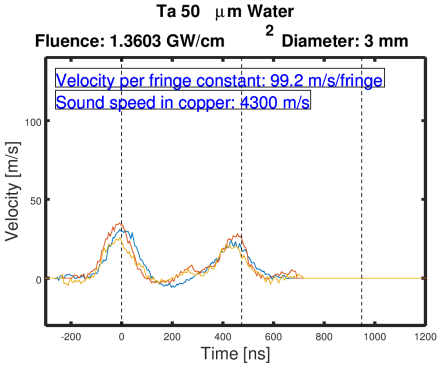

Figure D.42: Comparison of the VISAR measurements on a copper untreated sample of a thickness of 1 mm, with tape as confinement media, at the power density of 1.36 GW.cm^{-2}, with a 50-μm-thick Tantalum layer glue on the front surface.

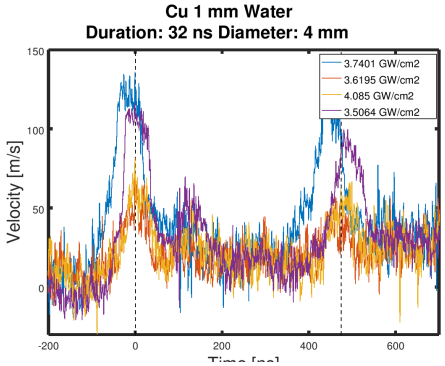

Figure D.44: Comparison of the VISAR measurements on a copper untreated sample of a thickness of 1 mm, with tape as confinement media, at the power density of 3.50 GW.cm^{-2}.

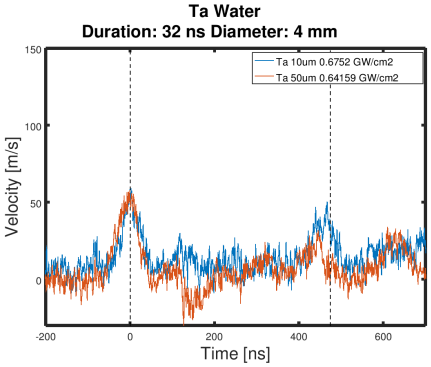

Figure D.46: Comparison of the VISAR measurements on a copper untreated sample of a thickness of 1 mm, with tape as confinement media, at the power density of 0.64 GW.cm^{-2}.

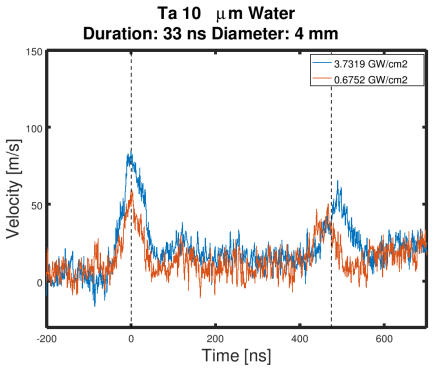

Figure D.45: Comparison of the VISAR measurements on a copper untreated sample of a thickness of 1 mm, with tape as confinement media, at the power density of 0.68 GW.cm^{-2}.

Sample thickness : 500 µm

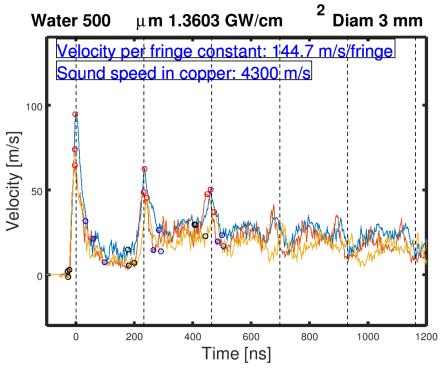

Figure D.47: Comparison of the VISAR measurements on a copper untreated sample of a thickness of 500 μm, with tape as confinement media, at the power density of 1.36 GW.cm^{-2}.

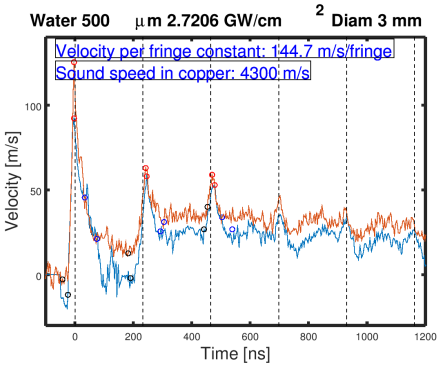

Figure D.48: Comparison of the VISAR measurements on a copper untreated sample of a thickness of 500 μm, with tape as confinement media, at the power density of 2.72 GW.cm^{-2}.

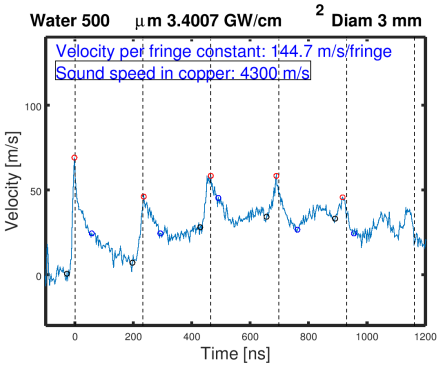

Figure D.49: Comparison of the VISAR measurements on a copper untreated sample of a thickness of 500 μm, with tape as confinement media, at the power density of 3.40 GW.cm^{-2}.

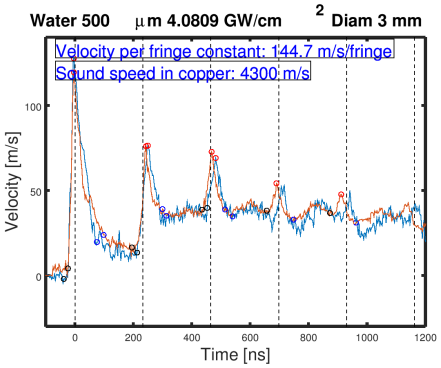

Figure D.50: Comparison of the VISAR measurements on a copper untreated sample of a thickness of 500 μm, with tape as confinement media, at the power density of 4.08 GW.cm^{-2}.

Sample thickness : 200 μm

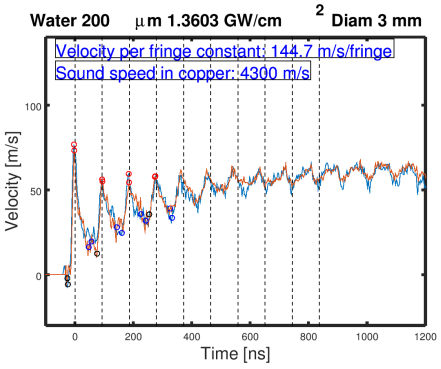

Figure D.52: Comparison of the VISAR measurements on a copper untreated sample of a thickness of 200 μm, with tape as confinement media, at the power density of 1.36 GW.cm^{-2}.

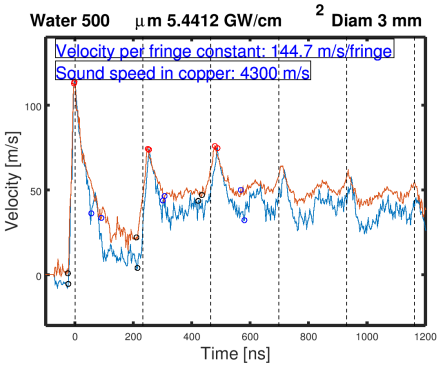

Figure D.51: Comparison of the VISAR measurements on a copper untreated sample of a thickness of 500 μm, with tape as confinement media, at the power density of 5.44 GW.cm^{-2}.

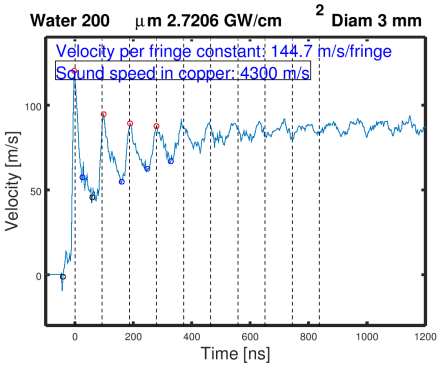

Figure D.53: Comparison of the VISAR measurements on a copper untreated sample of a thickness of 200 μm, with tape as confinement media, at the power density of 2.72 GW.cm^{-2}.

Sample thickness : Beam Screen type 74

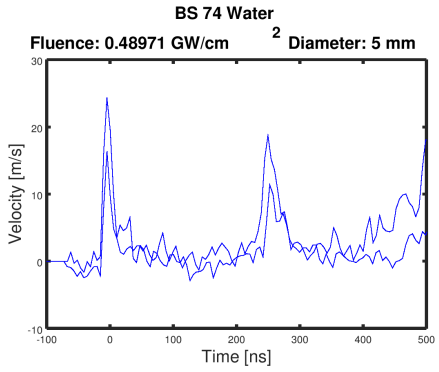

Figure D.54: Comparison of the VISAR measurements on a untreated BS74, with water as confinement media, at the power density of 0.49 GW.cm^{-2}.

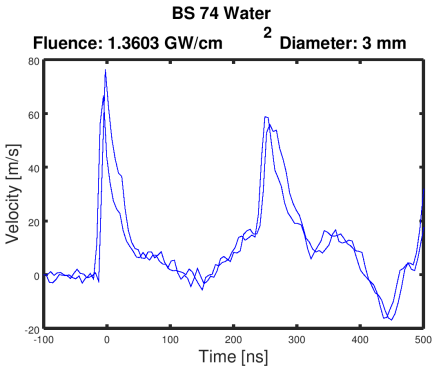

Figure D.55: Comparison of the VISAR measurements on a untreated BS74, with water as confinement media, at the power density of 1.36 GW.cm^{-2}.

With long pulses duration

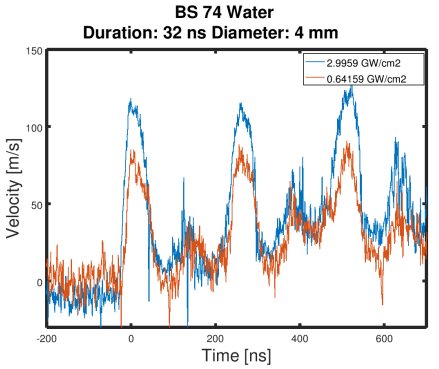

Figure D.56: Comparison of the VISAR measurements on a copper untreated sample of a thickness of 1 mm, with tape as confinement media, at the power density of 1.22 GW.cm^{-2}.

Tape confinement summary

Linear regressions of averaged maximum velocity peaks, accelerations and decelerations as functions of power density were calculated in the range between 0.48 and 4.76 GW.cm^{-2}.

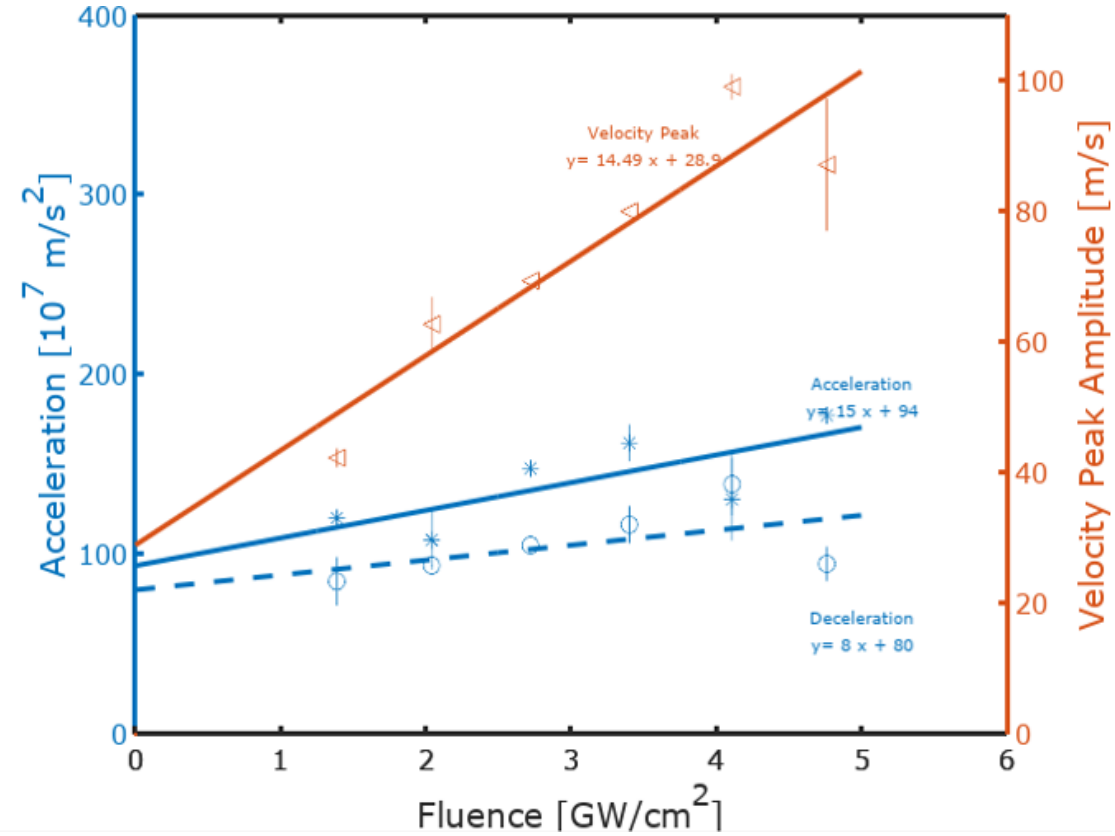

Figure D.57: Average amplitudes and calculated related accelerations and decelerations of the first peaks of measured velocities, as functions of irradiating power density. Water was used as confinement media on 1-mm-thick copper samples.

Table D.1: Expected time of the emergences of shock wave at the rear surface taking into account, the partial reflection at the interface, the shock celerity and the thickness of both the stainless steel and the copper of the layers.

Nb	Emergence	Expected time $[ns]$
1	incident shock wave	0
2	reflection at the interface of incident wave from the rear surface and peak	37
3	return from the front face of the first wave reflection at the interface	207
4	incidence shock wave after crossing the whole sample (one back and one forth)	244

D.4 Additional analysis

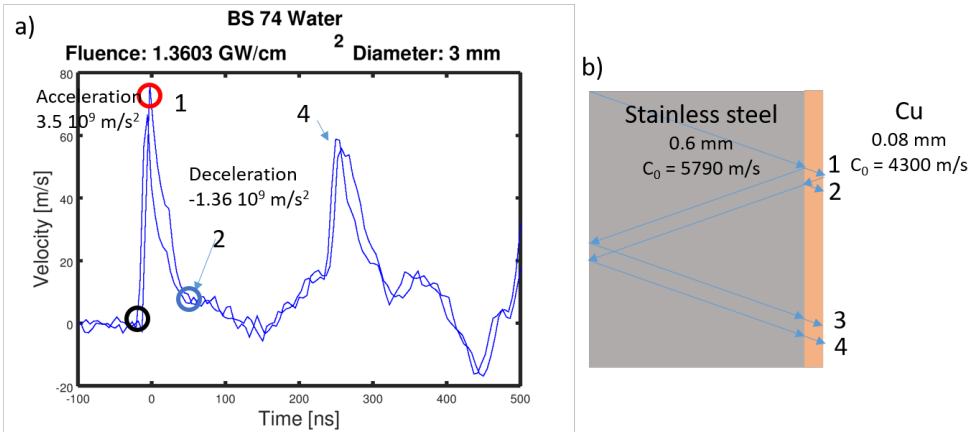

Figure D.58: a) VISAR measurements on a beam screen sample (type 74), with water as confinement media, at the power density of 1.36 GW.cm^{-2}. b) Schematic of the wave propagation and reflection at the free surfaces and at the interface between the copper and the stainless steel layers. The red circle corresponds to the maximum of the peak, The black circle correspond to the beginning of the peak. The average acceleration has been calculated between these two points. The blue circle corresponds to the end of the peak, The average deceleration has been calculated between the maximum of the peak and this point.

D.5 Wave propagation simulation

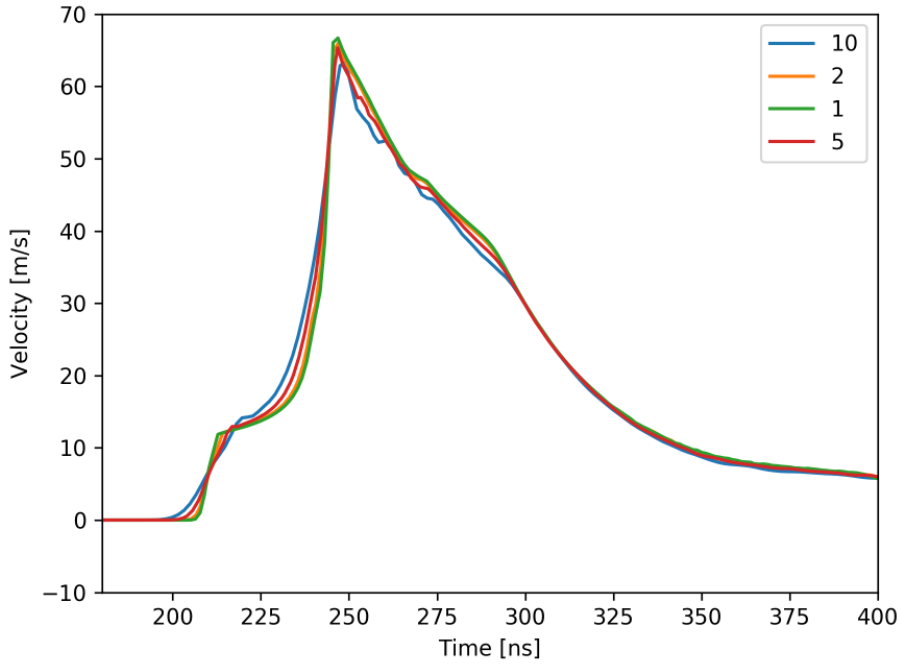

Figure D.59: First peak of velocity simulation in the axis of the the rear face with a mesh size of 10 mum, 5 mum, 2 mum, 1 mum, for the curves blue, red, yellow and green, respectively. Te curve obtained with 1 and 2 μm mesh size were mostly superposed.

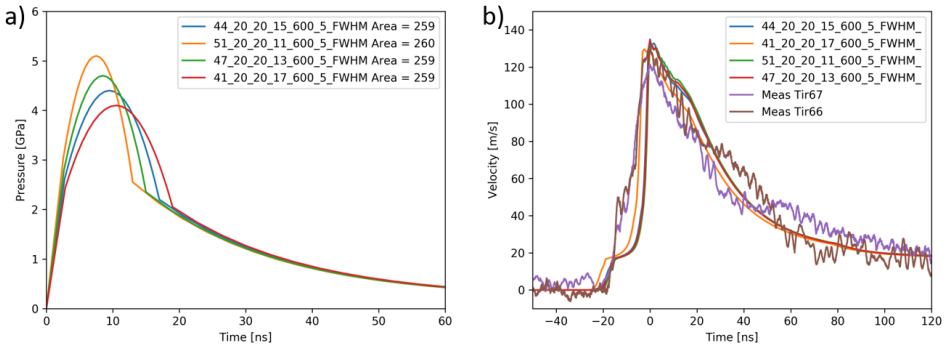

Figure D.60: a) Pressure load in simulation: various parameters but the same area under the curve. b) Comparison of the first peak of velocity of corresponding simulations and VISAR measurement.

Bibliography

[1] J. Ellis, "Beyond the standard model with the LHC," *Nature*, vol. 448, pp. 297–301, jul 2007.

[2] S. MYERS, "THE LARGE HADRON COLLIDER 2008–2013," *International Journal of Modern Physics A*, vol. 28, p. 1330035, oct 2013.

[3] M. Esma, "The CERN accelerator complex," 2016.

[4] O. Brüning, P. Collier, P. Lebrun, S. Myers, R. Ostojic, and J. Poole, *LHC Design Report*. CERN Yellow Reports: Monographs, v.2 : the ed., 2004.

[5] S. Dailler, "Cross section of LHC dipole," 1999.

[6] P. A. Gruber, *Mechanical Properties of Ultra Thin Metallic Films Revealed by Synchrotron Techniques*. PhD thesis, Max-Planck-Institut für Metallforschung Stuttgart, 2007.

[7] M. Month, S.-i. Kurokawa, and T. Stuart, *Frontiers Of Accelerator Technology - Proceedings Of The Joint Us-cern-japan International School*. World Scientific Publishing, 1999.

[8] M. Dohlus and R. Wanzenberg, "An Introduction to Wake Fields and Impedances," in *CAS-CERN Accelerator School: Intensity Limitations in Particle Beams* (W. Herr, ed.), vol. 3, (Geneva, Switzerland), pp. 2–11, CERN Yellow report, 2017.

[9] S. Calatroni, E. Bellingeri, C. Ferdeghini, M. Putti, R. Vaglio, T. Baumgartner, and M. Eisterer, "Thallium-based high-temperature superconductors for beam impedance mitigation in the Future Circular Collider," *Superconductor Science and Technology*, vol. 30, p. 075002, jul 2017.

[10] E. Métral, "RF heating from wake losses in diagnostics structures," *IBIC 2013: Proceedings of the 2nd International Beam Instrumentation Conference*, pp. 929–935, 2013.

[11] F. Ruggiero, "SINGLE-BEAM COLLECTIVE EFFECTS IN THE LHC," *Particle Accelerator*, vol. 50, pp. 83–104, 1995.

[12] V. Baglin, "The LHC vacuum system: Commissioning up to nominal luminosity," *Vacuum*, vol. 138, pp. 112–119, apr 2017.

[13] C. Benvenuti, J. Cazeneuve, P. Chiggiato, F. Cicoira, A. Escudeiro Santana, V. Johanek, V. Ruzinov, and J. Fraxedas, "A novel route to extreme vacua: the non-evaporable getter thin film coatings," *Vacuum*, vol. 53, pp. 219–225, may 1999.

[14] C. Benvenuti, "A new pumping approach for the large electron positron collider (LEP)," *Nuclear Instruments and Methods in Physics Research*, vol. 205, pp. 391–401, feb 1983.

[15] C. Benvenuti, P. Chiggiato, P. Costa Pinto, A. Escudeiro Santana, T. Hedley, A. Mongelluzzo, V. Ruzinov, and I. Wevers, "Vacuum properties of TiZrV non-evaporable getter films," *Vacuum*, vol. 60, pp. 57–65, jan 2001.

[16] V. Baglin, "VACUUM TRANSIENTS DURING LHC OPERATION," in *1st LHC Project Workshop,Accelerators and Storage Rings* (CERN, ed.), (Chamonix, France), pp. 275–282, 2004.

[17] I. Bellafont, M. Morrone, L. Mether, J. Fernández, R. Kersevan, C. Garion, V. Baglin, P. Chiggiato, and F. Pérez, "Design of the future circular hadron collider beam vacuum chamber," *Physical Review Accelerators and Beams*, vol. 23, p. 033201, mar 2020.

[18] V. V. Anashin, G. Derevyankin, V. G. Dudnikov, O. B. Malyshev, V. N. Osipov, C. L. Foerster, F. M. Jacobsen, M. W. Ruckman, M. Strongin, R. Kersevan, I. L. Maslennikov, W. C. Turner, and W. A. Lanford, "Cold beam tube photodesorption and related experiments for the Superconducting Super Collider Laboratory 20 TeV proton collider," *Journal of Vacuum Science & Technology A: Vacuum, Surfaces, and Films*, vol. 12, pp. 1663–1672, jul 1994.

[19] V. Baglin, P. Lebrun, and R. Van Weelderen, "Cryogenic Beam Screens for High-Energy Particle Accelerators," in *24th International Cryogenic Engineering Conference and International Cryogenic Materials Conference 2012*, no. January, (Fukuoka, Japan), 2013.

[20] V. Baglin, G. Bregliozzi, J. M. Jimenez, and G. Lanza, "Synchrotron radiation in the LHC vacuum system," in *IPAC 2011 - 2nd International Particle Accelerator Conference*, no. September 2011, pp. 1563–1565, 2011.

[21] G. Apollinari, I. Béjar Alonso, O. Brüning, M. Lamont, and L. Rossi, *High-Luminosity Large Hadron Collider (HL-LHC) Preliminary Design Report*. No. December, cern yello ed., 2015.

[22] O. Brüning and L. Rossi, *The High Luminosity Large Hadron Collider*, vol. 24 of *Advanced Series on Directions in High Energy Physics*. WORLD SCIENTIFIC, oct 2015.

[23] W. Herr and B. Muratori, *Concept of luminosity*, vol. 2. 2003.

[24] B. Bordini, L. Bottura, A. Devred, L. Fiscarelli, M. Karppinen, G. de Rijk, L. Rossi, F. Savary, and G. Willering, "Nb3Sn 11 T Dipole for the High Luminosity LHC (CERN)," in *Nb3Sn Accelerator Magnets*, ch. 9, pp. 223–258, Springer, Cham, 2019.

[25] R. B. Palmer, "Energy Scaling, Crab Crossing, and the Pair Problem," *Slac-Pub-4707*, vol. C8806271, pp. 613–619, 1988.

[26] R. Calaga, "CRAB Cavities for the LHC upgrade," in *Proceedings - Chamonix 2012 Workshop on LHC Performance*, no. 2, pp. 363–372, 2012.

[27] M. Morrone, *Thermomechanical study of complex structures in the aperture of superconducting magnets: Application to the design of the High-Luminosity Large Hadron Collider shielded beam screen.* PhD thesis, Imperial College, London, 2018.

[28] W. Fischer, M. Blaskiewicz, J. M. Brennan, H. Huang, H.-C. Hseuh, V. Ptitsyn, T. Roser, P. Thieberger, D. Trbojevic, J. Wei, S. Y. Zhang, and U. Iriso, "Electron cloud observations and cures in the Relativistic Heavy Ion Collider," *Physical Review Special Topics - Accelerators and Beams*, vol. 11, p. 041002, apr 2008.

[29] G. Rumolo, F. Ruggiero, and F. Zimmermann, "Simulation of the electron-cloud build up and its consequences on heat load, beam stability, and diagnostics," *Physical Review Special Topics - Accelerators and Beams*, vol. 4, p. 012801, jan 2001.

[30] R. Cimino and T. Demma, "Electron cloud in accelerators," *International Journal of Modern Physics A*, vol. 29, p. 1430023, jul 2014.

[31] P. A. Anderson, "The Work Function of Copper," *Physical Review*, vol. 76, pp. 388–390, aug 1949.

[32] G. Skripka and G. Iadarola, "Beam-induced heat loads on the beam screens of the inner tripletsforthe HL-LHC," Tech. Rep. February, 2018.

[33] V. Baglin, J. Bojko, O. Gröbner, B. Henrist, N. Hilleret, C. Scheuerlein, and M. Taborelli, "The secondary electron yield of technical materials and its variation with surface treatments," in *EPAC 2000*, (Vienna), pp. 217–221, 2000.

[34] G. Iadarola, *Electron cloud studies for CERN particle accelerators and simulation code development.* PhD thesis, Università degli Studi di Napoli Federico II, 2014.

[35] G. Rumolo and G. Iadarola, "Electron Clouds," vol. 3, no. November 2015, pp. 2–11, 2017.

[36] J. M. Jimenez, G. Arduini, P. Collier, G. Ferioli, B. Henrist, N. Hilleret, L. Jensen, K. Weiss, and F. Zimmermann, "Electron Cloud with LHC-type beams in the SPS

: a review of three years of measurements," in *Mini Workshop on Electron Cloud Simulations for Proton and Positron Beams* (CERN, ed.), (Geneva), p. 13, 2003.

[37] F. Zimmermann, "Beam Dynamics Challenges for Future Circular Colliders," in *European Particle Accelerator Conference*, (Lucerne, Switzerland), 2004.

[38] G. Iadarola and G. Rumolo, "Electron cloud in the CERN accelerators (PS, SPS, LHC)," sep 2013.

[39] F. Zimmermann, "Electron-Cloud Effects in past and future machines - walk through 50 years of Electron-Cloud studies," in *Joint INFN-CERN-EuCARD-AccNet Workshop on Electron-Cloud Effects: ECLOUD'12*, no. 2013, (La Biodola, Isola d'Elba, Italy), aug 2013.

[40] P. Chiggiato, "Beam Screen Treatment for LHC 's Point 2 and 8," in *LHC Performance Workshop*, 2018.

[41] S. Claudet, "HL-LHC Cryogenics Required Clarifications (1 / 2) Clarification on the e-cloud heat load and spare capacities in the triplet and," in *Chamonix workshop*, 2018.

[42] F. today, "Components of the inner triplet installed in building 181. April 2005," 2015.

[43] G. Arduini, J. Barranco, A. Bertarelli, N. Biancacci, R. Bruce, O. Brüning, X. Buffat, Y. Cai, L. Carver, S. Fartoukh, M. Giovannozzi, G. Iadarola, K. Li, A. Lechner, L. M. Medrano, E. Métral, Y. Nosochkov, Y. Papaphilippou, D. Pellegrini, T. Pieloni, J. Qiang, S. Redaelli, A. Romano, L. Rossi, G. Rumolo, B. Salvant, M. Schenk, C. Tambasco, R. Tomás, S. Valishev, and F. V. der Veken, "High Luminosity LHC: challenges and plans," *Journal of Instrumentation*, vol. 11, pp. C12081–C12081, dec 2016.

[44] G. Iadarola, G. Arduini, D. B. Zamora, S. Claudet, P. Dijkstal, R. D. Maria, L. Mether, E. Metral, G. Rumolo, and G. Skripka, "Beam induced heat loads on HL-LHC Beam Screens," in *7th HL-LHC Collaboration Meeting*, no. November, (Madrid, Spain), CERN, 2017.

[45] L. F. Wang, D. Raparia, J. Wei, and S. Y. Zhang, "Mechanism of electron cloud clearing in the accumulator ring of the Spallation Neutron Source," *Physical Review Special Topics - Accelerators and Beams*, vol. 7, p. 034401, mar 2004.

[46] Y. Suetsugu, H. Fukuma, M. Pivi, and L. Wang, "Continuing study on electron-cloud clearing techniques in high-intensity positron ring: Mitigation by using groove surface in vertical magnetic field," *Nuclear Instruments and Methods in Physics Research Section A: Accelerators, Spectrometers, Detectors and Associated Equipment*, vol. 604, pp. 449–456, jun 2009.

[47] J. R. Calvey, W. Hartung, Y. Li, J. A. Livezey, J. Makita, M. A. Palmer, and D. Rubin, "Measurements of electron cloud growth and mitigation in dipole, quadrupole, and wiggler magnets," *Nuclear Instruments and Methods in Physics Research, Section A: Accelerators, Spectrometers, Detectors and Associated Equipment*, vol. 770, pp. 141–154, jan 2015.

[48] M. Pivi, F. K. King, R. E. Kirby, T. O. Raubenheimer, G. Stupakov, and F. Le Pimpec, "Sharp reduction of the secondary electron emission yield from grooved surfaces," *Journal of Applied Physics*, vol. 104, p. 104904, nov 2008.

[49] R. Cimino, M. Commisso, D. R. Grosso, T. Demma, V. Baglin, R. Flammini, and R. Larciprete, "Nature of the Decrease of the Secondary-Electron Yield by Electron Bombardment and its Energy Dependence," *Physical Review Letters*, vol. 109, p. 064801, aug 2012.

[50] O. Hachenberg and W. Brauer, "Secondary Electron Emission from Solids," in *Advances in Electronics and Electron Physics*, vol. 11, pp. 413–499, 1959.

[51] B. Henrist, N. Hilleret, J. M. Jimenez, C. Scheuerlein, M. Taborelli, and G. Vorlaufer, "Secondary electron emission data for the simulation of electron cloud," in *Mini Workshop on Electron-Cloud Simulations for Proton and Positron Beams*, pp. 75–78, 2002.

[52] H. Seiler, "Secondary electron emission in the scanning electron microscope," *Journal of Applied Physics*, vol. 54, pp. R1–R18, nov 1983.

[53] M. Furman and M. Pivi, "Probabilistic model for the simulation of secondary electron emission," *Physical Review Special Topics - Accelerators and Beams*, vol. 5, p. 124404, dec 2002.

[54] E. L. Garwin, F. K. King, R. E. Kirby, and O. Aita, "Surface properties of metal-nitride and metal-carbide films deposited on Nb for radio-frequency superconductivity," *Journal of Applied Physics*, vol. 61, pp. 1145–1154, feb 1987.

[55] P. Chiggiato and P. Costa Pinto, "Ti-Zr-V non-evaporable getter films: From development to large scale production for the Large Hadron Collider," *Thin Solid Films*, vol. 515, pp. 382–388, oct 2006.

[56] B. Henrist, N. Hilleret, C. Scheuerlein, and M. Taborelli, "The secondary electron yield of TiZr and TiZrV non-evaporable getter thin film coatings," *Applied Surface Science*, vol. 172, pp. 95–102, mar 2001.

[57] C. Yin Vallgren, G. Arduini, J. Bauche, S. Calatroni, P. Chiggiato, K. Cornelis, P. C. Pinto, B. Henrist, E. Métral, H. Neupert, G. Rumolo, E. Shaposhnikova, and M. Taborelli, "Amorphous carbon coatings for the mitigation of electron cloud in the CERN Super Proton Synchrotron," *Physical Review Special Topics - Accelerators and Beams*, vol. 14, no. 7, 2011.

[58] P. Costa Pinto, S. Calatroni, H. Neupert, D. Letant-Delrieux, P. Edwards, P. Chiggiato, M. Taborelli, W. Vollenberg, C. Yin Vallgren, J. L. Colaux, and S. Lucas, "Carbon coatings with low secondary electron yield," *Vacuum*, vol. 98, pp. 29–36, 2013.

[59] M. Taborelli, P. Chiggiato, P. Costa Pinto, and P. Cruikshank, "Nine years of carbon coating development for the SPS upgrade : achievements and heritage," tech. rep., CERN, 2016.

[60] V. Baglin, I. Collins, and B. Jenninger, "Performance of a cryogenic vacuum system (COLDEX) with an LHC type beam," *Vacuum*, vol. 73, pp. 201–206, mar 2004.

[61] R. Salemme, V. Baglin, F. Bellorini, G. Bregliozzi, K. Brodzinski, P. Chiggiato, P. C. Pinto, P. Gomes, A. Gutierrez, V. Inglese, B. Jenninger, E. Michel, M. Pezzetti, B. Rio, A. Sapountzis, and R. Kersevan, "Recommissioning of the COLDEX experiment at CERN," in *6th International Particle Accelerator Conference, IPAC 2015*, pp. 3109–3111, 2015.

[62] R. Salemme, V. Baglin, S. Calatroni, P. Chiggiato, B. Di Girolamo, B. Jenninger, M. Sitko, A. Abdolvand, and S. Wackerow, "First beam test of laser engineered surface structures (LESS) at cryogenic temperature in CERN SPS accelerator preseries characterization," *International Particle Accelerator Conference*, pp. 2016–2019, 2016.

[63] R. Salemme, V. Baglin, S. Calatroni, P. Chiggiato, B. Di Girolamo, E. Garcia-Tabares Valdivieso, B. Jenninger, L. Prever-Loiri, M. Sitko, S. Wackerow, and A. Abdolvand, "First beam test of Laser Engineered Surface Structures (LESS) at cryogenic temperature in CERN SPS accelerator," *Journal of Physics: Conference Series*, vol. 1067, p. 082017, sep 2018.

[64] P. Costa Pinto, V. Baglin, S. Calatroni, P. Chiggiato, P. Cruikshank, and P. Demolon, "In-situ a-C coating performance and status of LESS & tunnel implementation," in *7th HL-LHC Collaboration Meeting*, (Madrid, Spain), 2017.

[65] K. Nishimura, T. Itotani, and K. Ohya, "Influence of Surface Roughness on Secondary Electron Emission and Electron Backscattering from Metal Surface," *Japanese Journal of Applied Physics*, vol. 33, pp. 4727–4734, aug 1994.

[66] G. Stupakov and M. Pivi, "Suppression of the effective secondary emission yield for a grooved metal surface," Tech. Rep. June, SLAC, Stanford, 2004.

[67] J. Kawata, K. Ohya, and K. Nishimura, "Simulation of secondary electron emission from rough surfaces," *Journal of Nuclear Materials*, vol. 220-222, pp. 997–1000, apr 1995.

[68] A. Krasnov, "Molecular pumping properties of the LHC arc beam pipe and effective secondary electron emission from Cu surface with artificial roughness," *Vacuum*, vol. 73, pp. 195–199, mar 2004.

[69] Y. Suetsugu, M. Tsuchiya, T. Nishidono, N. Kato, N. Satoh, S. Endo, and T. Yokoyama, "Application of a sawtooth surface to accelerator beam chambers with low electron emission rate," *Journal of Vacuum Science & Technology A: Vacuum, Surfaces, and Films*, vol. 21, pp. 186–195, jan 2003.

[70] L. Wang, T. Raubenheimer, and G. Stupakov, "Suppression of secondary emission in a magnetic field using triangular and rectangular surfaces," *Nuclear Instruments and Methods in Physics Research Section A: Accelerators, Spectrometers, Detectors and Associated Equipment*, vol. 571, pp. 588–598, feb 2007.

[71] M. Ye, Y. N. He, S. G. Hu, R. Wang, T. C. Hu, J. Yang, and W. Z. Cui, "Suppression of secondary electron yield by micro-porous array structure," *Journal of Applied Physics*, vol. 113, p. 074904, feb 2013.

[72] M. Ye, D. Wang, and Y. He, "Mechanism of total electron emission yield reduction using a micro-porous surface," *Journal of Applied Physics*, vol. 121, p. 124901, mar 2017.

[73] J. M. Sattler, R. A. Coutu, R. Lake, T. Laurvick, T. Back, and S. Fairchild, "Modeling micro-porous surfaces for secondary electron emission control to suppress multipactor," *Journal of Applied Physics*, vol. 122, no. 5, 2017.

[74] M. Kussmaul, M. J. Mirtich, and A. Curren, "Ion Beam Treatment of Potential Space Materials at the NASA Lewis Research Center," tech. rep., NASA, Cleveland, 1992.

[75] V. Nistor, L. A. González, L. Aguilera, I. Montero, L. Galán, U. Wochner, and D. Raboso, "Multipactor suppression by micro-structured gold/silver coatings for space applications," *Applied Surface Science*, vol. 315, pp. 445–453, oct 2014.

[76] M. Sitko, V. Baglin, S. Calatroni, P. Chiggiato, B. Di Girolamo, M. Taborelli, M. Colling, T. Jones, P. Mcintosh, D. Bajek, S. Wackerow, and A. Abdolvand, "Towards the implementation of laser engineered surface structures for electron cloud mitigation LHC vacuum system and electron screens in-situ treatment," in *IPAC 2018: the ninth International Particle Accelerator Conference*, (Vancouver), pp. 7–10, 2018.

[77] S. Calatroni, E. Garcia-Tabares Valdivieso, H. Neupert, V. Nistor, A. T. Perez Fontenla, M. Taborelli, P. Chiggiato, O. Malyshev, R. Valizadeh, S. Wackerow, S. A. Zolotovskaya, W. A. Gillespie, and A. Abdolvand, "First accelerator test of vacuum components with laser-engineered surfaces for electron-cloud mitigation," *Physical Review Accelerators and Beams*, vol. 20, p. 113201, nov 2017.

[78] W. M. Steen and J. Mazumder, *Laser Material Processing*. London: Springer London, 4 ed., 2010.

[79] T. Smausz, T. Csizmadia, C. Tápai, J. Kopniczky, A. Oszkó, M. Ehrhardt, P. Lorenz, K. Zimmer, A. Prager, and B. Hopp, "Study on the effect of ambient gas on nanostructure formation on metal surfaces during femtosecond laser ablation for fabrication of low-reflective surfaces," *Applied Surface Science*, vol. 389, pp. 1113–1119, 2016.

[80] T. Csizmadia, T. Smausz, C. Tápai, J. Kopniczky, X. Wang, M. Ehrhardt, P. Lorenz, K. Zimmer, L. Orosz, E. Varga, A. Oszkó, and B. Hopp, "Comparison of the production of nanostructures on bulk metal samples by picosecond laser ablation at two wavelengths for the fabrication of low-reflective surfaces," *Journal of Laser Micro Nanoengineering*, vol. 10, no. 2, pp. 110–118, 2015.

[81] J. Long, P. Fan, M. Zhong, H. Zhang, Y. Xie, and C. Lin, "Superhydrophobic and colorful copper surfaces fabricated by picosecond laser induced periodic nanostructures," *Applied Surface Science*, vol. 311, pp. 461–467, 2014.

[82] E. Allahyari, J. JJ Nivas, S. L. Oscurato, M. Salvatore, G. Ausanio, A. Vecchione, R. Fittipaldi, P. Maddalena, R. Bruzzese, and S. Amoruso, "Laser surface texturing of copper and variation of the wetting response with the laser pulse fluence," *Applied Surface Science*, vol. 470, no. September 2018, pp. 817–824, 2019.

[83] R. Valizadeh, O. B. Malyshev, S. Wang, S. A. Zolotovskaya, W. Allan Gillespie, and A. Abdolvand, "Low secondary electron yield engineered surface for electron cloud mitigation," *Applied Physics Letters*, vol. 105, p. 231605, dec 2014.

[84] L. Spallino, "Material properties compliance with cryogenic vacuum for particle accelerators," *Journal of Vacuum Science & Technology B*, vol. 38, p. 032803, may 2020.

[85] R. Valizadeh, O. Malyshev, S. Wang, T. Sian, M. Cropper, and N. Sykes, "Reduction of secondary electron yield for E-cloud mitigation by laser ablation surface engineering," *Applied Surface Science*, vol. 404, pp. 370–379, may 2017.

[86] S. Calatroni, E. Garcia-Tabares Valdivieso, A. T. Perez Fontenla, M. Taborelli, H. Neupert, M. Himmerlich, P. Chiggiato, D. Bajek, S. Wackerow, and A. Abdolvand, "Optimization of the secondary electron yield of laser-structured copper surfaces at room and cryogenic temperature," *Physical Review Accelerators and Beams*, vol. 23, p. 033101, mar 2020.

[87] E. Garcia-Tabares Valdivieso, "Laser-Engineered Surface Structured (LESS) Copper," tech. rep., CERN, Geneva, 2016.

[88] L. Spallino, M. Angelucci, R. Larciprete, and R. Cimino, "On the compatibility of porous surfaces with cryogenic vacuum in future high-energy particle accelerators," *Applied Physics Letters*, vol. 114, p. 153103, apr 2019.

[89] O. Berrig, N. Biancacci, F. Caspers, A. Grudiev, E. Metral, B. Salvant, and G. V. Stupakov, "LESS," tech. rep., CERN, 2016.

[90] N. Biancacci, "HLLHC impedance update," tech. rep., CERN, 2015.

[91] S. S. Kurennoy and G. V. Stupakov, "A New Method for Calculation of Low Frequency Coupling Impedance," *Particle Accelerator*, vol. 45, pp. 95–110, 1994.

[92] A. Chao, "Wake fields and Impedances," in *Physics of collective beam instabilities in high-energy accelerators*, ch. 2, p. 371, 1993.

[93] S. Calatroni, M. Arzeo, S. Aull, M. Himmerlich, P. Costa Pinto, W. Vollenberg, B. Di Girolamo, P. Cruikshank, P. Chiggiato, D. Bajek, S. Wackerow, and A. Abdolvand, "Cryogenic surface resistance of copper: Investigation of the impact of surface treatments for secondary electron yield reduction," *Physical Review Accelerators and Beams*, vol. 22, p. 063101, jun 2019.

[94] R. Valizadeh, O. B. Malyshev, S. Wang, T. Sian, L. Gurran, P. Goudket, M. D. Cropper, and N. Sykes, "Low secondary electron yield of laser treated surfaces of copper, aluminium and stainless steel," *International Particle Accelerator Conference*, pp. 1089–1092, 2016.

[95] G. Gold and K. Helmreich, "A Physical Surface Roughness Model and Its Applications," *IEEE Transactions on Microwave Theory and Techniques*, vol. 65, pp. 3720–3732, oct 2017.

[96] J. Polinski, "Materials in cryogenics Content," in *European Course in Cryogenics*, 2010.

[97] N. J. Simon, E. S. Drexler, and R. P. Reed, *Properties of copper and copper alloys at cryogenic temperatures*. 1992.

[98] L. A. Neely, E. M. See, H. D. Robinson, and V. Kochergin, "Thermal expansion of Cu(II)O nano- and micro-particles and composites at cryogenic temperatures," *Physica Status Solidi (B) Basic Research*, vol. 249, no. 9, pp. 1698–1703, 2012.

[99] J.-f. Croteau, E. Cantergiani, N. Jacques, A. E. M. Malki, G. Mazars, and G. Avrillaud, "Mechanical characterization of OFE-Cu at low and high strain rates for SRF cavity fabrication by electro-hydraulic forming," in *Congres Francais de Mecanique*, (Brest), pp. 1–12, 2019.

[100] N. Liang, Y. Zhao, J. Wang, and Y. Zhu, "Effect of grain structure on Charpy impact behavior of copper," *Scientific Reports*, vol. 7, p. 44783, apr 2017.

[101] L. Collini, *Copper Alloys - Early Applications and Current Performance - Enhancing Processes*, vol. 15. InTech, mar 2012.

[102] H. Hirakata, O. Nishijima, N. Fukuhara, T. Kondo, A. Yonezu, and K. Minoshima, "Size effect on fracture toughness of freestanding copper nano-films," *Materials Science and Engineering A*, vol. 528, pp. 8120–8127, oct 2011.

[103] E. Preiss, *Fracture toughness of freestanding metallic thin films studied by bulge testing*. PhD thesis, Friedrich Alexander Universität Erlangen Nürnberg, 2018.

[104] G. Irwin, "Analysis of Stresses and Strains near the End of a Crack Traversing a Plate," *Journal of Applied Mechanics*, vol. 24, 1957.

[105] K. Ravichandran and A. Vasudevan, "Fracture Resistance of Structural Alloys," *ASM Handbook: Fatigue and Fracture*, vol. 19, pp. 381–392, 1996.

[106] G. T. Méndez, S. I. C. Colindres, J. C. Velázquez, D. A. Herrera, E. T. Santillán, and A. Q. Bracarense, "Fracture Toughness and Charpy CVN Data for A36 Steel with Wet Welding," *Soldagem & Inspeção*, vol. 22, pp. 258–268, sep 2017.

[107] M. Malabaila, "TE / VSC Cleaning procedure for copper parts," Tech. Rep. September, CERN ORGANISATION EUROPÉENNE POUR LA RECHERCHE NUCLÉAIRE, 2014.

[108] D. Bajek, S. Wackerow, D. A. Zanin, L. Baudin, K. Bogdanowicz, E. G.-T. Valdivieso, S. Calatroni, B. Di Girolamo, M. Sitko, M. Himmerlich, M. Taborelli, P. Chiggiato, and A. Abdolvand, "Role of surface microgeometries on electron escape probability and secondary electron yield of metal surfaces," *Scientific Reports*, vol. 10, p. 250, dec 2020.

[109] V. Petit, M. Taborelli, H. Neupert, P. Chiggiato, and M. Belhaj, "Role of the different chemical components in the conditioning process of air exposed copper surfaces," *Physical Review Accelerators and Beams*, vol. 22, no. 8, p. 83101, 2019.

[110] V. Petit, M. Taborelli, D. A. Zanin, H. Neupert, P. Chiggiato, and M. Belhaj, "Impact of deconditioning on the secondary electron yield of Cu surfaces in particle accelerators," *Physical Review Accelerators and Beams*, vol. 23, no. 9, p. 93101, 2020.

[111] D. W. Müller, T. Fox, P. G. Grützmacher, S. Suarez, and F. Mücklich, "Applying Ultrashort Pulsed Direct Laser Interference Patterning for Functional Surfaces," *Scientific Reports*, vol. 10, p. 3647, dec 2020.

[112] L. Zhigilei, "Dynamics of the plume formation and parameters of the ejected clusters in short-pulse laser ablation," *Applied Physics A: Materials Science & Processing*, vol. 76, pp. 339–350, mar 2003.

[113] H. Garbacz, E. Fortuna-Zalesna, J. Marczak, A. Koss, A. Zatorska, G. Z. Zukowska, T. Onyszczuk, and K. J. Kurzydlowski, "Effect of laser treatment on the surface of copper alloys," *Applied Surface Science*, vol. 257, no. 17, pp. 7369–7374, 2011.

[114] S. Hamad, G. K. Podagatlapalli, S. P. Tewari, and S. V. Rao, "Influence of picosecond multiple/single line ablation on copper nanoparticles fabricated for surface enhanced Raman spectroscopy and photonics applications," *Journal of Physics D: Applied Physics*, vol. 46, p. 485501, dec 2013.

[115] C. A. Schaumberg, M. Wollgarten, and K. Rademann, "Metallic Copper Colloids by Reductive Laser Ablation of Nonmetallic Copper Precursor Suspensions," *The Journal of Physical Chemistry A*, vol. 118, pp. 8329–8337, sep 2014.

[116] K. Kobayashi, "Laser processing," ch. 5, pp. 89–119.

[117] K. Sugioka and M. Meunier, *Laser Precision Microfabrication*, vol. 135 of *Springer Series in Materials Science*. Berlin, Heidelberg: Springer Berlin Heidelberg, 2010.

[118] M. V. Shugaev, C. Wu, O. Armbruster, A. Naghilou, N. Brouwer, D. S. Ivanov, T. J. Derrien, N. M. Bulgakova, W. Kautek, B. Rethfeld, and L. V. Zhigilei, "Fundamentals of ultrafast laser–material interaction," *MRS Bulletin*, vol. 41, pp. 960–968, dec 2016.

[119] F. A. Müller, C. Kunz, and S. Gräf, "Bio-inspired functional surfaces based on laser-induced periodic surface structures," *Materials*, vol. 9, no. 6, 2016.

[120] S. A. Jalil, B. Lai, M. ElKabbash, J. Zhang, E. M. Garcell, S. Singh, and C. Guo, "Spectral absorption control of femtosecond laser-treated metals and application in solar-thermal devices," *Light: Science & Applications*, vol. 9, p. 14, dec 2020.

[121] L. B. Boinovich, E. B. Modin, A. R. Sayfutdinova, K. A. Emelyanenko, A. L. Vasiliev, and A. M. Emelyanenko, "Combination of Functional Nanoengineering and Nanosecond Laser Texturing for Design of Superhydrophobic Aluminum Alloy with Exceptional Mechanical and Chemical Properties," *ACS Nano*, vol. 11, no. 10, pp. 10113–10123, 2017.

[122] S. Wang, Y. Ren, C. Cheng, J. Chen, and D. Tzou, "Micromachining of copper by femtosecond laser pulses," *Applied Surface Science*, vol. 265, pp. 302–308, jan 2013.

[123] M. Fabian, E. Lewis, T. Newe, and S. I. Lochmann, "Novel multimode fibre-cavity for ring-down experiments," in *2009 IEEE Sensors*, no. January 2014, pp. 848–851, IEEE, oct 2009.

[124] D. J. Förster, S. Faas, S. Gröninger, F. Bauer, A. Michalowski, R. Weber, and T. Graf, "Shielding effects and re-deposition of material during processing of metals with bursts of ultra-short laser pulses," *Applied Surface Science*, vol. 440, pp. 926–931, may 2018.

[125] S. Anisimov, B. Kapeliovich, and T. Perel'Man, "Electron emission from metal surfaces exposed to ultrashort laser pulses," *Soviet Journal of Experimental and Theoretical Physics*, vol. 39, pp. 776–781, 1974.

[126] S.-S. Wellershoff, J. Hohlfeld, J. Güdde, and E. Matthias, "The role of electron-phonon coupling in femtosecond laser damage of metals," *Applied Physics A: Materials Science & Processing*, vol. 69, pp. S99–S107, dec 1999.

[127] Valette, *Effets thermiques due a l'interaction Laser- Matiere dans les metaux en regime fentosecond*. PhD thesis, Université Jean Monnet - Saint-Etienne, 2003.

[128] B. H. Christensen, K. Vestentoft, and P. Balling, "Short-pulse ablation rates and the two-temperature model," *Applied Surface Science*, vol. 253, no. 15, pp. 6347–6352, 2007.

[129] Z. Lin, L. V. Zhigilei, and V. Celli, "Electron-phonon coupling and electron heat capacity of metals under conditions of strong electron-phonon nonequilibrium," *Physical Review B*, vol. 77, p. 075133, feb 2008.

[130] B. N. Chichkov, C. Momma, S. Nolte, F. Von Alvensleben, and A. Tünnermann, "Femtosecond, picosecond and nanosecond laser ablation of solids," *Applied Physics A: Materials Science and Processing*, 1996.

[131] K. Ishihara, "Thermodynamics and Kinetics of Metastable phase formation," ch. 2, pp. 5–21.

[132] S. Preuss, A. Demchuk, and M. Stuke, "Sub-picosecond UV laser ablation of metals," *Applied Physics A Materials Science & Processing*, vol. 61, pp. 33–37, jul 1995.

[133] E. Leveugle, D. Ivanov, and L. Zhigilei, "Photomechanical spallation of molecular and metal targets: molecular dynamics study," *Applied Physics A*, vol. 79, pp. 1643–1655, nov 2004.

[134] C. Wu and L. V. Zhigilei, "Microscopic mechanisms of laser spallation and ablation of metal targets from large-scale molecular dynamics simulations," *Applied Physics A*, vol. 114, pp. 11–32, jan 2014.

[135] K. Ahmmed, C. Grambow, and A.-M. Kietzig, "Fabrication of Micro/Nano Structures on Metals by Femtosecond Laser Micromachining," *Micromachines*, vol. 5, pp. 1219–1253, nov 2014.

[136] J. Vincenc Oboňa, V. Ocelík, J. C. Rao, J. Z. Skolski, G. R. Römer, A. J. Huis In 'T Veld, and J. T. M. Hosson, "Modification of Cu surface with picosecond laser pulses," *Applied Surface Science*, vol. 303, pp. 118–124, 2014.

[137] L. V. Zhigilei, P. B. Kodali, and B. J. Garrison, "A microscopic view of laser ablation," *Journal of Physical Chemistry B*, vol. 102, no. 16, pp. 2845–2853, 1998.

[138] G. Paltauf and P. E. Dyer, "Photomechanical processes and effects in ablation," *Chemical Reviews*, vol. 103, no. 2, pp. 487–518, 2003.

[139] A. E. Mayer and P. N. Mayer, "Continuum model of tensile fracture of metal melts and its application to a problem of high-current electron irradiation of metals," *Journal of Applied Physics*, vol. 118, p. 035903, jul 2015.

[140] Z. Chen and A. Bogaerts, "Laser ablation of Cu and plume expansion into 1atm ambient gas," *Journal of Applied Physics*, vol. 97, p. 063305, mar 2005.

[141] K. H. Leitz, B. Redlingshöer, Y. Reg, A. Otto, and M. Schmidt, "Metal ablation with short and ultrashort laser pulses," *Physics Procedia*, vol. 12, no. PART 2, pp. 230–238, 2011.

[142] F. Di Niso, C. Gaudiuso, T. Sibillano, F. P. Mezzapesa, A. Ancona, and P. M. Lugarà, "Role of heat accumulation on the incubation effect in multi-shot laser ablation of stainless steel at high repetition rates," *Optics Express*, vol. 22, p. 12200, may 2014.

[143] R. Le Harzic, D. Breitling, M. Weikert, S. Sommer, C. Föhl, S. Valette, C. Donnet, E. Audouard, and F. Dausinger, "Pulse width and energy influence on laser micromachining of metals in a range of 100fs to 5ps," *Applied Surface Science*, vol. 249, pp. 322–331, aug 2005.

[144] E. G. Gamaly, N. R. Madsen, M. Duering, A. V. Rode, V. Z. Kolev, and B. Luther-Davies, "Ablation of metals with picosecond laser pulses: Evidence of long-lived nonequilibrium conditions at the surface," *Physical Review B - Condensed Matter and Materials Physics*, vol. 71, no. 17, pp. 1–12, 2005.

[145] J. Byskov-Nielsen, J.-M. Savolainen, M. S. Christensen, and P. Balling, "Ultrashort pulse laser ablation of metals: threshold fluence, incubation coefficient and ablation rates," *Applied Physics A*, vol. 101, pp. 97–101, oct 2010.

[146] Y. Jee, M. F. Becker, and R. M. Walser, "Laser-induced damage on single-crystal metal surfaces," *Journal of the Optical Society of America B*, vol. 5, p. 648, mar 1988.

[147] G. Raciukaitis, M. Brikas, P. Gecys, and M. Gedvilas, "Accumulation effects in laser ablation of metals with high-repetition-rate lasers," *High-Power Laser Ablation VII*, vol. 7005, no. December 2013, p. 70052L, 2008.

[148] N. Seifert and G. Betz, "Computer simulations of laser-induced ejection of droplets," *Applied Surface Science*, vol. 133, no. 3, pp. 189–194, 1998.

[149] T. D. Bennett, C. P. Grigoropoulos, and D. J. Krajnovich, "Near-threshold laser sputtering of gold," *Journal of Applied Physics*, vol. 77, pp. 849–864, jan 1995.

[150] J. P. Colombier, F. Garrelie, N. Faure, S. Reynaud, M. Bounhalli, E. Audouard, R. Stoian, and F. Pigeon, "Effects of electron-phonon coupling and electron diffusion on ripples growth on ultrafast-laser-irradiated metals," *Journal of Applied Physics*, vol. 111, no. 2, p. 024902, 2012.

[151] L. V. Zhigilei, Z. Lin, D. S. Ivanov, E. Leveugle, W. H. Duff, D. Thomas, C. Sevilla, and S. J. Guy, "Atomic/Molecular-Level Simulations of Laser–Materials Interactions," in *Springer Series in Materials Science*, vol. 130, ch. 3, pp. 43–79, Berlin: Springer Series in Materials Science, 2010 ed., 2010.

[152] L. V. Zhigilei, E. Leveugle, B. J. Garrison, Y. G. Yingling, and M. I. Zeifman, "Computer simulations of laser ablation of molecular substrates," *Chemical Reviews*, vol. 103, no. 2, pp. 321–347, 2003.

[153] T. E. Itina, K. Gouriet, L. V. Zhigilei, S. Noël, J. Hermann, and M. Sentis, "Mechanisms of small clusters production by short and ultra-short laser ablation," *Applied Surface Science*, vol. 253, no. 19, pp. 7656–7661, 2007.

[154] T. E. Itina and Gouriet Karine, "Mechanisms of Nanoparticle Formation by Laser Ablation," in *Laser Pulse Phenomena and Applications*, ch. 15, pp. 310–322, 2010.

[155] E. Povarnitsyn, M, V. Fokin, A. Voloshko, Delfour L, and T. E. Itina, "Numerical Analysis of Ultrashort Laser Ablation: Application for Fabrication of Nanoparticles and Nanostructures," in *AIP Conference Proceedings*, no. May, p. 8, may 2014.

[156] S. Noël, J. Hermann, and T. Itina, "Investigation of nanoparticle generation during femtosecond laser ablation of metals," *Applied Surface Science*, vol. 253, pp. 6310–6315, may 2007.

[157] P. Stefanov, N. Minkovski, I. Balchev, I. Avramova, N. Sabotinov, and T. Marinova, "XPS studies of short pulse laser interaction with copper," *Applied Surface Science*, vol. 253, no. 3, pp. 1046–1050, 2006.

[158] S.-B. Wen, X. Mao, R. Greif, and R. E. Russo, "Experimental and theoretical studies of particle generation after laser ablation of copper with a background gas at atmospheric pressure," *Journal of Applied Physics*, vol. 101, p. 123105, jun 2007.

[159] S.-B. Wen, X. Mao, R. Greif, and R. E. Russo, "Expansion of the laser ablation vapor plume into a background gas. I. Analysis," *Journal of Applied Physics*, vol. 101, p. 023114, jan 2007.

[160] S.-B. Wen, X. Mao, R. Greif, and R. E. Russo, "Laser ablation induced vapor plume expansion into a background gas. II. Experimental analysis," *Journal of Applied Physics*, vol. 101, p. 023115, jan 2007.

[161] I. Horn, M. Guillong, and D. Günther, "Wavelength dependant ablation rates for metals and silicate glasses using homogenized laser beam profiles - Implications for LA-ICP-MS," *Applied Surface Science*, vol. 182, no. 1-2, pp. 91–102, 2001.

[162] P. K. Pandey and R. K. Thareja, "Surface nanostructuring of laser ablated copper in ambient gas atmosphere and a magnetic field," *Physics of Plasmas*, vol. 18, p. 033505, mar 2011.

[163] S. Maragkaki, T. J. Derrien, Y. Levy, N. M. Bulgakova, A. Ostendorf, and E. L. Gurevich, "Wavelength dependence of picosecond laser-induced periodic surface structures on copper," *Applied Surface Science*, vol. 417, pp. 88–92, 2017.

[164] M. Huang, F. Zhao, Y. Cheng, N. Xu, and Z. Xu, "Origin of laser-induced near-subwavelength ripples: Interference between surface plasmons and incident laser," *ACS Nano*, vol. 3, no. 12, pp. 4062–4070, 2009.

[165] E. J. Y. Ling, J. Saïd, N. Brodusch, R. Gauvin, P. Servio, and A. M. Kietzig, "Investigating and understanding the effects of multiple femtosecond laser scans on the surface topography of stainless steel 304 and titanium," *Applied Surface Science*, vol. 353, no. April, pp. 512–521, 2015.

[166] E. Peng, R. Bell, C. A. Zuhlke, M. Wang, D. R. Alexander, G. Gogos, and J. E. Shield, "Growth mechanisms of multiscale, mound-like surface structures on titanium by femtosecond laser processing," *Journal of Applied Physics*, vol. 122, p. 133108, oct 2017.

[167] B. K. Meyer, A. Polity, D. Reppin, M. Becker, P. Hering, P. J. Klar, T. Sander, C. Reindl, J. Benz, M. Eickhoff, C. Heiliger, M. Heinemann, J. Bläsing, A. Krost, S. Shokovets, C. Müller, and C. Ronning, "Binary copper oxide semiconductors: From materials towards devices," *Physica Status Solidi (B) Basic Research*, vol. 249, no. 8, pp. 1487–1509, 2012.

[168] F. A. Akgul, G. Akgul, N. Yildirim, H. E. Unalan, and R. Turan, "Influence of thermal annealing on microstructural, morphological, optical properties and surface electronic structure of copper oxide thin films," *Materials Chemistry and Physics*, vol. 147, pp. 987–995, oct 2014.

[169] M. Heinemann, B. Eifert, and C. Heiliger, "Band structure and phase stability of the copper oxides Cu2O, CuO, and Cu4O3," *Physical Review B - Condensed Matter and Materials Physics*, vol. 87, no. 11, pp. 3–7, 2013.

[170] J. Li, J. W. Mayer, and E. G. Colgan, "Oxidation and protection in copper and copper alloy thin films," *Journal of Applied Physics*, vol. 70, no. 5, pp. 2820–2827, 1991.

[171] S. K. Lee, H. C. Hsu, and W. H. Tuan, "Oxidation behavior of copper at a temperature below 300 c and the methodology for passivation," *Materials Research*, vol. 19, no. 1, pp. 51–56, 2016.

[172] V. Figueiredo, E. Elangovan, G. Gonçalves, P. Barquinha, L. Pereira, N. Franco, E. Alves, R. Martins, and E. Fortunato, "Effect of post-annealing on the properties of copper oxide thin films obtained from the oxidation of evaporated metallic copper," *Applied Surface Science*, vol. 254, pp. 3949–3954, apr 2008.

[173] S. He, S. Amoruso, D. Pang, C. Wang, and M. Hu, "Chromatic annuli formation and sample oxidation on copper thin films by femtosecond laser," *Journal of Chemical Physics*, vol. 144, no. 16, 2016.

[174] L. Baudin, M. Sitko, C. Garion, P. Chiggiato, F. Delloro, F. Gaslain, M. Sennour, M. Jeandin, D. Bajek, S. Wackerow, and A. Abdolvand, "Morphological and Chemical Characterization of Laser Treated Surface on Copper," *Key Engineering Materials*, vol. 813, pp. 254–260, jul 2019.

[175] D. Bruneel, G. Matras, R. Le Harzic, N. Huot, K. König, and E. Audouard, "Micromachining of metals with ultra-short Ti-Sapphire lasers: Prediction and optimization of the processing time," *Optics and Lasers in Engineering*, vol. 48, pp. 268–271, mar 2010.

[176] T. PRILL, K. SCHLADITZ, D. JEULIN, M. FAESSEL, and C. WIESER, "Morphological segmentation of FIB-SEM data of highly porous media," *Journal of Microscopy*, vol. 250, pp. 77–87, may 2013.

[177] C. R. Phipps, M. Boustie, J. M. Chevalier, S. Baton, E. Brambrink, L. Berthe, M. Schneider, L. Videau, S. A. Boyer, and S. Scharring, "Laser impulse coupling measurements at 400 fs and 80 ps using the LULI facility at 1057 nm wavelength," *Journal of Applied Physics*, vol. 122, no. 19, 2017.

[178] C. Bolis, L. Berthe, M. Boustie, M. Arrigoni, S. Barradas, and M. Jeandin, "Physical approach to adhesion testing using laser-driven shock waves," *Journal of Physics D: Applied Physics*, vol. 40, pp. 3155–3163, may 2007.

[179] M. Arrigoni, *Study of the influence of interfacial roughness, porsity and sample thickness on the propagation of laser induced shockwaves in coated samples. Application to LASAT process (LASer... Mitigation of the effects of explosions View project International Journ.* PhD thesis, Université de Poitiers, 2004.

[180] S. Barradas, *Etude , à l ' aide du choc laser , des mécanismes d ' adhérence aux interfaces cuivre / aluminium et cuivre / cuivre obtenues par projection thermique To cite this version : HAL Id : tel-00273506.* PhD thesis, Ecole des Mines de Paris, 2008.

[181] L. Berthe, R. Fabbro, P. Peyre, L. Tollier, and E. Bartnicki, "Shock waves from a water-confined laser-generated plasma," *Journal of Applied Physics*, vol. 82, pp. 2826–2832, sep 1997.

[182] A. Sollier, *Etude des plasmas générés par interaction laser-matière en régime confiné. Application au traitement des matériaux par choc laser.* PhD thesis, DOCTEUR DE L'UNIVERSITÉ DE VERSAILLES ST-QUENTIN, 2002.

[183] B. Wu and Y. C. Shin, "Laser pulse transmission through the water breakdown plasma in laser shock peening," *Applied Physics Letters*, vol. 88, p. 041116, jan 2006.

[184] C. Bolis, *Étude numérique et expérimentale de la séparation par chocs brefs d'interface de revêtements multi-couches . Application au chocs laser.* PhD thesis, Université de Poitiers, 2004.

[185] G. Fabre, *Influence des propriétés optiques et de l ' endommagement de barrières thermiques EB-PVD pour la mesure d ' adhérence par choc laser LASAT-2D.* PhD thesis, École nationale supérieure des mines de Paris, 2013.

[186] S. Bardy, B. Aubert, T. Bergara, L. Berthe, P. Combis, D. Hébert, E. Lescoute, Y. Rouchausse, and L. Videau, "Development of a numerical code for laser-induced shock waves applications," *Optics and Laser Technology*, vol. 124, no. November 2019, p. 105983, 2020.

[187] D. Loison, *Etude expérimentale et numérique du micro écaillage de cibles métalliques soumises à des chocs laser.* PhD thesis, Ecole Nationale Supérieure de Mécanique et d'Aérotechnique de Poitiers (ENSMA), 2012.

[188] P. Peyre, L. Berthe, R. Fabbro, and A. Sollier, "Experimental determination by PVDF and EMV techniques of shock amplitudes induced by 0.6-3 ns laser pulses in a confined regime with water," *Journal of Physics D: Applied Physics*, vol. 33, pp. 498–503, mar 2000.

[189] C. Le Bras, A. Rondepierre, R. Seddik, M. Scius-Bertrand, Y. Rouchausse, L. Videau, B. Fayolle, M. Gervais, L. Morin, S. Valadon, R. Ecault, D. Furfari, and L. Berthe, "Laser Shock Peening: Toward the Use of Pliable Solid Polymers for Confinement," *Metals*, vol. 9, p. 793, jul 2019.

[190] R. Ecault, *Etude expérimentale et numérique du comportement dynamique de composites aéronautiques sous choc laser . Optimisation du test d ' adhérence par ondes de choc sur les assemblages composites collées.* PhD thesis, ECOLE NATIONALE SUPERIEURE DE MECANIQUE ET D'AEROTECHNIQUE, 2013.

[191] G. Prudhomme, *Étude du nuage de particules éjectées sous choc : apports de la Vélocimétrie Hétérodyne.* PhD thesis, Ecole Nationale Supérieure d'Arts et Métiers, 2015.

[192] B. T. Neyer, "Velocity Interferometer System For Any Reflector (VISAR)," in *Photonics: High Bandwidth Analog Applications*, vol. 0648, p. 301, 1986.

[193] P. M. Celliers, G. W. Collins, L. B. Da Silva, D. M. Gold, and R. Cauble, "Accurate measurement of laser-driven shock trajectories with velocity interferometry," *Applied Physics Letters*, vol. 73, no. 10, pp. 1320–1322, 1998.

[194] D. A. Dalton, J. L. Brewer, A. C. Bernstein, W. Grigsby, D. Milathianaki, E. D. Jackson, R. G. Adams, P. Rambo, J. Schwarz, A. Edens, M. Geissel, I. Smith, E. M. Taleff, and T. Ditmire, "Laser-induced spallation of aluminum and Al alloys at strain rates above 2 106 s-1," *Journal of Applied Physics*, vol. 104, no. 1, pp. 1–9, 2008.

[195] M. Boustie, J. P. Cuq-Lelandais, C. Bolis, L. Berthe, S. Barradas, M. Arrigoni, T. De Resseguier, and M. Jeandin, "Study of damage phenomena induced by edge effects into materials under laser driven shocks," *Journal of Physics D: Applied Physics*, vol. 40, no. 22, pp. 7103–7108, 2007.

[196] T. De Rességuier, E. Lescoute, D. Loison, J. M. Chevalier, and F. Ducasse, "Effects of cryogenic temperature on dynamic fragmentation of laser shock-loaded metal foils," *Journal of Applied Physics*, vol. 110, no. 12, 2011.

[197] E. B. Zaretsky, "Impact response of nickel in the 150-1150 K temperature range," *Journal of Applied Physics*, vol. 105, no. 9, 2009.

[198] E. B. Zaretsky, "Shock response of iron between 143 and 1275 K," *Journal of Applied Physics*, vol. 106, p. 023510, jul 2009.

[199] J. Hermann, *Caractérisation du plasma créé lors de l'interaction laser-cible métallique. Rôle du plasma dans le transfert d'énergie entre le faisceau laser et le métal, Thèse de l'Université d'Orléans, 19 mai 1991.* PhD thesis, Orleans, 1991.

[200] M. Grazka and J. Janiszewski, "Identification of johnson-cook equation constants using finite element method," *Engineering Transactions*, vol. 60, no. 3, pp. 215–223, 2012.

[201] M. Burley, J. E. Campbell, J. Dean, and T. W. Clyne, "Johnson-Cook parameter evaluation from ballistic impact data via iterative FEM modelling," *International Journal of Impact Engineering*, vol. 112, no. September 2017, pp. 180–192, 2018.

[202] T. de Rességuier, D. Loison, A. Dragon, and E. Lescoute, "Laser Driven Compression to Investigate Shock-Induced Melting of Metals," *Metals*, vol. 4, no. 4, pp. 490–502, 2014.

[203] C. Chauvin, "Contribution à la mesure de température des matériaux sous choc modéré par pyrométrie optique," 2010.

[204] K. Artoos, O. Calvet, and O. Capatina, "Experimental modal analysis and acceleration measurements during surface transport of a LHC cryodipole Table of Contents List of figures," tech. rep., 2002.

[205] L. Bottura, "Magnet Quench 101," *CERN Yellow Report*, pp. 1–9, jan 2014.

[206] B. Todd, A. Apollonio, A. Niemi, L. Ponce, C. Roderick, and D. Walsh, "LHC AND INJECTOR AVAILABILITY : RUN 2," in *9th LHC Operations Evian Workshop*, 2018.

[207] C. Rathjen, "Mechanical behaviour of vacuum chambers and beam screens under quench conditions in dipole and quadrupole fields," in *European Particle Accelerator Conference*, (Paris), 2002.

[208] C. Rathjen, "A model to calculate LHC beam screen deformation in a dipole field during quench," tech. rep., CERN, Geneva, 2000.

[209] C. Rathjen, "Bending Moment, Stresses, and Deformations of Beam Screens in a Quadrupole Field During Quench," tech. rep., CERN, Geneva, 2002.

[210] K. Artoos, P. Cruikshank, and C. Rathjen, "First quench tests of a LHC racetrack type beam screen in a short dipole magnet model," tech. rep., CERN, Geneva, 1999.

[211] J. Martinez-Darve, K. Artoos, P. Cruikshank, N. Kos, and C. Rathjen, "Measurement of the mechanical behaviour of the LHC beam screen during a quench," in *Proceedings of the IEEE Particle Accelerator Conference*, vol. 3, (Chicago), pp. 2162–2164, 2001.

[212] C. Rathjen, F. Caspers, P. Pugnat, S. Russenschuck, and A. Siemko, "Currents in, forces on and deformations/displacements of the LHC beam screen expected during a magnet quench," in *Proceedings of the IEEE Particle Accelerator Conference*, vol. 1, (Chicago), pp. 192–194, IEEE, 2001.

[213] K. Artoos, J. Martinez-Darve, and C. Rathjen, "Beam screen quench test in a 15 metre long LHC dipole magnet," tech. rep., CERN, Geneva, 2001.

[214] M. Morrone, C. Garion, M. Aurisicchio, and P. Chiggiato, "A coupled multiphysics FEM model to investigate electromagnetic, thermal and mechanical effects in complex assemblies: The design of the High-Luminosity Large Hadron Collider beam screen," *Applied Mathematical Modelling*, vol. 57, pp. 280–301, may 2018.

[215] R. Schmidt, "Beam loss scenarios and strategies for machine protection at the LHC," vol. 184, no. December 2003, pp. 184–187, 2003.

[216] L. Musinski, T. Liu, B. Gilchrist, and A. Gallimore, "Electrostatic charging of micro- and nano-particles for use with highly energetic applications," *Journal of Electrostatics*, vol. 67, pp. 54–61, feb 2009.

[217] J. Fransaer, P. M. Vereecken, and G. Oskam, *Semiconductors, Metal Oxides, and Composites: Metallization and Electrodeposition of Thin Films and Nanostructures 3*. 2015.

[218] D. S. Murali, S. Kumar, R. J. Choudhary, A. D. Wadikar, M. K. Jain, and A. Subrahmanyam, "Synthesis of Cu 2 O from CuO thin films: Optical and electrical properties," *AIP Advances*, vol. 5, p. 047143, apr 2015.

[219] K. S. Wanjala, W. K. Njoroge, N. E. Makori, and J. M. Ngaruiya, "Optical and Electrical Characterization of CuO Thin Films as Absorber Material for Solar Cell Applications," *American Journal of Condensed Matter Physics*, vol. 6, no. 1, pp. 1–6, 2016.

[220] J. B. Rubin, L. D. Sivils, T. Division, L. Alamos, A. A. Busnaina, P. Organic, C. Group, and A. A. Busnaina, "Precision Cleaning of Semiconductor Surfaces Using Carbon Dioxide-Based Fluids," no. January, pp. 1–26, 1992.

[221] NGL Cleaning Technology, "NGL 17.40 P.SP," tech. rep., NGL Cleaning Technology, Nyon, 2003.

[222] V. Petit, *Conditioning of Surfaces in Particle Accelerators*. PhD thesis, Toulouse, ISAE, 2020.

RÉSUMÉ

La structuration laser des surfaces a été développée au CERN pour le traitement des parois internes de l'enceinte à vide où circulent les protons.
Le balayage de la surface par le faisceau laser creuse des sillons en ablatant le cuivre dont une partie est redéposée sur la surface sous la forme d'agrégats de particules.
Cette rugosité a deux échelles absorbe efficacement les électrons, mais l'impact sur les autres fonctionnalités de la machine doit être vérifié.
Pendant son opération, la surface est soumise à des forces électromagnétiques et des variations de température qui pourraient l'endommager. Deux méthodes d'extraction de particules, chocs laser et centrifugation, ont été déployées pour tester l'adhésion des particules en laboratoire.
Bien qu'il ait été constaté que la surface préserverait ses propriétés, le détachement de particules, suite aux sollicitations mécaniques ou au traitement in-situ, est une question ouverte qui devrait motiver le choix de paramètres de traitement alternatifs ou d'une stratégie de nettoyage.

MOTS CLÉS

taux d'émission d'électrons secondaires, structuration de surfaces par laser, caractérisation morphologique, adhésion de particules, LASAT, application aux accélérateurs de particules

ABSTRACT

Laser-assisted surface structuration was developed at CERN for the treatment of the inside wall of the vacuum system. Grooves were created by material ablation while the laser scanned the surface. A part of this material was redeposed as particle aggregates. This two-scale rugosity efficiently trap electrons. The effects on other surface functionalities had to be assessed.
During its operation, the surface is submitted to electro-mechanical forces and cooling cycles which might deteriorate its performances.
Two extraction techniques have been developed - laser-shocks and centrifugation - to assess particle adhesion.
Although the surface properties are not detrimentally degraded, massive particle detachment during operation or during the treatment itself is an issue that should motivate the choice of alternative treatment parameters or of a cleaning strategy.

KEYWORDS

secondary electron yield, laser surface structuration, morphology characterisation, particle adhesion, LASAT, particle accelerator application